High Resolution Methods for the Aerodynamic Design of Helicopter Rotors

by

Alan Brocklehurst

June 6, 2013

This Thesis is submitted in fulfillment of the requirements for the degree of Doctor of Philosophy

CFD Laboratory

School of Engineering
Faculty of Science and Engineering
University of Liverpool

Dedication

This thesis is dedicated to my wife and family
who I thank for their patience, support and understanding.

Declaration

I hereby declare that this thesis is a record of my own work and was undertaken on a part-time basis from 2003 to 2005 in the Department of Aerospace Engineering at the University of Glasgow, and from 2006 to 2013 in the School of Engineering, Faculty of Science and Engineering at the University of Liverpool. This thesis is original in content except where otherwise indicated.

Alan Brocklehurst

March 2013

Abstract

The research reported here was driven by a desire to obtain a prediction method for helicopter rotor performance that would have sufficient resolution to evaluate changes to the design of the blade tip. This thesis examines the effectiveness of Computational Fluid Dynamics (CFD) methods to solve this problem.

An accurate, high-fidelity prediction is essential to quantify the performance of a new rotor tip shape which hitherto could not be properly assessed by a traditional approach. The CFD method lends itself to the resolution of the compressible, viscous flow around the helicopter blade tip. Starting from the surface shape required to generate a grid, together with the flow conditions, the flowfield naturally evolves from the numerical solution of the Navier-Stokes equations, based on the principles of conservation of mass, momentum and energy. Thus both the flow physics and the geometry of the tip are fully modelled by this technique.

In order to demonstrate the process, the Helicopter Multi-block solver (HMB) is used to predict the performance of a series of example tail rotor configurations. The various tip shapes are evaluated and compared, initially using an Euler approach to economically cover a wide range of designs, before going on to apply the Navier-Stokes method. The concepts behind each of the tail rotor blade (TRB) tip designs are explained in the thesis. As further computational resources became available, the datum blade, and the down-selected Küchemann-like and anhedral-Küchemann tip blades were the subject of Navier-Stokes predictions. Early in this work, the numerical method was validated against published data, and was also compared to existing model tail rotor test data for blades having different twist. In the central part of this thesis, the computational results are further analysed to reveal the influence of blade design changes on the time-averaged induced flow, and to extract more familiar aerodynamic parameters such as the angle of attack from the 3D rotor computations.

Steady Navier-Stokes predictions were obtained over a range of pitch angles such that the induced power factor could be reliably determined and the trends on profile power could also be established for the selected tip shapes. The research reported in this thesis has established that this numerical approach provides a good prediction of rotor performance, adequately resolving the flow-field and tip aerodynamics.

Since the assessment of helicopter rotors may involve additional interactional effects, or a degree of unsteady flow due to operating at high pitch angles near the onset of stall, an unsteady case was also demonstrated for a tail rotor blade adjacent to a fin.

It is concluded that only by using a CFD approach can a sufficiently high-fidelity prediction be obtained for helicopter rotor aerodynamics to allow progressive enhancements of future helicopter blade designs.

Acknowledgements

The writer wishes to thank his employers, Westland Helicopters Ltd (now part of AgustaWestland), and in particular, Rob Harrison and Bob Hansford, for their help and support, and for giving permission to use data from the model rotor tests. More recently, Pierre Abdel-Nour, Antonio Saporiti, and Andrea D'Andrea have also given their support to this research, prior to my retirement on 6th April 2011. The assistance of Richard Markiewicz of DSTL is also gratefully acknowledged for helping to release data into the public domain for the Twisted Model Tail Rotor experiments which were carried out in the 1980's with MoD funding.

Special thanks are due to Professor George Barakos for his supervision, help and encouragement, and his valuable time which was so freely given throughout the course this research. His enthusiasm for this subject is infectious and has sustained me through this part-time PhD programme. I have benefited greatly from our many discussions.

Sincere thanks are also due to Professor Ken Badcock for his help and support throughout this period of study, and to Rene Steijl and Mark Woodgate for their patience and assistance. The opportunity to meet and discuss many aspects of rotor aerodynamics with other researchers in the CFD lab, both in the early days at Glasgow and subsequently at Liverpool, is also much appreciated.

Contents

Nomenclature

Latin

A	Area of rotor disk
AR	Aspect ratio
AoA	Angle of Attack
b	wing span
c	chord
C_c	Chordwise Force Coefficient
C_D	Drag Coefficient
C_d	Sectional Drag Coefficient
C_L	Lift Coefficient
C_l	Sectional Lift Coefficient
C_M, C_m	Moment Coefficient
C_n	Normal Force Coefficient
C_T	Rotor Thrust Coefficient, Non-dimensional ratio of thrust to rotor disk area, density and tip-speed squared, $\frac{T}{\frac{1}{2}\rho S(R\Omega)^2}$
C_T/s	Blade Loading Coefficient, Thrust Coefficient divided by Solidity
C_p	Pressure Coefficient
C_P	Power Coefficient
C_Q	Torque Coefficient, Non-dimensional ratio of torque to rotor disk area, density, tip-speed squared and length, $\frac{Q}{\frac{1}{2}\rho SR(R\Omega)^2}$
e	Internal energy of fluid element
E	Total Energy per unit volume
f	Rotation frequency
FoM	Figure of Merit, Ratio of power required to produce thrust, P to total power required, $P+P_p$ where P_p is the profile power to overcome aerodynamic drag of blades, $\frac{C_T^{3/2}}{2C_Q}$.
k	Turbulent kinetic energy in $k-\omega$ model
k	constant
k_B	Fin Blockage Ratio, k_B=(Fin Force)/(Tail Rotor Shaft Thrust
k_i	Induced power factor
M	Mach number
N_b	Number of blades
P	Power
p	Pressure
q	Heat flux
r	Radial station along blade
R	Length of blade, radius of rotor, Residual
Re	Reynolds number, =U.c/ν
S	Area
s	rotor solidity, ratio of nominal blade area to rotor-disc area, $\frac{N_b c}{\pi R}$.
T	Temperature
t	time
U	Velocity in a generic direction
u	Flow velocity in x-direction
V_{tip}	Tip speed
v	Flow velocity in y-direction
v_i	Induced velocity
w	Flow velocity in z-direction
X	A generic direction
x	x direction, or fractional distance along rotor blade, x=r/R
y	y direction
z	z direction

Greek

α	Angle of attack
β	Rotor Blade Flapping Angle (Coning angle, β_o)
γ	Lock number, or Shaft Tilt Angle
Δ	Anhedral Angle
μ	Advance Ratio, Ratio of forward velocity to blade tip velocity
ξ	Vorticity
ρ	Density
λ	Induced inflow ratio
ν	Kinematic Viscosity
τ	Viscous stress tensor
σ	Relative Density, also used for Rotor Solidity when used to divide USA CT (ie without the 1/2), CT/σ
θ	Local pitch angle, θ_o referenced to rotor centre
ψ	Azimuth angle
Ω	Angular Velocity
ω	Specific Dissipation (defines scale of turbulence), ν_T=k/ω)
∇	Gradient

Subscripts and Superscripts

avg	Average
$\overline{c}$	Average value of c
c	Cosine term
s	Sine term
o	Constant term
B	Blockage
F	Fin
MR	Main Rotor
p	Profile Drag or Power
T, TR	Tail Rotor
tip	Blade tip conditions
W, WT	Wind or wind tunnel
∞	Freestream conditions

Acronyms and Definitions

AHS	American Helicopter Society
AIAA	American Institute of Aeronautics and Astronautics
AW	AgustaWestland (part of the Finemecanica Group)
AW (Yeovil)	Formerly Westland Helicopters Ltd, Yeovil, Somerset.
BERP	British Experimental Rotor Programme
BET	Blade Element Theory - considering the span of the blade as separate strips.
Bézier curves	Usually defined by 4 control points, located at the end points and with 2 intermediate points to define the gradient at the ends.
B-splines	Basis-splines are a more general form of Bézier curves, allowing local knots to have more weight to control the curve.
BVI	Blade Vortex Interaction
CFD	Computational Fluid Dynamics
CFL	Courant-Friedrichs-Lewy condition
DARP	UK Defence Applied Research Programme
Disk loading	Thrust divided by rotor-disk area
ERF	European Rotorcraft Forum
FoM	Figure of Merit
GOAHEAD	European research programme for the Generation Of an Advanced Helicopter Experimental Aerodynamic Database for CFD Validation
HART	Higher harmonic control Aeroacoustics Rotor Test
HB	Harmonic Balance
HMB	Helicopter Multiblock Solver
LE	Leading Edge
MoD	Ministry of Defence
N-S	Navier-Stokes
NURBS	Non-Uniform Rational B-Splines
PIV	Particle Image Velocimetry
RAE	Royal Aircraft Establishment
REACT	Rotor Embedded Active Control Technology
SST	Shear Stress Transport
TE	Trailing Edge
TM	Time Marching
TRB	Tail Rotor Blade
US, USA	United States of America
Vorticity	A measure of the rotation of fluid elements in fluid flow. Given as $\xi = \nabla \times V = 2\omega$
WHL	Westland Helicopters Limited, Yeovil, Somerset.

List of Publications

Journal Papers

Brocklehurst, A. and Barakos, G.N.,
A Review of Helicopter Rotor Blade Tip Shapes,
Progress in Aerospace Sciences,
pages 1-36, September, 2012,
(http://dx.doi.org/10/1016/j.paerosci.2012.06.003)

Conference Papers

Brocklehurst, A., Steijl, R. and Barakos, G.,
CFD for Tail Rotor Design and Evaluation,
34th European Rotorcraft Forum, Liverpool,
September, 2008.

Brocklehurst, A., Steijl, R. and Barakos, G.,
Using CFD to Evaluate Tail Rotor Tip Shapes in Forward Flight,
The University of Glasgow Helicopter Study Weekend, The Burn, Edzell, Scotland,
March, 2008.

Brocklehurst, A., Steijl, R. and Barakos, G.,
Using CFD to Understand and Evaluate Tail Rotor Blade Design,
AHS Aeromechanics Specialist's Conference, San Francisco, CA.,
January, 2008.

Brocklehurst, A., Steijl, R. and Barakos, G.,
Developing Insights Using CFD - Tail Rotor CFD Analysis and Design,
33rd European Rotorcraft Forum, Kazan, Russia,
September, 2007.

Brocklehurst, A. and Barakos, G.,
Effect of Tip Shape and Twist on Rotor Performance,
The University of Glasgow Helicopter Study Weekend, The Burn, Edzell, Scotland,
March, 2007.

Brocklehurst, A. and Barakos, G.,
Performance Analysis of Rotor Tip Shapes in Hover Using Computational Fluid Dynamics,
The University of Glasgow Helicopter Study Weekend, The Burn, Edzell, Scotland, March,
2006.

Barakos, G., Steijl, R., Badcock, K. and Brocklehurst, A.,
Development of a CFD Capability for Full Helicopter Engineering Analysis,
31st European Rotorcraft Forum, Florence, Italy,
September, 2005.

Brocklehurst, A.,
Recent Application of CFD to Helicopter Rotors at WHL,
The University of Glasgow Helicopter Study Weekend, The Burn, Edzell, Scotland,
April, 2005.

Brocklehurst, A. and Barakos, G.,
Helicopter Tip Shapes,
The University of Glasgow Helicopter Study Weekend, The Burn, Edzell, Scotland,
March, 2004.

Brocklehurst, A., Beedy, J., Barakos, G., Badcock, K. and Richards, B.,
Experimental and CFD Investigation of Helicopter BERP Tip Aerodynamics,
Conference on Computational and Experimental Methods, University of Glasgow,
September, 2003.

Brocklehurst, A.,
Application of CFD to Aerofoils, Blades and Helicopters,
The University of Glasgow Helicopter Study Weekend, The Burn, Edzell, Scotland,
April, 2003.

Other Recent Journal Papers

Antoniadis, A.F., Drikakis, D., Zhong, B., Barakos, G., Steijl, R. Biava, M., Vigevano, L.,
Brocklehurst, A., Boelens, O., Dietz, M., Embacher, M. and Khier, W.,
Assessment of CFD Methods against Experimental Flow Measurements for Helicopter Flows,
Aerospace Science and Technology, Elsevier (doi:10.1016/j.ast.2011.09.003),
September, 2011.

Other Recent Conference Papers

Zhong, B., Drikakis, D., Antoniadis, A., Barakos, G.,
Biava, M., Brocklehurst, A., Boelens, O., Dietz, M.,
Embacher, M., Khier, W., Renaud, T., Steijl, R., and Vigevano, L.,
Assessment of CFD Methods against Experimental Flow Measurements for Helicopter Flows,
36th European Rotorcraft Forum, Paris,
September, 2010.

Robinson, K. and Brocklehurst, A.,
BERP-IV Aerodynamics, Performance and Flight Envelope,
34th European Rotorcraft Forum, Liverpool,
September, 2008.

Boelens, O.J., Barakos, G., Biava, M., Brocklehurst, A., Costes, M., D'Alascio, A., Dietz, M.,
Drikakis, D., Ekaterinaris, J., Humby, I., Khier, W., Knutzen, B, LeChuiton, F., Pahlke, K.,
Renaud, T., Schwarz, T., Steijl, R., Sudre, L., Vigevano, L. and Zong, B.,
The Blind-Test Activity of the GOAHEAD Project,
33rd European Rotorcraft Forum, Kazan, Russia,
September, 2007.

Holton, S.A., Cotton, A., Brocklehurst, A. and Thompson, A.,
The Agusta-Westland EH101 Helicopter in the SAR Role and The Effect of Rotor Downwash,
60th Annual Forum of the American Helicopter Society, Baltimore, MD.,
June, 2004.

List of Prior Publications

Brocklehurst, A.,
Unsteady 2D Pitching Aerofoil in Compressible Viscous Flow,
Fluent CFD User Group Meeting,
March, 2002.

Chan, W. and Brocklehurst, A.,
Performance Enhancement Evaluation of an Actuated Trailing Edge Flap,
The Aeronautical Journal, Vol 105, No 1049, pages 391-399,
July, 2001 (Joint recipients of RAeS Hafner Award).

Chan, W. and Brocklehurst, A.,
Performance Enhancement Evaluation of an Actuated Trailing Edge Flap,
26th European Rotorcraft Forum, The Hague, Netherlands,
September, 2000.

Richardson, G. and Brocklehurst, A.,
Use of Fluent as a Solver for the Ice Acretion Code, ICREMO-1,
Fluent CFD User Group Meeting,
March, 1999.

Brocklehurst, A. and Pike, A.C.,
Reduction of BVI Noise Using a Vane Tip,
AHS Aeromechanics Specialists Conference on Aerodynamics, Dynamics and Acoustics,
Fishermans Wharf, San Francisco, CA.,
January, 1994.

Brocklehurst, A. and Duque, E.P.N.,
Experimental and Numerical Study of the British Experimental Rotor Programme Blade,
AIAA Paper AIAA-90-3008 presented at the 8th Applied Aerodynamics Conference,
Portland, Oregon,
August, 1990.

Brocklehurst, A.,
Aerodynamic Control of Horizontal Axis Wind Turbines,
Annual Conference of the BWEA, Edinborough,
April, 1988.

Brocklehurst, A.,
A Significant Improvement to the Low Speed Yaw Control of the Sea King using Eleventh
European Rotorcraft Forum, City University, London,
September, 1985.

Brocklehurst, A. and Taylor, P.,
Helicopter Tail Configurations to Survive Tail Rotor Loss,
Vertica, Vol 4, pages 107-119, 1980.

List of Industrial Patents

Brocklehurst, A.,
Aerofoil (Tail Rotor Blade Shape),
AgustaWestland, US 5992793 and EP2508423,
October, 2010.

Brocklehurst, A. and Scandroglio, A.,
Helicopter Tail Rotor and Tail Rotor Blade,
Agusta, CN 200910149769 and CN 200910149770
November, 2009.

Perry, F.J., Brocklehurst, A. and Harrison, R.J.,
Propellers with BERP Tip,
US Patent No 5927948 and European Patent No 968838,
July, 1999.

Brocklehurst, A.,
Low Airspeed Measurement for Rotary-wing Aircraft,
US Patent No 5750891 and EP0763743,
May, 1998.

Perry, F.J., Brocklehurst, A. and Harrison, R.J.,
Rotor Blades with a Gurney Flap,
US Patent No 5492448,
February, 1996.

Perry, F.J., Brocklehurst, A. and Harrison, R.J.,
Splitting Tip Vortex on Swept Tip,
US Patent No 5992793, and GB Patent,
January, 1996.

Brocklehurst, A. and Perry, F.J.,
The Vane Tip,
US Patent No 5199851,
April, 1993.

Brocklehurst, A.,
BERP Notch Shape,
EP0482788,
April, 1992.

Brocklehurst, A., Perry, F.J., and Isaacs, N.C.G.,
Flow Control for BERP Notch,
US Patent 5205715 and EP0481661,
April, 1993.

Brocklehurst, A. and Perry, F.J.,
BERP Notch Flow Control Vanes,
US Patent,
July, 1990.

Brocklehurst, A. and Cook, C.V.,
Strake on Helicopter Tail Boom,
EP0099185,
January, 1984.

1 Introduction

1.1 Motivation and Objectives

The research reported in this thesis was driven by a desire to establish a more accurate means of assessing the performance of helicopter rotor blades, such that the performance of new tip geometries may be properly predicted.

An accurate assessment of rotor performance is key to improving the aerodynamic design of helicopter main and tail rotors. Traditional methods, based on classical theory together with empirical corrections and incorporating measured aerofoil data, fall short of embracing all aspects of the flow physics. A 2D strip theory approach may offer rapid estimates of performance, but such methods are incapable of resolving the detailed blade loading, especially near the tip. This is the very region that has the strongest impact on performance. Even if a 3D panel method is adopted to capture the geometry of the tip, this idealised Laplace-based approach does not take into account compressibility, except by use of correction factors, and viscous effects must also be treated separately from the main solution. A prescribed-wake or free-wake method must also be employed to infer the induced flow. These lower-order methods provide a relatively rapid, but approximate, estimate of rotor performance, often relying on empiricisms, wind tunnel data, or past-experience to provide a correlated, rather than predictive solution.

In contrast, the Computational Fluid Dynamics (CFD) method lends itself to the solution of this problem. Starting with the surface geometry for the generation of the grid, together with the flow conditions, it avoids any assumptions or approximations, and the wake structure naturally evolves. This grid-based numerical approach makes use of the fundamental laws of fluid motion, conserving mass, momentum and energy to obtain a truly predictive 3D solution for the entire compressible and viscous flow field around the rotor. A computational method for solving the Navier-Stokes equations is therefore ideally suited to evaluating rotor blade tip designs.

However, obtaining an iterative solution to the Navier-Stokes equations for the complex 3D flow field of the helicopter requires significant computational resources, which until recently limited its application, leaving industry with little alternative but to continue using the more rapid and well established lower-order methods, and therefore unable to find benefits from design changes.

At the time this PhD study commenced, CFD methods were being used in industry to address relatively simple problems. To maintain a reasonable turn-around time, CFD was used, for example, to obtain snap-shots of rotor flows mainly for the advancing blade, and there was a clear gap between efforts to develop designs aimed at the retreating blade through fixed-wing wind tunnel tests and available modeling techniques that could transfer these results directly to the rotor. While the application of CFD to the hovering rotor appeared feasible, even an Euler solution was initially difficult for industry, and assessment of performance in hover relied heavily on either prescribed-wake, lifting-line rotor-codes or model rotor tests. The more complex task of determining control loads for, say a main rotor, in forward flight relied on use of modified strip-theory methods with empirical corrections, backed up by flight test experience. Over the last few years, better computational resources have become more widely available and, together with the continued development of CFD codes, this opens up the possibility of applying computational techniques to rotor design problems.

In this thesis, several tail rotor tip designs are evaluated using the Helicopter Multi-Block (HMB) code in an effort to verify the approach and develop a better understanding of the influence of tip shapes on rotor performance. An accurate, quantitative evaluation is sought which must have sufficient resolution to distinguish various design features such as rounding the tip leading edge, adding anhedral, or otherwise refining the shape of the tip. However, the aim here is primarily to explore and establish the computational method, and not necessarily produce an ideal tip shape for a specific application. Some of the tip shapes put forward, may offer advantages over existing designs, and might be considered as a range of fundamental shapes.

The tail rotor was chosen as an example application for several reasons. Through his career, the writer has had much experience with tail rotors, and existing model tail rotor test data was made available for comparison

with the computations. The relatively compact geometry of the tail rotor blade enables a hovering rotor to be simulated for a modest grid size compared to a main rotor, and this was considered a major benefit during the early part of this work, enabling a number of different tip geometries to be explored. However, tail rotors must be designed to operate at high thrust levels in hover, and proximity to stall makes this a challenging problem for computational fluid dynamics, leading to the need to consider an unsteady approach in some instances where grossly separated flows might occur, or where configurational, or interactional need to be taken into account.

For the most part, the research focuses on obtaining steady CFD solutions to evaluate the performance of the example tail rotor blades, although the techniques put forward here may be applied equally well to any type of rotor blade.

1.2 Background

In order to enhance the performance of helicopter rotors, the helicopter designer needs to have at his disposal an accurate method for quantifying the flow-field of the blade and, in particular, needs to be able capture the distributions of pressure and skin-friction that result from the flow around the tip.

The problem is that the blade tip aerodynamics cannot be easily modelled in the required detail, since this is a 3D question that can not be readily simplified.

Firstly, there is the problem of closely representing the precise 3D geometry of the tip. Near the blade tip, the design may involve the full range of aerodynamic design parameters, such as twist, taper, camber, thickness, sweep and anhedral, and (in the light of modern composite construction and CAD) the tip geometry itself is likely to be defined by B-spline, or NURBS, surfaces to provide the desired shape.

Secondly, the flow about the tip is highly 3-dimensional, compressible and viscous. Most helicopter rotors operate with hover tip Mach numbers in the moderate subsonic range, typically 0.59-0.64, although the narrow chord blades constrain the tip Reynolds number to moderate values in the region of $6x10^6$. Inboard these values are correspondingly lower. In hover, vortices from the preceding blade remain close to the tip, and in forward flight strong variations of angle of attack and side-slip come into play in this highly 3D flow-field. On the advancing blade, the onset flow may approach, or occasionally exceed, the speed of sound, depending on the combination of tip speed, forward speed, and temperature, and the outer part of the blade tip may be subjected to the development of strong shocks. On the retreating blade, where the dynamic head is much lower and high lift is required, the tip Mach number may fall to about 0.3, or less, and Reynolds number at the tip may be only about $3x10^6$. At these Reynolds numbers the stall may involve a combination of aerodynamic mechanisms, such as trailing edge separation, sudden separation from the leading edge, or bursting of the laminar bubble, sometimes with compressibility also playing a role. For the smaller-chord tail rotor blade, perhaps operating with a slightly lower tip speed than the main rotor, the Reynolds numbers may be in the region of only $2x10^6$ in hover. Consequently, the blade tips are flying in a flow that is both compressible and highly viscous. These effects are even more significant if model rotors are used as a means of correlating, or confirming the performance of new rotor designs.

In the past, classical lifting-line based methods, as used in many rotor-codes[286],[157] have provided a good overall indication of rotor performance, and the trends due to variations in tipspeed, chord, aerofoils, twist and taper have been able to be broadly identified. However, these so-called lower-order methods tend to be inadequate at the tip, and much development flight testing is required to confirm the characteristics of a particular blade design. Whilst some further advantage may be gained from the use of a panel method to get a better estimate of the loading,[88] the need to couple-in viscous effects, perhaps by reference to 2D aerofoil data, and apply compressibility corrections (that cease to be valid when shocks are present), leaves many details inadequately modelled. Transonic small perturbation theory,[121] and also full potential methods[105] have been applied in an attempt to capture the compressible effects, but again, coupling viscous effects and capturing induced flows remains a limitation.

In recent times has it become possible to apply Computational Fluid Dynamics (CFD) techniques to address the helicopter rotor problem. The numerical method is based on the conservation of mass, momentum and energy, and therefore is capable of modeling the viscous, compressible flow field. This process is ideally suited to modelling the physics of the flow about the tip, and is a truly predictive process, not hampered by use of empirical factors or arbitrary (sometimes biased) engineering corrections (except perhaps for the finer details and correlations necessary for the chosen turbulence model). Also, the blade geometry may be accurately represented by the 3D mesh, thus avoiding any compromises or approximation.

The HMB solver has been used throughout this thesis as a mean of obtaining, initially Euler, but later Navier-Stokes simulations for the example tail rotor blades (TRB's) put forward. On a good grid, such as the structured multi-block grids used here, this solver has third order spacial accuracy and is second order in time. Thus it should furnish CFD solutions which are adequate for the present purpose and of a much higher resolution

than were possible from the more traditional rotor code techniques. CFD solvers have been written with even greater resolution, up to 5th or 7th order,[131] and as such would offer a further improvement in accuracy for specific cases, and there is clearly a trade-off with mesh size, quality and computational requirements. A range of turbulence models are available, and advanced LES and DES, methods have found application on rotors and fuselages.[178] For hover performance evaluations, a steady solution should be adequate and is highly desirable to keep the computational time to a minimum, but an unsteady approach may be used in forward flight, or when the flow is highly separated. However, it is anticipated that the desire for a 'high-resolution' method, as suggested by the title of this thesis, should be satisfied by the application of HMB to the helicopter rotor problem.

For the main rotor, the design of the blade is inevitably a compromise between hover and forward flight requirements. In hover the aim is towards high efficiency, and therefore (for a given radius and aircraft weight range) the designer must take steps to minimise both the induced and profile components of the power to maximise the Figure of Merit. The induced power may be minimised by the use of twist as illustrated in Figure 1, although there is a concern that too much twist may compromise vibration in cruising flight. Tapering the blades may have a beneficial effect on the induced power and will also reduce the profile power, but reducing the chord toward the tip may lead to a conflict with the retreating blade lift requirements in forward flight. Figure 2 is included here to illustrate the impact that tapering the blade has on the hover performance. A clean low-drag tip shape would also be helpful in minimising the profile power, and for a highly loaded rotor the introduction of features such as anhedral in the tip design may also have a beneficial effect on induced power. Some benefit may be obtained from using a thinner aerofoil near the tip, and recently some attention has also been given to the use of laminar flow aerofoils to further reduce the profile drag coefficient. Such aerofoils must also need to avoid premature stall, if retreating blade lift is not to be sacrificed. In forward flight, the retreating blade stall and advancing blade compressibility boundaries limit the flight envelope, and here again some form of design compromise may be required. On the retreating blade the designer must ensure sufficient lift capability from the blade area, tipspeed and aerofoil camber, and a well designed tip planform may also be helpful. On the advancing blade, a highly cambered section is unwelcome due to the high pitching moments that would be generated, and the need is for thinner, less cambered, low-drag aerofoils that can operate at the elevated Mach numbers. Sweep may also be used to alleviate compressibility effects, but care must be taken with blade torsion deflections and additional pitching moment variations that may arise if the tip does not also have some forward off-set, or forward sweep inboard. The detail design of the tip may therefore play an important role in delaying stall on the retreating side whilst minimising shock-induced drag and acoustic propagation on the advancing blade. Figure 3 illustrates a range of tip shapes that have been considered for main rotors, and it is clear that the many different shapes result from different compromises between the conflicting requirements of advancing blade, retreating blade, and hover. Perhaps this is inevitable when changes to the many design parameters are not easy to evaluate. The evolution of main rotor tip shapes is discussed further in the literature review in Section 1.4.

Compared to the main rotor, the tip shape of the tail rotor has received less attention, and there have been few tip shapes put forward specifically for the tail rotor. In some cases, the tip-caps have taken the form of a rounded aerofoil or volume-of-revolution tip, but this early, and quite elegant solution seems to have given way to square-cut tips which are simpler to produce, Figure 4. This is the case for many military applications, although some recent civil helicopters, such as the A109 and AW139 have parabolic tips which are cut-off square at the ends similar to those of the main rotor. With the ongoing development in composite construction, the need to enhance rotor performance, and at the same time reduce noise signatures, there is now an opportunity to move towards more sculptured tip shapes that should have better aerodynamic characteristics. Several example tail rotor tip shapes are put forward and evaluated in this thesis.

Simplistically, one might expect that a tip shape that worked well on the main rotor, might also find application on the tail rotor, and indeed, sometimes the style of the main rotor tip is carried over to the tail rotor. However, the design requirements for tail rotors is sufficiently distinct from those described above for the main rotor that design solutions do not usually carry over. While the main rotor encounters the stall boundary on the retreating blade in forward flight, the tail rotor main design requirement is to produce high useful thrust in low-speed manoeuvring flight, in and around the hover.

The tail rotor is designed to both compensate the torque of the main rotor and provide a yaw acceleration capability. The main design requirement occurs in hover, since it is here that the main rotor torque is generally

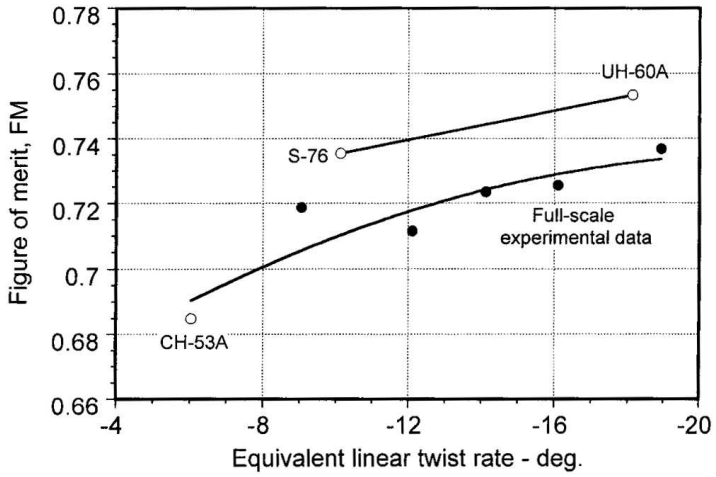

Figure 6.9 Measured effect of blade twist on hovering figure of merit. Data source: Paul & Zincone (1977).

Figure 1: Effect of Blade Twist on Figure of Merit from Leishman's Book[181]

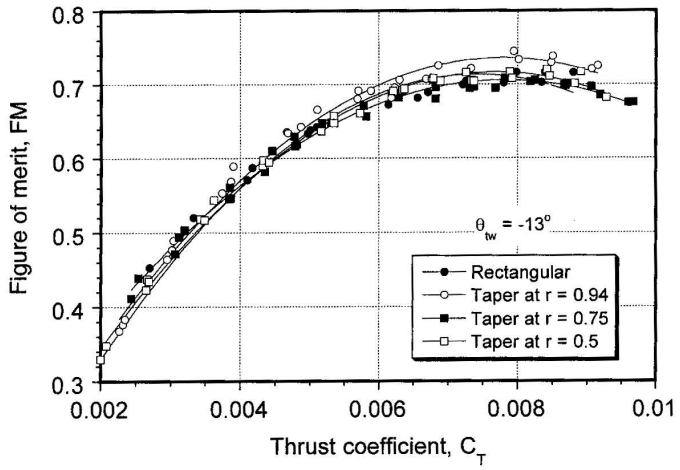

Figure 6.11 Measured effect of blade taper on the figure of merit of a hovering rotor. Data source: Althoff & Noonan (1990).

Figure 2: Effect of Blade Taper on Figure of Merit from Leishman's Book[181]

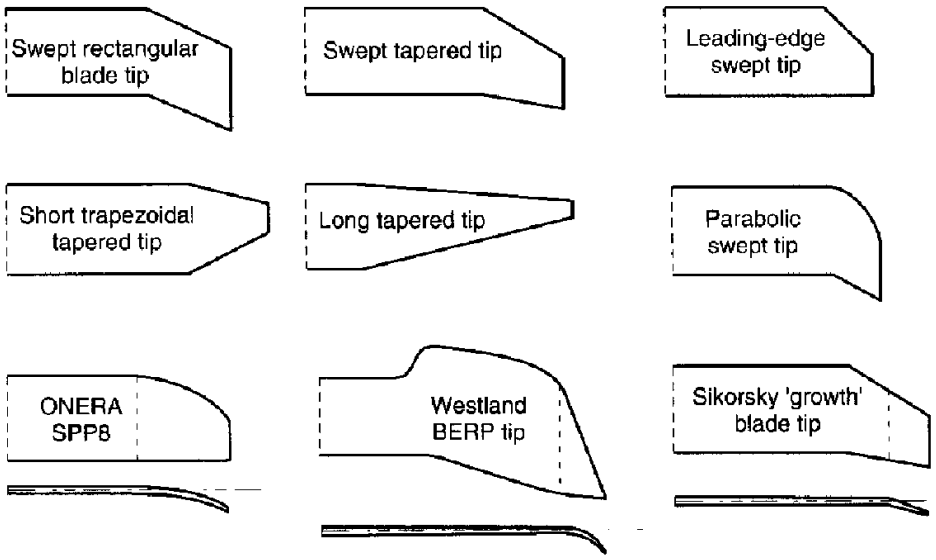

Figure 6.12 Some advanced main rotor blade tip designs. Note: Not to scale.

Figure 3: Examples of Main Rotor Tip Shapes from Leishman's Book[181]

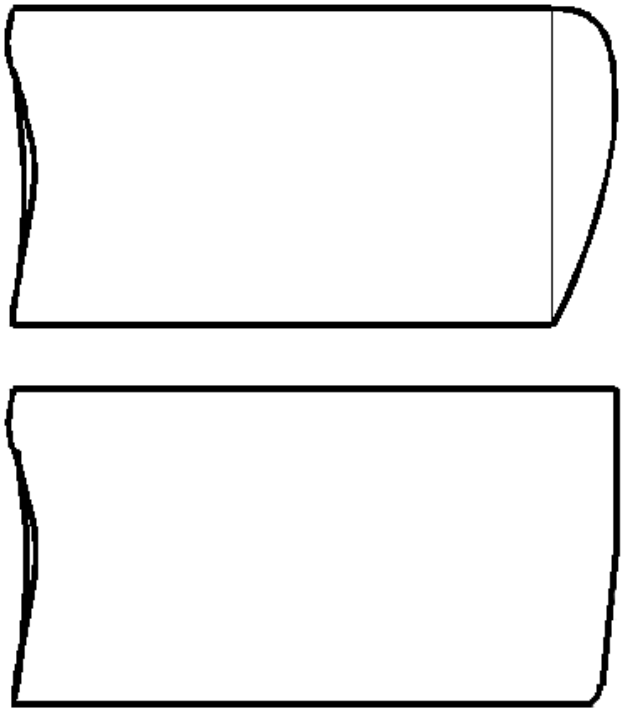

Figure 4: Old Style Tail Rotor Tip Shapes: Rectangular and Volume-of-Revolution Tip Caps.

a maximum. Adverse interactional aerodynamic effects of the main rotor wake over the fuselage and tail boom, or interactions between the tail rotor and the fin, may give rise to local maximum thrust requirements and may lead to the need for higher than expected pitch angles to provide adequate yaw control. Pitch, and power requirements in right sideways flight (for a helicopter with conventional clock-wise rotation viewed from above) can therefore be demanding. The need to handle the associated high power may lead to an undesirable increase in gearbox weight. While the single-main-rotor configuration has been preferred since the days of the Sikorsky R-4 due to its mechanical simplicity, any weight increase at the rear end of the aircraft will lead to a significant loss in overall payload, and must therefore be minimised. For lightweight helicopters the tail rotor is often small, but for heavier transport helicopters the tail rotor can become relatively large and may consume a significant amount of power (although this is still a relatively small fraction of the total power required). General weight growth during the life of the helicopter may lead to greater demands for tail rotor thrust, and is often accompanied by an increase in fuselage yaw inertia, adding to the demands on the tail rotor during manoeuvring. In some cases, this demand requires the addition of extra blades, or blades with increased chord. Increasing the radius could also provide additional thrust, but this change is often less desirable since it would require an increase in the tail cone length, and moving the tail rotor further aft would adversely affect the centre-of-gravity. Also, modern design requirements seek to reduce the significance of tail rotor noise, and thus the tail rotor may be constrained to operate at a slightly lower tipspeed than the main rotor. These engineering problems make the task of producing additional thrust quite a challenge. In the past, large benefits have been gained by use of specially designed cambered sections.[79] The addition of twist has been investigated by the writer and put forward as a mean of delaying the inevitable rise in profile power that occurs as the rotor approaches stall.

However, it would appear that one avenue that has not been generally researched in detail is the use of an improved tip shape that might be used in combination with twist and camber to augment the performance of the tail rotor. A good tip shape, should help to maintain the maximum thrust available, and would save power through suppression of premature separation in the tip region. By careful design, the tip could also help to minimise the induced power by maintaining as large an effective radius as possible. The application of anhedral may be especially useful in reducing the power on the highly loaded tail rotor.

Until now, it has not been possible to reliably evaluate the performance a new rotor tip design, since the tools available have not been able to model the aerodynamics of the tip region in sufficient detail. The prospect of a high-fidelity CFD method that can provide a predictive solution with the desired accuracy would enable this important rotor design issue to be effectively addressed.

The writer has been involved with tail rotor aerodynamics during much of his career in the helicopter industry. After the turn of the millennium, following work on the BERP-IV main rotor blade and tip design[250] for which intensive wind tunnel tests and 'snap-shot' CFD computations were carried out, a need arose to design a new tail rotor blade for an up-rated version of the Lynx. Prior to the start of this academic research, the writer designed a new tail rotor blade for what is now the AW159 Wild Cat, using a combination of twist, a variation of aerofoils (a new root section, and existing high-lift mid-Mach number aerofoil and a thinner, less cambered tip aerofoil), and employed a Küchemann-type tip closure. A little anhedral was added in the form of tip droop, but conservatism and the lack of a means of evaluating the effect in cruising flight prevented the use of a significant amount of anhedral. While this design of tip brought together several sound aerodynamic principles, there was no opportunity for any wind tunnel, or model rotor, tests and attempts to evaluate the benefits of the tip shape were hampered by the lack of a high resolution method. This type of tip shape was also later applied to the AW101 'advanced' tail rotor, replacing the original tip cap which had the forward leading edge corner shaped at 45 degrees. Early application of CFD to the original EH101 tail rotor tip design showed a tendency for weak shocks to form at the radiused corners, and in the final design the new curved-leading edge tip shape was preferred. Subsequent flight tests showed that the redesigned tail rotor consumed less power in low speed manoeuvres. At the time these tail rotor blades were designed, it was not possible to verify the finer details of performance prior to flight.

These recent examples of tail rotor tip design are mentioned here to provide background to the research presented in this thesis, where the focus is on the provision of a more accurate evaluation process, and the more basic properties of the tip design are of interest. All the tip shapes considered in this thesis are entirely separate from any industrial propriety, and are entirely those of the writer, designed solely to provide examples for the computations presented in this thesis.

For convenience, the series of tail rotor tip shapes put forward in this thesis were all defined to fit on the datum blade from the WHL (1980) model rotor tests. This carrier blade is an untwisted, rectangular blade with a simple NACA0012 aerofoil, and the rectangular tip was simply cut off square. The model tail rotor was initially used to test blades with 0, 8 and 16 degrees of linear twist, before moving on to tail rotor-fin blockage tests in the mid 80's. The results appeared to confirm that a blade that has too much twist might run the risk of a sudden loss in thrust due to the stall spreading rapidly along the blade, however, a notable reduction in induced power and a delay in power divergence even for moderate twist was observed. The model rotor data presented here has not been previously published, and despite some scatter in the data, it serves to provide a first-hand comparison with HMB computations for the model rotor.

During the period of this research, the author has been involved professionally in several research programs that have stimulated further development of the solver and, in this same period, computational resources have grown from a small, initially 10, now 48-processor (32-bit) cluster, to 96-twin (64-bit) Opterons (at AW), and about 500 processors at Liverpool. Through the UK Rotorcraft DARP and EU-GOAHEAD programs, which in turn led on to the UK REACT program, and other internal AW work, the solver capability and computer resources have grown from a capacity only able to run aerofoils, wings and Euler solutions, to one which is now capable of running unsteady Navier-Stokes forward flight cases in industry, and at Liverpool complete helicopter configurations have been completed[280].[281] In parallel with the research presented here, the HMB solver has been further developed to allow the use of sliding planes[278] and the code has recently been re-structured to allow implementation of faster solution methods. An harmonic balance method is now available which offers to greatly speed up design explorations for forward flight cases, by reducing the time consuming unsteady problem to a number of solutions.[324] Facilities for handling active aerodynamic devices on the blades have also been developed, and aeroelastic deformations can now also be taken into account.

This thesis aims to investigate the application of the HMB CFD code to the problem of resolving the impact of tip design changes on the performance of helicopter rotor blades. The method is illustrated through the evaluation of a series of example tail rotor tip designs, while the technique is equally applicable to any rotor application. The literature review in the following section further investigates the development of rotor blade tip design, together with the development and application of analysis methods leading to the gradual adoption of CFD for helicopter performance predictions. The literature review also considers development in fixed-wing tip design and any carry-over of ideas, before summarising the trends observed for helicopter tip design and evaluation.

1.3 Thesis Outline

As stated in section 1.1 of this thesis, the overall aim is to show that Computational Fluid Dynamics (CFD) methods can provide predictions of rotor performance with significantly greater resolution and accuracy than traditional rotor-code methods. At the start of this research it was not feasible to go directly to full Navier-Stokes solutions due to constraints on computational resources, and therefore an Euler approach was initially used. The idea was that a good tip shape would tend to reduce the power obtained from the blade pressure integrations mainly through a reduction in induced losses and, even without the viscous terms, insight would also be gained into the aerodynamics of each tip shape. The Euler studies were used to provide an initial screening of a variety of tail rotor tip designs in anticipation of further, more detailed analysis to be carried out on a few selected designs as additional computing resources became available. Navier-Stokes solutions were subsequently used to predict the impact of selected tip shapes on power divergence.

The techniques developed in this thesis are demonstrated for some example tail rotor blade (TRB) designs, but would apply equally well to performance evaluation of main rotors. The focus is on the aerodynamic design of the tip, since a well designed tip is key to enhancing rotor performance.

The first step in this investigation was to carry out a literature survey to determine trends in tip design and the state of the art of contemporary analysis techniques, as described in the following section of this first Chapter.

Chapter 2 briefly describes the numerical method and other tools employed in this research. As its name suggests, the Helicopter Multi-Block solver, HMB, provides an iterative solution to the Navier-Stokes equations on a structure multi-block grid. This strategy helps to maintain the desired spacial and temporal accuracy required for the type of problems encountered for helicopter rotors, and also minimises run-time by lending itself to parallel execution across a large number of processors. The multi-block approach is sufficiently flexible to provide good quality grids for the long-slender main blades without the need for approximation at the tip, even for the most complex geometries. The shorter blades of the tail rotor therefore offer some economy. The ICEM grid generator is used throughout as the main tool to generate 3D grids, using CAD (NURBS) surfaces imported from RHINOCEROS (RHINO) solid modelling (CAD) software, and is used here as an alternative to CATIA which might be considered as the industry standard. In a few instances, the GHMB grid generator (a deliverable of the UK Rotorcraft DARP from the University of Bristol) has also been used for some of the aerofoil validation work. Results from HMB are also compared to the MSES aerofoil code. Tecplot was used as a solution visualisation tool, together with an add-on to determine the Q and λ_2 vortex identification parameters. The author also created a Fortran based 'Rotor-Analyser' tool (see Appendix G) which has been used to obtain blade-loading distributions by integrating the computed surface pressures after taking slices in Tecplot (a version of this is now also available to HMB users as a Tecplot add-on). Several turbulence models have been explored in the course of this work, and the final Navier-Stokes cases settled on the use of the modified k-w model which was chosen because results in attached flow gave realistic profile drag values. However, other available turbulence models were also explored at high-pitch angles near stall. There may well be an ultimate need to obtain an unsteady Navier-Stokes solution for cases with severe separation, and this approach is certainly necessary where the rotor is adjacent to a stationary object, such as a fin.

Validation of the CFD process for helicopter rotors is provided for several test cases in Chapter 3 of this thesis. These range from 2D aerofoils, at appropriate Mach and Reynolds numbers, both in steady and unsteady flow to validation against published data for the UH-60A model rotor in hover. Grid sensitivity studies are also included for the case of the WHL model tail rotor and early sensitivity studies for 2D Euler cases are given in Appendix A. A 3D wing study is documented in Appendix B and a further model rotor validation case for the higher aspect ratio rotor of Tung is also included in Appendix C. General validation of the HMB solver for a wide range of test cases was also reviewed and presented by the writer in 2005.[22] The WHL model tail rotor is also simulated in this section of the thesis to provide a first-hand comparison between the computational predictions of HMB and the model rotor data, with the aim of confirming the effect of twist and comparing with measured vortex trajectories in hover.

In Chapter 4 a series of several different tip designs are put forward, using the rectangular, square-cut tip of the untwisted WHL model tail rotor blade as a datum. The design ideas behind each tip shape are presented and the resulting geometry is described and illustrated. It is important to point out that the aim of this research is to prove the computational method, and not necessarily to design a best tip-shape for any particular application. However, some of the tip shapes put forward clearly offer an advantage over the basic rectangular blade, and these benefits may be adopted in future practical tail-rotor blade designs by industry. Curves and surfaces for all the example tip shapes were generated using the RHINO solid-modeling (CAD) software, from which 3D rendered images and 2D drawings may also be obtained.

Since the computational requirements for multiple Navier-Stokes solutions were initially prohibitive, even taking advantage of periodicity in hover to minimise the grid size, a series of Euler solutions were obtained as a first-pass at determining the relative performance of the various tail rotor tip designs. The Euler investigations are presented in Chapter 5. The Euler option provides a somewhat idealised solution, taking into account compressibility, but omitting skin-friction and associated viscous effects on the pressure recovery. For low to moderate pitch cases, where the flow should be attached, the loading distributions should be fairly realistic and the induced flow-field, and hence the induced power, should be well predicted. A series of Euler results for each tail rotor tip design allows a good estimate of the induced power factor to be determined. A curve fitting process was adopted, and later refined, to ensure consistent results for the induced power factor from an economic number of points. A simple correction to the Euler results is put forward to allow for the missing profile-power to provide a more realistic Figure of Merit. Tip shapes which allow the tip vortex to form cleanly and roll-up as far outboard as possible should have a favourable effect on induced power, and the effect of anhedral is also expected to be beneficial for a highly loaded rotor. The possibility exists that these benefits may be cumulative, and could also complement the effect of twist. Results were also compared for each tail rotor tip shape at a fixed pitch angle of 10 degrees to provide a direct comparison of the potential performance. The most promising tip designs were then down-selected for more detailed evaluation. The next step, reported in the final section of Chapter 5, was to run a cursory check on the impact of the selected tip designs in forward flight, before moving on to a viscous analysis to more thoroughly evaluate performance of the selected tail rotor blades in hover. The fact that tail rotors have low radius/chord ratios tends to suppress compressibility effects compared to main rotors. Also, the modern trend towards wide-chord blades and high rpm could lead to relatively high moments due to dynamics in forward flight. Nevertheless, it was felt worthwhile to check that features such as sweep and anhedral would not introduce any undesirably large pitching moments. Taking advantage of the fact that most tail rotors in high-speed forward flight are (at least to some extent) off-loaded by the fin, an Euler solution was again used (for economy) to provide an early insight into pitching moments generated by the different tip shapes in cruising flight. The results also reveal the extent of shock development on the advancing blade, which may adversely affect the power required in this flight condition, or could impact the noise if shock de-localisation was to occur.

The results of the Navier-Stokes simulations for the selected blades are presented and compared in Chapter 6. Building on the experience gained from the Euler studies mentioned above, finer grids were prepared for the Navier-Stokes solutions of the down-selected tail rotor blade tip configurations. Again, the aim was to first determine the induced power factor from a series of solutions at relatively low pitch angles, and then to further compare the performance of the selected tip designs by extracting the profile power. As pitch is increased, the profile power gradually increases and then diverges more rapidly as stall is approached. This characteristic is also reflected in the shape of the Figure of Merit curve. The power consumed by the tail rotor depends on detailed design features such as twist, aerofoil section(s), and tip shape, the latter being the focus of this investigation. For the untwisted blades of the model tail rotor, it is likely that the stall will first occur in the tip region, thus leading to a dramatic rise in power. A good tip design should usefully delay the rise in power, but even so, this tendency for separating flow may lead to problems in economically settling to a steady state solution. In the tip region, trends in local loading coefficients provide an indication of the onset of stall and both leading edge and trailing edge pressures were used as stall monitors to more accurately determine the point of power divergence from the available Navier-Stokes solutions. Evaluating the performance of the selected tip shapes in this manner allows the benefits of using a Küchemann-type tips to be quantified.

In Chapter 7 some of the available CFD solutions are further analysed to discover the effect of different blade designs on various aerodynamic parameters which may be extracted by post-processing the CFD solution. Parameters familiar to the helicopter designer, such as the local lift coefficient, angle of attack and downwash are not readily available from the CFD results. The lift coefficient cannot be directly obtained because the

3D numerical solution is based in a global xyz-axes system, while the classical rotor model usually employs aerofoil data in local wind axes which requires a prior knowledge of the free stream direction. The angle of attack is also implicit in the solution, but for many rotor applications the direction of the upstream flow is not readily apparent, especially near the tips of the blades. However, away from the root and tip regions, the angle of attack may be approximated by subtracting the mean downwash angle from the local blade pitch angle. A method was devised to interpolate the computed results onto a cylindrical grid to ease the task of obtaining the time-averaged axial wake velocity for a range of radial stations, making it possible to show the influence of blade twist and anhedral on the downwash. The effect of blade design changes may also be observed in the wake trajectories. Alternatively, the angle of attack may be found from a knowledge of the chordwise position of the stagnation point. A unique relationship between the angle of attack and the stagnation point was discovered from use of 2D CFD for the NACA0012 aerofoil, at Mach numbers and Reynolds numbers appropriate to the model blades under consideration. The angle of attack may also be determined from a knowledge of the leading edge pressure, and the idea of matching the entire chordwise pressure distribution was also considered. This approach allows the angle of attack to be deduced where the flow is essentially 2-dimensional, and also reveals the differences that occur towards the tip due to the 3-dimensionality of the flow. The desire to extract the familiar parameters of downwash and angle-of-attack, raises the more philosophical question of whether it is sensible to attempt to break down the aerodynamics near the tip (and root) of the blade using supposedly simple 2D strip concepts. At the tip it may be preferable to extract surface pressure distributions normal to the leading edge, thus furnishing the rotor engineer with valuable insight into the performance of the tip. This part of the research highlights the implicit benefits of applying a 3D CFD solution to the tip design problem with all the geometry and physics well represented.

While the main theme of this thesis is to explore a method capable of resolving rotor performance such that detailed changes to the tip shape could be properly evaluated, the issues raised at high pitch lead to the need to consider an unsteady CFD solution for certain cases where stall may be present, or hub-blockage and turbulence may have an effect on the flowfield, and/or when the tail rotor is operating close to the fin. These aspects are considered in Chapter 8. For rotors at high pitch where a significant degree of separation occurs, a question arises over the continued use of a single-blade computational domain and the use of periodic boundaries. Also, it might be anticipated that establishing the wake and identifying an adequately repeatable solution may take some time. Nevertheless, use of an unsteady method also has the potential to simulate the response of the rotor in manoeuvre conditions. Aerodynamic interactions with the main rotor, fuselage and fin which occur in low-speed flight also raise the ultimate need to carry out unsteady simulations on a complete helicopter configuration. In Chapter 8, both an isolated rotor case and an example of a tail rotor and fin interaction in hover is computed to illustrate the future potential of the unsteady computational approach. The results are compared to available data from the WHL model tail rotor fin-blockage tests. In addition to predicting the mean fin force, the unsteady computations revealed the cyclically fluctuating loads as the blades pass over the fin, which are a source of aerodynamic excitation on the airframe that adds to vibration. The influence of the fin on the rotor is also apparent through changes in the vortex wake trajectories, although the flapping motion is prescribed rather than predicted in this demonstration case.

Finally, conclusions will be drawn with regard to the effectiveness of the CFD process for evaluation of rotor performance. CFD offers a unique capability to provide both steady and unsteady high-resolution predictions which are closely representative of the physics of the flow, and this is of prime importance for future improvements to helicopter rotor blade design. The process needs only the surface geometry and a set of boundary conditions to capture the aerodynamics of the helicopter rotor, as will be demonstrated for several different tail rotor blade tips in this thesis.

1.4 Literature Survey

This literature survey is divided into two sections, researched in parallel to provide a comprehensive knowledge of current trends in tip design. Firstly ideas are considered from fixed wing aircraft which may be usefully applied to the rotorcraft problem. In the second part of the survey tip shapes used on past and current helicopter blades are identified, and the reasons for their development are probed. The available methods for analysis of blade tip aerodynamics are also reviewed.

1.4.1 Review of Fixed-Wing Tip Shapes

Since there may be considerable carry-over in tip design thinking between fixed-wing and helicopter tip shape, fixed-wing aerodynamic developments are considered in this first section of the literature review. However, it is recognised that there are major differences in the flow environment in which the tip shapes must function, not least of which for the helicopter are centrifugal effects and vortex wake interactions, and indeed dynamic and manufacturing constraints may also differ. Nevertheless, there is commonality of purpose towards enhanced performance, and in certain cases, design ideas may be adapted from one application to another. In addition, modern CFD methods are being eagerly applied in both fields, and it may therefore be possible to learn new techniques, or gain additional insight from the fixed wing field, which could be applied to the helicopter problem.

As with helicopters, early aircraft were generally of wooden construction and commonly had rounded wing tips on an otherwise rectangular planform. The wing planform later became influenced by the lifting-line theory of Prandtl (1921),[242] which established that an elliptic planform produces a uniform downwash to give minimum induced drag. However, since this type of planform was not easy to manufacture when metal construction was adopted, much more basic planforms rapidly became the norm. Pope (1951)[241] and Glauert (1959),[119] amongst others, present factors to account for the effect of wing taper and/or twist on the induced drag and lift-curve slope. In the US, the inverse of the induced drag factor is known as the Oswald efficiency factor, as given in McCormick (1979).[207] The concept of breaking down the drag of an aircraft (or helicopter) into induced (vortex) drag due to lift, and profile (viscous and wave) drag, is fundamental to aircraft performance analysis.

While lifting-line theory is fundamental to wing design, and is often used to estimate the spanwise loading, it represents an idealisation of the flow over a real wing. Most notably lifting-line theory is not able to represent the chordwise loading which is known to vary markedly near the root and tip. More advanced (swept) planforms therefore demand the use of more sophisticated methods, such as lifting surface theory or panel methods, or Transonic Small Perturbation (TSP) methods if the flow speed is near sonic.

As numerical methods and computational resources evolved, 3D panel methods were developed to account for planform and tip shape effects, and this approach is now often used to model a complete aircraft. Despite their inviscid nature, most panel methods now also take into account viscous effects through the use of coupled integral methods for the boundary layer. Strong coupling is relatively common in 2D aerofoil codes, such as Xfoil and MSES, Drela and Giles (1987).[99] Most 3D panel codes, such as VSAERO, employ only weak coupling where the boundary layer development is computed along streamlines, Nathman (2003),[220] and responds to the predicted inviscid flowfield (although further developments are underway to improve the coupling). These methods work well provided the flow is attached, or separation points can be estimated with confidence. However, when modelling the flow around complex bodies and wing tips, it may be necessary to judiciously position the shedding location of the trailed vortices to represent edge separations. Panel methods usually solve the Laplace equation for incompressible flow, given boundary conditions on the surface of the body, but may also take compressibility into account by using Prandtl-Glauert or Karman-Tsien compressibility corrections, provided the flow remains well below sonic so that shocks are not present.

Where high sub-sonic Mach number flows are of interest (for high speed sub-sonic aircraft and helicopter rotors) TSP Methods, Full-Potential, or Euler methods may be used, or when viscous effects are also important, Navier-Stokes CFD methods are required to simulate details of the flow. While CFD methods are good at capturing the local flow field, and conserve mass, momentum and energy, it is also important ensure that the wake well represented if the induced drag is to be computed correctly.

In practice, the viscous nature of the flow often makes it difficult, if not impossible, to distinguish between induced (drag-due-to-lift) effects and profile drag due to viscous separations. For wing tip design an accurate model of the flow which contains all the physics is required.

In his book, Fluid Dynamics of Drag, Hoerner (1965),[140] presents a series of wing tip shapes which had been previously tested in Germany and documented in the USA by Hoerner (1949),[139] Figure 5. The tests were carried out a in a low speed wind tunnel on model-scale wings of relatively low aspect ratio fitted with different tip caps. Hoerner summarises their induced drag performance by determining an effective aspect ratio for each tip, and in his report also compares their total drag polars and lift characteristics. Hoerner also considered the effect of cross-section shape on various styles of tip, Figure 6. Hoerners preference was to blend the lower surface up to meet the upper surface to achieve an overall beneficial effect, as on Tip No. 5, and the suggested roll-up mechanism is sketched in Figure 7. Modern computational methods now have the potential to offer a deeper insight into the tip design problem, and it should be possible to reproduce the Hoerner results for a wing by a numerical approach, provided that adequate details of the flow can be captured.

So-called Hoerner tips are featured on many light aircraft, and there seems to have been some disagreement as to what comprised a Hoerner tip. Some early Cessnas have tips that curl slightly downwards, while Beech tend to employ a slightly curved up, or slanted up tip shapes, and Mooney use a simple square-cut tip. However, replacement tip caps are now available for range of light aircraft that appear to closely resemble the tip shape preferred by Hoerner, Sakrison (2012)[253].[254]

Hall (1990)[125] also clarifies the use of the Hoerner tip on sailplanes and compares several other shapes. The tip shape illustrated at lower-left of Figure 8 appears to be a logical development to encourage the tip vortex to roll-up as far outboard as possible, and the tip edge now curves back to form a right-angle trailing edge corner, while retaining the cross-section of Tip No. 5, as shown in Figure 8.

The choice of tip shape may also be influenced by aesthetic, or even marketing considerations. Nevertheless, the manufacturers are keen to enhance the performance of their aircraft, and the main aim is influence the roll-up, and position the tip vortex as far outboard as possible. The tip shapes used in practice may vary from those sketched by Hoerner, to much more extreme examples.

Some composite tip caps, known as 'Booster Tips' were fitted to the otherwise rectangular wing a Cherokee light aircraft, and were demonstrated to enhance performance during flight tests. These tips were strongly curled down, Ferguson (1980),[112] Figure 9. Gains in the take-off distance, rate of climb (+200 ft/min) and maximum speed (+10 mph) were reported, together with a stalling speed reduction of 5 mph. Similar tips are also used on the Fox light aircraft, Figure 10, and have also been seen on a Husky crop-sprayer aircraft where the aim may also have been to increase maximum lift, or avoid tip stall. The opposite, though less extreme, configuration is seen on the curled-up tips of the Eurostar, Figure 11, and has also been used in a milder form on sailplanes.

Wind tunnel tests on different tip shapes are reported by van Aken (1985) ,[301] who found relatively small changes in the overall wing loads for different tip planform configurations, Figure 12. Van Aken reports that the lowest drag was found drag with the tapered tip, and that the tapered-drooped (anhedral) tip caused high drag without increasing the tip-lift, perhaps as a consequence of the high taper and sweep. This is opposite to the effect anticipated from applying anhedral to the tip of a helicopter rotor blade. As can be seen from the Figure, van Aken's tip shapes have no sophisticated tip cap shaping like that of the Hoerner tips discussed above.

For an aircraft, not only must the tip have good low drag qualities, and avoid a sudden stall, but it must complement the basic design of the wing. An economic means of approximating an ideal elliptic loading is to employ double, or triple, tapered wing (although care must be taken not to reduce the Reynolds number too much in the outer tip region of small wing tips). This style of wing planform and tip, which features a straight trailing edge and slightly swept leading edge, with increased sweep and taper at the tip, is employed on several aircraft, such as the Dornier 228, Zimmer (1987) ,[330] Figure 13. Zimmer discusses the influence of the wing tip design and aerodynamic optimisation, and explores many configurations, including planar and non-planar tips. Burkett (1989),[67] also investigated the induced drag of several non-planar wing configurations and points out that the vertical displacement of the tip relative to the root which occurs on an aft-swept-tip may have a beneficial effect, Figure 14. In particular, Burkett analysed the crescent shaped wing, and like van Dam (see later) found a reduction of up to 4% in the theoretical induced drag. The use of sweep in the region of the tip leading edge will reduce the propensity for the isobars to cluster near the leading edge, and so avoid premature

WING SHAPE	A	$\frac{d\alpha^\circ}{dC_L}$	$\frac{dC_D}{dC_L^2}$	ΔA_i	R_c
1	3.0	18.6	0.123	+.04	$1\ 10^6$
2	3.0	19.6	.133	−.18	LFA
5	3.0	18.6	.124	≈ 0	2412
4	3.0	19.2	.131	−.19	REF.
3	3.0	19.6	.131	−.20	(7,b)
I	5.0	14.4	0.067	≈ 0	$5\ 10^5$
II	6.4	13.8	.051	−.03	AVA
III	5.2	14.5	.063	−.04	GÖ
IV	5.2	14.2	.060	+.03	REF.
V	6.4	13.4	.050	≈ 0	(9,a)
a	5.0	14.5	0.071	≈ 0	$2\ 10^6$
b	5.1	14.5	.073	−.20	REF.
c	5.0	14.5	.071	≈ 0	(9,b)

Figure 5: Aerodynamic Performance of 3 Families of Wings as a Function of Plan-form and Wing Tip Shape, Hoerner (1965)[140]

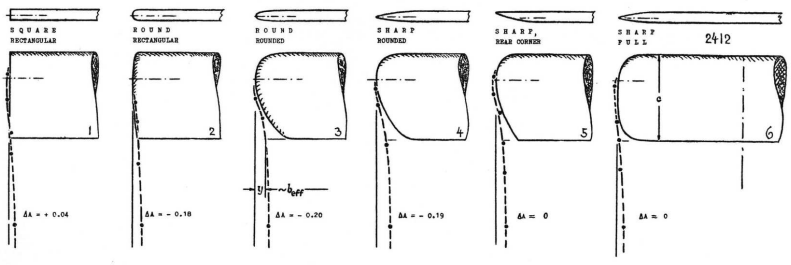

Figure 6: Wing Tip Shape and Wing Tip Vortex Location of a Family of Wings Tested at AR=3 and Re=1x10^6, Hoerner (1965).[140] Hoerner expressed a preference for Tip No. 5 because of the good overall lift-drag characteristics, but note that the rectangular tip has the highest effective aspect ratio

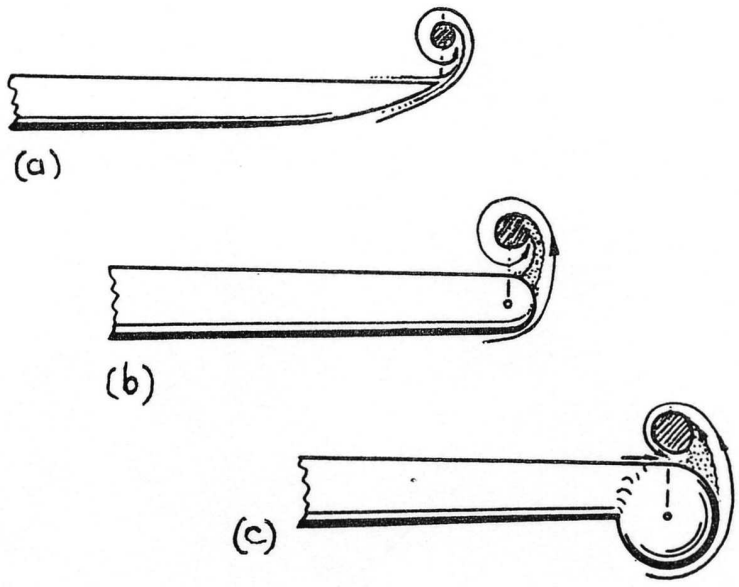

Figure 7: Location of the Vortex Core in Relation to the Wing Tip, (a) with Sharp Lateral Edge (as preferred by Hoerner), (b) on Wing with Round Edge, (c) Flow Around Tip Tank, Hoerner (1965)[140]

separation just inboard of the tip. However, the slanted outer tip edge and rapid taper could give rise to a large edge separation due to viscous effects, and possibly increase the vortex drag.

For the fixed wing case, the use of a tapered, or double tapered planform brings the loading towards elliptic, and therefore closer to the ideal of a constant downwash. For a rotor blade the situation is rather different, as most of the lift is generated outboard, although it may be advantageous to taper the blade towards to tip if the goal is to achieve a high figure of merit in hover. However, in either case, excessive taper may lead to increased loading in the tip region, and a tendency for the tip to stall early. This is a particular concern at high sub-sonic Mach number conditions where isobars may bunch-up in the forward leading edge corner and lead to premature shock-induced separation.

The design of swept wings is covered by Küchemann (1978),[169] who prescribed a parabolic tip cap which has become know as the Küchemann tip and is currently used on many jet-transport aircraft, Figure 15. In contrast to the so-called Parabolic Tip used on some European helicopters which are cut-off at the tip, the Küchemann tip has a smooth sweeping leading curve which extends to the (usually swept back) trailing edge. This type of tip shape has properties that would also be advantageous on the advancing blade of a helicopter rotor, in that it maintains the sweep and this helps to keep the drag low. These features may also have acceptable high-incidence characteristics for the retreating blade, and should have low drag in hover. However, it is understood that transport aircraft make use of flaps when landing and hence generate significant aerodynamic washout at the tips, which avoids the low speed stalling problem. In cruise, it is essential that the tip vortex forms cleanly to minimise energy loss and hence low drag, and the Küchemann tip would seem to offer an ideal shape in this respect.

The Küchemann tip has been applied on many civil aircraft and greatly enhanced the performance of high-speed, highly loaded military aircraft, such as the BAe Hawk and Harrier.

The need to relieve the isobars bunching up in the forward leading edge corner was recognised during the design of the tail rotor for the EH101 helicopter, and a tip cap with a 45deg blended chamfer at the leading edge corner was employed (see later).

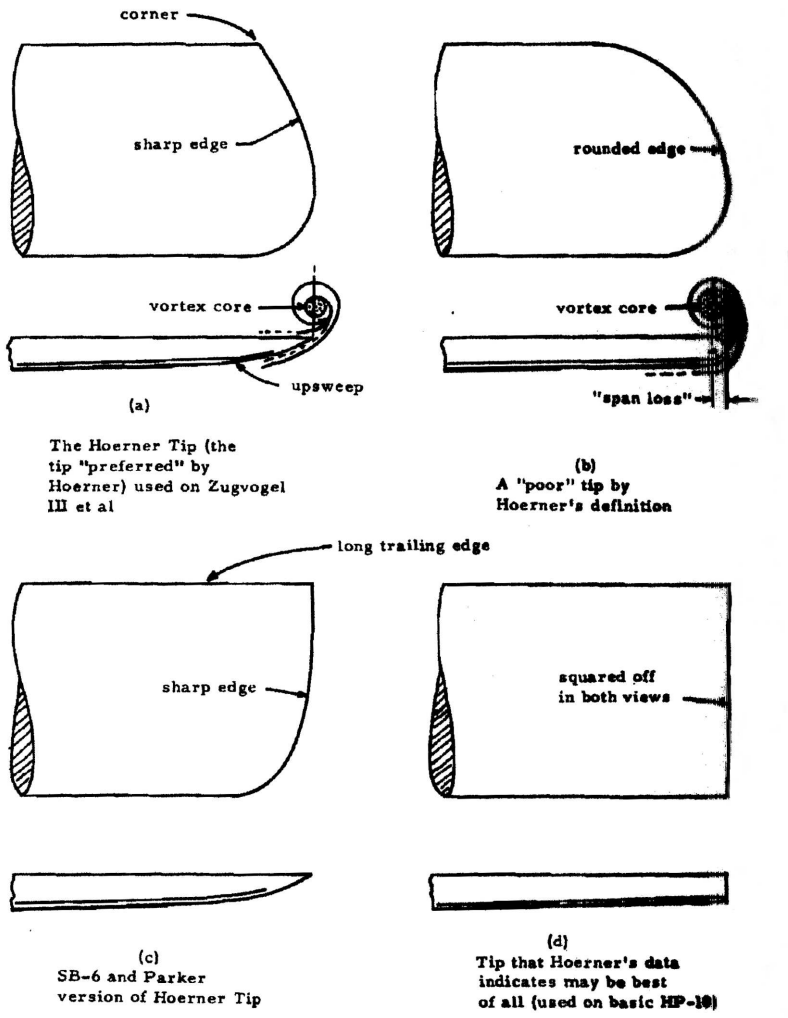

Figure 8: Various Applications of Hoerner Tip to Sailplanes, Hall (1990).[125] The Upper-Left Tip is the One Preferred by Hoerner, and at Lower-Left is a Further Development for a Modern Sailplane

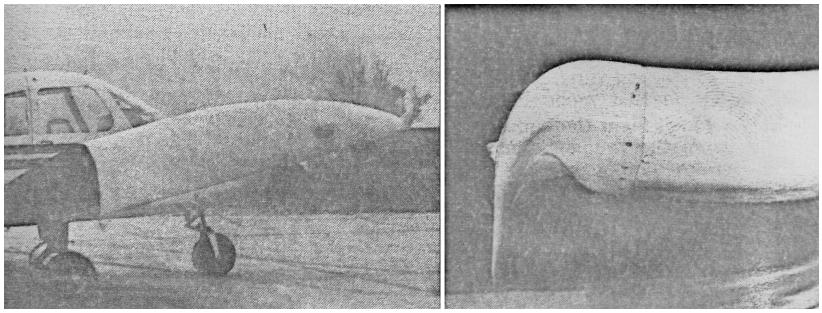

Figure 9: Side and Front View of the Booster Tip, Ferguson (1980)[112]

Figure 10: The Tip Shape used on the 'Fox' Light Aircaft, photographed at Kemble, 2003

Figure 11: The Upwards Curved Tip of the Eurostar Light Aircraft, photographed at Kemble, 2003

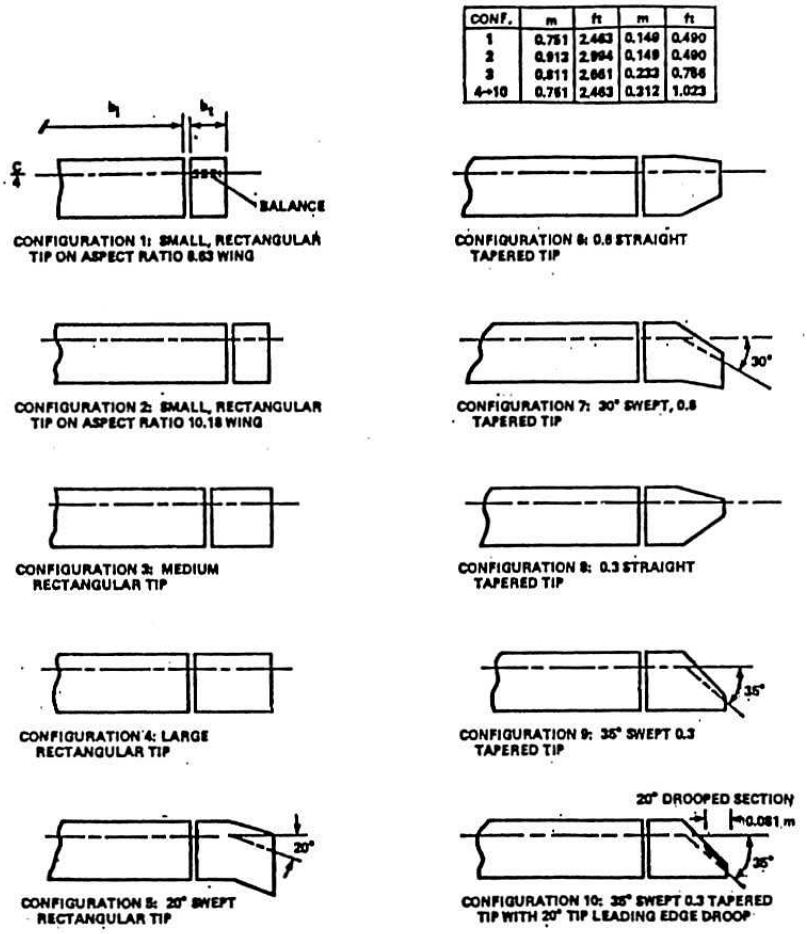

Figure 12: Wing Tip Configurations of van Aken (1985)[301]

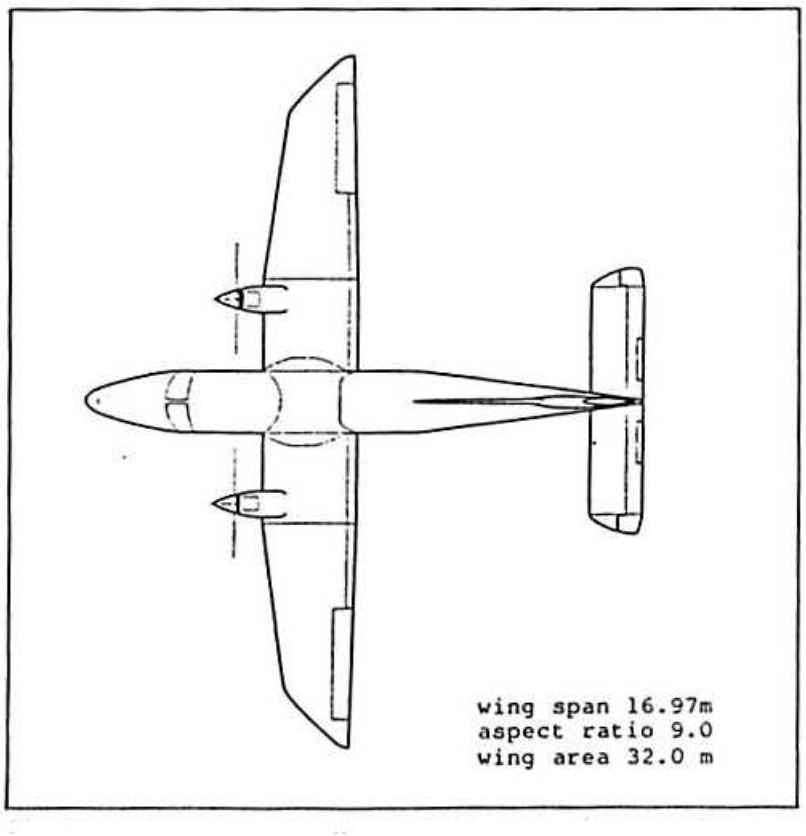

Figure 13: Dornier 228 Commuter Aircraft with Aft-Swept Triangular Tips, from Zimmer (1989) [330]

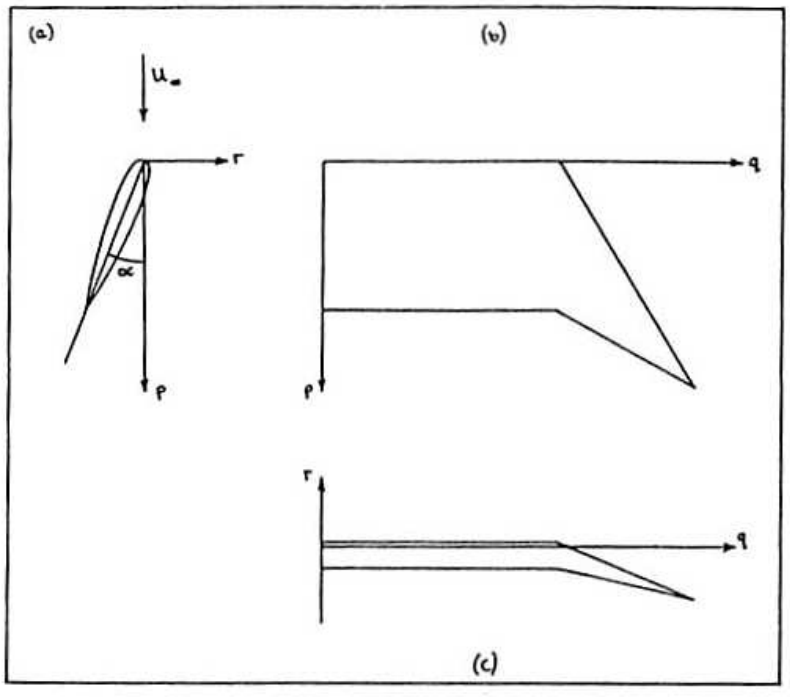

Figure 14: Wing with Aft-Swept Tip at Angle of Attack Showing Vertical Displacement of the Tip Relative to the Root, Burkett (1989)[67]

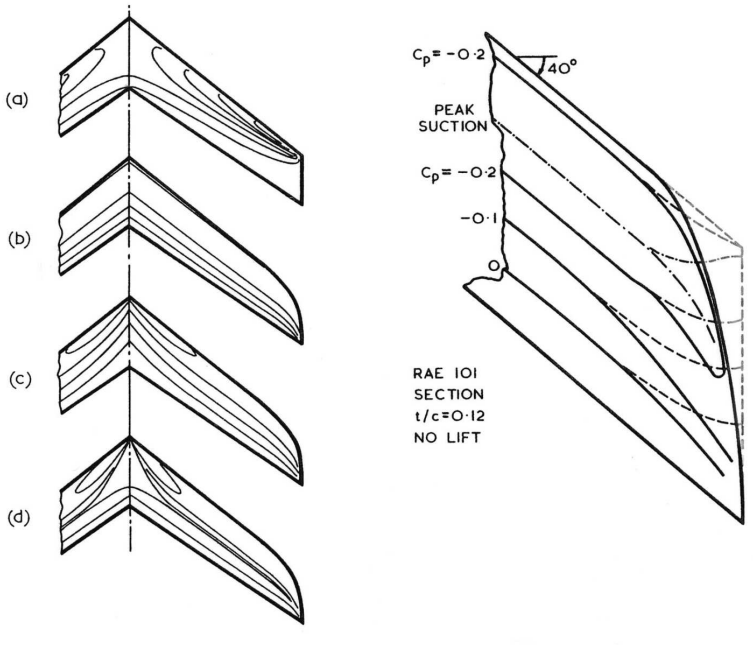

Figure 15: Left: Isobar Patterns on Sweptback Wings. Right: Isobars Near the Tip of Sweptback Wings: Dashed Lines Constant Sections and Streamwise Tip; Full Lines Curved Tip, from Küchemann[169]

The writer has also recently adopted Küchemann-like tip closures for both new main rotor and tail rotor blades, Robinson and Brocklehurst (2008).[250]

As with helicopters, composite construction now offers the designer greater scope, depending on the type of aircraft. The need to produce accurate laminar flow aerofoils for sailplanes led to early adoption of composites, despite the potential aeroelastic problems. This trend has been followed for light aircraft, and is gradually being adopted on larger aircraft, while aluminium alloys are still employed because of their stiffness which is necessary for the use of sweep. Many aircraft employ composite components, such as root fairings and tip caps, not only to simplify manufacture, but also to clean up the design to achieve nearer to the optimum aerodynamic performance. The question of what is the best planform has intrigued aerodynamicists for many years.

The goal of elliptic loading, and the idea that a straight, or a swept-back trailing edge (near the tips) may be advantageous in achieving low induced drag, has been taken a step further by van Dam (1986)[302] in his analysis of aft-swept pointed tips. Somewhat ironically, he also cites the early Etrich Taube aircraft and several helicopter tips, such as the BERP blade, as seeking low induced drag due to their sweep back. He also refers to the fins of various types of fish and birds, which feature crescent shaped aft-swept tips. This early paper includes a panel method analysis of some simple highly swept, and pointed tip planforms, Figure 16, which raised the question of whether this type of design really does offers a reduction in induced drag. While the inviscid panel-method analysis seems to confirm these ideas, in practice the question is clearly complicated by viscous effects and in particular the manner in which the tip vortex rolls up around the wing tip.

Vijgen, Van Dam and Holmes (1989)[309] present further analytical and experimental results for a high aspect ratio wing with swept-sheared wing tips and concluded that there was an increase in aerodynamic efficiency of about 3.3%, Figure 17.

These ideas were later followed by experiments on crescent wings, van Dam (1989).[303] The crescent wing configuration is really a generalisation of the elliptic wing, where the desired elliptic chord distribution is set out about an elliptic sweep line, such that the wing planform takes on a crescent (moon) shape, Figure 18. The problem is that changing from an elliptic planform to a crescent planform of the same span brings with it a change in the wing area, thus increasing the aspect ratio.

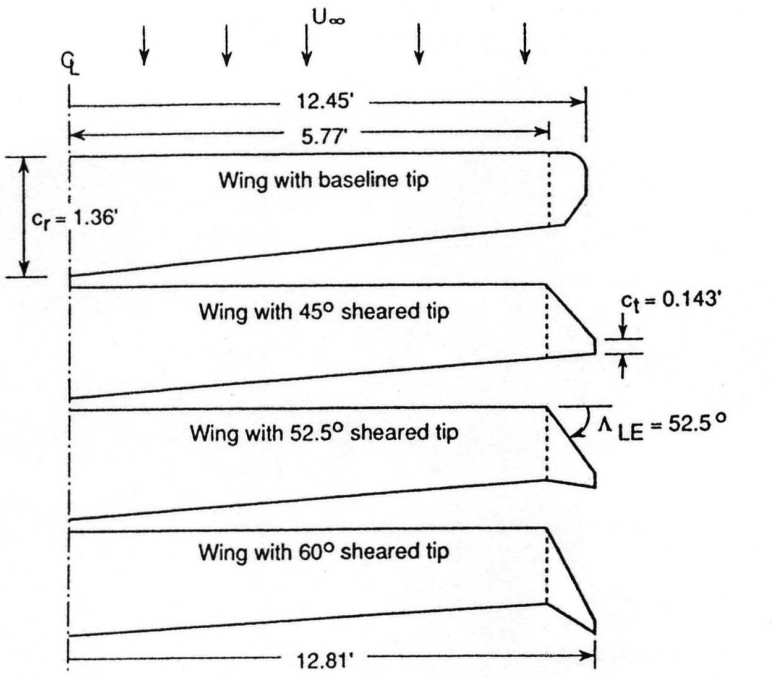

Figure 16: Planform Geometry of Sheared Wing Tips Configurations Tested by van Dam (1986)[302]

However, the curving swept back planform, and in particular highly swept tips, tends to lower the trailing edge and thus effectively raising the quarter-chord line out of plane when the wing is at incidence. Other examples of non-planar wings, are wings (or rotor blades) with anhedral, or dihedral as used on the tips of some aircraft (and free-flight model aircraft), and wings employing winglets, or tips which curl up or down.

The wind tunnel tests showed some small benefits, but at the time the results were regarded as rather marginal. Van Dam, Vijgen and Holmes (1991)[307] illustrates the surface flow on a curved (swept) tip compared to an elliptic wing, Figure 19. In the tests a transition trip was used, and this may have influenced the stall. In a further paper on the drag reduction characteristics of aft swept tips, van Dam, et al (1991)[306] again describes the wind tunnel tests and claims and average improvement in Oswald wing efficiency of about 3%.

Later, Ardonceau (1994)[16] carried out tests similar to van Dam's and analysed and compared the results in terms of total drag. Ardonceau found that the crescent planforms caused a reduction in wing efficiency as the mean sweep increases. However, a 10% lower drag was identified below a lift coefficient of 0.4 for the largest sweep case, and a trend of increased maximum lift with an abrupt stall was also noted for increasing sweep. Ardonceau highlights the difficulty of attempting to divide the drag into induced and profile components, and concludes that 'only small (second-order) effects, positive or negative, can be expected from deviations from the basic Prandtl definition of minimum induced drag'. Finally he states that 'what the aeronautical engineer needs is a lower total drag, irrespective of the balance between the components'. The author fully agrees with these sentiments, and would hope that the application of CFD to evaluate tip designs will provide the desired viscous,compressible solution.

One of the problems with the crescent shaped wing is that the tip vortex appears to form around an extended distance of the leading edge where the chord rapidly reduces. Hence, the flow may separate from the outer tip leading edge. At higher incidence, the tip vortex roll-up covers a significant portion of the span, and a stall cell develops inboard of this as shown by the flow visualisation. However, at moderate incidences, any premature drag rise near the tips takes place over a relatively small area such that its overall effect is small. The author has observed similar separation near the tip of parabolic and swept-parabolic tips that were tested in the Westland wind tunnel in early the 2000's.

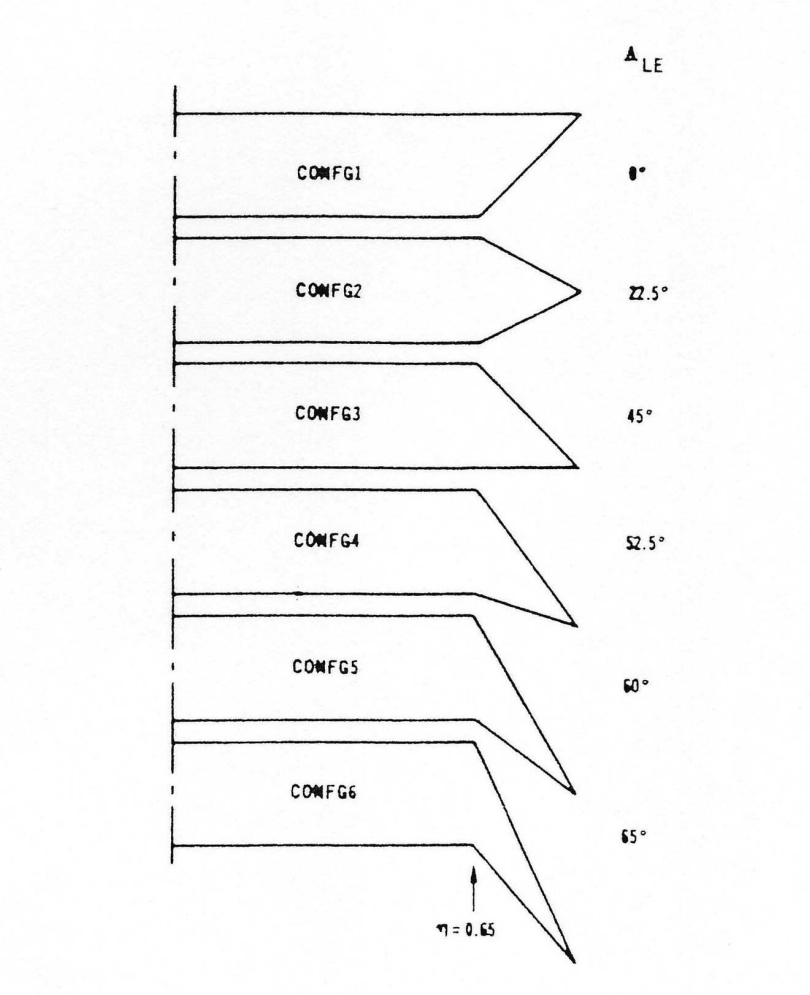

Figure 17: Various Aspect Ratio 7 Wing Planform Shapes, Vijgen, van Dam and Holmes (1989)[309]

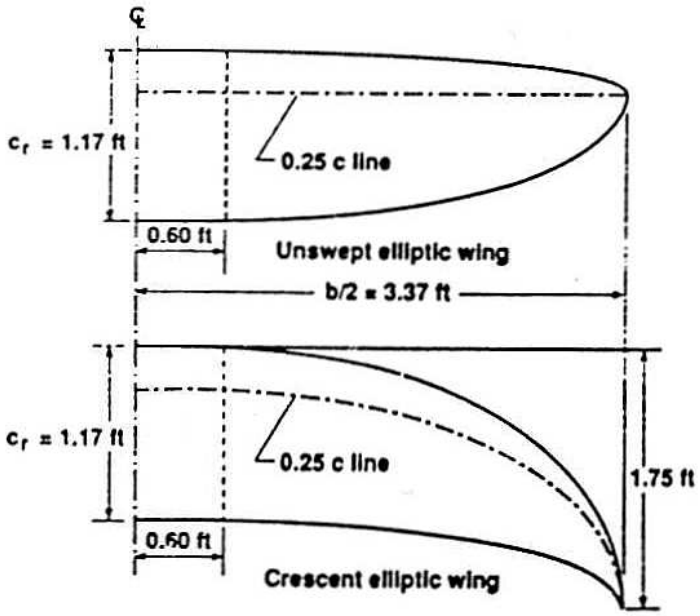

Figure 18: Planform Geometry of Elliptic and Crescent Wings for Wind Tunnel Testing, van Dam (1989) [303]

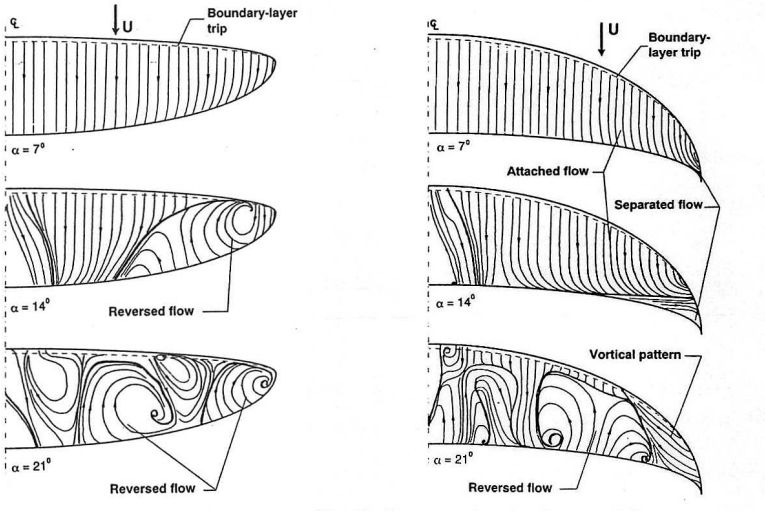

Figure 19: Surface Flow Streak-Line Pattern on Elliptic and Crescent Shaped Wings, van Dam, Vijgen and Holmes (1991)[307]

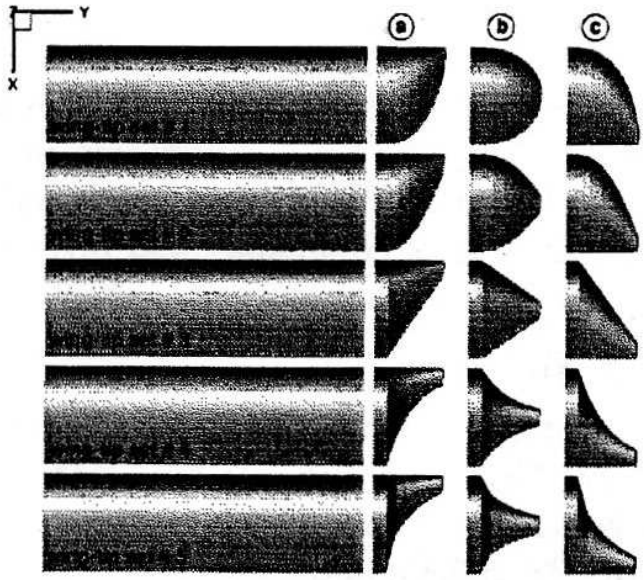

Figure 20: Geometry of the wing-tips added to a rectangular planform by Bourdin (2000)[50]

However, the high sweep of this style of tip may well make it suitable for high-speed applications, and a modest increase of chord and tip modifications may relieve the tip-separation problem.

The effect of planform on induced drag is also discussed in a recent paper by Bourdin (2002)[50] who reports a parametric study of a family of 15 different wing tip shapes, Figure 20, using a parametric geometry definition and grids generated in ICEM. However, Bourdin employed only an Euler solver, so while some induced drag benefits were discovered (for configurations that featured a straight trailing edge extending to the tip, column 'C' in Figure 20), it is not clear whether there would be an overall drag reduction. Some of the tip shapes illustrated are also similar to considered by Hoerner. The most successful of the tip shapes of Bourdin, although planar, leans towards the shape of a winglet.

Winglets for fixed-wing transport aircraft were originally developed by Whitcomb (1976) [315] and reported by Flechner, Jacobs, and Whitcomb (1976),[113] see Figure 21. Following tunnel testing winglets were initially flight tested on a KC-135A where a 7% increase in range was demonstrated. In this application, the objective is to reduce the total drag in cruise. Whitcomb discovered that, not only did the winglet push the roll-up of the tip vortex outwards, effectively increasing the span and therefore reducing the induced drag, but also brought about a reduction of wave drag by preventing the isobars bunching up near the leading edge of the tip. This transonic effect may also justify the purpose of the small lower tip fence. The opportunity to reduce wave drag therefore helps to offset any increase in profile drag due to the added area of the winglet. The addition of a winglet may increase root bending moments and the designer seeks a compromise between wing weight and maximising the effective span to improve the overall efficiency in cruise.

Winglets are now being incorporated into most commercial and business jets, including the Gulfstream III, IV and V, the Boeing 747-400, and the McDonnell Douglas MD-11 airliner and C-17 military transport. More recently, raked wing tips have been tried on the Boeing 767-400 and blended winglets have been applied to the Boeing 737-800 and Boeing 787 (Dreamliner), Figure 22.

Once the concept of winglets had been proven for commercial jets, they were tested in other applications, for example, on light aircraft, ultra-lights and sailplanes. In these applications, there is no wave drag to trade off, so the designer must be careful to minimise profile drag in cruise.

After several years of development, winglets have been used to advantage on high-performance sailplanes, Eppler (1997).[106] Eppler reports that although the winglets gave improvements in low speed performance,

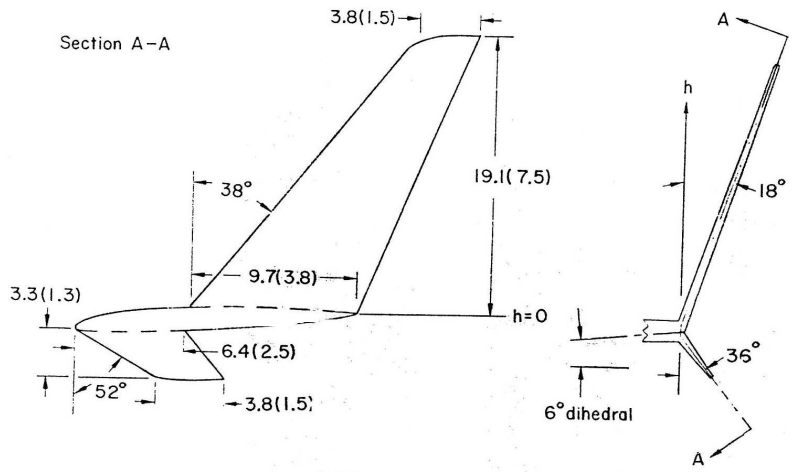

Figure 21: Winglet Details, from Flechner, Jacobs and Whitcomb (1976)[113]

Figure 22: Comparison of Winglet Designs: Boeing 737-800 compared to Airbus A319 (left), Raked Winglet on B767-400 (centre) and Boeing 787 Dreamliner (right)

Figure 23: Tapered 'flat' Winglet on Europa (photographed at RAF Kemble, 2003)

this had to be traded off against the additional profile drag incurred at high speed. Ironically, it was also reported that the pilots found that the winglets made the aircraft easier to circle in thermals, probably due to an improvement in lateral stability (dihedral effect), and an end-plating effect on the ailerons.

In contrast, the Europa motor-glider, Figure 23, features a winglet to extend the span with only a small amount of dihedral, perhaps to avoid problems landing in cross-winds.

Maughmer (2001)[203] also considers the design of winglets for sailplanes, as shown in Figure 24. The many geometric parameters make this a challenging design task, which lends itself to optimisation provided the geometry can be readily parameterised. The Winglet is required to reduce the induced drag at low speed (high CL), and should not give rise to any significant increase in profile drag at high speed (low CL). Parameters such as toe-in and twist must be chosen to give the best compromise between these conflicting design requirements. Maughmer reports that, at the world championships in 1991, only about 20% of the competitors used winglets, but by 1998 virtually every sailplane had some form of winglet.

A subsequent paper by Maughmer, Swan and Willits (2002)[204] considers the design of an aerofoil for a winglet on a high performance sailplane. This is a difficult design problem because the airfoil must operate over a wide range of angle of attack at relatively low Reynolds numbers, and the design of the aerofoil is intrinsically linked to the design of the winglet.

Hepperle (1993)[133] also considers the role of winglets for sailplanes and illustrates the 1976 Whitcomb (NASA) Winglets which have the form of an upper and lower winglet, and also quotes a VFW design from 1977 which has a larger aspect ratio lower vane. Hepperle remarks that that by 1986, Rutan's Voyager had blended winglets.

Some of the questions regarding winglet design are considered in a paper by deMattos, et al (2003),[90] where a figure of between 3.5-6.5% drag reduction is quoted. The need for extensive wind tunnel testing and CFD analysis is emphasised, and the trend towards optimising the wing tip design is highlighted. Blended winglets are used on the Embraer 170 airliner and Mattos makes the point that the navigation light was placed on the lower surface to minimise interference drag. As mentioned above, Boeing employed a raked wing tip for the 767-400 airliner instead of Whitcomb-like winglets. Compared to the Boeing 737-800 the raked wing tip provided a greater drag reduction. Fairchild-Dornier selected the so-called Super-Shark winglet for the Envoy-7 business jet which more gradually curve upwards. In some cases an extended trailing edge fillet has been added, to fair the angular junction region.

Brady (2003)[52] describes the blended winglets used on the Boeing-737, Figure 22. The new 777 and 7E7 airliner employs a refined tip design where the winglet has been integrated into the wing planform so that the tip is swept upwards, and has a considerable amount of sweep-back. The European Airbus series also employ a range of winglet designs, and the A340 uses a large lower upper winglet. Park (2003)[229] discusses rudders on winglets, but warns that the addition of a rudder may negate the benefit of the winglet.

The concept of displacing the tip vortex outwards or favourably modifying the flow over the tip is interesting, and at first sight appears compatible with the desire to enhance the performance of the helicopter rotor.

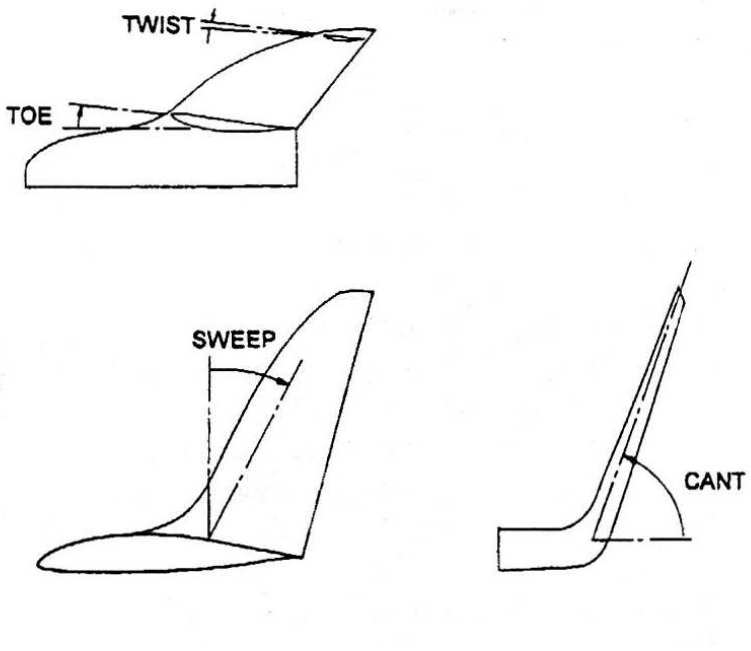

Figure 24: Geometric Quantities Used to Define Sailplane Winglets, from Maughmer (2001)[203] Note the Blending at the Junction of the Wing and Winglet

However, experience has show that it is advantageous to displace the tip vortex downwards in the wake to lower the induced power, and for a helicopter in forward flight, the large dihedral angle of a winglet, is not admissible due to the loads which would be generated in edgewise flight. On the other hand, a limited amount of anhedral is viable, since it may also counters pitching moments which arise from the use of sweep and offset. Anhedral has been used on the BERP main rotor blades of the Lynx and EH101, and also on the S-92. Downward pointing Winglets for helicopters were also tested by Muller, initially in hover, and later in forward flight (see Section 1.4.2).

The search for an efficient vehicle configuration has led to a consideration of joined wings, Nangia, et al (2003).[219] The benefits of this configuration are that there may be a reduction in the weight of the structure and a wide c.g. range.

The ability to model complex configurations in CFD has also enabled analysis of a spiral wing tip design, Grenon and Bourdin (2002),[123] Figure 25, which aims to gain greater amounts of forward suction (i.e. thrust) from the wing tip flowfield than obtainable from a simple winglet. However, the surface discontinuities in these new concepts may lead to viscous and wave drag penalty's which the writer feels may outweigh their benefits.

A natural extension of the winglet idea, is to emulate the tip feathers of certain (land-based) soaring birds by employing a series of tip vanes or sails. This challenge was taken up by Spillman (1978),[268] and Spillman and Allen (1987)[269] used up to 4 sails to sub-divide the vortex, while also generating a forward thrust on each sail.

After wind tunnel tests in the Cranfield wind tunnel, a set of 3 tip sails were tested in flight on the Morraine-Soulnier Paris 2-seat Jet, Figure 26. The twisted, tapered sails were fitted as extensions to the tip tanks, and according to Spillman, the L/D ratio improved from 12.5 to 15.8. Tip sails have also been tested on the Pawnee crop-sprayer, and later to the Centurion, Figure 27. However, tips sails have not been universally adopted, probably due to the profile drag penalty at high speed, for fixed sails. Indeed, the design of tip sails is complicated by the need to make such trade-offs, and the concept is best suited to reducing the induced drag at high lift coefficients. In nature, birds are able to overcome this compromise since they are able to re-configure

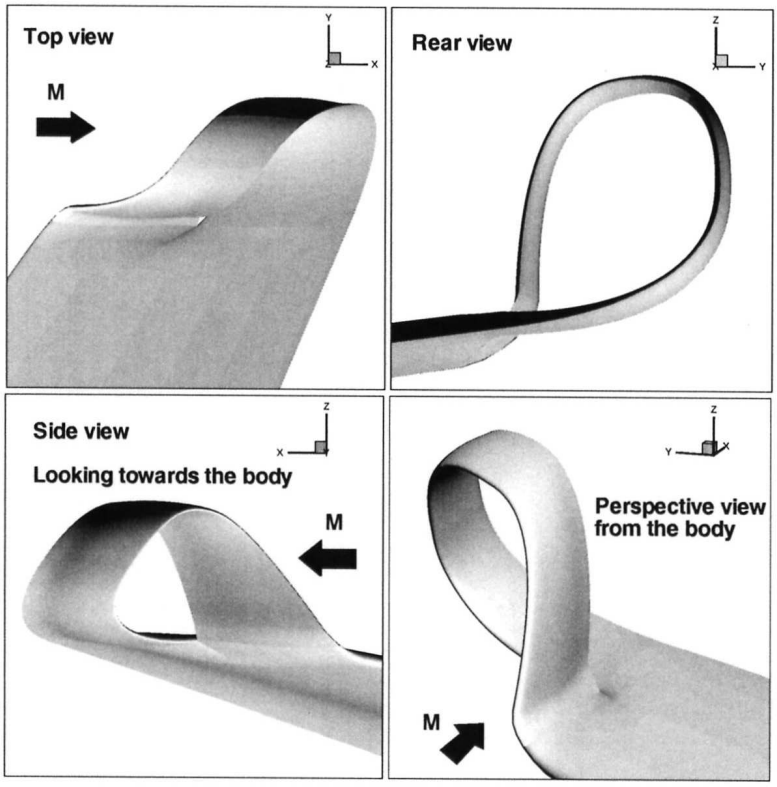

Figure 25: Spiroid Tips investigated by Grennon and Bourdin (2002) [123]

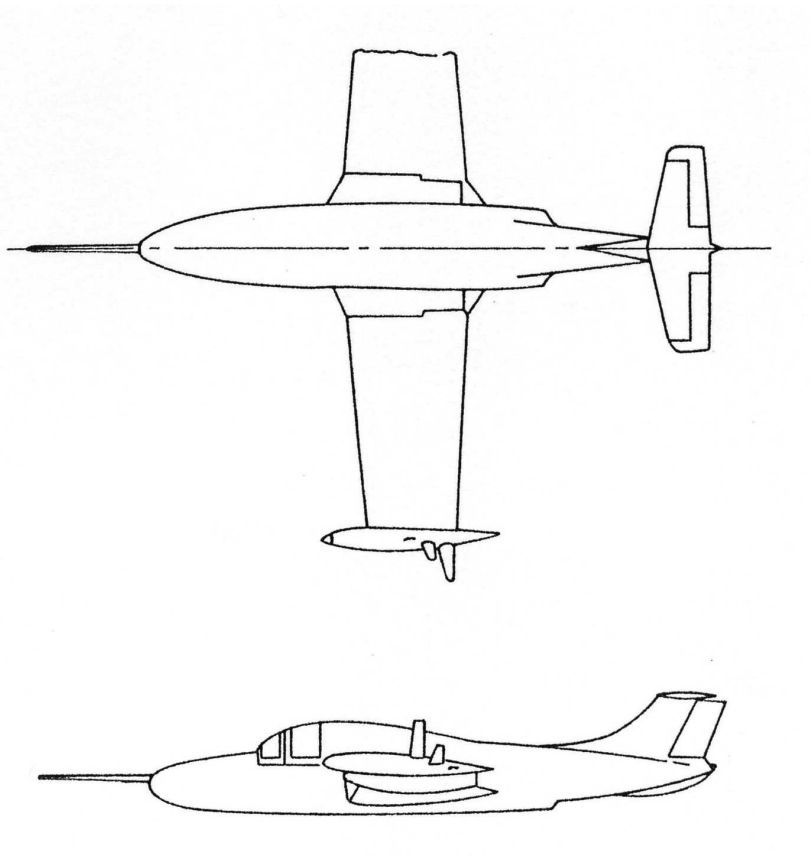

Figure 26: Tip Vanes Added to Tip Tanks of the Paris Jet Trainer, Spillman (1978) [268]

their tips to suit different modes of flight. Variable geometry sails would present mechanical difficulties and a weight penalty, and the writer is not aware of any such developments, although there may be some scope here for application of smart materials.

However, Spillman-like tip sails (mimicking those of birds such as the stork or condor) have been used on a Chinese version, Y5-B, of the Russian AN-2 light, high-wing transport aircraft, Shijianzhuang (2004),[259] Figure 28. As with Spillman's implementation, all three sails are set well aft on the otherwise rectangular tip.

The Wing-Grid concept takes The idea of mimicking the tip feathers of birds is taken a stage further with the Wing-Grid concept, as put forward by LaRoche and Palffy (1996).[177] The Wing-Grid comprises multiple (3 to 7) vanes, or winglets, mounted on (or initially between) end-plates on an otherwise rectangular tip and has been wind tunnel tested and tested in flight on a light-aircraft, LaRoche (2002).[173]

The functioning of tip sails contrasts to that of Winglets. The aim of tips sails is to divide the tip vortex, and in so doing generate a thrust component, while the objective of the winglet is to decrease drag by displacing the tip vortex upwards and outwards, and at the same time reducing the wave drag.

At first sight, tip-sails would appear to be unacceptable for the helicopter. However, the idea of dividing and therefore diffusing the tip vortex to reduce blade-slap noise was investigated by Tangler (1975)[291] with his sub-wing. Later, the concept of splitting the tip vortex into two smaller, separate vortices led to the Westland Vane Tip which greatly reduced the blade-vortex interaction (BVI) noise, Brocklehurst and Pike (1994)[59] (see Section 1.4.2).

A further reason for attempting to modify the tip vortex for fixed-wing aircraft is to overcome the landing separation problem at airports, and this topic has been much researched, but is not directly relevant to the

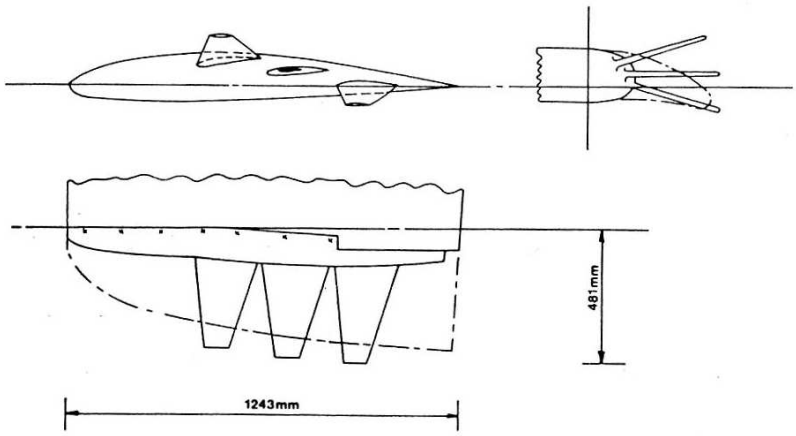

Figure 27: Tip Vanes on the Wing Tip of the Centurian, Spillman (1987)[269]

Figure 28: Chineese Built Version of Russian AN-2 Equipped with 'Winglets' to Improve Rate of Climb, Shijianzhuang (2004)[259]

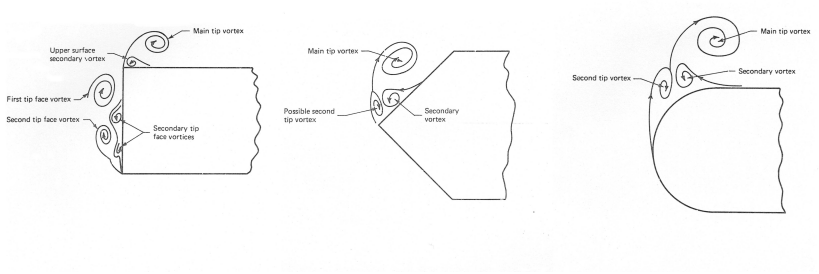

Figure 29: Crossflow Section Through Tip Vortex System using Dye Technique (a) Square Tip, α =12deg, x/c=0.5, (b) Bevelled Tip, α =16deg, x/c=0.4, (c) Rounded Tip, α=16deg, x/c=0.6, from Thompson (1998)[296]

topic of this thesis. Various techniques are available to diffuse the tip vortex, including the use of deployable tip spoilers and blowing.

Whilst perhaps not as efficient as splitting the tip vortex, diffusion of the tip vortex by blowing may be useful as means of reducing BVI noise. An alternative use of blowing, or suction (or other flow control devices) would be to clean-up the flow at the tip and, if possible, displace the tip vortex outwards and therefore reduce the induced drag by increasing the effective radius.

An experimental study on the use of wing-tip blowing aimed at diffusing the tip vortex are reported by Tavella, Wood and Harrits (1985).[294] Experiments on the adaptive control of the tip vortex have been carried out by Matthewson (1998),[202] and Maragaris and Gursul (2004),[197] and a flow deflector slot has been tested by Lin, et al (1996).[185] Vakili, et al (1998)[300] also presents hot film measurements and smoke flow visualisation of the impact of tip blowing on the characteristics of the tip vortex.

Understanding the formation and roll-up of the tip vortex, is an essential for accurate evaluation of tip aerodynamics, and measurements behind a wing tip may be used to supplement the full-scale hot wire rotor tip vortex measurements. Francis, and Kennedy (1979),[116] reported their experimental investigation of the formation of a trailing vortex, using hot-wire anemometry and helium bubble flow visualisation. The paper contains velocity contours in the cross-flow plane of the wing tip deduced from hot-wire measurements. Also around this time vortices on delta wings were being studied, for example at Boeing by Kulfan (1979),[172] where again details of the vortex structure were being observed. The delta wing is of interest here because of similarities with the flow on the outer swept tip of blades such as the BERP, and those proposed by Spivey at Bell (see Section 1.4.2).

The roll-up and structure of the tip vortex has a direct impact on both acoustics and performance, and is strongly influence by the tip design. Devenport, et al (1996)[92] presents a study of vortex development where the flow has been measured by hot wire anemometers. It is also possible to measure the circulation around a tip vortex. This was attempted by the writer during the Vane tip experiments using a five-hole yaw probe, but this approach has limitations when the vortex core is approached, Freestone (1983).[117] A vane type vorticity meter was used by Flowers and Collar (1966)[114] and Wigeland, et al (1978),[316] but a better method is to use a hot-wire traverse, Sampson (1976).[255] A rapid scanning (rotating arm) hot-wire anemometer surveys were carried out by Corsiglia, Schwind and Chigier (1973).[80] Johari and Moreira (1998)[155] and Desabrais and Johari (2000)[91] present circulation measurements for a delta-wing using an acoustic ultra-sound technique.

With regard to low drag tip shape, near field measurements at the start of the roll-up, where the vortical flow first detaches from the tip surfaces are of vital importance. The details of the flow around three type of tip caps; square, rounded, and square with bevelled edges, were recorded by Thompson (1998),[296] Figure 29. As with many visualisation studies, no pressure or force measurements were made, and in this case the Reynolds number was in the region of 20,000.

In order to separate out the drag component, and hence better understand the breakdown of the drag of modern transport aircraft, many researchers have resorted to a far-field drag-analysis technique to evaluate wing design for instance Li (2003),[184] and Hunt (2001).[149] The topic of drag prediction, and the breakdown of

the drag from CFD simulations, was discussed in a paper by van Dam (1995).[323] In this paper he computed the flow around one his characteristic, elliptic planform wings with a straight trailing edge using the TLNS3D solver for an inviscid subsonic flow with artificial viscosity. Van Dam also considered the effect of the tip-cap shape characteristics (rounded, bevelled and curved-bevel) on wing, concluding that the bevelled tip gave the highest Oswald wing efficiency factor. In another article, van Dam, et al (1995)[305] also computes the flow at higher subsonic Mach number over his crescent wing and the ONERA M6 wing, and compares the total drag from surface integration to that extracted from a wake analysis as induced and wave drag. Later, the topic of drag extraction is reviewed by van Dam (1999).[304] Other researchers have also employed a downstream, or Trefftz plane analysis, e.g. Yates and Donaldson, (1986)[328]extracted the induced drag and wave drag from CFD solutions of the flow-field. It is interesting to consider if a similar technique, such as taking a radial slice in hover, or a downstream plane in forward flight, could be similarly used to separate induced, profile and wave drag for rotorcraft CFD analysis.

Chao and van Dam (1999)[77] discuss airfoil drag composition to compare the surface integral and wake integration techniques in predicting the drag from computed solutions of the 2D RANS equations. Bushnell (2003)[68] also discusses drag break down in his review of Aircraft Drag Reduction.

Peace (2002)[232] describes the role of CFD in the design office (at ARA), and highlights drag prediction as one of the weak points of a CFD analysis. This view is confirmed by the writer's own experience, particularly with commercial codes such as Fluent, but as CFD methods become more developed, it is expected that the accuracy will improve. Studies at WHL have shown that HMB tends to over-predict the drag compared to the Drela 2D aerofoil code, MSES, but the predictions are much closer to test than Fluent, Brocklehurst (2003).[54] For a 2D aerofoil, the problem is to accurately predict both the pressure drag and skin-friction drag components, and here a method is required which is able to distinguish between laminar and turbulent boundary layers, as this will affect both of these components. In 3D, viscous drag is again important, and in the past has been notoriously difficult to predict, but the induced drag arising from the vortex system of the lifting wing depends upon accuracy in modelling the overall flow field, and especially the trailed wake. For compressible flow cases, wave drag is also important and requires adequate resolution and accurate modelling of shock-boundary-layer interactions. For the helicopter, accurate prediction of overall thrust and torque are of paramount importance in assessing the performance of new rotor blade designs. It is therefore essential that both the profile drag (which may include wave drag) and induced power are both well predicted. The later involves preserving the circulation strength and the trajectory of vortices in the rotor wake.

Uygun and Tuncer (2003)[299] consider the problems of accurate drag prediction for a complete CN-235 cargo aircraft, using a FASTRAN Navier-stokes solver.

Spall (2001)[264] examined the issue of excessive diffusion of wing tip vortex calculations using a second order accurate pressure-based finite volume method to solve the Euler equations, and concluded that with well-designed grid clustering the use of a second-order methods were viable. However, higher order methods may be needed when viscous terms are present. Snyder and Spall (2000),[263] investigated the multiple vortex structures formed over flat end-cap wing.

Since the drag prediction from CFD is crucial to the accuracy of any performance evaluation, it is important to be able to predict the transition location, and adjust the turbulence model of the solver accordingly to give the correct skin friction. Crouch, et al (2002)[85] has developed a transition prediction routine which can be invoked from within a 3D CFD code.

The EROS-UK project has led to a transition model being incorporated in to the HMB code, such that in future static and dynamic simulations, the transition point can be estimated. The solver may then be adjusted accordingly to give a more realistic representation of the flow and a better calculation of the resulting skin-friction, Hill (2004).[134] This implementation was initially for 2D aerofoils, but has since been developed for more general application by Zografakis, Barakos and Johnson.[331]

Further studies of drag breakdown into viscous and wave drag components from a knowledge of the far-field have been carried out by Paparone and Tognaccini (2003).[228] To determine the drag from the entropy variations in the flow, their approach was to allow for numerical and discretization error of the flow solver, such that accurate estimates of the drag components are available on moderately sized grids.

Methods of extracting of drag from numerical simulations has also been presented by Esquieu (2003),[108] again using Treffz-Plane methods.

The writer takes the view that the tip planform shape and the detail design of the tip-cap, will affect both the induced and profile drag components. The shape of the tip and the tip outer edge will also affect the structure of the tip vortex. Any edge separations that arise as incidence increases will present a source of disturbance which will be entrained into the vortex core. This idea is confirmed by the hot wire measurements of circulation and axial velocity within the vortex core which were carried out by Anderson and Lawton (2003)[11] on a NACA 0015 wing with a semi-span aspect ratio of 0.8. For small values of circulation, the axial velocity shows a velocity deficit, but as circulation increases, a progressive increase in axial velocity is observed. A linear relationship was found when the axial velocity exceeded 90% of the freestream value, and at high lift, the axial velocity near the centre of the vortex may exceed the freestream by as much as 70%. Anderson and Lawton also found that the axial velocity was sensitive to the shape of the end cap. Flat and rounded configurations were tested, and the axial velocities were found to be greater for the rounded cross-section tip-cap, while the vortex core also had a smaller diameter. Unfortunately, no measurements were made of the drag of the wing, so it is not possible to link the reported vortex properties to the performance benefits of having a particular tip-cap shape. Since the rounded tip cap produced a 'cleaner' vortex, it may be supposed that this would impose a lower drag.

Before going on to consider tip shapes specific to helicopters, it is perhaps useful to briefly summarise what has been learnt so far.

In this section of the literature review, the aerodynamic rationale behind several fixed-wing tip design concepts has been revealed. The work of Hoerner indicates that for good performance the tip should be designed so that the tip vortex forms as far outboard as possible, and the shape of the tip should encourage the tip vortex to roll-up cleanly with minimum energy loss. The cross-section preferred by Hoerner to achieve this was one where the lower surface blends up to meet the upper surface at the outer tip edge (based on the use of a cambered aerofoil section). Rounding of the leading edge corner is desirable for the best performance over a range of lift conditions, while excessive rounding of the tip near the trailing edge is to be avoided. Küchemann shows how to avoid isobars bunching up in the leading edge corner of the tip in compressible flow conditions, and this general principal should be effective even if the basic wing (or blade tip) is not highly swept, provided the effective Mach number is not too high so that a shock does not form inboard of the tip. This style of tip shape provides continuity of sweep and the sweep angle itself increases all the way to the tip. The tip also offers a nice clean outer edge for vortex formation. Küchemann employs a sharp trailing edge corner which places the roll-up as far outboard as possible, while maintaining sufficient sweep to suit transonic conditions. The basic Küchemann tip therefore addresses several of the problems encountered on helicopter blades, and in particular could be advantageously applied to a the tip of highly loaded tail rotor blades, which are a particular focus of this thesis. In recent times, the addition of a winglet has been found to provide some fine tuning to further reduce shock-induced drag, and this non-planar spanwise extension has been shown to further reduce the induced drag for a minimal increase in wing bending loads. While highly non-planar features may be inappropriate for helicopter rotors, the thought occurs that there may be some potential to exploit mild non-planar design features, such as anhedral, to enhance the performance of highly loaded rotor blades in conditions near hover. It is also clear from the review that to achieve an optimum tip design for a given application, it is necessary to employ a method of analysis which includes all the physics of the flow so that the total drag can be properly evaluated. This requirement should be able to be fulfilled by the application of a good CFD method with adequate resolution to capture the flow features.

1.4.2 Review of Helicopter Tip Shapes

Helicopter blade design has always been a compromise between aerodynamic efficiency, structural and mass properties, and ease of construction. Since wood was a natural choice of material for early helicopter blades, the designer initially had some freedom in the choice of shape although it is clear that the ease of manufacture of long, slender blades soon became the overriding consideration. For example, Cierva's C8L autogyro had blades with an elliptic planform, while the later C30A, had parallel chord blades with elliptical tips. As the helicopter developed, twisted, tapered blades best suited to hovering gave way to simpler parallel chord low twist blades, which were almost universally adopted, as they were easier to manufacture and gave a better compromise between hover and forward flight.

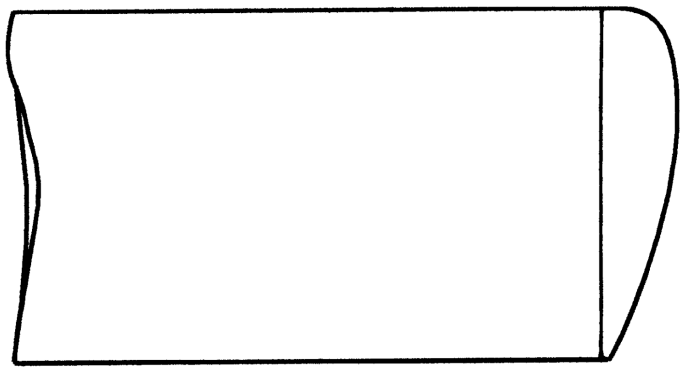

Figure 30: Illustration of Sikorsky/Westland Classical Hemispherical Tip Cap Used on Main and Tail Rotor of S-58 Wessex, S-61 Sea King, and Early WG-13 Lynx Metal-Spar Blades

While wood has good stiffness and fatigue properties, there are some drawbacks. One of the main problems was water ingress and the tendency for the ply to de-laminate or warp, not to mention the difficulty of maintaining aerofoil tolerances. Manufacture was also highly labour intensive, but the product was versatile, and had the potential been seen, the designer could have created more or less any tip shape he had desired.

However, through the 1950 and 60's the use of wood in blade construction gave way to extruded aluminium spars and trailing edge skins. When the writer joined Westland Helicopters in 1973, the Sea King and Wessex were in production with this type of construction, with the trailing edge comprising 'pockets' of alloy skin and Nomex honey-comb. The early Lynx blades had a titanium spar with glass-fibre skins. The tips of these blades (and there are many other examples from around the world) had tip caps of the classical hemispherical shape. That is to say, the end of the blade was closed with a surface, usually formed from aluminium, which was based on the aerofoil volume of revolution, Figure 30. In some cases, this shape was stretched in the spanwise direction giving an almost elliptic tip shape with some degree of thickness taper to the aerofoil. The symmetrical shape of the universally used NACA 0012 aerofoil lends itself to the creation of this type of tip. The tail rotor blades of the Wessex (S-58), Sea King (S-61) and early Lynx all followed similar styles of constant chord blades with aerofoil-of-revolution tip-caps.

Later, during the 70's and early 80's composite materials gradually replaced the metal construction and offered an immediate performance improvement and much improved fatigue life.

At Westland Helicopters in the UK, the composite technology was embraced in several stages. First, a tail rotor blade was built for the Sea King, Cook (1978).[79] For convenience of manufacture, the tip was simply cut square, and fitted with a flat metal tip cover. This blade was later produced with a cambered aerofoil, as reported by Byham (1987),[69] and has been used on both Sea King and Lynx, cropped to the appropriate length, and the tip is here illustrated in Figure 31. The next step, as part of the British Experimental Rotor Programme (BERP), was to build a replacement main rotor blade for the Sea King. These blades had similar dynamic properties to the blades they replaced, but had superior aerodynamics, not because of shape (since the NACA0012 aerofoil section and parallel chord was retained), but simply because the aerofoil contour was smooth and could now be manufactured within a finer tolerance. Somewhat disappointingly, the tip of the composite Sea King blade was also cut off square, and has a metal tip cover incorporating anti-static devices which contribute to profile power and disturb the tip vortex.

Elsewhere the industry was also looking for means of improving blade design to give enhanced performance and reducing noise and vibration, and parameters such as sweep, taper, and aerofoil section were being researched to take advantage of the freedom offered by composite construction.

The growing interest in dealing with the high tip Mach numbers encountered in cruising flight was discussed in a paper by RF Spivey (1968)[270] on 'Blade Tip Aerodynamics - Profile and Planform Effects'. This was

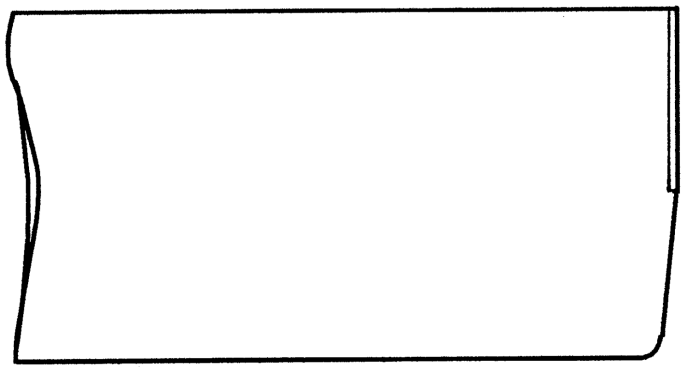

Figure 31: Sketch of Tip Shape Adopted for the Westland Composite Tail Rotor Blades for Sea King, W-30 and Lynx

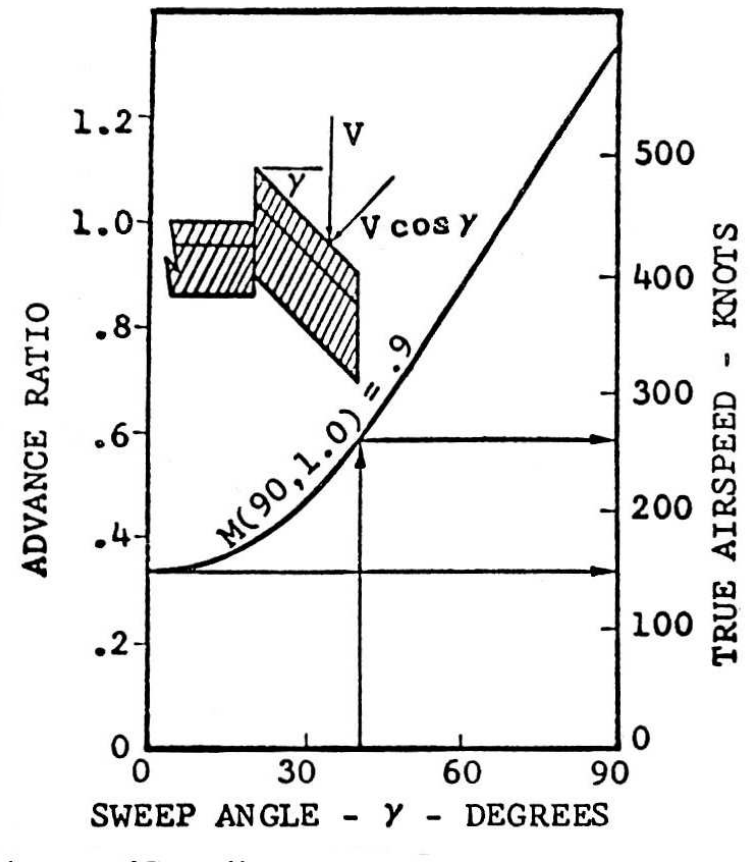

Figure 32: Method of Incorporating Sweep to Delay Compressibility Using Leading edge Sweep, from R.F. Spivey (1968)[270]

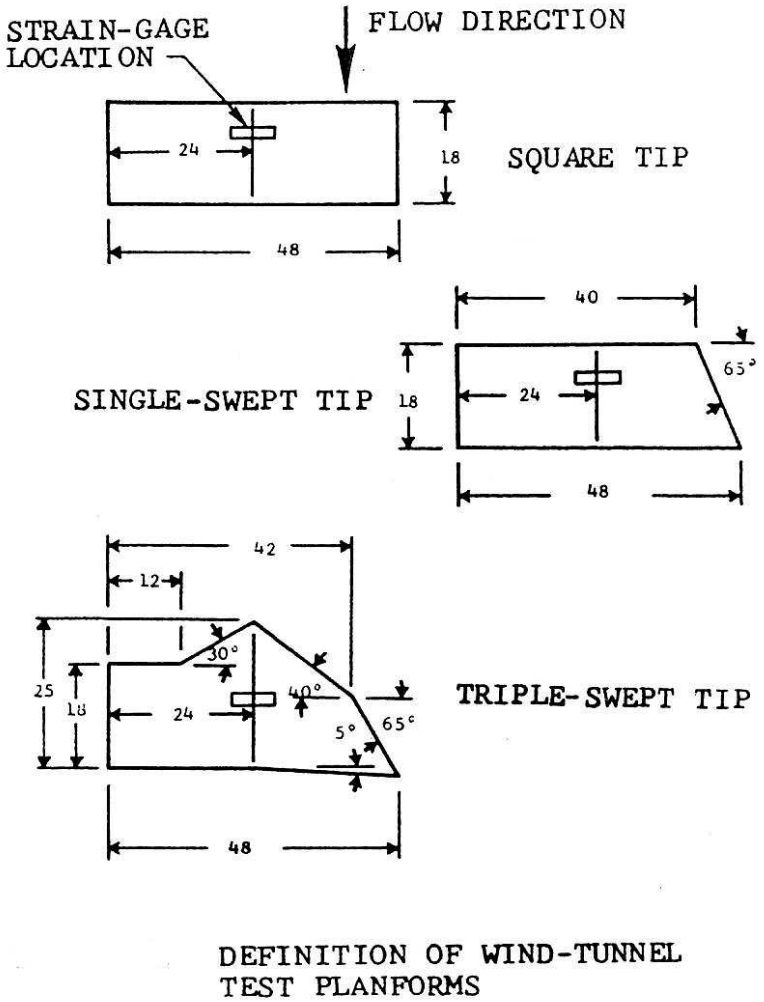

Figure 33: Design of Swept Tip Rotor Blades, W.A.Spivey (1970)[271]

followed 2 years later by another paper reporting work at Bell Helicopters, by WA Spivey, and GG Morehouse (1970),[271] entitled 'New Insights in to the Design of Swept Tip Rotor Blades'. The first of these papers describes the need for offsetting the swept tip panel forwards to maintain the aerodynamic centre near the blade feathering axis, Figure 32, and also suggests a highly swept outer edge, while the second paper discusses tests on a single-swept tip and a triple swept tip, Figure 33. The latter employs sweep forward and cranked aft-swept leading edge, with a small amount of trailing edge sweep. Although these tip shapes were not put into production at Bell, this work sowed the seeds for future development of swept tip blades.

The design emphasis in the US has mainly been on hover rather than forward flight performance, and this may have been one reason why the Bell tip shape was not adopted. Another reason may have been poor acoustics due to outboard location of the delta shape, and the high tipspeed of the UH-1.

The early 70's saw development on (mainly) prescribed-wake lifting-line rotor models, and experimental work to measure performance and determine the wake structure. In the UK, a full-scale test facility was used by Cook (1972),[78] to carry out hot-wire measurements of tip vortices. This paper became acknowledged as a major source of information on tip vortex structure and circulation strength, despite the difficulties involved in making measurement in a coastal environment . The test rig, which was located at Weston-super-Mare, was later used in the early development of the BERP blade.

Figure 34: The Westland BERP-III Tip which resulted from the British Experimental Rotor Programme

The design freedoms offered by composite construction lead to the unique shape of the BERP tip employed on the Lynx which later lead to the World Speed Record in 1986, see Perry (1987).[233] Later, this same type of blade tip planform, Figure 34, was employed on the EH101 because of its forward flight lift capability which allowed it to meet the constraints of operating a large helicopter from small ships. The main features that the BERP tip introduced were a large amount of sweep, and consequent use of notch offset, together with cambered aerofoils and the concept of an 'unstallable' tip. The change of aerofoil thickness-chord ratio and the notch off-set led to suppression of shocks on the advancing blade. The BERP tip provides an excellent example of the way manufacturers were embracing the potential for new technology to expand the flight envelope of the helicopter.

At Westland the BERP tip shape was assessed as a fixed-wing model in the wind tunnel by Newman and Byham in 1975, and although these tests were preliminary, they did confirm the high incidence performance potential of the BERP tip and the tendency for separations to start inboard of the tip. Some oil flow was attempted, and some tests were also carried out with a leading edge slat fitted inboard of the BERP notch to suppress the inboard stall in an attempt to quantify the benefit of the tip.

During the 70's, research in the USA was divided between improving hover efficiency, and the desire for low noise. Rotor models based on lifting-line or lifting-surface were developed, eg Kocurek and Tangler (1976),[166] and effort was put into wake measurements in order improve predictions of the tip loading in hover (due to the proximity of the tip vortex from the preceding blade). The lifting-line codes avoided the need to use Prandtl's tip loss factors which had been necessary in the earlier blade-element-momentum approach, eg Gessow and Myers (1952),[118] but they relied heavily on empirical tip corrections to account for compressibility and 3D shape effects in cruising flight. Landgrebe (1972)[174] reported measurements of the vortex wake in hover, and presented relationships which could be used in prescribed wake (hover) models. Kocurek and Tangler (1976)[166] made Schlieren measurements of the wake, and reviewed and generalised the vortex wake trajectory formulation. In this paper the authors put forward a lifting surface approach, which would have be capable of representing the effects of tip planform (although compressibility corrections would be required). Landgrebe and Egolf (1976)[176] also presented a forward flight wake analysis intended for incorporation into (lifting line) rotor performance codes.

The aim of reducing rotor noise led to several new tip shapes. The Ogee tip is described by Landgrebe and Bellinger (1974)[175] is shown here in Figure 35. This tip was aimed at reducing the peak velocities of the tip vortex. While the reduction in area at the extreme tip may also have given some improvement in Figure of Merit at low thrust, it may also have given rise to an early stall and an associated growth in profile power. Nevertheless, this type of tip was seriously considered as a low noise design, although it was never used on a production blade.

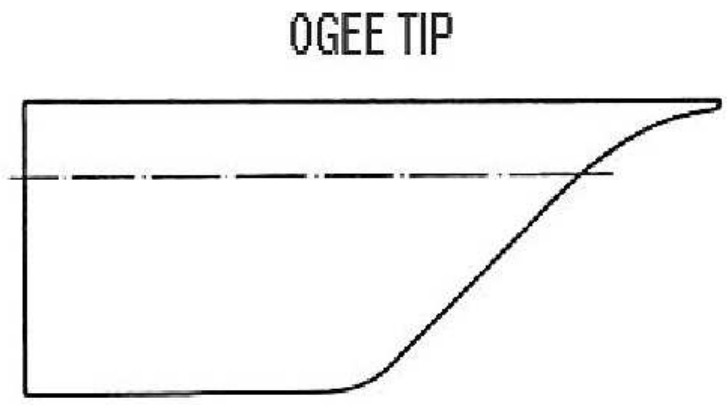

Figure 35: The Ogee Tip Designed to Reduce Noise, Landgrebe (1974)[175]

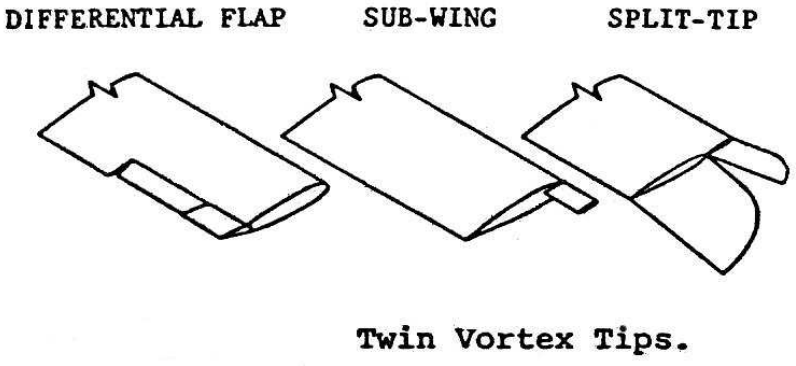

Figure 36: Sub-Wing and Split Tips, Tangler (1975)[291]

An alternative approach to reducing BVI noise, was put forward by Tangler (1975)[291] who presented experiments on blades fitted with a sub-wing to generate a secondary vortex and "so diffuse the vortex prior to interaction with the following blade". Other configurations also put forward were a differential flap near the tip, and a split-tip where the trailing panel was bent down and the forward part of the tip was bend up, Figure 36. However, in contrast to the Vane Tip developed by the writer (described later), the sub-wing comprised a small spanwise extension, which simply protrudes from the tip near the leading edge.

In this same timeframe, winglets were being developed for fixed wing aircraft by Whitcomb (1976),[315] and later Spillman and Allen (1987)[269] were active in promoting tip sails. These topics have already been covered in the first part of this literature review.

During the late 70's there was a continuing need for detailed experiments alongside developing strip-theory analysis for rotor performance. Shivananda, McMahon and Gray (1978)[261] made detailed pressure measurements near the (rectangular) tip of a hovering rotor, and from flow visualisation noted the presence of a secondary tip vortex. Later pressure measurement were compared for a baseline rectangular tip and a (rounded) volume-of-revolution tip, Gray, et al (1980).[122]

Huber (1979)[146] discusses the development of swept tip rotor blades on the Bo105 Advanced Geometry Blade (AGB-III). Several aft and forward swept tips were studied, including some like those proposed earlier by Spivey. However, the AGB-IV tip is illustrated as a tapered tip with a curved, swept leading edge, and a

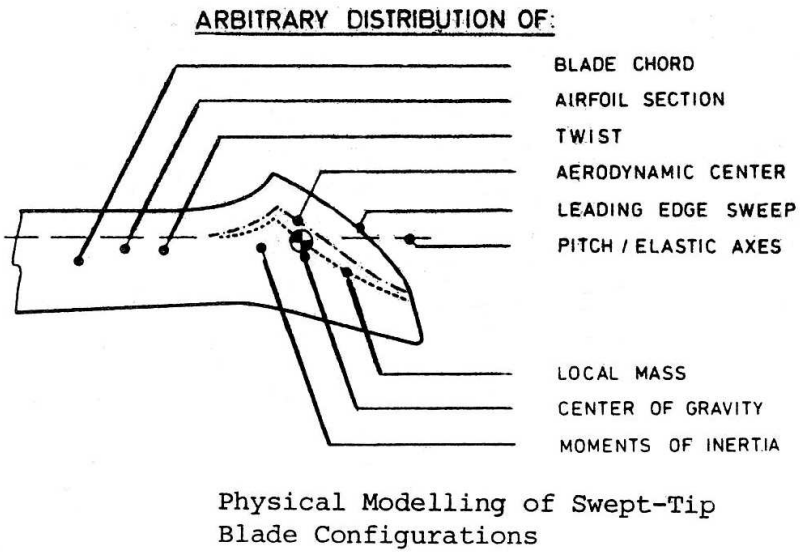

Figure 37: The Advanced Geometry AGB-IV Tip Combined Several Features such as Forward Offset to Facilitate Sweep together with a Tapered Curved Tip Shape, Huber (1979)[146]

slanted, highly-swept extreme tip edge, Figure 37. The paper by Huber is mainly concerned with blade stability and how the balance between dynamic and aerodynamic loading in the tip region would influence handling qualities. The AGB-IV tip has significant taper and this would probably help to minimise control loads and torsional deflections.

In the US, Maskew (1980)[201] applied an unsteady panel method to the tip design problem. In his paper entitled 'Influence of Rotor Tip Shape on Tip Vortex Shedding', he examined 4 tip shapes: rectangular, swept (sheared), straight tapered, and (once again) the Ogee tip. At Langley, Hoad (1980)[138] presented results from a wind tunnel test on rotor BVI noise on a similar set of tip shapes, which also included the sub-wing and end-plate tips, together with a 60 degree swept-taper tip, as shown in Figure 38. Summa (1985)[289] also applied a panel method to the case of a hovering rotor, thus improving the accuracy with which the 3D tip loading could be predicted. This approach is only valid for mildy compressible flow when compressibility corrections may be applied, and shocks are unlikely to be present. However, most dedicated rotor codes continued to use simpler and faster lifting-line methods, often relying on 2D wind tunnel data for aerofoil characteristics.

However, as early as 1980, Tauber and Hicks[293] applied a computerised full-potential method to the problem of improving advancing blade aerodynamics. They applied this method to aerofoil refinements on a blade with a straight trailing edge and 30 degrees of leading edge sweep. The analysis was also tested for a tapered Alouette tail rotor blade, where the 'low aspect ratio' was shown to reduce shock strength through tip relief. Tip relief is an important factor in tail rotor tip design and will be referred to again.

An empirical allowance for the relief of compressibility effects has been included in many traditional (lifting-line) rotor performance codes, e.g. in the WHL R314 code, by Beddoes (1976) at Westland. Tip relief was also analysed by Grant for blades at advancing blade conditions of transonic speeds and zero-lift using TSP methods, Grant (1977),[120] and this work was later developed by the same author to include arbitrary tip shapes in 1979.[121]

In the USA model rotor tests were being undertaken to support the development of rotor models, and Caradonna and Tung (1981)[72],[73] carried out their well known model rotor experiments on rectangular blades in hover and edgewise flight.

In search of improved hover performance, Bingham (1981)[47] considered blades with varying amounts of taper, twist, and RC-series aerofoils which are compared to the rectangular, NACA0012 blade of the UH-1 helicopter. As expected, the hover Figure of Merit improves with increasing taper, and with inboard location

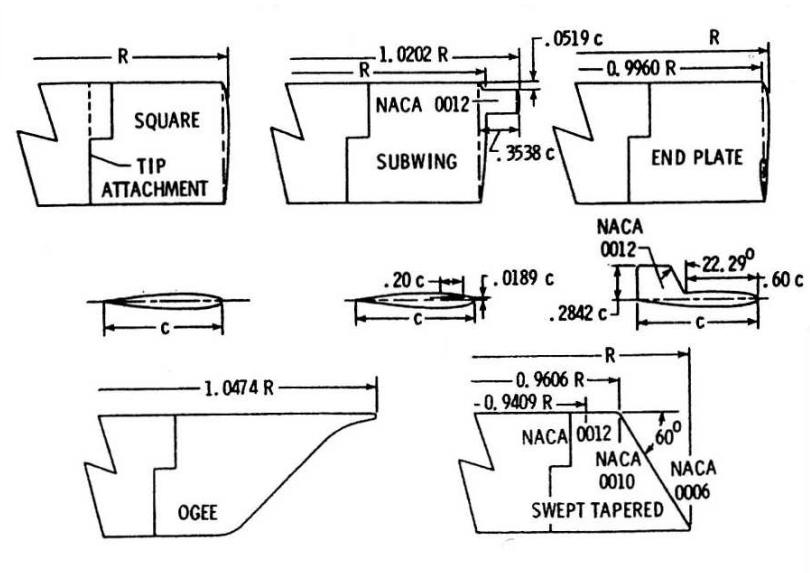

Figure 38: Tips used in BVI noise tests, Hoad (1980)[138]

of the initiation of the taper. However, it appears that twist (which is usually taken to be a powerful factor in enhancing hover performance) is less effective when the maximum chord of the blades is located well inboard such that the blades are tapered over most of their length. Bingham recognises that it would be necessary to maintain a constant thrust-weighted solidity [1], and cannot be relied upon to determine the retreating blade boundary in forward flight.

A quarter scale model of the UH-1, with a standard rotor and an advanced, tapered rotor was tested by Berry (1981),[37] Figure 39. The Mach scaled model demonstrated a full-scale equivalent 320kg (700lb) increase in hover thrust for a given power, despite a slight increase in the fuselage download (due to the increased inboard loading and downwash). The advanced blade also delivered a power reduction in forward flight. However, the advancing and retreating blade limitations of the tapered rotor blade were not fully explored. It is logical that a tapered blade would have a lower profile power in attached flow, since profile losses vary as radius cubed, provided the loading and tip Mach number is not too high (in hover a main rotor does not usually operate near maximum thrust). However, it is noted that the tapered blade has a narrow tip chord and no sweep. It would therefore be expected to be prone to advancing and retreating blade limitations.

Also in the USA, the UH-60 Black Hawk, and Sea Hawk blades, as described by Alansky, et al (1981)[6] featured a 20deg sheared-swept tip outboard of about 92% R, Figure 40. While this tip introduced much needed sweep to suppress shock development on the advancing blade, aeroelastic couplings were also introduced. The tip was not tapered, possibly to avoid any premature flow separation on the retreating blade (as observed in wind tunnel tests on a swept-tapered tip tested in the Westland wind tunnel). The Black-Hawk blade employs the SC1095 aerofoil section. During the late 80's, a scale model rotor was tested by Lorber (1991)[190] and this data has since been used by many researchers (e.g. Strawn, 1999, see later) to compare with CFD hover simulations.

While there may be some benefits in designing for a favourable aeroelastic response, simple application of a aft-swept tip to a rotor blade could lead to large one-per-rev pitching moment, and a possibly a reduction of control gradients in forward flight. The approach taken in the UK during the development of the BERP blade was to align the aerodynamic centre of the tip on the quarter-chord feathering axis of the blade, and this leads to a leading edge 'notch' which helps to suppress shock development on the advancing blade, and also contributes significantly to the high angle of attack performance. The BERP-III blade design also integrates

[1] The concept of thrust-weighted solidity is often used in the US to compare the lifting capability of different blade planforms. However, while this concept may be useful in project studies it is considered too simplistic to be applied to complex tip planforms, such as the BERP blade, Perry (1989)[234]

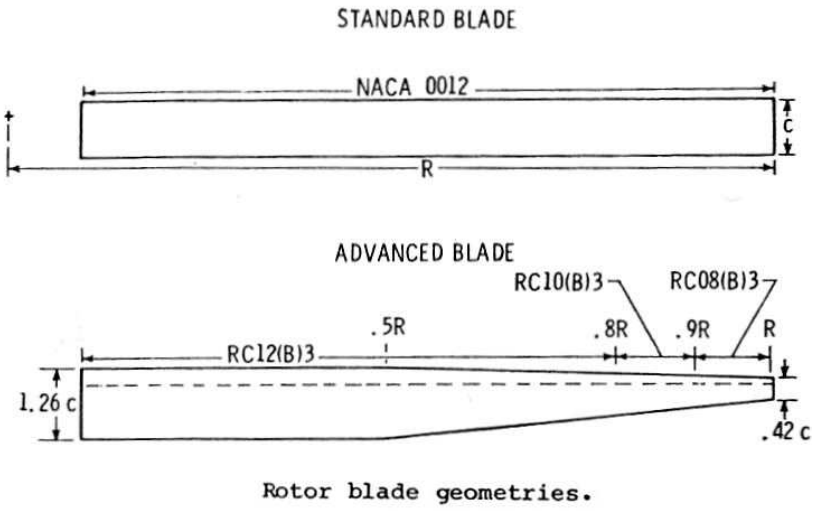

Figure 39: Advanced Tapered Tapered Tip Blade, Berry (1981)[37]

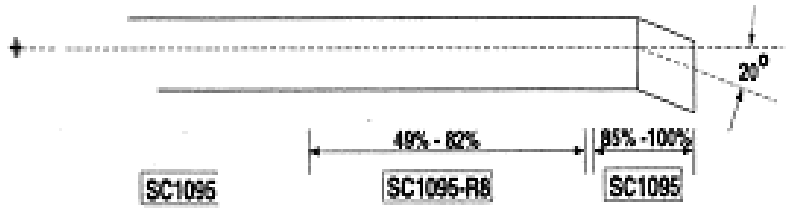

Figure 40: Swept Tip Blade, Alansky (1981)[6]

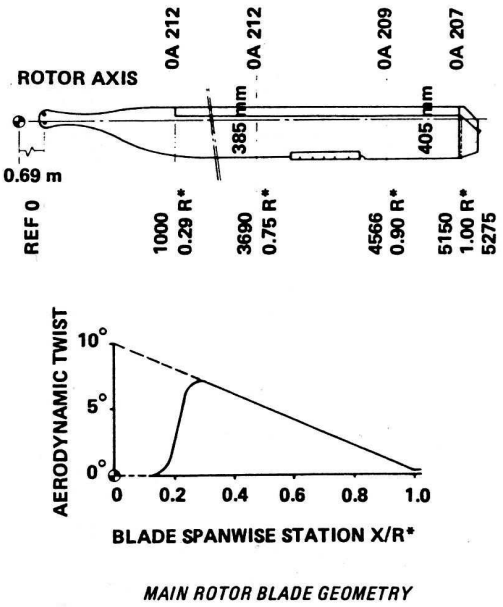

Figure 41: Blade with 10 deg twist and Swept-Tapered Tip, Roesch (1980)[251]

the properties of the tip with the use of a high-lift aerofoil just inboard of the tip. The aerofoils were designed by Wilby (1997 and 2001)[317],[319] and the cambered RAE9645 aerofoil is used as the main high-lift aerofoil, together with the thinner RAE934 in the tip region, a positive pitching moment aerofoil in the form of RAE9648 (later changed to a similarly reflexed RAE9683 for Lynx and the thicker RAE9651 on the EH101 blade) is used inboard to achieve moment balance, Perry (1987).[233]

In Europe, in the early 80's, Aerospatiale developed the SA365N Dauphin-2 Helicopter, Roesch (1980),[251] Figure 41, and compares the hover Figure of Merit for the old NACA0012 rotor with the new SA365N prototype rotor that replaced it. The latter used an increase in twist from 8 to 10 degrees, new OA2-series aerofoils (OA212 at the root, OA209 outboard, and OA207 near the tip). The new blade featured a tip-cap, which had the leading edge corner cut off at 45 degrees, and the trailing edge clipped at an angle of about 15 degrees. The tip cap also increased the diameter from 11.68m to 11.93m. The trailing edge tab was also used to extend the chord, outboard of the trim tabs to enhance the lifting capability of this blade.

A similar, 45 degrees leading edge corner tip cap, is found on the tail rotor of the EH101. This type of tip tends to relieve the clustering of isobars in the forward leading edge corner, and would therefore be expected to reduce the tendency for a profile power growth due to shock induced separation at high lift and moderate tip Mach number (except that a weak shock may form at the outer corner, as later identified in CFD simulations by the writer). As mentioned earlier, the low aspect ratio of the tail rotor blades gives rise to a significant amount of tip relief. This avoids the need for sweep, particularly if the aerofoil in the tip region is not too thick and low tipspeed is used. On the EH101, the tail rotor tipspeed is lower than that of the main rotor for noise reasons. Hence there is a greater need for sweep on the higher aspect ratio main rotor blades.

A similar tip shape to the swept constant chord tip of the UH60 was employed on the AH-64 Apache, as reported by Amer and Prouty (1983).[10] The aerofoil on this blade is a 9.5% HH02 airfoil, and uses a long reflexed tab to counter the slight nose droop, which would otherwise give a nose-down pitching moment. During the early stages of development the Apache suffered from interactional aerodynamic problems and a lack of tail rotor authority which lead to many fin and tail re-designs.[243] The tail rotor is a double teetering scissors type rotor with unequal azimuth spacing (of 60 and 120 degrees). The tail rotor blades are typically of constant chord with a classical hemispherical, or volume of revolution, tip cap.

Mantay and Yeager (1983)[196] considered parametric tip effects for conformable rotor applications. In this work, the focus was on the aft location of the aerodynamic centre which results from a simple swept (sheared)

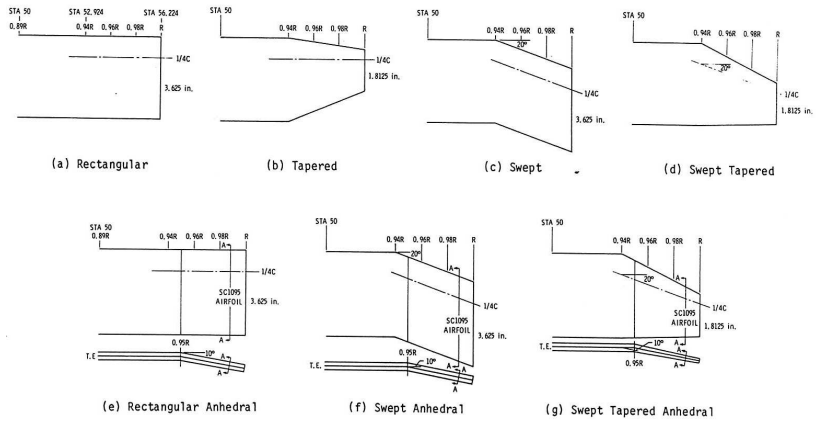

Figure 42: Tests on a range of Swept-Tapered tips, Mantay and Yeager (1983)[196]

back tip (Black Hawk and Apache). Tip shapes tested include rectangular, tapered, swept, swept-tapered, and for the first time tips with anhedral were tested in the form of rectangular anhedral, swept anhedral, and swept-tapered anhedral, Figure 42.

In the UK, there were initial concerns that the potential hover benefit of anhedral might not be able to be realised due pitching moments in forward flight. However, it was soon realised that blade tip anhedral produces a pitching moment variation around the azimuth that compensates for the effects of sweep and forward (notch) offset, and so could be used to reduce once-per-rev control loads on advanced tip shapes. The author carried out tests in the Westland wind tunnel in 1985 on a model rotor with various tip shapes, including the BERP tip with 10 and 20 degrees of anhedral angles. These tests were then followed by hover tests in 1986, which confirmed the expected beneficial effect of anhedral. It is now generally accepted that a tip with about 20 degrees of anhedral will yield an increase of about 0.02 in the Figure of Merit, with no performance penalty in forward flight. However, it was later discovered through computational work that this benefit might not be maintained on main rotor blades with high aspect ratio.

In parallel with preliminary design studies for the BERP-III blade, which commenced in 1981, a swept tip was tested by RAE on the Puma, Figure 43, as reported by Riley and Miller (1983) ,[249] following on from the collaborative work of Wilby and Phillipe (1982) .[320] The flight experiments were carried out with dissimilar tips, and showed that the new tip consumed less power due to the suppression of supercritical flow on the advancing blade. The flight measurements were compared with the earlier transonic small perturbation, TSP, analysis of Grant (1979) .[121]

Further wind tunnel tests together with rotor aerodynamic studies, and dynamics and composites design work, were carried out in the early 80's. The BERP tip was first demonstrated on Lynx in 1985.

While forward flight performance was being sought in the UK, acoustic measurements on a full scale rotor with four tip shapes (rectangular, tapered, swept, swept-tapered), tested in the NASA Ames 40 ft x 80 ft tunnel were reported by Marianne Mosher (1983).[212]

McVeigh of Boeing-Vertol (1984)[208] reports the effect of different tip shapes on hover Figure of Merit (FoM), and also includes a discussion of aerofoil performance, in addition to acoustics. McVeigh compares the performance of square, swept, swept-tapered and tapered blades, Figure 44. It is interesting to note that although the tapered tip has the best hover FoM, this rapidly falls off at high disc loading, presumably due to early power divergence which arises as a consequence of the vortex-induced loading peak near the tip, combined with a narrow tip chord. If the tip chord is too small, power divergence occurs despite the fact that most helicopter main rotors are not particularly highly loaded in hover.

Further 3D transonic computer analysis is reported by Tauber (1984)[292] of NASA Ames, who compares experimental and computed results for a tapered blade with a swept (sheared) tip, and shows shock de-localisation for a rectangular and 30deg swept-back tip. Here the sweep angle quoted is that of the leading

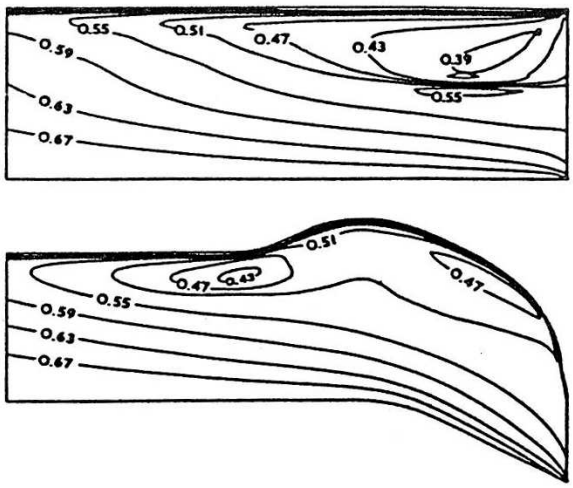

Figure 43: Pressure Contours on Rectangular and Swept Tip showing Reduced Tendency for a Shock to Develop, Riley and Miller (1983)[249]

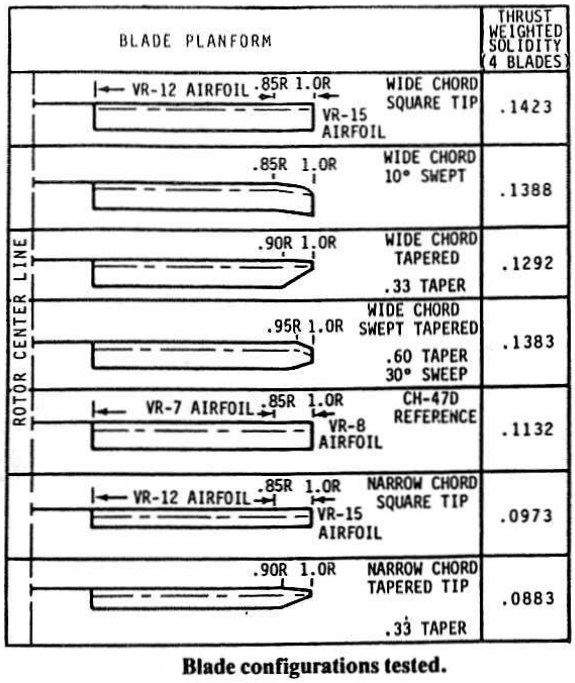

Figure 44: Variety of Tip Shapes Tested at Boeing Vertol, McVeigh and McHugh(1984)[208]

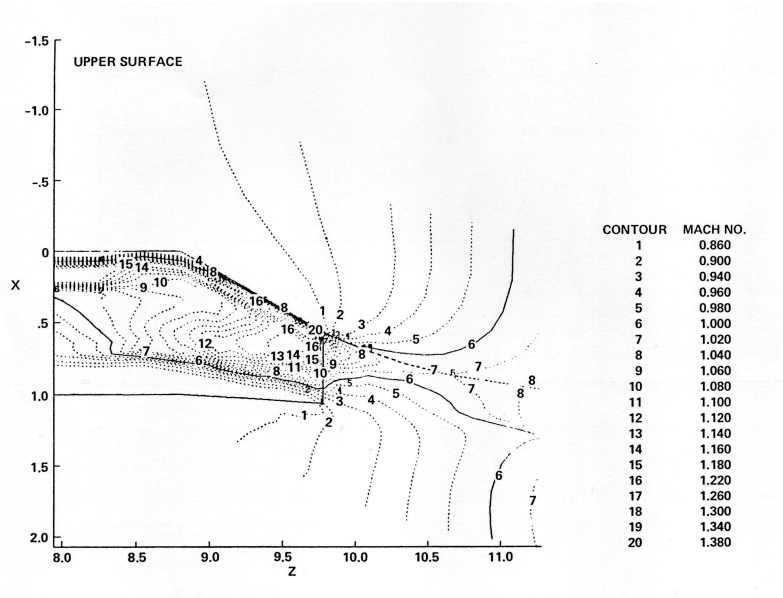

Figure 45: Prediction of Mach Number Contours on Swept-Tapered Tip showing De-localisation of Shock Outwards from the Tip, Tauber (1984)[292]

edge. It is apparent from these computations of compressibility effects on the advancing blade at zero lift, that this amount of sweep, whilst it relieves the shock strength, is not really sufficient, and at least 40deg swept tip was required to reduce de-localisation. Due to pitching moment considerations, recourse was made to the 30deg sweep with modified aerofoil sections, but the problem of de-localisation still persists, Figure 45. One feature of the swept-tapered tip is that there is an effective loss of leading edge sweep near the tip leading edge (sharp) corner. Also, when the shock is well aft, as in the computed conditions, the effective sweep of the trailing edge is relatively low and with the tip edge simply cut square the effective sweep is reduced where it is most needed. The reluctance to employ higher sweep is probably a consequence of the desire to suppress any adverse aeroelastic effects arising from a rearward aerodynamic centre.

Apparently, several tip shapes were considered for the Sikorsky UH-60 Black Hawk and S-76, as described by Balch (1984),[20] Figure 46. In this paper, the performance of the main rotor in proximity to the tail rotor is also considered. Again the emphasis is on achieving a good figure of Merit.

In Europe, Wagner (1984)[312] made comparative measurements of unsteady pressures on four oscillating wing tip models, of NACA 0012 aerofoil, having rectangular, swept, trapezoidal and Ogee tips, Figure 47. The tests were at low speeds, so any compressibility effects were not included. The paper shows how the isobars bunch up in the forward corner of the tip, especially on the Ogee tip, which experiences extreme CL's. Measurements of the vortex roll-up were made using an ultrasonic measuring device. Wagner reports observing up to 2 vortex cores behind the Ogee tip.

In the mid 80's techniques such as the wide-field shadowgraph were developed to study the rotor wake in hover, and Parthasarathy, et al (1985)[230] confirmed the earlier work of Landgrebe, and Kocurek and Tangler, already cited. These experiments supported the effort to obtain a better understanding of the wake and verify the prescribed wake and free wake methodologies, which were being developed at this time. Favier, et al (1985)[110] describe a lifting line vortex wake model for hover and axial climb, and later Quackenbush (1987)[244] describes the development of a free wake rotor model.

It is perhaps worth remarking that, most of the vortex wake visualisation and wake trajectory measurements, which were available to validate vortex wake models, were initially carried out on blades with rectangular tips. Only recently has there been interest in identifying the differences in vortex structure due to different tip shapes, as will be described later in this review.

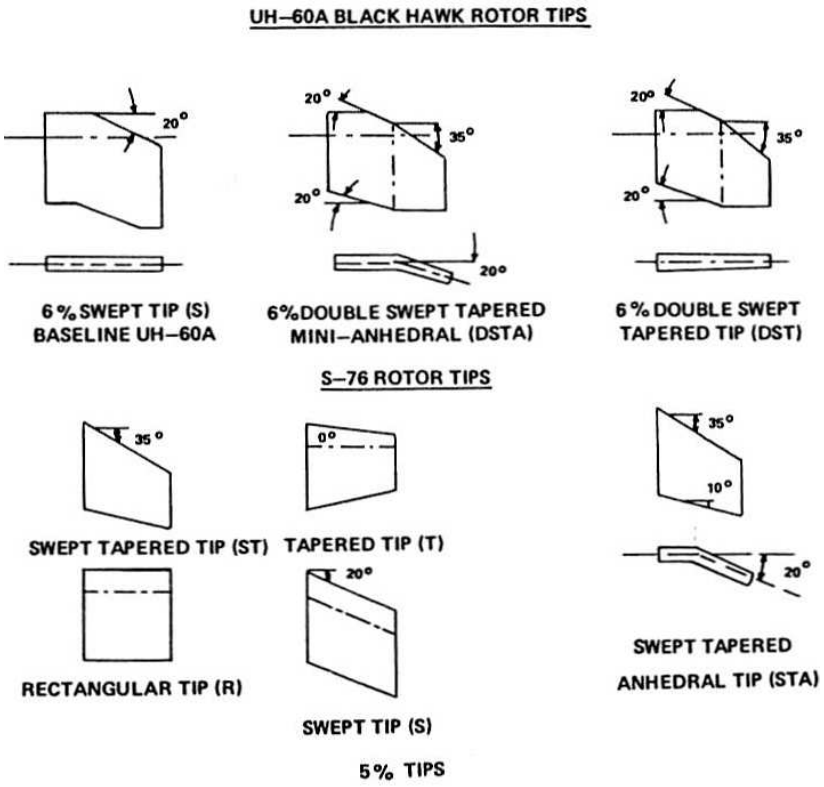

Figure 46: Tip Shapes Tested by Balch (1984)[20]

Also in the mid 80's a research effort was underway to design blades for the V22 tilt rotor, Felker, et al (1985),[111] and several tip shapes were considered for this application. These included a clipped-ellipse baseline tip, a swept-tapered tip, and a square tip, Figure 48. Again the aim was to maximise the hover FoM, while noise was probably also a consideration due to the high tipspeed of tilt rotor aircraft.

Development flying of the BERP blade was carried out in the early eighties on the Lynx. An extensive flight programme was undertaken to establish the loads on the new composite blade design and provide data for comparison with theoretical models. Vibration and loads were analysed by Hansford (1987)[129] to gain insight into the structural load characteristics of the and new composite BERP blade compared to the standard metal blade. The BERP blade gave the Lynx good manoeuvre capability and the expanded flight envelope has enabled weight growth from 8,500 lb to somewhere in the region of 15,000 lb for the latest variants.

The BERP blade enabled the Lynx to gain the World Speed Record, which still stands for this class of helicopter, and the blade design is described by Perry (1987),[233] Figure 49. The speed attained was 400.87 km/hr (216.3 kts or 249.1mph), corresponding to a tip Mach number of 0.977, and the rotor reached an advance ratio of 0.5.

The various fight trials of the BERP blade also included pressure measurements on the Lynx composite main rotor blade (CMRB), which were reported by Isaacs and Harrison (1989).[153]

In contrast to the BERP activity to expand the forward flight envelope, Kelly and Wilson (1985)[164] describe a model blade of an 'Advanced Rotor' for the AH-64 Apache aimed at improved hover performance. The model blade had constant chord out to 80% radius, and then had a 5:1 taper, see Figure 50. The test results showed that the tapered blade produced a 6.4% improvement in FoM, and had lower power in the forward flight tunnel tests. However, it is doubtful if the retreating blade envelope would have been maintained.

A team from Boeing Vertol, of Cowan, Dadone and Gangwani (1986)[84] also tested a model-scale advanced rotor, both in the Boeing Vertol Wind Tunnel and in the DNW tunnel where acoustic measurements were

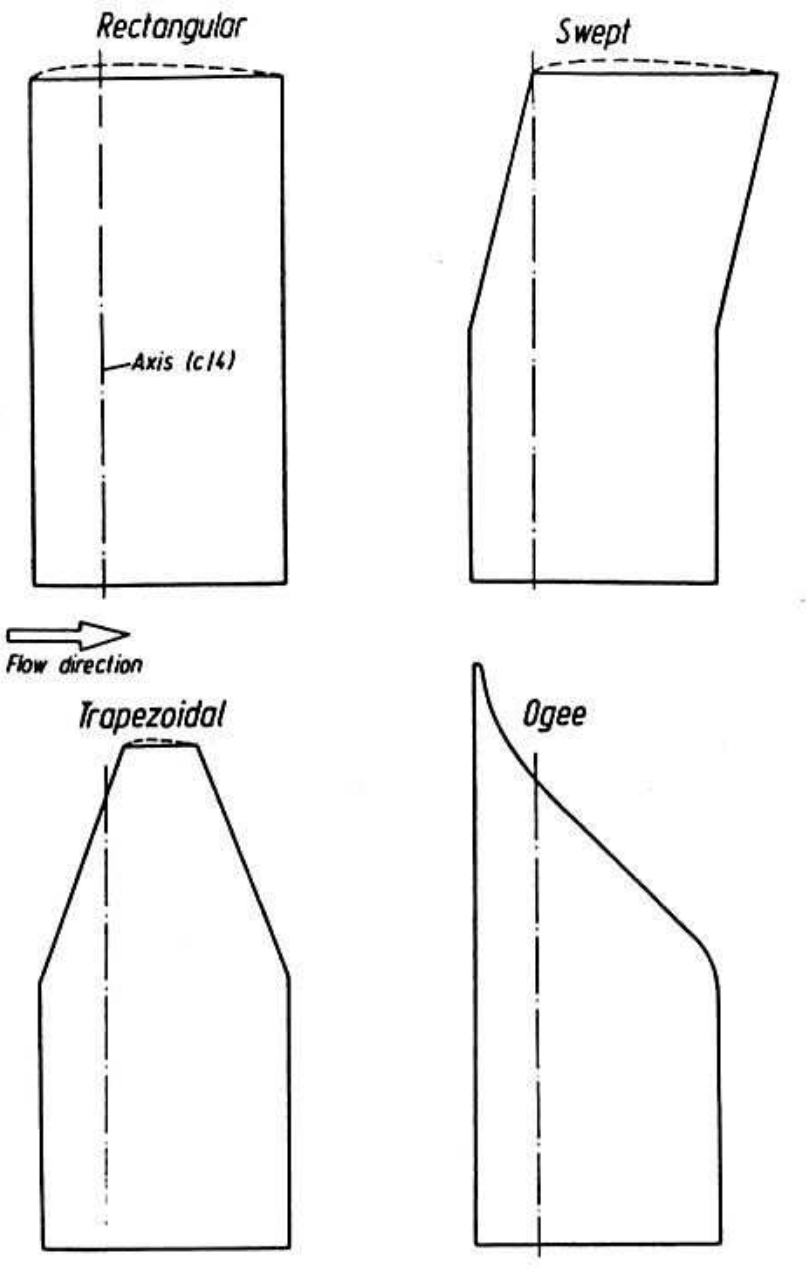

Figure 47: The four tips used by Wagner on oscillating wing tip model (1984)[312]

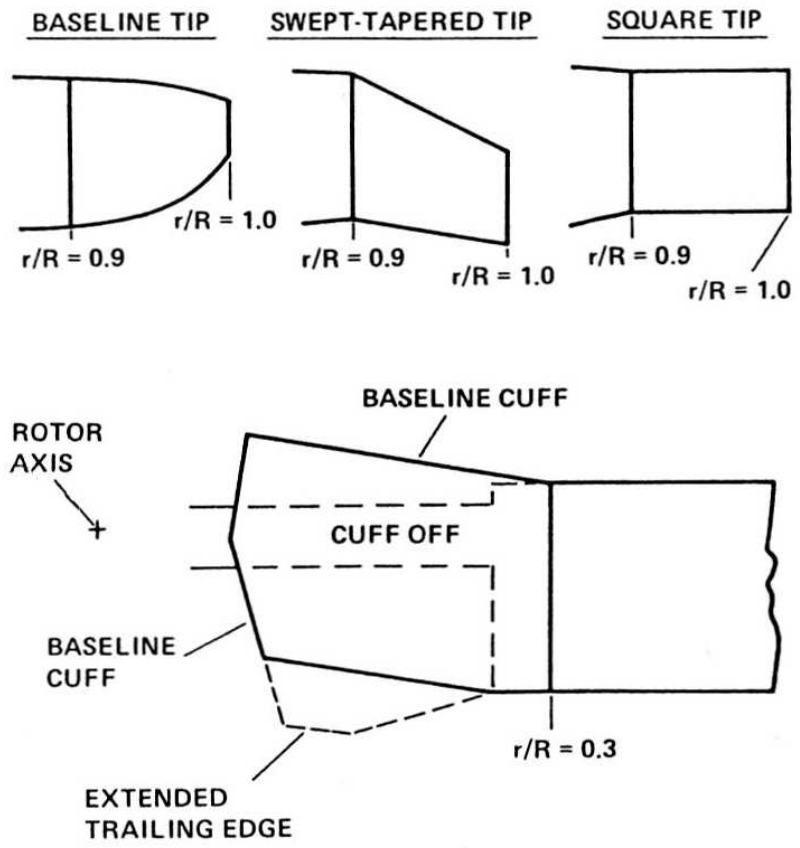

Figure 48: Tip shapes considered for the Advanced Technology Blade (ATB) of the V-22 Tilt-Rotor Aircraft, Felker, et al (1985)[111]

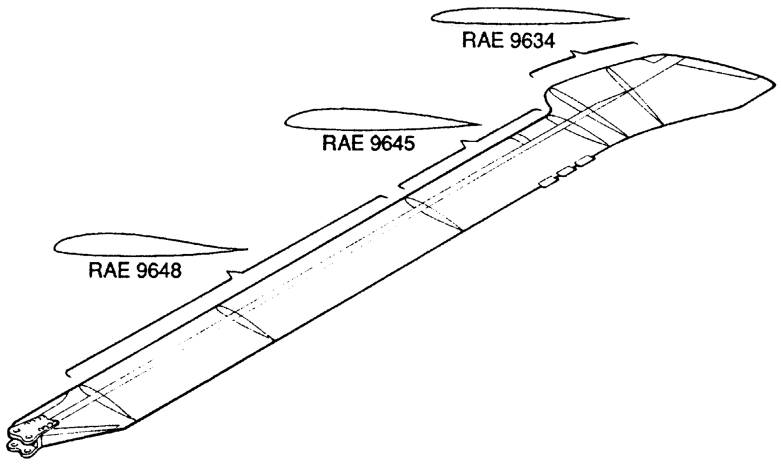

Figure 49: Distributed Aerofoil Section on the British Experimental Rotor Programme (B.E.R.P.) Blade, Perry (1987)[233]

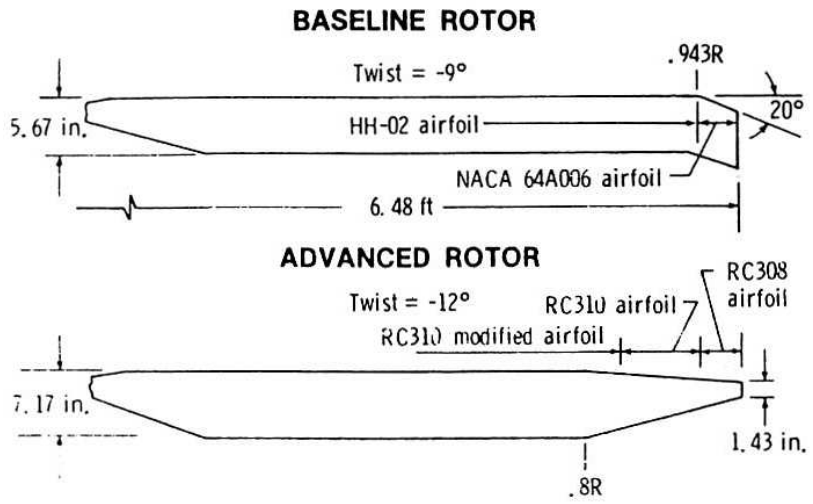

Figure 50: The Advanced Rotor for the AH-64 Apache designed to improve Figure of Merit in Hover, Kelley and Wilson (1983)[164]

obtained. In these tests the blades had VR12 and VR15 aerofoils, and were highly tapered (3:1) outboard of about 85%R, with a non-linear twist of 12.75 degrees. The highly tapered tip was probably intended to give a good Figure of Merit in hover and have a low acoustic signature. The tip planform has only a very small amount of sweep back, and so might be expected to suffer compressibility problems at high tip Mach numbers, and perhaps premature tip-stall at high loading. However, within the flight envelope, the torsional loads would be expected to be low on a blade with this type of tip planform. Data from the above tests was compared to a Boeing Vertol rotor analysis (B65), NASA Transonic Flow Analysis for Rotors (TFAR), and an Army Finite Difference Rotor (FDR) code. The TFAR and FDR codes were also coupled with the B65 rotor model in an attempt to match the chordwise pressures at 80%R for azimuths in the first and second quadrants.

While more sweep-back is often desirable to relieve compressibility effects, it also has some disadvantages. On an aft-swept tip it is almost inevitable that the c.g. will move aft, and in some cases the tip aerofoil may be wholly behind the blade quarter-chord line. Aft movement of the c.g. can be minimised by adopting very thin, light-weight materials for the trailing edge skins in the tip region, although this may make the blade vulnerable to damage and could incur a cost penalty. The use of lightweight trailing edge skins also helps to reduce the torsional inertia of the tip. In contrast to a simple aft-swept tip, the forward notch offset of the BERP tip helps to the bring the c.g. forward, and also avoids the aerodynamic centre becoming too far aft.

An alternative is to consider forward swept tips such as that proposed by Perry, in consultation with Dr. Nangia. Such a tip was tested in the Westland wind tunnel in 1987, but the general conclusion was that this tip had a tendency for premature flow separation due to the bunching of isobars in the junction region and at the tip. A typical tip planform considered in the tests is shown in Figure 51. A rearward protruding area distribution may help to alleviate this problem, but may reduce the effective the forward sweep. Attempts to overcome this drawback, tend to lead to a tip of large area, which would have an adverse impact on the hover performance. Also, since the aerodynamic centre is ahead of the torsional axis (shear centre), such that the blade would be aerodynamically unstable, and overall aeroelastic stability would certainly be an issue, although the c.g. can be placed well forward on a swept forward tip. More recently, the writer also reviewed the concept of a forward-swept tip in a subsequent design study. The aim was to alleviate advancing blade compressibility effects, while ensuring the c.g. would be well forward, but the design was not taken further due to concerns over retreating blade performance.

Later in this review, the subject of swept forward tips is raised once again, when the potential for avoiding shock de-localisation is discussed by Baeder and supported by CFD analysis.

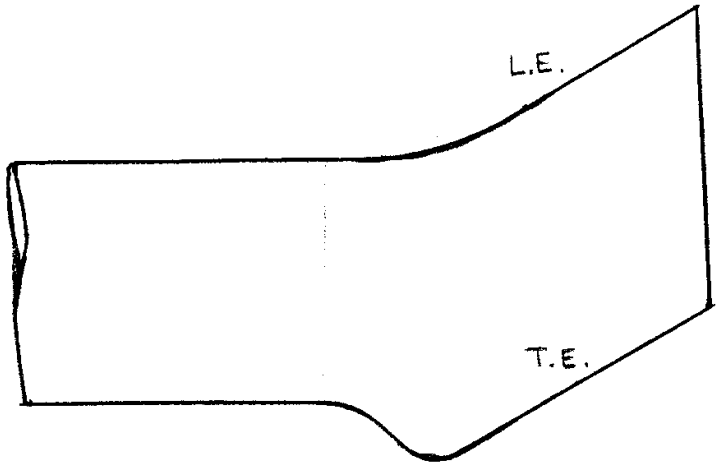

Figure 51: Sketch of a Forward Swept Tip similar to that Proposed by Perry and Nangia and Tested in the Westland Wind Tunnel in 1987

The topic of noise reduction is an important consideration in rotor design. The main driver is the tipspeed, and to a lesser extent blade loading. For this reason the EH101 was designed with a low main rotor tipspeed, and an even lower tail rotor tipspeed. Also the highly swept BERP tip has a thin aerofoil and low tip volume. The notch off-set and section change together with the sweep of the BERP tip eliminate any shock formation and de-localisation. However, helicopters such as early Lynx and Chinook, with rectangular tip blades, have higher tipspeed and BVI noise is often a concern.

In the late 80's, a new model rotor rig was developed at WHL with the intention of carrying out acoustic tests on a range of tip shapes. In a theoretical study, Beddoes (1986) found that splitting the tip vortex was more effective in reducing BVI noise than attempting to enlarge the core size. This led the writer to design the Vane Tip, Figure 52 which was then tested as a fixed-wing model in the WHL wind tunnel in 1987. These tests confirmed that the Vane Tip configuration generated twin vortices which remained distinct over a wide range of incidence, as shown by smoke visualisation in the working and diffuser sections of the wind tunnel. Following commissioning tests in hover, and shake-down tests in the WHL tunnel, the Vane Tip was tested on a model rotor in the acoustically lined 24ft wind tunnel at Farnborough. A 5.6dB reduction in BVI noise was demonstrated, as reported by Brocklehurst and Pike (1994).[59] The Vane tip has been included here as an example of the developments in rotor research which were taking place in this era. In contrast to Tangler's sub-wing, previously cited, which aimed to diffuse the trailing vortex, the Vane Tip produced two equal vortices that remained discrete for many chord lengths as verified by the wind tunnel tests. The Vane Tip was subsequently modelled using the VSAERO panel method in the early 1990's, Figure 53.

In the late 80's, interest in the effect of sweep on BVI was highlighted in a paper by Hardin and Lamkin (1987)[130] where a cranked blade is considered to 'reduce interaction length' and thus minimise the time during which the parallel blade/vortex interaction is taking place. The cranked rotor is not without dynamic problems, but was further tested in the mid 90's, and the concept of a forward swept tip has since been examined by Baeder (see later). The interaction length of the BVI event may work against an aft swept tip, since at some advancing blade azimuths the vortex may be aligned with the leading edge of the swept tip.

Towards the end of the 1980's, anhedral was introduced on the BERP blade to alleviate once-per-rev control loads, and back-to-back flight tests were carried out on EH101. As found in model rotor tests carried out by the writer, the effect of sweep and notch offset were balanced by anhedral in forward flight, and the benefit to hover performance was also confirmed.

Although used to advantage on the BERP blade, the mechanism by which anhedral reduces the hover power was not completely understood at the time, although it was clear that the position of the tip vortex was

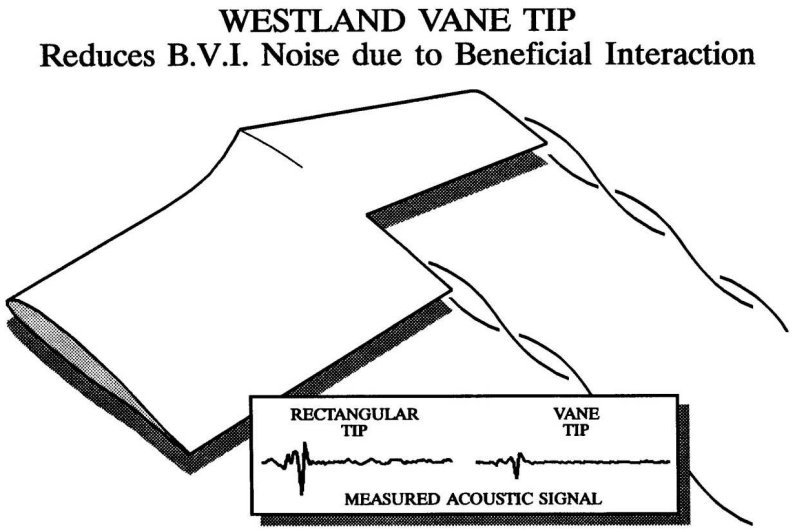

Figure 52: The Westland Vane Tip as tested on a Mach-scale Model Rotor Blade by Brocklehurst and Pike (1994)[59]

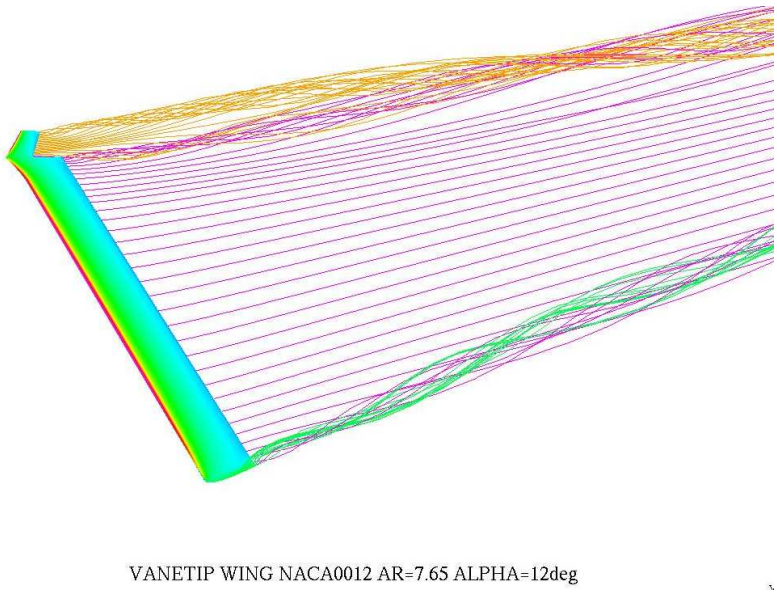

Figure 53: Analysis of the Westland Vane Tip using VSAERO, Brocklehurst and Pike (1994)[59]

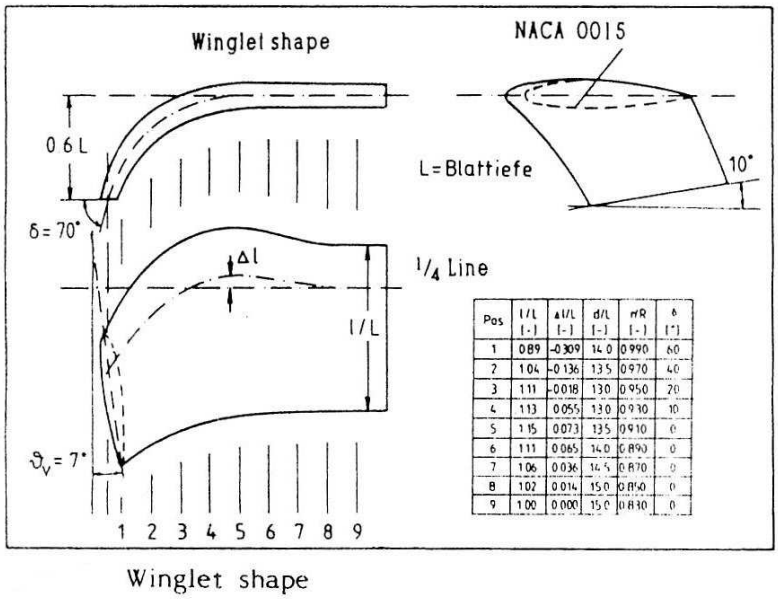

Pos	l/L [-]	Δl/L [-]	d/L [-]	r/R [-]	θ [°]
1	0.89	-0.309	14.0	0.990	60
2	1.04	-0.136	13.5	0.970	40
3	1.11	-0.018	13.0	0.950	20
4	1.13	0.055	13.0	0.930	10
5	1.15	0.073	13.5	0.910	0
6	1.11	0.065	14.0	0.890	0
7	1.06	0.036	14.5	0.870	0
8	1.02	0.014	15.0	0.850	0
9	1.00	0.000	15.0	0.830	0

Figure 54: Downward Pointing Winglets by Muller (1998)[214]

initially displaced downwards in the wake. Measurements by the writer at Westland in the 1983 on a model of the BERP blade showed that the tip vortex tends to snake back towards its usual position near the first blade passage. This snaking of the tip vortex trajectory has also been noted in the computational results presented later in this thesis for a tail rotor blade with a 20 degree anhedral tip, where it was found that the anhedral induced an inboard shift of the blade loading in the tip region.

The non-planar properties of the BERP swept-back anhedral blade tip may also come into play, as postulated by van Dam for swept-tip wings, and may become progressively more effective as incidence increases (as discussed in the first part of this literature review). Subsequent computational work at Westland has suggested that while the BERP blade benefits significantly from anhedral in hover, the same may not be true for high aspect ratio (R/c) main rotor blades with a more conventional tip shape.

Other researchers have also been intrigued by the idea of gaining performance through the use of anhedral or a small winglet. Muller (1986, 1988, 1990)[213214215] has investigated downward pointing winglets for rotorcraft, initially in hover, but also in forward flight, Figure 54. Muller mounted the downward pointing winglet on an otherwise rectangular tip, and found the winglet height limited by yawed flow considerations. As with anhedral, the hover efficiency was improved by a small amount.

Anhedral has also been used to improve the static thrust on propellers, although little information has been found in the scientific literature. A practical example is shown in Figure 55, as manufactured by the small American company, Prince Aircraft Inc. However, the impact of anhedral on propeller in cruise is likely to be minimal (unless other small benefits accrue from the tip design) since the vortices quickly pass downstream. Anhedral has also been suggested for use on Tilt-Rotor Blades by Patt and Karem (2011) as revealed in their US Patent,[231] again as a means of improving the hover Figure of Merit. Loading distributions are shown where the peak loading is reduced due to the trailing vortices being further away from the following blade.

In the 1987 Nikolsky Lecture, Drees (1987)[95] compares schematics of the roll-up from a square tip, a curved swept tip and a BERP tip, and ponders the question of placing the vortex roll-up further outboard to maximise the apparent rotor radius.

During the late 1980's, computer resources had reached the point where numerical solutions to the Euler and Navier-Stokes equations were now possible for 3D configurations, at least within research organisations, if not in industry. Srinivasan, et al (1988)[275] presents a numerical simulation of tip vortices from wings in

Figure 55: Propeller Blade with Anhedral to Improve Efficiency and Enhance the Static Thrust, as Manufactured by Prince Aircraft Inc

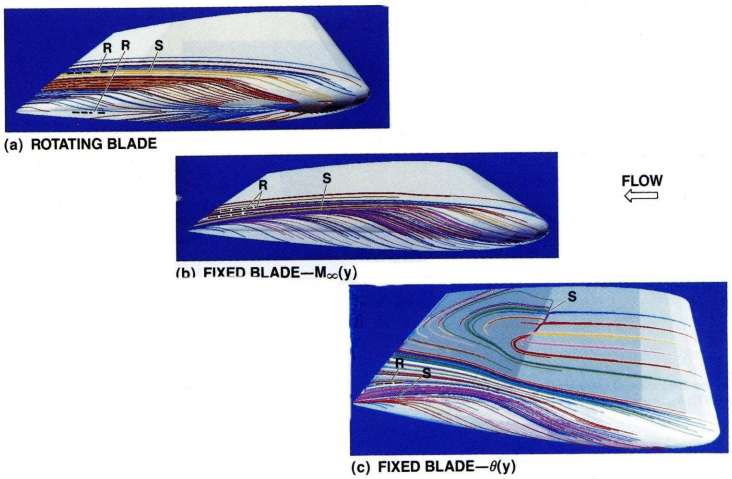

Figure 56: Surface Particle Flow Traces in the Tip Region of Rotating and Fixed Blades, M_tip=0.877, Re=3.93x10^6, Srinivasan and McCroskey (1988)[273]

subsonic and supersonic flow. In this paper Srinivasan modelled a rectangular wing with a square-cut tip (H-H grid), a so-called hemispherical or rounded tip (O-O grid), and a bevelled tip (H-H grid), together with a swept-tapered wing, the ONERA wing, and a modified ONERA Wing of AR 5. This paper is concerned with validation and demonstration of the potential of the CFD method, rather than making any pronouncements on the performance of the tips themselves, and shows that CFD provides a powerful tool for analysing and understanding the aerodynamic characteristics of wings and rotor blades. In a second paper, Srinivasan and McCroskey (1988)[273] extended the method to include a Navier-Stokes calculation for a hovering rotor. Results for a rotating blade are compared to the data of Caradonna and Tung (1981).[73] The surface particle traces and pressure contours from Srinivasan and McCroskey [273] are re-produced in Figure 56, together with some examples of the clustering of the pressure contours in the tip region of the blade, Figure 57. This work was the first application of CFD to a hovering helicopter rotor.

This ground breaking computational effort lead to the need to compare with high quality test data, and also a desire to explore and compare different rotor tip planforms to test and demonstrate the newly available CFD methods.

Through a collaborative US-UK agreement, a full-scale model of the Lynx-BERP tip was tested as a fixed-wing in the Westland wind tunnel by the writer in 1989 and the computational effort was reported by Duque (1989)[100],[101] Figure 58. Further comparisons, including some sideslip cases were reported by Brocklehurst and Duque (1990),[58] Figure 59 and some extreme Mach number/incidence cases, Figure 60. At that time CFD

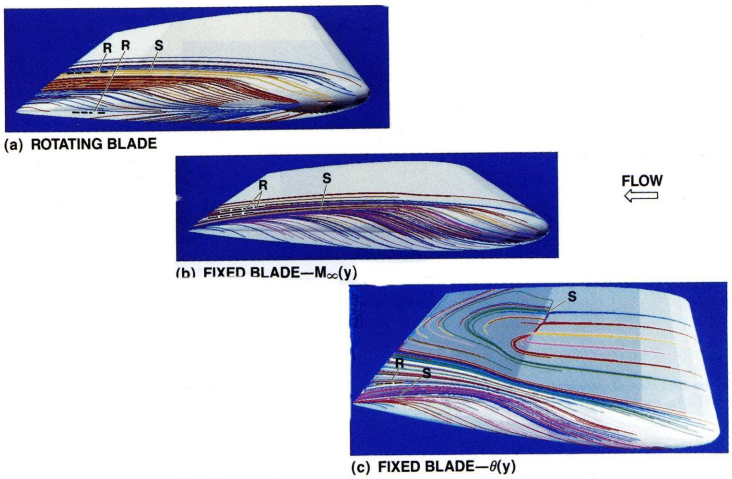

Figure 57: Surface Particle Flow Traces in the Tip Region of Rotating and Fixed Blades, M_tip=0.877, Re=3.93x10^6, Srinivasan and McCroskey (1988)[273]

methods were only available at large research establishments, and the LANS3D code was run by Duque on the Cray YMP at NASA Ames. These CFD calculations highlighted the favourable 'shock-eating' qualities of the BERP tip design. Different tip shapes, including the Puma tip, were also compared by Duque (1992),[102] Figure 61.

In addition to simulating the separation on the BERP blade at very high incidences, Beddoes (1991),[31] Figure 62, also modelled the stall pattern on a swept-tapered tip, Figure 63, which had been tested in the WHL wind tunnel.

The Lynx-BERP database has since been used to provide support for the development of rotor codes, such as ACROT, Beddoes (1992),[32] and CFD simulations, such as those presented later in this thesis. At the time the computational effort was similar to that required for the test, whereas simulations are nowadays much cheaper than parametric tests. However, the wind tunnel is still a valuable facility, and is has an important role in providing data for confirmation of a new design and for validation of CFD methods.

Recently, the HMB code has been used to simulate the BERP blade, and a means of extending reduced-order rotor models, Beedy (see later). Comparisons were made with the wind tunnel pressure measurement tests described above, and some of the simulations also included unsteady conditions, Brocklehurst, et al, 2003 .[60]

The agreement between the CFD of Duque and the pressure measurements on the BERP wing was particularly good at incidences below stall, but failed to provide a correct simulation when the inboard part of the wing was stalled. Nevertheless, the potential of the RANS method for predicting the performance of future rotor tip designs was clearly demonstrated.

Following the collaborative BERP tip investigations, NASA commissioned unsteady tests on a rectangular tip wing (with aerofoil of revolution end closure), Piziali (1994).[239] This data has been used by Beddoes at WHL to develop the ACROT model, and continues to form a useful database for further substantiation of 3D unsteady CFD simulations.

While the NASA Ames effort employed a full CFD analysis with structured grids to discretise the true geometry, Rajagopalan and Lim (1991)[245] at Iowa State University, developed a laminar Navier-Stokes solver to model a rotor in hover. They used point momentum sources distributed along the radius to represent the rotor blade. At Maryland, Kim and Chopra (1992)[165] investigated the aeroelastic response of various blade shapes, including straight (rectangular), swept (sheared, UH-60 type), anhedral and tapered tips, Figure 64.

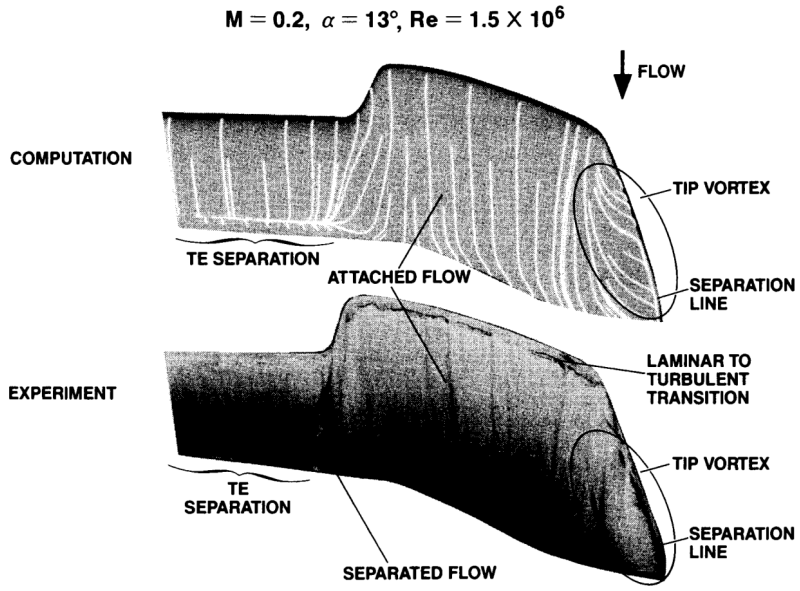

Figure 58: Surface Flow Validation, Duque (1989)[101]

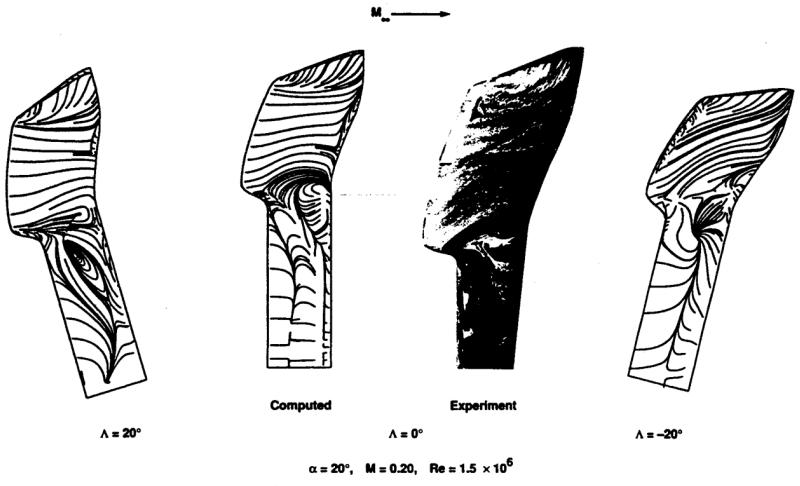

Figure 59: Computed and Experimental Surface Streamline Patterns at High Incidence and Sweep, Brocklehurst and Duque (1990)[58]

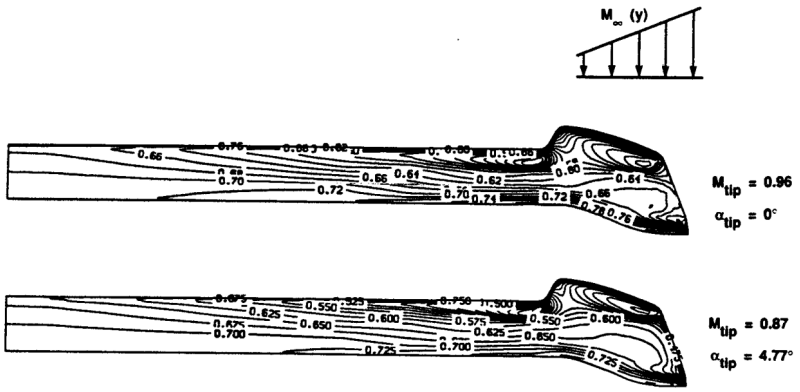

Figure 60: Computed Surface Pressure Contours with Sheared Free-Stream Mach Number, Brocklehurst and Duque (1990)[58]

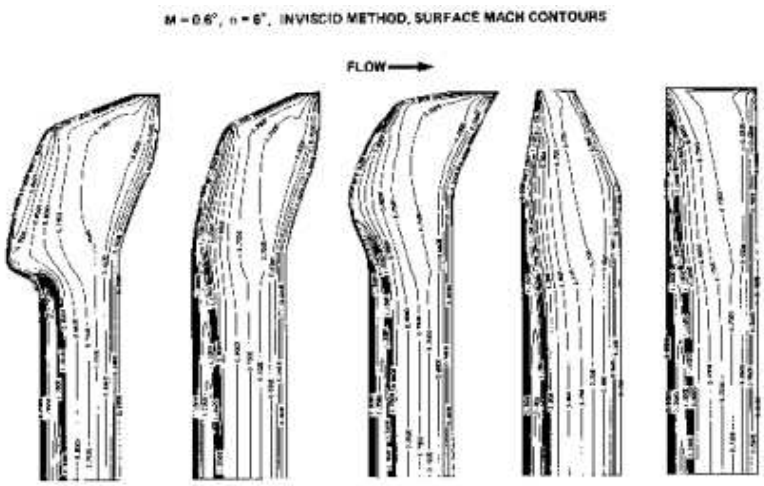

Figure 61: Planform Effects at Transonic Speed from Inviscid CFD Computations at M=0.6 and 6 degrees, by Duque[102]

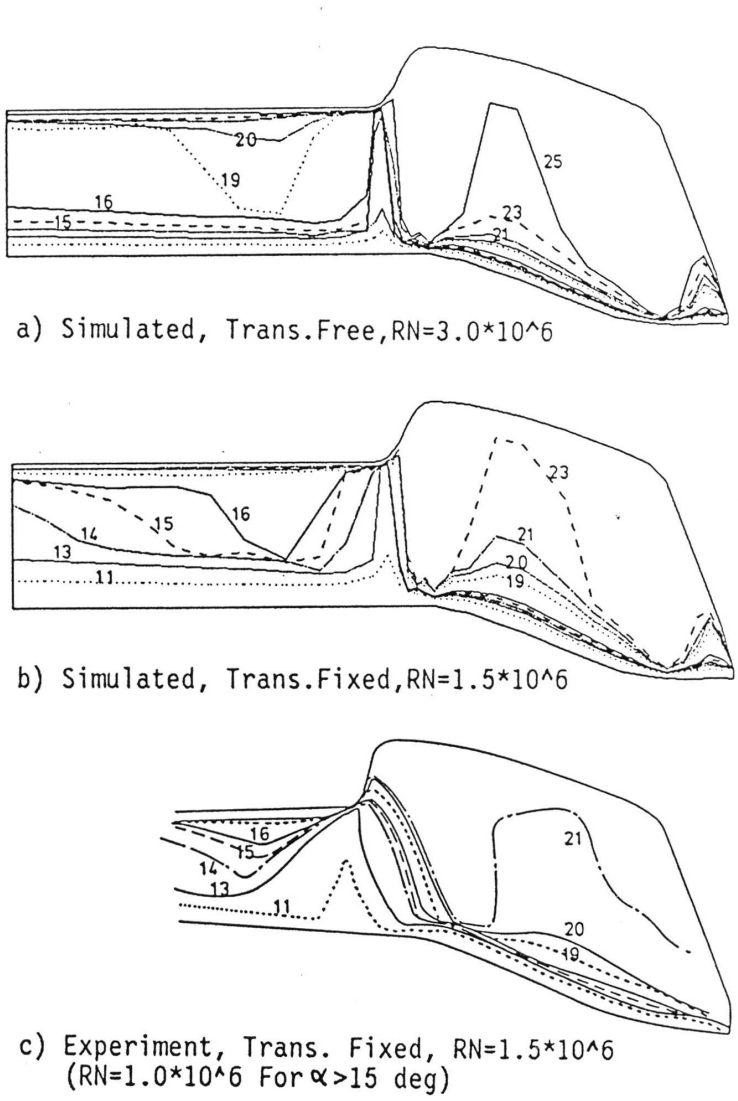

Figure 62: Progression of Separated Flow with Root Angle of Attack and Comparison of Prediction and Test, Beddoes(1991)[31]

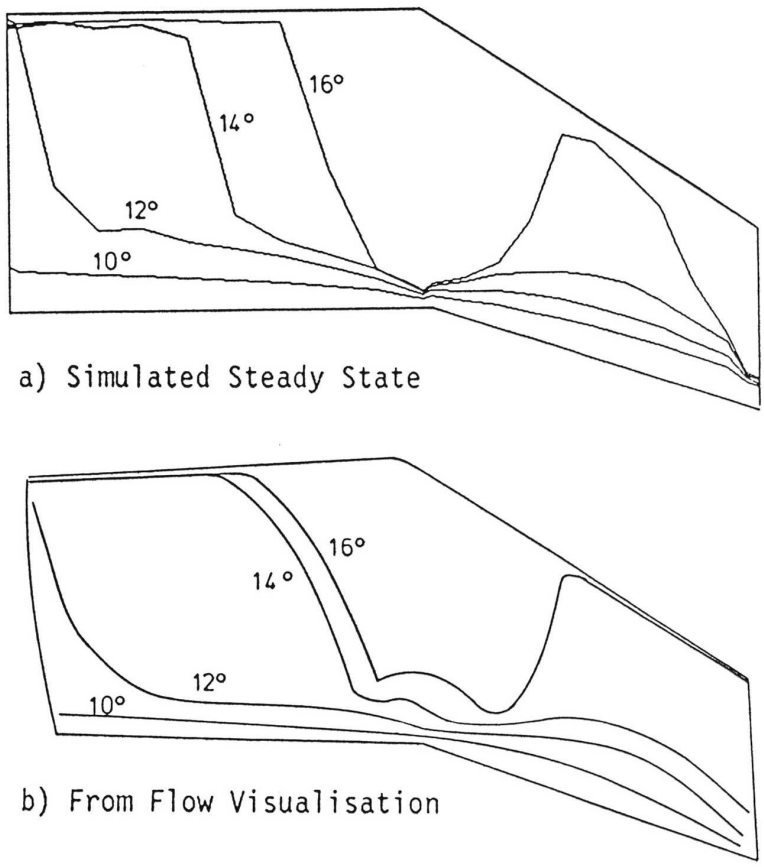

Figure 63: Progression of Predicted Separation on a Swept-Tapered Tip compared to Wind Tunnel Data, Beddoes(1991)[31]

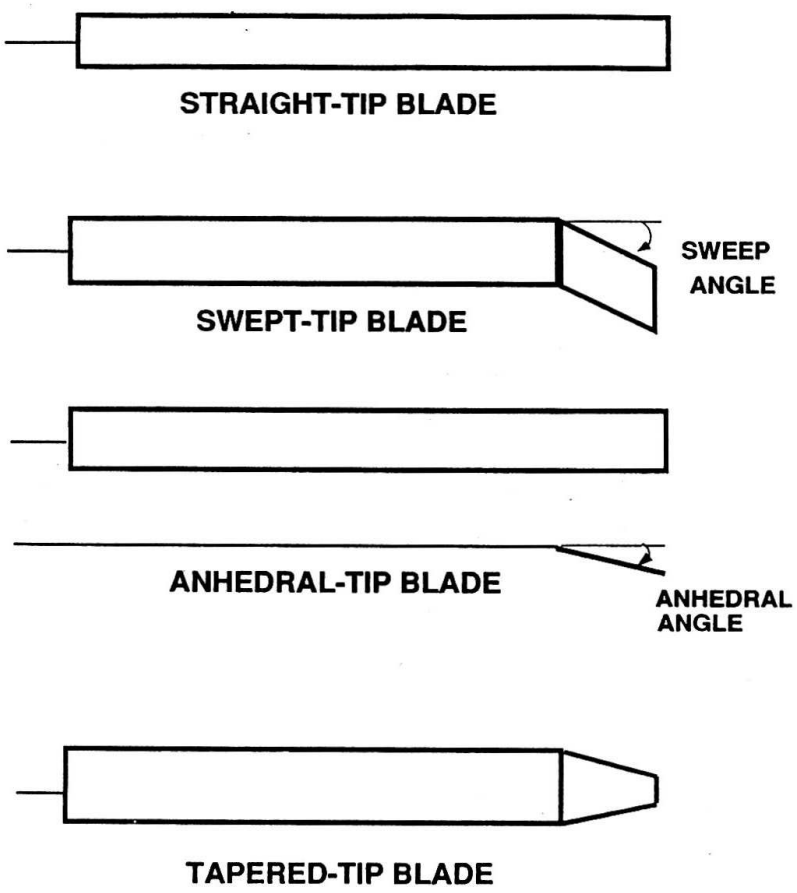

Figure 64: Tip Shapes Defined by Kim and Chopra (1992)[165]

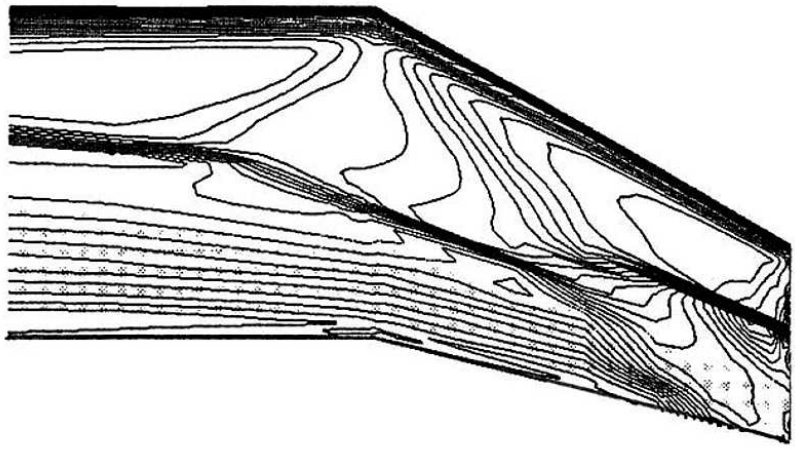

Figure 65: Surface Pressure Contours on the AH-66 Comanche Tip, Duque and Dimanlig (1994)[103]

A further example of these developments in the USA is provided by Srinivasan, Baeder, Obayashi, and McCroskey (1990)[274] where shock-induced separation on the tip of a hovering rotor is studied. This was followed by Duque and Srinivasan (1992)[104] where they illustrate the use of embedded, or overset grids (see later).

In a subsequent paper Srinivasan, et al (1993)[276] analysed a modern helicopter rotor in hover, and compared the UH60 and BERP blades. Duque (1994)[103] then simulated a complete helicopter model of the AH-66 Comanche in forward flight using an actuator disc for the rotor, and also presented results for the swept-tapered tip in hover. As an example of this work, the surface pressure contours on the tip are reproduced in Figure 65 . A double shock occurs on the swept panel, and the tendency is for the shock to strengthen towards the tip. This suggests that more sweep is required in the extreme tip region if this tip is not to generate a shock pattern which will adversely affect rotor (loading) noise, due to de-localisation of the shock beyond the tip of the blade. Similar compressibility problems have been noted by the writer in recent computational work at Westland during explorations of the advancing blade characteristics of a variety of tip shapes. The severity of the shock de-localisation problem depends on the planform, but a strong driver is the tip Mach number which stems from the forward speed and cold temperature design requirements of the helicopter.

Srinivasan and Baeder (1993) [272] summarised the capabilities of the Transonic Unsteady Rotor Navier-Stokes code, TURNS, to calculate simultaneously the aerodynamics and acoustic loading noise, using grids of 100,000 to 960,000 grid points.

Despite the rapid progress in CFD, traditional rotor tools continue to be used because of their fast turn around time. Aeroelastic optimisation was explored by Callahan and Straub (1993)[70] using CAMRAD/JA and CONMIN to vary several blade design parameters. Limitations in the simple aerodynamic model were recognised, especially when dealing with sweep. Blade twist was found to be a powerful design parameter affecting vibration, and somewhat surprisingly they found an optimum close to that required for best performance.

At Bell Helicopters, Yen (1994)[329] considered the effects of blade tip shape on dynamics, cost, weight and performance, and compared a swept-tapered tip design with swept, tapered and rectangular blades. In high speed flight the swept-tapered tip reduced pitch link loads and vibration, and depending on the thickness of the tip aerofoil, reduced the power requirement. Yen states that this tip gave a small increase in blade weight and manufacturing costs, and concluded that 'the performance of the swept-tapered tip depends on many design parameters, such as solidity, aerofoil thickness, tip speed, rotor dynamics and blade torsional stiffness. Therefore it is imperative that it is integrated into the overall design process'.

Meanwhile, manoeuvre trials proved the thrust capability of the BERP rotor, and noise tests were then carried out. The tests were arranged to avoid ground reflections, by flying the Lynx towards a microphone

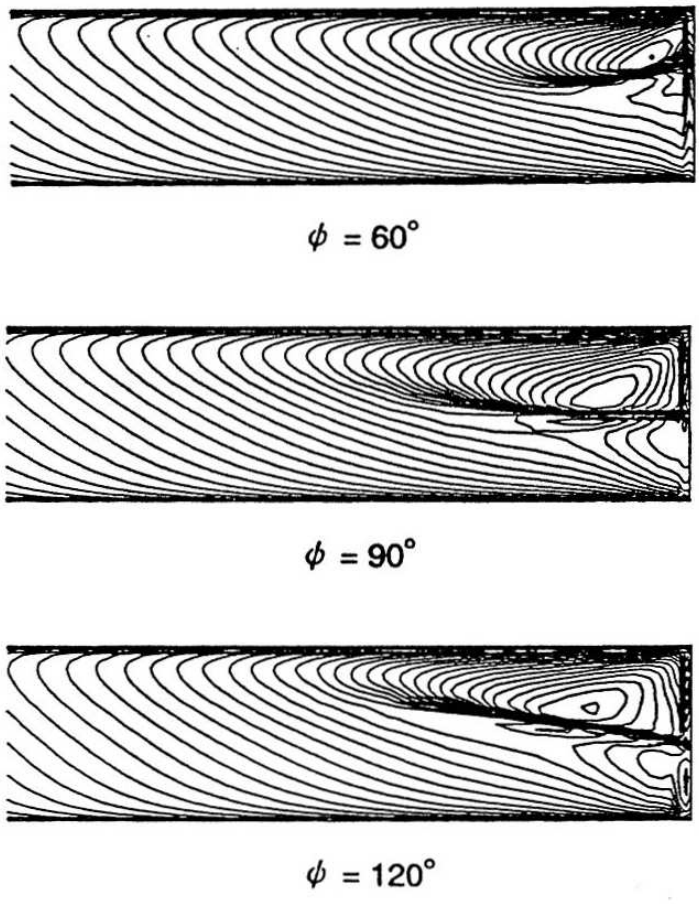

Figure 66: Mach Contours on Blade Surface, M_{tip}=0.7, μ=0.3, Non-lifting, Aoyama et al (1995)[15]

suspended below a hot-air balloon. In these tests a tip Mach number of 1.02 was reached with the BERP blade, as described by Pike and Harrison (1995).[238]

Also in 1995, a team from Japan, Aoyama, et al[15] computed the formation of shocks on the advancing blade using an Euler method for blades which had a NACA0012 aerofoil. In their paper, they present the location of the shock on a rectangular blade for advancing blade azimuths of 60, 90 and 120 degrees, where the shock reaches the tip and would de-localise, see Figure 66. They compare the pressure rise across the shock for several (sheared) swept tips and tapered tips, and even show the tip relief due to a change in aspect ratio. They then introduced a delta shaped extension to the leading edge, although the shock still persisted at the square cut tip, Figure 67 and finally they added a 75 degrees swept outer edge (similar to the BERP tip, but more abrupt) which helped to relieve this problem, Figure 68.

Wake and Baeder (1996)[313] evaluated the TURNS Navier-Stokes CFD method against the data of Lorber, et al (1991)[190] for the Black Hawk (UH-60A) model rotor and a 3:1 tapered tip for a range of thrust conditions in hover, Figure 69. The code used a low-dissipative 3rd order upwind solver. Periodic grids of 380,000 to 950,000 cells were used, and measured blade deflections were taken into account. Discrepancies with experimental results were found mainly in the tip region, although these were improved with the finer grid. While fair comparison with the measured FoM was obtained, there were compensating errors related to the lack of definition in the tip vortex which diffused by the time the following blade was reached, and the profile power was not accurately predicted.

By 1996, Ahmad and Duque[2] were testing computations in unsteady rotor cases in forward flight using overset grids. This method allows a well-formed structured grid to surround the blade, with the remainder of

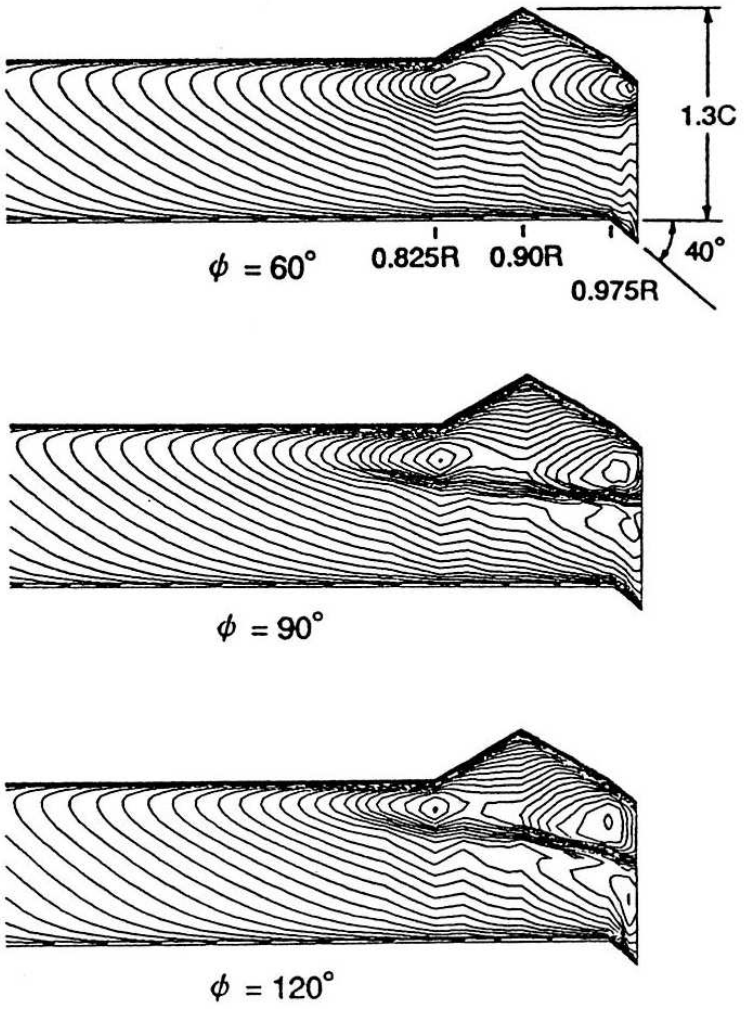

Figure 67: Mach Contours on Blade Surface, M_{tip}=0.7, μ=0.3, NACA0012, Aoyama, et al (1995)[15]

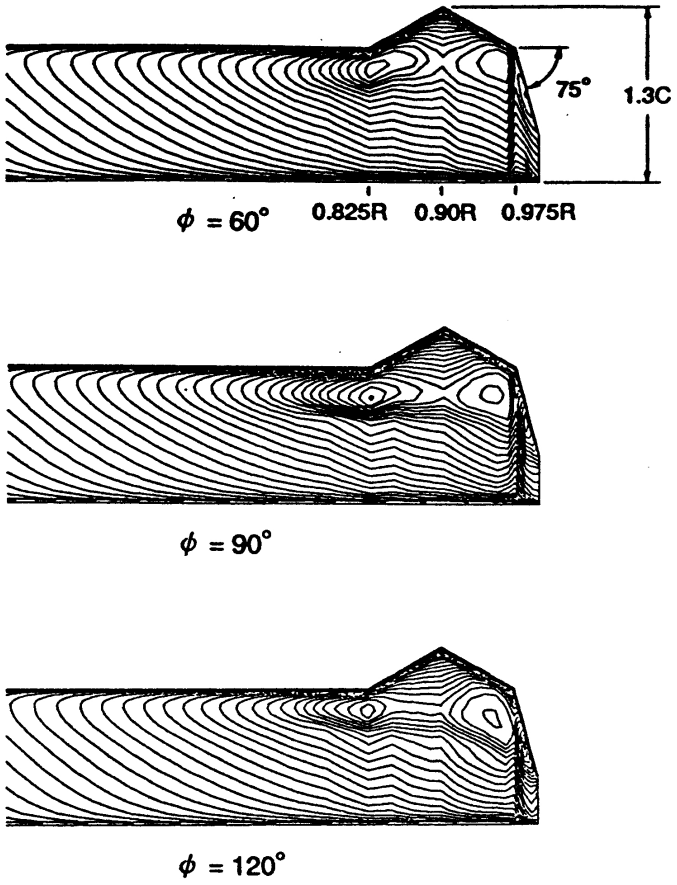

Figure 68: Mach Contours on Blade with Large Sweep-back and Delta-Shape Extension of Leading Edge, M_{tip}=0.7, μ=0.3, NACA0012, Aoyama, et al (1995)[15]

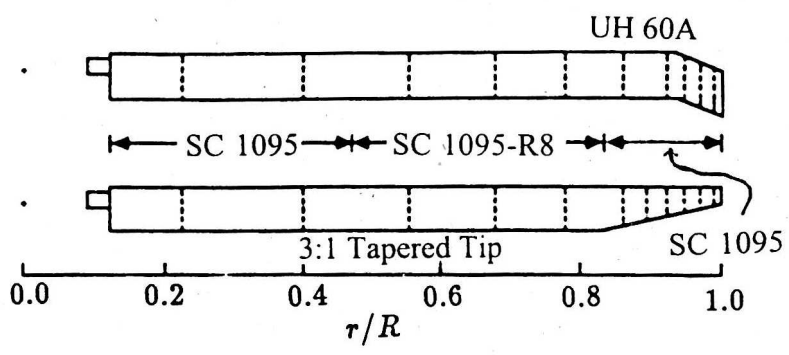

Figure 69: Model Rotor Planforms for UH60A and 3:1 Taper Tip, Wake and Baeder (1996)[313]

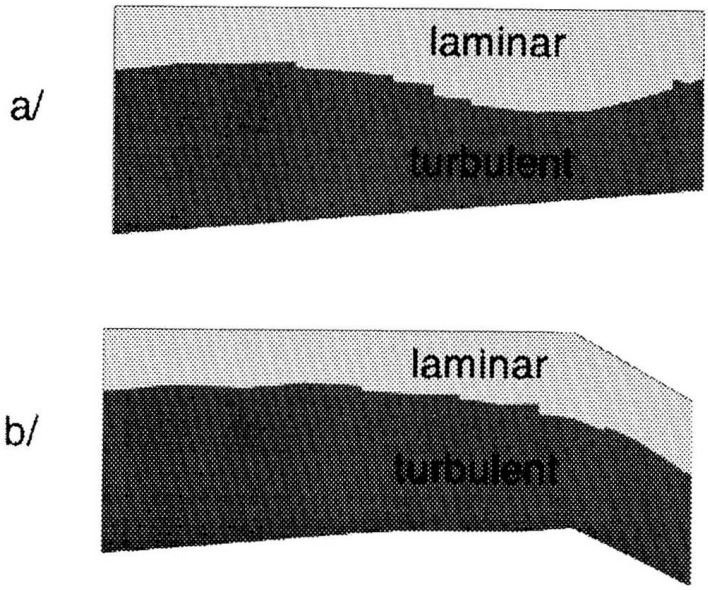

Figure 70: State of the Boundary Layer on Blades with Straight and Swept Tips, Beaumier, Zibi and Costes (1997)[27]

the domain meshed with a cartesian or cylindrical grid, as appropriate. The method involves interpolating (in 3D) between the results obtained on the two grids at each time-step, and this must be done without loss of accuracy.

In Europe, the overset grid concept was also tested in the EROS project, Renzoni (2000).[247] Subsequent development of a helicopter Navier-Stokes code by the EROS-UK consortium has concentrated on sliding grid-planes using a deforming mesh to accommodate blade motion. During the Rotorcraft DARP, and for the EU-GoAhead project (see later), this approach was developed and refined by.[279]

A numerical investigation of the tip vortex, and the effect of a tip spoiler for vortex diffusion is given by Russell, Sankar and Tung (1997)[252] using a 5th order accurate multi-zone Navier-Stokes code, and comparisons are made with the tests of McAlister, et al (1995).[205] Further work on a hovering rotor is presented by Liu, Sankar and Hassan (1999)[187] where the tip vortex structure is altered by blowing without incurring the drag penalty of a spoiler.

In France, Beaumier, Zibi and Costes (1997)[27] considered CFD predictions of power for a rotor in hover or forward flight, using a 3D Euler solver (WAVES) and a 3D unsteady full potential (FP3D) method, respectively. In each case, the inviscid flow solution was coupled to a laminar-turbulent boundary layer code (MI3DI) in order to compute the viscous drag. A straight tip with slight trailing edge taper and a swept tip were studied. The benefit of sweep in reducing the shock strength compared to the straight blade is readily apparent, and the state of the boundary layer shows a significant amount of laminar flow, Figure 70. Navier-stokes analyses are sometimes weak in the area of drag prediction, and the traditional assumption of using a turbulence model to compute the skin friction, while ignoring transition, must be questioned. Beaumier, Chelli and Pahlke (2000 and 2001)[25],[26] switch between laminar and turbulent solver options. In unsteady conditions, such as dynamic stall, modelling of transition will be important if accurate results are to be obtained.

Over the last few years, computational methods have been increasing in popularity to determine the performance of new tip designs. A paper by Manke, et al (1998),[195] supports the idea that 'semi-empirical tip corrections currently used in comprehensive rotor codes to model rotor tip-relief effects are not sufficient for designing (or representing) advanced blade tips'. The team from Boeing coupled their FPR code to the Tech-01 multi-disciplinary rotor code. The current coupling is limited to blade lift, but represents a 'significant advance' in modelling rotor aerodynamics and was successful in modelling tip-relief effects.

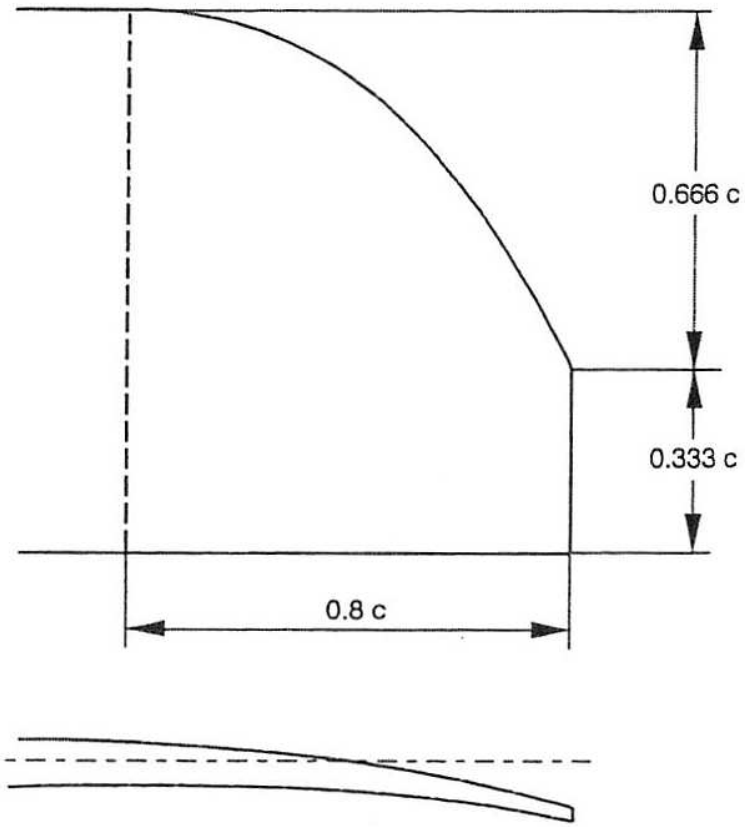

Figure 71: Parabolic Tip Shape (SPP8), Joncheray (1997)[158]

In Europe, a full-potential code was developed under a Brite-Euram programme, with the acronym, HELIFP, as described by Costes, et al (1997).[81] This collaborative development effort was aimed specifically at predicting compressible inviscid flow on helicopter rotor blades in hover and forward flight. A later version, HELIFP-X, included provision for an integral boundary layer model. In the UK, work has also been carried out at DERA, Farnborough to couple this full-potential code to a forward flight rotor code. In this approach, a first estimate of trim angles and induced flow are generated from a rotor code, and the full-potential code is used to compute the detailed pressure distribution and hence a better estimate of the aerodynamic loads on the blades, especially near the tips.

Despite the rapid development of CFD methods, lifting line methods are still in use in industry, since they have a fast turn-around time and lend themselves to parametric studies and design explorations. Provided the lifting-line approach is closely linked with a vortex wake model, it provides an acceptable method of studying parameters such as twist and taper, but is not able to accurately resolve the effects of tip shape. Despite this limitation Joncheray (1997)[158] uses a non-rectilinear modification of a lifting-line method to model the tapered 'dihedron' tip, SPP8, and compares to model rotor hover test data from the Modane wind tunnel. The SPP8 design is essentially a parabolic tip blade with a relatively small amount of anhedral, which gradually reaches a tip angle of 17 degrees. This style of blade, Figure 71, was subsequently demonstrated on the Super Puma.

Bridging the gap between lifting-line, or lifting-surface models, and full potential or Navier-Stokes CFD is the incompressible unsteady panel method described by Ahmed and Vidjaja (1998).[4] In this method a source sink distribution represents the blade thickness, while a doublet distribution is solved on the camber line, and the force-free wake is allowed to evolve at each time step. Ahmed remarks that, in contrast to the CFD methods, there is no diffusion of the vortex after it is formed, and the consequence could be an 'over-simulation' of vortical motion in comparison to the real viscous flow. The method was aimed at providing airloads for the

determination of BVI noise, and does not appear to include a coupled boundary layer to determine profile power, and hence overall performance. This method is restricted to conditions where compressibility is unimportant, but the panel method approach is otherwise capable of resolving the flow around arbitrary tip shapes (only the rectangular blade of the Bo105 was considered in the paper).

Interest also continues in developing free-wake models, such as the CHARM model of Quackenbush (see later), where the trailed circulation from the rotor is fed into the wake, and the vortices are displaced according to the induced flowfield. Laser Doppler Velocimetry (LDV) techniques have been used to make measurements in support of these and other numerical models. Bhagwat and Leishman (1998),[40] provide data on a hovering rotor. The aim of the tests was to determine the bound circulation along the blades, together with the swirl velocities and core sizes of the tip vortices.

A set of interesting tip shapes, are studied by Baeder (1998)[18] using an Euler/Navier-Stokes solver. Baeder argues that forward sweep is more effective in reducing noise than rearward sweep by effectively delaying de-localisation, although in the writer's opinion this is highly dependent on the outer tip shape, which was simply cut-off in the tip shapes presented in this reference. Figure 72 illustrates the effect of different tip shapes, and Baeder goes on to refine the detail design by introducing more area at the dog-leg and taper further outboard. At high speed, phasing effects become important, and forward sweep becomes more effective at reducing high-speed impulsive noise. A dog-leg planform is considered in order to maintain the aerodynamic centre on the quarter chord, and according to Baeder, the Forward Aeroacoustically Swept Thin and Tapered (FASTT) tip was seen to delay de-localisation well beyond a tip Mach number of 0.95. In comparison, computations by the writer for the BERP-III tip at Westland during 2001, were presented at The Burn 2003 ,[54] and later work on BERP-IV in 2008 ,[250] show no signs of de-localisation at this tip Mach number. As mentioned earlier, the BERP tip has been flown to a tip Mach number of 0.977 during the world speed record and up to 1.02 in subsequent acoustic tests.

An economical method of exploring the aerodynamic characteristics of a rotor blade tip shape using CFD is to consider the blade as a wing. This approach has its drawbacks, and ignores differences in radial loading, Mach number variation and induced velocity, however, the wing problem is much easier to compute, and allows comparison between test data and CFD, before attempting the rotor problem. The differences between the loading on a wing, and that on a rotating blade in hover, are discussed by Hu (1998).[144] In his paper, Hu describes the development of TLNS3DR code for rotary wing calculations, and shows examples of pressure contours for wings and rotor blades in hover. The comparisons are at zero-lift, although a lifting rotor case is shown for a high tip Mach number on a grid of about 545,025 points. The same author has also carried out computations on BERP-type blades, Hu (1995 and 1997)[142].[143]

One of the major problems in accurately computing the performance of a rotor in hover, is to conserve the vortices in the wake. For accurate performance predictions it is vital that the induced velocity at the blade is correctly represented, and this can only be done if the vortices in the wake have the correct location and strength. Dindar, et al (1998)[94] applies an adaptive refinement technique to an unstructured grid in order to study the effect of tip vortex resolution on the UH-60 blade in hover. The method works by computing error indicators to aid the efficient resolution of small scale features in the flow field.

In addition to ensuring an adequate description of the wake, it is also necessary to know the dynamic deflections of the blade. Torsional deflections are the most important, although flap and lag deflections may also have significant impact in certain flight cases. The topic of aerodynamic loading and aero-elasticity is discussed by Bousman (1999)[51] and the problem of correctly phasing of airloads is taken up by Datta in a more recent AHS Forum paper in 2003 .[89] In the latter reference, CFD was used to obtain a better prediction of the azimuthal variation of loading, based on measured torsional deflections from the comprehensive flight data obtained for the UH-60A Black Hawk. Recently, Kufeld and Bousman, 2005 ,[171] have pointed out that the data requires a 14 degree reduction in the azimuth previously quoted, due to a 7 degree error. This reduced the differences between prediction and measurements, but the phase-lag due to changing incidence and Mach number on the advancing blade is still significant. This phenomena has also been investigated recently by Steijl and Barakos, 2005 .[283]

In contrast to the UH-60 type of swept-sheared planform, hover performance and acoustic considerations have led to the development of the parabolic tip, which has become adopted for many European helicopters.

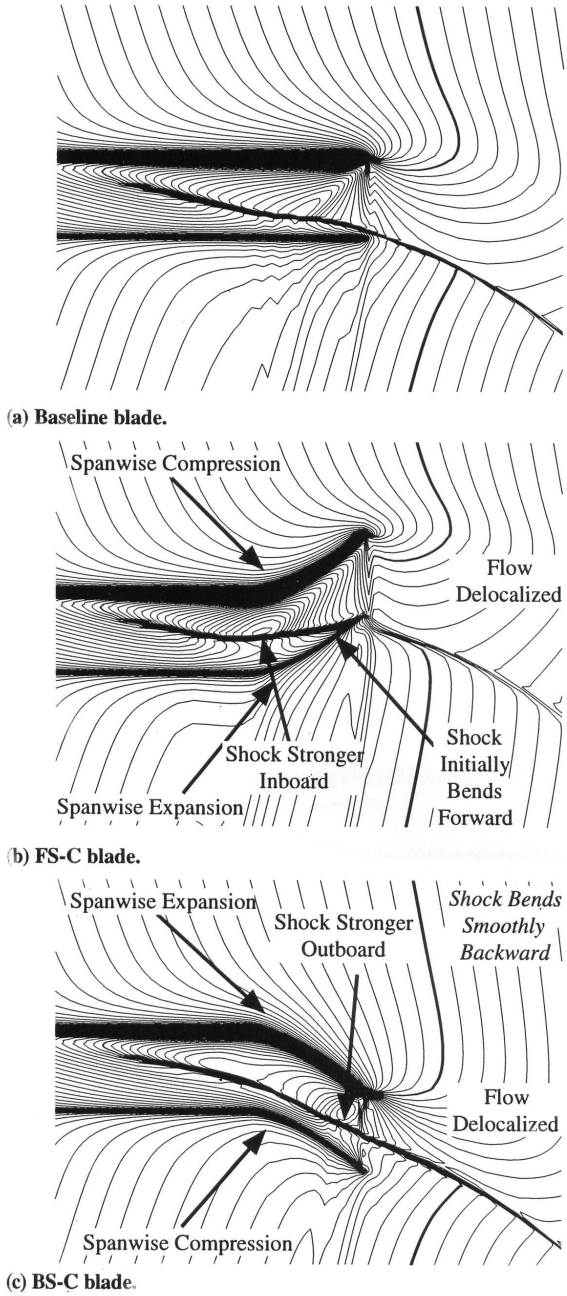

Figure 72: Mach Number Contours in the Plane of the Rotor at M_{tip}=0.95 for Blades with Different Sweep, Baeder (1998)[18]

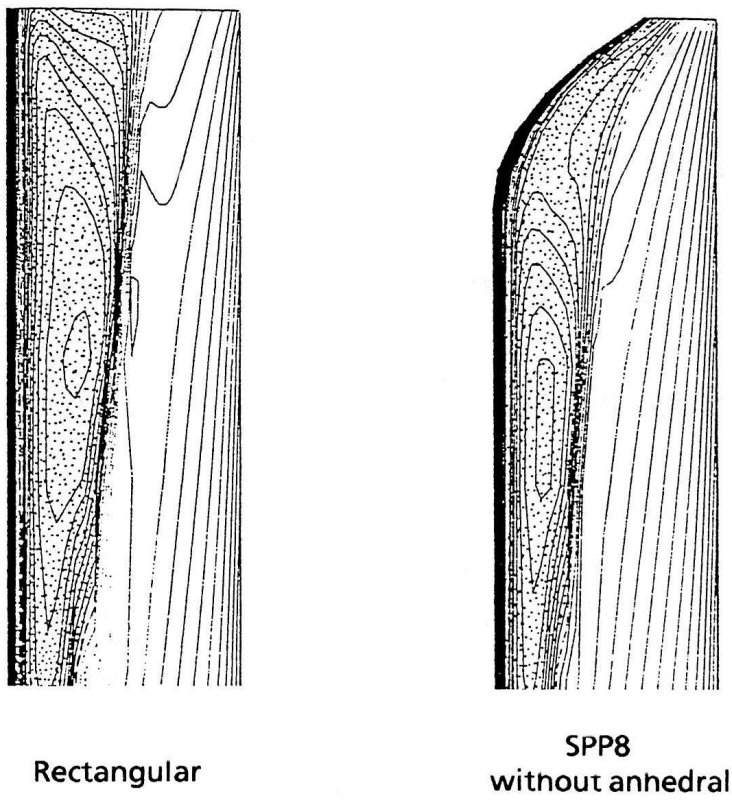

Figure 73: Iso-Mach Lines on Rectangular and Parabolic Tips, Philippe (1992)[237]

Philippe (1992)[237] shows the benefits of the parabolic tip relative to a rectangular blade, Figure 73. However, this style of tip design may pose some limitations at high forward flight, especially on highly loaded rotors, or rotors with a relatively high tipspeed. In a paper concerning the design of the EC135, Kampa, et al (1999),[159] shows Mach contours on a parabolic tip which suggest that a strong shock forms outboard, and is only slightly alleviated by the tip, suggesting that the tip has a lack of sweep, Figure 74. Similar results were obtained by the writer in 2002 for this type of tip in a representative sheared Mach number flow at zero-lift.

Bebesel, et al (1999),[28] discussed the development of the Advanced Technology Rotor (ATR) at Eurocopter Deutschland, Figure 75. A reference blade design with a parabolic tip (tip chord 1/3 of the main chord) was compared with EC3 and EC4 blades. The EC3 blade had reverse taper, together with a tapered parabolic tip (and trailing edge swept forward), while EC4 had a tip which was swept back at approximately 25 degrees from about 85%R. The main aim of these designs appears to have been towards noise reduction, hence the desire for a low tip volume. The ATR rotor was built with the means to test a variety of tip shapes, including a tapered parabolic tip, and an elliptic tip (to minimise the chord in the tip region). To accommodate a swept leading edge, while retaining the aerodynamic centre of the tip close to the quarter chord, a Bulge tip was put forward, and finally a Vane Tip was also tested (similar to that designed by the writer), Figure 76. The Figure of Merit plots indicate the superiority of the parabolic tip over the elliptic tip and the standard (rectangular) rotor blades of the BK117. Bebesel reports that the cruise speed was increased by 17 km/hr (9.2 kts), and the thrust in hover was increased by about 5% at the same power consumption. In all flight conditions tested, the parabolic tip showed a small noise improvement over the elliptic tip, presumably due to the benefit of sweep and a thin aerofoil in suppressing transonic loading. Variable rotor speed was also adopted for the ATR, which allowed a noise reduction in descending flight.

Allongue, et al (1999)[8] discuss a Quiet Helicopter demonstrator for the EC155 derivative of the Dauphin, Figure 77. Five blades and a larger diameter are used, and variable tipspeed was demonstrated. The tip

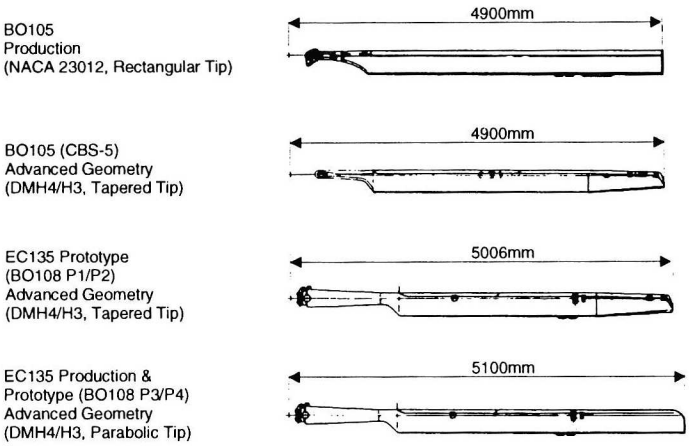

Figure 74: Advanced Blade Planforms Developed for the Bo105 and EC135, Kampa (1999)[159]

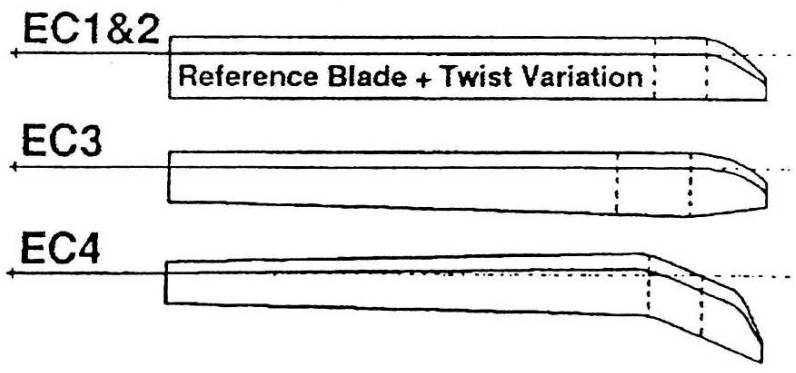

Figure 75: Optimised Rotor Blades, Bebesel (1999)[28]

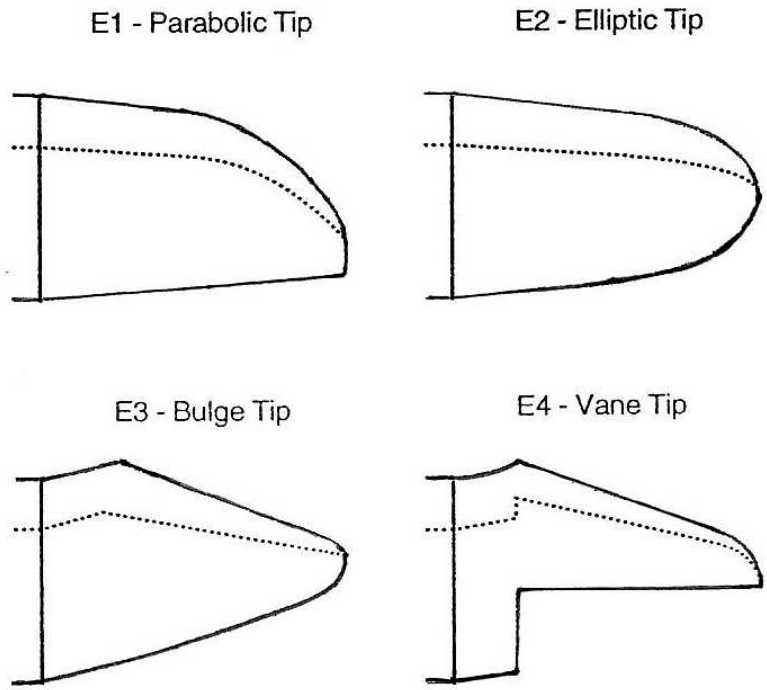

Figure 76: Advanced Technology Rotor (ATR) Blade Tip Shapes, Bebesel (1999)[28]

shape again has a parabolic leading edge and tapered trailing edge such that the tip is highly tapered, and therefore has low volume, but little sweep. The aerofoils employed are (inboard) OA415, OA312 and (towards the tip) OA409. While there is little doubt of the benefits with regard to the hovering efficiency and low noise performance of this type of tip design, use on heavier, faster helicopters may be limited by advancing compressibility and retreating blade stall. Judging by the planform, and the low pitching moment aerofoils, this blade design would exhibit low control loads during normal operations.

As noise regulations become more stringent, and With the ongoing development of the V22 tilt-rotor aircraft, there is a continuing interest in reducing rotor noise and, in particular, BVI noise on the approach, both for conventional helicopters and tilt-rotor configurations. The sub-wing topic has again been the subject of further experimental investigations, as reported by Bhagwat, et al (1999),[44] where hover smoke flow visualisation and wake measurements are given. Bhagwat reports that the sub-wing modification did not significantly affect the hover wake geometry, once the vortices had merged. Lower peak swirl velocities were observed, together with a larger core radius of the merged vortex, compared to the baseline tip. The sub-wing was found to be effective in enhancing diffusion of the tip vortex. However, the lack of twist and blending on the sub-wing may introduce turbulence into the vortex roll-up, and therefore cause an increase in the power required.

The effort to reduce BVI noise is the topic of a paper by McAlister, Tung and Heinech (2001)[206] where the effect of a small 'turbulence generating device', or spoiler, attached to the tip of a hovering rotor on the structure of the trailing vortex is discussed. As shown in Figure 78, several tip planforms were considered, including a new non-planar curved anhedral tip, an Ogee tip, stepped chord, several spoiler arrangements, lateral tip blowing, and a (deployable) 'spline' tip. The tip spoiler device was effective in reducing the peak velocities in the tip vortex, but caused an 18% increase in rotor torque, and should therefore be retracted when not required.

Yang, et al (2000)[326] describe an experimental and numerical investigation of the effect of tip blowing for fixed and rotary wings, as a step towards the reduction of BVI noise. The authors find that not only does

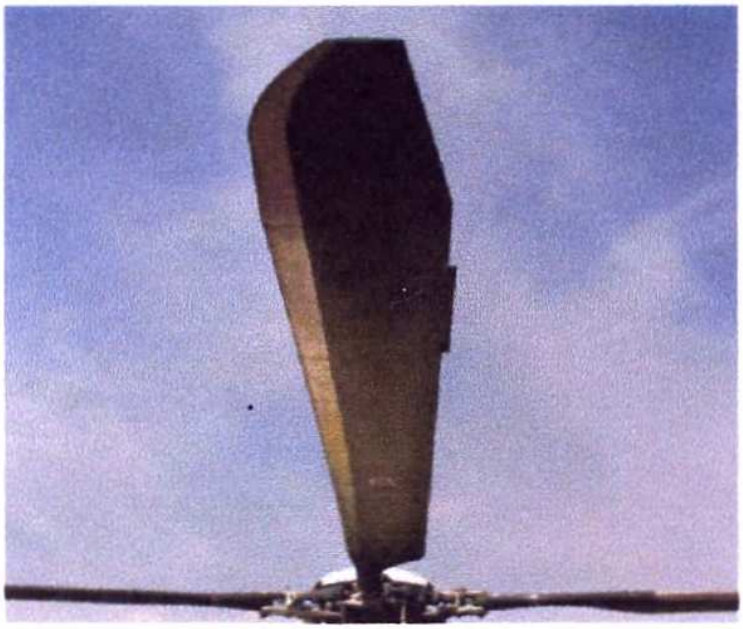

Figure 77: The Quiet blade for the EC155, Allongue (1999)[8]

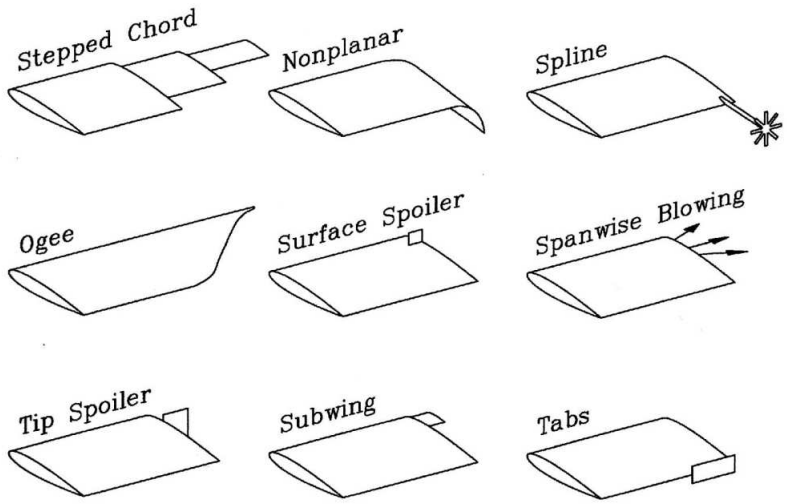

Figure 78: Examples of Attempts to Modify the Tip Vortex, McAlister, Tung and Heinech (2001)[206]

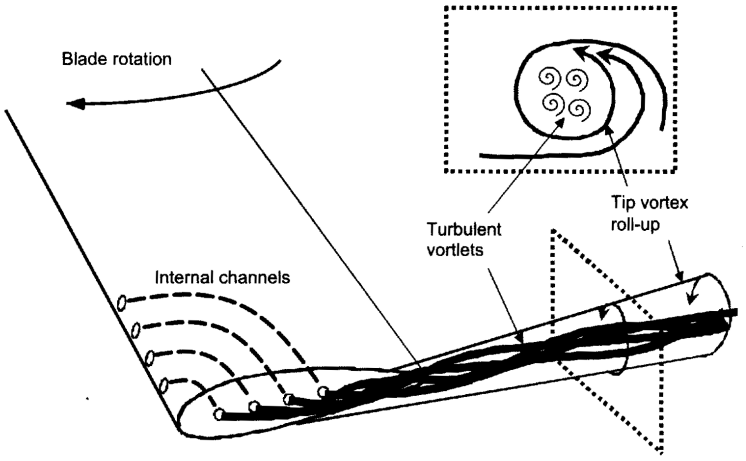

Figure 79: Illustration of the Method of Dissolving the Laminar Inner Region of the Tip Vortex by the Action of Turbulent Vortlets Generated at the Slot Exits, from Han and Leishman (2004)[128]

blowing diffuse the tip vortex, but may displace the tip vortex outwards, causing an effective increase in wing-span, or radius. In the UK, recent tests at the University of Bath were also reported by Margaris and Gursul (2004).[197] While the main aim of research on tip blowing has been to achieve a reduction in blade-vortex interaction noise, potential may exist to enhance performance and moderate control loads by active blowing techniques.

More recently, Han and Leishman (2004)[128] have put forward a tip which employs natural blowing to diffuse the tip vortex. A series of openings on the leading edge of the blade lead to outlets on the edge of the tip such that air is injected close to where the vortex forms and is therefore entrained into the tip vortex as illustrated in Figure 79. In their paper Han and Leishman present excellent flow visualisation and LDV measurements of the tip vortices, with and without blowing, on a model-scale rotor and conclude that the peak swirl velocity is reduced by nearly two-thirds and the core size is increased by two to three times for increase in power of less than about three percent.

In looking forward to applying high-resolution CFD methods to rotorcraft design evaluation problems, it is essential to be able to economically predict the vortex roll-up process and the trajectory of the wake vortices. In practice, the circulation strength of the trailed vortices will gradually decay through natural (viscous) diffusion, and one of the main challenges for CFD is to avoid accelerated diffusion due to numerical effects.

The use of a seventh order spatially accurate ENO method was implemented by Hariharan and Sankar (1999)[132] and benefits in efficient vortex capturing were assessed. A moving, tracking, overset grid technique was employed. A fifth order scheme was used to compute the tip vortex behind a wing, and the importance of capturing the axial momentum was highlighted. It is claimed that the high order scheme can capture the tip vortex for 180 degrees with less than 10% dissipation, and for a wing tip vortex a distance of fifty chord lengths was computed with negligible dissipation of the vorticity. Further work on 5th and 7th order schemes is also reported in a later paper by Hariharan (2002).[131]

While a higher order scheme is able to capture a trailing vortex with a minimum of grid points, these methods work best on a Cartesian grid. This implies the need to use of an overset grid to track the vortices in the rotor wake, and this process may present some difficulties. An alternative would be to use a very fine grid, which would then demand longer runtimes.

Tang and Baeder (1999)[290] present an improved Euler method for a hovering rotor and validate the results against the data of Baghwat and Leishman (1998),[40] using a third order accurate method. Improvements in both grid generation and flow solver reveal a numerical diffusion of the same level as viscous diffusion prior to the first blade passage.

Hall and Long (1999)[124] employ a fourth order Euler scheme and compare to the NASA CFL3D code. The lower diffusion of their simulation is shown to produce a stronger tip vortex that follows a trajectory closer to the experimental data for the development of the wing tip vortex of Devenport (1996).[92]

Several papers have been presented by Strawn on computational modelling of helicopter rotors. Ahmad and Strawn (1999)[3] present a Navier-stokes CFD analysis of a hovering rotor using an overset grid, and compare the results to the rectangular tipped blade of Caradonna and Tung, and to the UH-60 model rotor tests in the DNW tunnel by Lorber (1991).[190] The loading was under-predicted inboard and over-predicted at the tip. In their 2001 paper Strawn and Djomehri [287] again discuss the hovering rotor and wake aerodynamics, and employ grids of 10.6 million points and 64 million points to check grid sensitivity, and although the wake is better resolved with more points, the performance results were not particularly sensitive to the number of grid points. Again, the computations consistently over-predicted the thrust near the rotor tip and it was suggested that this was due to a mechanism of vorticity migration, although other factors, such as differences in boundary conditions for computation and test, and the over-prediction of the vortex core size, may also be at fault. The vortex core size may be affected by the local grid density in the region of the tip vortex, or could be influenced by the choice of turbulence model. Strawn and Djomehri (2002)[288] used structured overset grids with high resolution on the blades, and systematically vary the grid resolution in the rotor wake and the outer boundary locations. The solver used is now of 4th order, but even so, the thrust in the tip region is still over-predicted.

In the UK the alternative technique of employing a sliding grid (in the plane of the rotor) has been developed for forward flight simulations, and blade pitch variation is achieved via a distorting mesh. This technique has been adopted in the Helicopter Multi-Block code (HMB) because of its ease of programming and potentially greater accuracy.

The writer has also used the sliding mesh approach in the commercial FLUENT code for an unsteady 2D aerofoil, and to obtain quasi-steady solutions for a rotor blade at various azimuths in forward flight, Brocklehurst (2000)[53] and (2003).[54] Azimuth position was controlled using a large cylinder aligned with the axis of rotation of the rotor, but the requisite pitch angle of the blade was set by simply rotating the blade about the (coned) feathering axis within a local cylindrical grid. The idea of enclosing the blade in a fixed mesh, and convecting the flow and wake across a sliding mesh boundary, appears a sound idea provided that this can be done without loss of accuracy. This technique would also minimise the amount of distortion that has to be accommodated by the deforming grid, since the cyclic pitch rotation is handled by the sliding grid, and only the blade deflections need to be addressed by grid deformation. These test cases used an Euler solution (for economy) and an unstructured grid (for convenience), and could have been readily extended to a time-accurate solution for rotating blades, had sufficient computational resource been available at the time. However, a much finer, structured grid would be preferred.

The current deforming grid scheme within HMB is able to handle large pitching displacements by allowing movement of the block boundaries to minimised overall distortion, and so maintain the quality of the grid.

However, not only is it important to know the dynamic deflections of the rotor so that the loads can be accurately determined, but it is also necessary to understand how the aerodynamic design of the tip impact the dynamics. Maier and Abrego (2000)[194] discuss the aeroelastic stability of a model rotor with a swept-sheared tip, and establish good correlation of CAMRAD-II with regard to the dynamics.

Clearly, the trim of the rotor and blade deflections are of paramount importance in forward flight, but blade deflections, particularly torsion, may also be important in hover simulations. As mentioned previously, Beaumier, Chelli and Pahlke (2001)[26] computed the performance of a hovering rotor, and accounted for the aeroelastic torsional deflection in order to improve the loading in the tip region.

Yang and Zhuang (2000)[327] also discuss the numerical simulation of a rotor in hover, and compare with Caradonna and Tung. Yang introduces an angle correction from a vortex model to overcome the problem of vortex diffusion for the 8 degree lifting case.

As computational methods continue to be developed, there is a need to compare with high quality tests data. Phase-resolved stereoscopic PIV has been used to measure the wake of a model helicopter by Martin, et

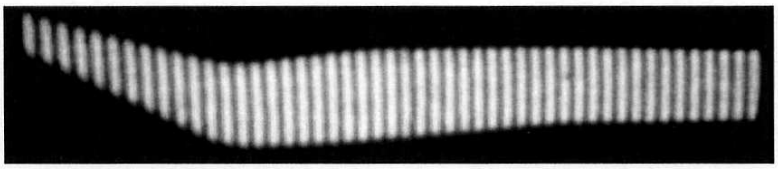

Figure 80: Fringe Patterns Indicate the Shape of the ERATO Blade, Muller et al (2000)[216]

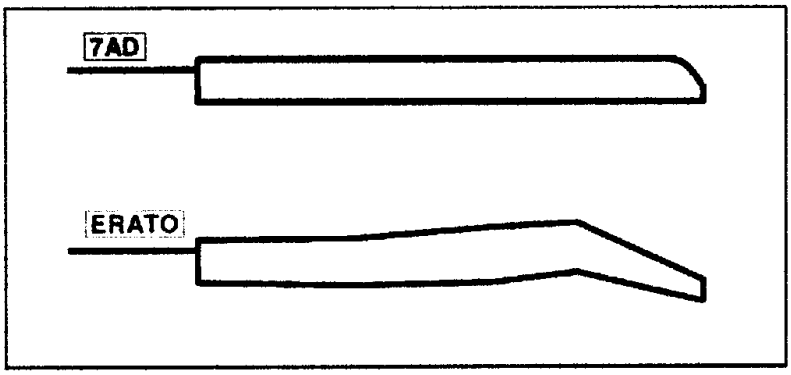

Figure 81: Comparison of ONERA 7AD and ERATO blades, Beaumier and Delrieux (2003)[24]

al (2000)[198] and Bhagwat and Leishman (2000)[4241] have measured the bound and trailed circulation. High-resolution measurements of the wake of a hovering rotor were also reported by Martin, et al (2001)[200] using LDV. This information is important in establishing the wake structure, and provides a good database to support the development of both high-order computational techniques and free-wake methods for noise and performance predictions. Stability of the wake in hover is also considered by Bhagwat and Leishman (2000).[43]

Wind tunnel studies have also been undertaken in Europe, and a low noise rotor blade was designed and tested in the DNW tunnel by ONERA and DLR in a bilateral project, Muller, Pengel and van der Wall (2000).[216] On the ERATO rotor the blade curves forwards and the main sweep-back starts well inboard, at about 75% radius. The highly tapered blade planform sweeps back at about 25 degrees, as shown in Figure 80 and 81. At the tip, the blade is simply cut off normal to the inboard-quarter-chord reference axis, perhaps risking some de-localisation due to the shock re-forming since the sweep is limited, depending on the advancing blade tip Mach number. With this type of planform, torsional deflections are important, and the paper describes the analysis of strain gauge data, and the non-intrusive optical fringe correlation method (FCM), also known as the projected grid method (PGM). The aim of this blade design is to reduce blade-vortex interaction(BVI) noise as described by Beaumier and Delrieux in their 2003 ERF paper.[24]

Pahlke and Chelli (2000)[226] through the French/German CHANCE program, have developed CFD methods for multi-bladed rotors in forward flight, and compare results for the 7A (rectangular tip) and 7AD (parabolic tip) rotors with data from tests in the S1-Modane tunnel. The blades are here assumed rigid and the chimera technique is used to allow for the relative blade motion, by surrounding the blade with a grid, which moves with the blade, and overlaps the background grid. It is concluded that the results could be improved with rotor trim changes and by taking the aero-elastic deflections into account.

As expertise with CFD methods is steadily developing, the more ambitious goal of simulating a complete helicopter has been taken up. In Europe, collaboration between ONERA and DLR is reported by Sides, Pahlke and Costes (2001)[262] where the aim is to develop the CFD methods and enhance high speed impulsive aero-acoustic predictions using Euler/Kirchoff methods. Sides also describes the application of Navier Stokes codes

Figure 82: Illustration of the ATR blade analysed by D'Alascio (2001)[87]

to the prediction of the flow around helicopter fuselages, including the effects of boundary layer transition. This collaborative work formed the basis for the CHANCE project (Complete Helicopter AdvaNced Computational Environment). The DLR FLOWer code makes use of overlapping grids, while the elsA software at ONERA employs moving grids.

The development and application of CFD methods in the French/German CHANCE programme is also described by D'Alascio (2001).[87] The elsA software combines the former ONERA models of CANARI, FU3M and WAVES, while FLOWer was further developed by DLR. The paper focuses on the Advanced Technology Rotor (ATR), and the ATR-A rotor is the subject of analysis, see Figure 82. This rotor has a small amount of inverse taper, such that the chord at about 85%R is wider than the chord at the root, and the tip is a tapered parabolic planform with a swept leading edge. The trailing edge has a slight forward sweep, and the end of the blade is cut off square to the reference axis. Such a blade tip would have low torsional loads. The aerofoils used are the ONERA OA-4 series and the 3-series OA312 at mid span. The aerofoil section is 15% thick at the root, and in the tip region the thickness tapers from 9 to 7% at the tip. Such thin aerofoils are required to cope with advancing blade compressibility when the sweep is not large, and could give an early stall on the retreating blade. However, this tendency may well be alleviated by the use of sufficient blade area in the region of 75-85%R. One would also expect such a blade with a tapered parabolic tip to have a high peak Figure of Merit in hover.

Pahlke and van der Wall (2001)[224] introduce weak fluid-structure coupling, and present test cases for the 7A and 7AD isolated rotors using the FLOWer code with Chimera grids. This improved the solution and the performance difference between the two sets of blades was fairly well predicted. In a later paper, Pahlke and van der Wall (2002)[225] report progress on the use of weak fluid-structure coupling for multi-bladed rotors in high speed flight, and show much improved phase agreement with experiment when coupling is used.

Pomin and Wagner (2002)[240] from the University of Stuttgart have also applied a Navier-Stokes method to the hovering rotor case and compared to the 7A test data. Use of a Chimera grid is being developed to encompass the forward flight, complete helicopter problem.

The combined efforts of ONERA and DLR are used to support ECF and ECD in the development of improved rotor blades. Application of the ATR blade on the EC145 is described by Humpert and Schley (2001).[147] Details of the ATR blade configuration are shown in Figure 83 and 84. A similar tip shape (on a parallel chord blade) is also used on the civil EC225 and military EC725, which supersedes the Super Puma, Faury (2001).[109]

In parallel with the European effort, the ATIC team from Japan has carried out a programme of research into rotor design, performance, loads and noise in a series of tests in the DNW wind tunnel, Kondo, et al (1998),[167] Figure 85. A baseline rectangular blade was compared to the AT1 rotor, which had a BERP-type tip with a forward offset of the trailing edge as well as the leading edge, while the AT2 rotor has a swept tip with no forward offset and 20 degrees of anhedral, Sato (2001),[256] Figure 86 . The AT-2 tip has leading edge sweep and a straight-swept trailing edge, such that there is a small increase in chord at the tip. This contrasts with the NH-90 style rotor blade where the tip planform is highly tapered towards the tip.

In the second series of tests, summarised by Murashige, et al (2001),[218] the main objectives were noise and Higher Harmonic Control (HHC). Flow-field PVI data was gathered and blade deflections were also measured to aid the subsequent analysis and enhance understanding. The results were compared to CAMRAD-II and a multi-bladed CFD forward flight analysis, and a reduction of torque was established for the AT-2 rotor. Level flight noise was reduced, although there was an increase in BVI noise for this swept, anhedral tipped rotor. It

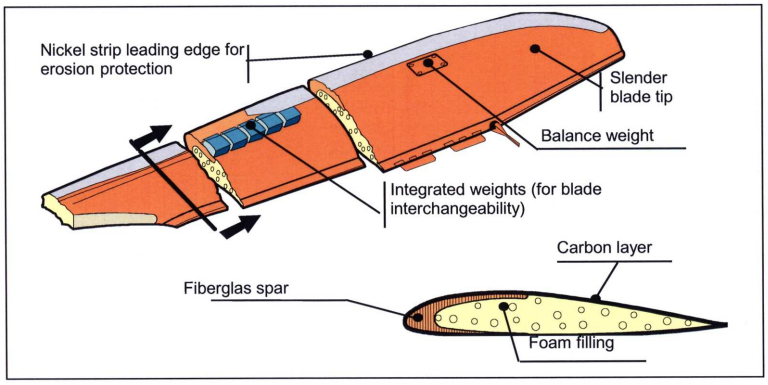

Figure 83: Detail Design Features of the Advanced Technology Main Rotor Blade, Humpert and Schley (2001)[147]

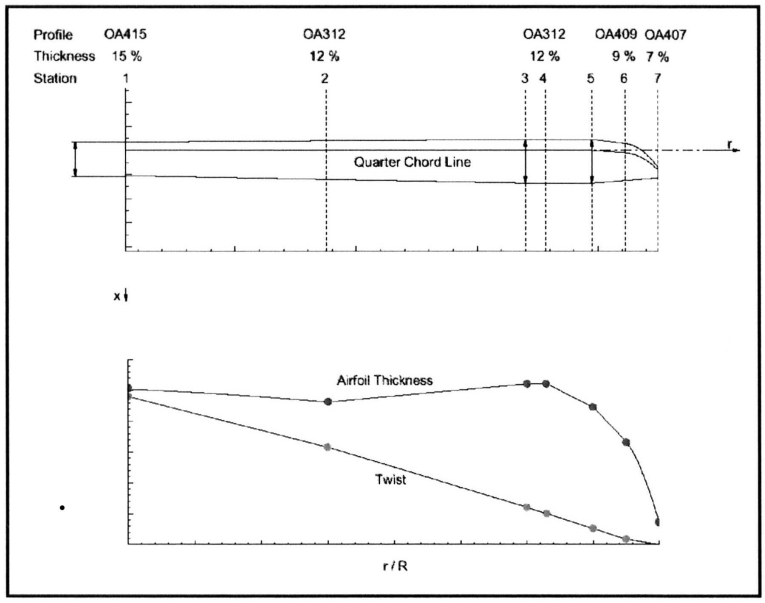

Figure 84: Aerodynamic Layout of the Advanced Technology Main Rotor Blade, Humpert and Schley (2001)[147]

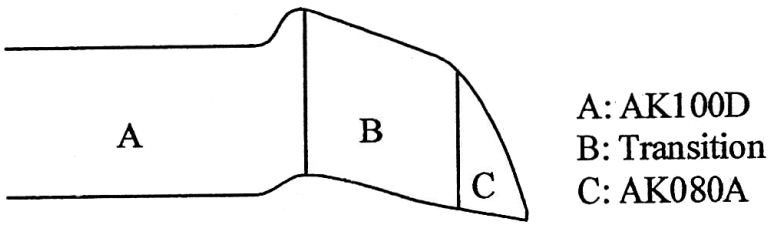

Figure 85: The AT1 Blade was Selected from Several Similar Tip Shapes, Kondo (1998)[167]

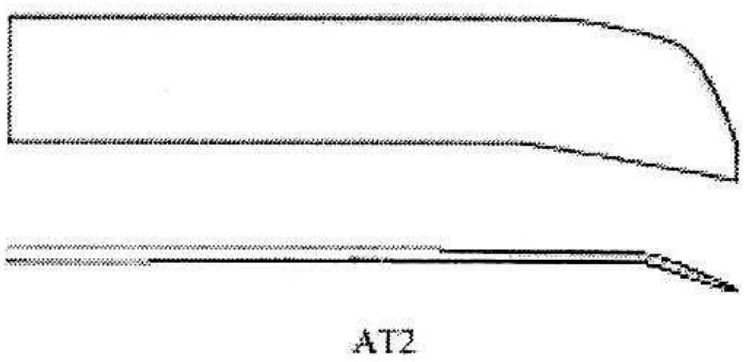

Figure 86: The AT2 Blade Described by Sato (2001)[256]

was suggested that the BVI noise was due to twin vortices arising from the anhedral, and that this could be cured by removing the anhedral. This conclusion is interesting and highlights the complexity of the tip design and BVI problem.

Further validation of Japanese rotor aerodynamic and acoustic prediction methods based on the second ATIC model rotor test is also reported by Kondo, et al (2000).[168] The performance, acoustic and flow visualisation tests are reported in detail by Murashige (2000).[217]

Also in Japan, a novel Canard Tip configuration was put forward by Ota, et al (2001).[223] The Canard Tip was tested on a model rotor, and featured rectangular lifting surfaces towards the leading edge and trailing edge of the main blade, Figure 87. A noise reduction of 2.5 dbA is reported (compared with 5.6 dB for the Westland Vane Tip). One of the main problems with attempting to develop a tip of this nature is the difficult design compromise between advancing and retreating blade performance, and the Canard Tip of Ota therefore employs a leading vane which may be controlled in pitch. However, even with active control, the simple rectangular shape of the Canard tip would probably impose some penalty on performance.

In the past, the lack of a detailed computational method has prohibited a thorough evaluation of blades with the added complexity of a tip vane(s), and such configurations have therefore been the subject of experimental investigation, usually focussed on acoustics as discussed above. However, there are some difficult design issues to be resolved if the advancing and retreating blade performance is not to be sacrificed.

The Vane Tip concept was taken a step further in the mid 90's by adding a vane to the BERP tip, and a several configurations were tested by the writer in the Westland wind tunnel. This work led to a patent entitled 'Splitting the Tip Vortex on a Swept Tip' (1999).[235] A related configuration is the KBERP tip as described by Hwang, Joo, Pike and Perry (2001),[150] where a vertical leading edge vane is employed to shed an additional tip vortex, Figure 88, but as far as is known neither tip was put into production.

A swept tapered tip was preferred for the 'new affordable' Apache blade, as described by Loftus (2004),[189] and shown in Figure 89.

While some new designs of helicopter blade tip test out new ideas, others, out of necessity, are more conservative. Curtiss, et al (2003)[86] report development of the 'Carson' replacement main rotor blades for the S-61. Curtiss describes several small refinements to the design in order to stay within centrifugal and control load constraints. The new rotor blade employs 12 degrees twist (increased from 8 degrees), the NASA Langley RC-series aerofoils and a swept-tapered tip, see Figure 90. The design emphasis was on hover performance enhancement and the analysis was done using the EPIC free-wake code of Quackenbush (2000).[310] This rotor model employs a free-wake methodology which is linked to a lifting surface solution for the loading distribution. Recent developments in this high-fidelity free-wake model used in the CHARM comprehensive rotor analysis code were described by Wachspress, Quakenbush and Boschitsch (2003).[311] The free-wake method has been developed over the last 20 years to be numerically efficient and has been designed to provide a 'first-principles' free-vortex method without the need to adjust model parameters from configuration to configuration. The

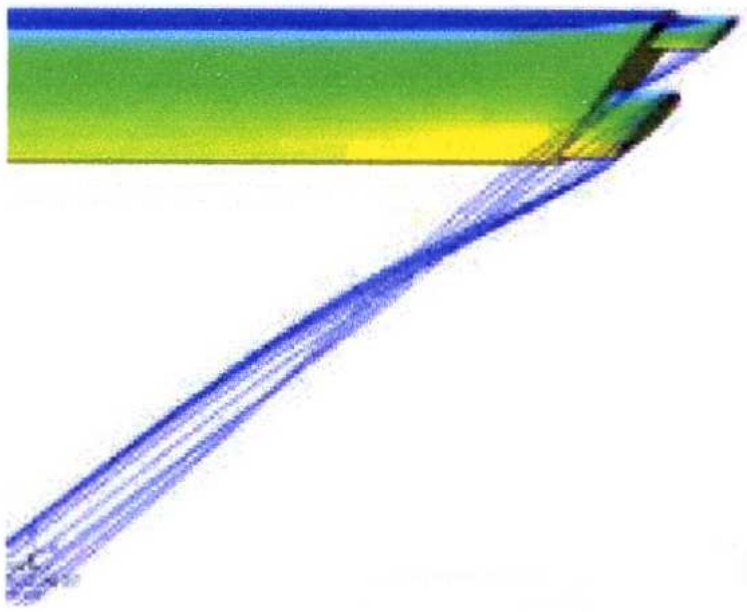

Figure 87: The Canard Tip has Twin Rectangular Tip Vanes, Ota (2001)[223]

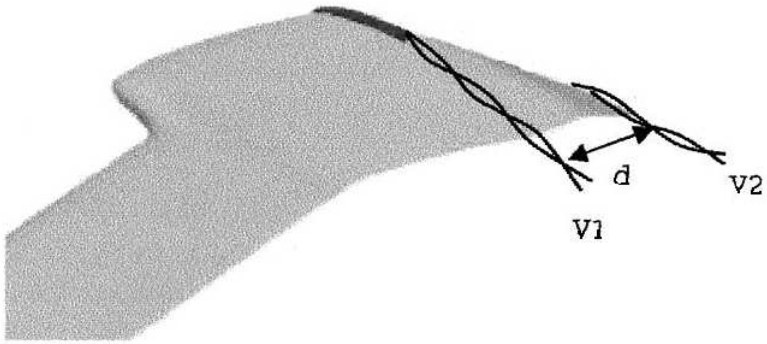

Figure 88: The Advanced KBERP tip, Hwang, et al (2001)[150]

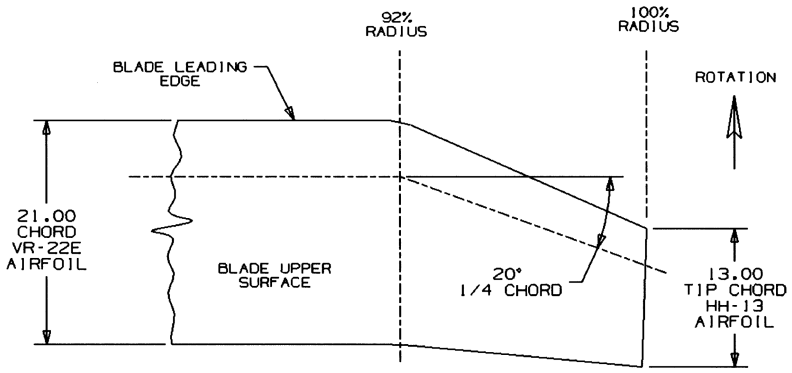

Figure 89: Plan View of Swept Tip Geometry for the 'New Affordable' Apache Blade, from Loftus (2004)[189]

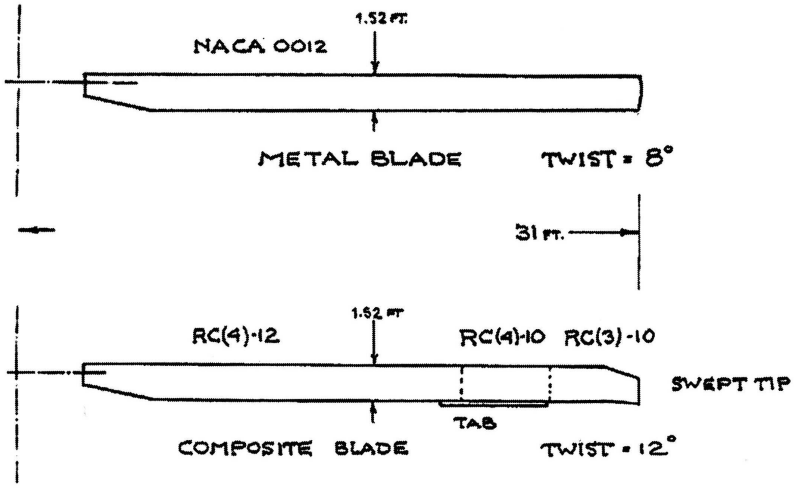

Figure 90: The Carson Replacement Blade for the S-61, Curtiss (2003)[86]

method also includes dynamic coupling, and has shown good agreement with rotor loads and BVI predictions. However, while the efficient computation of the induced velocities is an obvious strength, one area of weakness in common with all such models is the difficulty of adequately representing the compressible, viscous flow in the tip region.

In order to fully understand the detailed aerodynamics of the tip region recourse has often been made to wind tunnel tests, either on model rotors, or for convenience on fixed-wing models. In the latter case, low-speed static fixed-wing tests economically provide industry with useful insight into the characteristics of one tip shape compared to another, and provide data for validation the analysis methods in the process of applying the results to the rotational case. As mentioned earlier, the writer has carried out several wind tunnel campaigns covering a wide variety of tip shapes, and these were recently extended as part of the further development of the BERP-IV tip, Figure 91. These fixed-wing wind tunnel tests established the stalling characteristics, while the advancing blade aerodynamic characteristics were subsequently assessed using computational tools, Figure 92. Hover performance of BERP-III and BERP-IV was later compared using the Navier-Stokes solver of the Helicopter Multi-Block Code (HMB), as illustrated in Figure 93.

The idea of testing a wing rather than a rotor for validation of CFD codes is particularly useful for the unsteady case of a wing oscillating or ramping in pitch, since the test conditions can be more readily controlled

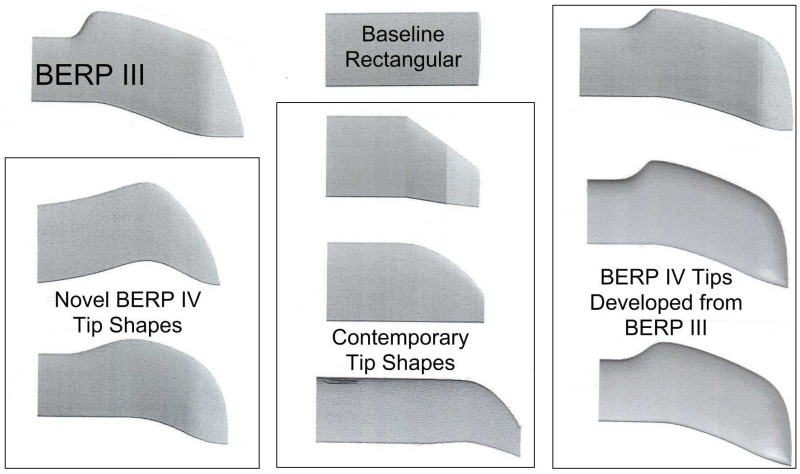

Figure 91: A Range of Rotor Tip Shapes Tested (by the author) as Fixed Wings in the Wind Tunnel During the BERP-IV Programme to Establish Their Stalling Characteristics, from Robinson and Brocklehurst (2008)[250]

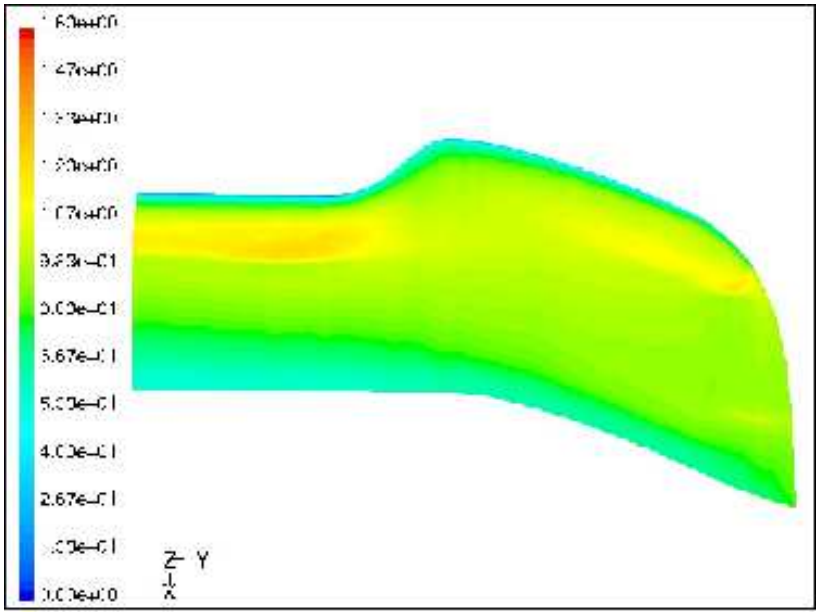

Figure 92: Advancing Blade Characteristics were assessed by computations carried out (by the author) during the early design phase of BERP-IV, from Robinson and Brocklehurst (2008)[250]

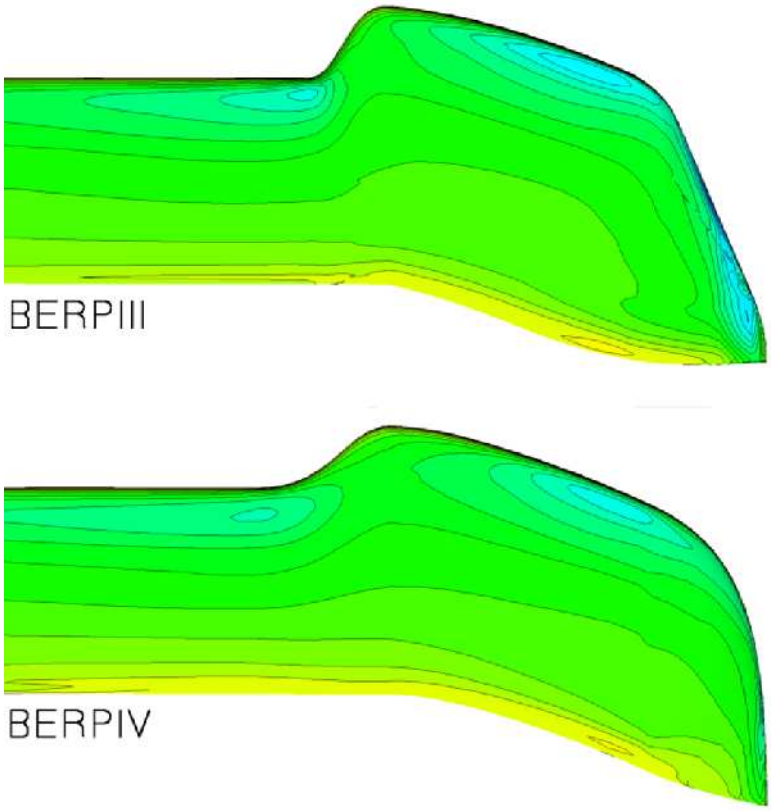

Figure 93: Comparison of BERP-III and BERP-IV tips in Hover using HMB, from Robinson and Brocklehurst (2008)[250]

and therefore boundary conditions are accurately known.

The work of Piziali in the early 90's has already been referenced, but other workers have carried out similar tests to provide a deeper insight into dynamic stall and to furnish data for CFD validation. Since Piziali's landmark effort on a rectangular tip, tests have been carried out in France at LABM by Berton (see later), in the US by Ramaparian (see later), and at the University of Glasgow on a range of tip shapes, including tips with a highly swept outer edge.

The unsteady stalling characteristics of three type of wing tips undergoing ramp motion have been studied experimentally by Coton, Galbraith and Green, (2001).[83] These included a rectangular tip, a swept-tip and a delta wing. The experiments were undertaken to meet the need to obtain a better understanding of the dynamic stall characteristics of helicopter blades. By way of comparison, the dynamic stall on the delta wing was characterised by a progressive lag in the forward movement of vortex breakdown, while on the rectangular and swept-tip wings generated a strong dynamic stall vortex that interacts with the tip vortex system. The study concluded that development of the vortex system during dynamic stall is highly dependent on the tip planform.

Coton and Galbraith (2003)[82] also describe an experimental study of the dynamic stall and vortex 'Omega' vortex shedding mechanism on a rectangular wing.

In Korea, Chang and Park (1999)[76] have carried out an experimental study of a tip vortex roll-up of an oscillating wing. In this work, the interest is focussed on the structure of the tip vortex, rather than on the loading of the wing. The authors present results for the variation of tangential velocity, axial vorticity, tip vortex circulation against angle of attack, and movement of the vortex centre during the oscillation cycle. During pitch-up, the axial velocity deficit increased, while the area of the axial velocity defect was much larger and the deficit was considerably smaller on the down-stroke. The turbulent intensity around the wing tip vortex being much greater on the up-stroke than on the down-stroke.

Berton, et al (2003)[38] describe a collaborative programme of research with TSAGI, Moscow, and model rotor tests undertaken at LABM, Marseilles, France. Two free-wake methods were used to analyse the hovering rotors with different twists and tip shapes, Figure 94. The work concludes that the methods are very efficient and there is good agreement with test, except in the case of the swept tip blades were further development of the analysis is required to overcome discrepancies in circulation distribution, vortex trajectories and instantaneous velocities in the far wake.

Schreck (2002)[257] has also carried out tests on a 2D NACA0015 aerofoil to study the boundary layer separation mechanism from measurements of shear stress obtained from hot film gauges. Ramaprian (1998)[246] has carried out tests to determine in the near field of the tip vortex behind an Oscillating Rectangular Wing.

Using the HMB code, Spentzos, et al (2004)[267] have performed unsteady computations and compared to the pitching wing tests of Ramaprian and Shreck, Beedy (2003)[33] has also carried out similar calculations for the BERP tip.

Against this background, the Helicopter Multi-block (HMB) code has been extensively validated against most of of the available aerofoil, wing and rotor data in the public domain leading to the development of a full-helicopter capability, as summarised and presented by the writer in an ERF paper, Barakos, et al (2005).[22]

Trailing vortex measurements in hover have also been carried out by Martin and Leishman (2002),[199] for various tip shapes including rectangular, tapered, swept, and a sub-wing tips. One of the primary differences noted was the change in wake geometry for a given tip shape. The tapered tip reduced the initial swirl velocity, increased the radial convection and decreased the axial convection, while the merging of the sub-wing and primary vortices created a less coherent vortical structure. The Black-Hawk style swept (sheared) tip of constant chord trailed a tip vortex outboard of 100% radius because of its geometry, and appeared to decrease both the radial and axial convection of the vortex core. Unfortunately no thrust and power measurements are presented, so the effect of tip shape on performance cannot be directly ascertained.

The formation of the tip vortex in hover has been captured numerically for two different tip edge designs; square-cut and aerofoil of revolution, Kang and Kwon (2000).[162] They employ a solution-adaptive unstructured

ROTORS TESTED IN THE EXPERIMENT AND CALCULATION

ROTOR NAME	LINEAR TWIST	PLANFORM	AIRFOIL TYPE
LABM 7	-8.3°	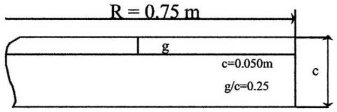	OA209
LABM 4	-8.3°	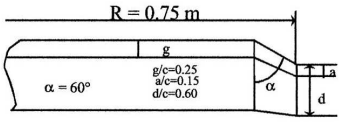	OA209
TSAGI 217	-5.5°	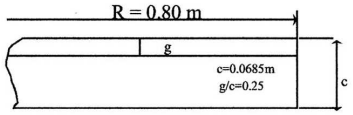	NACA 23010
TSAGI 217A	-5.5°	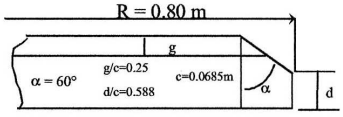	NACA 23010

Figure 94: Rotors Tested in the Experiment and Calculations, Berton (2003)[38]

mesh refinement technique, with a grid of 830,000 cells, and compare viscous and inviscid computational results. They conclude that the inclusion of viscous effects significantly affects the surface pressures and the blade airloads for transonic tip Mach numbers, especially where strong shock-induced separations occur. The formation of the tip vortex was qualitatively investigated and revealed primary and secondary tip vortices merging in to a single tip vortex, coupled with a vortex sheet roll-up. They see the unstructured grid as a 'strong' alternative to previously used structured grids, however, some mesh dependency issues may still remain. The effect of wake adaption is also highlighted in a further paper by the same authors (2001).[161]

Several techniques are available to meet the objective of preserving the circulation of the vortices. Currently vorticity confinement methods are receiving attention, as represented in 2D by the work of Morvant (2003),[211] and for 3D hovering flows by Tsukahara, et al (2002)[297] who also compared with test data for a wing. Biava and Vigevano (2003)[46] also carried out an assessment of the vorticity confinement technique applied to rotorcraft and concluded that whilst a better representation of the flow field is achieved, further work was required to automatically determine a suitable confinement parameter. A numerical method for vorticity confinement in compressible flow was also presented by Hu, Grossman and Steinhoff (2002),[141] here the application is to vortex formation on a flat delta wing, but the method has clear application to 3D rotor wakes.

Wenren, et al, (2003)[314] apply vorticity confinement to the prediction of the flow over complex bodies, such as a helicopter fuselage, where bound vorticity is shed, and also for cases of convecting vortices for a complete helicopter configuration. The vorticity confinement techniques avoid the need for logic, or Lagrangian marker arrays, and according to Wenren, shed vortex filaments can be convected indefinitely with no numerical spreading.

At ONERA, Canonne, et al (2002)[71] described cylindrical mesh refinement to better capture to the wake of an isolated rotor in hover. The computations also employed Chimera overset grids to contain the rotor blades within the cylindrical background domain. The latter is then periodically adapted to allow the tip vortex to be captured for approximately 380 degrees on a grid of approximately 600,000 points. Pomin and Wagner (2002)[240] also develop techniques for preserving the tip vortices in the wake.

An alternative to the higher order CFD methods and vorticity confinement techniques described above, is to re-cast the Navier-Stokes equations in a vorticity conservation form as presented by Brown (2000).[64] This computational method was originally intended as an alternative to a free-wake model for the Glasgow RASCAL flight mechanics code. However, the method is computationally expensive, despite recent attempts to accelerate it, and excludes compressibility and viscosity in the primary formulation. Several papers have now been published where the Vorticity Transport Model (VTM) has been used to study the effect of blade twist on the vortex ring state, Brown, et al (2002)[65] and in cruising flight by Line and Brown (2003).[186] Further studies of the vortex ring state in forward descending flight were described by Brown, Line and Ahlin (2004).[66] The VTM provides a detailed description of the wake, but relies on a lifting-line or lifting surface model to provide the blade bound circulation, hence is not currently capable of capturing the effects of compressibility for specific tip design features. However, this limitation could be overcome by coupling this wake model to a RANS solver.

The multigrid TLNS3DR CFD code has been used by Hu (2003)[145] to model a tilt-rotor in hover with various tip shapes reminiscent of those tested in earlier acoustic studies in the US. These include an Ogee-type tip, a sub-wing, and a 45 degrees tapered tip, and datum rectangular tip (see earlier Figures). The two 'low noise' tips, while producing a weaker, or more diffused (pair of) tip vortices were found to consume more power. The author claims that this CFD code provides an efficient tip analysis tool for initial design analysis, and quotes a runtime of about 1.5 hours on a Cray-YMP single processor using grids of just over 500,000 points. However, this grid density seems rather low, and the studies appear to have been carried out with the rotor at low pitch.

CFD models for rotor performance still require further development, but have now advanced to the stage where it is possible to consider their use in an optimisation process. A paper on numerical optimisation of rotor performance in hover was presented by LePape and Beaumier (2003).[179] Here, the authors validate their method against the tests on the 7AD rotor, and show an optimised clipped-elliptical tip with no sweep, and a constant chord swept tip with no chord taper, and then go on to consider an anhedral tip. Their OPT-2 configuration employs a form of anhedral which arches over the tip vortex from the preceding blade (in hover),

before being angled downwards towards the tip (retaining a rectangular planform), Figure 95. They then apply the optimisation method to the ERATO rotor to obtain a curved planform shape, with a small amount of anhedral. The final design shows a significant improvement in hover Figure of Merit, due to reduced loading in the tip region.

If CFD methods are to be routinely used in the design environment to seek an optimum solution, both high-resolution and fast run-times are a pre-requisite. An alternative approach to the wake problem that would appear to hold promise of faster run-times is the embedded vortex wake technique of Bhagwat, Moulton and Caradonna (2004),[39] Figure 96. The authors describe the ideas behind embedding a force free vortex-lattice wake within a CFD simulation such that the convection velocity is determined by the solution of the full-potential equations, rather than by direct application of the Biot-Savart law. Whilst initial stability issues were explored with a constant circulation strength in the wake, the aim is to provide an 'outer flow' representation that will relieve CFD methods of the burden of resolving the (downstream) shed and trailed wake. The approach put forward by Bahgwat is clearly an alternative to the use of higher order schemes, or vorticity confinement methods, and would appear to offer a more economical solution. The paper presents some preliminary hover performance results for the UH-60A rotor using a 288,000 point grid. Whilst this new method is currently being developed in hover, it seems reasonable to expect that it will soon be extended to forward flight.

The application of hybrid CFD methods was anticipated by Aiken, Ormiston and Young (2000)[5] in a review of 'Future Directions for Rotorcraft Technology at Ames Research Center'. Aiken considers the optimisation of rotor performance through improvements in tip shape, Figure 97, using such methods. Aiken also recognises the trend towards smart actuation of aerodynamic devices, such as flaps, to enhance aerodynamic performance of future rotorcraft. While most flaps currently envisaged are located inboard of the tip, the addition of a flap (or other device) to provide closer to ideal aerofoil characteristics, may later have some influence on the choice of planform and tip shape, Figure 98.

An active flap mounted on the MD900 blade has been recently tested in the Ames 40 x 80 foot wind tunnel during a Boeing/NASA project, Figure 99. In this case the tip shape is parabolic, and vibration reduction aspects were discussed in a paper by Hall and Anand (2009).[126] This tip shape and flap combination is also shown during earlier hover tower tests in Leishman's RAeS Cierva Lecture (2006),[182] and in his subsequent book (2007).[183]

Imiela (2009, 2010)[151][152] provides a recent example of the further application of optimisation to enhance hover performance, taking into account the aeroelastic deformation as well as employing computational aerodynamics for a high fidelity solution, and arrives at a swept-tapered anhedral tip with enhanced hover performance. For this blade the tip starts well outboard, in contrast to his rigid blade optimal solution where he shows a swept forward blade with the sweep commencing further inboard. The result of the initial rigid blade optimisation is shown in Figure 100, while the final blade shape obtained taking aeroelastic deflections into account is shown in Figure 101. Both blades also have twisted which helps to increase the loading inboard and decrease it in the tip region.

A further example of optimisation is given by Chae, et al (2010)[75] where an improvement in the Aeroacoustic performance in Hover is sought. Their analysis leads to a blade, arising from a Self-Organisation Map (SOM) process, with a blended swept and tapered tip with forward notch offset, Figure 102, similar to that used on the BERP blade, although somewhat surprisingly the outer edge of the tip is cut-off square.

Clearly, the blade shape that results from any attempt at optimisation will depend on the flexibility of the design parameters, the constraints imposed, and the objectives set. Thus it is not surprising that widely differing blade geometries result, even for applications that are currently focused on the simpler hover case.

In addition to optimisation work being carried out in hover, Johnson and Barakos (2011)[156] have made a start in considering the optimisation of blade tip shapes in forward flight using the HMB CFD framework and a parametric changes to the geometry. In this way the effect of sweep and anhedral, etc, on performance and control loads can be assessed. It is anticipated that CFD will become mode widely used as a design optimisation tool as faster CFD methods, eg Woodgate and Barakos (2010),[324] are implemented and computational resources further enhanced. This latter method builds up the flowfield from several harmonics for which steady solutions

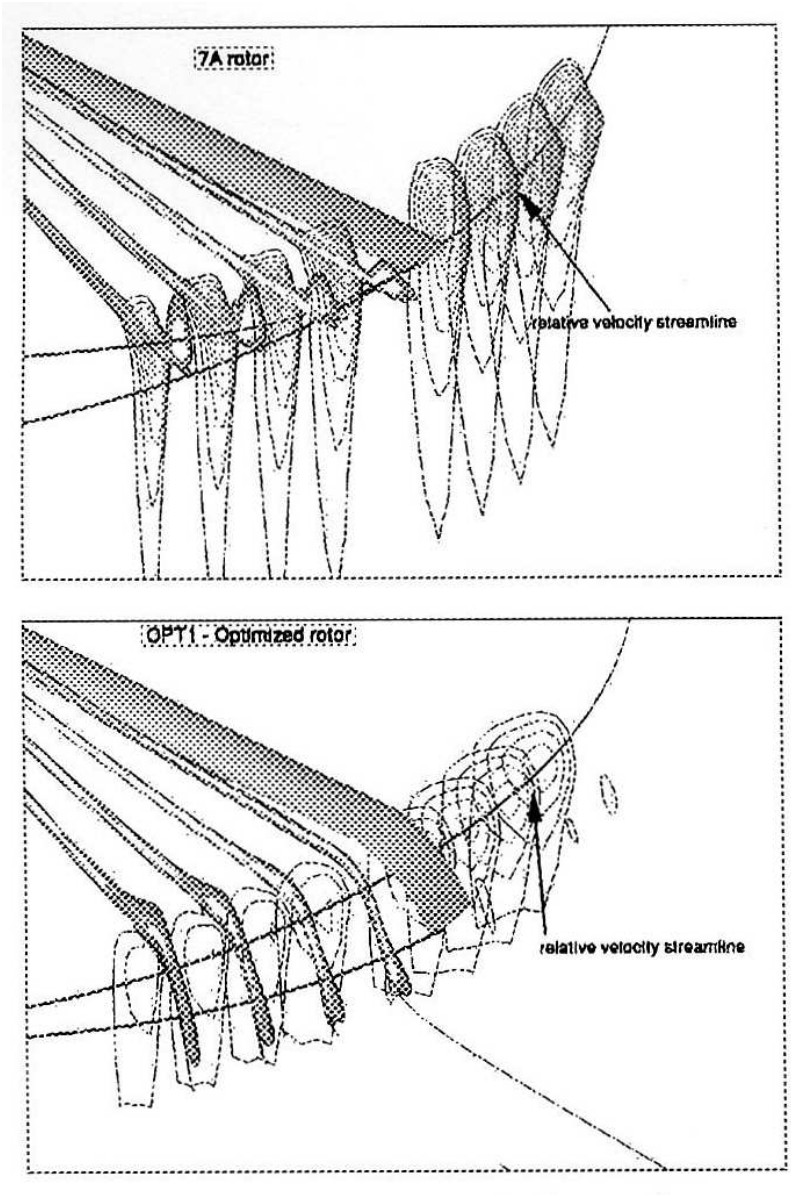

Figure 95: Vorticity Contours for 7A Reference Blade and Anhedral Tip Optimised Rotor Blade, LePape and Beaumier (2003)[179]

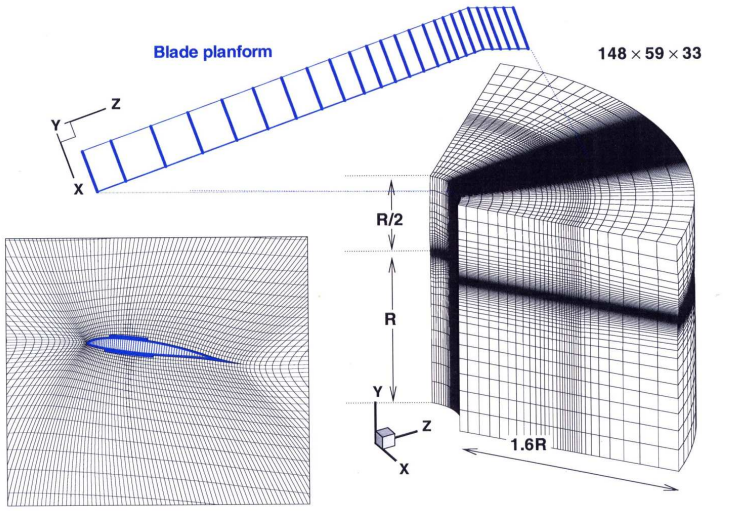

Figure 96: Application of CFD to a UH-60-type Blade with a Swept Tip, Bhagwat, Moulton and Caradonna (2004)[39]

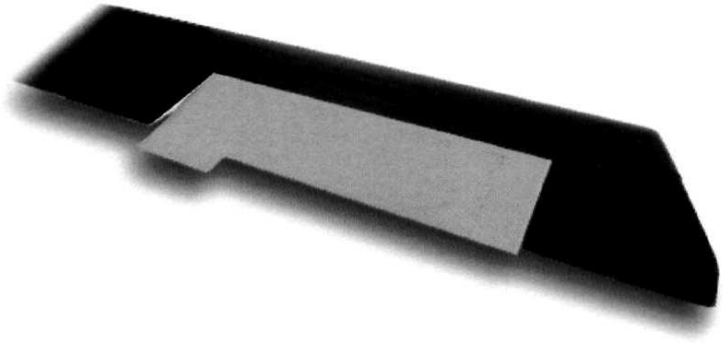

Figure 97: HeliFlap ElectroMagnetic Actuator for On-Blade Control Whirl Tested on OH58, Aiken, Ormiston and Young (2000)[5]

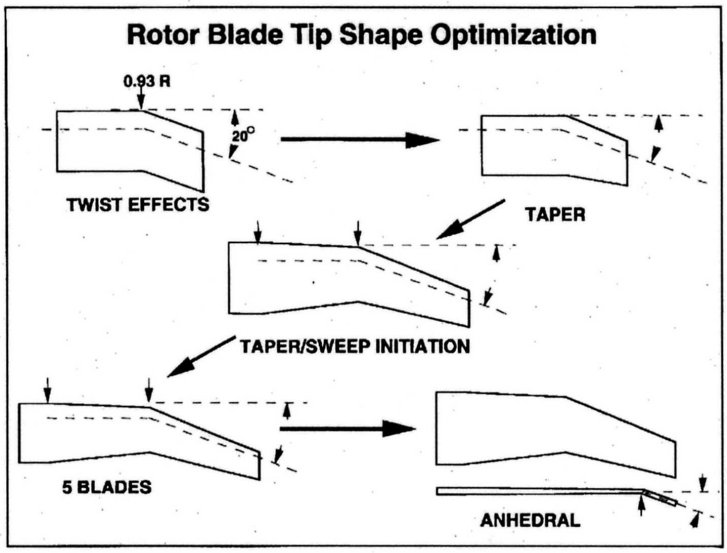

Figure 98: Advanced Design Methodology to Improve Rotor Hover Performance, Aiken, Ormiston and Young (2000)[5]

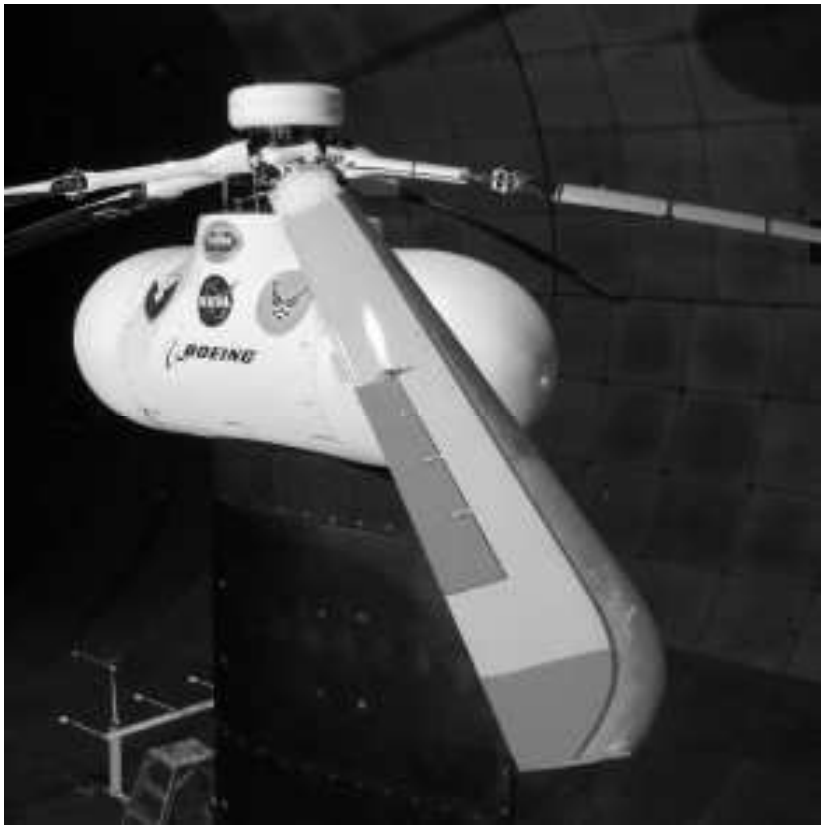

Figure 99: Active Flap and Parabolic Tip of the MD900 Blade as Tested by Boeing/NASA in the NASA Ames 40 x 80 Foot Wind Tunnel, from Hall and Anand (2009)[126]

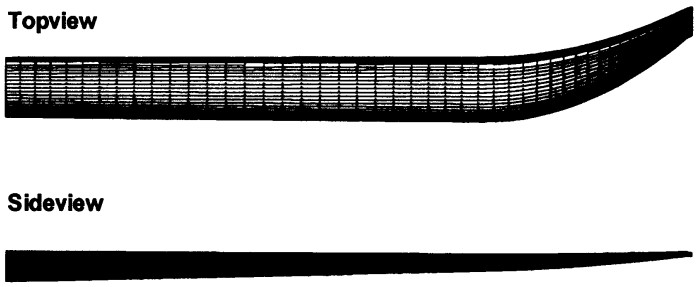

Figure 100: Forward Swept Blade Shape for Optimum Hover Performance Using an Initially Rigid Blade as Obtained by Imiela (2010)[152]

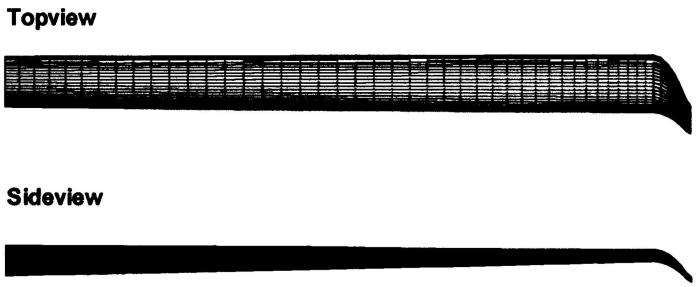

Figure 101: Final Aft Swept Anhedral Tip Shape for Optimum Hover Performance Using an Aeroelastic Blade, Imiela (2010) [152]

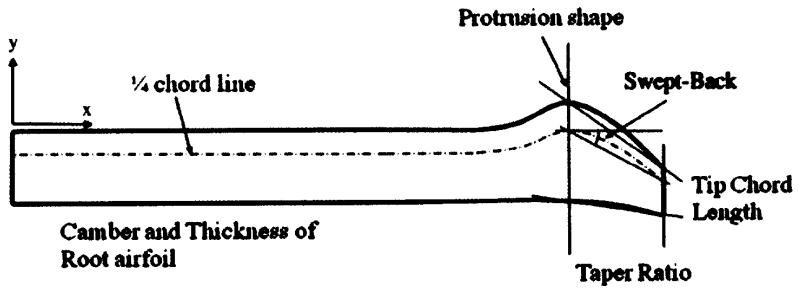

Figure 102: The Blade Design Shape Features used by Chae, et al (2010)[75]

Figure 103: The EuroCopter Blue Edge Blade, as announced by ONERA (2011)[221]

may be obtained, in lieu of the more traditional time-stepping approach, thus offering a substantial reduction in runtime for each flow solution, whilst still capturing the salient non-linear flow feature such as shocks which occur on the advancing blade.

The trend toward coupled CFD/CSD analysis and the continuing demand for a quiet blade with good hover performance has led to the development of the EuroCopter Blue-Edge blade, as recently annouced by ONERA (2011),[221] and shown in Figure 103.

This section of the literature review has discussed the evolution of helicopter blade designs and tip shapes, and the development of methods for their analysis and evaluation. The review has also revealed sources of data suitable for CFD validation, either from model rotor tests, or from steady or unsteady fixed-wing wind tunnel data where these tests have been specifically aimed at the helicopter problem. The review has identified three main types of helicopter tip design: the parabolic tip, the swept (tapered) tip, and the BERP tip. In addition there are several tip shapes intended to alleviate BVI noise by splitting, or diffusing the tip vortex. Despite a considerable research effort over the last 30 years, no single best tip shape has emerged, perhaps because the tools required for accurate evaluation have not previously been available, or because design requirements and manufacturing constraints have also been evolving. Modern high-resolution CFD methods now offer an opportunity to gain deeper insight into the aerodynamics of blade and tip design, and with continued rapid development, will soon have sufficient maturity to make a major impact on the design process.

1.4.3 Conclusions from Literature Survey

Reported developments in rotor blade design and fixed-wing aerodynamics have been surveyed with particular focus on the aerodynamic design of the tip. It is evident that a wide variety of tip shapes have been explored over the past 20-30 years, although there is no clear consensus as to a best design for helicopters.

The helicopter is a unique vehicle which lends itself to fulfilling a variety of roles, and therefore spends varying amounts of time in hover and forward flight. In the past it has been difficult to accurately assess the overall impact of design changes by use of simple tools due to the complex physics involved. Manufacturers are

now faced with the need to produce more efficient vehicles, and so it is more important than ever to quantify detailed improvements to the design. Modern computational methods now have the potential to do this.

The major emphasis for rotor blade design has been on aerodynamic performance, with efforts to reduce noise playing an important, but somewhat secondary role. For main rotor performance, two main themes have emerged. On the one hand, there has been great focus on improving the hover Figure of Merit by employing twist and taper. On the other hand, high-speed forward flight requirements have also given rise to important design considerations, and in some cases have dominated the blade tip design. While it is highly desirable to relieve compressibility effects through sweep, it is difficult to incorporate sufficient sweep into the overall blade design, leaving a need to employ relatively thin aerofoils at the tip. Thin aerofoils and some degree of planform taper will give advantages in hover as they offer to minimise the profile power, however, they may lead to premature separation and a reduction of lift on the retreating blade. Modern helicopters tend to operate at high disc loading, and this places even greater emphasis on good blade and tip design to provide the maximum possible retreating blade performance, at the same time requiring the optimum Figure of Merit to be achieved at ever increasing thrust coefficients. This in turn places greater demands on the tail rotor to provide more thrust to compensate torque and maintain or expand control margins, although little has been found in the literature on developments in tail rotor aerodynamics in general, or tip design in particular. The modern ethos is also to minimise fuel consumption and noise. The design of the tip plays an important role in all aspects of main and tail rotor performance. Blade structural design, dynamics, vibration, ease of manufacture and cost are also strong design drivers.

Three types of main rotor blade tip designs have been identified. In the USA, the simple sheared-swept tip or swept-tapered-anhedral tip represents the state of the art, while in Europe the parabolic tip has been widely adopted, except in the UK where the BERP tip remains a unique option. Each tip is probably well suited to its particular operating requirements, which perhaps vary according to locally perceived mission requirements, although no doubt fashion and company bias have played a role. These three types of tip still tend to dominate the choice for helicopter main rotors, whilst variety of simpler tip shapes are generally found for tail rotors. For the tail rotor, the modern trend towards blades with low radius/chord ratio is also helpful in relieving compressibility effects, and perhaps explains why tail rotors tend not to feature large amounts of sweep at the tip.

Anhedral has been used to good effect on several main rotor design, and appears to be particularly effective on the BERP-type tip at high rotor loadings and offers an improved hover Figure of Merit. In forward flight anhedral can be useful to balance the effects of sweep and notch offset. Anhedral has also been used on propellers and tilt-rotor blades, and has potential to be used advantageously on tail rotor blades which are required to efficiently produce high thrust to compensate the main rotor torque and provide a good manoeuvre margin in hover.

A separate design challenge has been to reduce rotor noise, and BVI noise in particular. Several tip shapes have been put forward to achieve this goal, sometimes with little regard to performance. Several examples have been seen of tip shapes which have been designed to split, or diffuse the tip vortex, but these have not been subsequently adopted due to their limited performance potential, and perhaps an easier option has been to use low volume tips at lower tipspeeds and/or adopt alternative descending flight procedures. In general, a main rotor blade with a well designed thin swept-tip shape that has good advancing blade aerodynamics, may need only small refinements to also have acceptable thickness and loading-noise, especially if the tip speed is moderate.

This literature review has also identified some overlap with fixed-wing aircraft, particularly with regard to tip aerodynamics and the details of vortex formation. While there are some obvious fundamental differences, both fixed-wing and rotary-wing configurations require accurate resolution of the flow-field if the results are to be useful in tip design studies. The nature of the helicopter problem is, however, much more complex than fixed-wing and is much more demanding from a modeling point of view due to the need to preserve wake vortices, take into account variations in incidence and sideslip (in cruising flight), and also include unsteady effects. The design must also work within much tighter moment constraints. Nevertheless, much can be learnt from validating the methods against fixed-wing tests, and there is considerable carry-over in some of the detailed design thinking. In particular, the work of Hoerner and Küchemann provide a basis for generating improved tip shapes.

The review has also covered the development of computational methods. Analysis techniques have developed from rotor models based on lifting-line and lifting-surface theory, with a prescribed or free wake, to the application of sophisticated CFD methods. Initially the numerical approach required some of the world's largest computers, but these modern methods are now becoming available in industry, and offer greater insight and higher resolution than traditional design methods.

Two main features of the computational approach would appear to require further development for helicopter applications. One is that it is important to fully capture the wake in order to determine the correct flow-field around the rotor blade, and the other is that the solver needs to include boundary layer transition in both steady and unsteady (3D) conditions, if accurate overall performance and the effects of retreating blade stall are to be predicted. Much effort has been expended on coupling wake models with near-field Navier-Stokes solutions in an effort to obtain the desired accuracy at acceptable computational cost. It is also clear that rotor trim and blade deflections are important aspects of helicopter simulation. Often, the rotating and pitching blades may operate in proximity to a stationary fuselage, or fin, and this presents challenges in grid generation, requiring the use of sliding grids, or Chimera overset grid techniques. From the literature there appears to be a preference toward structured grids to resolve the flow features, but some developers favour the Chimera approach. It is also clear that CFD methods are maturing quickly and through rapidly growing computer resources will soon be universally accepted and are likely to become indispensable for rotor blade design evaluations.

Recent research effort on CFD has been directed towards tackling the challenging problems of whole helicopter simulations. Coupling of CFD with structural dynamics to take into account blade deflections has also been a focus of attention, and offers to greatly improve the fidelity of the simulation. Most recently, fast harmonic-balance methods have begun to emerge which promise further run-time reductions for forward flight simulations. However, while CFD has been applied to a range of rotors problems, including investigations of tilt-rotors, little new work has been found on the use of CFD for the design of new tip shapes, particularly for tail rotors.

2 Numerical Methods

2.1 Helicopter Multiblock Solver

The CFD Solver used in this research was the Helicopter Multi-block Solver (HMB). Since computational sources were initially limited, Euler solutions were used for a first appraisal of a series of tip designs by comparing the induced power and observing the pressure distributions in the tip region. Since helicopter blades operate at mid-subsonic Mach numbers, it is essential to take compressibility into account, especially for tip design. However, helicopter blades also have small chords and consequently operate at relatively low Reynolds numbers (although still considered high in mathematical terms), such that viscous effects also play a key role in determining the performance of the tip and the rotor as a whole. For the subsequent evaluation of three selected tip shapes the Reynolds Averaged Navier-Stokes (RANS) method was used with the $\kappa - \omega$ turbulence model. HMB solves the RANS equations in integral form and discretises using a cell-centred finite volume approach on structured multiblock grids. Temporal integration is done using an implicit dual-time stepping method. The details of the theory behind this method and the derivation of its equations can be found in Anderson[12] .
The Navier-Stokes equations defines the flow by mathematically stating the conservation laws of physics:

- Conservation of mass (Continuity equation):

$$\frac{\partial \rho}{\partial t} + \frac{\partial (\rho U_i)}{\partial X_i} = 0 \tag{1}$$

  where ρ is the density, U_i is the velocity in the i^{th} direction which is X_i.

- Conservation of momentum (Newton's 2$^{\text{nd}}$ law):

$$\frac{\partial (\rho U_i)}{\partial t} + \frac{\partial (\rho U_i U_j)}{\partial X_j} = \partial f_i + \frac{\partial p}{\partial X_i} - \frac{\partial \tau_{ij}}{\partial X_j} \tag{2}$$

  where f_i are the body forces (such as gravity, coriolis effect and so on) in the i^{th} direction, p is the pressure and τ_{ij} is the Newtonian stress tensor given as,

$$\tau_{ij} = \mu \left[\left(\frac{\partial U_i}{\partial X_j} + \frac{\partial U_j}{\partial X_i} \right) - \frac{2}{3} \delta_{ij} \frac{\partial U_k}{\partial X_k} \right] \tag{3}$$

  where μ is the molecular viscosity and δ_{ij} is the Kronecker delta given as

$$\delta_{ij} = \left\{ \begin{array}{l} 1 \text{ if i=j} \\ 0 \text{ otherwise} \end{array} \right\} \tag{4}$$

- Conservation of energy (1$^{\text{st}}$ law of thermodynamics):

$$\frac{\partial \rho E}{\partial t} + \frac{\partial}{\partial X_j} \left[U_i \left(\rho E + p \right) \right] + \frac{\partial}{\partial X_j} \left(U_i \tau_{ij} + q_j \right) = 0 \tag{5}$$

  where E is the total energy (internal and kinetic) per unit volume and q_i is the heat flux with respect to the i^{th} direction. Both are given as:

$$E = e + \frac{1}{2} U_i^2 \tag{6}$$

$$q_i = -k_T \frac{\partial T}{\partial X_i} \tag{7}$$

$$\tag{8}$$

  where e is the internal energy, k_T is the heat transfer coefficient and T is the temperature.

For fluids, all of the above are functions of the three velocity components in each perpendicular direction, the density, the pressure and the internal energy. They can be expressed in matrix form for a fluid element fixed in space (i.e. conservation form of the equations). So the N-S Equations can be expressed as

$$\frac{\partial Q}{\partial t} + \frac{\partial F}{\partial x} + \frac{\partial G}{\partial y} + \frac{\partial H}{\partial z} = J \tag{9}$$

where Q is the vector of conserved variables, F, G and H are the flux vectors in the x, y and z directions and J contains the source terms as shown:

$$Q = \begin{bmatrix} \rho \\ \rho u \\ \rho v \\ \rho w \\ \rho(e + \frac{U^2}{2}) \end{bmatrix} \tag{10}$$

$$F = \begin{bmatrix} \rho u \\ \rho u^2 + p - \tau_{xx} \\ \rho uv - \tau_{xy} \\ \rho wu - \tau_{xz} \\ \rho \left(e + \frac{U^2}{2}\right) u + pu - k\frac{\partial T}{\partial x} - u\tau_{xx} - v\tau_{xy} - w\tau_{xz} \end{bmatrix} \tag{11}$$

$$G = \begin{bmatrix} \rho v \\ \rho uv - \tau_{yx} \\ \rho v^2 + p - \tau_{yy} \\ \rho wv - \tau_{yz} \\ \rho \left(e + \frac{U^2}{2}\right) v + pv - k\frac{\partial T}{\partial y} - u\tau_{yx} - v\tau_{yy} - w\tau_{yz} \end{bmatrix} \tag{12}$$

$$H = \begin{bmatrix} \rho w \\ \rho uw - \tau_{zx} \\ \rho vw - \tau_{zy} \\ \rho w^2 + p - \tau_{zz} \\ \rho \left(e + \frac{U^2}{2}\right) w + pw - k\frac{\partial T}{\partial x} - u\tau_{zx} - v\tau_{zy} - w\tau_{zz} \end{bmatrix} \tag{13}$$

$$J = \begin{bmatrix} 0 \\ \rho s_x \\ \rho s_y \\ \rho s_z \\ \rho(us_x + vs_y + ws_z) + \rho q \end{bmatrix} \tag{14}$$

i.e. the first rows of each matrix are part of the continuity equation, the 2nd, 3rd and 4th represent the conservation of momentum and the last row represents the conservation of energy[12] . The source terms, s_x, s_y, s_z, $us_x + vs_y + ws_z$ and q are typically zero except in the case of a hovering rotor where a Froude condition is applied as explained later.

The N-S equations completely describe turbulent flow, however, at high Reynolds numbers, there are many turbulent scales that vary with time and space. Therefore, the number of turbulent scales are reduced by time averaging the Navier-Stokes equations to give the Reynolds-Averaged Navier-Stokes equations (RANS). This results in additional unknowns (called Reynolds stresses) which must be modelled with a turbulence model. This is described in more detail later on in this chapter.

As mentioned, the HMB flow solver uses a cell-centred finite volume approach combined with an implicit dual-time stepping method. The governing equations are applied to each cell in turn. The spatial discretisation of Eqn 9 leads to a set of ordinary differential equations in time,

$$\frac{d}{dt} Q_{i,j,k} \vartheta_{i,j,k} + R_{i,j,k} = 0 \tag{15}$$

where $\vartheta_{i,j,k}$ is the volume of the cell and $R_{i,j,k}$ is the flux residual.

The solution marches in pseudo-time iterations for each real time-step to achieve fast convergence. The following system of equations is then solved in the implicit scheme during the time integration process

$$\frac{\Delta V Q^{m+1}_{i,j,k} - \Delta V Q^{m}_{i,j,k}}{\Delta V \Delta \tau} + \frac{\Delta V Q^{n+1}_{i,j,k} - \Delta V Q^{n}_{i,j,k}}{\Delta V \Delta t} = R^{n+1}_{i,j,k} \tag{16}$$

where n represent real time step iterations, m represents pseudo time step iterations, $\Delta\tau$ is the pseudo time-step increment and Δt is the physical time step increment. ΔV is the cell volume change. The term $Q^{n+1}_{i,j,k}$ is

obtained when the pseudo time steps converge (first part of Eqn 16) to within a user-defined tolerance. An implicit scheme is used for the pseudo time integration and $R^{n+1}_{i,j,k}$ is approximately given as

$$R^{n+1}_{i,j,k} \approx R^{n}_{i,j,k} + \frac{\partial R^{n}_{i,j,k}}{\partial Q^{n}_{i,j,k}}(Q^{n+1}_{i,j,k} - Q^{n}_{i,j,k}) \tag{17}$$

The pseudo time integration is typically carried out until a convergence of 0.001 is reached. To ensure convergence, for most cases, the maximum number of pseudo time steps was set to between 100 and 200.

Combining Eqns 16 and 17, the linear system becomes,

$$\left(\frac{1}{\Delta t} + \left(\frac{\partial R_{i,j,k}}{\partial Q_{i,j,k}}\right)^{n}\right)\left(Q^{n+1}_{i,j,k} - Q^{n}_{i,j,k}\right) = -R^{n}_{i,j,k} \tag{18}$$

The convective fluxes are resolved using Osher's scheme[222] . Second-order accuracy is provided using the Monotone Upstream-centred Schemes for Conservation Laws (MUSCL) variable extrapolation method[308] and any spurious oscillations across shock waves is removed using the Van Albada limiter. Central differencing spatial discretisation is used to solve for the viscous terms. The linearisation results in a set of non-linear equations. This is solved by integration in pseudo-time using a first-order backward difference. A Generalised Conjugate Gradient (GCG)[17] method is then used in conjunction with a Block Incomplete Lower-Upper (BILU)[17] factorisation as a pre-conditioner to solve the linear system of equations, which is obtained from a linearisation in pseudo-time.

Turbulent flow causes aerodynamic structures that vary with time and space quite frequently. To run the full Navier-Stokes equations to obtain all of these structures would require a high resolution in time and space. However, with increasing Reynolds number, it is found that the larger scale turbulent structures carry more of the energy than the small ones. To avoid the high computational cost, therefore, the variables can be split into two components: an average value and a fluctuating component. So if the conservation equations are time averaged, then a number of additional terms, Reynolds stress terms, appear in the equations (denoted with '^{R}' in the following equations):

$$\frac{\partial(\rho U_i)}{\partial t} + \frac{\partial(\rho U_i U_j)}{\partial X_j} = \partial f_i + \frac{\partial p}{\partial X_i} - \frac{\partial}{\partial X_j}\left(\tau_{ij} + \tau^R_{ij}\right) \tag{19}$$

$$\frac{\partial \rho E}{\partial t} + \frac{\partial}{\partial X_j}\left[U_i\left(\rho E + p\right)\right] + \frac{\partial}{\partial X_j}\left(U_i(\tau_{ij} + \tau^R_{ij}) + q^R_j\right) = 0 \tag{20}$$

where q^R_j is the turbulent heat flux. The turbulence model is then employed to model these Reynolds stress terms. A number of turbulence models are available in HMB. For the cases presented here, the two-equation $\kappa - \omega$ model was used[321] . In a few cases Menter's Shear Stress Transport (SST)[210] blending was also applied as it improves the performance where adverse pressure gradients exist. For this model, two transport equations are used: the turbulent kinetic energy, κ, and the κ-specific dissipation rate, ω which is a function of the length. The eddy viscosity is obtained as:

$$\mu_T = \rho\frac{\kappa}{\omega} \tag{21}$$

The full turbulent transport equations used in the formulation of the $\kappa - \omega$ model are given as

$$\frac{\partial}{\partial t}(\rho\kappa) + \frac{\partial}{\partial x_j}(\rho U_j \kappa) = \frac{\partial}{\partial x_j}\left[\left(\mu + \frac{\mu_T}{\sigma_\kappa}\right)\frac{\partial \kappa}{\partial x_j}\right] + \rho\left(P_\kappa - \beta^*\omega\kappa\right) \tag{22}$$

$$\frac{\partial}{\partial t}(\rho\omega) + \frac{\partial}{\partial x_j}(\rho U_j \omega) = \frac{\partial}{\partial x_j}\left[\left(\mu + \frac{\mu_T}{\sigma_\omega}\right)\frac{\partial \kappa}{\partial x_j}\right] + \rho\left(\frac{\alpha}{\upsilon_t}P_\omega - \frac{\beta}{\beta^*\omega^2}\right) + \rho S_l \tag{23}$$

The values for the coefficients are given in Table 4 for the model. The flow solver was used in parallel for the large grid cases. Message Passing Interface (MPI) was used for the communication between the processors in parallel.

α	β	β^*	σ_κ	σ_ω	S_l
$\frac{5}{9}$	$\frac{3}{40}$	$\frac{9}{100}$	2	2	0

Table 4: *Table of coefficients for the $\kappa - \omega$ turbulence model from Wilcox*[321] .

2.2 Grid Generation

Multi-block structured grids were used with the HMB solver. The use of the multi-block method provides the versatility to accommodate complex geometries and at the same time preserves a good grid quality, such that HMB maintains 3rd order spacial accuracy. For the rotor grids, the Ansys ICEM-Hexa[13] grid generation software was used throughout, while the GHMB was also used for convenience in some 2D aerofoil cases.

The Ansys ICEM-Hexa software is designed to import geometry from CAD files. As described in greater detail in the following chapters, the Rhino 3D solid modelling (CAD) software was used to generate the surface geometry of the blade (or aerofoil) together with any other components and support curves. This geometry was then imported into ICEM-Hexa via an IGES file. In contrast, the GHMB grid generator was developed during the UK Rotorcraft DARP research programme (building on earlier work carried out in the EU-EROS project, as reported by Renzoni[248]), and the basis for GHMB is described by Allen and Rogers.[7] The input to this grid generator is simply a list of aerofoil ordinates and a set of grid size parameters. For the rotor grids the ICEM-Hexa software was preferred for its versatility, and the blocking topology was varied in the tip region to accommodate the shape of the tip.

Most of the grids used were based on a C-H topology. For the 2D aerofoil cases the outer radius was set at about 15 chords and the downstream boundary at least 20 chords from the aerofoil. These grids were built with either ICEM-Hexa or the GHMB grid generator was used.

For a hovering rotor, the wake may be assumed to be symmetrical and a steady state solution may be used. The boundaries of each blade segment are therefore assumed to be periodic. This places constraints on the topology of the grid (unless non-matching grids can be used, as now possible in the HMB framework, building on the development of sliding planes, Steijl[277]), and required that the topology around the aerofoil section of the blade changes from H to C to H. A 2D 'rotor-grid' was generated during the early stages of this research to verify the grid quality, as illustrated in Appendix A.

For Euler cases a first cell spacing of 10^{-3} chords was used (see Appendix A for the effects of varying this spacing and the grid density), and for Navier-Stokes grids the first spacing was set to 10^{-5} chord in order to achieve $y^+ < 1$. The grid spacing away from the wall was governed by either the exponential or hyperbolic functions available in ICEM, ensuring a smooth variation and the expansion rate was generally less than 2 and preferably less than 1.3. Details of the Euler grids for the model tail rotor application are described in Chapter 5, and the refinements made for Navier-Stokes are detailed in Chapter 6. For the Navier-Stokes case, it was found advantageous to reduce the size of the blocks around the blade to help control the expansion of the grid.

2.3 Boundary Conditions

For the case of a hovering rotor, potential sink inflow and so-called 'Froude' outlet boundary conditions were used such that the wake exhausts the domain in a jet on the downstream boundary, based on the rotor thrust and outflow radius as described by Steijl.[284] This technique avoids any re-circulation in the domain. The downstream boundary was set at 6R below the rotor. A central cylindrical hub was used as a convenience in the centre of the domain, and a gap was left between the blade and the hub to facilitate pitch adjustment. Although this allows the root vortex to form naturally, the tail rotor has a large root cut-out and an upwash was therefore experienced in the central region of the rotor disc. The simplification offered by the cylindrical hub also had unforeseen consequences at high pitch as discussed in Chapter 6. For the forward flight case, a elliptical hub was used, and the blade segments were copied and rotated to complete a full rotor grid on which an unsteady solution was obtained.

The grids for the rotor-fin blockage case study employed a sliding plane between the upper (stationary) domain of the fin and lower rotating domain of the rotor. The fin was surrounded by an O-grid topology and the rotor had a simplified central hub and the feathering bearings were also represented. As in the forward flight case, the blades were allowed to flap and change pitch due to pitch flap-coupling. For this case, however, the solver was modified to non-dimensionalise on the tipspeed for this initially stationary flowfield, in contrast to the more usual forward flight case where there is a predominant freestream and the non-dimensionalisation is based on the forward flight Mach number.

2.4 Wake Visualisation and Vortex Criterion

Locating the position of vortices in the wake of the rotor depends on the vortex definition used. In this research, most of the vortex location work was carried out using vorticity as generated in Tecplot,[295] however, later in this project, the Q and λ_2 criteria were also used to identify tip vortices, and the two methods were compared (see Chapter 3.4).

The vorticity, and vorticity magnitude, as computed in Tecplot is given by:

$$\begin{aligned} \xi_x &= \frac{\partial w}{\partial y} - \frac{\partial v}{\partial z} \\ \xi_y &= \frac{\partial u}{\partial z} - \frac{\partial w}{\partial x} \\ \xi_z &= \frac{\partial v}{\partial x} - \frac{\partial u}{\partial y} \end{aligned} \tag{24}$$

and hence:

$$|\xi| = \sqrt{(\xi_x^2 + \xi_y^2 + \xi_z^2)} \tag{25}$$

Alternatively, using the eigenvalues of the velocity gradient tensor, ∇u, it has been proposed that a vortex core is a region with complex eigenvalues of ∇u. Complex eigenvalues imply that the local streamline pattern is closed or spiral in a reference frame moving with the point[154] .
Q is the second invariant of ∇u. If it is positive and the pressure is lower than the ambient pressure, then an eddy exists. Q represents the balance between shear strain rate and vorticity magnitude. Q vanishes at a wall unlike vorticity strength.

Haller[127] analyses a few definitions, including the Q and λ criteria. Q is defined as

$$Q = \frac{1}{2}[|\Omega|^2 - |S|^2] > 0 \tag{26}$$

and must satisfy the condition in Equation 26 for there to be a vortex. Here, Ω is the norm of the vorticity tensor (or the spin tensor) and S is the strain rate i.e. Ω must exceed S.
On the other hand, the λ criterion states that

$$\lambda_2(S^2 + \Omega^2) < 0 \tag{27}$$

for a vortex to exist. Jeong and Hussain[154] start from the idea that a pressure minimum is not a characteristic unique to vortices and that pressure minimums that do exist in vortices can be removed by viscous effects. Therefore, they break down the velocity gradient tensor and obtain S and Ω and define a vortex as a region where the $S^2 + \Omega^2$ has two negative eigenvalues. More details on the formulation of these definitions can be found in Haller[127] and in the original paper by Jeong and Hussain[154] .

2.5 2D Aerofoil Code - MSES

In addition to running HMB for 2D aerofoils, the MSES Code of Drela[99] [97] was also found to be useful for obtaining rapid results for the compressible viscous flow around an aerofoil. It was found particularly useful for comparing with HMB, and provided a cross-check on the pressure drag and skin-friction. Like HMB, the MSES code has been well validated over the years, and is routinely used at Westland Helicopters as an aerofoil design and optimsation tool.

To take into account compressibility, the solution of the Euler equations is obtained along streamlines, using an H-H grid topology. MSES is therefore able to capture shocks and the coupled boundary layer solution responds accordingly. If the flow has a low Mach number, the results are essentially the same as the well known public domain Xfoil code, described by Drela.[96]

However, MSES is only applicable in steady flow up to the point of stall, and although it has robust boundary layer, perhaps tends to slightly overestimate the maximum lift and underestimate the drag in extreme high incidence conditions. At more moderate angles, MSES has an initially laminar boundary layer, and transition is triggered by an e^N stability criterion. An integral boundary layer method is then used to represent the turbulent boundary layer. The drag at low to moderate incidence is therefore well predicted by MSES, since it takes into account the laminar drag bucket.

The location of the transition point may be either prescibed, or controlled by the N_{crit} parameter of the e^N transition model. Typical values of this parameter are 7-9 for low-turbulence freestream, and the author found that an Ncrit of 2 correlated wel with aerofoil tests in the WHL wind tunnel [Proprietary WHL Internal Report, April 1997]. Values as low as unity were sometimes required to match the drag values obtained from the ARA pressurised 2D transonic tunnel which is thought to have higher turbulence. If the N_{crit} parameter is set to a low value, say 0.5, transition may be made to occur near the leading edge, and in this case very close agreement is found with HMB for 2D aerofoils over a range of flow conditions.

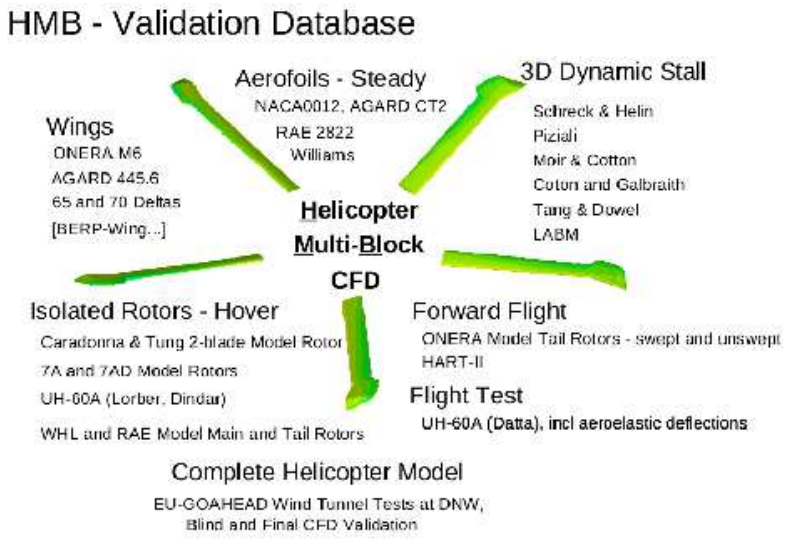

Figure 104: Presentation Slide Describing the HMB Validation Database

3 Validation

The aim of the validation section of this thesis is to show that results from the HMB CFD code provide a realistic simulation of helicopter rotor aerodynamics, and also that the validations can be extended to the practical (highly loaded) rotorcraft problem in support of the blade tip design theme of this thesis.

The HMB computational fluid dynamics code has already been widely validated against a range of test cases and has an associated Validation Database,[21] and was subsequently refined and expanded under the UK Rotorcraft DARP initiative to include a hover and forward flight trim capability, Steijl and Barakos[285].[284] A description of validation cases in the public domain was also presented by the author at the 31st European Rotorcraft Forum in Florence in 2005,[22] and later a slide sumarising the contents of the HMB Validation Database, reproduced here as Figure 104, was also presented by the author at conferences in 2008[62].[61]

Although the tip design question is a 3D problem, 2D aerofoil characteristics provide a vital under-pinning for understanding the aerodynamics of the rotor, and a useful starting point for the current research.

At an early stage in this research, some 2D cases were run for the NACA 23012 aerofoil to get a feel for grid requirements and the limitations of the Euler solution. Depending on the first spacing and gridsize, it was found that the numerical diffusion which manifests itself as a residual drag (due to pressure losses) could either be raised to a higher level with gradual divergence, or a relatively low drag polar could diverge quite suddenly as incidence was increased. This work is included in Appendix A .

Further grid sensitivity studies have been carried out for the case of the model tail rotor, as discussed in Section 3.2.

At the start of this work, several validation cases were available for aerofoils such as the NACA0012 and RAE2822 in high sub-sonic Mach number conditions at moderately high Reynolds numbers, together with some comparisons from the low Reynolds number unsteady tests for NACA 0012 at LABM.

For the present research it is essential to confirm that the solver performs well at the relatively low Reynolds number mid-Mach number conditions of the example model tail rotor blades. Further validation of the HMB code was therefore undertaken, firstly for a typical aerofoil, NACA 23012, which has been used in the past for rotor applications and for which test data exists in the public domain from two different sources, and secondly for the NACA0012 aerofoil of the model rotor blades as used later in this thesis for design demonstration

purposes. Subsequently, a series of unsteady cases were run to explore aerofoil characteristics as the stall is encountered. This work is the topic of Section 3.1

Various wings, such as the tapered ONERA M-6 wing, are already included in the HMB Validation Database. Beedy[34] has explored the characteristics of a BERP-III-like planform wing, and results were compared to wind tunnel data by Brocklehurst and Beedy.[60] [2] Spentzos[265] has simulated dynamic stall on a rectangular wing, and also 3-dimensional stall on various planforms.[266] Early in the current research the author simulated a wing of AR=5 to verify the code against classical lift-curve slope and induced drag theory, and these results are included in Appendix B.

A well known rotor validation case in the public domain is that of the Caradonna and Tung, low aspect ratio, R/c=6, 2-blade model rotor,[73] and this rotor was used as a foundation of the HMB Validation Database. The results of the validation has been reported by Steijl,[284] together with the 7AD rotor (R/c=15) of Le Pape and Beaumier [2003].[179] These comparisons with blade surface pressure measurements have been repeated several times to test the code, but since these have already been published they are not reproduced here. The Sea King has an even higher main rotor aspect ratio and was investigated by the author as part of his duties at WHL,[57] where it was observed that the tip vortices passed closer to the blades than expected, although there is some anecdodal photographic evidence which suggests that this may be the case. These main rotor issues contrast to the tail rotor where the vortices tend to be spaced further from the blades, giving a more rounded loading peak. Unfortunately, there is a general lack comprehensive rotor tests cases where all aspects of the loading, wake and overall performance have been measured.

In an effort to confirm the overall performance, the author has more recently run cases for the higher aspect ratio, R/c=13.7, 2-blade model rotor of Tung, Pucci, Caradonna and Morse[298] where fair comparison with measured thrust and torque was found. Unfortunately surface pressure data does not exist for this rotor configuration as the purpose of the test was to investigate the structure of the tip vortices rather than to specifically measure the power, hence the data is sparse and some scatter is present. These comparison therefore fall short of full validation case. Nonetheless this work helps to increase confidence in the HMB method for the assessment of rotor performance and is briefly presented as a further comparison case in Appendix C.

The UH60A model rotor tested by Lorber[191][192] has been chosen as a primary validation case in the current work because it is a model rotor with an interesting tip shape for which both blade surface pressure measurements and wake trajectories are both available. In recent times the full-scale Black Hawk has been the subject of a significant research effort following the development of an extensive flight test database (but restricted to the US), Kufeld and Bousman[170].[171] Aeroelastic coupling due to the swept tip is a strong feature, and corrections needed to be made even for the model rotor in hover. This validation case is presented in Section 3.4, before going on to compare with the Westland model tail rotor.

The application of HMB to practical tail rotor simulations is demonstrated in Section 3.5 of this validation chapter, through comparison with the authors own model rotor hover tests from the early 1980's. While these experiments were part of an industrial test program, and may therefore lack the precision necessary for a thorough validation of CFD, it is useful to make these comparisons and thus build further confidence in the use of the solver. [3]

In this PhD study, the focus is on evaluating tip shapes on an example model tail rotor blade, where the design is dominated by hover performance. The aim of this chapter is to support that aim. However, an Euler forward flight case was also run to provide an assessment of the impact of tip shape, as presented in Chapter 5. Fortunately, in forward flight the tail rotor is often off-loaded by the fin, and the solidity is also relatively large, so that the loading on the retreating blade is not as high as for a main rotor, making the Euler solution viable for an initial evaluation. For more highly loaded cases a much more computationally demanding Navier-Stokes case would be required.

[2] The BERP tip is not explored further in this thesis, since the detailed geometry of the Lynx and EH101 main rotor blades is not readily available in the public domain, and the focus here is on evaluating a range of tip shapes for an example tail rotor.

[3] Over recent years, the code has also been intensively used, by the author and others, at AgustaWestland (UK,Italy) in pursuance of rotor design, development and research tasks, allowing some further in-house comparisons to be made against flight test experience and additional model main rotor test data. Comparisons have also been made against more traditional rotor prediction methods, but unfortunately the work is proprietary. Nevertheless, this additional experience increases the confidence with which HMB can be applied to practical helicopter problems.

Validation of CFD codes in forward flight places great demands on both experimental resources and computational resources, and is beyond the scope of this thesis. However, the author has gained first hand experience of validation in forward flight through his professional involvement in a parallel project.

The recently completed EU-GOAHEAD project now provides a comprehensive dataset for a complete helicopter model which was tested in the DNW wind tunnel. The timescale of this project ran in parallel with this PhD study, and the author was the lead engineer for the Westland (WHL) contribution. This collaborative test and validation program encompassed a range of forward flight conditions, including a challenging highly loaded stall-flutter case and a very high-speed test case. Computed 'blind' test cases and 'post-test' CFD simulations were carried out by partners from academia, research institutions and industry. An overview of the GOAHEAD project has been presented by Pahlke[227] and results were compiled by Boelens.[48] The WHL contribution comprised an initial Euler simulation (constrained by computational resource limitations at that time), and this first UK industrial unsteady forward flight case clearly demonstrated the need to employ a Navier-Stokes solution to properly simulate the viscous effects on the retreating blade of a main rotor. In the final phase of the project, such a case was run by the author for an isolated rotor, and the results compared well to the test data, as summarised in the public domain by Antoniadis, et al,.[14] Other partners completed whole helicopter simulations, for example see Dietz,[93] Boelens,[49] Steijl and Barakos,[278],[280] and Barakos, Steijl and Woodgate.[23]

All the following public domain validation cases described in this section of the thesis were completed with HMB version 1.4 during the course of this PhD research. Permission to use and publish the WHL model rotor test data was given by WHL and MoD/DSTL, and access to ARA steady data for NACA0012 at mid sub-sonic Mach number and low Reynolds number is gratefully acknowledged.

3.1 Aerofoils

The NACA 23012 and NACA 0012 aerofoils were chosen for 2D Navier-Stokes validation cases because these aerofoils have, for many years, found application on helicopter rotors, and data for these aerofoils is available in the public domain. The NACA 0012 aerofoil was chosen for the example tail rotor blade (TRB) designs put forward in this thesis, and was also used on the WHL model tail rotor.

The symmetrical NACA 0012 is well known for providing a good compromise between helicopter requirements in forward flight for low drag at high (sub-sonic) Mach number, and moderate lift at low Mach number, with near-zero pitching moment. However, the concept of using leading edge camber to increase the usable CL on the retreating blade, without significantly degrading the advancing blade drag, or introducing unmanageably high nose-down pitching moments, is exemplified by the NACA 23012. Both these aerofoils have interesting mixed-phenomenon stalling characteristics at the relatively low Reynolds numbers and moderate Mach numbers appropriate to typical helicopter applications.

The NACA 0012 and NACA 23012 aerofoil may be generated from mathematical expressions which make up the NACA 4-digit and 5-digit aerofoil series, as described by Abbott and von Doenhoff,[1] and are therefore smooth. The co-ordinates used for these validation cases were generated by the author and written out to 7 significant figures prior to use in Rhino/ICEM or the GHMB grid generation software. The co-ordinates for NACA 23012 are listed in Appendix E and for NACA 0012 in Appendix F, both of which were defined with sharp trailing edges to simplfy grid generation.

In recent years, aerofoil design and evaluation methods have been developed for compressible flow, and incorporate a coupled integral boundary layer method to account for viscous effects. These methods have become more widely available to the rotorcraft design engineer and require only a short runtime on a modern desktop workstation. Quite accurate results are known to be available from methods such as MSES[99] and BVGK[188] at conditions where separation is not too significant (and for 2D incompressible flow, XFOIL[96] and the EPPLER[107] airfoil code may also be used with some confidence). The author has used these methods which compare well to one another and have been well validated against a wide range of test data over many years. MSES tends to have advantages over BVGK at low Mach number and high incidence, whereas BVGK converges more readily at higher Mach number. It therefore seemed logical to not only compare HMB to test data, but to also compare against at least one of these codes, and MSES was the preferred choice.

The MSES aerofoil prediction code of Drela and Giles (1987) [99] was also used to provide a comparison with the test data and CFD predictions. This Multi-Element Euler Streamline code includes a coupled boundary layer, and has a parameter, Ncrit, which controls the growth of instabilities in the laminar boundary layer following the e^N method of transition prediction. The author's experience in comparing results from this code with tests in the Westland wind tunnel [WHL Internal Report, 1997] suggests values for Ncrit in a typical tunnel test may be between 2 and 5, while a value of 8 would represent a very low turbulence tunnel and values of 9 to 11 are used in free-air. [4]

Like most RANS methods, HMB is normally used with turbulence models which do not fully take into account the initial run of laminar flow and the transition process, and so there is a tendency to overpredict the drag. In comparison to the inviscid/viscous-coupled methods such as MSES, the RANS CFD methods are, however, better able to cope with shock-boundary layer interactions which play an important role in limiting aerofoil performance at moderate to high sub-sonic Mach numbers. For hovering rotors, and model tail rotors in particular, aerofoil performance at low to mid Mach numbers and relatively low Reynolds number conditions is important, and perhaps presents a greater challenge with regard to drag prediction than cases at higher Reynolds numbers that have been validated previously.

Several turbulence models are available for HMB-1.4, ranging from the the Spallart-Almaras to the standard k-ω model of Wilcox,[322] a modified k-ω model, and a Shear Stress Transport (SST) model of Menter[209].[210] The choice of turbulence model will affect the development of the boundary layer, the tendency for separation, and consequently the skin-friction.

[4] A much lower value of Ncrit, in the region of 0.5, appears be required to compare with data for rotor aerofoils tested in the ARA 2D transonic wind tunnel, suggesting that the turbulence level may be high.

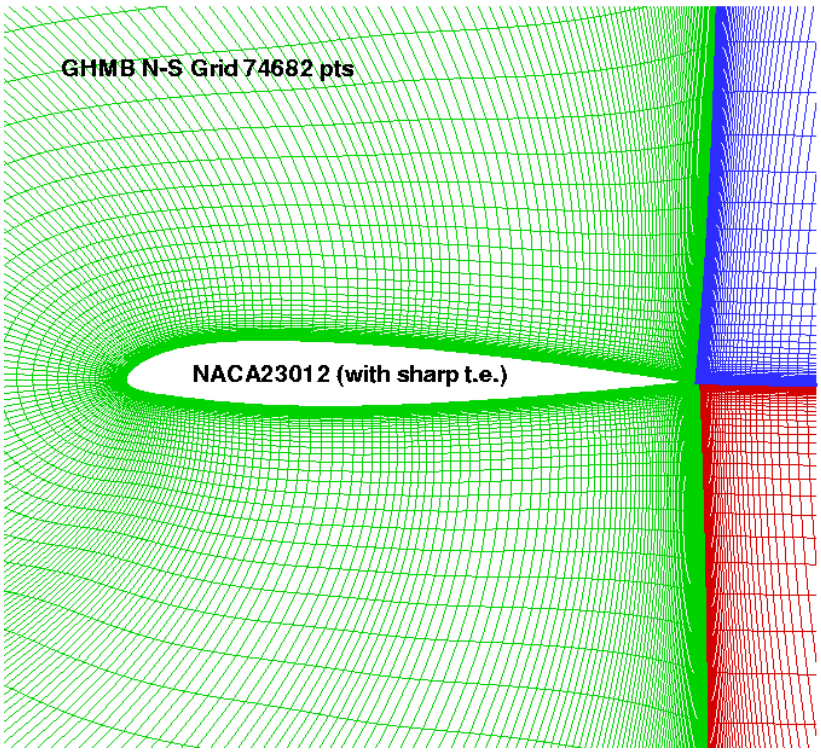

Figure 105: Grid used for 2D Navier-Stokes Solutions for NACA 23012

A transition model has been introduced into the HMB solver through the work of Hill [2005],[135] and Hill, Shaw and Qin [2004][137],[136] and while the transition location appears to be well predicted, the lower drag resulting from the laminar boundary layer was not computed, and question remain about the accuracy of the model in unsteady conditions. This work was carried out at Cranfield and was mainly based on Michel's criterion. In the Liverpool CFD LAB Zografakis[331] has carried out further research on transition using an intermitency approach, which is now implemented in HMB, but was still being finalised at the time of writing this thesis and was therefore not employed in the current research. The use of a good transition model should improve not only the accuracy of the drag predictions, but should also offer a better physical model of the flow separation mechanism near stall.

Although the focus of the work of this thesis is towards steady state performance evaluation of new tip shapes, the flow state at high pitch angles may become unsteady as the stall is approached. To illustrate the capability of HMB to model this type of unsteady separating flow, a series of unsteady aerofoil cases are also included in section 3.1.4, after first considering steady state comparisons.

3.1.1 NACA 23012, M=0.2, Re=3 million

The NACA 23012 aerofoil was chosen for this first validation study because it is representative of a typical rotor aerofoil and published test data is available from more than one source. Data from tests in the NACA low-turbulence pressurised (3ft x 7.5ft) wind tunnel was published by Abbott and van Doenhoff ,[1] and Althaus [9] also provides data from the low-speed wind tunnel at the University of Stuttgart. Both these well respected sources of data provide good quality lift, drag and pitching moment data, and the datasets have the case of a Reynolds number of 3 million in common.

A grid suitable for HMB Navier-Stokes runs was prepared using GHMB, and for convenience, a sharp trailing edge version of NACA 23012 was used (the trailing edge thickness of the true NACA aerofoil is, in any case, fairly small, having a dimensionless t.e. ordinate of +/-.00126). The grid is shown in Figure 105, and comprised 74682 points with the first spacing set to .00002 which gave y^+ values close to, or just greater than,

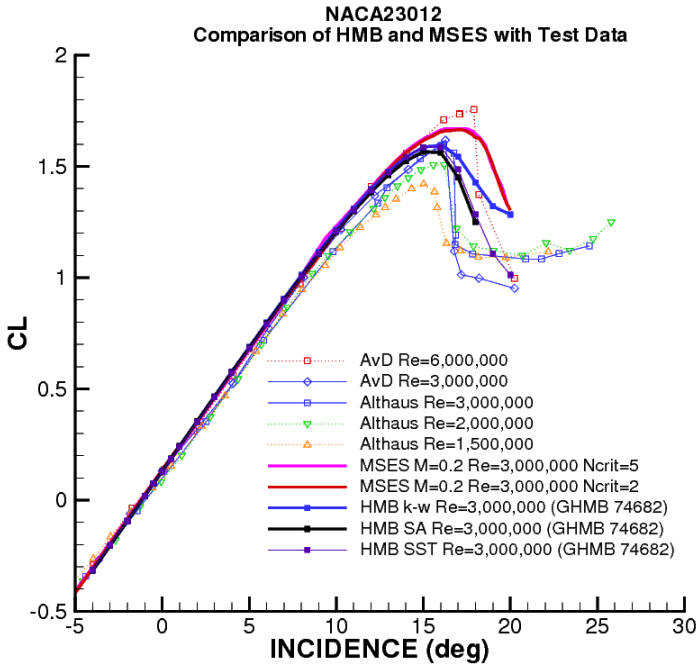

Figure 106: Comparison of HMB Predictions and Test Data: CL vs Incidence

unity at low to moderate incidence conditions. No attempt was made to optimise the grid for each incidence. The HMB solver was run at a Mach number of 0.2, appropriate to that of the test conditions.

At a Reynolds number of 3 million the data from the above mentioned sources for NACA23012 are in close agreement. Figure 106 also includes (NACA) test data at higher Reynolds number and lower Reynolds numbers (Althaus) to show the effect of varying the Reynolds number through the range 1.5, 2.0, 3.0 to 6.0 million. The predicted lift-curves in Figure 106 from HMB and MSES are in good agreement with the test data, and with one another, below stall. However, at the stall, MSES tends to over-predict the lift and the drop-off in lift is delayed. This over-prediction in the lift as come to be expected from MSES, and is related to the way in which the boundary layer develops and affects the Kutta condition (which is difficult to predict at stall). HMB predicts CLmax in close agreement with the test data, and captures the reduction of lift-curve due to trailing eddge separation prior to stall. At the stall the predicted curves show a more gradual break, whereas the test data shows a more sudden break due to leading edge separation (and this might be further improved by use of a transition model).

The lift-drag polar is compared in Figure 107, and as expected, the Spallart-Almaras (HMB, 2000) and k-ω models (HMB, 3000) over predict the drag due to the relatively high turbulent skin friction, while the drag from the Shear Stress Transport (SST) model (HMB, 3007), falls much closer to the test data, showing close agreement at low incidence beyond the bottom of the laminar drag bucket, and again at the top of the drag bucket. The predicted drag curves have a smooth parabolic shape, since they do not include any effects of changes in transition location with incidence, and the low-drag laminar bucket is not modelled. Using the e^n transition model, MSES showed good agreement with the test data and in particular the lower part of the laminar drag bucket is extremely well predicted. Again, it is noted that while the e^n transition model in MSES captures the laminar drag-bucket, while the coupled Euler-streamline and integral boundary layer method tends to underpredict the drag at high lift.

Finally, Figure 108 shows a general growth in nose-up pitching moment prior to a sudden break in the test data at stall, as predicted by both HMB and MSES. There is also some apparent disparity in the pitching moment data (perhaps due to 3D effects in the tests), mainly at the higher Reynolds numbers, although it is clear that the moment break is predicted at too great an angle by HMB, and more so by MSES. The closest

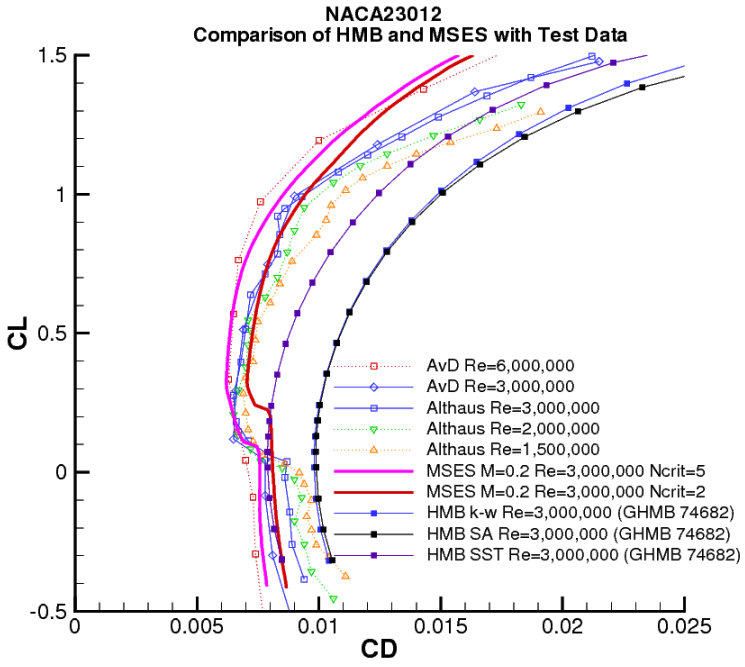

Figure 107: Comparison of HMB Predictions and Test Data for NACA 23012: CL vs CD

agreement with the test data for the moment break is achieved using HMB and the Spalart-Almaras turbulence model option, although the SST k-ω model provides a similar lift break and has the advantage of offering very good agreement on drag.

It is anticipated that the introduction of a boundary layer transition model in HMB will bring the drag predictions and lift and moment breaks into much closer agreement with steady test data, and should also have the potential to capture the stall mechanism under dynamic conditions typical of the helicopter.

It is concluded that predictions of aerofoil characteristic at low Mach number and moderate Reynolds number, obtained from HMB compare quite well to measurements, although the finer details drag-bucket is not yet predicted as accurately as with specialised aerofoil methods. The above validation studies were presented by the author at The Burn in April 2005 .[55]

3.1.2 NACA 0012, M=0.5, Re=5 million

NACA 0012 was chosen for the various tail rotor blades defined later in this work, which were developed from the baseline NACA0012 blade of the WHL model tail rotor. HMB predictions for the NACA 0012 are here validated against ARA wind tunnel test data and compared to MSES at a Mach number of 0.5, and a Reynolds number of 5 million (the effect of Reynolds number is covered in the following sub-subsection).

In contrast to the above comparisons where the data was from low-turbulence tunnels, the ARA 2D-transonic tunnel[148] is thought to have a moderate amount turbulence, but for many years the (steady and unsteady ramp and oscillatory pitch) data obtained has been taken to be representative of practical helicopter aerofoil sections, Wilby.[318] Since the ARA tunnel is pressurised (up to 3 atmospheres), this data has the advantage that the Reynolds number is usually close to that of a typical full-size rotor blade (nominally Re=10 x M x 10^6, and in addition some limited data is also available at reduced pressure ratios, and hence lower Reynolds numbers, over the same range of Mach numbers, 0.3-0.85, for application to tail rotors.

The validations for NACA 0012 presented here have therefore been carried out at M=0.5, Re=5.0 million and 2.2 million, and an HMB case for Re=1 million has been included to highlight the trend with Reynolds

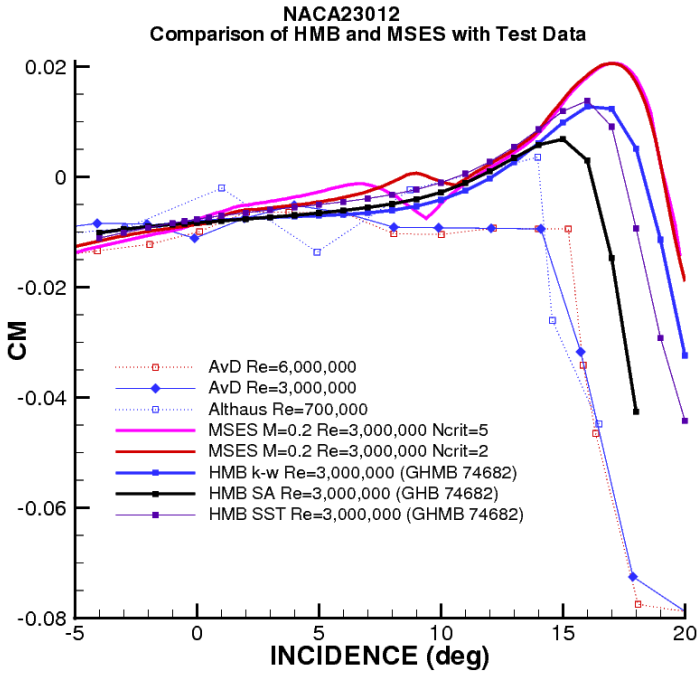

Figure 108: Comparison of HMB Predictions and Test Data: CM vs INCIDENCE

number. This Reynolds number is also of interest for the Navier-Stokes hover computations (presented later in this thesis), for a blade-section with chord based on the WHL model rotor, while M=0.5 relates to about 83%R and a tip Mach number of 0.6.

As for the above NACA 23012 validation, several turbulence models were used, including the modified k-ω model which had been well tested for HMB Navier-Stokes hover cases due to its robustness. [5] A range of Ncrit (2.0, 0.5 and 0.1) was used for the MSES aerofoil analysis code to facilitate comparison with the HMB fully-turbulent model predictions and also to represent the effects of turbulence of the ARA tunnel (based WHL experience, see also Drela's Turbulence-Ncrit graph in the MSES documentation[98]).

The grid size used for these 2D aerofoil computations totalled 96,390 points, 291 around the aerofoil, 81 normal and 151 in the wake, the distance to the farfield boundary was 15 chords around the aerofoil and 20 chords downstream and the first cell height was set to 1 x 10^{-5} to obtain a y+ value near unity.

The following Figures present comparisons for NACA 0012 at a Reynolds number of 5 million. Figure 109 compares the CL-alpha curve for HMB predictions with the 3 turbulence models, as described above, with MSES predictions and the ARA test data. NACA 0012 was computed here with the standard finite thickness trailing edge to be compatible with the tests. Generally there is good agreement for the lift-curve slope, although on close examination, MSES shows the steepest slope, while HMB lies nearer to the test data, which has the lowest slope, with little difference whether transition free or fixed (with .0021"-.0025" balantini balls at 7% chord). As the stall is approached the lift-curve flattens at the Mach number and the lift does not break. Both MSES and HMB with the k-ω (3000) model capture the maximum lift, but all the predictions show a reduction in CL post-stall. While the data is thought to be reliable, the values must represent the mean of a signal with some unsteadiness and the stall pattern in the wind tunnel would be influenced by roof (vented to a plenum chamber) and wall effects, and perhaps even the formation of stall cells, in contrast to the purely 2D simulations.

[5] Recently, main rotor hover cases have been run by the author at AW(Yeovil) using the range of HMB k-ω models, and the profile power characteristics reflected the trends identified here.

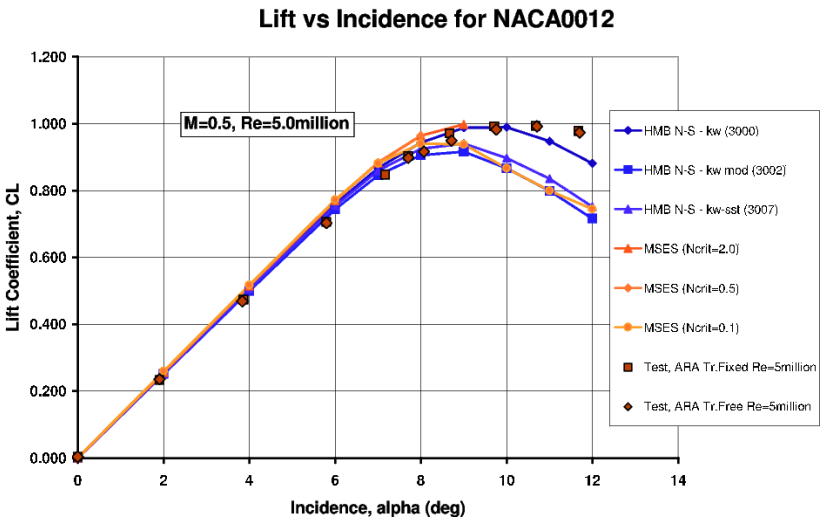

Figure 109: Predicted lift-curve for NACA 0012 at M=0.5 and Re=5.0 million together with ARA test data

While the 3000 turbulence model gives the highest CLmax, the 3007 and 3002 models are in close agreement with the MSES predictions with fairly low Ncrit, with the later turbulence model perhaps giving pessimistic results.

Figure 110 compares the drag. As found previously, the standard k-ω (3000) model tends to over-predict, while the modified model and SST k-ω models are in excellent agreement with the test data. MSES tends to under-estimate the drag, but both predictions cpature the drag divergence trend quite well. Figure 110 also shows the skin friction component of drag (obtained from the HMB .intv file, and from MSES), and this data is plotted on large scales in Figure 111 where it can be seen that the results from HMB straddle the skin friction values from MSES. The sst model (3007) is in close agreement with MSES with Ncrit=2.0. [6] As expected the skin friction drag gradually decreases with incidence while the pressure drag increases, slowly at first, but then diverges as the stall develops with increasing incidence, Figure 112. In terms of pressure drag the HMB estimates are slightly greater than those produced by MSES.[7]

Comparisons of predictions and test data for the pitching moment of NACA 0012 at M=0.5 and Re=5 million are shown in Figure 113. The moment increases strongly with incidence due to the formation of a shock on the upper surface near the leading edge. This trend tends to be over-predicted both MSES and HMB, although the moment break occurs at a similar incidence to the test, and shows a downward trend in the region of 12 degrees.

Figure 110 compares the MSES and HMB predictions for total drag and skin friction drag, both with the ARA test data, and with points obtained for the drag coefficient of the rotor blade as described above. While the steady drag test data at the higher Reynolds number lies close to the MSES predictions, the 3002 or 3007 turbulence model of HMB may be considered to provide a good estimate of the drag at a Reynolds number of 1 million. The solid points from the measured drag coefficients coincide with the 2D trends, giving confidence in the overall approach. Figure 111 shows the skin friction drag on an expanded scale, confirming good agreement between HMB and MSES, and Figure 112 shows the trends for the pressure drag to be similar for both sets of predictions, and with the residual pressure drag (obtained from the total minus the skin friction) showing similar drag divergence trends.

Finally, the predictions and test data are compared in terms of a CL-CD polar in Figure 114, and the HMB results are seen to be in excellent agreement with the test data, particularly for the modified and sst k-ω models

[6] A value of Ncrit=2 was identified as matching the onset of transition from flow visualisation tests carried out by the author in the WHL wind tunnel in 1997.

[7] While the static pressures measured on the surface of the wind tunnel model may be integrated to give an estimate of the pressure drag, the sparcity of data is generally considered to limit the accuracy of the integration, even with 39 tappings. While this topic has not been pursued further here, separate fitting of the skin friction and pressure drag has been used in methods developed at WHL by Beddoes[30] to provide a semi-empirical model of the drag for application in rotor codes.

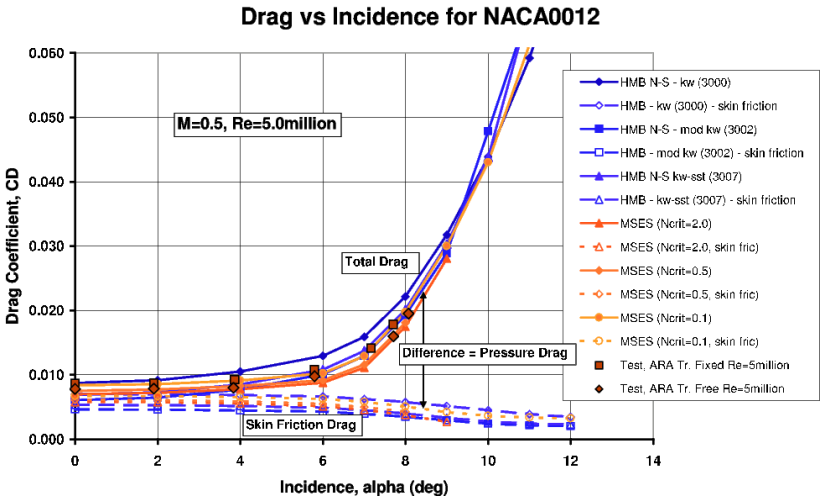

Figure 110: Profile drag coefficient predicted from MSES and HMB compared to blade profile drag coefficient from Navier-Stokes hovering rotor simulations

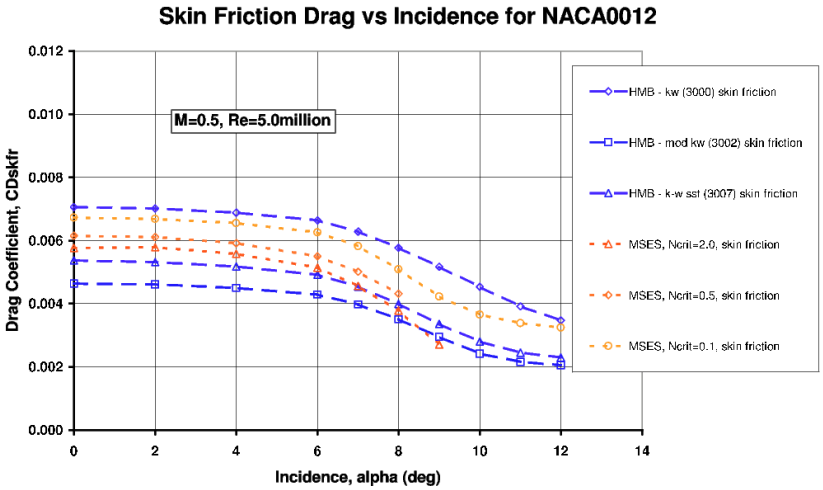

Figure 111: Skin Friction drag predicted from MSES and HMB on expanded scale compared to blade skin-friction drag coefficient from Navier-Stokes hovering rotor simulations

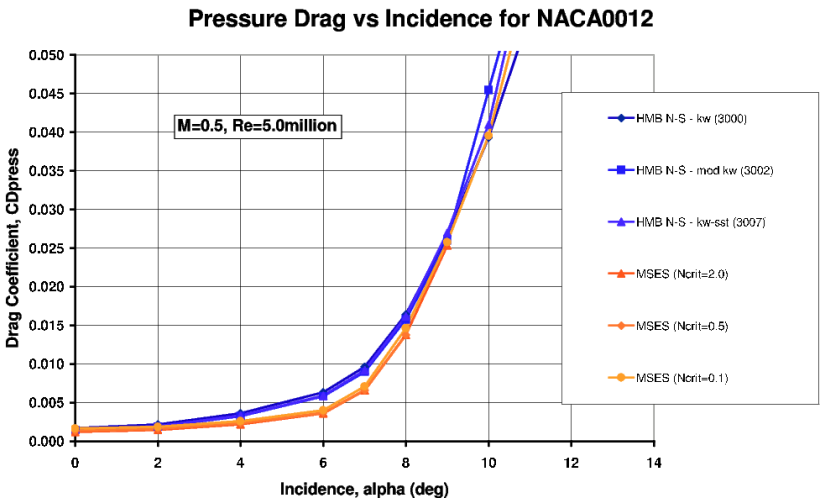

Figure 112: Pressure drag predictions from HMB and MSES compared to ARA test data for NACA 0012 at M=0.5 and Re=5 million

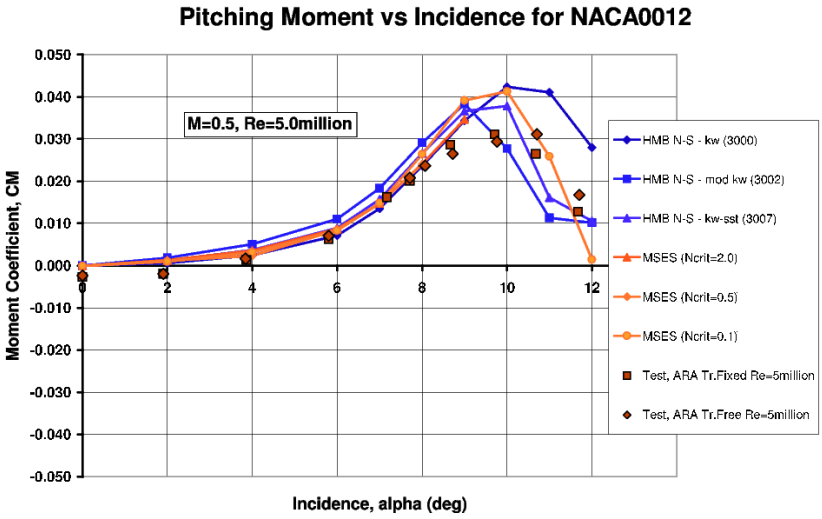

Figure 113: Pitching Moment predictions from HMB and MSES compared to ARA test data for NACA 0012 at M=0.5 and Re=5 million

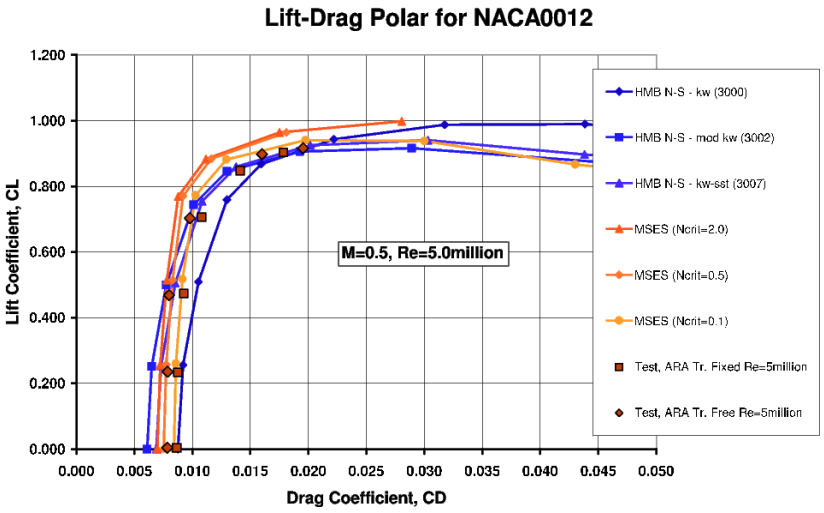

Figure 114: Lift-Drag Polar predictions from HMB and MSES compared to ARA test data for NACA 0012 at M=0.5 and Re=5 million

(3002 and 3007). As might be expected the MSES predictions tend to over-estimate the CL/CD at the top end of the drag bucket, while they also show good agreement at low lift.

3.1.3 NACA 0012, M=0.5, Effect of Reynolds Number

The above validation for NACA 0012 at M=0.5 has shown excellent agreement with test data at Re=5 million. However, for tail rotors and especially model rotors the Reynolds number has a generally lower value, reducing to 1 million in the case of the model tail rotor considered in this project. The effect of Reynolds number was investigated by comparing HMB and MSES predictions over the range from 1.0 to 5.0 million, and comparisons were also made against a further set of ARA test data at Re=2.2 million. In all the following cases, HMB predictions were run with the modified k-ω model (3002) (as preferred for the Navier-Stokes hovering rotor simulations, as described later) and the MSES predictions assumed a low value of Ncrit=0.1. Figure 115 shows that there is a gradual reduction in lift-curve as Reynolds number is reduced, and while HMB and MSES show similar trends, HMB is in best agreement with the test data (although the test data appears to have a relatively low lift-curve slope for this particular case).

The ARA data for NACA 0012 (at M=0.5 and Re=2.2 million) again suggests that the lift remains high near stall whist the predicted values tend to fall off. In these extreme conditions the drag again appears to be slightly over-predicted at high angles, Figure 116.

As expected, at lower incidences, the drag was predicted to increase at lower Reynolds numbers, and Figure 116 shows generally good agreement between HMB and MSES and the ARA data at Re=2.2 million. As stated above, the skin friction drag is initially nearly constant and then slowly decreases with incidence, while the pressure drag tends to increase parabolically. As Reynolds number decreases, both the skin friction drag and the pressure drag are found to increase due to strengthening viscous effects.

The more dominant viscous effects at lower Reynolds number initially accentuate the nose-up trend of the pitching moment, but then the curves come together as the stall is approached and, as might be expected, the low Reynolds number predictions diverge slightly earlier towards zero and then negative pitching moment values post-stall.

Comparing the CL-CD polar shows how the lift/drag ratio is reduced at the lower Reynolds number, Figure 118. Again, good agreement is seen between HMB, MSES and the ARA test data at 2.2 million throughout most of the usable lift range.

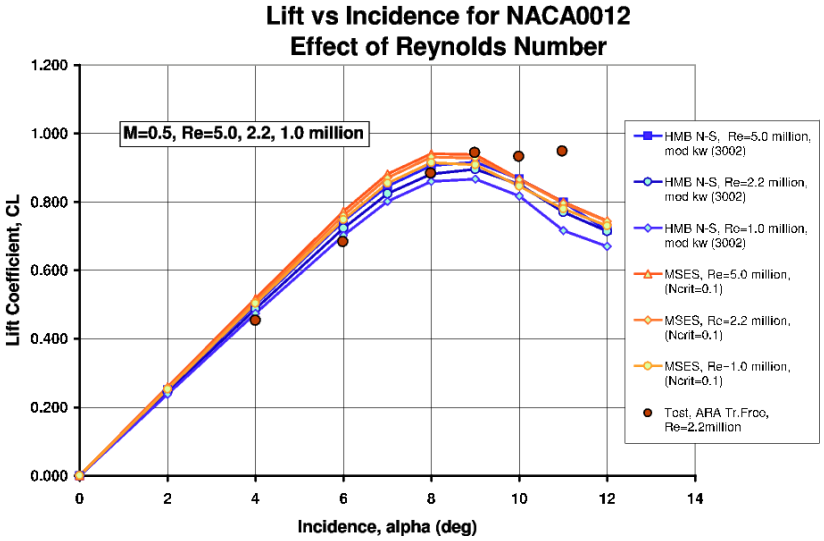

Figure 115: Effect of Reynolds number on lift-curve slope as predicted by HMB and MSES for NACA 0012 at M=0.5, and comparison with ARA test data at Re=2.2 million

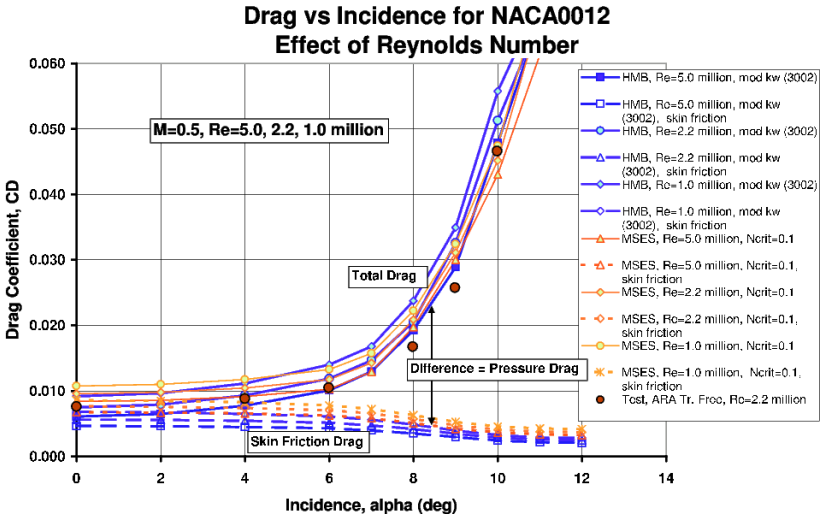

Figure 116: Effect of Reynolds number on drag as predicted by HMB and MSES for NACA 0012 at M=0.5, and comparison with ARA test data at Re=2.2 million

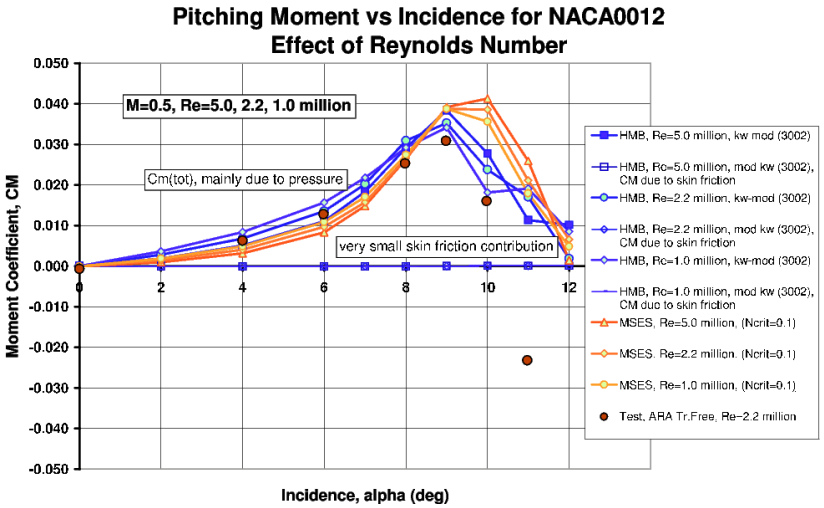

Figure 117: Effect of Reynolds number on pitching moment as predicted by HMB and MSES for NACA 0012 at M=0.5, and comparison with ARA test data at Re=2.2 million

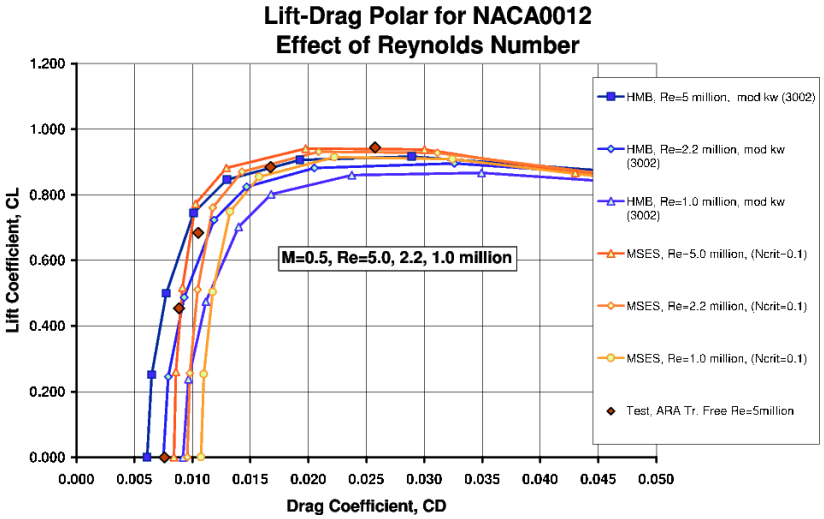

Figure 118: Effect of Reynolds number on pitching moment as predicted by HMB and MSES for NACA 0012 at M=0.5, and comparison with ARA test data at Re=2.2 million

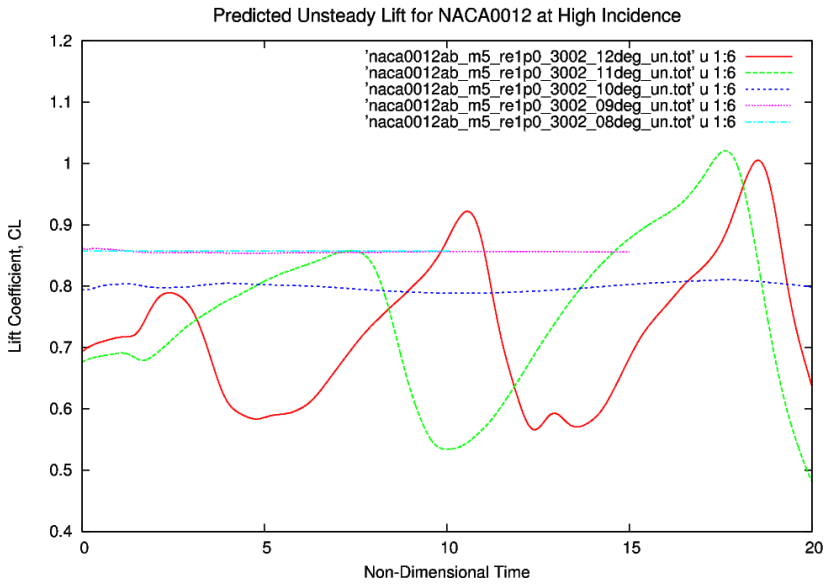

Figure 119: Lift predictions from an unsteady HMB 2D simulation of NACA 0012 at high incidence, M=0.5 and Re=1.0 million

From the above comparisons it is clear that the greatest discrepencies occur at the stall, and indeed, it was observed that the residuals from the steady HMB solutions did not converge to the same low levels (usually 10^{-7} as the angle of attack was increased. In fact, the residuals tended to rise and oscillate about a mean of the order of 10^{-4} or 10^{-3}, suggesting that the solution was fluctuating due to inherent unsteadiness in the flow. This problem may be overcome by running an unsteady simulation to capture the fluctuating flow separations that occur near stall, however, such solutions are more expensive on cpu time.

3.1.4 NACA0012, M=0.5, Re=1 million, Unsteady Stall

Later in this thesis, different rotor tip designs are explored with the HMB Navier-Stokes code, and while steady results were obtained at high pitch angles similar difficulties of convergence were eventually encountered as the stall was reached, and it was found difficult to settle on final values of CT and CQ. Attention then turned to the prospect of running high-pitch (tail) rotor cases as unsteady solutions, thus accepting any flow separation and vortex shedding that might occur (perhaps ultimately exceeding the bounds of RANS applications). It was therefore of interest to take a similar approach here for the 2D aerofoil case, and while unsteady ramp and oscillatory cases have been modelled with HMB in the past, eg Spentzos,[265] it is unusual to find unsteady solutions for aerofoils at a steady high pitch near the separation boundary. Experience with model rotors, has also revealed a tendency for unsteady torsion loads and control moments to grow rapidly as the stall is approached in addition to the expected increase in nose-down mean pitching moments. Such effects would, of course be automatically included in an unsteady N-S simulation of forward flight, offering to capture both unsteady shock movement and shock-boundary layer interactions on the advancing blade and unsteady separation and vortex shedding from the retreating blade. On a tail rotor in low-speed flight, many disturbances, such as gyroscopic flapping and pitch-flap coupling, and rotor-fin and main rotor-tail rotor interactions could exacerbate the stall, and even in a steady hover the stalled flow will not leave the blade in an ordered fashion.

The unsteady cases were run at 8, 9, 10, 11 and 12 degrees, using a GHMB grid of similar size (104,000 pts) to that used for the steady cases described above. However, for the unsteady cases, the aerofoil was set at the desired incidence angle in the grid and the flow angle was set to zero. Various non-dimensional time-steps were tried with .002 being finally chosen and the simulations were run to 20.0 (chord lengths through the fluid) over a period of typically 2.5 days, per case, on a P4 3.2 GHz 64-bit processor. All cases employed the modified k-ω

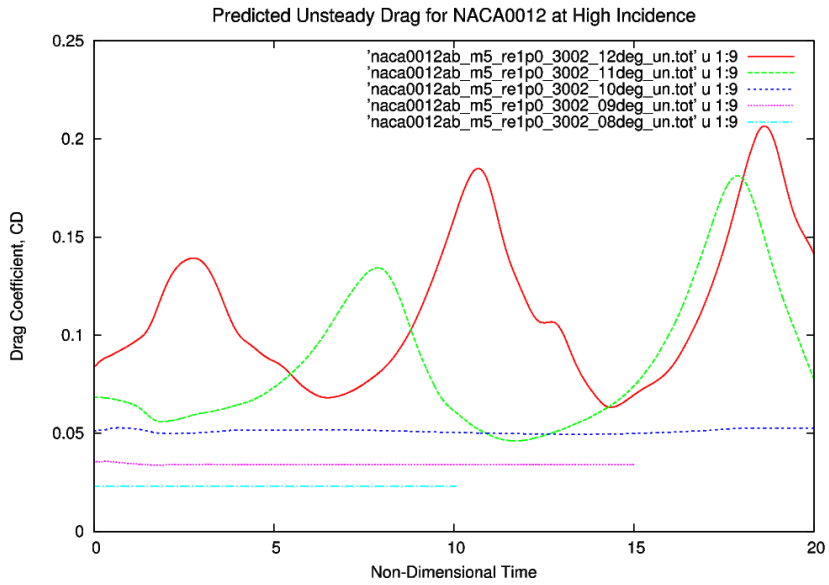

Figure 120: Drag predictions from an unsteady HMB 2D simulation of NACA 0012 at high incidence, M=0.5 and Re=1.0 million

(3002) turbulence model. The Mach number was 0.5 and a Reynolds number of 1.0 million was chosen, to be consistent with the above steady cases and compatible with the model tail rotor simulations to follow.

As seen from visualisation of the results, separation first develops at the trailing edge and gradually moves forwards along the upper surface, until it meets the adverse gradient at the foot of the shock (near the leading edge) which causes it to suddenly separate and shed vorticity into the stream.

The unsteady lift response for the incidences considered is shown in Figure 119 and it can be seen that, as expected, the unsteadiness increases with increasing incidence, with the trends showing some signs of settling to a repeatable pattern, although the total time was not extended to fully confirm this expectation. Nonetheless, these results showed that the peak unsteady values far exceeded the initial steady values. Perhaps because of the modified k-ω (3002) model used, or perhaps due to the RANS methods itself, results for the lower incidences showed less unsteadiness than perhaps might have been expected.

Results for the unsteady drag, Figure 121, where the drag coefficient at the higher angles was at already very high values in steady flow, showed much larger values at the peaks and only values similar to the initial steady value in the troughs. As expected, these large fluctuations are caused by changes in pressure drag due to fluctuating separation, shock movement and vortex shedding. In contract the skin friction term is small and changes only slightly in sympathy with the incidence and length of attached boundary layer.

While the steady pitching moment, discussed earlier, had shown a gradually increasing nose-up trend with incidence prior to stall (due to shock formation near the leading edge at this mid-Mach number), with a reversal of this trend at stall, the unsteady results revealed large fluctuations in pitching moment (about the 1/4 chord) which reached values in the region of -0.15 due to aft movement of the centre of pressure arising from separation, recovering to -0.03 to -0.05 during re-attachment.

The steady state validations discussed earlier have demonstrated good accuracy for HMB predictions of lift, drag and pitching moment at incidence angles ranging from those for attached flow conditions to those near the stall. However, at the stall, strong vortex shedding is likely to occur which demands the use of the unsteady solver, and this then reveals large fluctuating force and moments on the aerofoil. HMB may therefore be used with confidence to predict the flow around 2D aerofoils, and the next step is to validate the code for 3D problem of the hovering rotor.

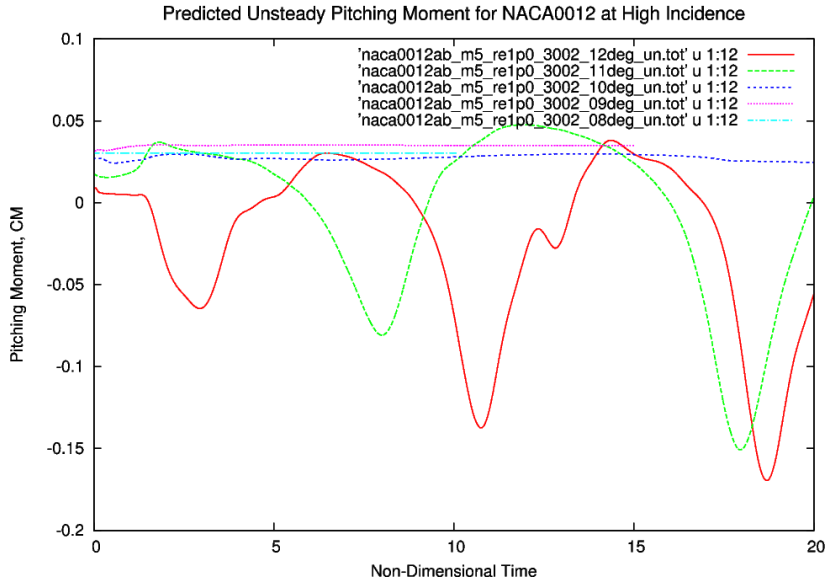

Figure 121: Pithcing moment predictions from an unsteady HMB 2D simulation of NACA 0012 at high incidence, M=0.5 and Re=1.0 million

3.2 Grid Sensitivity Studies

Ahead of rotor computations, a 3D Euler solution was also used to explore the performance of an unswept wing of AR=5 with Küchemann-like tips. The grid was progressively refined from about 250,000 to near 3,500,000 points, until close agreement was obtained in comparison to the expected lift-curve slope and induced drag from lifting-line theory. This preliminary work not only gave confidence in the capability of HMB to predict the correct (inviscid) performance (from surface pressure integrations), but also helped to develop a feel for 3D grid requirements. These studies are reported in Appendix B.

Building on the aerofoil and wing studies, several Euler grids were generated for the example model tail rotor blade. Initial grid size was about 1.5 million points, but with further refinements to improve grid quality and obtain better resolution of the flow, the grid size gradually increased to approximately 2.5 million points. Some finer grids were used in the search for grid independency, and some coarser grids were also explored to better understand the sensitivity of the solution to grid spacing. This grid dependency study is reported in this section of the thesis.

While the model tail rotor has relatively short blade (R/c=6.402), main rotors have much longer blades (13<R/c<20), and consequently require a greater number of cells to populate the computational domain. A case in point is that of the Sea King which has a main rotor blade with R/c=20.4, and requires at least 3 million points. Some preliminary cases were reported in a seminar, Brocklehurst,[57] where the proximity of the tip vortices to the preceding blade was noted. As the work [8] progressed, 5-6 million points were commonly used for Euler hover solutions in an attempt to resolve the finer details of the flowfield arising from various design features, and a fine grid of just over 10 million points was used to show that the results were essentially grid independent.

Navier-Stokes grids were later developed, initially for 2D aerofoils, by the addition of points within the boundary layer region with exponential refinement, and a first cell height of about .00001 to obtain y^+ near unity. The quality of these grids was gradually refined as experience was gained (mainly using ICEM, but GHMB was also used for aerofoils). The 2D aerofoil profile drag results were scrutinised by comparing to test data and other prediction methods. Good agreement was reached, as shown by the validation results presented in the previous Section.

Initial attempts to run Navier-Stokes cases for hovering rotors were hampered by the need to economise on grid size which resulted in severe stretching of the grid and therefore undesirably large cells outside the boundary layer and in the blocks surrounding the blades. Eventually, as computational constraints became less of a problem, and the necessary experience and insight was gained to allow the generation of rotor grids which had a smooth transitions from the boundary layer at the surface, through the region around the blade, and out towards the far field. An adequate number of cells are also required to resolve the wake and capture the flow features around the root and tip of the blades. Moving the block-boundaries (and their support curves) nearer to the blade helped greatly in this respect, as did an extra block downstream of the trailing edge to control the spacing. These refinements for a viscous rotor grid increased the number of points from about 2.5 million up to about 8 million points for a blade-quadrant of the 4-blade model tail rotor example, as used later in this thesis.

Up to 16 million points were used to obtain a high-fidelity hover Navier-Stokes solution for the 2-blade model rotor (R/c=13.7) of Tung, Pucci, Caradonna and Morse,[298] which was computed recently and is presented in Appendix C.

The following sub-section describes the results of varying the grid size for Euler solutions for the example model tail rotor. The grid size relates to a single blade segment with periodic boundaries faces.

[8] In parallel with this research project, several main and tail rotor cases relating to EH101, Lynx and Sea King were run by the author at Westland Helicopters Ltd (WHL). This background provided additional experience and gave confidence in generating good quality grids to obtain meaningful solutions to practical problems.

3.2.1 Model Tail Rotor - Hover - Euler

Most of the Euler hover simulations presented in the thesis have used a 'standard' grid size of about 2.5 million cells for the tail rotor cases. This choice was based on experience gained through preliminary work for this thesis (as noted above), together with tail rotor and later main rotor design studies at WHL. A grid of this size gives a reasonable turn-around time (approx 24 hrs on 8 x 2.8GHz cpu's), and provides sufficient resolution of the tip vortices to give good performance predictions. The number of grid points may also vary slightly depending on the blocking scheme necessary to accommodate the tip shape.

To ensure that the results obtained were reasonably independent of grid size, a series of different grid densities were run for the datum, rectangular (square-cut) tail rotor blade. Use of a coarse grid will clearly minimise runtime, but could lack the resolution required to yield reliable performance estimates. It is expected that a finer grid will better resolve and preserve the tip vortices and other weaker features of the wake, such as the inboard vortex sheet and the root vortex system, all of which may affect the blade loading and influence rotor performance. However, the requirement to use a really fine grid is perhaps not as necessary for an Euler solution as it would be for a Navier-Stokes case where the aim would be to simulate more details of the physics, and the grid must match the requirements of the type of turbulence model used.

The 'standard' case quoted here comprises 2,875,680 points, and the geometry is that of the datum rectangular (square-cut) tail rotor blade with no twist and NACA0012 aerofoil. The radius of the cylindrical hub was 0.25 chords for this particular case (TRB-000-00). All cases are compared with a coning appropriate to the model rotor tests and the tip Mach number was 0.448.

To check on grid sensitivity a coarse grid of about 1.0 million points and a fine grid of 8.5 million points were generated. Subsequently, further cases of 0.75 million and 8.0 million points were also added in order to confirm the various trends seen in the results.

In modifying the ICEM grids, the node spacing was re-adjusted in each case to give a smooth variation of grid points in regions of greatest interest, and the spacings were matched as closely as possible at block boundaries. In all cases an intermediate blocking plane was used at 0.75R below the rotor to give fine control of the grid spacing just below the blocks attached to the blades. For these Euler solutions, the blade-attached blocks started about 1-chord above and below the blade surface, whereas for a Navier-Stokes grid this would be reduced to about 0.25 chords, or less, to avoid stretching.

The results for the 'coarser', 'coarse', 'standard', 'fine' and 'finer' grids are compared at pitch angles of 4, 6 and 10 degrees impressed pitch in Figures 122 to 126, for grid sizes of 746,372, 1,041,788, 2,875,680, 7,900,456 and 8,479,876 respectively, where the standard size grid of 2,875,680 points is that used for TRB-000-00 for the model rotor twist study, as described later in this validation section. All grids contained 170 blocks.

Figure 122 shows that the thrust for a given pitch is not very sensitive to changes in the grid size, provided of course that the grid is fine enough to capture suction peaks on the blades. The coarser grids considered here produced an artificially high thrust (perhaps because the mean induced downwash in the wake was under-resolved), while the finer grids gave a thrust comparable to that of the standard grid (when adequate wake resolution had been established). When the thrust variation is plotted against gridsize, as in Figure 123, this trend becomes clearer. It is seen that the differences become greater at higher pitch and thrust, and this is a point worth bearing in mind for future work, particularly where it is desired to apply very high pitch angles to achieve maximum thrust (for which purpose a full Navier-Stokes analysis would be necessary).

Greater effects of changing the grid size in these Euler cases was observed in the torque results, Figure 124, where it is clear that the coarser grids result in a significantly higher torque value, while the finer grids give reasonable agreement, with the torque perhaps decreasing as the grid is refined. This trend is confirmed and shown in greater clarity in Figure 125.

The combined effect of variations in the thrust and torque due to use of the various grids is illustrated in Figure 126, where a significant impact on the (inviscid, Euler) Figure of Merit is found. A grid that is too coarse will result in an artifically low Figure of Merit, while too fine a grid would waste valuable computer resources. The overall trend with grid refinement is fairly flat, and any small variations for the finer grids are

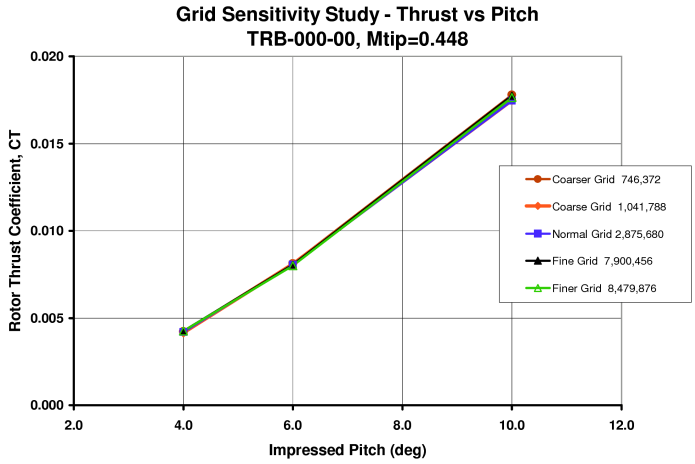

Figure 122: Effect of Grid Size on Thrust-Pitch Characteristics: Euler Solution for Configuration TBR-000-00 at a Mach Number of 0.448

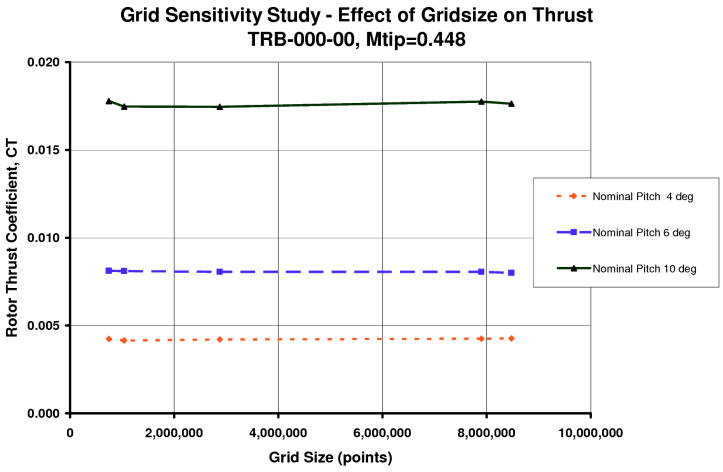

Figure 123: Effect of Grid Size on Thrust Coefficient: Euler Solution for Configuration TBR-000-00 at a Mach Number of 0.448

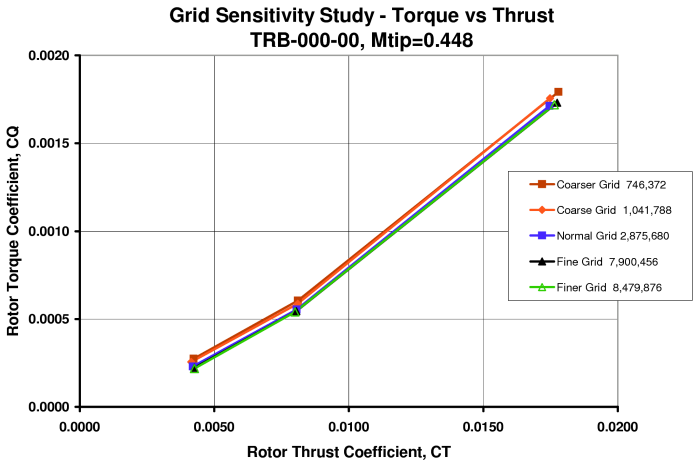

Figure 124: Effect of Grid Size on Torque-Thrust Characteristics: Euler Solution for Configuration TBR-000-00 at a Mach Number of 0.448

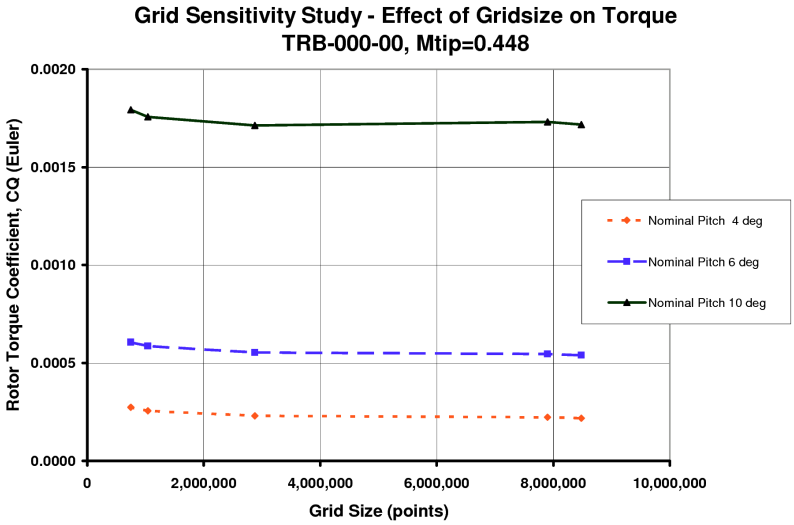

Figure 125: Effect of Grid Size on Torque Coefficient: Euler Solution for Configuration TBR-000-00 at a Mach Number of 0.448

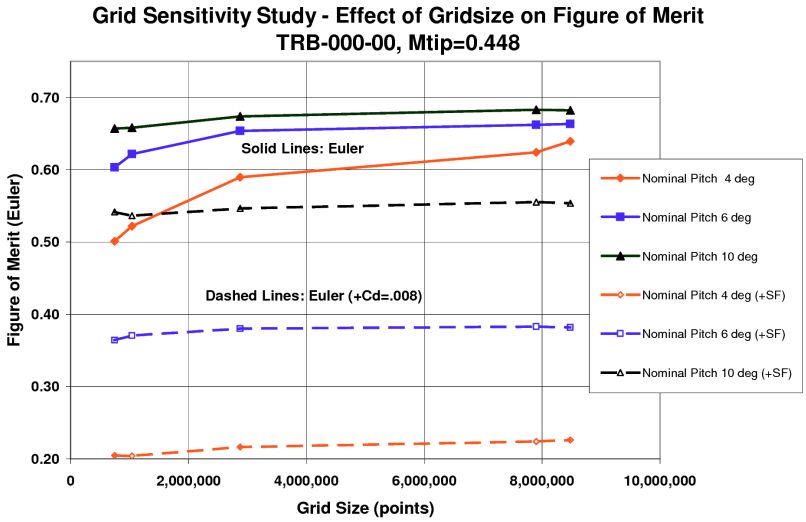

Figure 126: Effect of Grid Size on Figure of Merit: Euler Solution for Configuration TBR-000-00 at a Mach Number of 0.448

almost completely masked by the addition of a notional 'profile' drag (the addition of an estimated profile drag to the Euler solution to make the Figure of Merit more realistic is discussed further in Section 5).

Conclusions for Tail Rotor Grid Sensitivity Study

While a relatively coarse grid may offer some economy during initial trials, it is likely that pessimistic performance predictions would result due to under-resolved flow features. The results of this grid sensitivity study confirm that a grid of about 2.8 million cells is sufficient to obtain good resolution of the vortex wake structure, and has been found to preserve vortices to an age of about 360 degrees. Use of a finer Euler grid did not appear to significantly affect the vortex trajectories. Therefore correctly predicted values of the hover thrust and induced power should be obtained for the example model tail rotor blade(s) considered in this research project.

For subsequent Navier-Stokes analysis, additional points must be added to capture the boundary layer and resolve the flow near the tip, and near the vortex sheets and cores in the wake, so that grids of up to about 8-10 million cells are anticipated for viscous simulations using one quadrant of the example model tail rotor in hover.

3.3 UH60A Model Rotor with Swept Back Tip in Hover

The Sikorsky UH-60A Black Hawk has been the subject of many studies aimed at performance assessment and method validation in the USA, where there is ready access to the original model rotor data and more recent flight test data from the Airloads Programme. However, the fullscale data is not readily available in the open literature and therefore the UH60A model rotor data is used here for the further validation of HMB.

Test data for the UH-60A model main rotor is available from Lorber,[191] and has been used for CFD validation by several authors, such as Srinivasan, Raghavan, Duque and McCroskey,[276] Wake and Baeder,[313] Berkman, et al,[36] Dindar et al,[94] Strawn and Djomehri,[287] and Bhagwat et al,[39] and others. It is of interest to note that the first aplication reference also includes CFD comparisons with the Lynx-BERP rotor, following the earlier work of Duque.[100] Usefully, Dindar includes the effect of aero-elastic deflections (due to the aft-swept tip) which are significant even in hover, and this has been taken into account in the current work.

More recenty full-scale pressure measurements and strain gauge data is emerging from the NASA/US Army Airloads Programme, Kufeld and Bousman,[170] mainly in terms of integrated loads, as also available from tests in the NASA Ames 80-by120ft wind tunnel, Shinoda, Yeo and Norman,[260] but at the time of writing the model rotor data offers the most detailed pressure measurements in hover.

3.3.1 Rotor Geometry

The UH-60A model rotor has 4 blades, a radius of 1.4325 m (4.7ft) and a chord of .0924m (3.64in). Several papers state that in all other respects the model blade is identical to the full-scale blade (R=26.83ft, c=1.73ft). The blade tip has 20 degrees of sweep, starting at 92.9%R, and no taper. Although not obvious from some of the illustrations of the model rotor, the leading edge has a curved blend region between 92.9%R and 95%R to achieve the required sweep angle, while the trailing edge has a sharp kink. The chord normal to the leading edge in the tip region is the same as the basic blade chord. The model blade is illustrated in Figures 127 and 128 and the full-scale blade planform is shown in Figure 129 for reference.

The swept-back tip appears to have a classical end-closure, perhaps a bit blunter than hemispherical, and such a tip shape has been included in the geometry used here. For simplicity in this CFD validation study, the root was simply cut-square at 13%R, although the bluff sections inboard of the blade root station will influence the (low speed) flow in the hub region (close to the periodic boundary) and therefore have a small effect of the rotor performance. In the present work, however, the main focus is on the pressure distributions and vortex roll-up in the tip region.

The twist comprises a 17.45 degrees radial rate from the root to 75%R, after which the rate reduces to 12 deg, before increasing again outboard of 85%R to a rate of 27 degrees per unit radius to 95%R. Relative to the root, the twist reaches a maximum of 13.3 degrees, while outboard of 95%R the twist is reversed and the tip is twisted 2.2 degrees nose up, Lorber.[191] The collective pitch setting is measured relative to 75%R. However, according to Dindar,[94] at moderate collective there is over a degree and a half of aeroelastic nose down twist which arises from the rearward lift offset on the tip (the tip itself appears almost rigid). Dindar also quotes a coning angle of 2.31 degrees for a collective pitch setting of 10.47 degrees. The twist distribution is plotted in Fig 135 where the effect of the aero-elastics can be readily seen.

In the literature, comparisons have been made with the test data at several approximate pitch angles, ranging from 9 to 11 degrees. Specific collective pitch angles are not available from Lorber[191] due to US Army restrictions, but may be deduced from the other references cited above. Following Dindar,[94] a collective pitch setting of 10.47 degrees was used to compare with measured pressures. After allowing for aeroelastic effects the blade angle at 75%R is 9.164 degrees.

3.3.2 Aerofoils, and Smoothing

The co-ordinates for the SC1095 and SC1095R8 were obtained from Lednicer's internet site,[180] and are specified to more decimal places than those from the UIUC web site, which are otherwise consistent. The aerofoils are compared in Figure 130 where it can be seen that SC1095R8 is a nose-drooped version of SC1095, and the aerofoils are essentially common aft of about 20% chord. The SC1095R8 would be expected to have a greater lift capability prior to stall, and so is used for the main lifting part of the blade, with SC1095 at the tip.

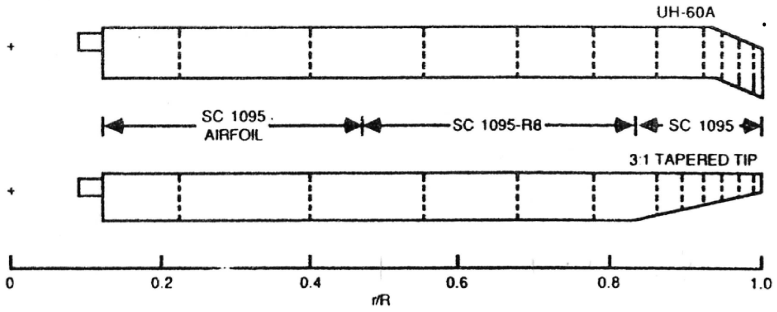

Figure 127: UH-60A Swept Tip and 3:1 Taper Tip Model Rotor Planforms, from Lorber[191]

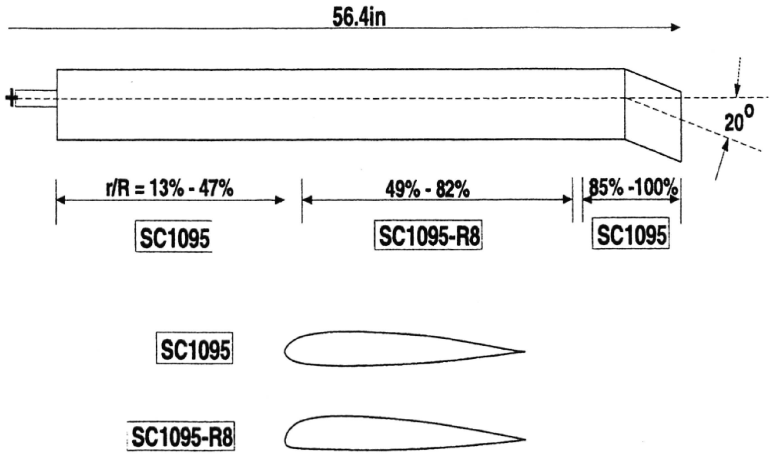

Figure 128: UH-60A Model Blade, from Dindar[94]

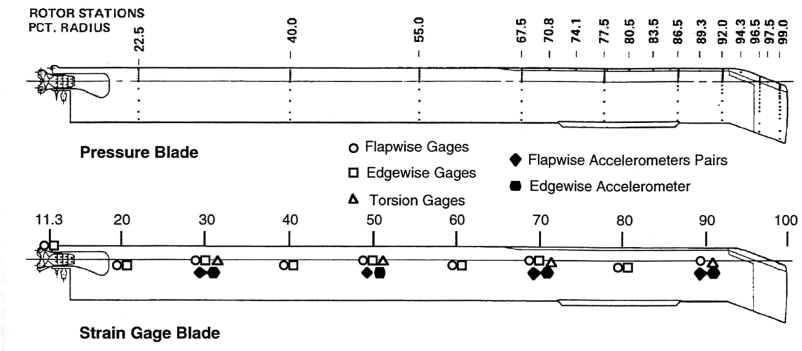

Figure 129: Full-Scale UH-60A Blade from Kufeld and Bousman[170]

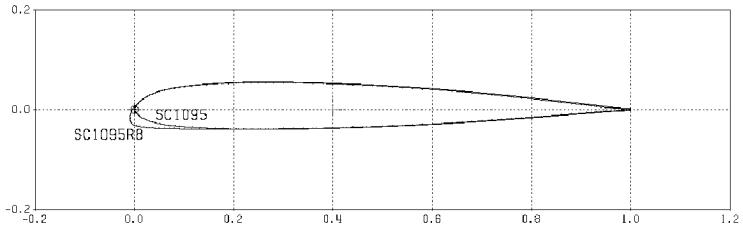

Figure 130: Comparison of SC1095 and SC1095R8 Aerofoils

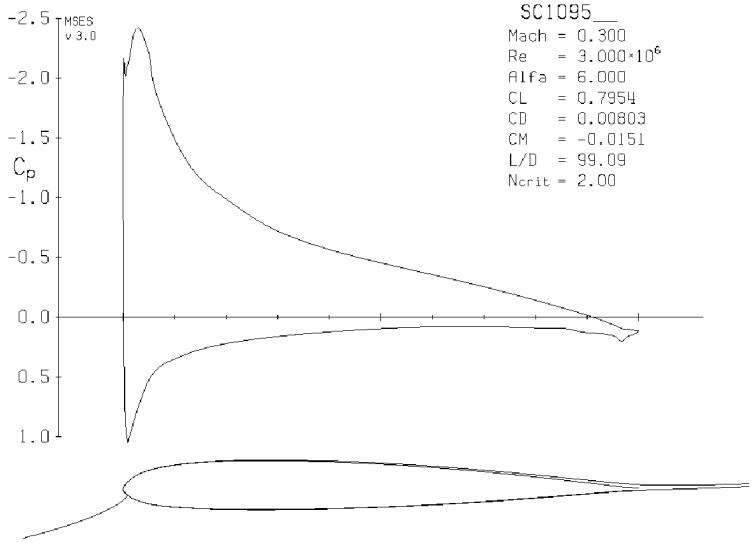

Figure 131: SC1095 with L.E. Suction Spikes from Lednicer's Co-ordinates

While the SC1095 is defined about the chordline, the SC1095R8 is set-out about a datum line which is nose up relative to the true chord line, hence the two aerofoils have similar zero-lift angles relative to their datum lines (MSES: -0.729 degrees SC1095, and -0.636 degrees SC1095R8). The blade twist angles are therefore taken to be relative to the datum line. Both aerofoils have a thickness/chord ratio of 9.5%, and SC1095 has a very low pitching moment, CMo=-.015, while SC1095R8 has CMo=-.026. Perhaps the low pitching moment of the SC1095 is the reason that it is also used over the inboard part of the blade. Another reason may be the desire to minimise the profile power in hover, as an aerofoil with a low thickness/chord ratio is clearly acceptable on a blade with a titanium spar. More contemporary practice (with composite construction) might be to use a thicker, more nose-cambered and reflexed aerofoil inboard to avoid inboard stall and minimise defleections due to blade sailing during start-up in wind.

The 2D aerofoil code, MSES, was used to provide a quality check of the aerofoil definitions. The UIUC co-ordinates were found to give spikely pressure distributions and were discarded in favour of those from Lednicer, which provided co-ordinates to 6 figures. However, while the SC1095R8 was acceptable at most conditions, Figure 132, the SC1095 still revealed a significant numerical problem at the leading edge, Figure 131, due to discontinuities in curvature (second derivative). Both aerofoils were therefore carefully smoothed by plotting second differences of the ordinates, prior to being used for grid generation. As part of the smoothing process, the leading edge of SC1095 was re-drafted in RHINO, making only very small changes to achieve the desired continuity prior to final numerical smoothing (alternatives would have been to use ICEM DDN, or preferably CATIA where both the aerofoil geometry and curvature can be simultaneously plotted in detail). For the present purpose, the trailing edge was made sharp to simplify grid generation. The smoothed co-ordinates for

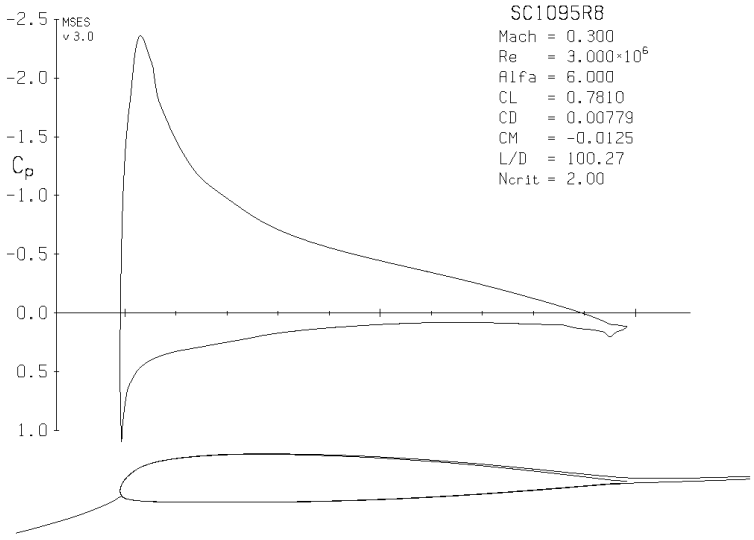

Figure 132: SC1095R8 Aerofoil from Lednicer's Co-ordinates

the sharp trailing edge SC1095 and SC1095R8 aerofoils are given in Appendix D.

Using the smoothed ordinates, computed 2D pressure distributions from MSES (using a relatively low value of Ncrit) and HMB (with a k-ω turbulence model) showed good agreement for a SC1095 in typical UH60A model rotor hover conditions of M=0.55, Re=1,200,000 at 87.5%R, as shown in Figure 133, and confirm that the leading edge suction spike has been removed. For this quick 2D check-case, GHMB was used to generate the grid of 40,000 points for the 2D HMB solution.

3.3.3 Blade Drafting and Mesh Generation

Using the above twist prescription and smoothed aerofoils, a FORTRAN program was used to determine the xyz locations of all the aerofoils making up the blade for the UH-60A Black Hawk model rotor, and the geometry was then completed and surfaced in ICEM DDN. This process has since been superceded both in industry and academia by the use of Rhino 3D solid modelling (CAD) software. The geometry was exported to the ICEM Hexa multi-block structured mesh generator.

ICEM HEXA was used to generate the structured mesh with 33 points in each of 6 blocks around the blde aerofoil. At the tip the grid accomodated the volume-of-revolution tip cap.

3.3.4 Boundary Conditions

The model rotor was tested in a large building, 12.8m wide x 18m long x 9.1 m high, and the rotor height was between 3 and 4 diameters above the ground level, with the rotor wake able to exhaust through doors 2.45m high. For convenience, a cylindrical mesh with periodic boundary conditions was used for HMB in the present computations. The top and bottom of the domain were considered as non-reflecting, pressure far field conditions, and a pre-determined outlet velocity was imposed below the rotor.

3.3.5 Comparison with Measured Pressure Distributions

Measured pressure data for a tip Mach number of 0.628 has been scanned and re-plotted from Lorber, and are compared to the results of the HMB computations in Figures 136 to 144. Excellent agreement is found

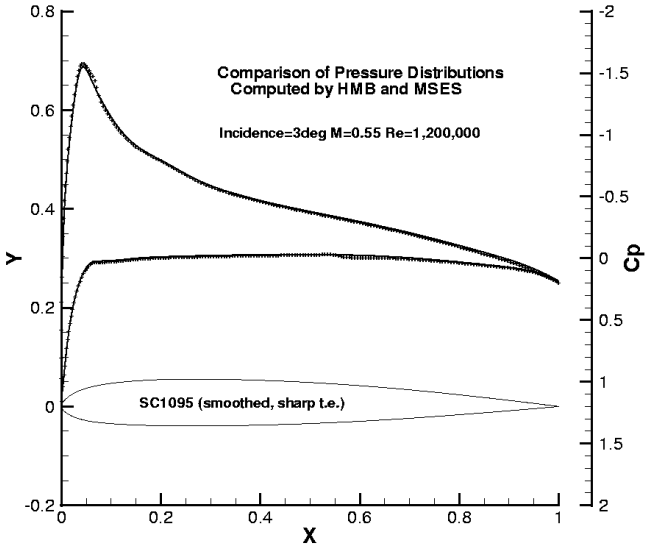

Figure 133: Comparison of 2D Pressure Distribution for the Smoothed SC0195 from MSES and HMB Preditions (note that the MSES results show a pressure disturbance due to boundary layer transition)

at all radial stations, and the predictions are well within the scatter of the data. Since the sectional pressure-distributions are in good agreement, the thrust predictions should also be very close to the actual thrust and it would also be expected that the induced torque would well predicted.

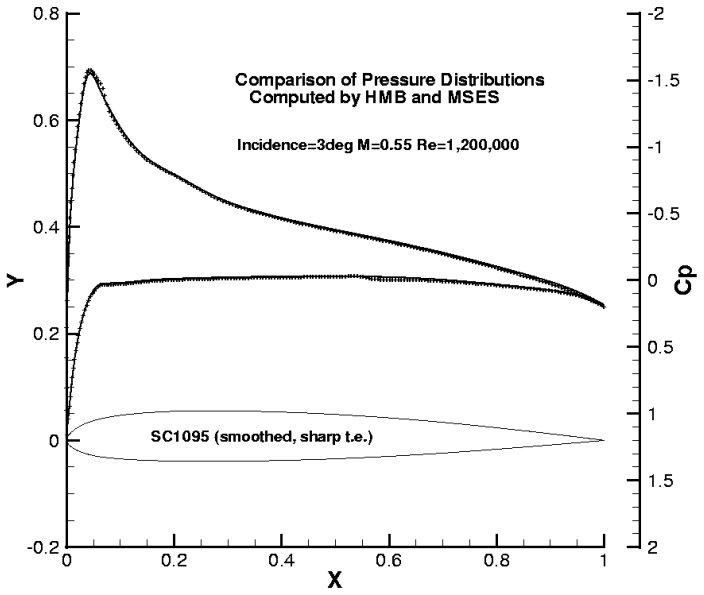

Figure 134: Smoothed SC1095 with Sharp T.E. at Typical Hover Conditions Comparison of MSES (Ncrit=2) and HMB(k-ω)

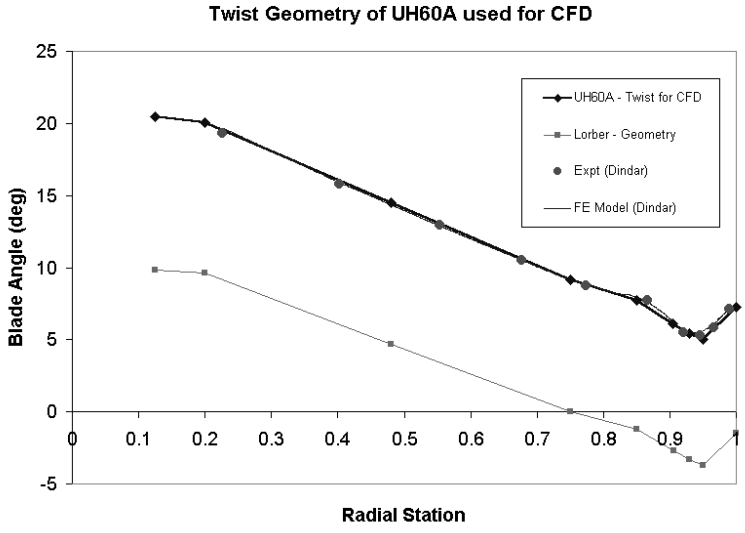

Figure 135: Twist Distribution for UH60A Model Rotor

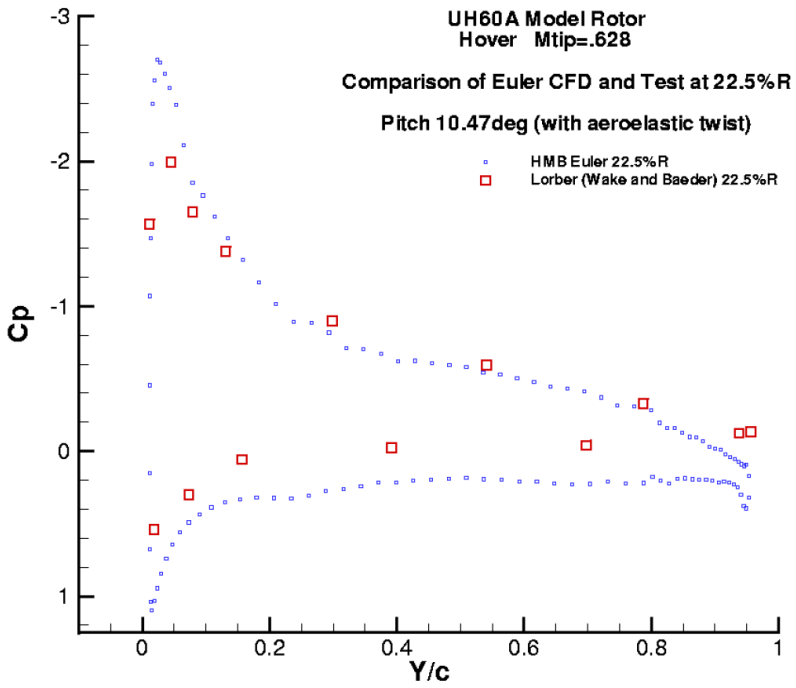

Figure 136: HMB Predicted Cp-x/c for UH-60A isolated model rotor in hover compared to Lorber's measurements at 22.5% radius

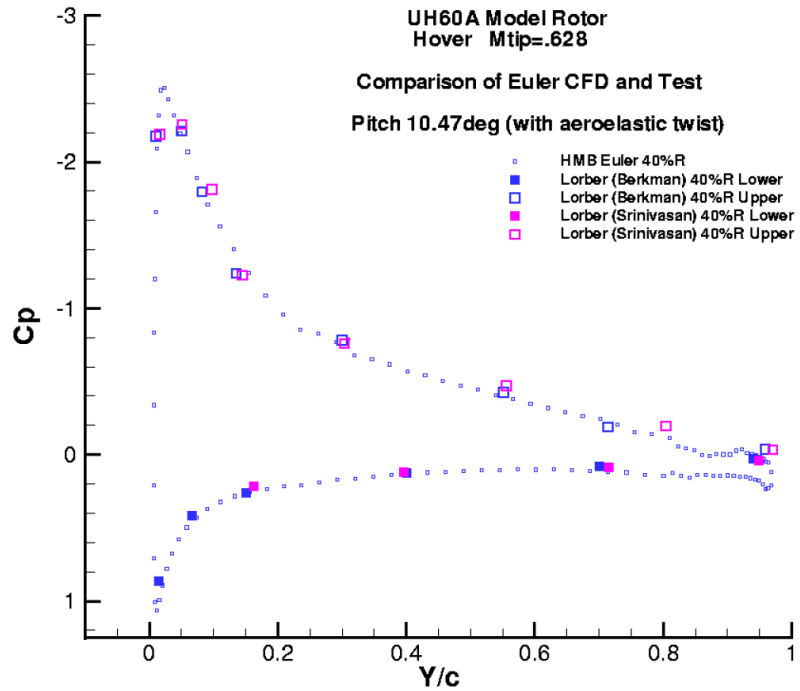

Figure 137: HMB Predicted Cp-x/c for UH-60A isolated model rotor in hover compared to Lorber's measurements at 40.0% radius

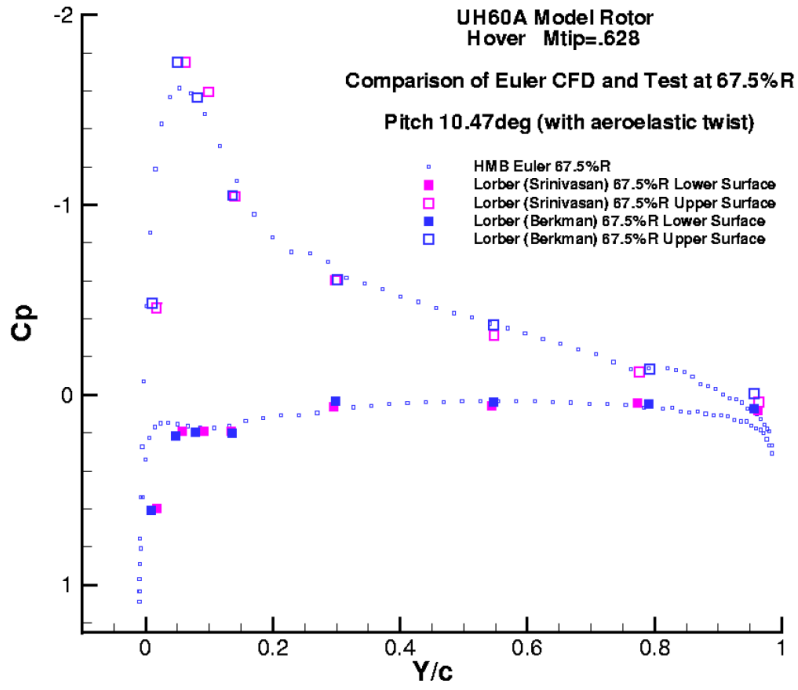

Figure 138: HMB Predicted Cp-x/c for UH-60A isolated model rotor in hover compared to Lorber's measurements at 67.5% radius

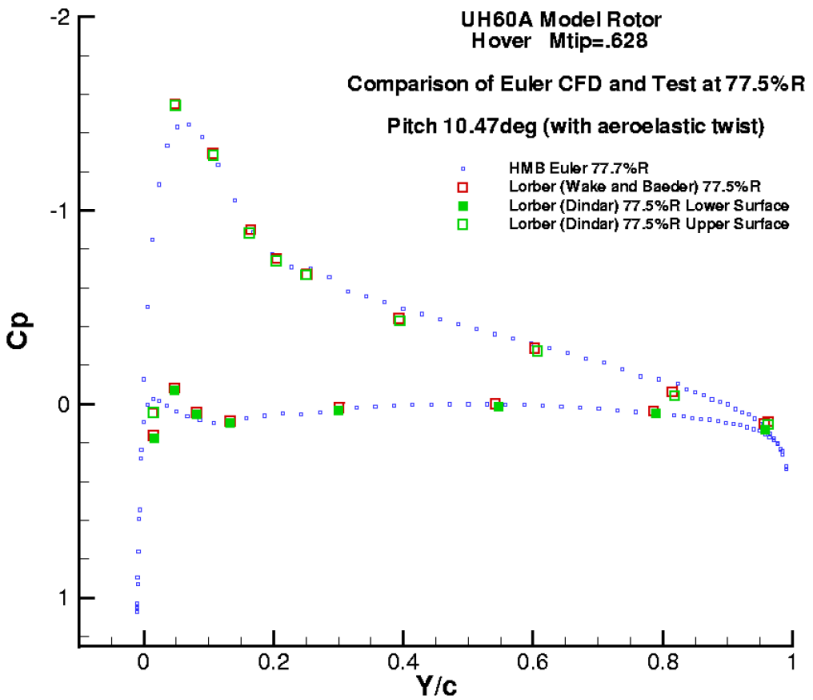

Figure 139: HMB Predicted Cp-x/c for UH-60A isolated model rotor in hover compared to Lorber's measurements at 77.5% radius

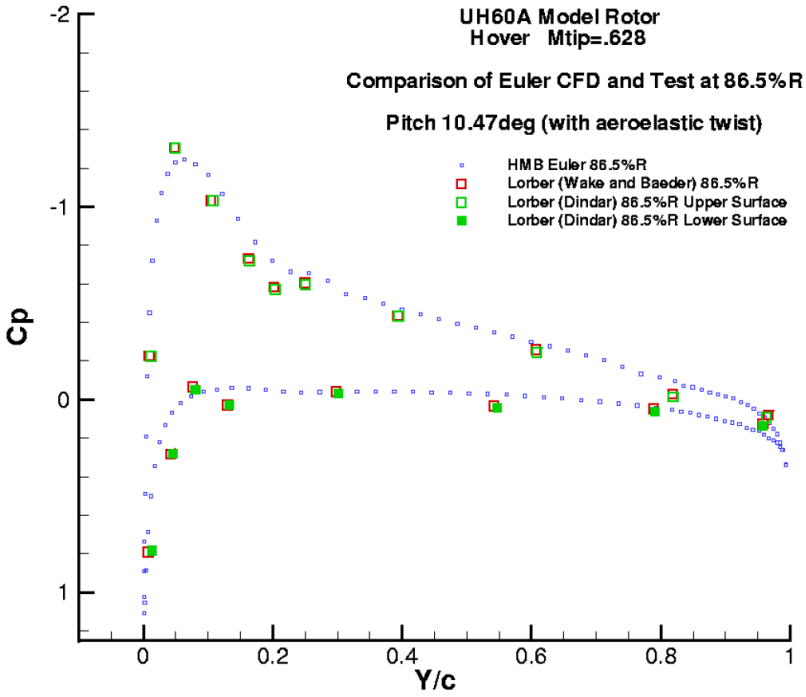

Figure 140: HMB Predicted Cp-x/c for UH-60A isolated model rotor in hover compared to Lorber's measurements at 86.5% radius

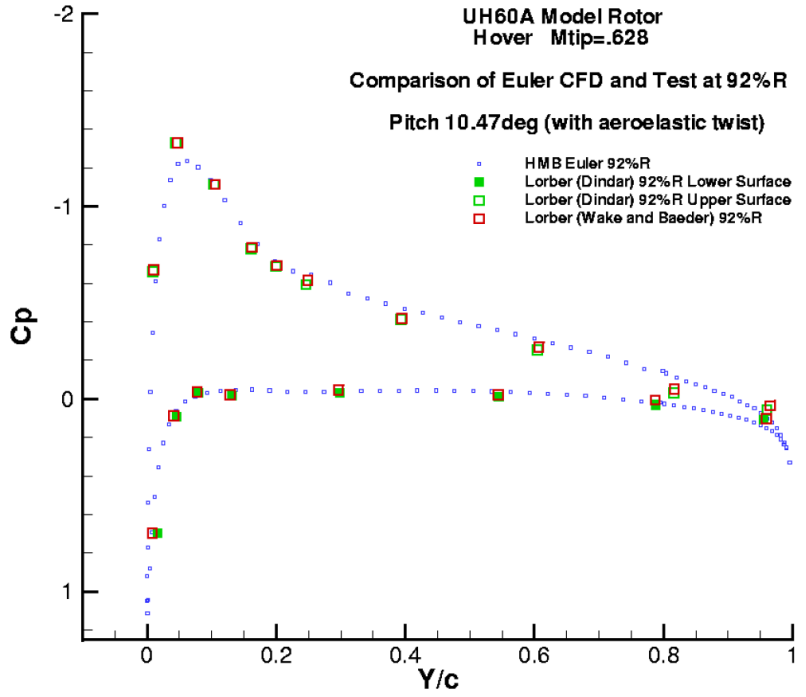

Figure 141: HMB Predicted Cp-x/c for UH-60A isolated model rotor in hover compared to Lorber's measurements at 92.0% radius

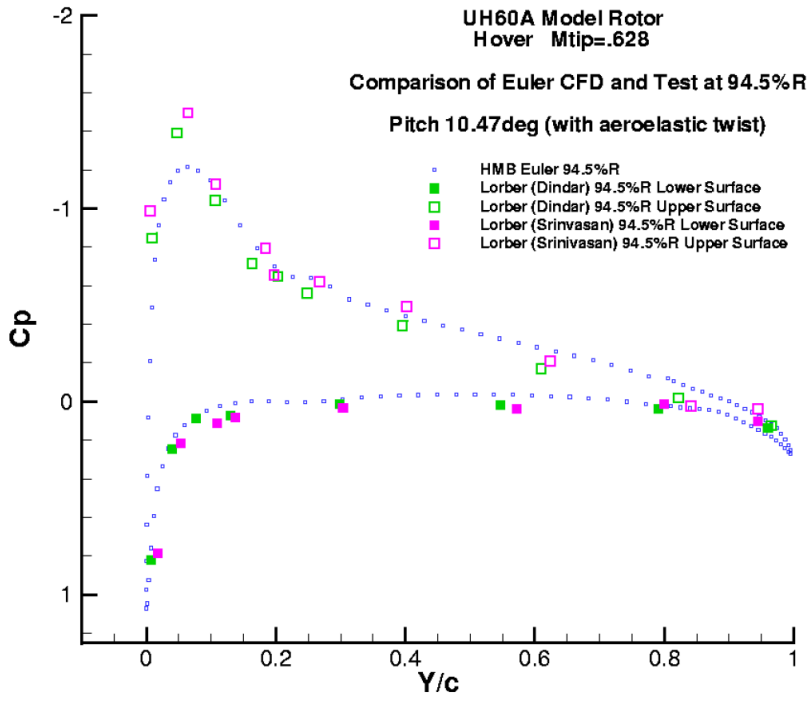

Figure 142: HMB Predicted Cp-x/c for UH-60A isolated model rotor in hover compared to Lorber's measurements at 94.5% radius

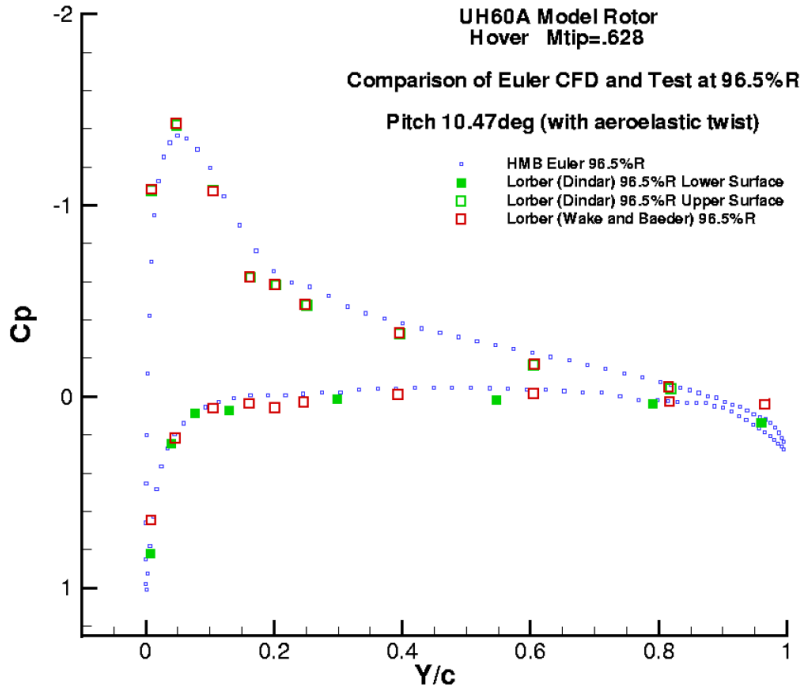

Figure 143: HMB Predicted Cp-x/c for UH-60A isolated model rotor in hover compared to Lorber's measurements at 96.5% radius

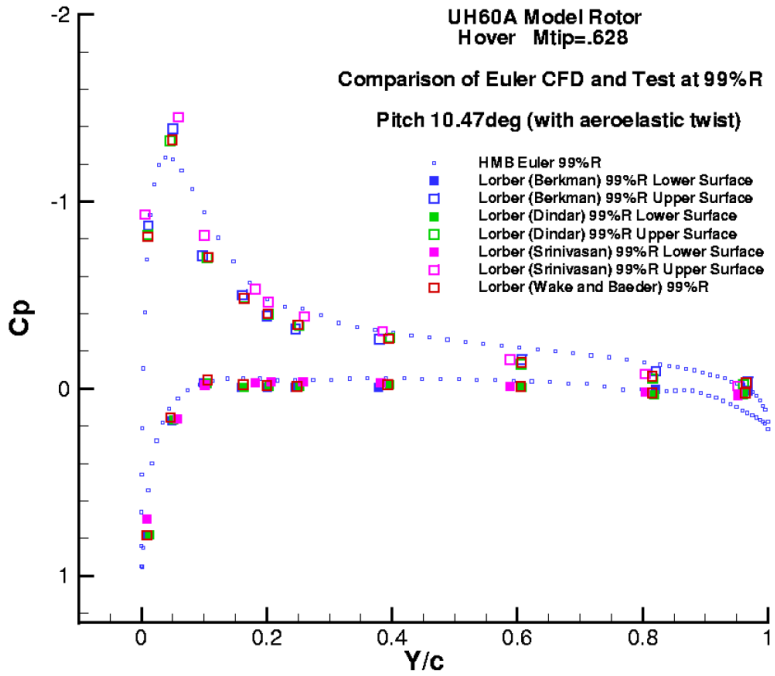

Figure 144: HMB Predicted Cp-x/c for UH-60A isolated model rotor in hover compared to Lorber's measurements at 99.0% radius

3.4 WHL Model Tail Rotor

In this section of the thesis, CFD results are compared to the Model Tail Rotor tests carried out by the author at Westland Helicopters Ltd (WHL) (now AgustaWestland UK) in 1980 and 1984. The aim of the 1980 tests was to demonstrate the effect of linearly twisted (rectangular) blades on tail rotor performance and to confirm predictions from a new lifting-line, prescribed wake hover performance model which had been written to support the development of Sea King and Lynx. It therefore seems appropriate to re-use this data here to verify that the computational method of HMB can be used to realistically model the case of a highly loaded tail rotor, so that this numerical method can be subsequently used with confidence to evaluate changes in blade tip design.

The tests were carried out using the hydraulically powered TREMOR rig [9]. The 4-blade model rotor had a radius of 21" (533.4 mm) and a constant chord of 3.28" (83.312 mm), and employed NACA 0012 aerofoil (the details of the aerofoil and tab are noted in Appendix F together with the co-ordinates of the sharp trailing edge NACA 0012 aerofoil which was used for the computations). The tips were simply cut-off square, and at the root the trailing edge corner was cut-away, such that the root cut-out (first full-chord aerofoil) was at 33%R, typical of a tail rotor blade. The pitch was adjusted mechanically via a spider, and the articulated hub had conventional ($d\theta/d\beta = -1$) pitch-flap coupling, Figure 145. The hover tests were carried out in a large building of approximately 8m x 8m x 8m, such that re-circulation was not present at the limited tipspeed and disc loadings used in these tests. While this early test data contains some scatter, the effect of twist on thrust and power was clearly demonstrated. The experiment showed that as the blade twist was increased, power divergence at the onset of stall was delayed, although the power did eventually diverge more rapidly once the stall occurred. The thrust also appeared to peak more abruptly when using 16 degrees of twist on the model rotor. However, practical limitations on both power and pitch-range prevented the investigation of the model tail rotor in more deeply stalled conditions. The test results were compared to a lifting-line model, and it was concluded that twist causes an increase in loading over the inboard part of the blade while off-loading the tip, such that when stall occurs on a highly twisted blade separation tends to spread quite rapidly along the entire blade.

While there are clear benefits in using twist, recent tail rotor designs have been conservative, partly due to the remaining uncertainty in the behaviour of a highly twisted blade at stall, and partly because of design compromises (eg dynamic stability and loads) and the need to operate in many different flight conditions. In the model rotor tests, a rectangular, square-cut tip was used, together with a constant NACA 0012 aerofoil, and the tests were carried out over a range of less-than-full-scale tipspeeds ($0.263 < \text{Mtip} < 0.55$), giving relatively low Reynolds numbers ($520{,}000 < \text{Re} < 960{,}000$) on this approx half scale model. Of course, subtle changes in Mach number, aerofoil distribution and tip shape, may significantly change the stall characteristics and the modern trend is towards a moderately twisted blade with distributed aerofoils. Later in this thesis the effect of changing just the tip shape is investigated.

Unfortunately, the tests did not extend to measurement of blade surface pressures. However, some smoke flow visualisation of the wake was carried out using the datum, zero-twist, blades and this provided further valuable data with which to compare with prescribed wake formulae, and is here re-used to verify the vortex trajectories predicted by CFD for a given pitch and blade geometry. In all cases, the pitch was set with the blade stationary and at zero-coning (impressed pitch), therefore in order to determine the actual blade angle an allowance must be made for the coning angle and the existence of 45 degrees of pitch-flap coupling.

Flow visualisation of the vortex wake was carried out at a relatively low tipspeed to ensure that re-circulation was not present in the enclosed test facility. The vortices were visualised by introducing smoke into the vortex wake pattern, and using strobe lighting with a variable phase-delay synchronised to the rotor. The locations of the vortices were measured via a video position analyser, and averaged in real time. It was found that the wake remained stable with vortices persisting to an age of about 360 degrees for this 4-bladed rotor, provided that the rig was carefully balanced and the blades were well tracked. New and larger stroboscopes were used to illuminate as much of the wake as possible, and a moderately long persistence theatrical smoke was used. Following the 1980 tests on linear-twist, where wake trajectories were measured at 5, 10 and 15 degrees of collective pitch for the datum blades, the fin-blockage tests in 1984 provided an opportunity to make similar

[9] The TREMOR rig was the first of a series of 3 model rotor rigs used by the author during his career at WHL, the subsequent ADAM and MERCURY rigs were mainly used for (proprietary) main rotor tests. The MERCURY rig was also used for main rotor Vane Tip acoustic tests in the RAE Farnborough 24ft tunnel, Brocklehurst and Pike[59]

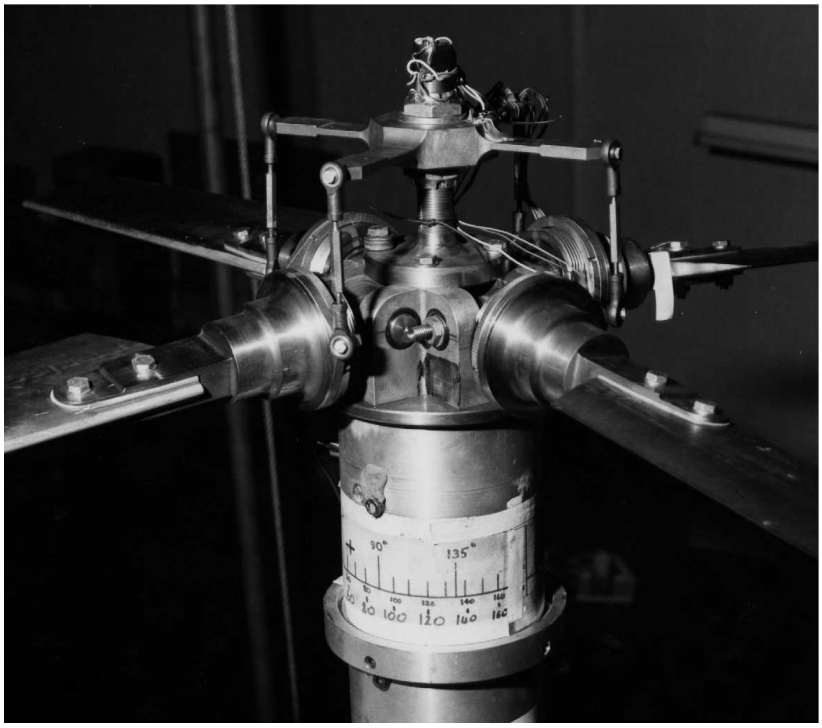

Figure 145: Photograph of Model Tail Rotor Showing Articulated Hub, Feather Bearings, Pitch Links, Spider, Blade Attachment Forks, and Carbon Fibre Blades

measurements at 8 degrees pitch, with no fin present, using the same zero-twist blades. As expected, the results from these later tests fall between the 5 and 10 degrees datapoints of the earlier tests, giving confidence in the experimental procedure.

It was therefore considered useful to compare the HMB predictions against both the thrust-pitch-power, and vortex trajectory data for the model tail rotor, before proceeding further with the research aims of this thesis. Ideally, it would be nice to have highly accurate thrust-pitch and power readings at full-scale conditions, accompanied by blade pressure measurements, vortex wake trajectories and wake velocities, quantified by PIV and LDA, and in well controlled conditions, but such data is exceptionally rare and does not exist in the public domain. The following sections of this Chapter therefore presents comparisons against the model rotor data with which the author has had first-hand experience.

3.4.1 Geometry and Grid for Model Tail Rotor Comparisons

The geometry and grid used for the model rotor simulation was developed and refined from the initial studies described under the grid sensitivity heading earlier in this Chapter.

The computational domain was set at 2R above, 6R below the rotor datum location and extended 3R in the radial direction. A cylindrical hub of 55mm (0.66chords) radius was used throughout. The root end of the blade was tapered in the same fashion as the model tail rotor blades although the aerofoil section had a sharp trailing edge to meet the requirements of the Euler solver. The rectangular tip of the blade was simply cut-off-square, exactly the same as the carbon composite model rotor blades. The blade geometry was drawn and surfaced in Rhino, and grids of about 2.5 million points (170 blocks) were constructed in ICEM. The Grid Trimmer utility was used to provide the appropriate coning and to correct the blade angle for pitch-flap (delta3) coupling. The model rotor blades, together with the larger-than-scale feathering bearings, gave a relative high flapping inertia and hence have a low Lock number, and consequently the coning angle is relatively small, as shown in Figure 146.

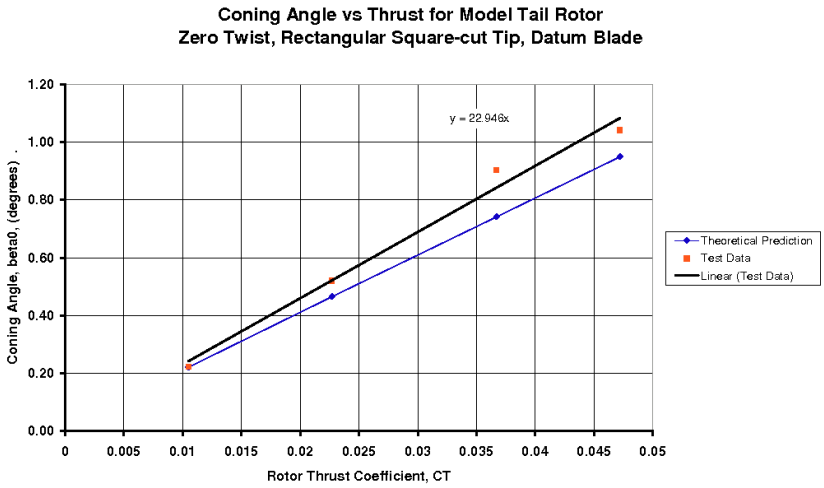

Figure 146: Measured and Predicted Coning Angle for the Model Tail Rotor with an Effective Lock No of 1.276. The Coning Angle must be Subtracted from the Impressed Pitch due to the -45 deg Conventional Pitch-Flap Coupling

3.4.2 Performance Comparisons (Zero Twist)

Initially, CFD comparisons were made with the model tail rotor test data at tip Mach numbers of 0.263 (1600 rpm) and 0.492 (3000 rpm) for zero twist, as reported here, while later a series of runs was carried out at a tip Mach number of 0.448 (2730 rpm) with twisted blades as reported in Sections 3.4.4 and 3.4.5.

Some problems were encountered with early Euler CFD results underpredicting the thrust, and this raised a concern over re-circulation within the computational domain, which led to the adoption of so-called Froude boundary conditions. In fact, any re-circulating velocity was found to be extremely small, but was accentuated by the continuous nature of Tecplot streamtraces. It was later found that at the low tip Mach number used for the comparisons, the solution took a large number of iterations to settle. Note that the model rotor (R=533.4 mm (1.75 ft), c=83.312 mm (3.28 inches), N=4) was tested in a large building, and was free from re-circulation (confirmed by tuft-wand visualisation).

The final CFD results are shown compared to the test data in Figures 147 and 148 at the two Mach numbers mentioned above. The computed thrust results compare well to the test data. The higher Mach number cases were run for a larger range of pitch angles, and show a tendency for the thrust to be slightly overpredicted by the Euler solution, as might be expected. The thrust-pitch slope is likely to be artificially high beyond about 15 degrees due to the inviscid nature of the computations which may also include some numerical diffusion effects as the Euler solution reaches its practical limits.

The power measurements from the 1984 tests (without fin) are thought to be of better quality than those obtained in 1980, although at the time, the induced power factor of 1.4 which was deduced from the tests was considered to be rather high. Despite a slight difference in the tip Mach number, comparisons were therefore made with the more recent data, as shown in Figures 149 and 150 (the test Mach number was 0.361, since the values are low, the differences are not significant, as confirmed by early exploratory CFD runs). A momentum theory line has been added to Figure 150 to illustrate the power based on a profile drag coefficient of 0.018 (inclusive of hub drag), and an induced power factor of 1.4. Except for the very high pitch cases, the CFD results run parallel to this line, suggesting that the Euler method has resulted in the correct amount of induced power, with any residual 'profile' (pressure) drag being very small indeed. (For an alternative, more accurate method of determining the induced power factor, see Section 5.1).

Although a true Figure of Merit cannot be obtained directly from Euler computations since the viscous effects are absent, it is nevertheless interesting to gain some idea of the Figure of Merit by casting the computational results and test data into this form. As shown in Figure 151 the raw Euler results give an artificially

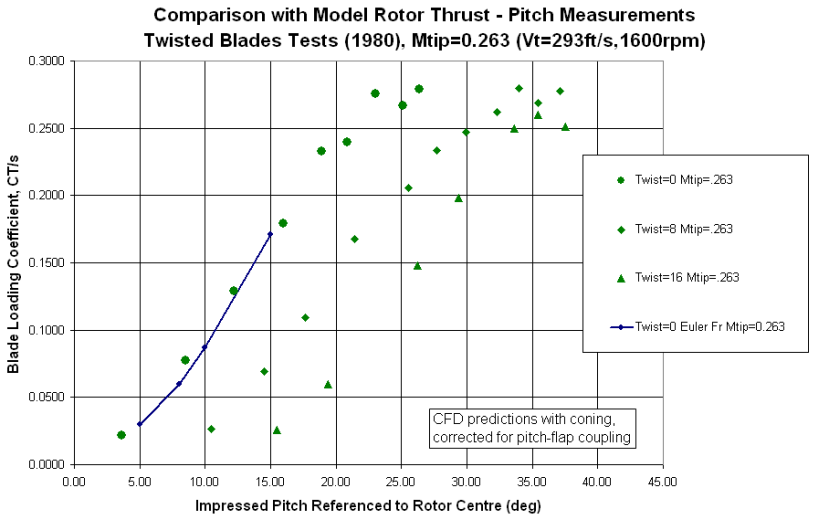

Figure 147: Comparison of Euler CFD Thrust-Pitch Predictions with Measurements from 1980 Model Tail Rotor Tests at a Tip Mach Number of 0.263

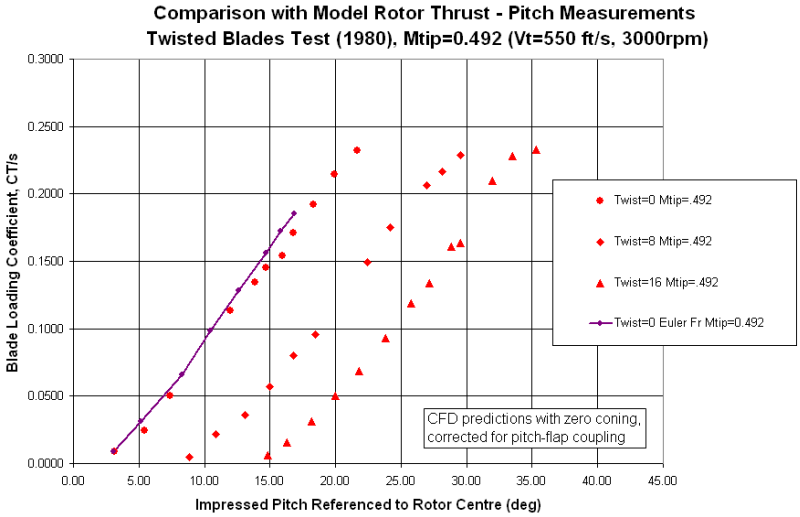

Figure 148: Comparison of Euler CFD Thrust-Pitch Predictions with Measurements from 1980 Model Tail Rotor Tests at a Tip Mach Number of 0.492

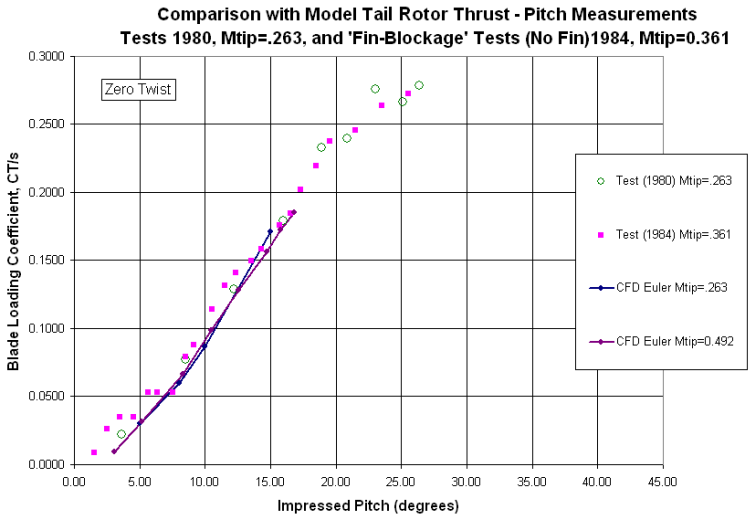

Figure 149: Comparison of Euler CFD Thrust-Pitch Predictions with Measurements from 1980 and 1984 Model Tail Rotor Tests at a Tip Mach Numbers of 0.263, 0.361 and 0.492

high result for Figure of Merit (as expected, this is close to the reciprocal of the induced power factor) and a constant profile power term has therefore been added (based on the above integrated-mean hub and blade profile drag coefficient of 0.018, minus .002 to allow for the Euler residual drag, giving an additional blade and hub drag coefficient of 0.016). This almost brings the computed results into agreement with the test data, except at very high thrust levels where the profile drag diverges due to the onset of stall and the Figure of Merit accordingly reduces. Wilst the scatter in the test data makes it difficult to be precise, a maximum figure of merit for the model tail rotor with zero twist blades is in the region of 0.55 to 0.56.

3.4.3 Predicted and Measured Vortex Locations (Zero Twist)

When the later model tail rotor tests were originally reported, it was shown that the measured vortex trajectories fell between the prescribed displacements and contraction given by Landgrebe[174] and Kokurek and Tangler,[166] although there was some doubt about the thrust coefficient which was used for the original comparisons (due to scatter of the test data, and the fact that the theory used at the time tended to over-predict the thrust). However, in the present work, the CFD has been set up to replicate the pitch and coning of the experiment (and from the above comparisons, the thrust is in good agreement with the trends of the test data). Since it is generally accepted that the Kocurek and Tangler prescribed-wake provides a superior formulation to the earlier work of Landgrebe, especially for high solidity rotors, the vortex positions have been re-computed to provide a comparison at the same CT as predicted by the CFD.

Since much of the model tail rotor vortex position data was obtained on video, only a few still photographs of relatively poor-quality were taken during the tests, Figure 152. Better photographs were later obtained for a sequence of vortex ages from a model main rotor, as presented by Brocklehurst,[56] and an example is included here to illustrate the quality of wake visualisation that was achieved, Figure 153.

The vertical displacement, Figure 154, and contraction, Figure 155, together with the wake overall trajectory plot in Figure 156, show excellent agreement between the measured vortex locations and those extracted from the CFD results. In general there is better agreement between the (Euler) CFD results and the test measurements, than between the test data and the Kocurek and Tangler prescribed wake, and the latter appears to under-predict the wake displacements at low pitch and over-predict at high pitch (although the primary descent rate at low pitch and secondary descent rate at high pitch are in good agreement). Apart from instances of vortex 'pairing', or 'gearing' which is evident in the wake contraction plotted from test data at the highest and lowest pitch angles in the far-wake, the agreement between test, prescribed wake and CFD

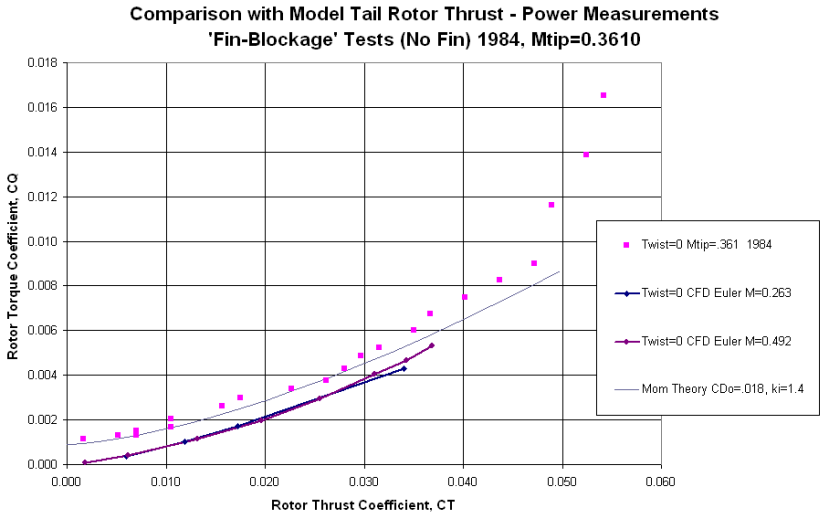

Figure 150: Comparison of Euler CFD Torque-Thrust Predictions with Measurements from 1984 Model Tail Rotor Tests at a Tip Mach Number of 0.263, 0.361 and 0.492

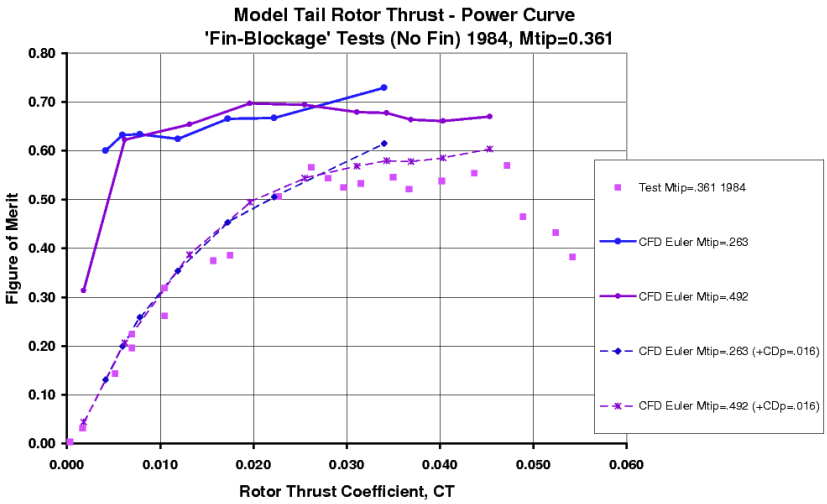

Figure 151: Comparison of Euler CFD Corrected Predictions for Figure of Merit with Measurements from 1984 Model Tail Rotor Tests at a Tip Mach Number of 0.263, 0.361 and 0.492

Figure 152: Early Flow Visualisation Photograph of Wake of the Model Tail Rotor, Taken Prior to Employing New Strobes and Improved Video Techniques to Extract Vortex Locations

is good. The CFD results, however, shows some 'lobing' between each blade passing (every 90 degrees), and although it is difficult to be sure, a similar effect is perhaps just discernable in the test data.

Looking again at Figure 155, at 5 degrees pitch the CFD and prescribed wake show similar contraction, while the test data shows a lack of contraction. For the 15 degree case, the test data and prescribed wake show slightly more contraction than predicted by the CFD, but overall, and at 8 and 10 degrees in particular, the wake positions are in excellent agreement.

Despite viscous effects being missing from the Euler solutions, the vortices were found to be well formed and closely follow the expected trajectories, giving confidence in the capability of an Euler CFD method to correctly predict the overall induced flow field and give good predictions of the thrust and induced power in attached flow conditions.

The Euler computations discussed above were carried out at an early stage in this research, and later the 8 degree impressed pitch case was repeated using Navier-Stokes as it was of interest as a baseline for the unsteady isolated rotor (no fin-blockage) case of Chapter 8. This allows a direct comparison to be made between Euler and Navier-Stokes, and between Navier-Stokes and test data for this particular model rotor case. As before, the actual blade angle for the datum rectangular blade, TRB-000v, allowing for pitch-flap coupling and 0.402 degrees of coning was 7.598 degrees. In the tests, the flow visualisation was carried out at a reduced rotational speed of 1600rpm, giving a tip Mach number of 0.2625 and a tip Reynolds number of only 510,000. The modified k-ω turbulence model based on Wilcox[321] was used in the computations. For this low tipspeed cases, 90,000 iterations were needed (at CFL=1.0) for the solution to completely settle. Even so, the wake did not completely connect to the Froude outlet at the far field, although judging by the vortex trajectories, this may not be very significant as most of the contraction has already taken place by the time the wake has descended 0.4R and the wake does not spread until about 1.5R beneath the rotor plane.

Figure 157 shows the vortex trajectories, vertical displacement and contraction for Euler and Navier-Stokes predictions compared to the test data and the prescribed wake of Kocurek and Tangler.[166] The vortex locations were obtained from the vorticity computed in Tecplot, by taking planes at 5 (or 10) degree intervals and using the probe tool to obtain the required co-ordinates of the centre of the vortices. As mentioned previously, some of the vortices appear non-circular in shape due to proximity to the blade and the inboard vortex sheet breaking away from the tip vortex. The trajectory from the Navier-Stokes predictions lies outside that obtained from the Euler solution. It can be seen from the separate contraction and vertical displacement plots that the Navier-Stokes results show a reduced contraction, while the vertical displacement is initially almost identical

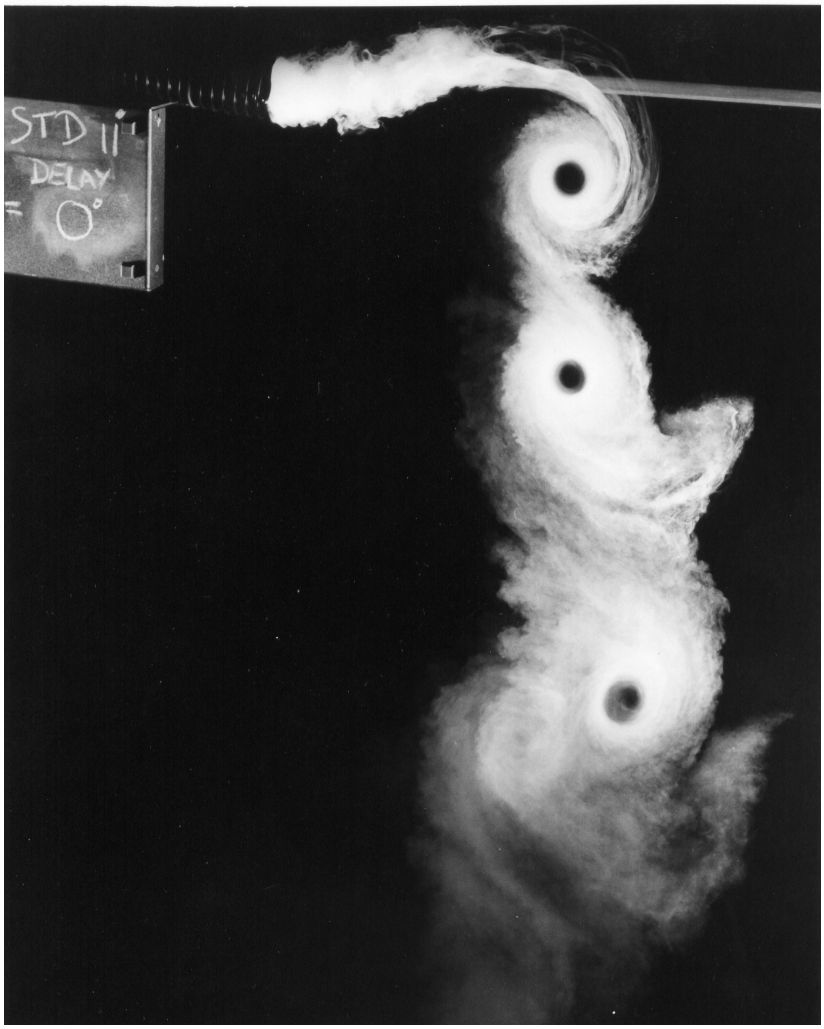

Figure 153: Illustration of Better Quality Flow Visualisation Photography on a Rectangular 2-blade Model Main Rotor Showing Improved Clarity of Vortex Trajectories, Similar to that Achieved on Model Tail Rotor Using Video Techniques

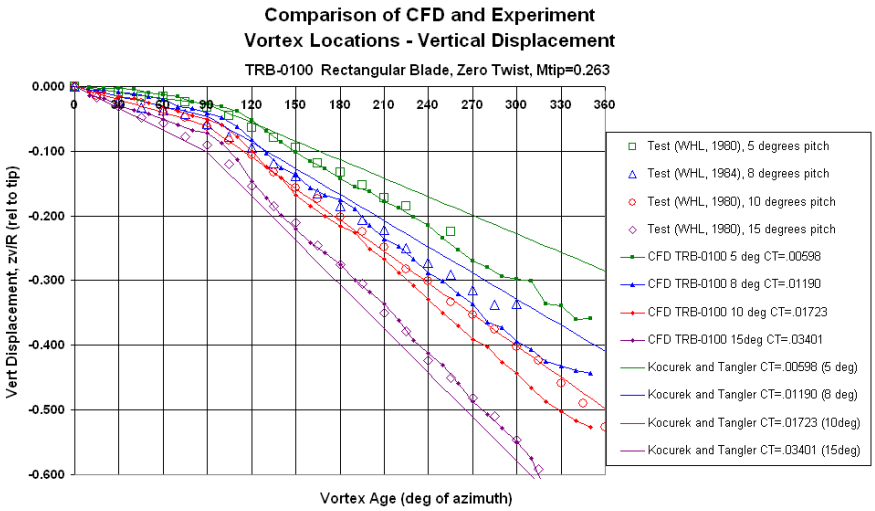

Figure 154: Comparison of Euler CFD Vortex Displacement with the Prescribed Wake of Kocurek and Tangler, and Measurements from 1980 Model Tail Rotor Tests at a Tip Mach Number of 0.263

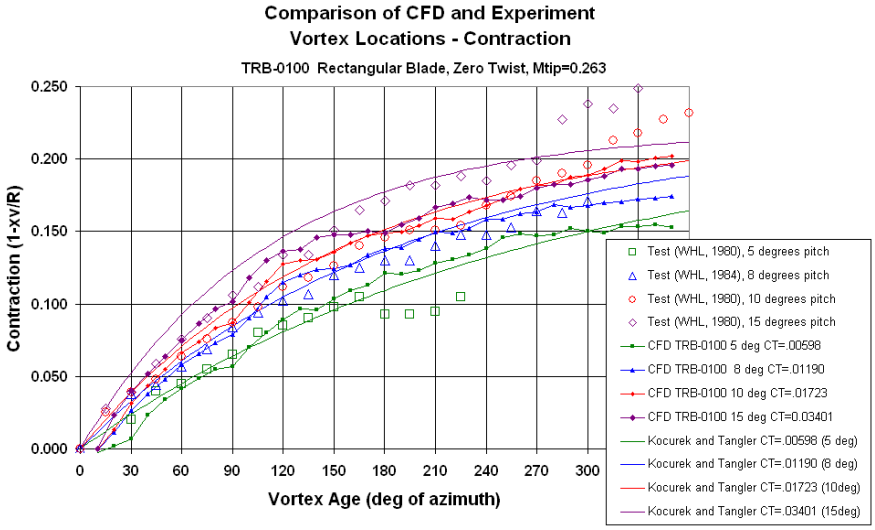

Figure 155: Comparison of Euler CFD Wake Contraction with the Prescribed Wake of Kocurek and Tangler, and Measurements from 1980 Model Tail Rotor Tests at a Tip Mach Number of 0.263

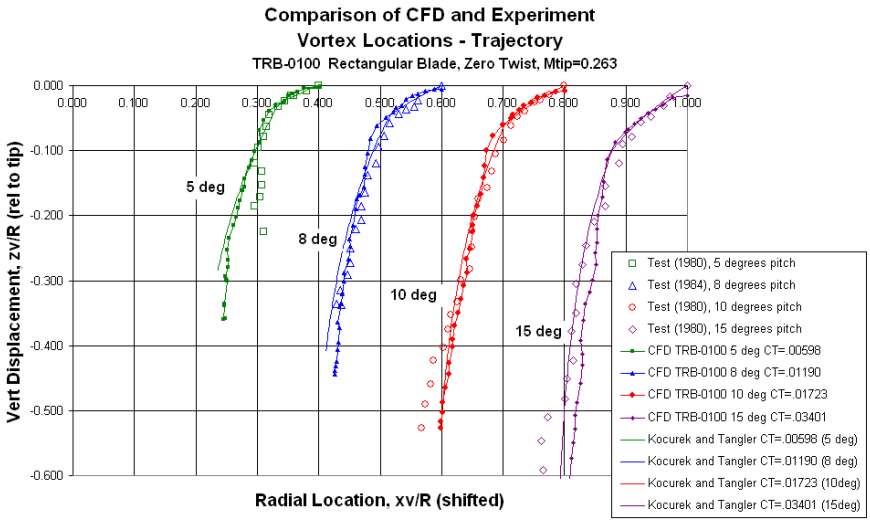

Figure 156: Comparison of Euler CFD Vortex Trajectories with the Prescribed Wake of Kocurek and Tangler, and Measurements from Model Tail Rotor Tests at a Tip Mach Number of 0.263

up to about 180 degrees, except for a slight inflexion just after the first blade passage. Further down in the wake, the descent rate of the viscous solution continues to match that of the test data, while the Euler points suggested a steeper descent. For the Navier-Stokes results, the computed solutions better reflect the distortions of the trailed vortices as they leave the blade than was able to be measured in the experiment, and these details (which might be crucial to the performance) are also ignored by the prescribed wake model.

Most of the vortex locations in the wake were obtained as described above by using Tecplot to compute the vorticity in a post-processing operation, and the majority of the wake trajectory information presented in this thesis were formed using this technique. However, late in this research program the λ_2 vortex identification parameter was also computed using a Tecplot add-on, following the work of Jeong and Hussain.[154] This parameter takes into account the pressure and density field of the vortex as well as the velocities, and so should provide a better indication of the centre of the vortex.

Vortex trajectories, vertical displacement and contraction obtained from λ_2 are compared to those from vorticity in Figure 158. The differences in the initial part of the wake, close to the rotor, are surprisingly small, while after about 180 degrees age, the λ_2 results show a greater contraction and fall closer to the prescribed wake trend. The two methods of determining the vortex locations fall either side of the test data in this last half-turn of the wake for which vortex locations were extracted. The vertical displacement graph shows close agreement between the two sets of results, with perhaps slightly less inflexion after the first blade passing for the λ_2 case. After about 180 degrees of vortex age the λ_2 results fall slightly above the vorticity results, but rejoin after 270 degrees. The agreement between the two methods is good, particularly prior to the vortex interacting with the blade at ψ=90 degrees.

In summary, there appears to be little difference between the vorticity and λ_2 methods when used to simply extract the centres of the vortices, except in the second half-turn of the wake development, towards the end of which the vortices are starting to decay. Both approaches show the vortices to contract less than the prescribed exponential and lie above the expected descent path. While care was taken to align the test measurements to the rotor centre, it may be possible that part of the discrepancy in vertical displacement might be a shift due to coning, or measurement datum error. However, the predictions have an initially flatter trend compared to the simplistic linear descent rate of the prescribed wake. Also, the predictions show a slower initial contraction which would appear to originate in the vortex formation process.

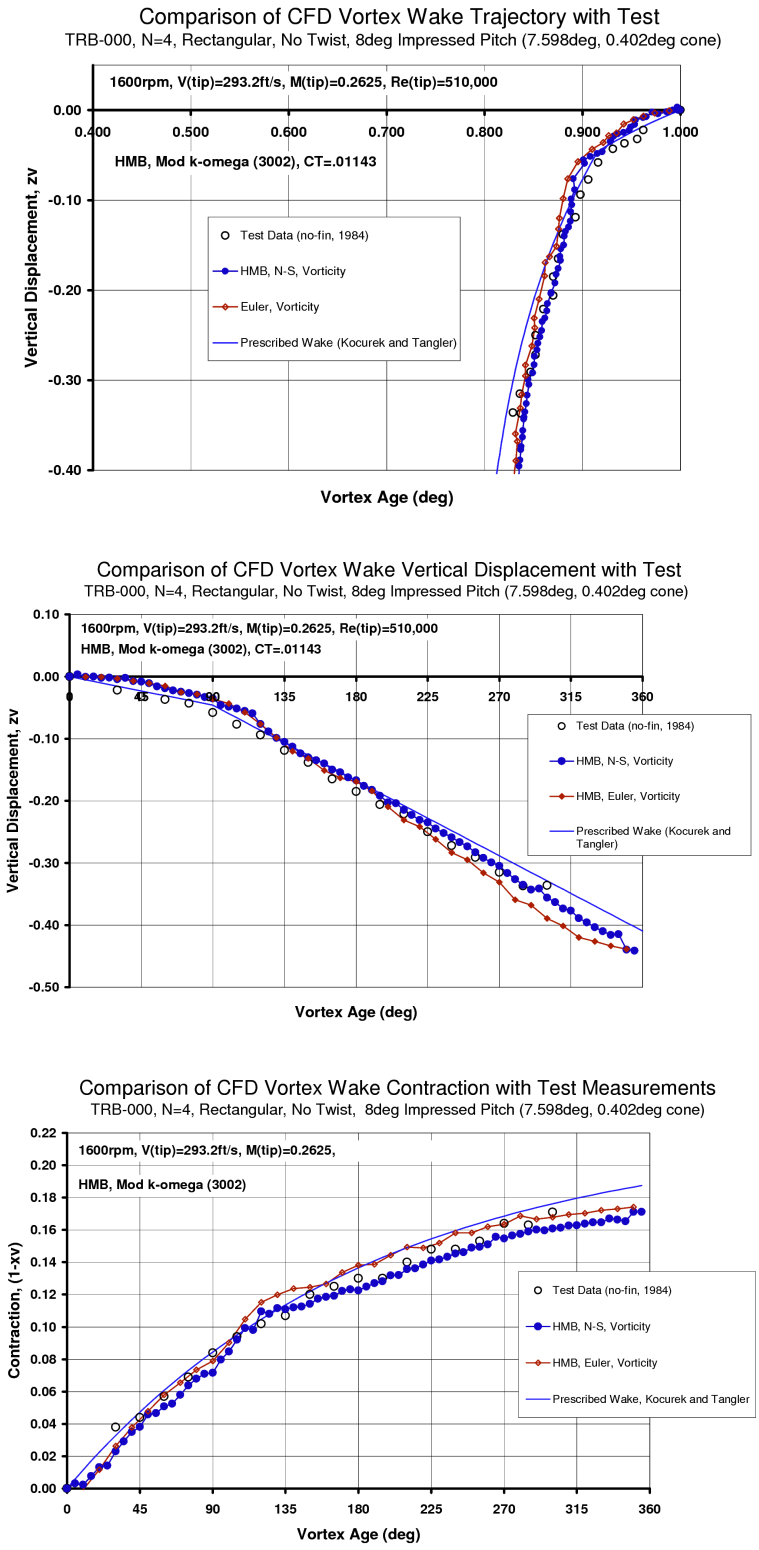

Figure 157: Vortex Trajectories from Euler and Navier-Stokes Predictions (using Vorticity) for the Datum Blade, TRB-000 (Mtip=0.26), compared to WHL Model Tail Rotor Measurements and the Prescribed Wake of Kocurek and Tangler.[166]

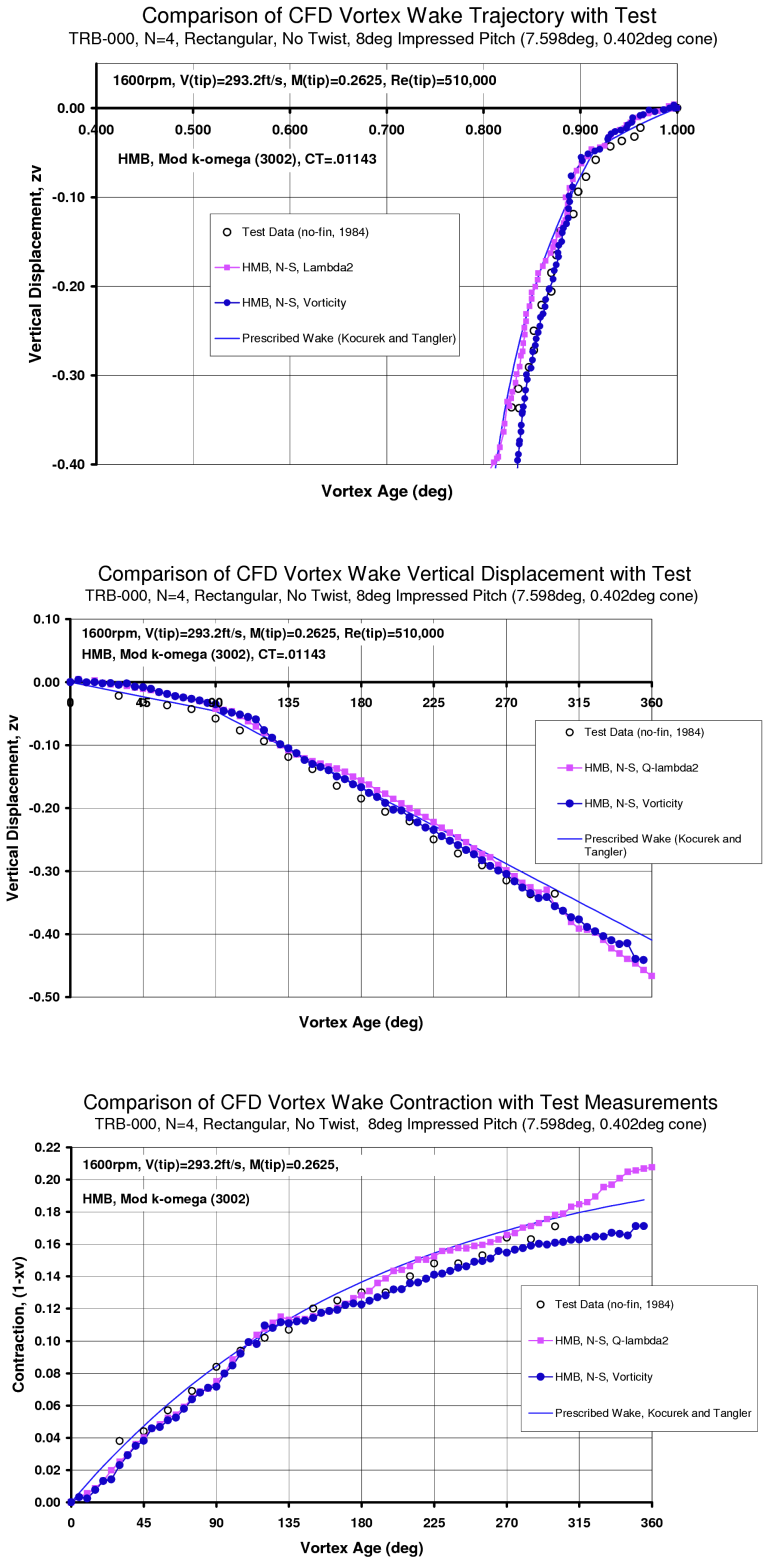

Figure 158: Vortex Trajectories from Navier-Stokes Predictions (using Vorticity and λ_2) for the Datum Blade, TRB-000 (Mtip=0.26), compared to WHL Model Tail Rotor Measurements and the Prescribed Wake of Kocurek and Tangler.[166]

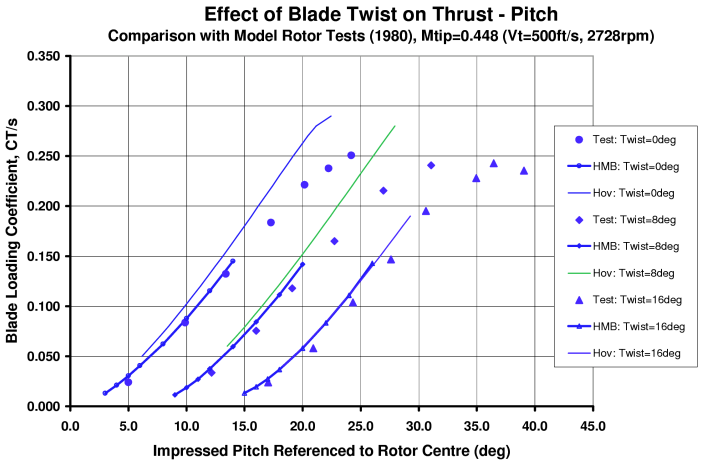

Figure 159: Comparison of Thrust-Pitch Characteristics from HMB and WHL Hover Program with Test Data for the Rectangular Model Tail Rotor Blades with 0, 8 and 16 Degrees Twist

3.4.4 Further Performance Comparisons (0, 8, 16 degrees Twist)

Having made comparisons with the zero twist case, the question naturally arose as to whether Euler predictions would show the correct trends of thrust and torque with increasing twist. A series of blade geometries, representative of the WHL tail model rotor, were therefore prepared with 0, 8 and 16 degrees twist in Rhino, and ICEM grids were generated as before, with care being taken to make the grids consistent. For these twist cases, a cylindrical hub of 0.25 chords in radius was used at the centre of the computational domain, while the domain size was the same as before, 2R above, 3R in radius and 6R below the rotor. Away from the periodic boundaries, so-called 'Froude' boundary conditions were used on the farfield boundaries to allow the wake to exhaust from the bottom of the domain, balanced by a tiny inflow elsewhere, and so avoid any concerns of re-circulation.

A series of cases were run using HMB over a range of pitch angles from 3 to 14 degrees (additional pitch was added for the twisted blades to notionally align the blade angles at 75%R). The thrust-pitch results are compared to the test data for the 3 different blade twists, and also to results from the WHL Hover Program [10], in Figure 159. Here the pitch angles are plotted in absolute terms (if plotted in terms of the angle at 75%R they nearly, but not quite, fall onto a single line). For zero twist excellent agreement was found between CFD and the test data for the thrust-pitch gradient, but the WHL Hover Program results exhibited a steeper gradient. At high twist the CFD and WHL Hover Program results fall more into line, and lie slightly to the left of the test data.

The corresponding comparison in terms of thrust and torque is presented in Figure 160. The test data, which includes blade (and hub) profile drag losses as well as the induced power, shows how the power consumed by the rotor grows with increasing thrust until power divergence is reached at stall. It is perhaps just discernable that the power for the higher twist blades diverges later, but the situation is masked by scatter in the test data. Perhaps not surprisingly, the Hover Program results under-estimate the profile power at the low Reynolds number of the model rotor, and the slope of the curves show less growth of power with thrust. The inviscid HMB results run parallel to the test data (the off-set being expected due to the absence of profile power).

The value of the induced power factor, ki, can be determined by plotting the torque coefficient against thrust coefficient raised to the power of 1.5, as in Figure 161. Here a second order polynomial has been fitted

[10] The WHL Hover program is a prescribed wake, lifting line model with an extensive aerofoil database. It was put together following the early work of Cook,[78] and was developed by Isaacs, Harrison, and others, to become one of the main tools of the WHL Aerodynamics Department. Unfortunately it is a proprietary code, details of which have not been published. Permission from WHL to use this code for the current work is gratefully acknowledged.

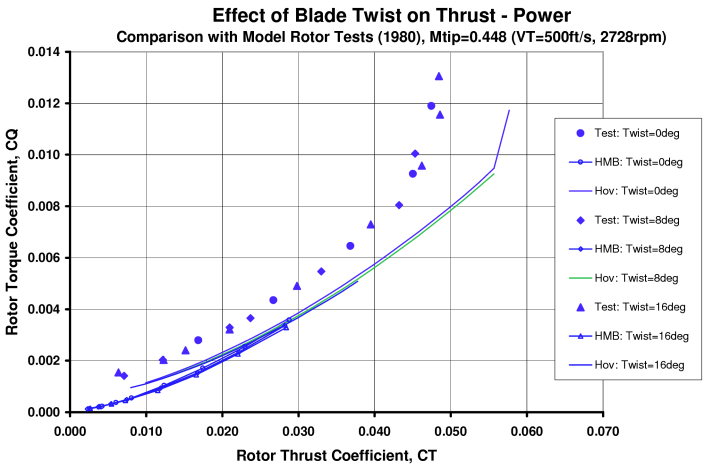

Figure 160: Comparison of Torque-Thrust Curves from HMB and WHL Hover Program for the Rectangular Model Tail Rotor Blades with 0, 8 and 16 Degrees Twist

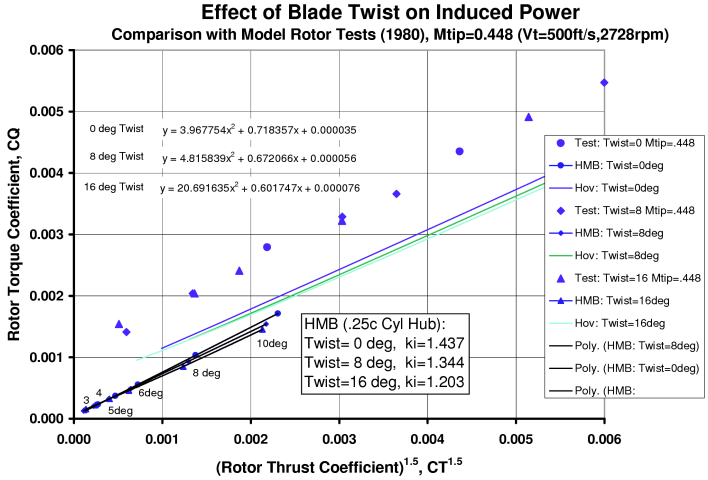

Figure 161: Extraction of Induced Power factor from HMB and WHL Hover Program for the Rectangular Model Tail Rotor Blades with 0, 8 and 16 Degrees Twist

to the HMB results to give the induced power factors (this new technique of extracting the induced power factor from either test data or computational results is described in detail in Chapter 5). Based on the slope parameter, the induced power factors from HMB are predicted to be 1.437, 1.344, and 1.203 for blade with 0, 8 and 16 degrees of twist, respectively. Unfortunately, the sparseness of the data together with a small amount of scatter makes it difficult to give an accurate numerical comparison of ki, but the trend of the data points is very similar to that predicted by HMB. The prescribed wake model also provides an indication that the induced power factor decreases significantly with twist, thus enhancing the performance of the tail rotor. It is gratifying that an Euler solution from HMB has provided a realistic estimate of the induced power, and this capability will be later employed to make a first-pass assessment of the performance of rotor blade design features that might affect the induced power.

3.4.5 Comparison of Predicted Loading and Effect of Twist

In addition to the validation work reported in Section 3.3 for the UH-60A model rotor, blade chordwise pressure distributions from HMB have also been validated against both the (low R/c) Caradonna and Tung model rotor and the ONERA 7A and 7AD rotors for several tip Mach numbers with radial stations distributed over the radius and clustered near the tip, Steijl.[284] The close agreement achieved between the CFD predictions and test leaves little doubt that when these chordwise pressure are integrated that HMB would then correctly predict the loading distribution along the radius. Qualitative comparisons between HMB predictions for the volume of revolution tip, TRB-006, and the tip pressure measurements of Gray,[122] presented later in Chapter 5, also confirm the fidelity of the computational approach.

In the absence of blade surface pressure measurements from the model tail rotor tests, and since one of the aims of applying the computational method to the design of helicopter rotors is to be able to evaluate the performance, and hence quantify improvements in blade design, it is of interest here to compare the loading predicted by the HMB numerical approach with that obtained from a more traditional hover code, based on a prescribed wake and lifting line method.

Two methods of predicting the loading distribution on the 0, 8 and 16 degree linearly twisted blades have been compared. A recent version of the WHL Hover Program has been used to reproduce loading distributions for the same cases as tested on the model tail rotor. HMB has also been run under these conditions using the Euler option. The results are compared at a tip Mach number of 0.448 (2728 rpm, Vtip=152.4m/s, 500ft/s) for the case of 0, 8 and 16 degrees of twist for the rectangular tip, NACA 0012 blades. All runs were carried out at an impressed pitch equivalent to 8 degrees, giving a blade angle of 7.679 degrees at 75%R in all cases, after allowing for 0.321 degrees of coning of the model rotor blades.

The effect of twist on the blade loading is shown in Figures 162 to 165 where Euler results from HMB are compared to lifting-line predictions from the WHL prescribed wake Hover Program. Figure 162 shows the non-dimensional blade loading distribution. The overall trends in the predicted loading are similar, except that the Hover Program produces a more rounded peak loading towards the tip. The loading peak predicted by HMB is also slightly further outboard and whilst of similar magnitude at zero twist, becomes relatively greater at increased twist. The HMB predictions include a loading spike at the tip, due to the suction generated towards the rear of the tip under the rolled-up tip vortex (at first sight this feature appeared somewhat surprising and is not picked up by the traditional method). There are also some loading differences in the root region.

Plotting the results in terms of Cz (which is approximately equal to CL for small pitch angles) reveals some major discrepencies between the two methods near the root of the blade. The Hover Program locates the root vortices vertically below the blade in the prescribed wake model. This is probably too simplistic, and the loading is over predicted outboard of the root, and dips negative in the root region. In contrast, the CFD results reflect the predicted flow field and may be more realistic. However, in the current simulation, the hub and feathering bearings are ignored, and only the geometry of the blade itself is represented. Also, it might be that there is some interaction between the root vortex and the 'wall' of the cylindrical hub used for convenience in the numerical simulation. The CFD predicts some local regions of high non-dimensional loading due to the presence of the root vortex, together with the influence of the root vortex from the preceding blade. These interactions change dramatically with twist, although the overall impact on thrust and torque is small. Looking ahead to Figure 166 shows how the position of the vortices in the wake and the inboard vortex sheets and root vortex are influenced by twist in the numerical simulation.

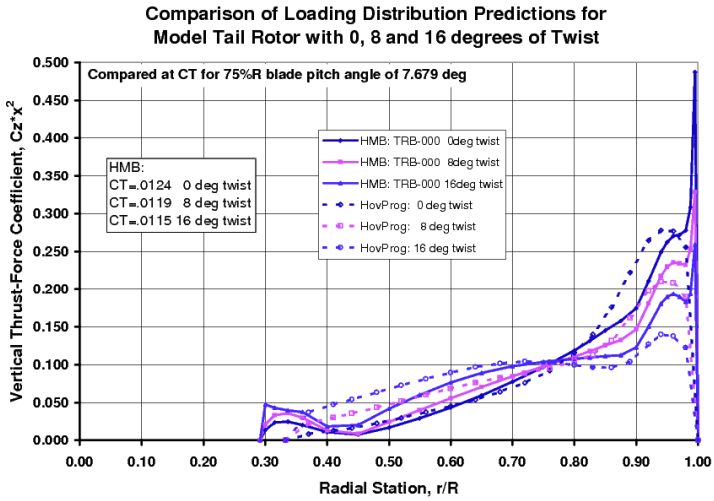

Figure 162: Comparison of Non-Dimensional Blade Loading ($Cz.x^2$) Results from HMB and WHL Hover Program for the Rectangular Model Tail Rotor Blades with 0, 8 and 16 Degrees Twist

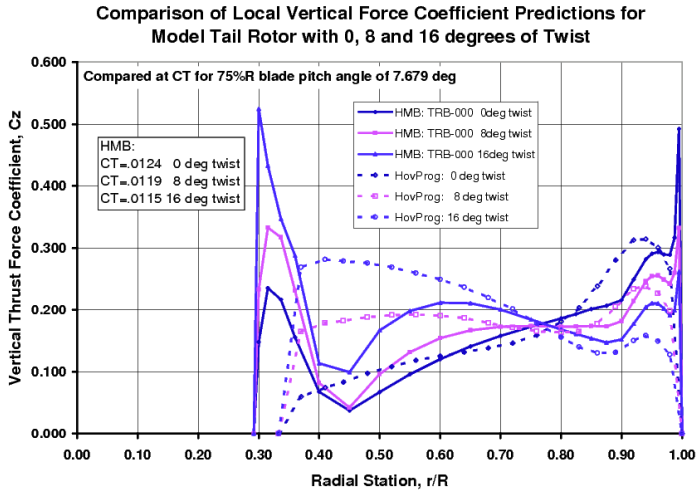

Figure 163: Comparison in Terms of Local (Aerofoil, Cz) Vertical Force (Lift) Coefficient from HMB and WHL Hover Program for the Rectangular Model Tail Rotor Blades with 0, 8 and 16 Degrees Twist

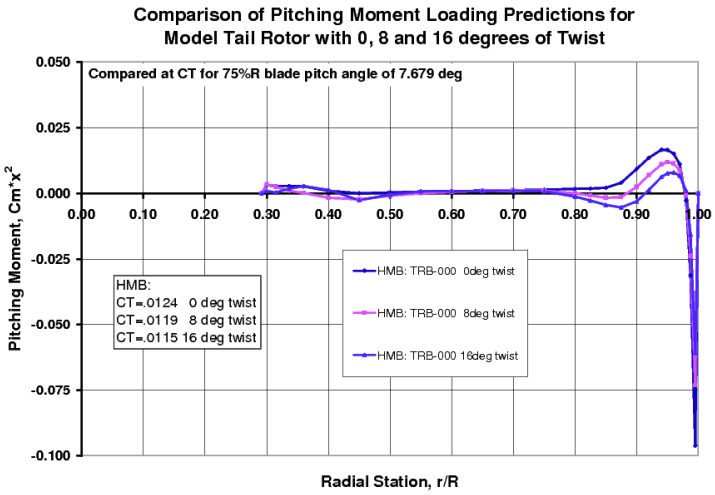

Figure 164: Comparison of Blade Pitching Moment (Cm.x^{2}Results from HMB and WHL Hover Program for the Rectangular Model Tail Rotor Blades with 0, 8 and 16 Degrees Twist

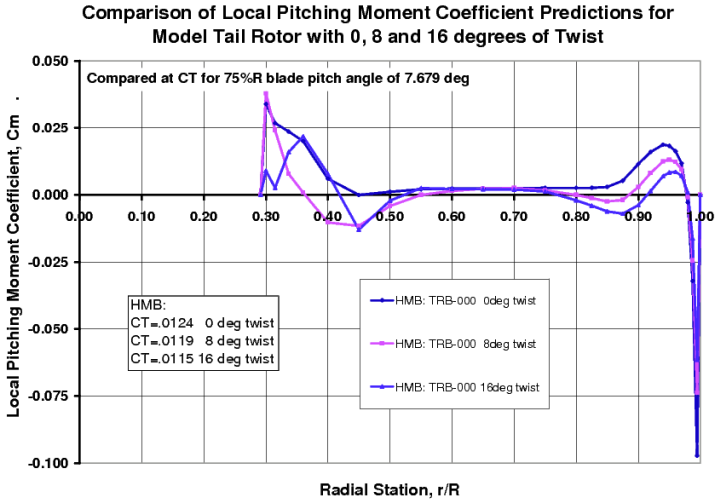

Figure 165: Comparison in Terms of Local (Aerofoil, Cm) Pitching Moment Coefficient from HMB and WHL Hover Program for the Rectangular Model Tail Rotor Blades with 0, 8 and 16 Degrees Twist

The blade pitching moment distribution in Figure 164 reflects how the loading towards the tip of the blade first moves a little aft (negative moment), and then forwards (positive moment) under the influence of the (downwash and upwash, respectively) of the tip vortex from the preceding blade, augmented by a planform effect arising from the rectangular tip itself. At the extreme tip, the roll-up of the tip vortex over the upper surface of the blade generates a suction region which gives a locally strong negative (nose-down) moment at the tip. Ironically, these effects tend to cancel out when integrated along the blade, such that (for a blade with a symmetrical aerofoil in hover) the overall blade pitching moment is generally fairly small at low pitch conditions, but may grow slowly with increasing pitch. For the rectangular blade and NACA 0012 aerofoil, the positive (nose-up) trend arising from suctions near the leading edge is accentuated by the increased Mach number near the tip due to the presence of a weak shock. This nose-up moment is counter-balanced by the aft suction under the tip vortex (until the suction on the aerofoil moves aft at the stall). The effect of twist is to suppress this trend as the tip is unloaded and a greater proportion of the thrust is carried inboard. Again, the differences near the root of the blade become more noticeable when the local pitching moment is plotted, as in Figure 165. Much of this detail would normally be missing from the traditional rotor model, but is captured by the computational approach.

The change in location of the root and tip vortices is shown in Figure 166 which provides a cross-section view of the vorticity in the wake of the model tail rotor for the three different blade twists of 0, 8, and 16 degrees at a similar loading, since the pitch is the same at 75%R. Notice that at the tip, the tip vortex soon separates from the end of the vortex sheet which then convects downstream at a greater rate than the tip vortices themselves. In addition to the visualisation of the tip vortex, the inboard vortex sheet is clearly visible and is positioned differently for each value of twist, becoming less inclined with increasing twist until with 16 degrees of twist it is near horizontal. For zero twist the root vortex is found to be well above the inboard blade, but as twist is increased, the loading and hence the downwash near the root-end of the blade increases, and the root vortex is pulled downwards until for a twist of 16 degrees it lies firmly below the plane of rotation. It is interesting to note that many flow visualisation photographs of rotor flows, eg as in Fradenburg[115] are indistinct in the root region, probably due to the general turbulence caused by the rotor hub.

The changes in the structure of the vortex wake due to twist will also be seen in the downwash distribution below the rotor. The downwash was extracted from the Euler solutions for the twisted model rotor blades by averaging the w-velocity over the blade segment at each radial station (as described later in Chapter 7). The effect of twist on the downwash distribution is shown in Figure 167, both in the plane of the rotor and well below the rotor plane in the fully contracted wake. It is observed that the greater the twist, the more uniform is the distribution of downwash, although after the wake has contracted the maximum w-velocity still found towards the edge of the wake but with a significant increase in downwash inboard. Carrying more load inboard clearly helps to make the rotor more efficient by making the downwash much more uniform. Note also that close to the rotor there is some upwash outside the wake, as expected. Inside the central region, between the cylindrical hub and the root cut-out, there is a considerable amount of upwash in the plane of the rotor due to the absence of any hub-blockage, or turbulence that would have been generated by the feathering bearings, which were not included in the simulations. Further down in the wake, these upwash effects at the edges of the wake are no longer apparent.

In the preceding sub-sections, results from HMB have been compared to test data and to results from a more traditional rotor code for the WHL model tail rotor with twisted blades. The comparisons have covered integrated quantities, extraction of induced power, blade loading distributions, vortex trajectories, wake visualisation and downwash, and in all cases the results appear to be realistic and have furnished valuable detailed information, hitherto unobtainable from lower-order methods. It is therefore clear that the HMB solver, which has third-order-accurate spacial resolution on a good quality multi-block structured grid, is capable of providing a high-fidelity simulation of rotor flows.

At the start of this section of the thesis, validation was established for viscous, compressible (Navier-Stokes) computations on aerofoils, while the rotor validation cases presented here have employed an Euler solution (as a necessary economy during the early stages of this research). Nevertheless, the induced flow features have been well captured and the method can now be used for a preliminary assessment of various rotor blade tip shapes, as defined next in Chapter 4, and evaluated using Euler solutions in Chapter 5. The performance of selected tip shapes is then more fully determined using a steady Navier-Stokes method in Chapter 6.

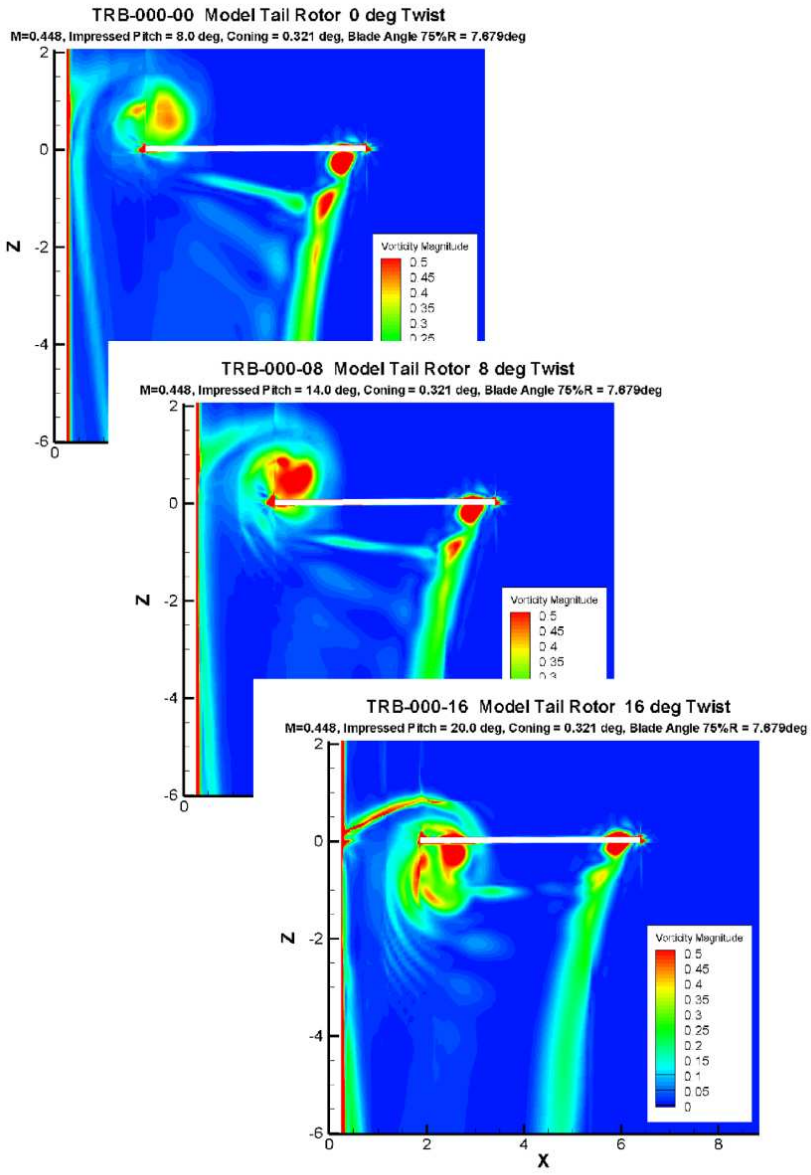

Figure 166: Visualisation of HMB Computational Results for the Wake Below the Model Rotor with Blades having 0, 8 and 16 Degrees of Twist

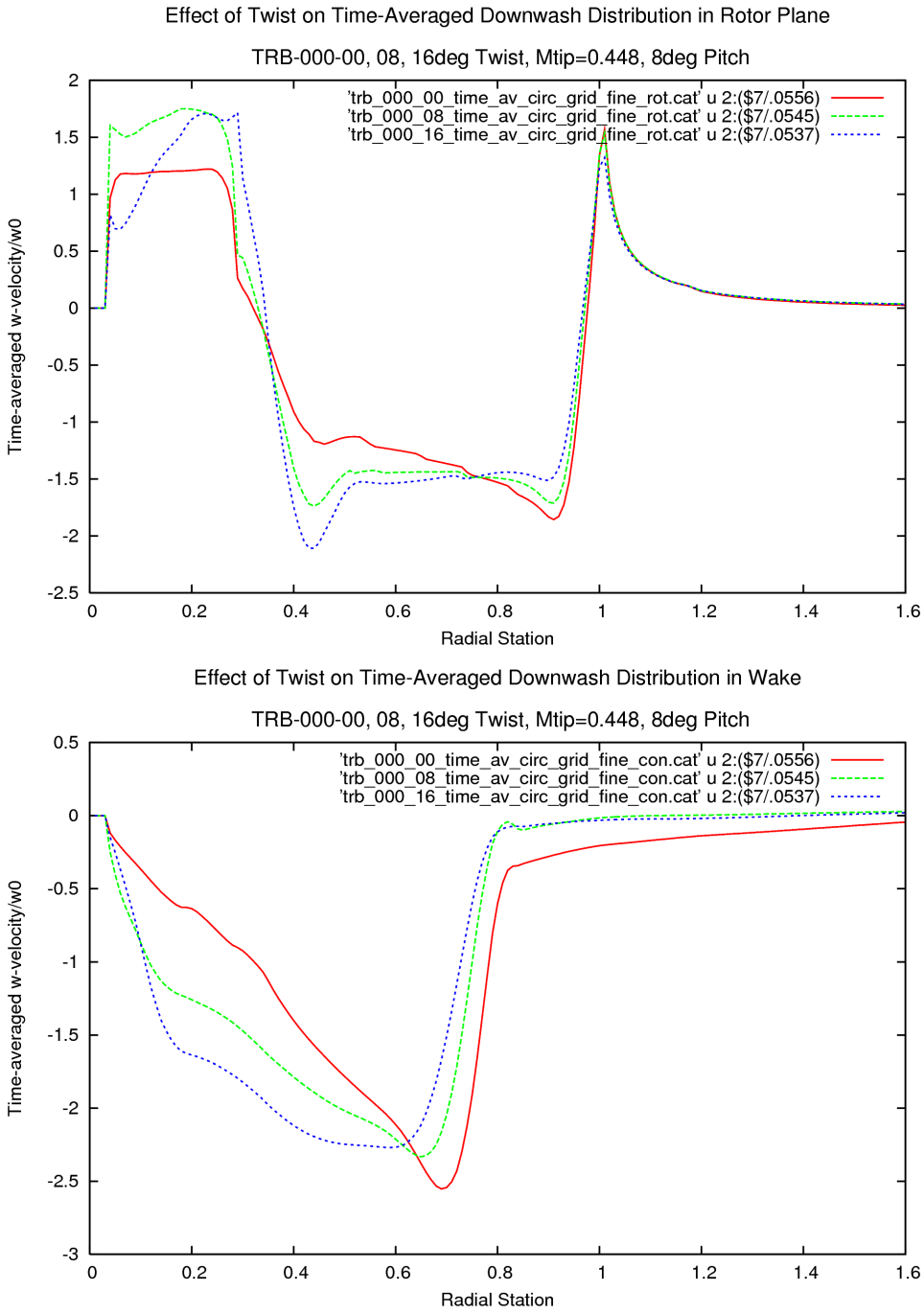

Figure 167: Comparison of the Time-Averged Downwash from Euler Solutions for the Twisted Model Tail Rotor Blades having 0, 8 and 16 degrees of Twist at 8 degrees of pitch (at 75%R) and Mtip=0.448. The Change in Loading due to Twist is Reflected in the Distribution of Downwash. Top: Averaged Downwash Distribution in the Plane of the Rotor Disc. Bottom: Averaged Downwash Distributions at 12 chords, or 1.874R below the rotor where the Wake is Fully Contracted.

The validation cases in this thesis expand the Validation Database of HMB, and the solver has been further verified by comparison with the WHL model tail rotor test data. In parallel with this research, the solver has also been employed in industry for the analysis and design evaluation of several main and tail rotor configurations. This background work provides the confidence needed to now examine blade tip aerodynamics in greater detail.

4 Tip Design

One of the main objectives of this research is to show that modern CFD methods are capable of accurately resolving the differences between various tip designs, thus permitting improvements in rotor performance to be obtained by a process of gradual refinement and perhaps, in the future, by optimisation. A high fidelity simulation will also allow a deeper insight into the compressible and viscous flow-field about the tip, and indeed, will provide details of the tip vortex itself. The ability to accurately quantify the tip aerodynamic loading should lead to improved designs of main and tail rotors which will enhance the mission effectiveness of the helicopter.

While the computational methods used here could equally well be used to evaluate the performance of either main or tail rotors, the design examples considered here focus on the tail rotor. This choice brings about a modest economy in the grid size required, and also allows comparison with available test data for the datum blade as already presented in Chapter 3.

The model rotor tests carried out by the writer at WHL in 1980-84 [WHL Internal Report(s), 1980-1986] addressed the question of the optimum twist that should be used on a tail rotor. Since then, a moderate amount of twist (8 to 10 degrees) has been employed on several new tail rotor designs, but little research work has been done to determine the best tip shape. A well designed tip should complement the chosen twist and the specialised aerofoils that are now used on modern tail rotors. However, in this thesis the emphasis is placed solely on the design of the tip and a blade with no twist and a simple symmetrical aerofoil was chosen as a carrier for the tip designs. The datum rectangular blade is compatible with the baseline model rotor blade.

In this section of the thesis, design requirements for tail rotors are briefly reviewed to establish the aerodynamic tip design features that offer the most potential for a highly loaded tail rotor. A series of tip design concepts are then described in detail and the reasoning behind each design is presented. The surfaces of the blades were defined using the Rhino 3D solid modelling software package, in readiness for meshing in ANSYS ICEM Hexa, for subsequent evaluation with HMB. Far-field curves and surfaces, and other supporting curves for block boundaries around the aerofoil were also defined in Rhino.

Later, in Chapter 5, Euler (compressible, inviscid) methods were used for an initial and economic screening of the series of tail rotor tip designs, with the most promising designs being down-selected. Following further explorations of flow-solutions in Chapter 6, a final performance evaluation was carried using Navier-Stokes in hover, as presented in Chapter 7. This latter step of taking viscosity into account is essential to accurately quantify the performance of rotor tip shapes, and is fundamental to the aims of this thesis.

4.1 Design Aims

Whereas the main rotor reaches its fundamental limits in forward flight, due to stall on the retreating blade, and the effect of compressibility on the advancing blade, the design requirements for the tail rotor are set in low speed manoeuvring flight by the need to provide an adequate thrust margin to initiate yaw manoeuvres. For agile helicopters, a maximum yaw acceleration requirement in excess of 1 radian/sec is not uncommon, with the need to retain at least 1/3 of this capability at the extremes of the low speed flight envelope, in yaw manoeuvres and for safe take-off in hot and high conditions. These requirements are often idealised to a design thrust target in hover, which may be about twice the thrust needed to balance the main rotor torque. Some limitations may also arise in forward flight, and these may be alleviated to some extent by fin off-loading (which reduces thrust and hence flapping). The low 'aspect ratio' (R/c) blades typical of most tail rotors also provides some compressibility relief. However, these factors are not always sufficient to avoid drag rise and achieve low noise.

Growth of the helicopter maximum all-up-weight is another factor that places further demands on the tail rotor. As aircraft weight and yaw-inertia increase, the tail rotor is required to produce a higher thrust in hover for a given tipspeed and blade area. Aerofoils which produce high lift at mid-Mach numbers are often employed to enhance the maximum useable thrust, and while pitching moments constraints may be more relaxed than for main rotors, control loads arising from both aerodynamic and dynamic sources may also be an important issue. However, unlike the main rotor, for which a high Figure of Merit is paramount, the requirement to produce maximum possible thrust from the tail rotor perhaps out-weighs the desire for the highest possible induced power efficiency, save for the benefits of employing a small amount of twist (which is constrained due to the need to avoid any possibility of thrust-loss as stall develops). Indeed, there is a conflicting need to maintain area outboard to achieve the design thrust instead of tapering the blade for better efficiency. The blade chord required is often set by practical constraints on the radius and tipspeed. Also, in order for the tail rotor to operate within tail gearbox torque constraints, and therefore avoid weight penalties in the tail, it is highly desirable to delay the divergence of profile power by good aerodynamic design. The choice of tip shape will play an important role in achieving this goal, but in the past the tip predictive tools lacked the resolution to provide a reliable indication of performance, and the design may have been constrained by manufacturing considerations.

Uniquely, the tail rotor often operates at high pitch and frequently encounters a degree of stall when initiating manoeuvres or hovering at high weight or altitude. The absolute pitch available may be constrained by torque limits or blade stability issues, but even so collective pitch values as high as 26 to 28 degrees are the norm, and are essential to meet manoeuvre requirements. While it is acknowledged that the tail rotor operates in a highly dynamic environment, it is common practice to carry out design evaluations in a nominal, steady hovering condition.

The main design aim for a tail rotor blade is therefore to provide a high thrust capability and the aerofoil, twist and tipshape should be chosen to delay the onset of separation at high incidence. The tip should also be designed to avoid drag rise on the advancing blade, and ensure acceptable pitching moments in forward flight. Compressibility relief via low R/c may be sufficient to avoid the need for any significant sweep, except as incorporated into the tip shape itself. A secondary requirement may be to suppress tail rotor noise by use of a relatively thin tip section, and for tail rotors which must operate at very high forward speeds, or with particularly high tipspeed, there may be a need to alleviate any tendency for shock delocalisation by use of sweep at the extreme tip. However, the modern trend is towards lower tipspeeds for tail rotors, with the intention that the noise signature should be less than than of the main rotor.

The tip shape must also be suitable for economic manufacture, and may need to include provision for spanwise and chordwise balancing. Fortunately, modern composite construction and electro-deposited erosion shields provides an amount of scope for sculpturing the tip.

Having reviewed the general aerodynamic requirements for the tail rotor, it is now possible to translate these into several strategies for tip design, as will be described in detail in the following sections of this Chapter. Clearly, the tip needs to avoid adverse chordwise pressure gradients that may arise from isobars bunching up in the forward leading edge corner, where adverse pressure gradients may be compounded by compressiblity effects. It is also desirable that the formation of the tip vortex takes place in an efficient manner, with minimal

energy losses due to edge separations. The tip shape should have a favourable effect on the stability of the tip vortex to delay vortex bursting at high lift and therefore delay gross flow separation and possible lift-loss. The tip shape should also help to minimise induced power losses by encouraging the tip vortex to form as far outboard as possible (ie to maximise the effective rotor radius).

Since the notional design point is in hover, use of Anhedral in the tip region may be beneficial for a highly loaded tail rotor, although care must be taken to balance any associated pitching moments in forward flight. While, simplistically, anhedral may be expected to displace the tip vortices downwards in hover, and perhaps bring about a power saving, the detailed effects of a downwards deflection of the tip are likely to be quite subtle. This level physics should be captured by the CFD analysis, perhaps helping to understand how the benefits of anhedral are accrued.

On the example tail rotor designs that are described in the following sections, a 12% thick symmetrical NACA 0012 aerofoil has been retained up to the radial station which marks the start of the tip shape. For a modern tail rotor design the aerofoil sections may vary along the blade, perhaps starting from a section optimised for high-lift at relatively low Mach numbers at the root, blending to a good lifting section suitable for use at mid Mach numbers outboard, and then to a slightly thinner, lower cambered aerofoil near the tip. While the NACA 0012 may therefore not be the best choice, it is deliberately used here, in combination with zero twist, to simplify the comparison between different tip designs.

4.2 Tip Designs

Starting with a simple datum design adopted from the model rotor tail rotor tests, a series of blades have been generated to test several tip design concepts with the overall aim of enhancing the performance of the tail rotor. The idea is to build on the knowledge obtained from the CFD solutions to gain a better understanding of how each design functions, and identify any potential improvements or limitations. Most of the following designs were generated to test perceived advantages, but a few were deliberately defined to test what may be regarded as high-risk strategies, which may, or may not, yield overall benefits.

Since the primary role of the tail rotor is to produce high thrust in hover at mid-subsonic tip Mach numbers, the tip shape should be designed to alleviate local separations near the tip which may adversely affect the growth in profile power, or invoke an early stall. It is therefore desirable to round the leading edge corner of the tip to avoid high suction peaks or shock-induced separations. The first two designs exploit this idea, while a third seeks to employ vortex lift with a shape that would also be well suited to delaying drag rise on the advancing blade in forward flight, and may reduce noise by avoiding delocalisation. However, if the tip design is too biased towards forward flight it may not perform well in hover. Tip design for the tail rotor is therefore a compromise, between the conflicting requirements of obtaining high thrust in hover (as distinct from main rotor hover efficiency requirements), and the need to achieve acceptable characteristics in forward flight by staying within pitching moment constraints and advancing blade compressibility limitations (although these may be less critical for a tail rotor than a main rotor), and for the tail rotor there should be less concern for the retreating blade stall.

One design parameter which may be beneficial in hover, but has not been used on tail rotors previously is anhedral, and this design parameter has therefore been included in the set of tip shapes. CFD will be used to first quantify the hover performance and then to investigate any adverse effects which may arise in forward flight.

Twist has already been shown to be advantageous from the model rotor tests, and by comparison with CFD results in Section 3. A moderate amount of twist has also been used on several recent tail rotor designs which the writer has worked on in industry. Since the aim here is to investigate only the tip design, twist has been set aside in these studies.

Initial studies therefore focus on the effect of tip shape in hover, and employ Euler methods for a preliminary assessment. The most promising designs were also evaluated in forward flight to identify any pitching moment limitations. Once initial ideas had been explored, the performance of the selected tip shapes was evaluated in hover using Navier-Stokes. Taking into account viscous effects allows the chosen tail rotor tip designs to be compared at the onset of power divergence, at moderately high pitch angles (high thrust) conditions which are key operating conditions for the tail rotor.

The series of tail rotor blades were all evaluated at a tip Mach number of 0.6, representative of a modern full-scale tail rotor, but it was chosen to retain a relatively low, model-scale Reynolds number of 1,168,000, the philosophy being that this Mach number was just high enough for the presence of transonic flow effects and the low Reynolds number would help emphasise viscous effects.

A detailed description of each design and the ideas on which it was founded are put forward in the following sections. The series of tail rotor blades generated with various tip shapes for evaluation in this thesis are illustrated in Figure 168.

4.2.1 Datum Blade, TRB-000

A datum blade, TRB-000, was defined with a rectangular square-cut tip, zero twist, and a NACA 0012 aerofoil section with a sharp trailing edge (co-ordinates for this aerofoil are listed in Appendix F). This blade design is also typical of many early tail rotors, and is compatible with the zero twist blade used in the model rotor tests. Starting with this simple blade, the outer portion of the blade has been modified to generate various tip shapes. All the following blades have zero twist and have the same basic blade chord and radius. The blades were all drafted in Rhino with a model-scale chord of 83.312mm and radius of 533.4mm, in keeping with

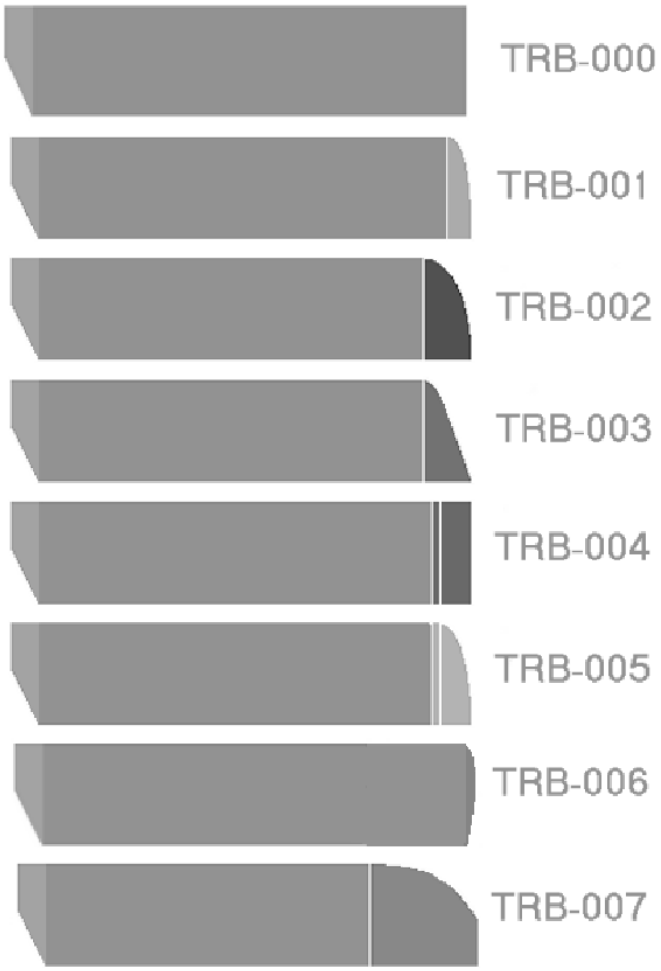

Figure 168: Series of Seven Tail Rotor Blade Tip Shapes

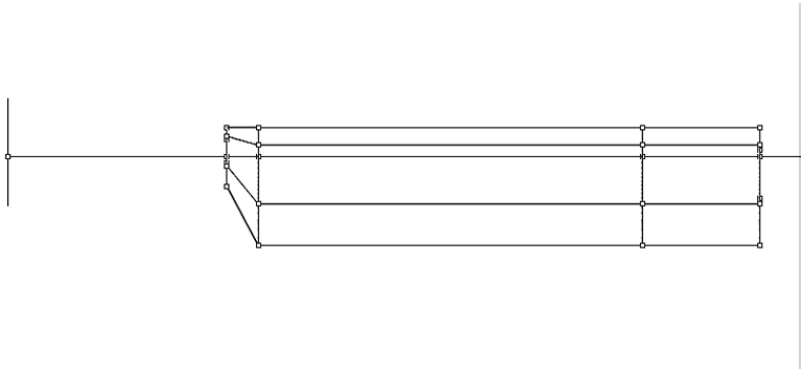

Figure 169: Plan View of Datum Tail Rotor Blade Tip Shape Definition: TRB-000, R/c=6.402439

Figure 170: Front View of Datum Tail Rotor Blade: TRB-000

the WHL model tail rotor. However, for the computational work, unit chord was used giving R/c is 6.402439 chords. The root of the blade tapers inboard of the root cut-out at the first aerofoil station at 33% radius, to 50% chord at the blade attachment or 'cuff' (centred on the blade reference axis). The rendered surfaces of the datum blade are shown in Figure 172. The thickness of the blade remains constant at the root, giving an aerofoil of 24% t/c at the cuff, twice the 12% thickness/chord ratio of the NACA 0012 aerofoil. All blades were evaluated in hover using a cylindrical hub of 10.3% radius (0.66 chord). The designs selected for evaluation in forward flight had a spherical hub of the same radius. In all cases a clear gap was left between the blade cuff and the hub to facilitate pitch change. Hub configuration and root vortex issues are discussed in more detail in the following section.

All blades were defined with a sharp trailing edge to facilitate the Euler computations, and this also brought some useful economy through simplification of the multi-grid blocking for the Navier-Stokes simulations.

4.2.2 TRB-001, Küchemann-Type Tip (0.25c Wide)

The first new tip shape, TRB-001, Figure 173, follows the style of a so-called Küchemann tip[169],[19] and has a smoothly curved leading edge generated by a 3rd order Bezier curve, while the trailing edge is straight. The tip extends over a quarter of the blade chord inboard from the tip, such that the tip aerofoil station is at 96% rotor radius. The tangent of the outer tip edge is normal to the blade reference axis.

The aim of this tip is to provide sufficient rounding of the forward leading edge corner to avoid isobars bunching up and causing premature stall or shock-induced separation at the tail rotor design condition of

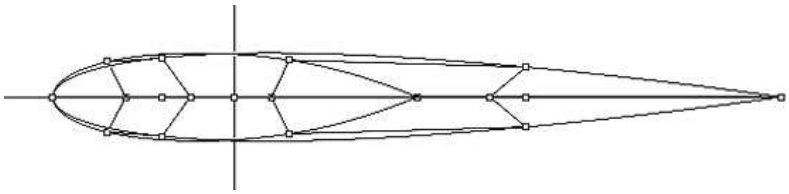

Figure 171: All Tail Rotor Blades have NACA 0012 Aerofoil

Figure 172: Datum Tail Rotor Blade Rectangular Tip Shape: TRB-000

Figure 173: Küchemann-Type Tip Shape (0.25c Wide): TRB-001

high lift at mid-subsonic Mach number in hover, but yet maintain as much lifting-area as possible in the tip region. The Küchemann type tip is perhaps the best shape to do this and also avoid any rearward facing suction area. The 'streamwise' tip edge allows the tip vortex to roll-up as far outboard as possible, maximising the effective rotor radius, and hopefully delaying vortex bursting by facilitating a small core size. The design takes advantage of natural tip relief, which occurs due to the low aspect ratio of tail rotor blades, to alleviate compressibility effects on the advancing blade in forward flight.

In a final design the tip aerofoil may be reduced in thickness (and camber) outboard of the hover loading peak to further reduce compressibility effects, thus eliminating the need for more general sweep if the advancing blade Mach number is high. However, for simplicity, and to allow direct comparison against the datum blade, the NACA 0012 aerofoil has been retained up to the 96% radial station, outboard of which the tip is smoothly blended and gradually reduces in thickness. The leading edge radius therefore gradually reduces from that of the NACA 0012 (1.58%c) at the tip leading edge to zero at the trailing edge (in this instance, due to the use of a sharp trailing edge). On a practical tail rotor blade, a finite trailing edge tab may employed and the tip edge would then blend to a small finite radius at the trailing edge.

4.2.3 TRB-002, Küchemann-Type Tip (0.5c Wide)

The second tip design, TRB-002, is similar to TRB-001, but extends over a half chord width, starting from 92% rotor radius, thus introducing a small additional sweep effect, which together with the reduced thickness due to the longer blend, may be beneficial on the advancing blade. This tip shape may also provide further relief from shock-induced separation at high incidences in hover, but with the possible risk of extending the spanwise extent of the tip-vortex roll-up region. A rendered image of this TRB-002 is shown in Figure 174. While the tip suffers a small reduction in area outboard, it retains a 'streamwise' outer edge. The favourable design features of TRB-001 are therefore balanced against the use of a longer tip region. In high speed forward flight the tip should display some advantages with regard to advancing blade drag, pitching moment, and acoustics, although in the latter case the 'streamwise' outer edge may still suffer a degree of delocalisation at high-subsonic Mach numbers. However, for the tail rotor the main emphasis is in maximising hover thrust for a given radius and basic chord.

Figure 174: Küchemann-Type Tip Shape (0.5c Wide): TRB-002

Figure 175: Tip Shape with 70 degree Swept Leading Edge: TRB-003

4.2.4 TRB-003, 70-degree Swept-Edge Tip

The third configuration, TRB-003, Figure 175, seeks to take advantage of a slender delta wing-tip to provide a high-lift capability (almost independent of the main aerofoil). This tip has a 70 degrees swept outer tip edge, reminiscent of the BERP-III blade, and is similar to the wing tested dynamically in the wind tunnel at the University of Glasgow by Coton and Galbraith.[83] This tip also sacrifices some area in the outer tip region, which may be compensated by increased vortex lift capability, since the roll-up takes place over an increased radial extent, there may be a chance of the tip vortex migrating inboard as it rolls-up. If the tip vortex is generated with a larger viscous core, there may also be some risk of it bursting prematurely on an otherwise unswept, rectangular blade.

The additional sweeping and thinning of the tip, together with the 70 degrees outer swept-edge, should give favourable acoustics through the likely elimination of delocalisation on the advancing blade.

It will therefore be interesting to discover exactly how this tip behaves in the critical hover design conditions for a tail rotor.

4.2.5 TRB-004, Rectangular Tip with 20 degrees of Anhedral

A design parameter which has previously been found to enhance performance in hover by reducing the power requirement is anhedral. While anhedral is used on the BERP-III main rotor in combination with sweep and notch-offset, and was tested on the NH-90 parabolic-tip main rotor, it has not previously been used in any significant amount on tail rotors. The reason is probably the potential it has to generate high pitching moments at the front and rear of the disc in forward flight. However, if a tail rotor tip were designed to accommodate anhedral, there would appear to be potential for a significant power saving in hover.

The fourth tail rotor tip design, TRB-004, introduces 20 degrees of anhedral, whilst retaining a rectangular, square-cut tip to enable direct comparison with the datum blade. The anhedral-crank is located at 94.0% rotor radius and the junction is smoothly blended over a distance 0.75% radius either side. Hence the outer 6.0% of the blade is bent downwards, and the blend-curves have a mean radius of about 22.68 mm at the leading and

Figure 176: Rectangular Tip with 20 degrees of Anhedral: TRB-004

Figure 177: Küchemann-Type Tip (1/4c wide) with 20 degrees of Anhedral: TRB-005

trailing edges. The centre of the tip aerofoil is therefore displaced by 2.18% of the radius, or 14% chord. The tip is illustrated in Figure 176.

The aim of this tip design is not only to capitalise on the anticipated power saving bought about by anhedral for highly loaded rotors, but also to understand the mechanism by which the performance in hover is enhanced. Should a useful reduction in power be found, it will then be necessary to quantify any detrimental pitching moments in forward flight. After evaluation of any adverse effects, the results obtained may point the way to further design refinements, such as employing a Küchemann type tip shape (as TRB-005 below), or the incorporation of some sweep and perhaps some forward off-set, that would alleviate one and two per rev torsional loads.

4.2.6 TRB-005, Küchemann-Type Tip (0.25c Wide) with Anhedral

This tip design anticipates the need to refine the simple rectangular planform of the anhedral tip of TRB-004, described above. TRB-005 therefore incorporates a Küchemann tip shape identical to that used on TRB-001, while keeping the geometry of the anhedral break identical. The TRB-005 tip shape is shown in Figure 177. Thus comparing results for TRB-005 with TRB-001 should again confirm the benefit of anhedral, and comparison with TRB-004 should determine if the anticipated advantages of the Küchemann tip are retained when anhedral is used.

The simple combination of a .25c wide Küchemann tip facilitates a direct comparison with TRB-001. However, blending the tip shape from the end of the anhedral-break blend would provide a more aesthetically pleasing design (by eliminating the small region of parallel chord just outboard of the anhedral blend). Comparison between TRB-001, and the wider TRB-002 tip may provide an indication of whether this would be beneficial. Alternatively, a more gradual anhedral blend region might be preferable, and indeed, the results of this evaluation may be used to guide further design changes.

4.2.7 TRB-006, Rectangular with Volume-of-Revolution Tip Cap

The tail rotor tip designs have so far considered two types of tip closure; either a square-cut rectangular tip, or a curved and blended Küchemann-style tip effectively radiused at the leading edge and becoming sharper

Figure 178: Blade with Volume-of-Revolution Tip Cap: TRB-006

towards the trailing edge. While the Küchemann tip offers perhaps the greatest efficiency, the square-cut tip would appear to be the simplest to manufacture.

A further concern with the square-cut tip is that edge separations might adversely affect the vortex formation, perhaps to the extent of generating strong additional (secondary and tertiary) vortices which may consume energy. These details should be captured by a Navier-Stokes solution, but may not be well represented by an Euler method.

A less extreme type of tip cap, which perhaps avoids edge separations and so should help the tip vortex to roll-up cleanly, is the simple volume-of-revolution, or hemispherical tip shape. While perhaps most suited to lower tip Mach numbers, this tip has minimal rearward facing suction area, and little loss of area at the trailing edge. This tip shape should therefore help the tip vortex to roll-up cleanly to minimise power

Such a tip shape has been defined as TRB-006, Figure 178 in order to gain an appreciation of the benefit of rounding the tip edge. To allow direct comparison with TRB-000, and the other blades, the overall blade radius of TRB-006, measured along the blade quarter-chord reference axis, has been maintained, while the swept-radius (from the rotor centre to the tip rear corner) is very slightly reduced to 99.7525%R.

4.2.8 TRB-007, Parabolic Tip

The final tip shape considered in the exploratory phase was a parabolic tip, TRB-007, shown in Figure 179. The parabolic tip has proved popular in Europe for both main and tail rotors, and introduces a tapered planform over a greater part of the tip region for improved aerodynamic efficiency. TBR-007 employs a Bezier-defined parabolic tip shape, starting at 84.3% radius (ie one-chord width from the tip) and tapering to 0.55 chords at the tip. The taper ratio was chosen to be modest in view of the need to maximise the thrust from the tail rotor, while the tip-relief arising from the relatively low aspect ratio reduces the need to maximise the sweep that is introduced by this style of tip. Hence the sweep angle of the leading edge at the tip of the blade is 42 degrees. For simplicity, and to compare with the datum rectangular tip (TRB-000), the tip is cut-square (as in many practical designs).

The thickness-chord ratio was maintained at 12% over the entire tip region using NACA 0012, giving an absolute thickness at the tip of only 6.6% of the basic blade chord, although in a practical design, a thinner tip aerofoil (of relatively low camber) may be used if advancing blade considerations and acoustics are a major concern. However, excessive thinning of the tip aerofoil will erode the hover thrust capability. It is anticipated that this tip should have an improved Figure of Merit due to reduced wetted area near the tip, and the fact the more loading will be carried inboard should reduce the induced power. However, whilst improved hover efficiency is vital for a main rotor design, and also beneficial for a tail rotor, the need to maximise the thrust for a given blade size may out-weigh the benefits of aiming for a high Figure of Merit. Much will depend on the location of the loading peak, and the occurrence of any flow separation due to increased local lift coefficients in the tip region, which may well adversely influence the formation of the tip vortex.

Figure 179: Blade with Parabolic Tip Shape: TRB-007

4.2.9 Thoughts for a Final Design

In the thesis, blade twist has been considered only in the model rotor comparisons in Chapter 3, while the focus here has been solely on the effects of tip geometry, with all blades having zero twist and a uniform aerofoil section.

The authors prior research into the effect of twist on tail rotor performance has influenced several new tail rotor designs, which employ a moderate amount of twist to take advantage of benefits in induced power while avoiding any danger of a sudden thrust loss when the stall is reached.

Twist influences how the loading is distributed between the root and tip of the blade, and this, together with the choice of aerofoils and tip shape, controls the development of stall. It is therefore clear that a final design should include appropriately designed advanced aerofoils and twist, as well as the best tipshape, arising from this work, possibly with some anhedral.

However, it is not the objective of this thesis to fully specify a best tail rotor design, but to establish the methodology required to achieve such goals, for either helicopter main or tail rotors. The method and some of the tip design concepts put forward here may also be extended to propellers, wings and wind-turbines.

4.3 Tip Design Summary

A series of eight tip shapes for low 'aspect ratio' (R/c=6.402) helicopter tail rotors has been put forward for evaluation by computational methods.

The tip designs start from a simple NACA0012 rectangular tip blade, consistent with that used in the WHL model rotor tests. Building on this basic untwisted blade with symmetrical aerofoil, various tip shapes have been generated, as described and defined above. RHINO 3D solid modelling software was used to generate the required CAD surfaces for subsequent grid generation with ANSYS ICEM-Hexa software.

This series of tip shapes represents several alternative aerodynamic design concepts aimed at controlling flow separation characteristics in the tip region and enhancing the vortex roll-up process, thus delaying power divergence at high pitch angles as the onset of stall is approached.

In particular, a Küchemann style tip has been employed on three of the tip shapes and is expected to be effective in both suppressing the bunching of isobars in the forward leading edge corner and enabling efficient vortex formation.

While blade twist and aerofoil design have been deliberately set aside to focus on the tip shape itself, two of the designs include anhedral since it is thought that this may be effective in reducing the power requirements of highly loaded rotor blades. It was also decided to retain a constant blade chord, since the tail rotor has a unigue requirement for lifting area in the outer region of the rotor blade, and again this helps to separate planform and tip shape effects. However several of the tip shapes employ a variation of chord locally in the tip region, with perhaps the parablic tip and the 70 degree tapered tip being the most extreme examples. A classical volume of revolution tip cap has also been included to compare with the square-cut tip of the datum blade.

Computational fluid dynamics in the form of the Helicopter Mutli-Block code, HMB will now be used to evaluate the performance of these tip shapes in hover, and for selected tips in forward flight. For economy, Euler computations were used for an initial assessment, and certain chosen tip shapes were then evaluated using Navier-Stokes simulations, as described in the following sections of this thesis.

5 Euler Evaluation

The objective in this Chapter of the thesis is to carry out an initial evaluation of the series of tail rotor blade (TRB) tip shapes that were described in Chapter 4. As stated earlier in this thesis, hovering flight is one of the main design points for the tail rotor, and so it was natural to start with a series of hover computations. The Euler solver option was chosen for these first evaluations because the computational cost, and hence turn-around time, is much lower than would be required for a Navier-Stokes solution. Based on experience gained from the validation work of Chapter 3, a typical grid size of about 2.5 million points was used to ensure that all the flow details were well captured. A series of cases were therefore able to be run for each configuration within the available computing resources (using 8-10 processors) to provide an initial screening of the tip designs prior to selection of the most promising designs for subsequent evaluation using Navier-Stokes, as discussed later in Chapter 6.

In contrast to traditional methods, the Euler approach is able to furnish a close prediction of the 3D loading in the tip region, inclusive of compressibility effects, and through conservation principles the effects of blade design features will be reflected in the wake, allowing new ideas such as anhedral to be explored (while the effects of twist were confirmed earlier in Chapter 3). While an Euler solution is restricted to low to moderate pitch angles, where attached flow is present and any viscous separation effects are small, this approach should nevertheless provide a fairly good indication of the induced power. Observation of adverse pressure gradients may also give an early indication of any potential separation problems for a given tip shape at higher pitch.

For these comparisons the tip Mach number was chosen to be 0.60, representative of a modern full-scale tail rotor. In retrospect, this tip Mach number was perhaps rather low to bring compressibility effects to the fore, but this situation is quite typical of a modern tail rotor design where the trend is to reduce tipspeed to minimise tail rotor noise. It was later discovered from Navier-Stokes computations that, depending on the Mach number and Reynolds number, the combination of compressibility and viscous effects may strongly influence flow separation in the tip region, and hence impact the performance via changes in profile power, as discussed in Chapter 6.

The tip designs considered here were all based on an untwisted blade with a constant NACA0012 aerofoil section (see Appendix F). The more detailed design issues of aerofoil selection and twist optimisation were purposely left to one side, placing the emphasis on the tip shape. For simplicity the comparison cases presented here were run at zero-coning (the effect of coning was taken into account in the earlier validation in Chapter 3, even though the coning of the model tail rotor was small). Coning was also separately investigated at an early stage in this research effort, and has a small effect onthe induced power which increases with the coning angle. Conversely, a negatively coned rotor may bring about a reduction in the induced power in a similar manner as anhedral. However, these changes were small unless the positive or negative coning angles were made particularly large.

The Euler solutions obtained provide a comparison of rotor performance mainly in terms of thrust, pitch and induced power, and allow the blade loading distribution, downwash and vortex wake trajectories to be investigated and compared for the various blade tip designs. These comparisons provide a first insight into the effects of tip shape, and in particular, have revealed how anhedral brings about a reduction in the induced power. The performance of selected blades will be assessed in greater detail using Navier-Stokes in Chapter 6.

While the main emphasis for tail rotor design is in hover, it is also necessary to consider the relative merits, or indeed any limitations, of the selected TRB designs in high speed forward flight. For instance, use of anhedral provides a benefit in hover, but may give rise to unwanted pitching moments in high speed flight (unless used to balance sweep, or notch offset effects, Perry et al[236]). The tip shape itself could also signifcantly affect the moments experienced by the blade in a time varying aerodynamic environment. A modern tail rotor may also employ a cambered aerofoil to provide high lift at the hover tip Mach number, and this camber may lead to strong 1 and 2 per rev variations in pitching moment, or control force, in forward flight, Cook.[79] It would be useful to know at an early stage in the design process if the use of an advanced tail rotor tip shape would exacerbate, or have the potential to alleviate, these effects. A series of unsteady forward flight simulations for selected tip designs were therefore undertaken to identify any potential constraints on the down-selected tip shapes, and are described later in this chapter.

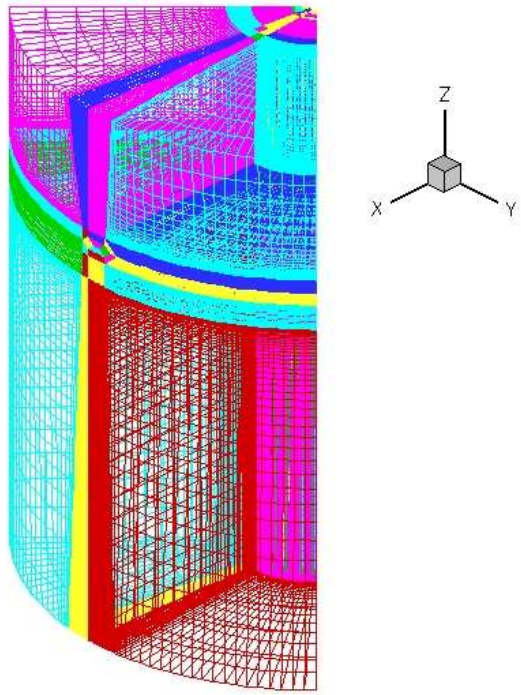

Figure 180: Periodic Domain Segment used for Euler Hover Computations for 4 bladed Tail Rotor

5.1 Comparison of Tip Shapes in Hover

The Euler option of the HMB 1.4 solver has been applied to obtain a first comparison of the performance and flow field of the various TRB designs of Chapter 4, all of which use a NACA0012 aerofoil and zero twist. In all, eight different tip shapes have been evaluated in this section of the thesis, including the rectangular, square-cut datum blade, TRB-000. The blades were all defined with a realistic root cut-out with the first full aerofoil at 33.33%R, together with a tapered portion extending inboard which maintains the sharp trailing edge and resulted in a 0.5c aerofoil of 24% thickness-chord ratio at the root cut-off, or notional blade-attachment, radius of 29.17%R. In all cases, the radius was defined to the most outboard point of the blade and was held constant, giving a radius/chord ratio of 6.402439, compatible with the datum blade of WHL model tail rotor.

As described in Chapter 4, the surface geometry of all the blades, TRB-000 to TRB-007, was defined in the Rhino solid modelling package and scaled to unit chord before being imported into ANSYS ICEM-Hexa (v10) grid generator via an IGES file. The computational domain, illustrated in Figure 180, was 4R in radius, and extended 2R above and 6R below the rotor, and used a so-called 'Froude' boundary condition as previously described in Chapter 2.

A cylindrical hub of 0.660c radius (.1031R) was used in all cases [11]. The first cell spacing normal to the blade surface was set at .001c and the block boundaries in this initial work were set at +/-0.84c above and below the blades with a further boundary at -2.52c to help control the cell size variation below the rotor for better wake capture. The support curves for the multi-block mesh are illustrated in Figure 181.

While it was desired to retain a similar mesh spacing around all the blades, it was found necessary to vary the blocking to accommodate the different tip shapes. Two major blocking strategies were employed, and in

[11] Various cyclindrical and spherical hub configurations were explored in preliminary Euler hover computations, but were found to make little difference to the overall result. Some concern remains, however, that the flow induced by the root-vortex, which may also be affected by the 'wall' of the hub, may lead to an unrealistically high upwards flow inboard of the root cut-off, whereas in reality this may be diffused by the presence of a physical rotor hub. The hub configuration used here was constrained by the requirements for an Euler solution.

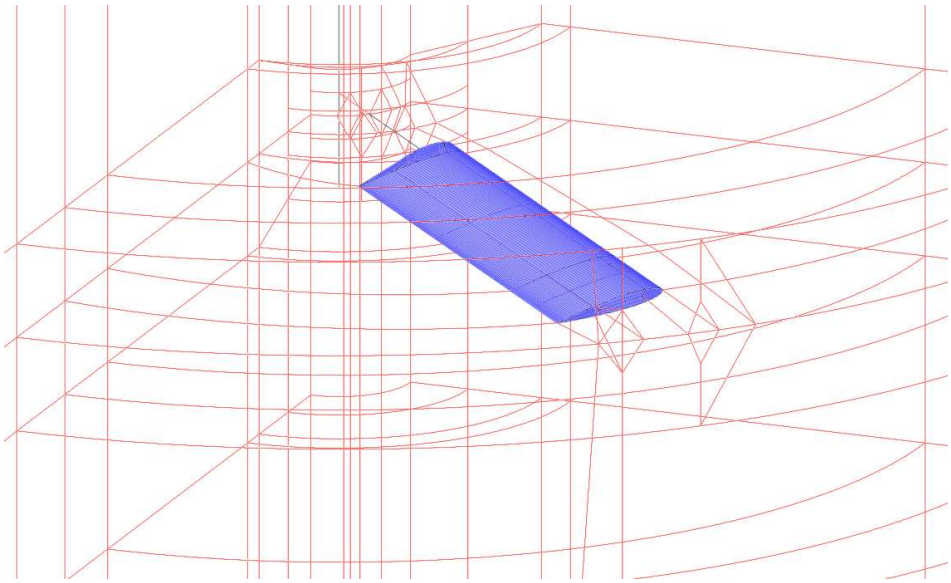

Figure 181: Multi-Block Grid Support Curves Generated in Rhino v3 for Datum Tail Rotor Blade

some cases the number of blocks around the aerofoils were varied to obtain a more even mesh. In the near field, the mesh surrounding the blade therefore used either 2x3x30 or 2x4x23 nodes around the aerofoil. The latter option being used as a means of improving mesh quality to suit the more complex tip shapes, as illustrated in Figure 182. This figure also serves to illustrate the different tip shapes which include two different styles of Küchemann-type tips (TRB-001 and 002) and a 70 degree swept-edge tip (TRB-003). Anhedral is used on a rectangular tip (TRB-004) and also on a Küchemann-type tip (TRB-005). A volume-of-revolution tip cap was also considered (TRB-006) and a parabolic tip (TRB-007) was designed to complete the comparisons.

The comparisons were carried out at a full-scale tip Mach number of 0.60 with zero coning. Each run commenced with about 400 explicit iterations, followed by implicit iterations using a relatively low CFL number which was gradually increased from 1.0 to 5.0 as the run progressed. The histories of the residuals, thrust, and torque, etc, were moniotored during the runs and are illustrated for a typical case in Figures 183 and 184. At low to moderate pitch angles, the residuals converged well, and in most cases the solver was run for about 16,000 iterations. At high pitch angles, the thrust and torque did not readily settle due to pending Euler-breakdown, and these results were therefore ignored when determining the induced power factor. In some early cases for the datum blade pitch angles up to 17 degrees were reached before Euler break-down of the flow occurred, however, time did not permit such a wide range of pitch angles to be explored for every tipshape.

The majority of the TRB cases used in the comparisons were therefore run at low to moderate pitch angles, where numerical diffusion effects are small, and well converged solutions were obtained, allowing the thrust-pitch curve to be established and the induced power factor to be determined in a consistent manner. Figure 185 shows that residuals of about 10^{-5} were achieved for most configurations for pitch angles below about 10 degrees.

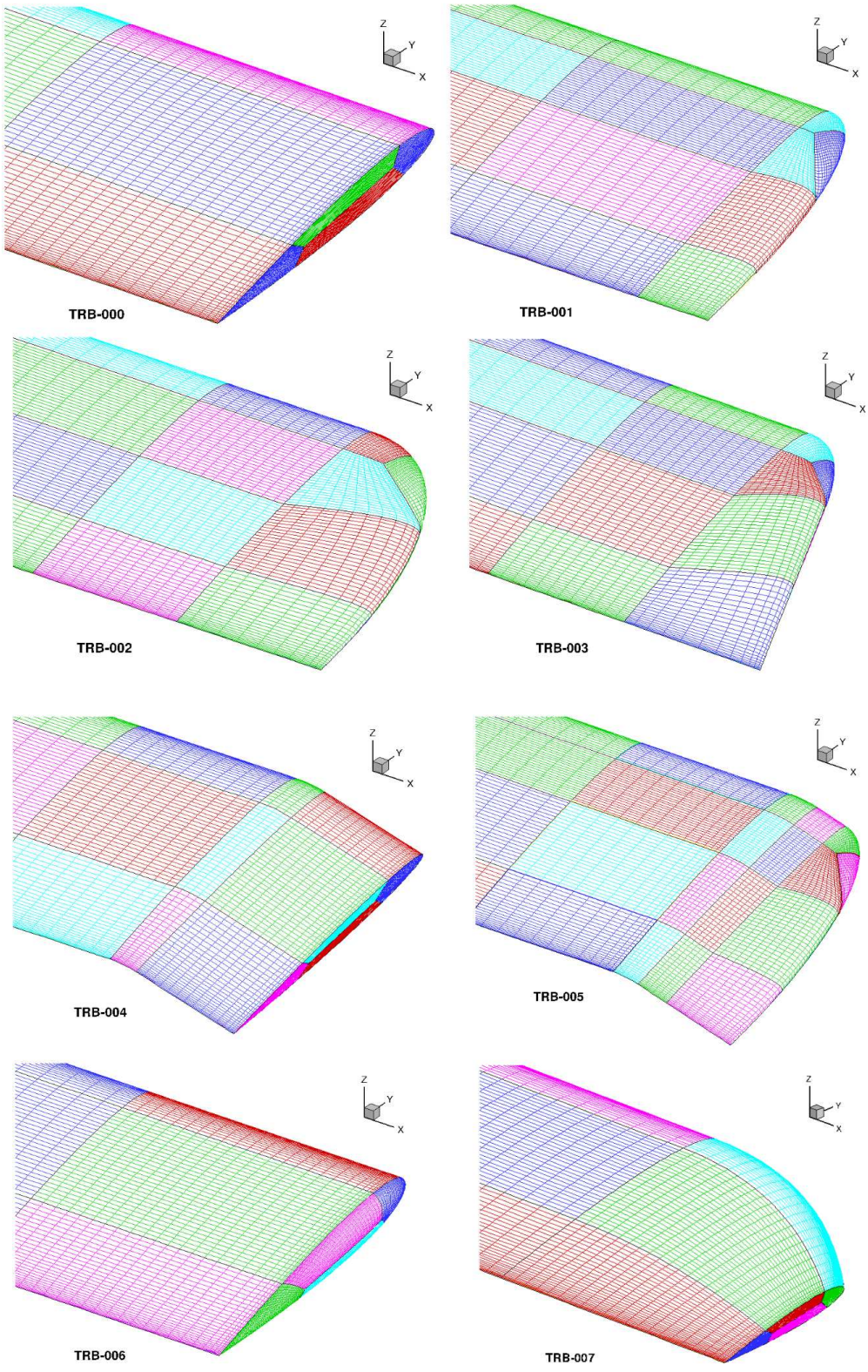

Figure 182: Surface Meshes in the Tip Region for all 8 Tail Rotor Blades, TRB's 000-007. The Blocking was Varied as Necessary to Accommodate the Tip Shape, whilst Retaining a Similar Mesh Spacing.

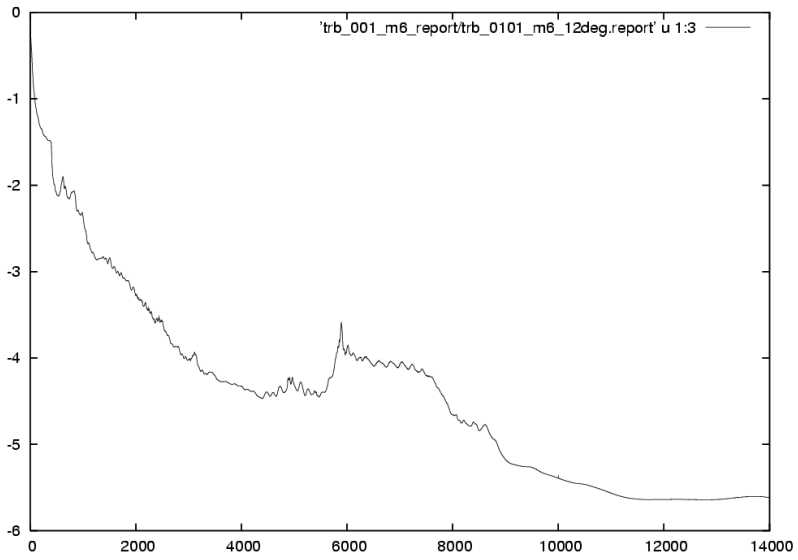

Figure 183: Typical Convergence History of Residuals for Euler Hover Computations for TRB-001 at 12 degrees Pitch and Tip Mach Number of 0.60

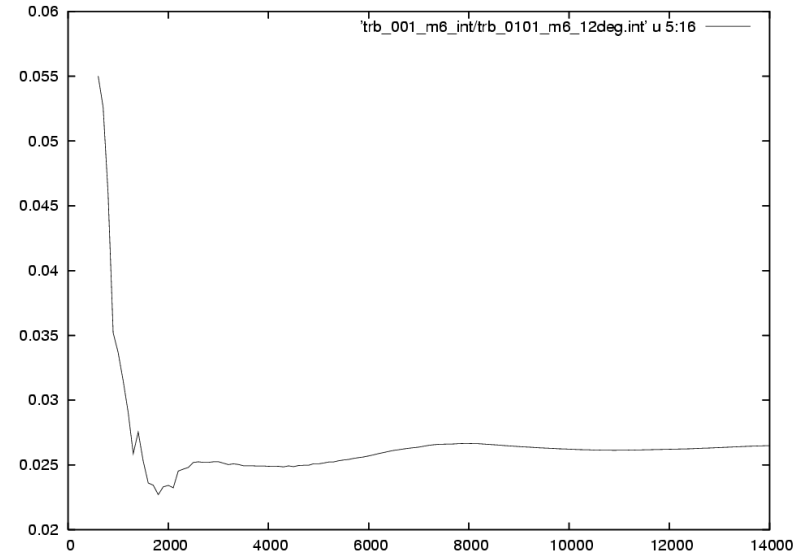

Figure 184: Typical Convergence History of Thrust Coefficient for Euler Hover Computations for TRB-001 at 12 degrees Pitch and Tip Mach Number of 0.60

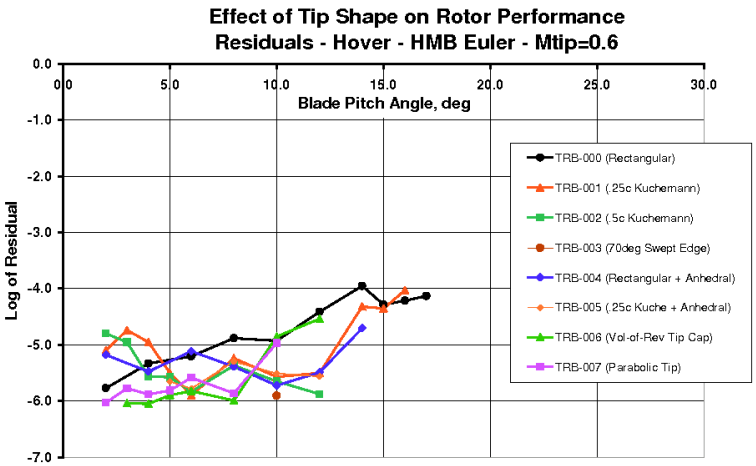

Figure 185: Trend of Final Euler Hover Solution Residuals with Pitch Angle for Several Tip Configurations at Tip Mach Number of 0.60

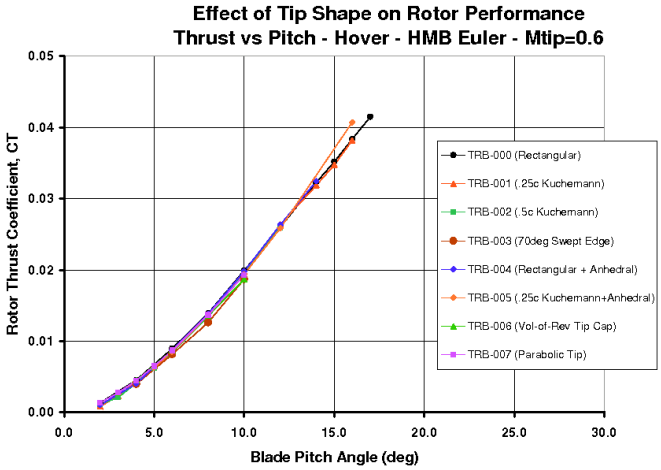

Figure 186: Comparison of Thrust-Pitch Curve for Tail Rotor Blades with Various Tip Shapes from Euler CFD Predictions in Hover at a Tip Mach No of 0.6

5.1.1 Thrust and Induced Power Factor

The predicted thrust-pitch curves for several tip configurations are shown in Figure 186. The results are surprisingly close, perhaps due to the lack of viscous effects for the different configurations.

A relatively high thrust-pitch gradient was found for TRB-000 (datum rectangular blade), and also for TRB-004 (rectangular, anhedral blade), despite the possibility of anhedral off-loading. These tips maintain the maximum chord in the tip region. TRB-001 (.25c wide, Küchemann) also exhibits a similarly steep thrust pitch characteristic, as does TRB-005 (.25c wide, Küchemann with anhedral), since the tip shape has little impact on the effective lifting area of the blade. At very high pitch, the thrust was sometimes difficult to determine, leading to some spread in the results, and perhaps an artificially high point for TRB-005 at 16 degrees (well beyond the region of interest for induced power and possibly near Euler breakdown). However, as the tip shapes of TRB-002 (.5c wide, Küchemann), and TRB-003 (70deg Swept Edge) progressively reduce the area in the tip region, the thrust for a given pitch is reduced, and TRB-003 has the lowest lift-curve slope for the computed pitch angles below 10 degrees, perhaps due to its slender-delta like behaviour. The rectangular, hemispherical tip, TRB-006, was expected to have a similar thrust pitch gradient to the datum blade, and this was the case for low pitch angles, but the 8 and 10 degree results suggest the gradient reduces, perhaps due to numerical effects (despite efforts to improve the grid). The parabolic tip, TRB-007, also has a slightly low thrust-pitch gradient, probably due to the reduction of area in the tip region, and on this basis may have limited application for tail rotors, since the surface pressure results (see later) also indicate high suction peaks in the tip region which could lead to premature separation and a further loss in thrust at stall.

The thrust-torque curve of Figure 187 shows that some of the tip shapes are predicted to have a beneficial effect on the rotor performance compared to the datum blade while others show little or no improvement. For reference, a simple momentum-based estimation of the induced power was also included in this figure, using an induced power factor of 1.3. At the higher pitch angles and blade loading conditions, a tendency for power divergence is observed, mainly due to flow separation which may occur as a consequence of increasing adverse pressure gradients near the tip, as exhibited here by growing pressure losses which arise from the Euler solution in these extreme cases.

In order to obtain a comparison of the induced power for each tip design, CQ has been plotted against $CT^{1.5}$ in Figure 188, as would normally be done to linearise the data if analysing model rotor tests, or full-scale

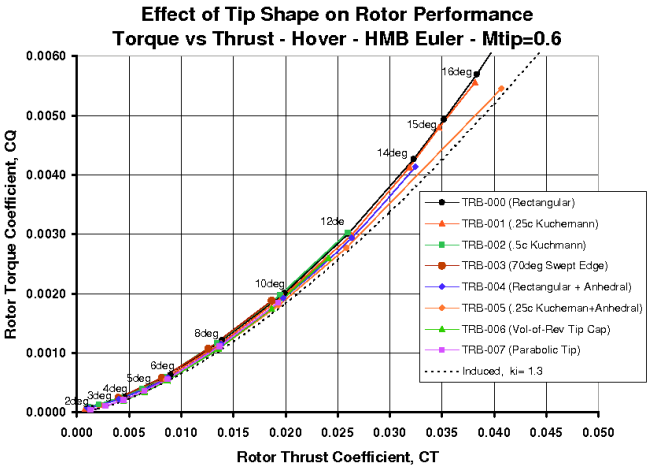

Figure 187: Comparison of Torque-Thrust Curve for Tail Rotor Blades with Various Tip Shapes from Euler CFD Predictions in Hover at a Tip Mach No of 0.6

measurements, according to equation 28. This process allows the induced power factor, k_i to be determined from the slope of the fitted line. The technique of curve fitting used here has been further developed from earlier work at WHL, as described in the Vane Tip model rotor hover tests reported by Brocklehurst and Pike.[59] Instead of approximately fitting a straight line to the linearised data until the growth of profile power looked sensible, this process has now been improved by including a quadratic term in what was previously a linear best fit. For the Euler results the power predictions will comprise mainly induced power, and what may be thought of as residual 'profile' power losses only arise due to numerical diffusion. These effects are expected to be small, although like the actual profile power these numerical (pressure) losses will tend to increase with pitch when the pitch angle becomes moderately high, and may diverge rapidly when the Euler solution for the flow eventually breaks down.

To precisely determine the induced power factor, k_i, for each tip shape, the CQ-$CT^{1.5}$ data were individually fitted with a second order polynomial, rather than attempting a simple linear fit which, as mentioned above involves an amount of judgement to fit the available data points. This approach has been found to yield a more consistent result for the induced power factor, which is then given by the coefficient of the linear term (and is effectively the minimum slope at zero thrust). The quadratic term in equation 29 represents the non-linear growth of the induced power factor with thrust and might be expected to be relatively small, as was found to be the case here, and the constant term, or intercept, gives the residual 'profile' power at zero-thrust, for blades with zero-twist. Note that if the blades were twisted, as was the case for the twisted model tail rotor in chapter 3, the curve fit should start from the zero-thrust condition where there is no induced power. The induced power factor may then be different for positive or negative pitch.

Since the torque can be written as:

$$CQ = (k_i/2).CT^{1.5} + s.CD/4 \tag{28}$$

where the induced power factor, ki, and the overall blade drag coefficent, CD, may also be functions of CT. For the curve fit:

$$CQ = A.(CT^{1.5})^2 + B.CT^{1.5} + C \tag{29}$$

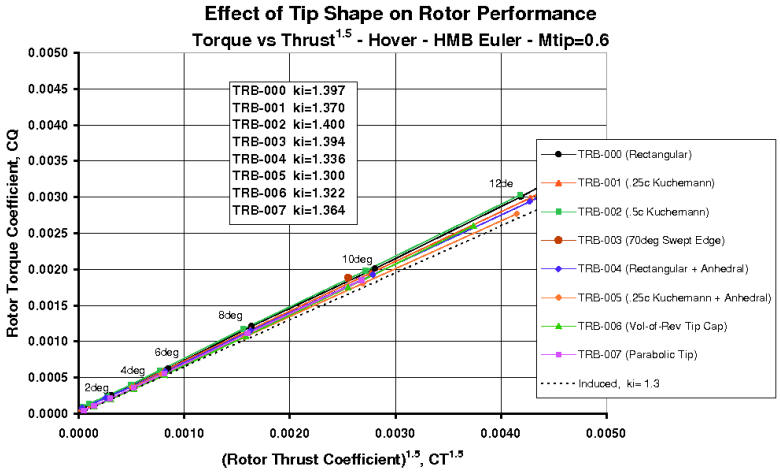

Figure 188: Comparison of Torque-Thrust$^{1.5}$ Curve for Tail Rotor Blades with Various Tip Shapes from Euler CFD Predictions in Hover at a Tip Mach No of 0.6

hence, the induced power factor (at zero thrust), k_i, is found from the slope, B:

$$k_i = 2 \text{ x } B \tag{30}$$

In order to avoid any power divergence due to numerical effects from the Euler solutions at high incidence, only results for pitch angles below 12 degrees were fitted. This choice was later verified by plotting the residual power due to Euler (pressure) losses which manifests itself as a small amount of profile power. As with the model rotor measurements, several data points at low thrust conditions are necessary to establish a good quality curve-fit. For a model or full-scale test, it is notoriously difficult to obtain accurate thrust and torque data at very low thrust, due to the difficulty of measuring small values at the same time as catering for the maximum thrust and torque levels that are also required to be measured, and many repeat points are required to minimise scatter. While the CFD results settled well at most low to moderate pitch angles, at very low pitch, some cases were initially difficult to settle, possibly due to the close proximity of the tip vortex from the preceding blade. This problem was overcome by use of additional iterations which also allowed time for the wake to settle and propogate down to the 'Froude' outlet. Care was also necessary at the higher pitch angles of 10 and 12 degrees to ensure that a well converged result was obtained, and indeed such high angles could probably not have been attained from an Euler solution for a more lightly loaded main rotor. A small amount of twist may have helped the tail rotor solutions settle better at the higher pitch angles.

The results obtained suggest that there is little non-linearity in the induced power, which is perhaps surprising, considering the complexities of the wake. In fact, it was found that the induced power factors obtained from the Euler hover solutions were independent of thrust, and vary according to the tip configuration. The results of extracting the induced power factor from the results of the Euler computations for all the TRB designs are presented in the bar-chart in Figure 189. The induced power factors found for each of the tipshapes, together with the coefficients obtained from the curve fitting, are also presented in tabular form in Table 5.

It was found that anhedral has a significant impact on the induced power factor, and gives a benefit of about 4 to 5%. A further benefit of about 2 to 2.5% arises from the use of the narrower (0.25c wide) Küchemann tip shape of TRB-001. The results for the anhedral, .25c wide, Küchemann tip shape, TRB-005, suggests that these

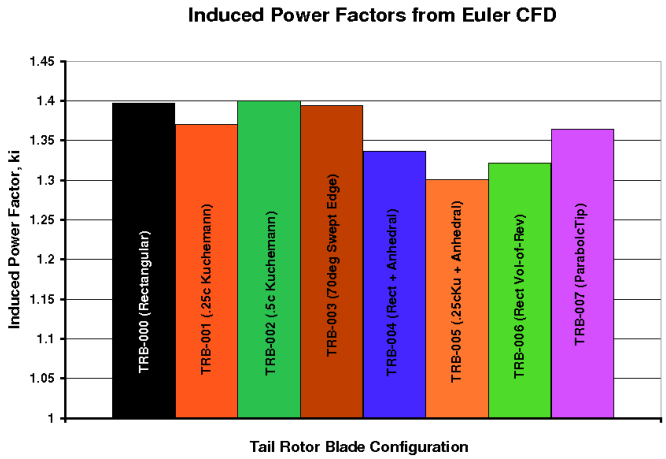

Figure 189: Comparison of the Induced Power Factor as Determined from the Euler Computations for the Tail Rotor Blade designs in Hover at a Tip Mach No of 0.6.

	A	B	C	ki	CDe
TRB-000	1.660176	0.698463	0.0000443	1.397	0.00089
TRB-001	0.682780	0.684946	0.0000447	1.370	0.00090
TRB-002	1.981565	0.700005	0.0000655	1.400	0.00132
TRB-003	8.108728	0.697167	0.0000669	1.394	0.00135
TRB-004	1.973900	0.668000	0.0000500	1.336	0.00101
TRB-005	1.809266	0.650123	0.0000383	1.300	0.00077
TRB-006	9.456553	0.661001	0.0000001	1.322	0.00002
TRB-007	2.171519	0.682310	0.0000007	1.364	0.00014

Table 5: Results of Quadratic Curve Fit to Determine the Induced Power Factor

benefits can be combined to give potential for an overall improvement in the induced power factor of about 7%. It is also clear that two of the tip shapes, TRB-002 (0.5c wide Küchemann) and TRB-003 (70 degree swept edge) exhibited relatively large induced power factors, similar in magnitude to the datum, rectangular blade. The residual profile drag coefficients are also relatively high for these tip shapes. By comparison, the results for TRB-006 appear surprisingly low, compared to the datum blade. In this case, refining the tip by employing a volume-of-revolution tip cap appears to have made a significant difference to the performance (in the absence of viscous effects). As expected, the induced power factor for the parabolic tipped blade, TRB-007, is lower than that of the datum blade, but its relative value is, perhaps, somewhat disappointing. In the next two sub-sections of this Chapter the CFD solutions will be further examined to reveal the underlying aerodynamic causes for these performance differences, first by comparing loading distributions and later by examining the wake, prior to selecting tip shapes for further study.

Having determined the induced power factor as described above, the residual power losses can now be separated out in terms of an equivalent profile drag coefficient, Figure 190. Since these losses result from an Euler computation, the equivalent profile drag represents only the pressure-losses which arise through numerical effects. As expected, the residual profile losses are small, and amount to only about 1/10 of the drag of a typical aerofoil. Using this approach (with the induced power factor based on the linear term of the curve fit), the trend of profile drag is fairly flat at low thrust and then gradually increases with pitch, for pitch angles below about 12 degrees. Whilst the split between the induced power and residual losses is somewhat arbitary, this

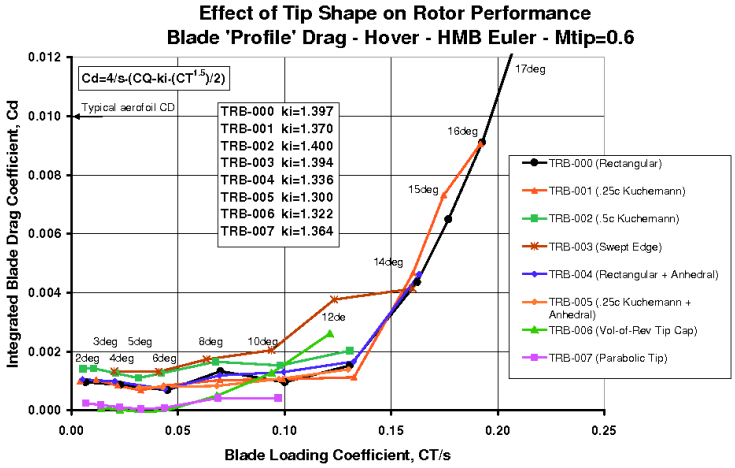

Figure 190: Equivalent Profile Drag versus Thrust Coefficient for Tail Rotor Blades with Various Tip Shapes from Euler CFD Predictions in Hover at a Tip Mach No of 0.6

shallow slope gives confidence that the logic used to deduce the induced power factor was sound, and again confirms that the induced power factor is insensitve to thrust variation. Clearly the Euler solutions should not be considered as valid above about 12 degrees, and the residual power grows in a similar manner to the profile power divergence which occurs in reality, but of course the divergence depicted here is artificial in that it arises solely from numerical effects as the Euler method is pushed to its limit. Therefore no attempt has been made to home-in on the point of power divergence since such details are better evaluated using Navier-Stokes.

However, it is interesting to note that the results in Figure 190 fall into three distinct groups. The equivalent profile drag values for most of the blade designs (TRB-000, 001, 004, 005) cluster together at about CDe=.001. The drag values for the wider tips with more higly swept outer edges (TRB-002 and 003), which also did not perform so well in terms of induced power, have a higher equivalent profile drag (.0015-.002). The 70 degree swept tip (TRB-003) showed the highest (Euler) pressure drag which grew most rapidly, probably due to aft-facing vortex-induced suction over the wider tip region. At low pitch angles, very low residual drag values are found for both the volume-of-revolution tip-cap design (TRB-006), and the parablic tip (TRB-007). The latter result is probably a consequence of reduced area in the tip region for TRB-007, while TRB-006 may benefit from a reduction in edge separation losses. However, as the blade loading increases, the line through the results for TRB-006 curves upwards and tends to diverge more quickly than for the datum blade, suggesting that this initial benefit may not persist. For TRB-007, there is one further low-point at 10 degrees of pitch, but the surface pressures (see following sub-section) suggest that the tip may become highly loaded and this may then limit the thrust and cause the profile power to grow prematurely.

While much can be deduced from these Euler results, it must be remembered that the observed trends are not from Navier-Stokes results and so may not be a good indication of the actual performance. The results may also contain some small errors due to slight differences in mesh density and the quality of the grids for the various tips which are difficult to quantify, and/or eliminate. Nonetheless, it is encouraging that the numerical losses in the Euler solutions have been found to be small and the above trends seem sensible.

For the tail rotor, the magnitude of the induced power factor is an important consideration, but tends to be over-shadowed by the divergence of profile power due to stall since the tail rotor is often operated close to its maximum thrust limit during yaw manoeuvres, particularly when hovering in hot and high conditions. Whilst it was instructive to think in terms of a residual profile power arising from numerical diffusion in the Euler solution, the profile power growth for a given blade design requires a Navier-Stokes simulation, and simulations

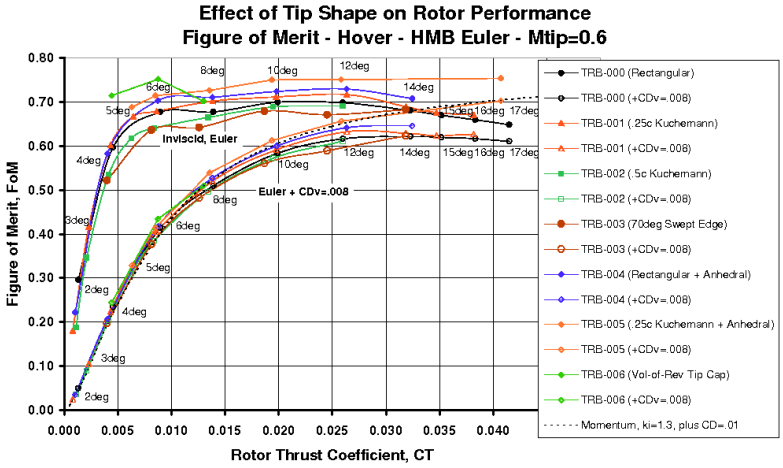

Figure 191: Figure of Merit versus Thrust Coefficient for Tail Rotor Blades with Various Tip Shapes from Euler CFD Predictions in Hover at a Tip Mach No of 0.6. Realistic results obtained by including an allowance for skin friction drag

of this nature will be carried out later in Chapter 7. Dividing the power into induced and profile components, although sometimes fraught with dificulties, allows each component to be dealt with separately during the aerodynamic design. However, another parameter which gives a sensitve measure of rotor performance is the hover Figure of Merit (FoM). This parameter offers an overall comparison between different rotor designs, and results were obtained for Figure of Merit for all the tail rotor designs considered here.

As expected, the results obtained for Figure of Merit directly from the Euler solutions are high because of the omission of viscous effects. At very low thrust, the Figure of Merit is relatively poor due to the dominance of the (residual) profile drag, and then asymptotes towards a notionally constant value, while at high thrust levels the curve should roll-over as the profile power increases due growing numerical losses (similar to how it would in reality due to stall). If the power losses were precisely zero, the Figure of Merit would be equal to the inverse of the induced power factor (which here would range from 0.715 to 0.769).

For these Euler tail rotor cases, only a relatively small residual drag is present and so, as discussed above, the Figure of Merit is unrealistically high. Ahead of obtaining a Navier-Stokes performance prediction, it is possible to approximately correct the FoM values to bring them closer to reality by adding a drag increment. In Figure 191 an arbitrary increment (of Cd=0.008) has been added to the Euler 'profile' drag, to account for skin friction and other pressure losses due to viscous (boundary layer thickness) effects (no attempt was made to introduce a profile drag coefficient that diverged at high thrust conditions near stall). Using this simple Cd correction, more realistic values for the peak Figure of Merit of the example tail rotors may lie between about 0.62 and 0.68, and the corresponding likely benefits due to the 20 degree anhedral tip and the (0.25c) Küchemann tip shape are estimated to be about 4% and 2% respectively.

The relative benefits of the various tail rotor tip shapes can also be illustrated by simply comparing the thrust/power ratio, or CT/CQe, as plotted in Figure 192. Here the Euler results have been used directly, and therefore the values indicated on the y-axis will be higher than in reality, and represent primarily the induced power (more realistic values are presented from Navier-Stokes computations in Chapter 7). The relative benefits of the various tip designs should be compared at a realistic loading for a hovering (and manoeuvring) tail rotor, say in the region of CT=0.02. From the graph, and also from the above Table, the ranking on this basis is the same as that for FoM and k_i.

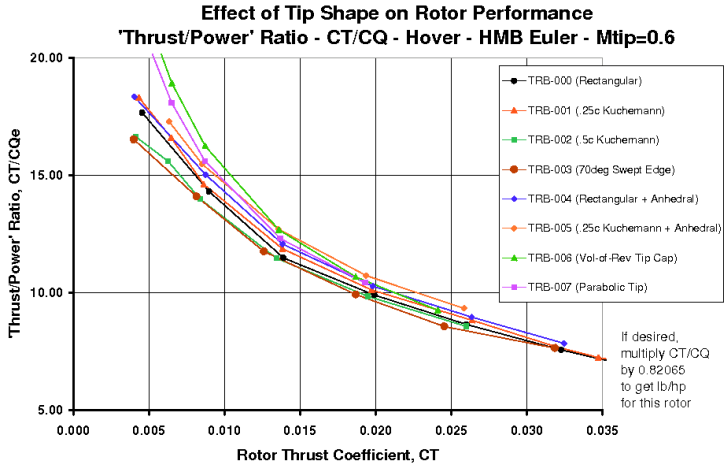

Figure 192: Non-Dimensional Thrust-Torque Ratio for Tail Rotor Blades with Various Tip Shapes from Euler CFD Predictions in Hover at a Tip Mach No of 0.6

From the Euler results, it was found that the ranking (from best to worst) is TRB-005, 004, 001, 006, 007, 000, 002, and 003. On average, the CT/CQ ratio for the TRB-005 (Küchemann, anhedral) tip is about 4% better than the datum. The TRB-001 (1/4c Küchemann) tip shows about 2% improvement, while TRB-002 shows a reduction of about 1%, similar to the differences seen in the Figure of Merit.

It is noted that the two anhedral tips both perform well in terms of induced power, with the combined anhedral and 1/4c Küchemann, TRB-005, doing particularly well, consistent with the idea that the 1/4c Küchemann, TRB-001, is superior to the datum, rectangular blade, TRB-000. Unfortunately, extending the Küchemann tip further inboard did not appear to increase the advantage of using this type of tip - perhaps because the vortex-roll-up extends over too great a radial distance near the tip - so it is concluded that the tip should have just enough rounding at the leading edge to avoid excessive loading peaks, and the best outer edge for vortex formation is one that is more nearly streamwise, as in TRB-001.

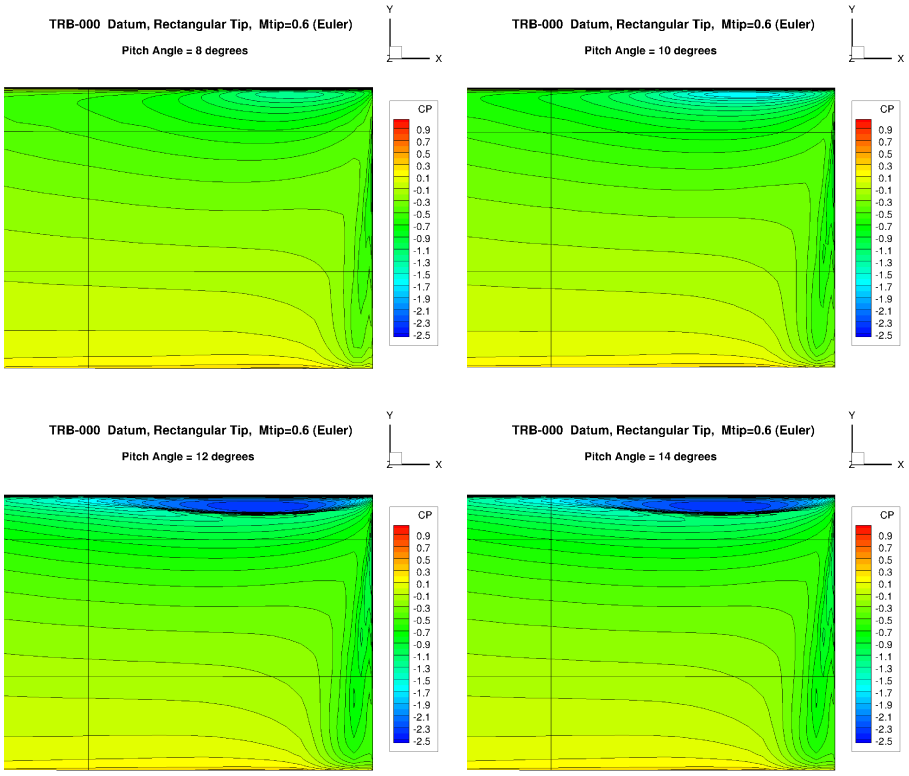

Figure 193: Comparison of Pressure Contours in the Tip Region of the Datum, Rectangular Blade, TRB-000, Over a Range of Pitch Angles at Mtip=0.6 from HMB Euler Predictions in Hover, Showing the Gradual Development of a Strong Suction Peak Near the Leading Edge Corner of the Tip.

5.1.2 Loading Distributions

In the aforegoing sub-section, the integrated loads were used to compare the performance of the various tail rotor blade tip shapes. In the current sub-section, surface pressures from the Euler solutions are examined in more detail to gain a deeper insight into the aerodynamics of the tip shapes, and to further justify the relative ranking of the tips.

Surface pressure contours are shown for the tip region of the datum, rectagular blade, TRB-000, in Figure193. It is clear that as the pitch angle is increased a peak in loading occurs near the leading edge corner of the tip (just inboard of the tip). On a rotor in hover, the natural tendency for isobars to cluster in the forward leading edge corner of a rectangular tip is augmented by the upwash field of the tip vortex from the preceding blade. The development of the suction peak, and the associated adverse pressure gradient just downstream of it, is such that above a pitch angle of about 10 degrees the Euler results reveal a tendency for a shock to form. In reality, this may cause shock-induced separation on a blade with a rectangular tip planform, and could lead to an undesirable rapid growth in profile power. At the tip Mach number of the present computations, this effect is relatively mild, but will become stronger if the tip Mach number is increased. Another notable feature, that may not be apparent from use of a lower order method, is the suction that is present on the outer edge of the tip towards the trailing edge, and which originates from the formation of the tip vortex. As will be discussed again later, these features affect the pitching moment of the blade, although on a rectangular tip the leading edge and tip edge suction regions may counter-balance each other until the stall is reached, at which point the pitching moment will become increasingly nose-down.

Pressure contours on the upper surface of each of the eight blade tip designs are compared in Figure 194 at 10 degrees of pitch. As expected, the blades with a rounded leading edge corner, either in the form of

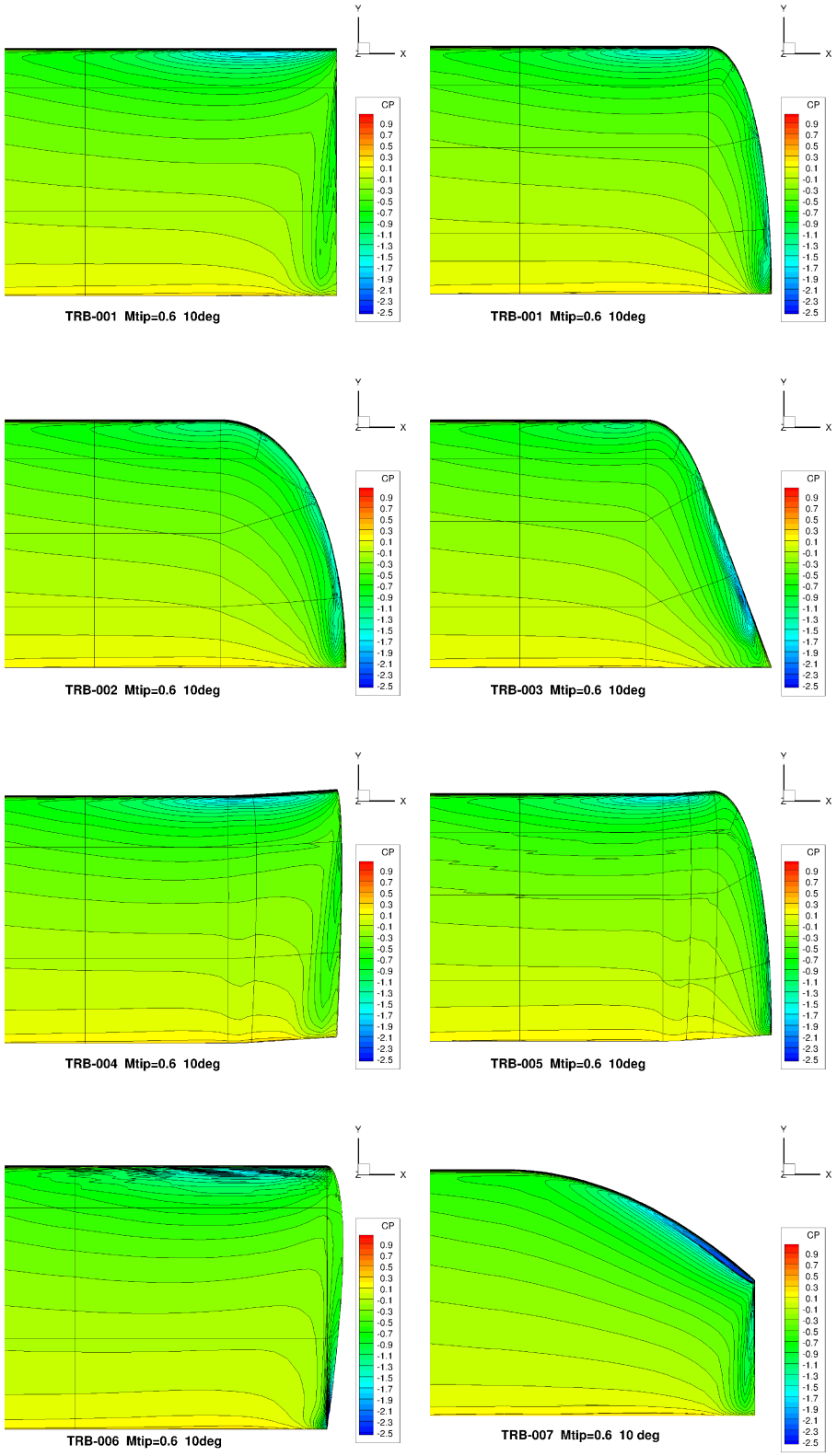

Figure 194: Comparison of Pressure Contours in the Tip Region for the Full Range of Tail Rotor Blades at Mtip=0.6 and 10 degrees Pitch from HMB Euler Predictions in Hover. The Magnitude and Location of the Leading Edge Suction Peak is Strongly Influenced by the Tip Shape.

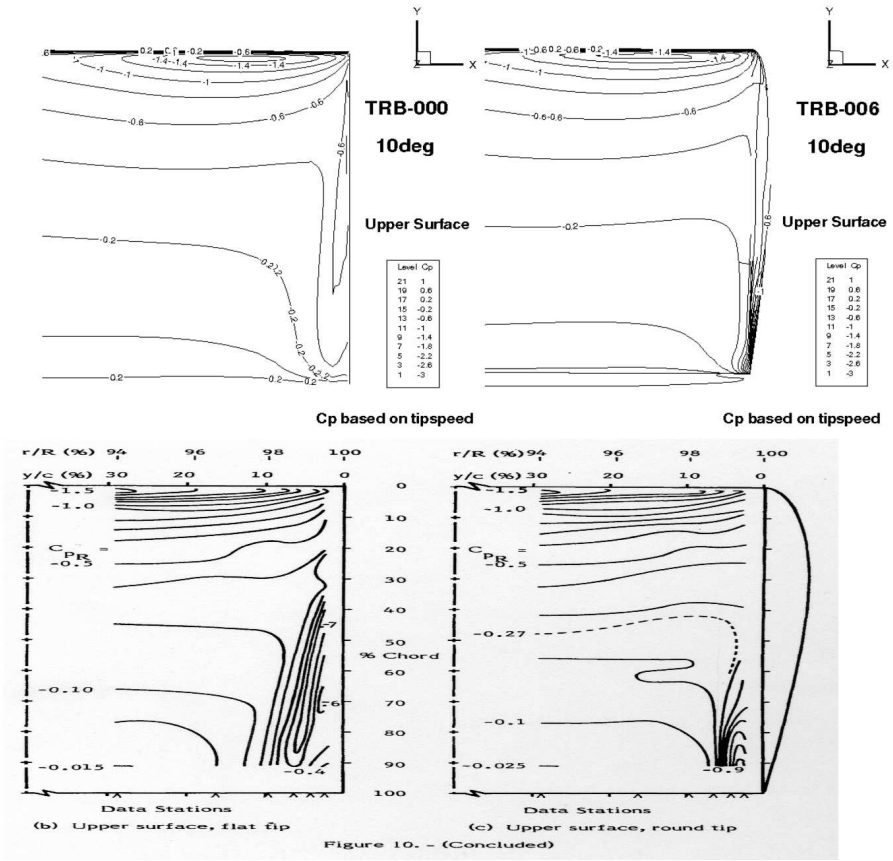

Figure 195: Comparisons of Pressure Distributions on Square-Cut and Volume of Revolution Tips. TRB-000 and TRB-006 CFD Predictions for 4 Blade Tail Rotor at 10 degrees Pitch Compared to Measurements at 11.4 degrees Pitch on a Single Blade Rotor of Similar R/c Ratio from Gray et al[122]

a Küchemann-type tip shape (eg TRB-001,2,5), or the rounded corner of the 70 degrees swept edge blade (TRB-003) reduce the tendency for isobars to bunch at the forward leading edge corner as was evident on the rectangular tip shapes (eg TRB-000 and TRB-004). However, as will be shown in more detail later, the wider tips, TRB-002 and TRB-003, have strong local suctions from the tip vortex which extend over the tip surface, and tend to impose an induced power penalty via an increase in lift-dependent drag. The anhedral tips, TRB-004 and TRB-005, were found to have better performance, and it is just discernible on TRB-004 that the suction peak is perhaps slightly weaker and more distributed than on TRB-000. A similar subtle effect of anhedral is also seen by comparing TRB-001 and TRB-005, and the later tip appears to have relatively smooth surface pressure contours. On TRB-006, the addition of the tip cap apparently makes little difference to the leading edge suction peak and the associated adverse gradients, although the rounded tip edge probably enables the flow to roll-up into the tip vortex more cleanly. The parabolic tip, TRB-007, exhibits a build-up in suction further outboard as the chord width reduces, and a strong shock is seen to form on the outer part of the curved leading edge, despite the sweep. It is likely that shock-induced separation will become a major problem here, particularly at higher angles, whereas at low pitch this potential drag source may not be noticeable, given the small area of the tip.

Further details of the presure contours near the tip of a rectangular blade, and one with a volume-of-revolution tip cap, are given by the comparison shown in Figure 195, where results from the HMB Euler computations for TRB-000 and TRB-006 are compared to the measurements of Gray, et al.[122] The measured data is from tests on a single blade rotor, but there is a strong similarity between the isobar patterns. Unfortunately, time did not permit a one-to-one comparison, but it is clear that, as stated above, the main suction peak is little affected by the addition of a tip cap. However, on close inspection of the computed isobars, there may be some slight improvement in the smoothing of the isobars due to rounding the tip leading edge, and there

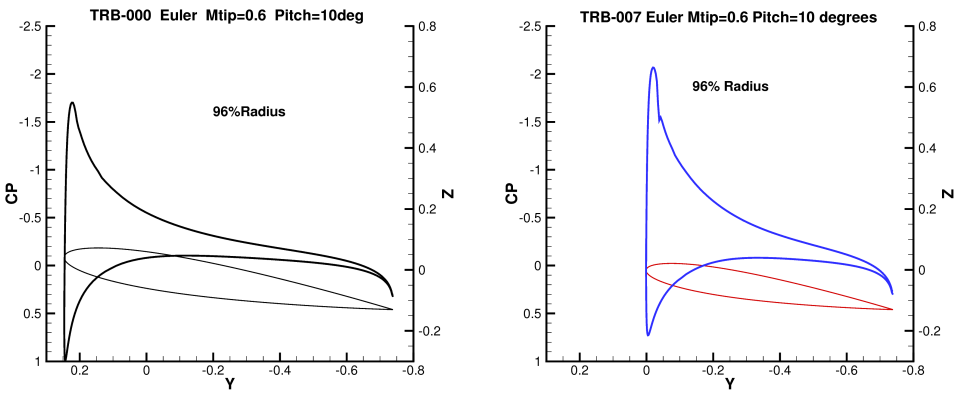

Figure 196: Comparison of Chordwise Pressure Distributions for TRB-000 (Datum, Rectangular Tip) and TRB-007 (Parabolic Tip) at 96%R for 10 degress Pitch Angle, Close to the Location of Peak Loading. The Taper of the Parabolic Tip Generates a Higher Suction Peak and a Shock is Formed, Despite the Sweep. The Strong Adverse Pressure Gradient is Likely to Cause Early Flow Separation In the Tip Region.

is perhaps some evidence to suggest that the slightly elongated tip cap of Gray might further help to alleviate the isobar bunching problem. The suction under the tip vortex shows additional contraction compared to the computed results, perhaps due to the wider tip cap, and also affected by the higher pitch. Clearly the cleaning up of the flow around the tip cap has served well in the past to minimise the drag losses at the tips of several tail rotors, eg on the Wessex and Sea King, as referenced earlier in the literature review in Chapter 2. However, while this type of tip has plenty of thrust potential due to maintaining area outboard, and is to be preferred to the datum blade, there is a likely to be a performance penalty, compared to a more advanced tip shape, due to the high leading edge suction peak and associated adverse gradients.

Further important information can be obtained from the CFD results by plotting the chordwise pressure distribution at chosen radial stations along the blade. This has been done in Figure 196 to compare the suction peaks for the datum, rectangular blade, TRB-000, and the parabolic tip blade, TRB-007, at 96%R. As in the contour plots, the pressure coefficients are based on the rotor tipspeed (and therefore represents the actual loading at the specified radial station), and in most cases a classical inviscid (Euler) pressure recovery is observed at the trailing edge. At 96%R the parabolic tip blade has a smaller chord and carries a higher loading (suction) peak than the datum blade. The large, narrow suction peak gives rise to a shock as the pressure starts to recover, and in a viscous flow field would probably cause separation to occur, perhaps leading to premature stall and a rapid growth in profile power.

Pressure distributions were also taken at several radial stations spanning the width of the 70 degrees swept edge tip, TRB-003, as shown in Figure 197. For this tip, the peak leading edge suction is not as great as for the datum blade, due to the rounding of the leading edge corner, but along the swept edge a large suction region arises due to vortex formation over the outer tip surface. As can be seen from the Figure, this suction is on a rearward facing slope and therefore is deterimental to performance.

Chordwise pressure distributions are compared for the two flat Küchemann-type tips, TRB-001 (0.25c wide), and TRB-002 (0.5c wide) at 10 degrees pitch, in Figure 198. For the narrower Küchemann tip, TRB-001, the leading edge suction peak occurs just inboard of the tip station, near 92-94%R, and as expected is of lower magnitude than that of the datum blade. The loading then falls off as the tip leading edge starts to curve, as shown by the blue line at 96%R, which slices the tip just inboard of the influence of the tip vortex (a slight increase in suction over the trailing edge is visible in the Cp-distribution). In comparison, the Cp-distributions for the wider Küchemann tip, TRB-002, show a further reduction in the leading edge suction peak, and this lower level of suction is maintained at 95 and 96%R. The greater rounding of the leading edge is also apparent in Figure 198. The negative pressures, or suctions, are slightly greater over the area of this tip, than they were for the narrower tip, and consequently this tip has inferior performance due to this greater rearward facing

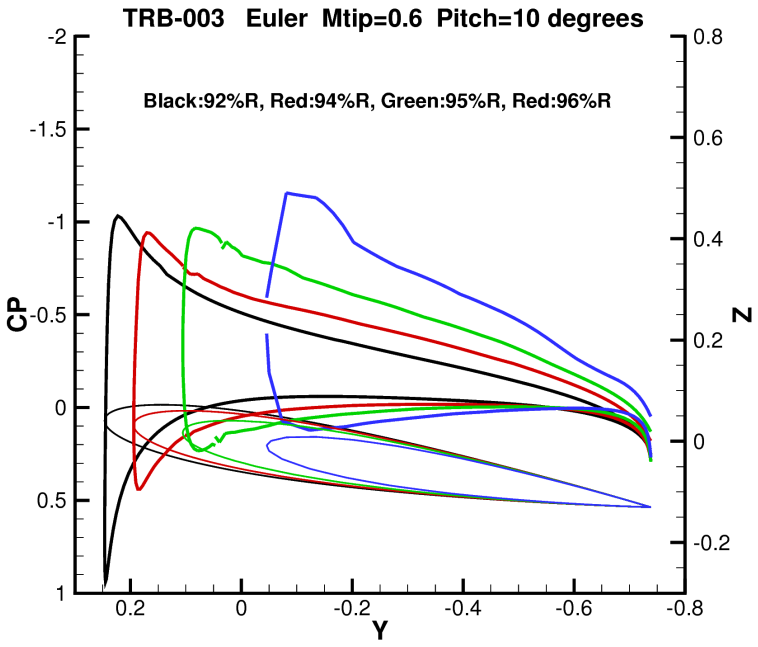

Figure 197: Chordwise Pressure Distribution for the 70 degree Swept-Edge Blade, TRB-003, Showing the Loss in Loading Accompanied by Strong Rearward Suction Giving Rise to High Power Consumption

suction region. Of these two tips, TRB-001 would appear to have a better potential performance for a tail rotor in hover.

Figure 199 shows a similar comparison for the rectangular, anhedral tip, TRB-004, and the Küchemann-type, Anhedral Tip, TRB-005, at a pitch angle of 10 degrees. In this Figure, additional chordwise cross-sections are shown at 97, 98 and 99%R in an attempt to provide a more detailed comparison. For TRB-004, the leading edge suction peak builds to a maximum at about 94%R, similar to the datum blade, and then starts to fall more rapidly towards the tip, due to the anhedral. The effect of the tip vortex elevates the suction toward the trailing edge of the outer tip edge, by a small amount at 98%R, but more significantly at 99%R. The pressure distributions for TRB-005 show how the loading falls off in the tip leading edge corner and at 99%R suction is present due to the tip vortex roll-up along the outer, near-streamwise edge of the tip.

Further insight into the effect of the various tip shapes may be obtained by integration of the chordwise pressures and plotting the resulting loading along the radius of the blade. This has been done for the datum blade, TRB-000, to highlight several fundamental flow features, and for TRB-004 and TRB-005 to show the effect of anhedral.

The pressure distribution on the surface of the blade has been extracted at several radial stations using chordwise slices obtained via Tecplot, although this could also be done by interpolating the data in the HMB '.plt' files. This information was then integrated using a Fortran program to determine the values of Cz, Cy and Cm at each radial station extracted (Appendix G for a listing of 'Rotor-Analyser'). Resolution of these coefficients also provides results in terms of Cn and Cc. For small angles, the axial thrust coefficient, Cz, and the normal force coefficient, Cn, are very similar (and provide an approximation to CL), the inplane force coefficient, Cy, contributes to the torque, while the chordwise coefficient, Cc, comprises mainly forward suction due to the inviscid nature of the Euler solution. However, the pitch angles at which tail rotors operate cannot always be considered as small, and comparisons between CFD results, in body-axes, and more traditional strip theory approaches, which often employ CL and CD in wind axes, can become misleading at high pitch angles. Unfortunately, it is not a simple matter to determine true lift (and drag) coefficients (in wind axes) from the CFD pressure data, since neither the angle of attack, nor the induced inflow angle can be easily extracted

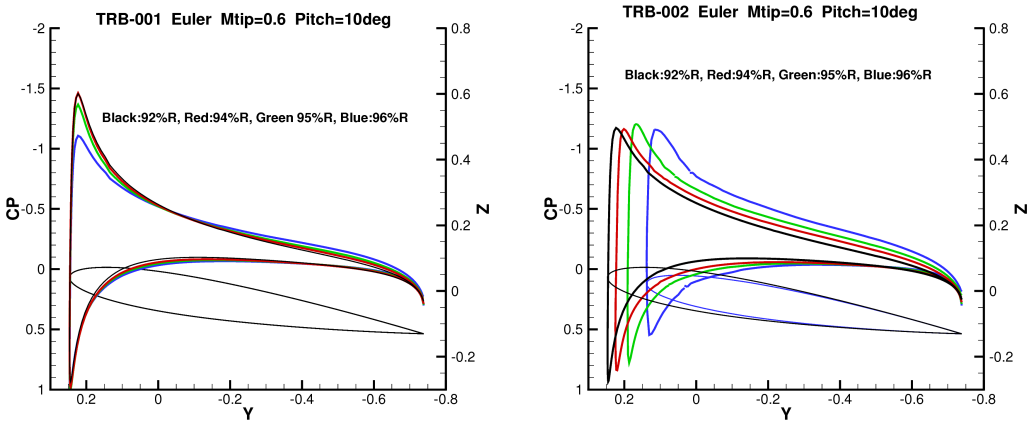

Figure 198: Comparison of Chordwise Pressure Distributions for the Flat Küchemann Tip Blades, TRB-001 (1/4c wide), and TRB-002 (1/2c wide), Showing Increased Rearward Suctions Over the Tip of TRB-002

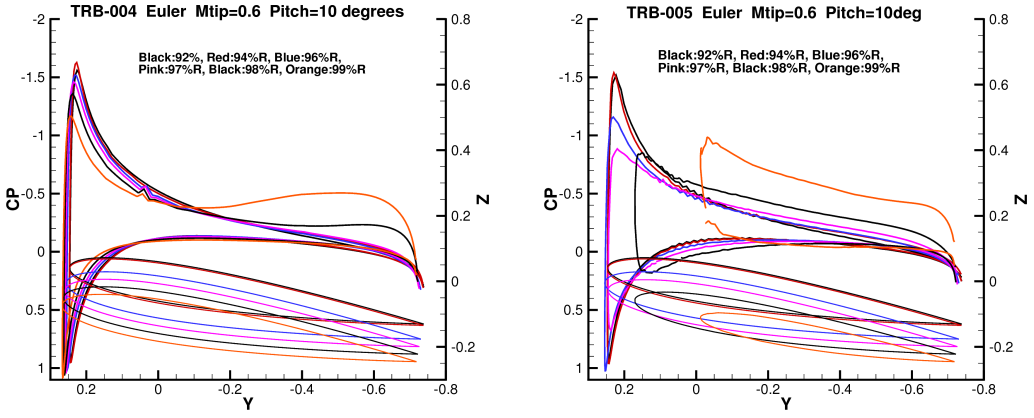

Figure 199: Comparison of Chordwise Pressure Distributions for the Anhedral Blades, TRB-004 (Rectangular) and TRB-005 (Küchemann) Showing a Reduction in Loading Near the Tip Leading Edge Corner of TRB-005 and Effect of Tip Vortex at the Most Outboard Radial Stations.

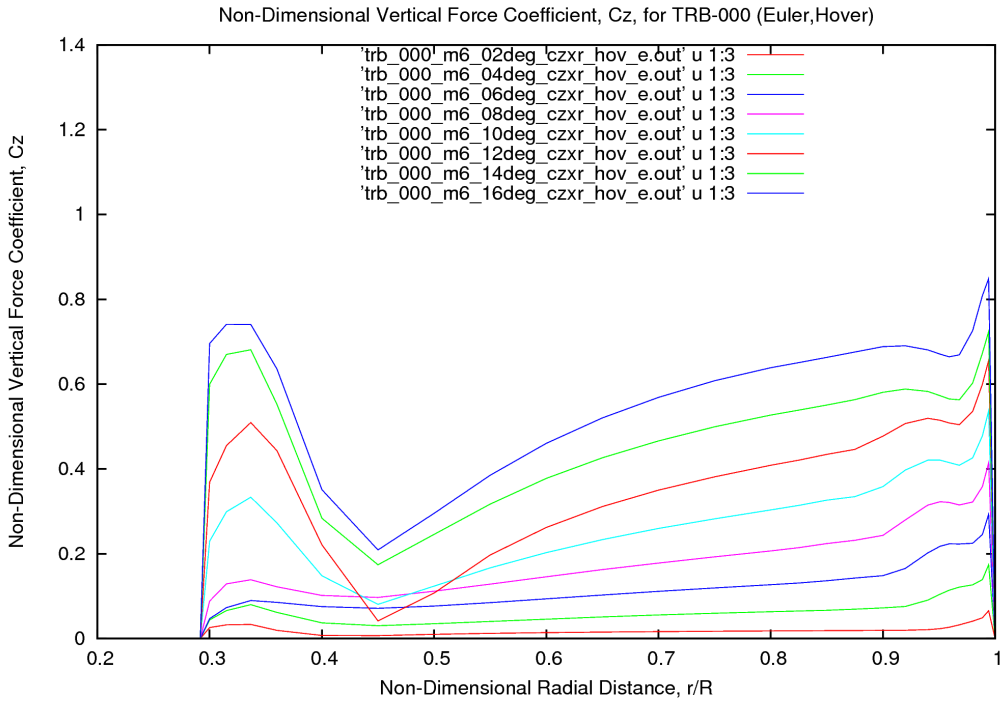

Figure 200: Non-Dimensional Vertical (Thrust) Force Coefficient (Cz) Distribution for TRB-000 from Euler CFD Predictions in Hover at a Tip Mach No of 0.6 over a Pitch Range of 2-16 degrees

from the complex 3D flow field about the tip. It is therefore convenient to compare the loading distributions using Cz (or if desired, Cn, and Cy or Cc), and Cm (and these quantities are also available from lower order methods). While scope exists to 'calibrate' lower order methods by comparison with CFD, as discussed by Beedy,[35] the main aim of the present work is to use the CFD results to gain a better understanding of how the tip design impacts on rotor performance. Extraction of angle of attack and downwash to enable comparison with strip theory is discussed later in Chapter 7.

The non-dimensional sectional loading in terms of the force coefficient in the thrust direction, Cz, for the datum, rectangular blade, TRB-000, is given for a range of pitch angles in Figure 200, while the product of Cz and the radius squared gives a non-dimensional form of the actual blade loading distribution, as shown in Figure 201. It is clear from the Cz results in Figure 200 that the loading towards the inboard end of the blade is strongly influenced by the proximity of the root vortex, although Figure 201 shows this to have only a relatively small impact on the overall blade loading, and hence it does not play a significant role in the thrust produced. Looking towards the outboard end of the blade, the Cz distribution shows the influence of the upwash and downwash field of the tip vortex from the preceding blade and the angle of attack is reduced inboard and increases further outboard. Further towards the tip, the tip shape also affects the loading (as already described), and while the leading edge suction peak starts to fall away, a loading spike is seen at the extreme tip due to the suction generated by the roll-up of the tip vortex on the outer edge of the tip. These influences are then weighted by the tipspeed (or at constant rotational speed, the radius squared), but are still noticeable in the loading. [12]

The induced-flow effects of the root vortex, the tip vortex from the preceding blade, the tip shape effect and tip-vortex loading are also visible in the sectional pitching moment characteristics shown in Figure 202 and in Figure 203 for the pitching moment loads. In the latter Figure, note the minor effects near the root, but the much stronger nose up moment caused by the wake vortices (together with an effect of Mach number which increases the loading towards the leading edge, and so augments the nose up pitching moment), which in this case is balanced by the strong nose-down effect of the tip vortex over the outer trailing edge surface

[12] In traditional lifting line rotor models, the suction generated by the tip vortex over the outer edge of the tip may be missed entirely, or indeed, in the past the expectation might have been that the loading would fall-off in a more gradual manner.

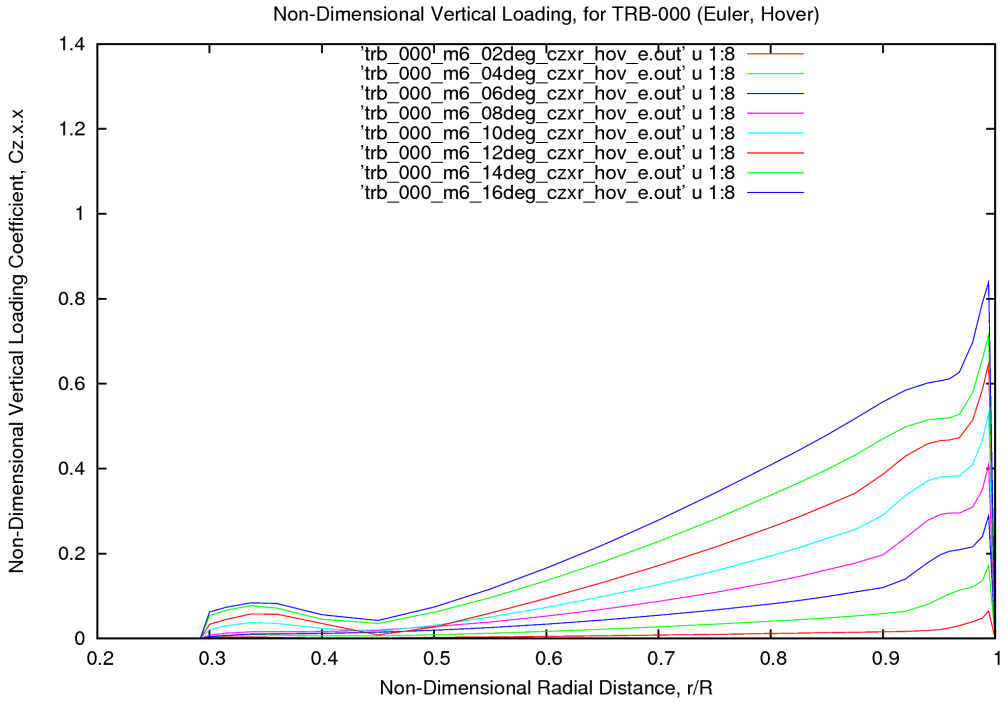

Figure 201: Non-Dimensional Loading ($Cz.x^2$) Distribution for TRB-000 from Euler CFD Predictions in Hover at a Tip Mach No of 0.6 over a Pitch Range of 2-16 degrees

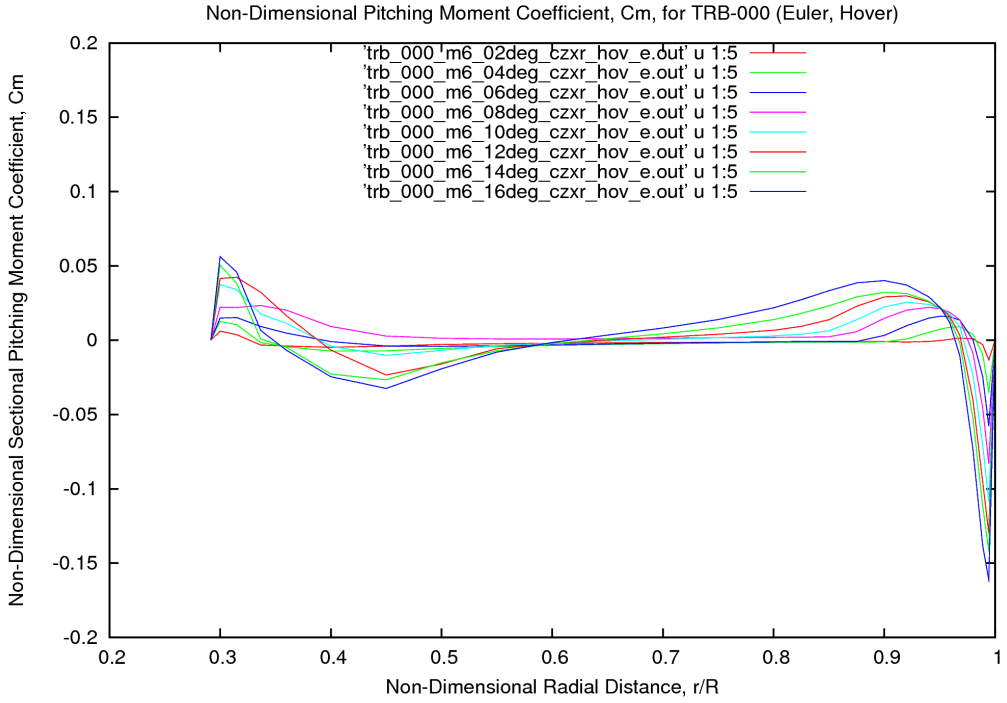

Figure 202: Non-Dimensional Pitching Moment Coefficient (Cm) Distribution for TRB-000 from Euler CFD Predictions in Hover at a Tip Mach No of 0.6 over a Pitch Range of 2-16 degrees

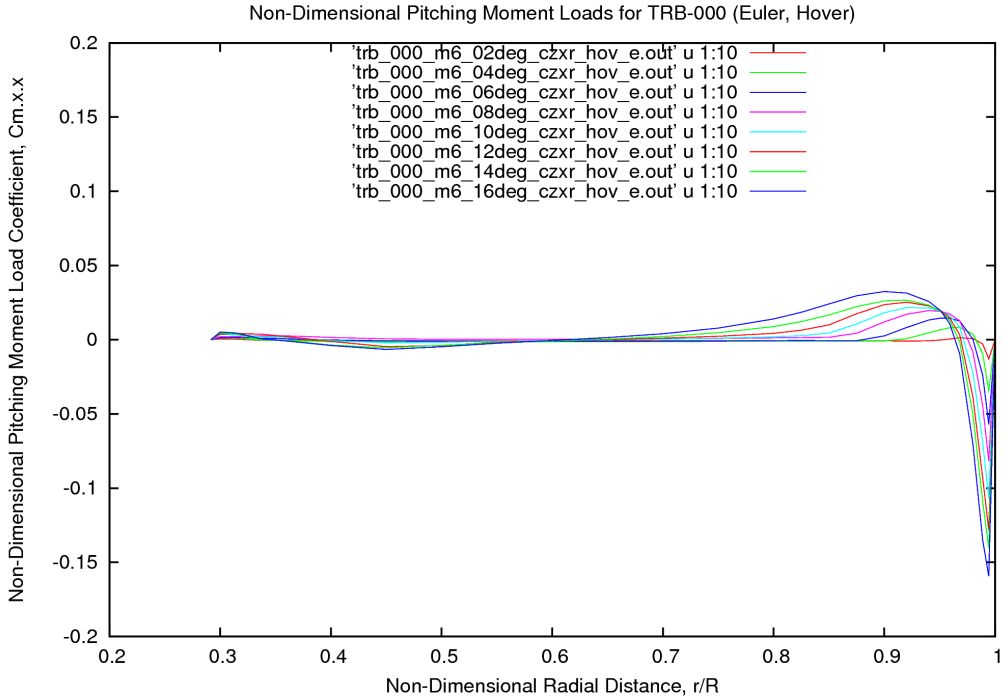

Figure 203: Non-Dimensional Moment Loading ($Cm.x^2$) Distribution for TRB-000 from Euler CFD Predictions in Hover at a Tip Mach No of 0.6 over a Pitch Range of 2-16 degrees

of the tip. On the rectangular tip of TRB-000, the (inviscid, Euler) overall (root) pitching moment is small, but gradually becomes more nose up as incidence increases below stall. In a viscous flow, the moment would become strongly nose down when the stall is reached due to collapse of the leading edge suction and large aft suctions appearing due to separation (see Chapter 6 for comparison of integrated blade-root pitching moments for the datum blade and down-selected tip shapes).

The effect of anhedral on the loading distributions is shown in Figures 204 to 207 for the flat Küchemann-type tip, TRB-001, and the anhedral, Küchemann-type tip, TRB-005. Both these tips are 0.25 chord wide in the radial direction, and therefore have a nicely rounded leading edge with the tip edge straightening out towards the trailing edge. From the loading distributions (presented here at the given pitch angle of 10degrees), it is clear that anhedral has the effect of off-loading the tip and through changes in the induced flow (arising from a re-positioning of the vortices in the wake) loads up the blade in the mid-outer region (60-85%R) by a small amount. Minor differences are also visible near the root-end of the blade, but these are not significant in the overall loading, Figure 205, although they could be a consquence of small changes in the wake structure. Interestingly, the green curve for TRB-005 shows a minor inflection at about 94%R, which probably arises due to the fact that the anhedral crank is at this radial station, and there is a small radial extent of constant chord blade prior to the commencement of the tip at 96%R. Notice also that the off-loading due to anehdral brings about a reduction in the nose-down moment.

Examination of the surface pressure distributions in this sub-section of the thesis has provided further insight into the aerodynamics of the various tip shapes, and supplements and supports the deductions made from comparison of the integrated performance results presented previously. The detailed information available from the CFD solutions will be invaluable to the rotorcraft designer in understanding and improving the design of helicopter tip shapes. In the next sub-section the vortex wake trajectories predicted by the Euler CFD method will be examined to complete the comparisons for the example tail rotor tip shapes, before making the final choice of tips to be studied further.

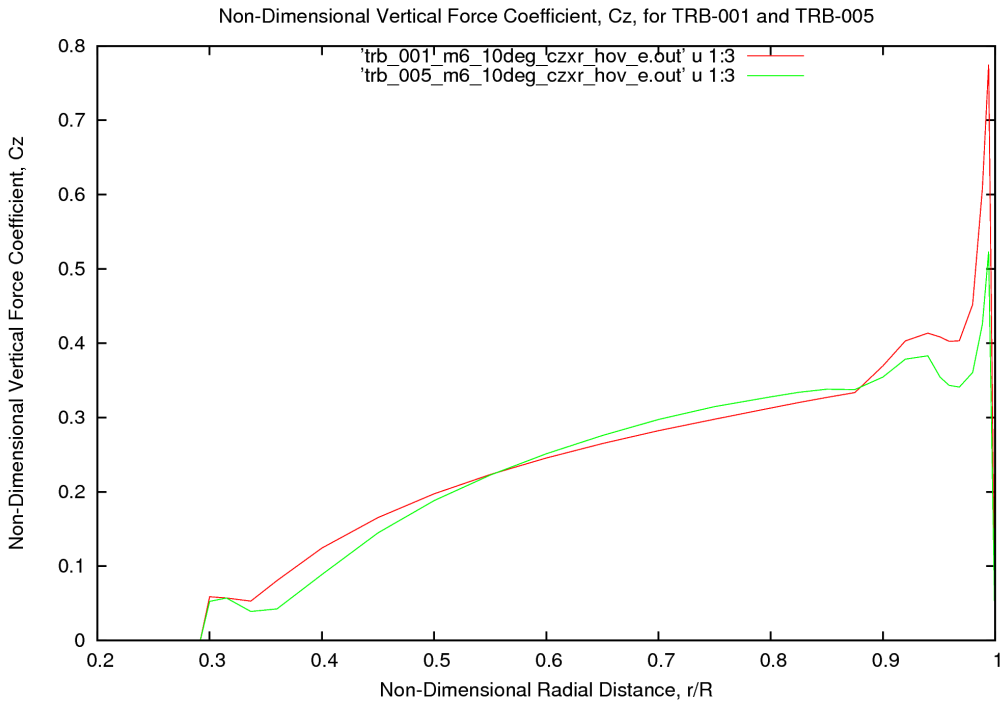

Figure 204: Comparison of Non-Dimensional Vertical (Thrust) Force Coefficient (Cz) Distributions for TRB-001 (1/4c wide Küchemann) and TRB-005 (Anhedral, 1/4c wide Küchemann) from Euler CFD Predictions in Hover at a Tip Mach No of 0.6 and a Pitch Angle of 10 degrees (Cz based on local chord).

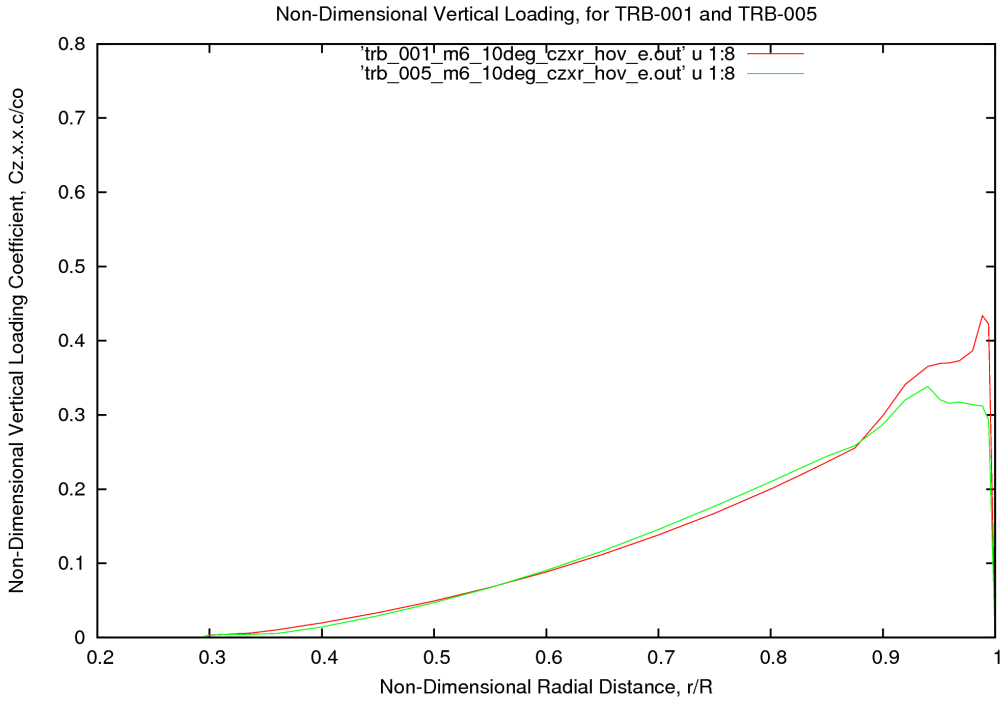

Figure 205: Comparison of Non-Dimensional Loading ($Cz.x^2.c/co$) Distributions for TRB-001 (1/4c wide Küchemann) and TRB-005 (Anhedral, 1/4c wide Küchemann) from Euler CFD Predictions in Hover at a Tip Mach No of 0.6 and a Pitch Angle of 10 degrees.

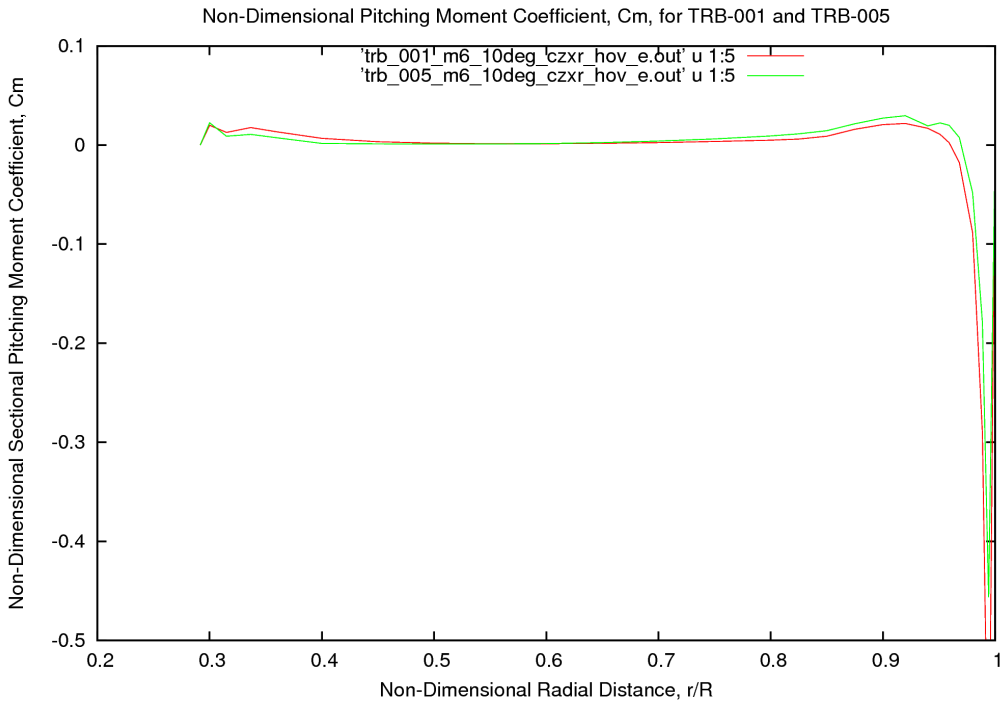

Figure 206: Comparison of Non-Dimensional Pitching Moment Coefficient (Cm) Distributions for TRB-001 (1/4c wide Küchemann) and TRB-005 (Anhedral, 1/4c wide Küchemann) from Euler CFD Predictions in Hover at a Tip Mach No of 0.6 and a Pitch Angle of 10 degrees (Cz based on local chord).

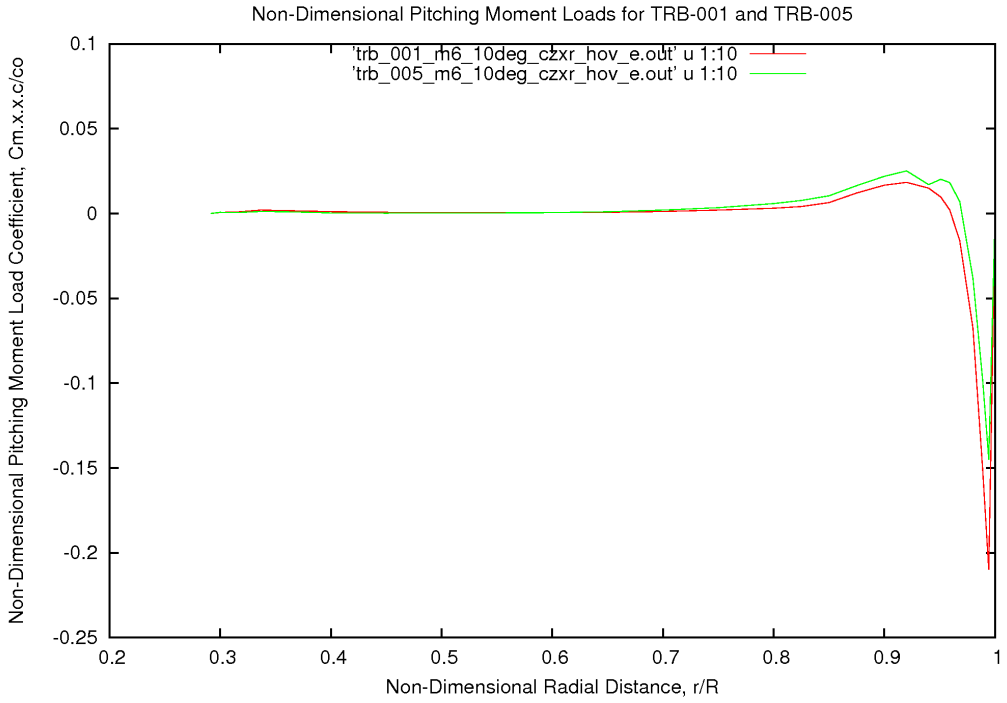

Figure 207: Comparison of Non-Dimensional Moment Loading ($Cm.x^2.c/co$) Distributions for TRB-001 (1/4c wide Küchemann) and TRB-005 (Anhedral, 1/4c wide Küchemann) from Euler CFD Predictions in Hover at a Tip Mach No of 0.6 and a Pitch Angle of 10 degrees.

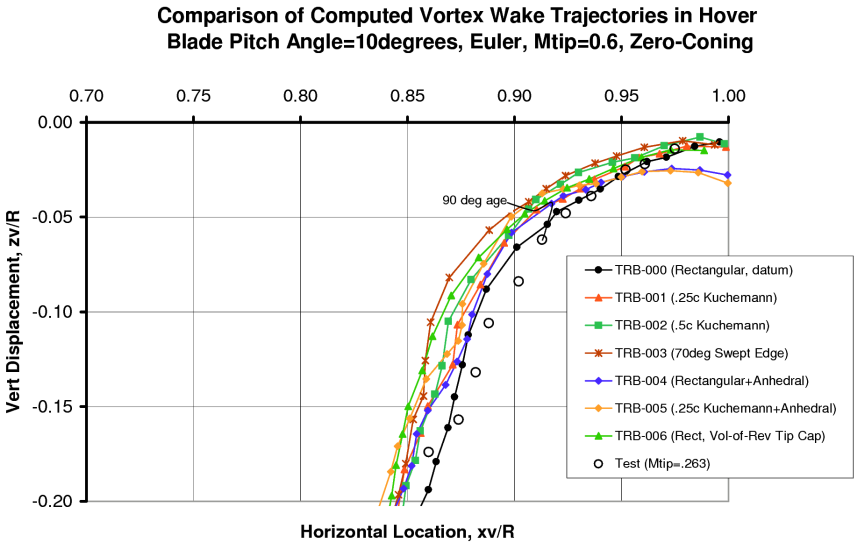

Figure 208: Wake Trajectories for Tail Rotors with Various Tip Shapes from Euler CFD Predictions in Hover

5.1.3 Vortex Trajectories

The comparisons with test data in Chapter 3 showed that the computed vortex locations from an Euler solution were in reasonably close agreement with measurements for the datum blade over a range of pitch angles. The aim here is to examine the vortex trajectories to gain a better understanding of the effect of the various tip shapes. It is recognised, however, that some of the physics in the vortex formation and diffusion processes are missing, but nonetheless it is hoped that some underlying trends can be identified.

While vortices can be seen in density and pressure contours, the vorticity in the flow field was computed in Tecplot to more readily identify the location of the vortices in the wake of the rotor (later in this thesis, the $\lambda 2$ criterion is used to obtain a more accurate vortex location from Navier-Stokes solutions). Radial cross-sections of the wake were obtained from Tecplot for a range of azimuthal planes relative to the blade reference axis. The vertical displacement and contraction were measured for each tip shape using the Tecplot probe tool. It was noted that in some cases, particularly when the vortices are in close proximity to the blade, that the vorticity contours are not necessarily circular, and/or the peak vorticity is not always central. Inevitably, this leads to some uncertainty and variability in the plotted vortex trajectories. For the grid density used here of approximately 2.5 million points (per blade segment), vortices could be traced to about 360 degrees of age (ie one revolution of the 4-bladed tail rotor).

For expediency, vortex positions were extracted and plotted only for the 10deg pitch cases, and it is assumed that similar trends would be observed at other pitch angles. Unlike the model tail rotor comparisons (reported earlier in Chapter 3), the Euler hover CFD cases were all run at zero coning, which was considered reasonable in view of the Euler limitations on pitch range, and the fact that the model tail rotor and many full-scale tail rotor have only a small coning angle.

The vortex trajectories for a range of tip shapes are plotted in Figure 208. The points plotted here represent the vortex locations at azimuthal intervals of 10 degrees. In general, the trajectories start with the vortex leaving the trailing edge of the tip and moving rapidly inboard as the wake contracts. Subsequent to the passage of the following blade, the vortices move downwards more rapidly in the wake. The vortex trajectory of the

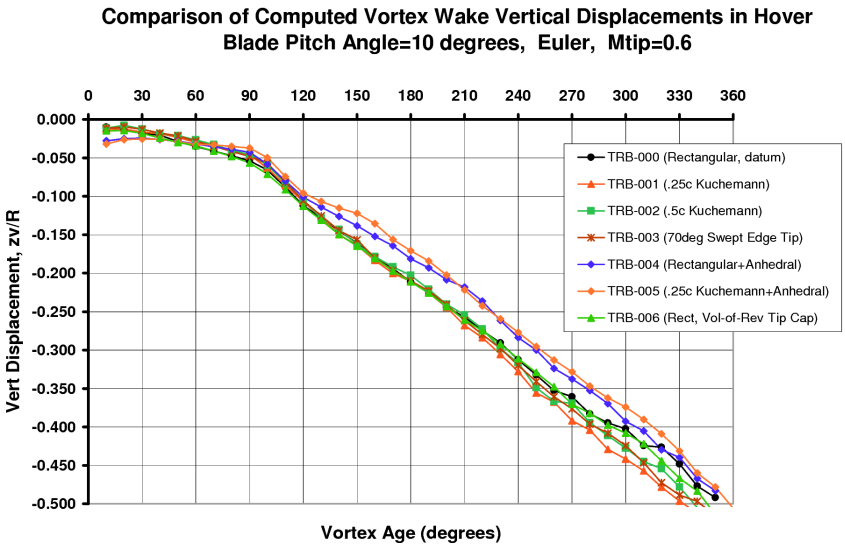

Figure 209: Vertical Displacement of Vortices for Tail Rotors with Various Tip Shapes from Euler CFD Predictions in Hover

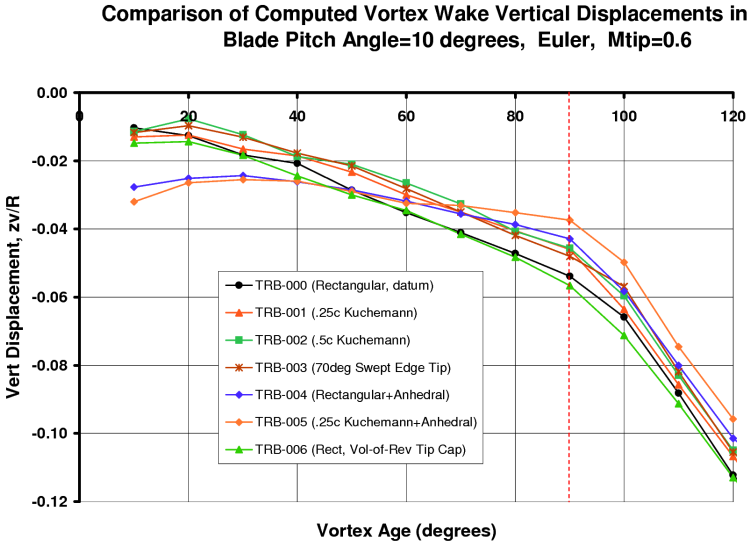

Figure 210: Closer View of the Vertical Displacement of Vortices in first 120 degrees for Tail Rotors with Various Tip Shapes from Euler CFD Predictions in Hover

datum blade, TRB-000, shows the greatest vertical displacement and least contraction, and lies closest to the measured data from the model rotor tests which has also been included for comparison (see Chapter 3 for additional comparisons with the wake formulae of Kocurek and Tangler[166]). The trajectories for the blades with tip anhedral, TRB-004 and TRB-005, start from a lower initial position, cross over the trajectories of the datum and some other blades before they start to descend in the wake. The blades with a better performance ranking tend to show slightly less contraction, while one of the poorest, TRB-003 (with the 70 swept edge), exhibits a stronger contraction. The trajectories of the 0.5c wide Küchemann tip, TRB-002, and the rectagular, volume-of-revolution tip cap blade, TRB-006, also cluster near the latter blades.

While Figure 208 shows the general shape of the wake trajectories, a deeper insight into the trends obtained from the Euler results for the various tip shapes can be obtained by plotting the contraction and vertical displacement separately. This has been done in Figures 209 to Figure 212, where the whole wake to an age of 360 degree (1 revolution of the 4-blade rotor) is presented first, followed by an expanded view over 120 degrees to help identify the details of the radial contraction and vertical (axial) displacement of the vortices in the wake.

The vertical displacement of the predicted wake vortices is presented in Figure 209 and Figure 210. For the anhedral tips, the vortex is initially displaced downwards, but rises up to a similar, if not higher position than the other blades. This type of 'snaking' has been noted in earlier experimental studies at WHL on BERP blades with anhedral, Brocklehurst and Thomas [WHL Internal Report, 1983]. The classical increase in descent rate following the first blade passage can be clearly seen, and while the anhedral blades start this second descent quite steeply, the rate of descent reduces and the traces for the anhedral blades remain noticably higher than for the blades without anhedral. The rectangular blades, TRB-000 (datum), and TRB-006 (with the volume-of-revolution tip cap) initially fall below the others, but shortly after the first blade passage rejoin and remain amongst the other flat-blade results. However, it is perhaps questionable as to whether an euler solution could correctly model the vortex formation process from such different tip-cap shapes, and this and the fact that an element of judgement was required in extracting the vortex locations, may have resulted in a small amount of scatter in the results. Further down in the wake, where the vortex strength is reduced, the vortex cores are less easy to identify and some variation is inevitable. Nevertheless, there is a notable difference between the vertical location of vortices from the flat blades and the blades which have tips with anhedral.

The contraction of the wake is shown in Figures 209 and 212 and lobes are observed in the results every 90 degrees, with the first dip at 90 degrees being most pronounced. This phenomenon is observed in the results for both the flat and anhedral blade tip shapes. A similar effect was noted in the model rotor test data, but was less regular (probably due to external disturbances). On the enlarged plot, several tip shapes cluster together initially, while TRB-006 and TRB-003 exhibits the strongest contraction, and TRB-002 is seen to exhibit greater contraction between 60 and 90 degrees. The datum blade, TRB-000 and the 0.25c wide Küchemann tip blade, TRB-001, both fall close to the anedhral blades, and these better performance blades show the least initial contraction. It may be that these trends would be realised in reality, such that tip-shapes that exhibit a slower contraction may have a better performance in terms of induced power. However, the lack of viscosity in these Euler solutions could perhaps cause some anomalies in the vortex formation and diffusion process, also there could be some small differences in the convergence of the Euler solution, or feature extraction inaccuracies might also be present. Nevertheless, it does not seem unreasonable that the less efficient tip shapes should cause the wake to contract more rapidly, while anhedral affects mainly the vertical displacement.

Finally, a further comparison was made by plotting the results close to the blade tip in a more pictorial format to show more clearly the effect of anhedral. The rectangular datum blade, TRB-000, and the rectangular anhedral tip blade, TRB-004, are compared alongside the flat 0.25c wide Küchemann tip blade, TRB-001, and the 0.25c wide, Küchemann, anhedral blade, TRB-005, in Figure 213 and 214. For the rectangular tip blades, the vortex positions were extracted at 1 degree increments, while the results for the Küchemann tip blades were added at the original 10 degrees spacing to complete the comparison. Even so, the trends are clear, and the vertical displacement and contraction results can be compared for 15 degrees ahead and aft of the blade.

As expected, the vortex traces from the anhedral tips start off lower down in the wake. They then snake their way to a higher position, passing relatively close to the anhedral tip of the following blade, as shown in Figure 213. It is observed that the vortex trailed by TRB-005 starts slightly lower and rises higher than that of TRB-004, even though the anhedral is the same. The vortex stemming from the flat Küchemann blade,

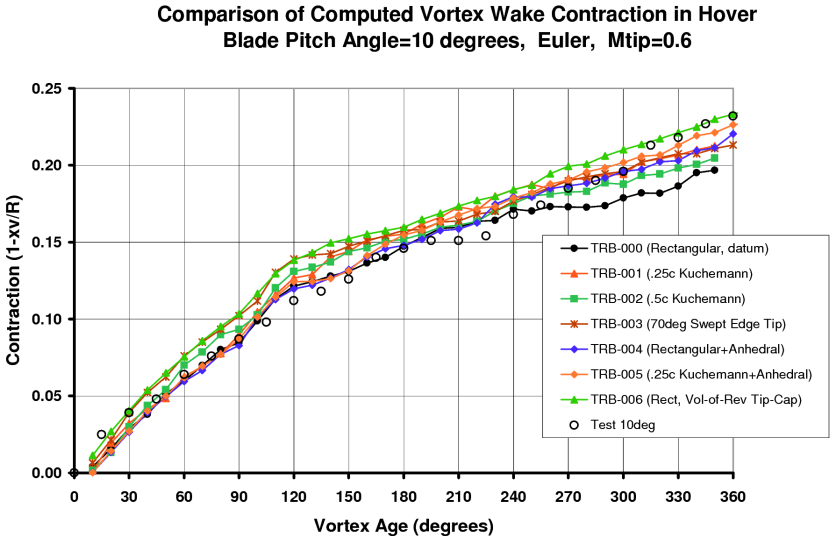

Figure 211: Wake Contraction for Tail Rotors with Various Tip Shapes from Euler CFD Predictions in Hover

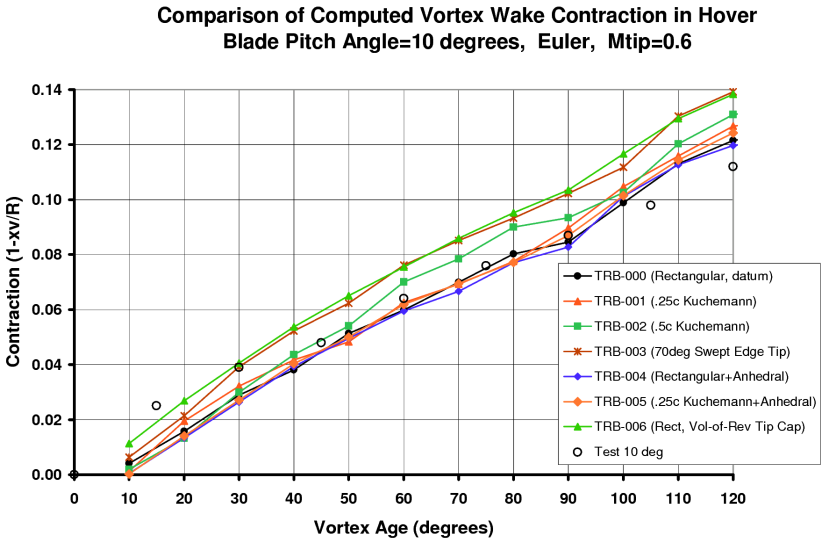

Figure 212: Closer View of the Wake Contraction in first 120 degrees for Tail Rotors with Various Tip Shapes from Euler CFD Predictions in Hover

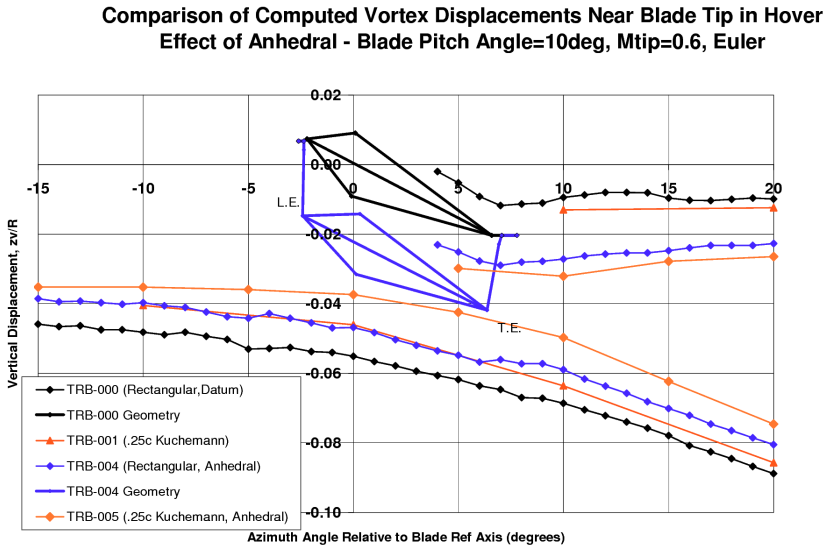

Figure 213: Vortex Displacements for +/-15 degrees Age for TRB-004 (Rectangular Tip with Anhedral) from Euler CFD Predictions in Hover

TRB-001, also starts slightly lower than that from the datum blades, and simlarly rises higher in the wake than that of the datum blade (and to a similar absolute height as the anhedral blade, TRB-004). Therefore, the effect of the Küchemann tip is to allow the vortex to start lower and rise higher than a vortex from a rectangular tip, irrespective of anhedral. The effect of anhedral is also for the vortices to start low and then snake up to pass closer below the following blade, while vortices trailed from the flat blades lie relatively low at the first blade passage.

It is also apparent from Figure 214 that there is little variation in the contraction of the wake due to either changes in anhedral or the tip shape, at least not for this set of tips where the roll-up occurs along the outer edge of the tip. If anything, the vortices from the flat blades contract slightly more rapidly than those from the anhedral blades, but in all cases pass below the following blade at the same radial location.

The opportunity to examine the vortex trajectories for several tip shapes has revealed a number of subtle changes to the displacements which may in turn relate to the induced power. Whilst the comparisons here are formed from an Euler solution, some underlying trends for the beneficial effects of Küchemann tips and anhedral have been identified. Tip shapes which have not been selected for further study generally have vortex trajectories that differ from these beneficial trends. It will therefore be interesting to see if these trends persist in the more physically representative Navier-Stokes (compressible and viscous) computations which are to follow in subsequent chapters of this thesis.

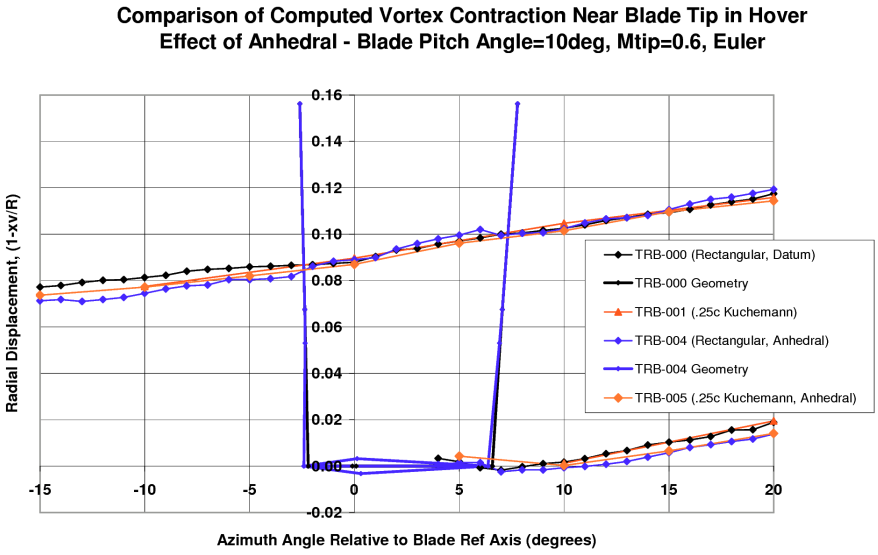

Figure 214: Wake Contraction +/- 15 Age for TRB-004 (Rectangular Tip with Anhedral) from Euler CFD Predictions in Hover

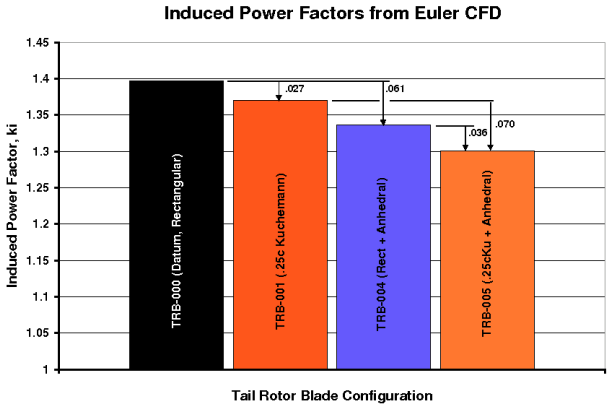

Figure 215: Comparison of Induced Power Factor for Tail Rotor Blades with Selected Tip Shapes from Euler CFD Predictions in Hover at a Tip Mach No of 0.6

5.2 Selection of Tip Shapes for Further Study

From the outset it was recognised that a full Navier-Stokes solution would ultimately be required to obtain a high-fidelity simulation of a helicopter rotor and so provide an accurate prediction for any given blade design. It was also clear that it was not practicable to perform viscous, compressible solutions for all the different tip shapes under consideration over a wide range of pitch angles and conditions, due to the high computational cost imposed on the available computer resources. The further evaluation of candidate tip designs in high speed forward flight also poses a daunting prospect for which down-selection prior to further investigation seems a reasonable approach.

The aforegoing Euler hover computations have provided a useful insight into the fundamental aerodynamic characteristics of a series of different tip shapes, taking into account compressibility effects, to allow the blade design with the best performance potential to be selected.

In comparison to traditional methods, the Euler approach is able to furnish a close prediction of the 3D loading in the tip region, and through conservation principles these effects will be properly captured in the wake, allowing new ideas such as sweep and anhedral to be explored. While an Euler solution is restricted to low to moderate pitch angles, where viscous effects are not dominant, this approach should provide a fairly good indication of the induced power. An Euler solution was used earlier in Chapter 3 to confirm the effect of twist on the induced power factor of model tail rotor. The blade tip designs considered here were all based on an untwisted blade with a symmetrical NACA0012 aerofoil section, and the focus here was soley on the effect of the tip shape. The sequence of Euler solutions presented in this Chapter therefore represent a first screening to learn something of the fundamental aerodynamics characteristics prior to selection of just a few designs for further study.

The Euler results described and compared in the aforegoing sections of this chapter have provided sufficient information to down-select some tip shapes for further study from the 8 different 'TRB' tip shapes put forward. It seems sensible to retain the datum blade, TRB-000, as a basis for future comparison and to select a further 2 designs which offer potential improvements, perhaps one representing a modest benefit, and the other seeking to greatly enhance performance, but perhaps carrying some additional risk.

From the induced power results presented earlier, the 0.25c wide Küchemann-type tip, TRB-001, showed a marked benefit compared to the rectangular datum blade. This result was not improved upon by extending

the spanwise region of this tip shape, as with TRB-002. The highly-swept-edge blade TRB-003 showed the worst level of thrust-power performance. These results were not entirely unexpected and were probably due to the tip vortex rolling up further inboard on the broader tips, together with an increasely likelihood of flow separation, with adverse pressure gradients being evident in the Euler solutions. Both TRB-002 and TRB-003 reduce the effective lifting area in the tip region, and while there was generally not much difference between any of the tips with regard to thrust-pitch gradient, TRB-003 possibly has the lowest slope. Therefore, while tip designs TRB-002 and TRB-003 may have some favourable acoustic properties in very high speed flight, they do not appear to offer any apparent benefits in thrust-power characteristics in the hover, and therefore will not be considered further in this study.

Clearly, the Euler hover results have highlighted anhedral (TRB-004 and TRB-005) as having a beneficial effect on the induced power factor of the relatively highly loaded tail rotor (solidity of 0.1989). The improvement due to the addition of a 0.25c wide Küchemann-type tip shape, found previously for TRB-001 compared to the datum blade, TRB-000, is also retained for TRB-005 compared to TRB-004. These results are summarised and compared in Figure 215. Certainly, it will be interesting to see if the benefit of anhedral is retained and maintained to higher pitch angles through use of a viscous simulation. As mentioned above, the use of anhedral is not without risk of increased blade pitching moments in high speed forward flight and this aspect of tip design will be addressed before progressing to a final Navier-Stokes hover investigation.

The rounded tip shape, TRB-006, gave surprisingly good results for induced power, and this is probably due to a reduction in rearward-facing suction regions on the more rounded tip closure, compared to the square-cut tip of the datum blade (some evidence was also found to suggest that if this tip cap was extended radially, then more rapid contraction of the wake might occur). While it would be interesting to see if the benefits were retained by such a simple tip cap (which has been used previously for tail rotors eg. S-61 Sea King, S-58 Wessex, as referenced earlier in Chapter 1), the limited number of configurations which could be considered further was limited, and further study of the new tip shape TRB-001 was preferred. Nonetheless, it is worthwhile to underline how well the Euler (CFD) solutions already obtained, have revealed a good level of detail in the pressure distributions in the important tip region, and the impact of these details on the performance (except for the lack of viscous effects).

The tapered-chord, swept-back-leading-edge parabolic tip, TRB-007, showed a slight reduction in thrust-pitch gradient, in keeping with the effective reduction in solidity. As expected, the induced power factor (or Figure of Merit) was improved slightly, but the presence of a shock near the leading edge of the tip suggests that this benefit may not be maintained to high thrust levels and it was concluded that this tip design would probably have a limited maximum thrust capability, together with rapid drag divergence, both of which are important to avoid for a tail rotor design.

On the basis of the Euler hovering rotor solutions, TRB-001 is identified as offering a reduction in induced power factor, with the potential to maintain this and also achieve high thrust levels at high pitch angles due to adequate rounded leading edge corner and control of the vortex formation over the straight tip outer edge. The small amount of sweep may also help in high speed flight, in combination with the compressibility relief naturally available on the relatively low aspect ratio blade, provided the (advancing blade) Mach number is not too high. It also seems logical to retain this tip shape when further exploring the effect of anhedral, and hence TRB-005 is selected as a second tip planform for more detailed evaluation. The datum blade will also be further evaluated to provide an ongoing datum-case to provide a basis for comparison.

Thus 3 tip designs have been selected for further evaluation. These configurations are the datum blade, TRB-000, the 0.25c-wide Küchemann-type tip, TRB-001, and TRB-005 which again uses this preferred tip shape and also features 20 degrees of anhedral. In the next section of this Chapter, the selected tips will be assessed in forward flight using (for economy) an Euler solution. The selected tip shapes will be evaluated in greater detail in hover using a Navier-Stokes method in Chapter 6.

5.3 Forward Flight Comparisons

The prior sections of this chapter provided an initial screening of the proposed tip designs using Euler solutions in hover, leading to the selection of 2 particular blade designs, TRB-001 (Küchemann type tip) and TRB-005 (Küchemann type tip with 20 degrees cranked anhedral), which will now be evaluated in forward flight, again using Euler, together with the datum, rectangular blade, TRB-000, to provide a simple baseline for comparison.

While cruising flight may be considered as an off-design condition for a tail rotor, of concern are the 1 and 2 per rev pitching moments that feed into the control system and arise from the cyclic variation in loading near the tip. For a main rotor this may become a major consideration in the design process and it is well known that swept tips can generate a significant variation of pitching moment around the azimuth, eg Spivey,[270] and indeed the BERP tip used anhedral to counteract these moments by production of a cancelling out-of-phase pitching moment, Perry.[233] The anhedral of TRB-005 might therefore be expected to give rise to some variation in pitching moment, due (simplistically) to the tip off-loading around the front of the disc and loading-up around the rear.

It was noted in the hover studies just carried out, that the integrated blade pitching moment depends on the chordwise balance of loading in the tip region. The suctions near the leading edge just inboard of the tip produce a nose-up moment, and on the aft-outer edge of the tip a nose-down moment is experienced due to the formation of the tip vortex. As the blade rotates in forward flight, the sideslip seen at the blade tip varies, as does the angle of attack and Mach number, thus the loading on the tip will vary accordingly and the resulting moments will also depend upon the geometry of the tip. In forward flight, even the rectangular tip, TRB-000, experiences a cyclical variation in loading, which governs the variation of pitching moment. The different geometry of TRB-001 might be expected to change the phase of this variation, but it is difficult to estimate whether the magnitude will increase or decrease, relative to the datum blade.

In a practical design, other detail design features such as a cambered aerofoil, or twist, may also affect the aerodynamic moments, but these additional features have been left aside to allow a simple comparison between Rectangular, Küchemann-type, and a Küchemann-type tip with anhedral.

Another issue worth mentioning here is that the aerodynamic pitching moment is just one contributor to the total blade pitching moment, and it may be that, particularly for wide-chord blades, the dynamically generated moments dominate. Nevertheless, it is worthwhile to undertake an analysis to quantify the aerodyanmic moments due to a new tip design using computational methods since the established comprehensive rotor design tools are unable to represent the loading in the tip region.

CFD provides an excellent tool to determine the variation in the detailed blade loading in forward flight, and indeed is the only method that is capable of predicting the required details of the blade loading distribution. An accurate analysis therefore not only aids understanding and could provide a basis for further design refinements, but will also quantify the aerodynamic pitching moments that are of concern.

For economy, the Euler method was chosen since the tail rotor should be lightly loaded in forward flight and viscous effects should be much less important than they are for main rotors, since main rotors have to maintain roll-balance, and provide 'g' capability in turns, thus demanding high lift on the retreating blade and also around the front and rear of the disc. For a modern helicopter, it is expected that the tail rotor will be off-loaded (at least to some extent) by the central fin, augmented by any end-fins on the tailplane. Many helicopters employ such a configuration to provide some measure of 'fly-home' and 'run-on-landing' capability in case of tail rotor failure. The off-loading also reduces the flapping and hence alleviates the Coriolis lag loads which in turn extends fatigue life. Most tail rotors also tend to be somewhat over-bladed compared to the main rotor since they are designed to provide about twice as much thrust in hover as needed to simply overcome the torque of the main rotor, and even at high speed where to main rotor torque again increases, they should not approach a retreating blade limit. In fact the tail rotor should have sufficient (negative) pitch range to provide control in auto-rotation in forward flight. Hence it seems reasonable to use an unsteady Euler solution to obtain a first indication of the characteristics of a new tail rotor tip design[13].

[13]Since undertaking these unsteady Euler runs, an harmonic balance method has become available in the most recent version of the solver.[325] This allows a forward flight solution to be reconstructed from a number of harmonics which are solved as steady solutions. This greatly reduces runtime, and now makes a full Navier-Stokes more feasible for assessing helicopter main and tail rotors in forward flight.

Advance Ratio	μ	0.4032
Forward Flt Mach Number	Mfwd	0.24193
Tip Mach Number	Mtip	0.6
Collective Pitch (no twist)	θ_0	4.0 deg
Pitch-Flap Coupling	δ_3	-45 deg
Flap-Hinge Offset	e_f	0.065 R
Coning Angle	β_0	0.6689 deg
First Harmonic Flapping	$\beta_1 c$	1.7971 deg
First Harmonic Flapping	$\beta_1 s$	-1.3773 deg
Second Harmonic Flapping	$\beta_2 c$	0.1016 deg
Second Harmonic Flapping	$\beta_2 s$	0.0347 deg

Table 6: Trim Conditions for the Example Tail Rotors used in the HMB Euler Forward Flight Computations. Note the Flapping Angles are Specified as Coefficients of a Negative Fourier Series

A typical helicopter high-speed cruise case of 160kts was chosen for these comparisons, giving an advance ratio of about 0.4 based on the same tip full-scale Mach number of 0.6, as used in the hover comparisons. In order to determine the thrust and flapping, the model rotor dimensions were scaled up by 2.25 times, to produce a tail rotor suitable for a typical Lynx-size helicopter. Then, using typical values for Lock number, and assuming that about 50% of the typical tail rotor thrust requirement would be supplied by fin off-loading, the momentum-based WHL Tail Rotor Program was used to obtain a first estimate of the collective pitch and flapping, taking into account conventional pitch-flap coupling. The resulting thrust coefficient for the tail rotor was CT(UK)=0.019, or CT(US)=0.0096. Further calculations were also undertaken using the WHL Forward Flight Program to confirm the collective pitch, blade loading and determine the vortex intersection pattern, and to obtain an estimation of blade pitching moments due to pitch-rate effects for the datum rectangular blade. The trim conditions that were used as input for the HMB CFD code are presented in Table 6.

When running the Euler solutions, the tail rotor configurations, TRB-000, 001 and 005, were all run at the same pitch angles for expediency. In retrospect, it may be more desirable to adjust the trim to provide a comparison at the same thrust, since the CFD results showed that the style of the tip had some influence on the thrust obtained, and a small effect on flapping. This is perhaps more significant for a main rotor, than for the current evaluation which assumes significant tail rotor off-loading from the fin.

Despite the low R/c which provides some tip relief, a fairly strong shock occurs on the NACA0012 blades in this high speed case on the advancing side and the tips experience a significant cyclical sideslip effect at this high advance ratio. Figure 216 compares the selected blades at the four cardinal azimuths. At the rear of the disc, the loading is fairly benign on TRB-000 and TRB-001, but the anhedral blades show an increase in the the loading contours. The results on the advancing side of the disc show how a shock builds up on the rectangular datum blade, TRB-000, and how this problem is alleviated as the isobars curve-back in the extreme tip region to provide further relief for the Küchemann tip, TRB-001. TRB-005 appears to have a shock that is slightly stronger than TRB-001, but weaker than the datum blade TRB-000. At the front of the disc, the flat blades pick up some loading on their outer edges and near their leading edge, while the anhedral blade tip, TRB-005, is off-loaded. On the retreating blade, the blades appear to be relatively lightly loaded and the loading is biased towards the tip, where the effect of the Küchemann tip is to usefully smooth the isobar pattern. The CFD results clearly reveal how the tip loading is influenced in detail by the tip shape, as the blades undergo the effect of changes in incidence, side-slip, and varying Mach number around the azimuth.

The vorticity in the wake for the forward flight case is illustrated in Figure 217, and several blade-vortex intersections are visible. Note that at this instant in time, at the advance ratio of 0.4, the retreating blade is about to encounter the trailed vortex from the preceding blade which is now at the rear of the disc and has left a cycloidal vortex pattern behind it. This interaction produces transient airloads which give a nose-down pitching moment at about 280 degrees for each of the blade designs. While the Euler solution may have broken down prematurely during this interaction, such transients will occur in practice, depending upon the advance ratio, thrust and flapping.

The aerodynamic pitching moments obtained from the CFD simulations are compared in Figure 218. Here the datum blade is first compared to the aerodynamic component of the pitching moment from a lifting-line

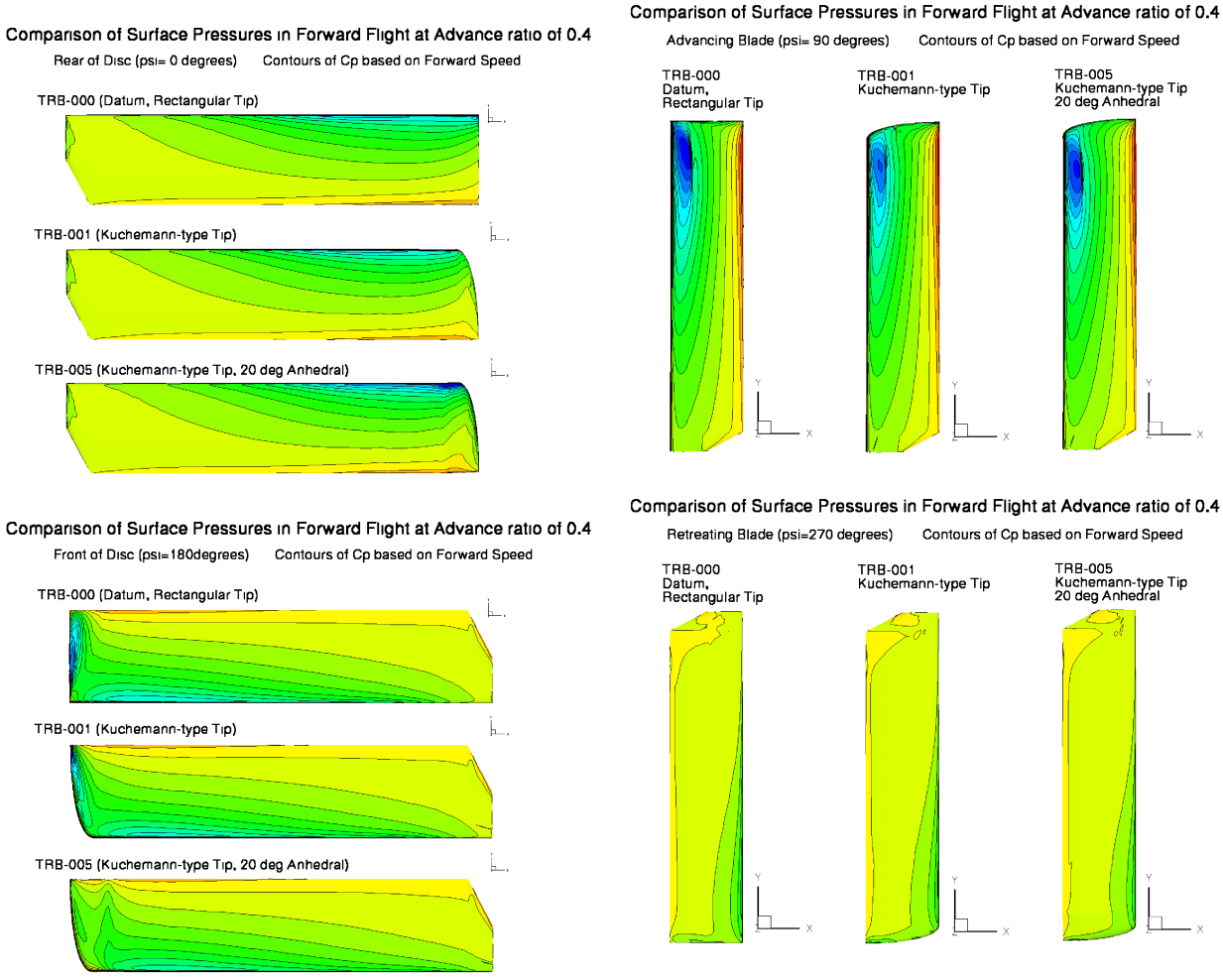

Figure 216: Surface Pressure Contours at 0, 90, 180 and 270 degrees Azimuth for the 3 Selected Tail Rotor Blades in Forward Flight at an Advance Ratio of 0.4 (Mtip=0.6, Madv=0.84)

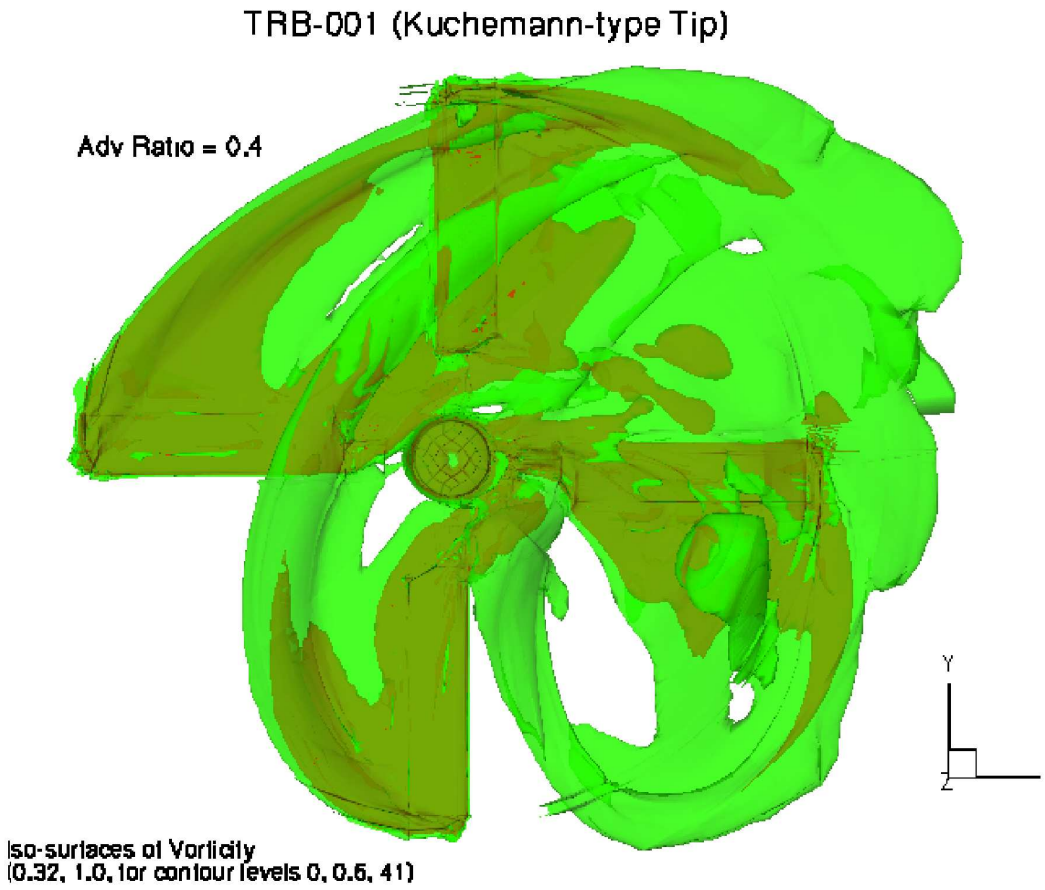

Figure 217: Iso-Surfaces of Vorticity for TRB-001 (Flat Küchemann-type Tip) in Forward Flight Showing Vortex Ahead of Retreating Blade (as Viewed Here the Rotor has Top-Blade-Forward Rotation and the Free-Stream Flow is From Left to Right).

forward flight program prediction, in the top part of Figure 218, and it can be seen that while the peak-to-peak variation is similar, the inviscid computational results are offset due to compressibility effects and the fact that the aerofoil data for NACA0012, as used in the performance program, contains a small positive moment coefficient, depending upon the angle of attack and Mach number.

The total blade pitching moments for the three tip shapes are compared in the middle part of Figure 218. There is little difference in the results for the datum and (flat) Küchemann tip, while the anhedral blade, TRB-005, shows a slightly larger peak-to-peak variation, and an increased nose-up moment in the first quadrant, indicating a phase-shift. All blades react to the blade-vortex interaction at about 280 degrees azimuth.

In order to gain further insight, the computational results were the subject of a Fourier analysis which identified the phase shift in the first harmonic as almost 50 degrees for TRB-005 relative to TRB-001, due to anhedral. The pitching moments for TRB-005 have been reconstructed using the mean, first and second harmonics, and are shown superimposed on the computed pitching moment predictions, as shown in the lower part of Figure 218. For illustration and comparison, this figure also contains a moment variation arising from use of a typical cambered tail rotor aerofoil with an arbitrary (constant) pitching moment coefficient of -.02. It is clear that this variation is approximately in anti-phase to the predicted moments from the computational results for the anhedral tip, and the combined effect is to leave mainly the second harmonics, as illustrated by the dashed line in the lower part of Figure 218.

Of course, as experience at WHL has revealed, the aerodynamic loading only makes up part of the total tail rotor control loads, and may only account for about 25% of the pitching loads for modern wide-chord tail rotor blades which operate at relatively high rotational speed. Nevertheless, the current work illustrates the usefulness of CFD for determining rotor aerodynamic moments (which may take on even greater importance in main rotor applications) and has confirmed that tip anhedral may be a viable solution for tail rotor applications.

In summary, only a small difference in pitching moment in the second quadrant was found for the flat Küchemann-type tip, TRB-001, compared to the datum rectangular blade, TRB-000. In comparison to these flat blades, the 20degree anhedral Küchemann-type tip, TRB-005, showed a modest increase (of about 30%) in peak-to-peak aerodynamic pitching moments around the azimuth for this high speed design case, together with a 50 degree phase shift. However this level of aerodynamic pitching moment may well be acceptable for a pratical tail rotor design, and the possibility remains to refine the tip design to alleviate pitching moments if desired. Improved accuracy would be obtained by using Navier-Stokes solutions for further evaluations of a final design, where separation may occur if more highly loaded cases were required to be considered.

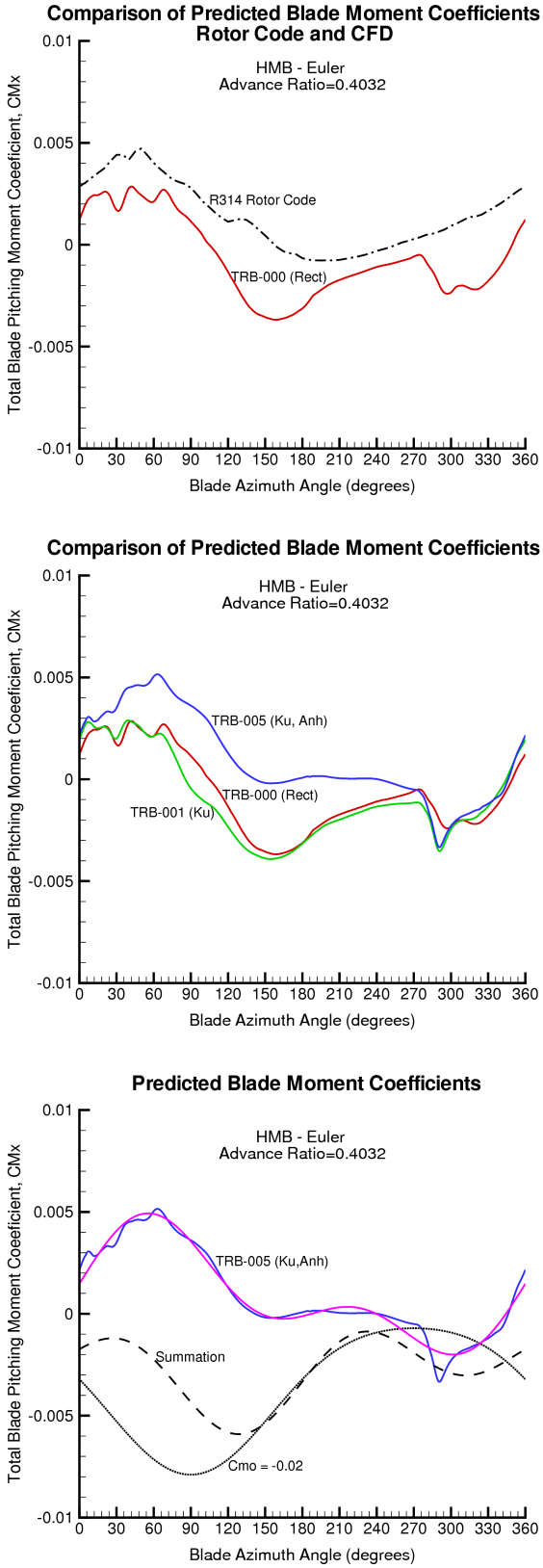

Figure 218: Azimuthal Variation of Total Blade Pitching Moments. Top: Compared to Lower Order Method, Middle: Effect of Anhedral, and Bottom: Compared to Cambered Aerofoil

5.4 Summary of Euler Evaluations

This final section of Chapter 5 brings together the findings from an initial evaluation of a range of tip designs using Euler computations, before going on to further investigate selected designs using a Navier-Stokes simulation.

The Euler computations gave a relatively economic assessment by using a compressible, but inviscid simulation of the 3D flow field about a helicopter rotor, which through conservation principles naturally includes the influence of the vortex wake. The induced flow field appears to have been captured quite well and thrust and torque on the blade vary according to the loading distribution in the tip region which depends on both the induced flow and the tip design. For the datum blade, the predicted values of the induced power factor were comparable with those found experimentally for the model tail rotor and, as expected, were greater than for a main rotor, due to the high disc loading and lack of twist, increased swirl losses and relatively large root-cut-out of the tail rotor. The series of new tip shapes revealed varying degrees of potential to improve tail rotor performance.

The results from the Euler hovering rotor analysis have allowed the blade tip designs to be ranked in terms of their induced power factor. This was done by fitting the integrated results for each tip shape with a quadratic to reliably determine the induced power factor from the slope of the linearised power characteristics, CQ-$CT^{1.5}$. These cases were run at low to moderate pitch angles, where flow separation was not an issue. However, since the Euler solution leaves aside the effects of viscosity, the resulting Figure of Merit (and Thrust-Power ratio) was artificially high. It was found that a more realistic estimate of these quantities could be obtained by adding a correction for the profile power (below the onset of stall), in advance of Navier-Stokes computations.

However, other factors also have bearing on the selection of best tip shape for a tail rotor, and the detailed surface pressure information available from the Euler solutions provides a good guide to the magnitude of loading peaks and adverse pressure gradients on the various tip planforms. These features control the propensity for flow separation, and therefore affect the maximum thrust and the divergence of profile power for any given rotor blade.

The 0.25c wide Küchemann-type tip, TRB-001, ranked well in terms of induced power, and the detailed surface pressure distributions indicated a clean formation of the tip vortex over the tip edge and gave confidence that the rounding of the leading edge corner was sufficient to suppress adverse gradients at high incidence.

The fact that the Euler method is able to capture the flowfield around a given tip design also highlighted the beneficial effect of anhedral on tail rotor performance. This was first revealed in a straight comparison for rectangular tips, TRB-000 and TRB-004, and the same relative improvements in induced power factor were confirmed for the two similar (0.25c wide) Küchemann tip designs, TRB-001 and TRB-005, with the latter having 20 degrees of anhedral. The results showed that anhedral tends to off-load the tip in a similar manner to twist, causing the loading to move slightly further inboard to give a more uniform downwash distribution and therefore an improved induced power factor.

Examination of the vortex wake trajectories for different tip shapes also revealed changes in the vortex wake which may account for the changes experienced in induced power. It would appear that the the use of anhedral causes the tip vortex to rise higher in the wake at the first blade passage, closer to the following blade. A similar behaviour was observed for the Küchemann tip, but with a greater blade-vortex separation. The effects appear to be additive, as were the beneficial effects on the induced power factor. Further down in the wake, the vortices from the anhedral tips are not displaced as much as for the other tips. Comparisons for anhedral and Küchemann tips showed little difference in contraction.

The two Küchemann-type tips, one flat, TRB-001, and one with anhedral, TRB-005, together with the datum rectangular blade, TRB-000, were therefore selected for further investigation.

A new tip shape must also be shown to have desirable aerodynamic and acoustic characteristics in high-speed forward flight, and at the same time impose no significant adverse effects the dynamic loading. Both sweep and anhedral are known to carry some risk of increased pitching moments which feed into the control

system. The 3 selected tip shapes were therefore investigated in forward flight, using an unsteady Euler simulation, to provide an economic first assessment of integrated blade pitching moments at an advance ratio of 0.4. The results revealed the expected 1 and 2 per-rev aerodynamic moments, although little difference was found between the datum rectangular blade, and the flat Küchemann-type tip, with only a small change notable in the second quadrant. The anhedral Küchemann-type tip blade design, TRB-005, was found to give 30% greater peak-to-peak blade pitching moments around the azimuth than the datum blade, but the phase of this moment variation was such as to partially compensate for any pitching loads which might arise from the use of a cambered aerofoil (which is a common feature of modern tail rotors, but was not investigated here). It is also worth noting that the aerodynamic component of the total moments is relatively small compared to the contribution arising from the blade dynamics, especially with the modern trend towards wide-chord blades and moderately high rotational speed.

An Euler approach has been successfully used to obtain a first appraisal of the aerodynamic characteristics of the range of tail rotor tip designs put forward in this thesis. A preliminary quantification of the induced power factor was obtained, and the details revealed by the numerical solutions was found useful in developing a better understanding of the impact of the different tip designs. The Euler solutions have identified the mechanism by which anhedral enhances the performance of highly loaded rotors and pitching moments have been quantified in high-speed flight. The following section, Chapter 6, a further evaluation of the selected tip designs using Navier-Stokes is reported.

6 Navier-Stokes Hover

The Euler simulations in the previous chapters provided a preliminary analysis at relatively modest computational expense and proved useful to predict the broad impact of rotor design features on induced power. They also provided a useful early insight into the blade loading distribution and revealed interesting trends in vortex trajectories, from which the rotor designer can start to formulate ideas. However, a proper evaluation of rotor performance demands accurate prediction of both compressibility and viscous effects, particularly in the tip region, such that the thrust and total power can be accurately determined. A numerical approach is perhaps the only way of obtaining a high-fidelity simulation which includes the full physics which are present in the rotor problem.

Most helicopter blades operate at moderate sub-sonic tip Mach numbers, but have a small chord such that the tip Reynolds number of a hovering main rotor is about 3-8 million, depending on the size of the helicopter. For acoustic reasons the tip speed of the tail rotor is often about 5% lower than that of the main rotor and due to their smaller chord tail rotors may have a Reynolds number in the range 2-4 million. The example model tail rotor considered here has a tip Mach number of 0.6, typical of a modern tail rotor, and a Reynolds number of just over 1 million. Use of a Navier-Stokes solution is therefore essential for accurate performance predictions.

The relatively low Reynolds number means that viscous effects generate a thicker boundary layer which is more prone to separation, particularly if adverse pressure gradients are strengthened by compressibility effects, and consequently the pressure drag may be relatively high. This together with skin friction (and any wave drag) may lead to relatively high profile power for small rotors. The helicopter multi-block code, HMB, offers a well validated Navier-Stokes solver with a range of turbulence models that are well suited to the rotor problem. Given sufficient grid resolution, a Navier-Stokes solver such as HMB which computes the flow down to the surface should allow prediction of the growth in profile power up to, and perhaps just beyond, the onset of stall. However, an unsteady and computationally more expensive solution may be required as the stall develops and strongly fluctuating flow separations are encountered. The unsteady aspects are explored further in Chapter 8. The current focus here is on obtaining steady solutions to evaluate, as far as possible, the chosen tip shapes in hover.

The total power of a rotor is made up of induced and profile power, although these components can be difficult to separate out from either test data or CFD simulations. Splitting the power is useful to the helicopter designer, and the technique of fitting a second order polynomial to the linearised power curve is again employed in the following analysis to facilitate this process. For both main and tail rotors, an accurate estimate of the total power is essential to determine the Figure of Merit, and for a tail rotor it is also important to be able to predict the growth in profile power that occurs as the stall is approached. This latter scenario is perhaps more difficult to simulate due to the propensity for separated flow. Both twist and tip shape strongly influence the stall development, as well as influencing induced and profile power in attached flow conditions.

In this section of the thesis the performance of the three selected tip shapes (as previously defined in Chapter 4 and initially appraised and selected in Chapter 5) are compared using a steady Navier-Stokes analysis. The chosen example blades are:

TRB-000v	Datum, rectangular blade with square-cut tip
TRB-001v	0.25c wide Küchemann-type tip
TRB-005v	0.25c wide Küchemann-type tip with 20 degrees of anhedral

where the suffix ‘v’ has been used to denote the viscous solution. All blades have a radius of 21” (533.4mm) and a chord of 3.28”(83.312mm), giving R/c=6.402439, and the blade root cut-out extends to 33%R.

For compatibility with the Euler computations of Chapter 5, the Navier-Stokes simulations were all run at a tip Mach number of 0.6, this being typical of a modern tail rotor and just sufficient to produce some compressibility effects in hover. The tip Reynolds number was chosen to to be consistent with the model rotor blade chord (Re=1,168,000). In retrospect, a higher tip Mach number would have better illustrated the effects of compressibility. Most importantly, use of a full-scale Reynolds number may have avoided concerns that the

low Reynolds number was partially responsible for the problems that were encountered with convergence of the solutions. For convenience, all cases were again compared at zero coning angle and, in line with the desire to focus solely on the tip aerodynamics, the blades had a constant NACA 0012 aerofoil section and zero twist (the co-ordinates of the sharp trailing edge NACA 0012 aerofoil are given in Appendix F).

Section 6.1 describes the necessary grid refinements required for a Navier-Stokes solution, such as the need to accommodate the boundary layer and define blocks close to and around the surfaces of the blade to avoid excessive stretching. Controlling the quality of the grid leads to more consistent and reliable solutions. This section includes an illustration of the subject tip shapes that also shows the radial stations at which cross-sections of the blades were taken to obtain the loading distributions.

The reporting of the Navier-Stokes evaluation of the selected model rotor blades is divided into 2 main parts, for low-to-moderate and moderate-to-high pitch cases.

Section 6.2 presents performance predictions at low-to-moderate pitch angles to establish an induced power factor for the selected tip shapes, and provides a straightforward comparison of performance where the solutions were found to be generally stable and well converged. The induced power factor was obtained by fitting the computed results for pitch angles up to 10 degrees, to avoid any significant growth in profile power. However, to show the trends in profile drag and Figure of Merit, together with an indication of the blade pitching moments, results for pitch angles up to 16 degrees have also been included. Further insight into the blade tip aerodynamics was obtained from the blade loading distributions. However, for some of the tips, between 12 and 16 degrees, some variation in the thrust and torque were found. It was later discovered that this was due to instabilities in the flowfield that gradually became more significant as the pitch was increased to 16 degrees and beyond. For these cases, the rotor is apparently clear of stall, but with increasing pitch many iterations were necessary to settle the solution.

Section 6.3 discusses the difficulties which were encountered in obtaining a steady state solution as the pitch angle was gradually increased to larger values. Whilst it had been anticipated that the presence of flow separation would limit the application of a steady solution, a flow instability problem originating from the movement of the root vortex proved troublesome at even moderate pitch angles. With hindsight, an early indication of this problem may have been present in some of the higher pitch Euler solutions (prior to Euler breakdown), but it was thought that this variability would have been suppressed when going to a Navier-Stokes solution. At higher pitch angles these changes in flow state may couple with the effect of flow separation near the tip, causing the solution to fluctuate when stall is present. What was surprising was that the changes in loading over the inboard region of the blades had such a great impact on the thrust and power. In retrospect, this problem was aggravated by the decision to use blades with zero twist which also had a large root cut-out.

Towards the end of Section 6.3 some suggestions are put forward for geometry changes in the hub and root regions which may alleviate the central pumping and root-vortex re-positioning problem for steady solutions. Such changes could lead to more reliable use of a steady Navier-Stokes solution for the performance evaluation of highly loaded rotors with low twist and large root-cut out. The use of a steady solution is much more economical than resorting to an unsteady method where hub and bearings could be modelled in detail, especially when the objective is the evaluation of a new tip design, up to the point of stall.

Despite the problem of flow variations ocurring over the inboard part of the blade, the steady hover Navier-Stokes results obtained for the three tip shapes at high pitch angles have furnished much useful information about the characteristics of the selected tip shapes. Section 6.4 presents and analyses the computed results at moderate-to-high pitch angles in the range 12 to 20 degrees. For this untwisted rotor blade, the profile power starts to diverge in the pitch range between 15 to 17 degrees, where it is desired to evaluate the benefits of refinements in the tip design for tail rotor applications. A range of stall indicators were used to obtain further useful insight into the tip aerodynamics and rate of stall development. Analysing the results in this manner enabled much useful information to be obtained from the CFD predictions, despite the variations found in the thrust and power at moderate-to-high pitch.

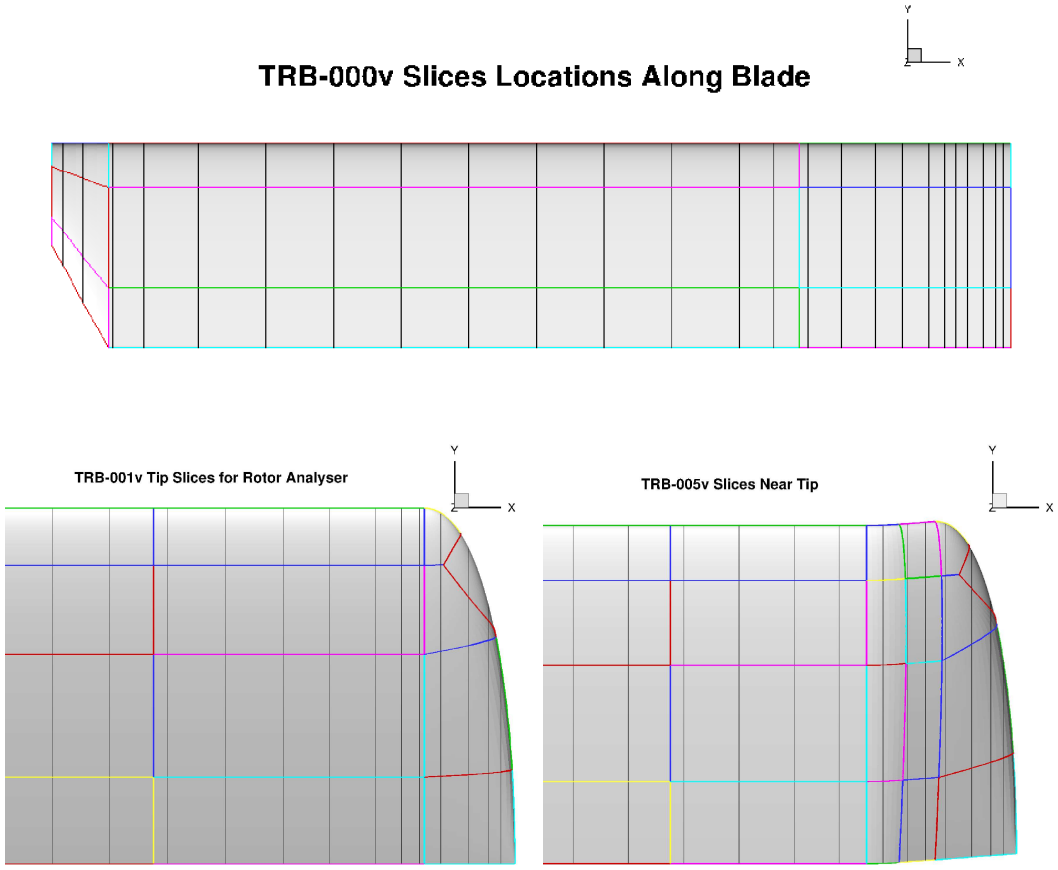

Figure 219: The Three Tip Shapes Selected for Navier-Stokes Analysis. TRB-000v Datum Rectangular Blade, TRB-001v Küchemann Tip, and TRB-005v Küchemann tip with 20 degrees Anhedral. This Figure also shows the Distribution of the Cross-Sections at which the Surface Pressures were Extracted for Input to Rotor-Analyser

6.1 Tip Shapes and Grid Considerations

The three selected tip shapes for the model tail rotor blades have been previously defined in Chapter 4, and are illustrated again here in Figure 219. The datum blade, TRB-000v, has a rectangular tip which was cut off square at the tip. In all cases, the blades were cut-off just inboard of the root and the root itself tapered rapidly from the aerofoil at 33%R to the cut-off at 29%R, as is typical of many tail rotor blades. The flat Küchemann-type tip, TRB-001v, is shown on the left in the Figure, while on the right, TRB-005v, has the same tip shape and 20 degrees of anhedral. The tip starts at 96%R and the anhedral crank is at 94%R with blends from 93.25 to 94.75%R. This illustration also depicts the stations at which the surface pressures were extracted during post-processing to obtain the loading distributions via Rotor-Analyser (see Appendix G).

The style of the grid for the Navier-Stokes computations was chosen to be consistent with that used previously for the Euler studies, and featured a cylindrical hub of 55mm radius (0.660 chords, or 0.103R, left at this size to avoid extremely small blocks of cells near the centre of the domain in an effort to maintain grid quality). All grids used periodic boundaries on the (vertical) planes between the blades to allow a single blade quadrant to be used (an alternative would be to model the whole rotor, although a 4 times larger grid would give a substantial runtime penalty). The size of the computational domain was the same as had been used for the Euler solutions and extended 4R is the radial direction, 2R above and 6R below the blade. The so-called 'Froude' type boundary conditions (see Steijl, et al,[284] and Biava and Vigevano[45]) were again used (this boundary condition may allow some economy in reducing the distance to the far-field outlet, but the policy here was to keep this distance large). In retrospect, it may have been advantageous to reduce this distance,

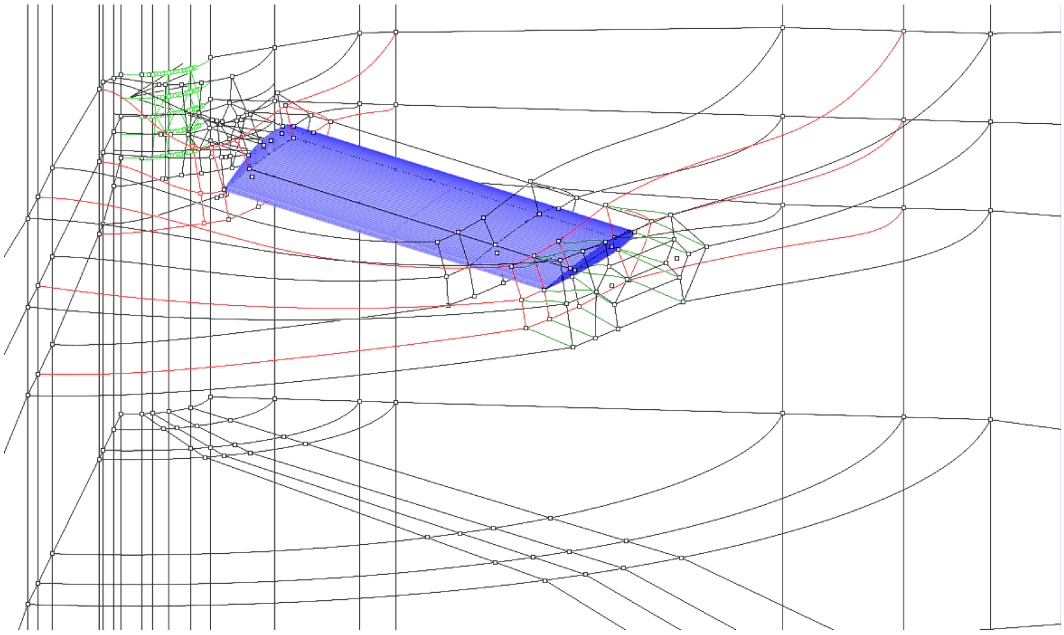

Figure 220: Illustration of mesh construction curves generated in Rhino3 for Navier-Stokes Grid for TRB-000v at 20 degrees Pitch

especially for the more lightly loaded cases where the wake was sometimes slow to join up, but for consistency it was kept the same throughout.

For application of the Navier-Stokes solver, the Rhino 3D CAD software was used to rotate the blade to higher pitch angles. Grids were built at pitch angles of 8, 12, 15, and 20 degrees with further fine adjustments to pitch made using GridTrimmer. Rhino was also used to make refinements to the support curves around the blade. These additional curves were added to provide closer control of the block boundaries and mesh spacing, prior to import into Ansys/ICEM-Hexa for the generation of a structured multi-block Navier-Stokes grid for HMB.

The meshing topology closely paralleled that used for the Euler meshes, except that it was found useful to surround the aerofoil by a frame (at about 25-30% chord distance) to control the orthogonality and grid-spacing normal to the aerofoil/blade surface. This was particularly helpful in the preparation of Navier-Stokes grids with the need to cluster the cells close to the blade. An exponential expansion was used to grow the cell spacing away from the blade surface. An additional block downstream of the aerofoil trailing-edge was also found helpful in controlling the spacings and orthogonality of the mesh downstream of the blade in the plane of the rotor. The curve-matching function in Rhino3 was used to ensure a smoothly blended shape of the supporting curves defining the block boundaries, such that these were then available for projection in the Ansys/ICEM-Hexa grid generator. This approach to thoroughly preparing the underlying geometry of the grid takes a little extra time in Rhino, but saves much time and effort in Hexa and, with practice, allows a better quality grid to be produced. These improvements to the underlying geometry are illustrated in Figure 220.

The number of mesh nodes upstream and downstream of the blade was also significantly increased to improve vortex capture, as were the spanwise and chordwise spacings to provide cells of sufficiently low aspect ratio (of the order of 100 radially, and 10 or less at the leading and trailing edges of the blades). The split in the blocking below the rotor which had been introduced for the Euler grids was retained because it allows fine control of the mesh spacing (using Ansys/ICEM-Hexa's bi-geometric spacing near the rotor and exponential spreading near the outlet plane).

The target first-cell spacing was taken as 1 x 10^{-5}, although some 2D aerofoil computations for NACA0012 at representative (83%R) Mach number and Reynolds number conditions suggested a first cell spacing of double this spacing might be more appropriate due to the low Reynolds number. However, HMB can deal with y^+

less than unity close to the surface. The mesh spacing was therefore relaxed to a slightly larger first spacing if meshing problems were encountered near the root-end of the blade.

Initial grids were aimed at about 5.6 million points, but due to the changes in grid topology necessary to accommodate the Küchemann-type tip shapes, the final grid size had to be increased in order to ensure sufficient cells in the boundary layer and to avoid excessive stretching producing regions of sparse cells. Use of finer grid spacings also improved the capture of tip vortices and in the wake.

As the results were scrutinised and the surface pressures and skin friction effects were examined, various refinements were made to the grids. The grid size of the datum blade, TRB-000v, gradually increased to 6,819,324 points (205 blocks). Later some runs were repeated with 8,765,799 points with little change in the results. The final grid size for TRB-001v was 9,166,422 (270 blocks) and for TRB-005v was 9,058,368 (344 blocks) mainly due to the use of additional blocks in the tip region to accommodate the anhedral.

The HMB solver has a wide variety of turbulence models available of varying complexity and, for the current rotor application, the modified k-ω model was preferred. This model was used throughout, except for some additional test cases at high pitch. This model is quite robust and appropriate for turbulence that originates near the wall and is then convected downstream in the shear layer and vortical wake structures. Experience has shown that the drag levels predicted by this model agree well with practice and are lower than those obtained from the standard k-ω model of Wilcox,[322] whilst generally slightly higher than the full SST model of Menter[209].[210] These ideas were confirmed by a few runs carried out during the course of this research (and also by work in industry).

The following sections of this Chapter present the results obtained using the refined Navier-Stokes grids and the chosen turbulence model in all cases, except for a few additional runs. At low-to-moderate pitch angles realistic results have been obtained, although some variability was encountered at higher pitch angles as the changes in the flow state near the root of the blade were encountered. The problems that hindered the convergence now appear to be due to a flowfield instability issue, and do not appear to be related to the choice of turbulence model or a grid quality issue.

6.2 Navier-Stokes Evaluation at Low-to-Moderate Pitch

The Navier-Stokes solutions presented in this section of the thesis were obtained once the grids had been refined and were run at Mtip=0.6 and a tip Reynolds number of 1.1668 million, using a k-ω turbulence model (HMB 1.4 option 3002). All angles below 10 degrees were very well converged. At small pitch angles, the residuals settled well to the order of 10^{-6}, or better, and the histories of the integrated quantities, such as thrust and torque, were smooth and remained within about 0.5%. As the pitch angle increased up to about 10 degrees, the histories showed convergence to within 1 or 2%. Between 12 and 16 degrees the convergence histories were less settled, but this was initially only considered a minor inconvenience, with the first established solution, at say, 30 to 40,000 iteration being taken before any significant tendency for drift became apparent. However, some cases near 15 or 16 degrees started to show signs of a significant solution shift and were eventually run to a far greater number of iterations to explore the issue. These problems at the higher pitch angles are deferred for the present and will be fully discussed in the following section.

6.2.1 Performance Predictions

Figure 221 presents the thrust pitch curve using results up to 16 degrees for blades with the 3 selected tip shapes, together with the Euler results for the datum blade for comparison at the same tip Mach number. As expected, the effect of including viscosity is to reduce the thrust-pitch gradient. At first sight the amount by which the slope is reduced might seem large, but a similar reduction is observed between Euler and Navier-Stokes predictions for a 2D NACA 0012 aerofoil, Figure 222, at a Mach number of 0.5 and Reynolds number of 1 million, representative of the blade at 83%R. Since the Mach number is now at a full-scale value to allow a realistic appraisal of the tips, a direct comparison with the model rotor data is no longer possible, but referring back to Chapter 3, it was noted that the Euler results generally exhibited a slightly steeper gradient, and this was most apparent in Figure 148 at the higher tip Mach number. Looking again at Figure 221 it is seen that there is little difference in the thrust-pitch results for the different tip shapes. The results for TRB-000v and TRB-001v are very close, with the points for TRB-005v just very slightly lower, perhaps due to the effect of the anhedral. Some slight variation from the expected (near linear) trend is just noticeable towards the higher pitch angles, and this is perhaps a first indication of the convergence problems which are discussed later. The single point obtained with the basic k-ω model (HMB 3000) for TRB-001v sits just on the high side of the thrust curve.

The computed total torque, CQ, is plotted against the blade pitch angle in Figure 223 and here the differences between the tip shapes are more apparent. The datum blade, TRB-000v, consumes the greatest torque for a given pitch, while the two Küchemann tip blades each consume less, with the anhedral tip consuming the least torque for a given thrust. The trends for the datum blade and the Küchemann tip blades seem to diverge slightly as pitch increases, although again there is some slight variability in the results at the higher pitch angles above about 13 degrees. These benefits from the improved tip shapes are quite significant and will be quantified further in terms of induced and profile power savings as this analysis of the Navier-Stokes results progresses. Note that the single standard k-ω result has a slightly higher torque than found for the collected results for TRB-001v with the preferred, modified k-ω, turbulence model.

The benefits from the more refined tip shapes are again apparent in the CQ-CT curve of Figure 224, and here some simple momentum-based curves have been added to clarify the trends. The induced power factor, k_i, and the (effective) profile drag coefficient, CDp_o, have been extracted as described in the following paragraph.

In Figure 225 the torque versus thrust has been linearised, by plotting against $CT^{1.5}$. Here only results up to 10 degrees have been used to fit the trend of the predictions which also include several points at low pitch angles. Although results were not obtained at 2 and 3 degrees for all the blades, there are sufficient points to allow good curve fits to be made.[14] Following the ideas put forward in Chapter 5.1, a second order polynomial curve was fitted to the results using a least squares method and the coefficients for the equation of the curve,

[14]These runs were carried out using HMB-1.4 and the grids at these low pitch angles were generated using an early version of the GridTrimmer utility to reduce the pitch from an 8 or 10 degrees grid. For Küchemann-type tips, and the anhedral tip in particular, it is thought that some distortion of the grid may have occurred which prevented solutions being obtained at the lowest pitch angles. Since the number of solution points are sufficient, and the focus of the work was mainly concerned with higher pitch cases, these issues were not pursued. However, if the blade was first rotated to a low angle, prior to meshing in Ansys/ICEM-Hexa then these problems would be overcome. In fact, several grids were subsequently generated at 8, 12, 15 and 20 degrees to minimise these effects for the higher pitch cases. Improved TFI techniques for deformation of the grid are now available.

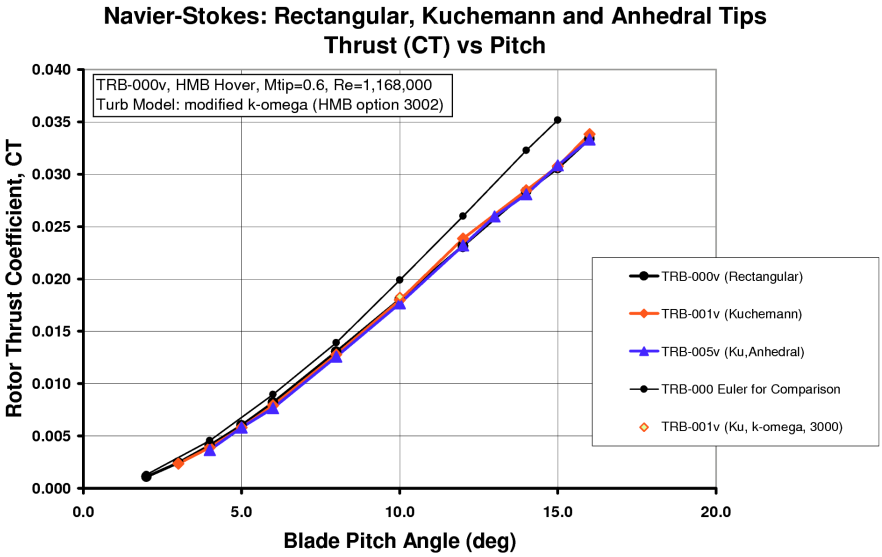

Figure 221: Comparison of Steady Navier-Stokes Thrust-Pitch Predictions for the 3 Tip Shapes, TRB-000v (Datum, Rectangular), TRB-001v (Küchemann) and TRB-005v (Küchemann with Anhedral), Computed Using HMB with a Modified k-ω Turbulence Model, Mtip=0.6

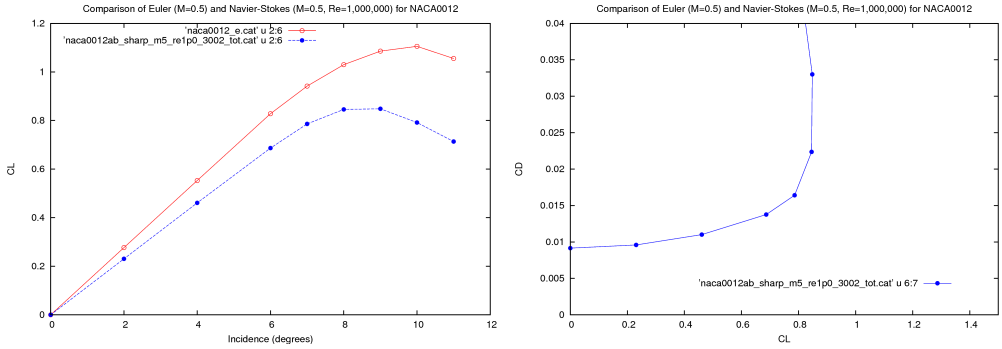

Figure 222: Comparison between Euler and Navier-Stokes results for NACA 0012 at a Mach number of 0.5 and Reynolds Number of 1 million, appropriate to 83%R on the Model Rotor. The Reduction in Lift-Curve Slope is similar to that seen in the Thrust-Pitch results for the Model Rotor, while the Drag Growth with Lift may be compared to the Profile Power of the Model Rotor. A Modified k-ω Turbulence Model was also used for these Navier-Stokes predictions.

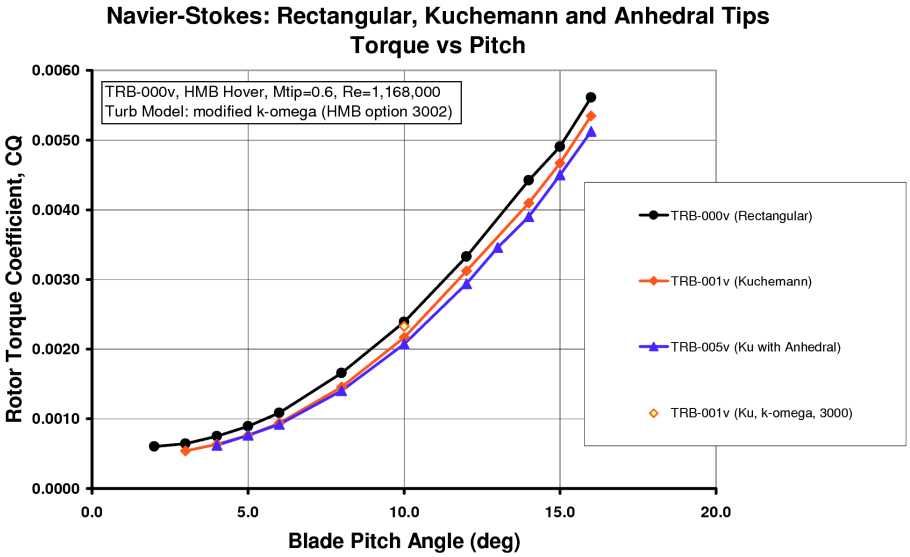

Figure 223: Comparison of Steady Navier-Stokes Torque-Pitch Predictions for the 3 Tip Shapes, TRB-000v (Datum, Rectangular), TRB-001v (Küchemann) and TRB-005v (Küchemann with Anhedral), Computed Using HMB with a Modified k-ω Turbulence Model, Mtip=0.6

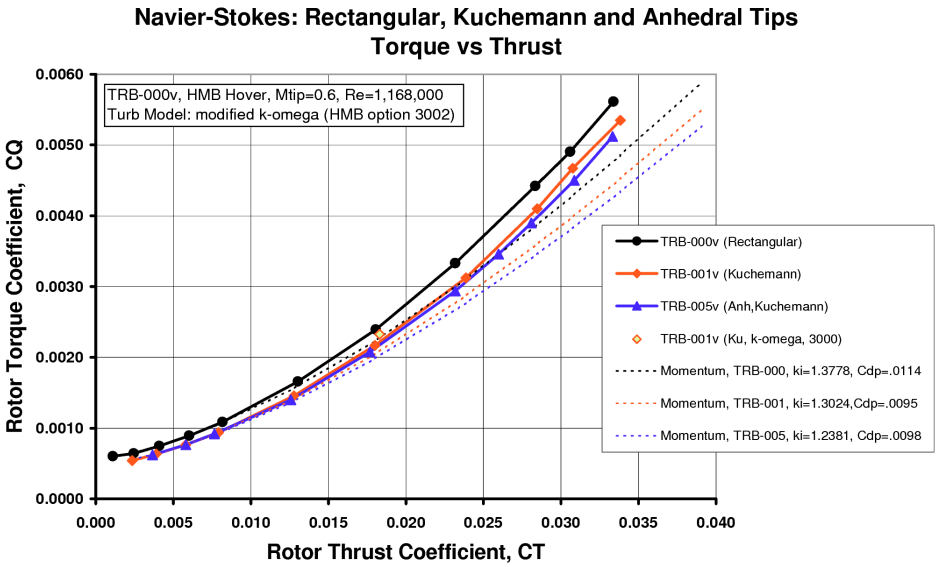

Figure 224: Comparison of Steady Navier-Stokes Torque-Thrust Predictions for the 3 Tip Shapes, TRB-000v (Datum, Rectangular), TRB-001v (Küchemann) and TRB-005v (Küchemann with Anhedral), Computed Using HMB with a Modified k-ω Turbulence Model, Mtip=0.6

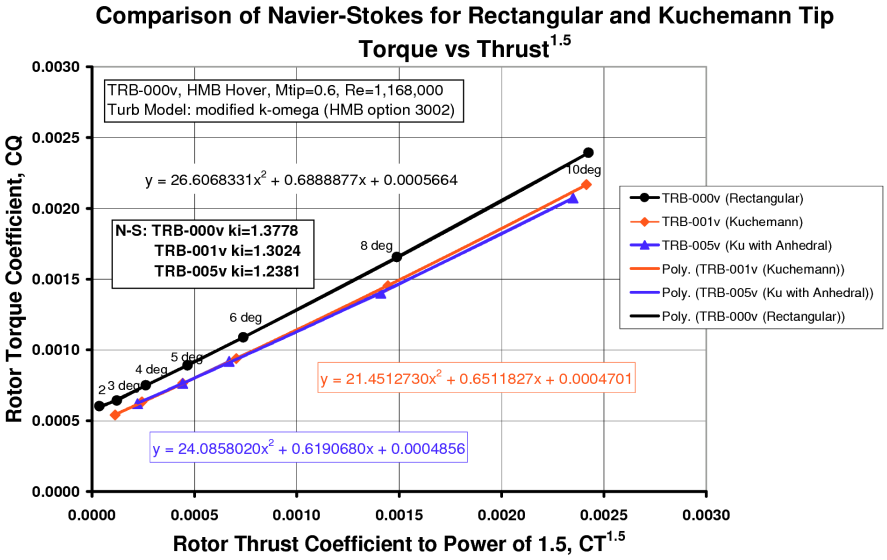

Figure 225: Comparison of Steady Navier-Stokes Torque-Thrust$_{1.5}$ Predictions for the 3 Tip Shapes, TRB-000v (Datum, Rectangular), TRB-001v (Küchemann) and TRB-005v (Küchemann with Anhedral), Computed Using HMB with a Modified k-ω Turbulence Model, Mtip=0.6

	A	B	C	ki	CDe
TRB-000	26.6068331	0.6888877	0.00005664	1.3778	0.0114
TRB-001	21.4512730	0.6511827	0.00004701	1.3024	0.0095
TRB-005	24.0858020	0.6190680	0.00004856	1.2381	0.0098

Table 7: Results of Quadratic Curve Fit to Determine the Induced Power Factor and Effective Profile Drag Coefficient from the Navier-Stokes Predictions for the Model Rotor with 3 Different Tip Configurations.

Equation 29, were obtained as shown on the graph, and tabulated below. Compared with the Euler results, the first coefficient (controlling the growth of the induced power factor with thrust) is now larger, but still within reasonable bounds, and suggests some gradual growth in either induced or profile power with thrust. The induced power factor, k_i, is again taken to be twice the slope of the curve fit (at zero thrust), while the profile power, CDp_o (also at zero thrust) is obtained from the constant term of the curve fit. An alternative least-squares curve fitting method was also used to verify the coefficients, since the k_i for TRB-005v seemed rather low. However, the first coefficient is almost as high as for the datum blade, and the slope, and hence the 'efective' induced power factor, calculated at, say 10degrees, is similar to that for TRB-001v. This non-linear increase is probably due to changes in profile power. The results of the curve fitting process and the values of k_i and CDp_o are given in the following table:

The benefits on induced power arising from the use of an enhanced tip shape is therefore about 5.5% for the Küchemann tip compared to the datum, and the anhedral tip provides a further 4.5% benefit (at zero CT). However, using the slope of the CQ-CT^1.5 curves at, say 10degrees, gives a benefit of 7.6% for TRB-001v, and a further 0.7% for TRB-005v which is still 8.3% better than for the datum blade.

The zero-CT equivalent drag coefficient for the TRB-001v Küchemann tip blade is 16.6% lower than that of the datum blade, while the reduction for the anhedral blade, TRB-005v, was 14%. All these improvements

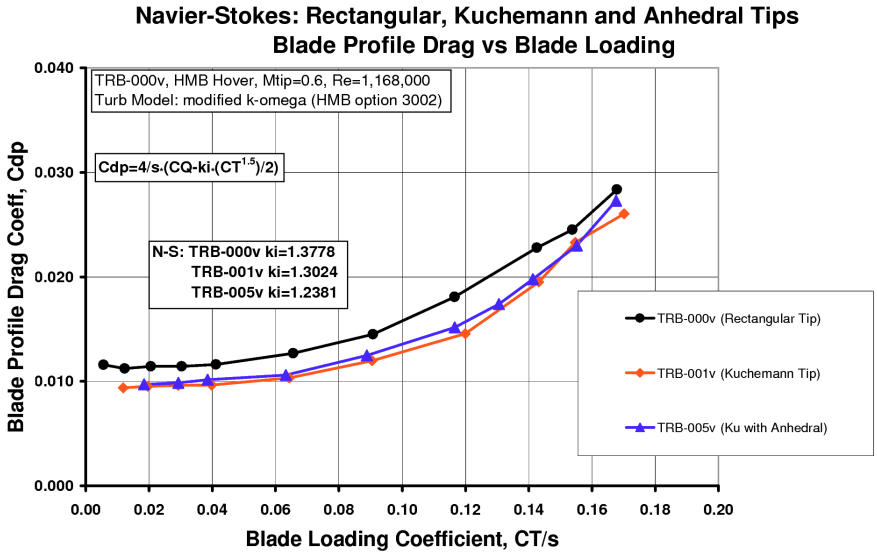

Figure 226: Comparison of Steady Navier-Stokes Profile Power Results for the 3 Tip Shapes, TRB-000v (Datum, Rectangular), TRB-001v (Küchemann) and TRB-005v (Küchemann with Anhedral), Computed Using HMB with a Modified k-ω Turbulence Model, Mtip=0.6

are quite substantial, considering they have been achieved by detailed design changes in the tip region.

These substantial performance improvements arise from simply rounding the leading edge corner of the tip and providing a tip outer edge around which the tip vortex can form cleanly. Compared to the earlier Euler results, the induced power benefits are greater for the flat Küchmann tip relative to the datum blade (the reduction in k_i has increased from .027 to .055), while the change in k_i due to anhedral was similar (the reduction in k_i decreased slightly from .070 to .064). The additional benefits would appear to be brought about by the Küchemann-type tip shape cleaning up the viscous separations at the tip edge and thus reducing the drag of the tip, in addition to favourably influencing the induced power.

The benefits in profile power are shown in Figure 226, plotted against the blade loading coefficient, CT/s. The results shown were obtained from the difference between the total torque and the induced torque, as given by the linear term of the curve-fit described above. Hence the effective profile drag coefficient presented here may also include a small amount of thrust-dependent drag, but probably the greatest effect is associated with the non-linear growth in blade profile drag at low Reynolds numbers. If this drag curve for the rotor is compared to that in the right hand part of Figure 222, which shows the predicted variation of aerofoil profile drag with lift coefficient, the assumption of this being mainly profile power seems reasonable (using the rule of thumb is that CL is approximately 3 times CT/s to make the comparison).

The effective blade profile drag coefficient in Figure 226 reflects the higher zero-lift drag coefficient of the datum, rectangular blade, compared to the Küchemann tip blades. The flat Küchemann blade was predicted to have similar, but slightly lower drag than the anhedral tip blade, perhaps as a consequent of closer spacing of the tip vortex for the anhedral blade, or additional drag due to the anhedral bend. Above about 8 degrees (CT/s=.10), the profile drag starts to grow more rapidly for the rectangular tip, compared to the Küchemann tips. The Kücheman tip blades have effective drag coefficients nearer to the 2D aerofoil predictions. The results in Figure 226 suggest that the rectangular tip blade may suffer drag due to adverse pressure gradients aft of the loading peak near the tip of the blade, whereas the rounding of the leading edge corner has suppressed this

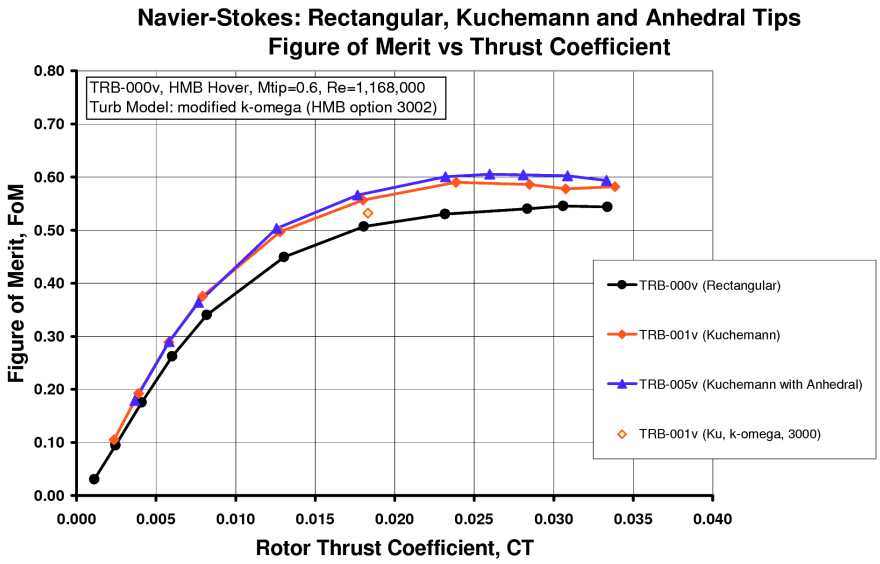

Figure 227: Comparison of Steady Navier-Stokes Figure of Merit Predictions for the 3 Tip Shapes, TRB-000v (Datum, Rectangular), TRB-001v (Küchemann) and TRB-005v (Küchemann with Anhedral), Computed Using HMB with a Modified k-ω Turbulence Model, Mtip=0.6

tendency for the Küchemann tip. The rectangular blade may also suffer a drag penalty due to edge separations, whereas the Küchemann-type tips allow the tip vortex to roll-up more cleanly.

As the blade loading increases further (for pitch angles 14-16 degrees), the trends in profile drag become a little less clear. The results in these important operating conditions for the tail rotor will be considered again later.

Re-plotting the results in terms of the Figure of Merit also reflects the benefits of the Küchemann tip blades, and shows that the best Figure of Merit is obtained for the anhedral blade, TRB-005v, as shown in Figure 227. For the example model tail rotor the peak Figure of Merit for TRB-005v is about 0.6, closely followed by the flat Küchemann tip, TRB-001v, at about 0.59, while the datum blades of TRB-000v only reach a Figure of Merit of about 0.54. The Figure of Merit is a sensitive measure of rotor performance and it is good to note that these results are quite realistic for the example model rotor. These values of Figure of Merit are in line with those found from the model rotor tests data, presented earlier in Section 3.4. The Figure of Merit is starting to flatten off at thrust coefficients in the region of 0.025 to 0.030, corresponding to pitch angles in the range 13 to 16 degrees. Depending on the reliance placed on the last few predicted points, it could be that the performance is be starting to fall-off as the onset of stall is approached. For an untwisted tail rotor blade, with a NACA 0012 aerofoil at relatively low Reynolds number, the onset of tip stall may be anticipated to follow the drag divergence already observed although, as will be discussed later, some of the variability in the last few points may arise for other reasons, and the stall onset may occur post 16 degrees.

Finally, the predicted pitching moments are plotted in Figure 228. The cases for the datum blade were run first, and a problem with the integrated moments meant that the results had to be replaced with results from Rotor-Analyser (see Appendix G) after post-processing. This problem was corrected for the remaining cases, and the results for TRB-001v and 005v are taken from the integrated output of the solver (after adding a very small viscous term and scaling appropriately). Some variation was found at very low pitch, and this could be a consequence of grid distortions (as mentioned earlier) affecting this very sensitive parameter. As exhibited by

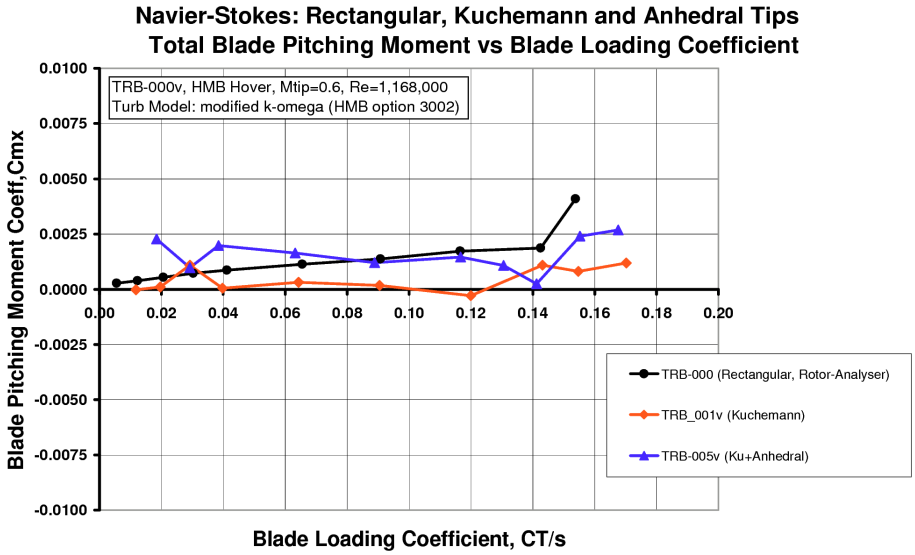

Figure 228: Comparison of Steady Navier-Stokes Total Blade Pitching Moment Predictions for the 3 Tip Shapes, TRB-000v (Datum, Rectangular), TRB-001v (Küchemann) and TRB-005v (Küchemann with Anhedral), Computed Using HMB with a Modified k-ω Turbulence Model, Mtip=0.6

the datum blade, a slight nose-up moment may be expected, following the predicted and measured trends for the NACA 0012 aerofoil in these conditions (as illustrated in Chapter 3). The resulting moments also depend upon how quickly the forward loading peak develops near the tip of the blade, compared to amount of suction produced beneath the tip vortex on the outer edge of the blade. The total blade pitching moments about the blade 1/4-chord reference axis show that the aerodynamic loads approximately balance out to leave a relatively flat gradient and the magnitude of the pitching moments remain quite small in most hover conditions, with those for TRB-001v being particularly close to zero. At the higher pitch angles, the convergence was less straightforward. The pitching moment, CMx, was the slowest to settle and in some cases can show small oscillations which probably accounts for the lack of smoothness in the results and, as discovered later, was linked to changes in the induced flowfield which occur near the root of the blade at the higher pitch angles.

The Navier-Stokes predictions just described have revealed some significant performance improvements for the Küchemann-type tips, and have also confirmed that anhedral provides a further small benefit for this example tail rotor in hover. In order to provide further insight into the reasons behind these improvements, the surface pressure data is now used to examine the aerodynamic loading. This information may be obtained by taking sections along the blade so that the resulting chordwise pressure distributions can be integrated to give the force coefficient, Cz, in the thrust direction, together with the pitching moment, Cm. From these non-dimensional (2D-like) coefficients, a loading distribution may be derived by simply multiplying by the radius squared and the local chord ratio (or the local chord-ratio squared in the case of the moments), since the blade velocity is proportional to the radius. Therefore the distribution of Cz, and the loading distribution, $Cz.(c/co).x^2$, look considerably different due to the radial weighting and chord taper, as does the pitching moment, Cm, and $Cm.(c/co)^2.x^2$. All four distributions are given for the 3 tip shapes, in Figures 229 to 232. The load distributions presented here are for pitch angles between 4 and 12 degrees, where the cases were well converged, although not all the flowfield data (.plt files) were retained for each case. In some instances, at 10 or 12 degrees pitch some variation is apparent in the loading at the root of the blade. The reasons for this will be discussed in the next section.

6.2.2 Loading Distributions

Figure 229 compares the non-dimensional sectional thrust-force coefficient, Cz, distributions for the three different blades. As observed from the previous Euler computations, there is a loading spike at the tip of the blade that originates from the vortex formation over the outer edge of the tip. Just inboard of this (near the start of the shaping for the Küchemann tip) the aerodynamic loading reaches a maximum at about 94%R and is again influenced by the tip shape. The Cz given here also includes the effect of the tip (and root) chord tapering in the extreme tip region (since this coefficient is based on the local chord). The loading distribution in the next figure allows for this and also includes the velocity-squared weighting. As for the earlier comparisons in Chapter 5, the effect of anhedral is to reduce the loading in the tip region and increase it slightly in the middle-outer region of the blade. For the anhedral blade, there is a noticeable dip in the non-dimensional loading at about 96%R near the blended anhedral crank.

The actual airloads distribution is shown in Figure 230, and hence the loading spikes in the tip and root regions do not appear as dramatic as they did on the first set of graphs. Also the differences in the root region are less apparent. The loading peak in the tip region is clearly greater for the datum blade, TRB-000v, than for the Küchemann tip blades, TRB-001v and TRB-005v, and this peak also blends into the tip-edge loading spike. The peak in loading due to the upwash of the vortex from the preceding blade is noticeable, particularly for the anhedral blade, TRB-005v, at the higher pitch angles.

Figure 231 presents the non-dimensional sectional pitching moment coefficent. Note the very large negative peaks at the tip, due to the tip vortex (magnified by the reducing chord), and the effect of the leading edge loading peak in the 80-95% region which gives a balancing nose up moment. Inboard, the pitching moment dips negative before rising steeply near the root, but note that about half of this loading peak is due to the sudden chord reduction in the root region. This peak and dip near 40 to 50% radius is the effect of the circulatory induced flow near the root of the blade, and will be discussed further in the next section of this thesis.

When multiplied by the radial velocity-weighting and chord ratio, as in Figure 232, the moments at the root of the blade are seen to make only a small contribution to the total blade moments. Far more important is the balance between the nose-up loading further outboard and nose-down spike at the tip. The results presented in Figure 232 confirm that the datum blade has a slightly stronger nose up moment than the Küchemann tip blades, consistent with the trend of the total pitching moment shown earlier in Figure 228.

The Navier-Stokes predictions presented above have revealed a significant performance improvement, and the reasons for this have been explained by examination and analysis of the integrated results from the solver and an examination of the blade loading obtained from the surface pressure information. Changing to a more refined Küchemann-type tip shape, TRB-001v, provided a 5.5% reduction in induced power together with a reduction of about 16% in profile power, equivalent to a 5 point improvement in peak Figure of Merit. The addition of anhedral (to a blade with a Küchemann tip) also brought about a further 4.5% reduction in induced power factor (at zero-CT) and the profile drag was similarly low (14% better than the datum blade at zero-CT), although the growth in profile drag was a little more rapid than for the flat blade. Compared to the datum rectangular blade, the anhedral Küchemann tip achieved an extra 6 points in Figure of Merit.

For a tail rotor, the manner in which the profile power starts to diverge more rapidly near the onset of stall is also an important feature of any new tip design, and one of the aims of this research was to investigate this further. Unfortunately, convergence at higher pitch angles was found to be more difficult, and the reasons for this are discussed in the following section, before presenting further analysis of the results that were obtained from steady Navier-Stokes simulation at higher pitch angles.

6.2.3 Vortex Trajectories - Comparisons of Euler and Navier-Stokes

In this section of the thesis, the vortex location in the wake are examined. Firstly the Euler results obtained earlier are compared to Navier-Stokes and secondly the effect of tip shape on the vortex trajectories is obtained by comparing extracted locations from Navier-Stokes solutions. All the comparisons presented here were obtained from computing the vorticity magnitude using Tecplot as a post-processing tool. [15]

[15]The Tecplot add-on for λ_2 developed in the CFD lab at Liverpool only became available after most of the wake comparisons presented here had already been made. However, as shown by the comparison with the model rotor tests which were presented in

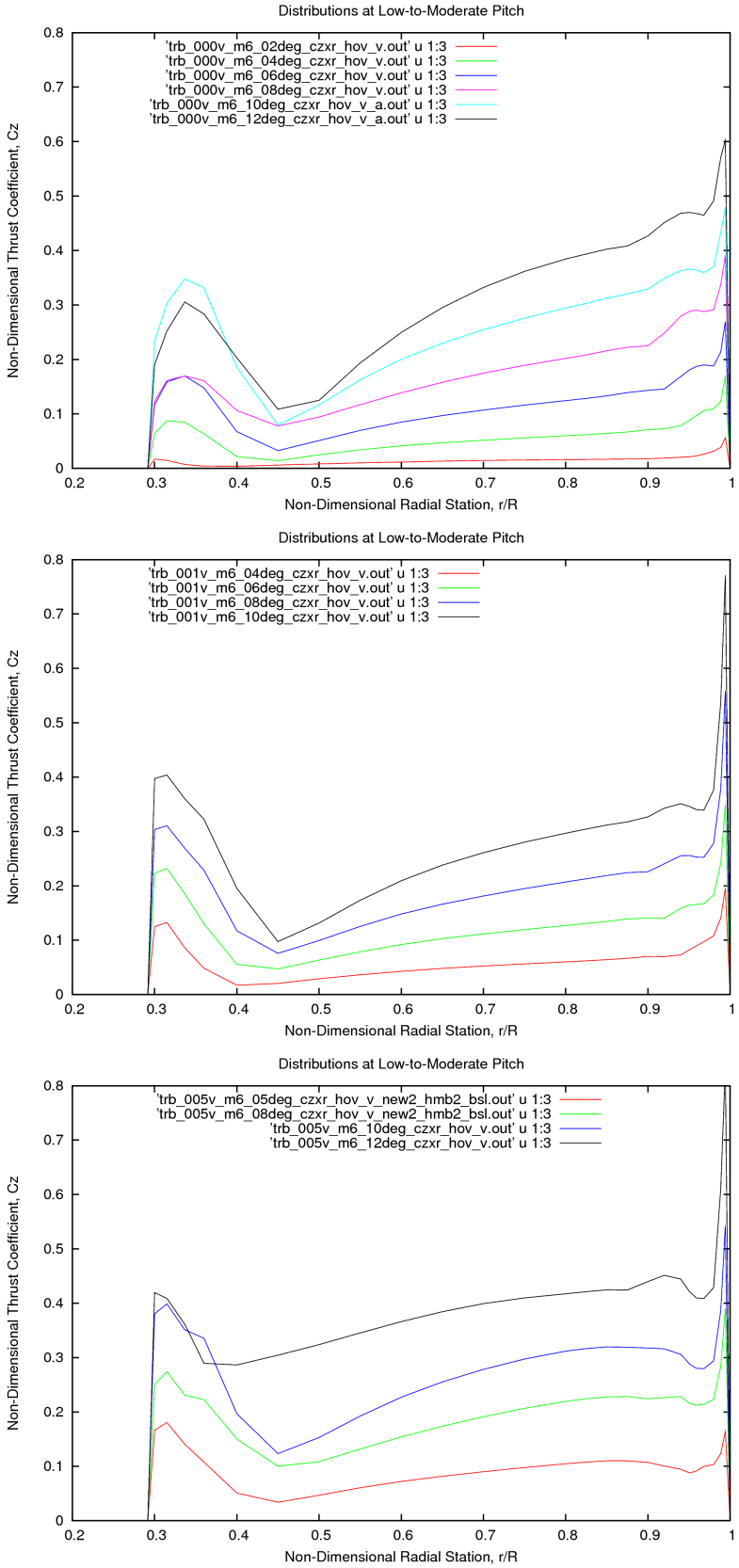

Figure 229: Predicted Thrust Coefficient Distributions for the 3 Tip Shapes at Low-to-Moderate Pitch, TRB-000v (Datum, Rectangular), TRB-001v (Küchemann) and TRB-005v (Küchemann with Anhedral)

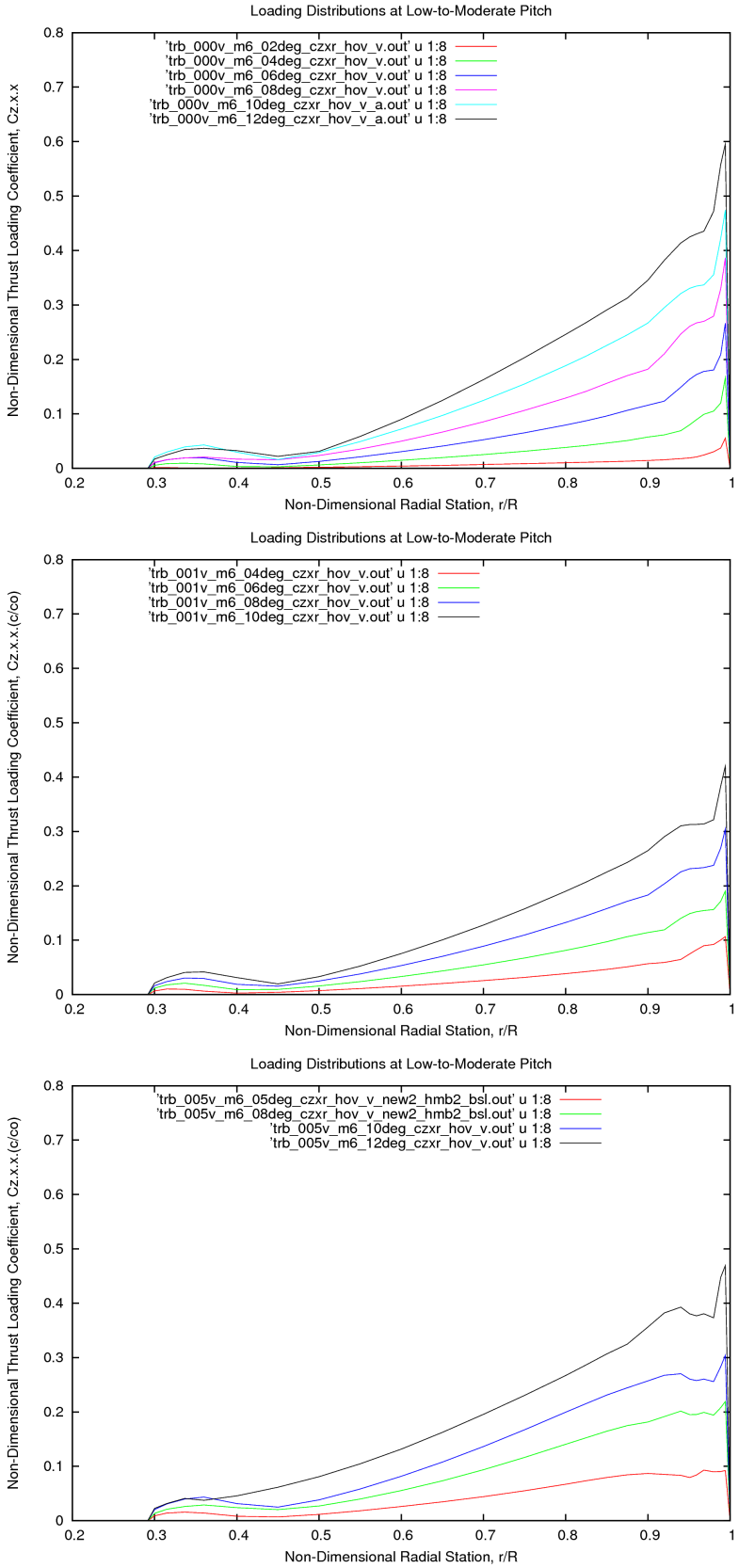

Figure 230: Predicted Thrust-Loading Distributions for the 3 Tip Shapes at Low-to-Moderate Pitch, TRB-000v (Datum, Rectangular), TRB-001v (Küchemann) and TRB-005v (Küchemann with Anhedral)

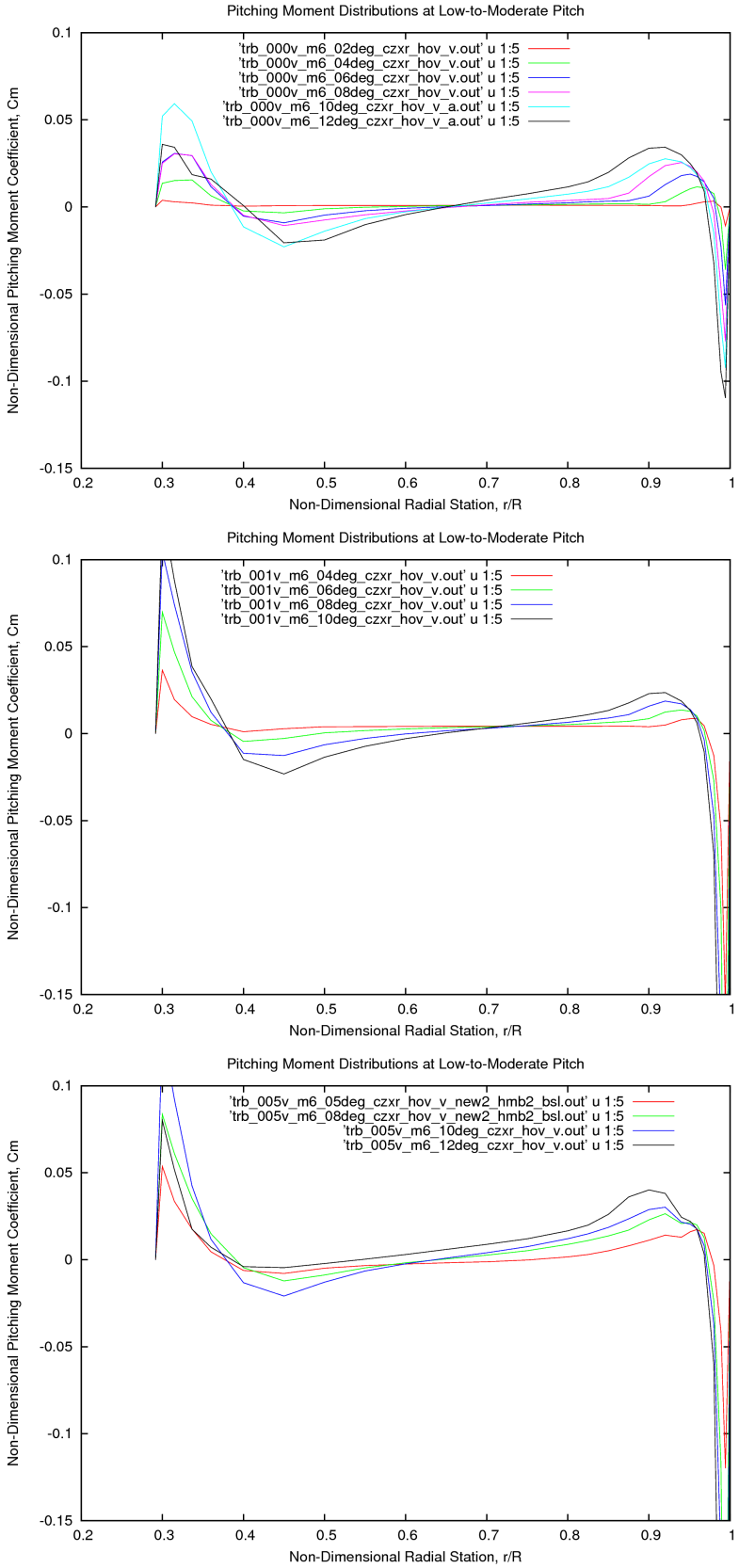

Figure 231: Predicted Pitching Moment Coefficient Distributions for the 3 Tip Shapes at Low-to-Moderate Pitch, TRB-000v (Datum, Rectangular), TRB-001v (Küchemann) and TRB-005v (Küchemann with Anhedral)

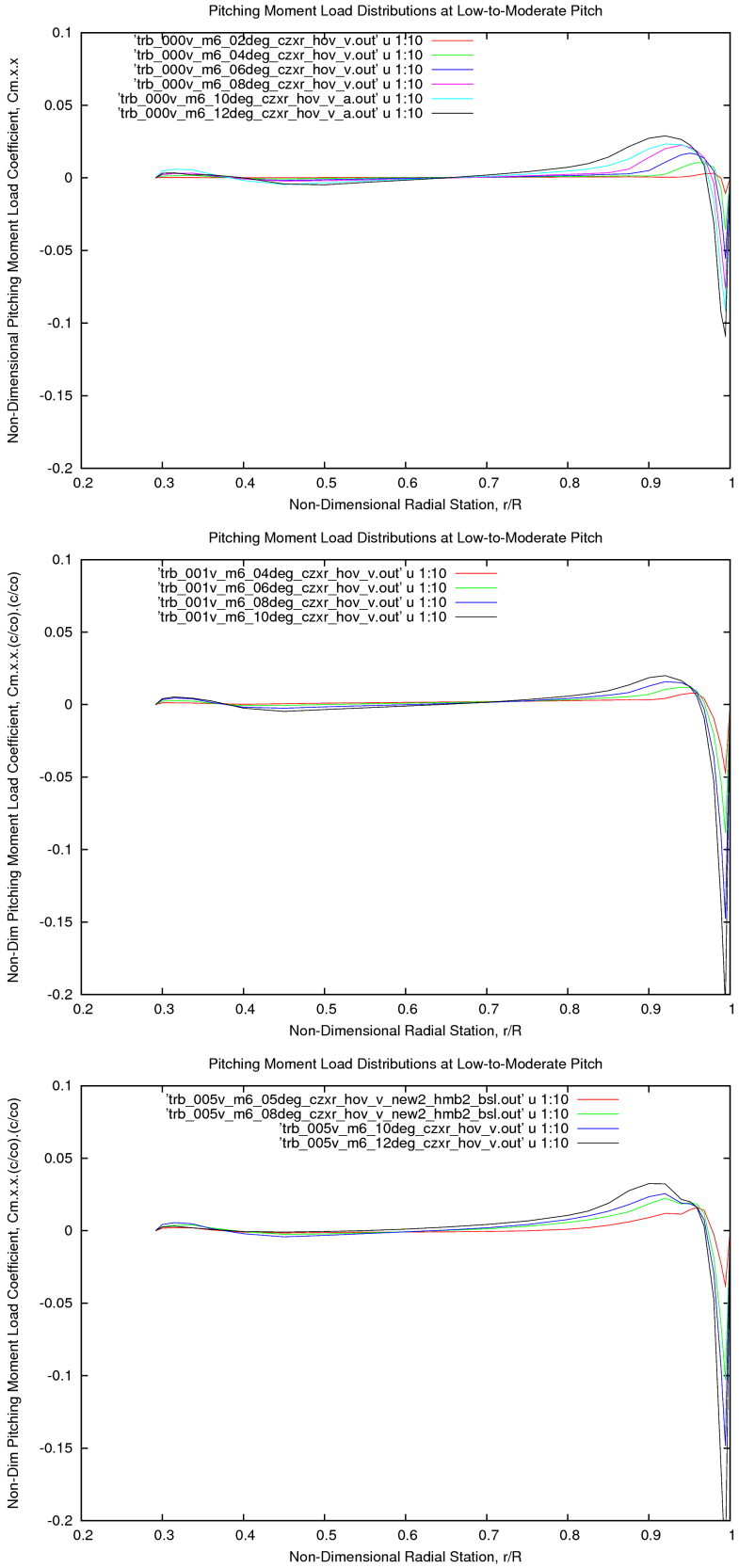

Figure 232: Predicted Pitching Moment Load Distributions for the 3 Tip Shapes at Low-to-Moderate Pitch, TRB-000v (Datum, Rectangular), TRB-001v (Küchemann) and TRB-005v (Küchemann with Anhedral)

In general, the Navier-Stokes wake lies outside that initially predicted by Euler, suggesting that the final contraction achieved in inviscid flow is not now possible due to viscous energy losses in the flowfield. It might also be argued that part of this difference could be due to the fact that these trajectories are compared at the same geometric pitch, and are therefore not at the same thrust. On average, the inviscid Euler solutions generate about 8% more thrust for a given pitch than obtained from the Navier-Stokes simulations, and this translates to an increase of about 4% in the mean downwash. However, the vertical displacement is generally less for the Euler case than found from a Navier-Stokes solutions, perhaps because of the way the vortex forms and trails from the tip of the blade where viscous effects are significant. After the first blade interaction (in this case at 90 degrees of vortex age) the vortices then descend at a similar rate. These trends have been observed in all cases where Euler and Navier-Stokes comparisons have been made.

The wake trajectory, and the separated vertical displacement and contraction trends are shown for the 0.25c wide, flat, Küchemann Tip, TRB-001, in Figure 233. The general features outlined above are visible in the wake and, particularly for the viscous case, the tip vortex descends more rapidly after about 10 degrees. After 90 degrees the Navier-Stokes results show a reduced contraction and a smoother transition towards an ultimately similar vertical displacement.

Figure 234 for the 20deg anhedral Küchemann tip shows a similar picture, although here the Euler results stay remarkably flat in the first 90 degrees, while Navier-Stokes shows a greater spacing between the following blade and the tip vortex. Again the ultimate contraction is less for the Navier-Stokes case (as it probably is in reality), while the final descent rate is similar. Thus the close proximity of the tip vortex to the anhedral blade which was previously observed in the Euler results is now perhaps of less concern, and for both the flat and anhedral Küchemann tips the viscous results show the blade/vortex spacing at ψ=90 to be about 0.025 to 0.03R (or 0.16 to 0.19 chords) greater than before (for the 10 degree pitch case), which is quite a significant change.

6.2.4 Vortex Trajectories - Navier-Stokes - Effect of Tip Shape

In this sub-section, vortex trajectories from the Navier-Stokes results are compared for the selected tip shapes. Firstly, the effect of changing from the square-cut rectangular tip of the datum blade, TRB-000v, to a 0.25c wide Küchemann tip (without anhedral), TRB-001v, is considered. This is followed by a comparison between the flat blade, TRB-001v, and the 20deg anhedral blade, TRB-005v, which both have the same style of Küchemann tip.

Interestingly, the wake for the rectangular tip blade lies inside the wake trajectory for the flat Küchemann tip blade, as shown in Figure 235. The differences in these Navier-Stokes comparisons are now smaller than seen previously between the Euler and Navier-Stokes results, and perhaps opposite to what might be expected from a knowledge of the relative performance of these tips. Both blades have a trailing edge which extends to the outer tip edge and the main difference is in the rounding of the leading edge corner. In extracting the vortex positions, it was observed that the tip vortex of the Küchemann tip tends to form further aft on the tip and therefore starts-off slightly lower, and also has slightly less initial contraction. Within about 20 degrees of azimuth the contractions become similar, while the tip vortex of the Küchemann blade remains very slightly lower, and remains so at the interaction with the following blade. Following this interaction, the vertical displacements become similar until at about 135 degrees the (second) rate of descent shows a small difference. A difference is also noted in the contraction for vortex ages greater than about 200 degrees. In these regions, the Küchemann tip has the greatest rate of descent and the least contraction. As found in Chapter 5, and discussed again earlier in this Chapter, the Küchemann tip has a lower induced power than the datum blade.

The effect of anhedral on the vortex wake trajectories (for blades having the same outer tip shape) is shown in Figure 236, where wake information is compared for TRB-001v and TRB-005v. In this case the wake trajectories cross-over due to the vortex from the anhedral tip starting off lower in the wake. The tip vortex from the anhedral blade remains fairly level in the wake for the first 45 degrees of azimuth, and then starts to descend at a similar, but slightly lower rate such that by 90 degrees it is slightly higher in the wake

Chapter 3, there appears to be little to choose between the two methods away from the immediate vicinity of the blade, for vortex ages of less than about 180 degrees, although the λ_2 method is probably preferable when the vortices are starting to diffuse in the second half-turn of the wake (although here they have less influence on the rotor).

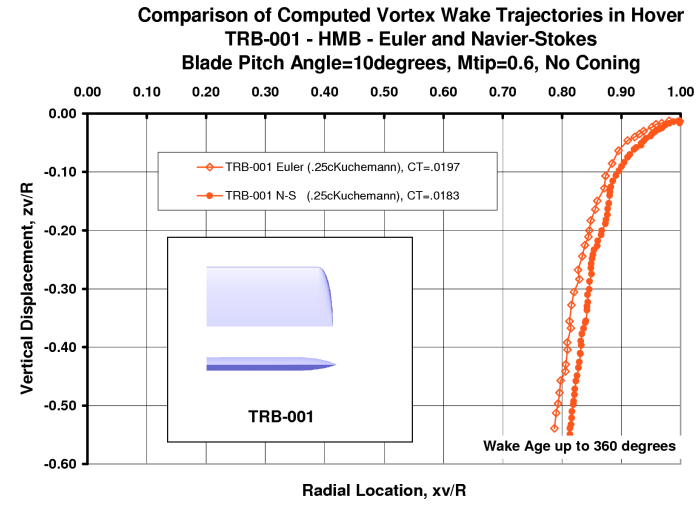

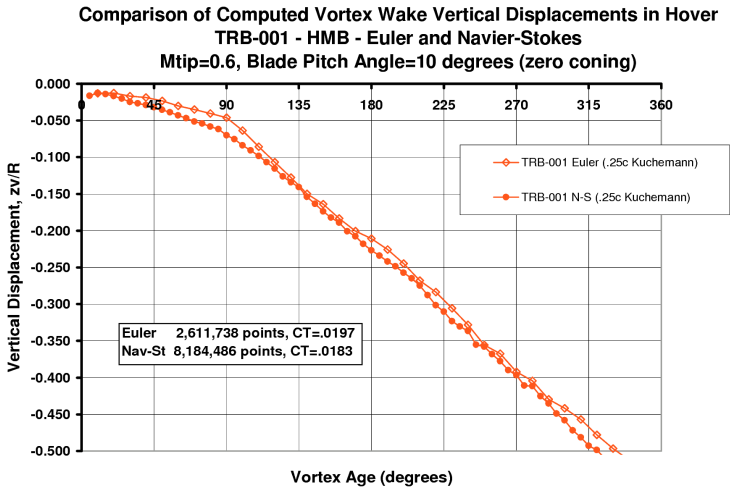

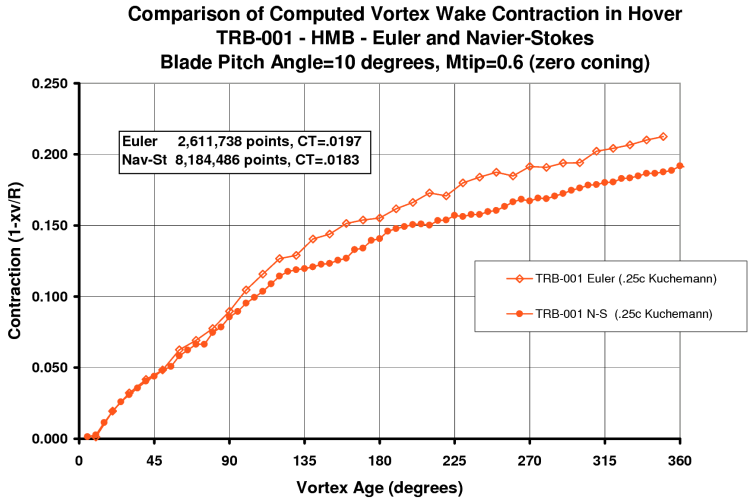

Figure 233: Vortex Trajectories from Euler and Navier-Stokes Predictions for the Flat Küchemann Tip, TRB-001 (Mtip=0.60). The Viscous Solution shows Similar Initial Contraction, Less Final Contraction and Increased Vertical Displacement.

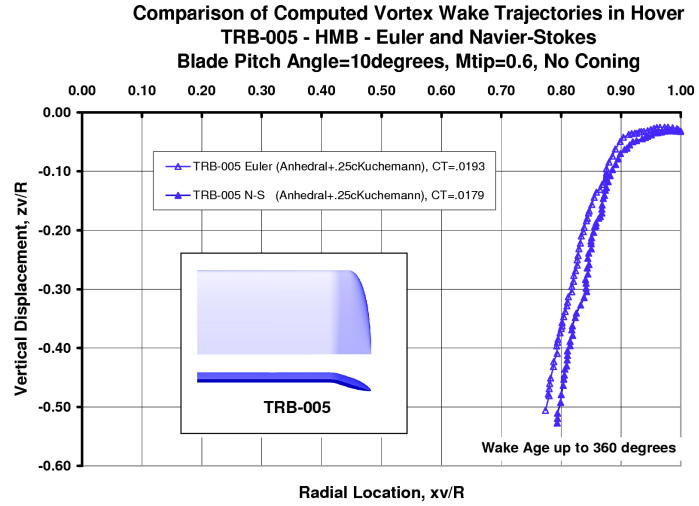

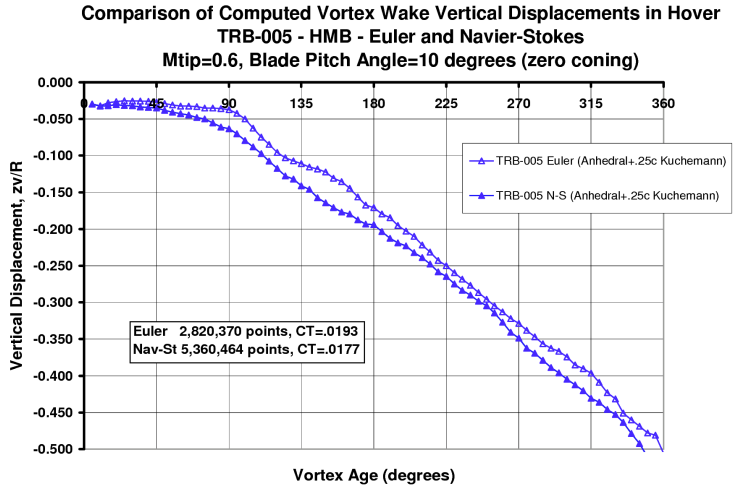

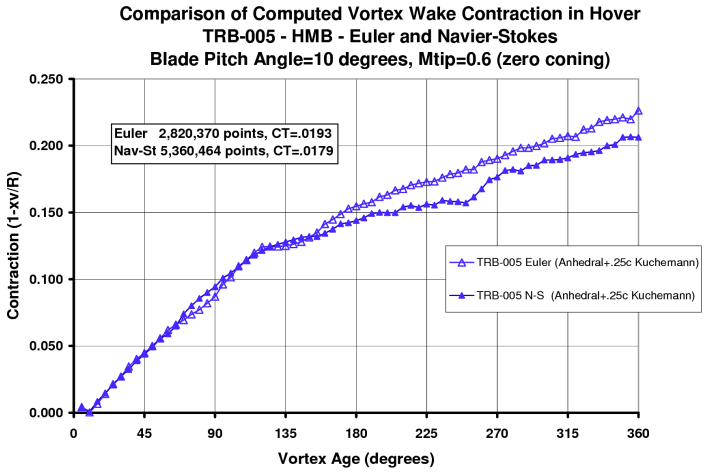

Figure 234: Vortex Trajectories from Euler and Navier-Stokes Predictions for the 20deg Anhedral Küchemann Tip, TRB-005 (Mtip=0.60). The Viscous Solution shows Similar Initial Contraction, Less Final Contraction and Increased Vertical Displacement.

and therefore in closer proximity to the blade (but by only about .01R, or .06 chords) with a small increase in contraction. Following the interaction with the following blade at ψ=90 degrees, the two trajectories show similar rates of descent and (between 180 and 260 degrees) similar rates of contraction. In the final half turn, the anhedral blade shows a greater final contraction and a lower rate of descent.

Inspection of the vortex trajectories for TRB-000v compared to TRB-001v and TRB001v compared to TRB-005v have revealed some interesting trends. Compared to the Euler predictions of the previous chapter, the difference in vortex location at the first blade passage is here shown to be much smaller when viscosity is taken into account, although the underlying trends are basically the same. It is concluded here that small changes in the vortex trajectories near to the blades are directly linked to the tip shape, and these effects also change the way in which the wake then continues to develop.

It is also worthwhile mentioning here that the Navier-Stokes predictions of the rotor flowfield provide a wealth of information that may be useful for the construction and verification of more traditional lower-order vortex-wake models. For instance, the vortex sheet trailed by the blades can also be seen in the wakes and even the double regions of vorticity stemming from the upper and lower boundary layers of the blades were clearly visible. The slope of these sheets, and the manner in which they curl up at the ends as the tip (and root) vortices detach from them, could also be extracted from the CFD solutions, together with information about the root vortex (once issues with stabilising the wake have been resolved). This information should be helpful in fine tuning prescribed vortex wake models, or could be used to compare with and hence verify the results from a free-wake analysis, such that small changes due to blade design may be better represented.

In the future, CFD has the potential to evaluate the performance in near-hover conditions when the wake may not be entirely symmetrical and large distortions of the vortex wake may be present during low speed manoeuvres and transitional flight. This is an area where accurate vortex wake measurements are more difficult to make, since the wake geometry is more complex than in forward flight. Application of CFD in these complex flow regimes may help to provide a better understanding and prediction of the effect of hovering in a natural environment rather than the idealised axi-symmetric hover simulated here. To do this an unsteady approach would be required, and some of these aspects are discussed in Chapter 8.

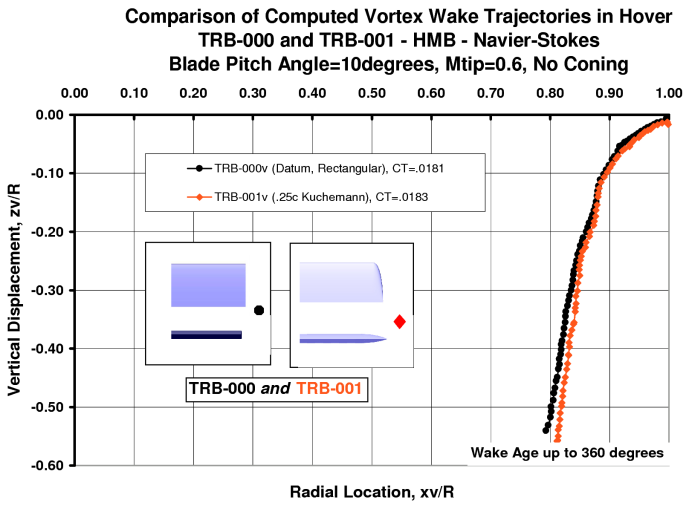

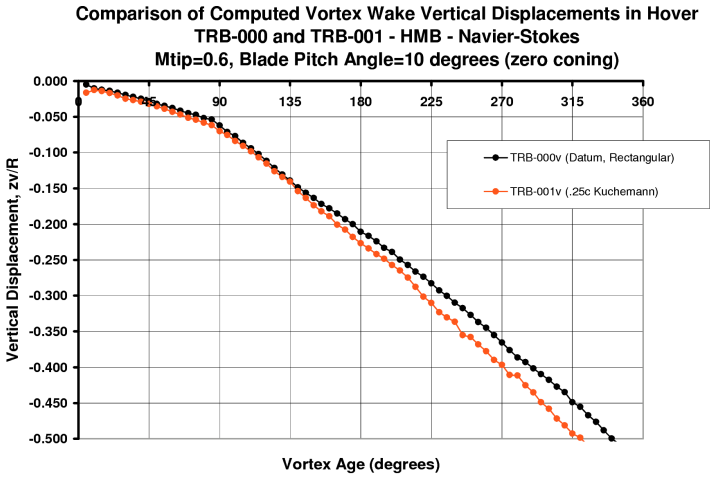

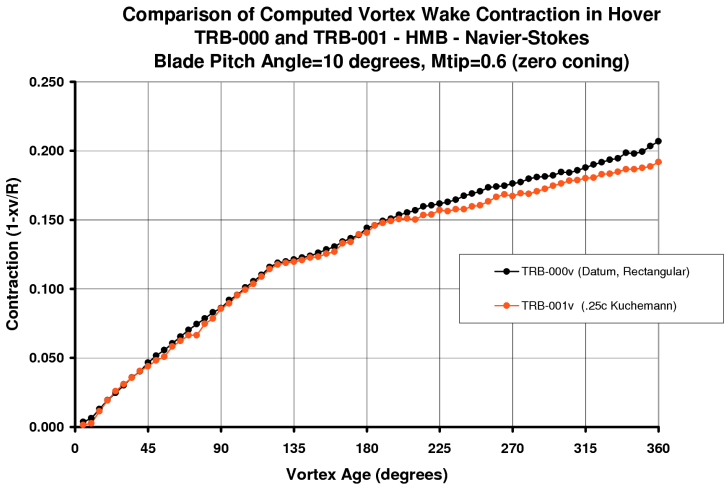

Figure 235: Vortex Trajectories from Navier-Stokes Predictions for the Datum Rectangular Blade, TRB-000v, and Flat Küchemann Tip, TRB-001v (Mtip=0.60). Compared to the Datum, the Küchemann Tip shows Similar Initial Contraction, Less Final Contraction and Increased Vertical Displacement.

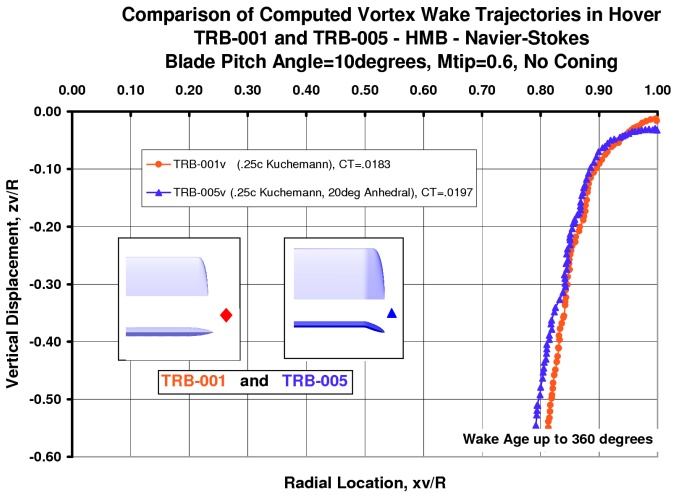

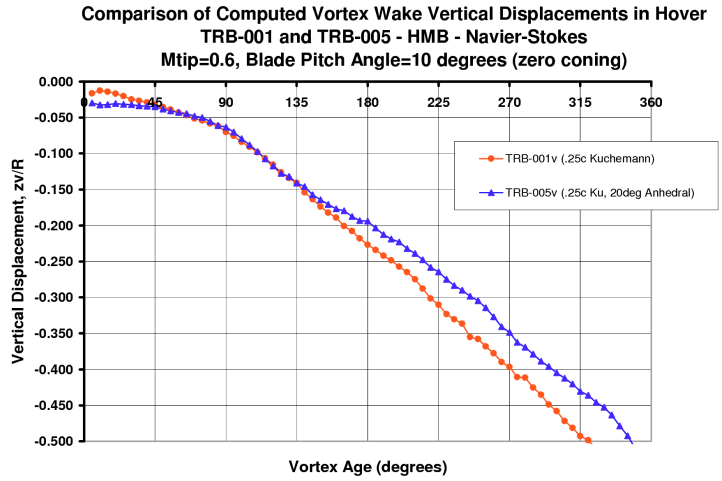

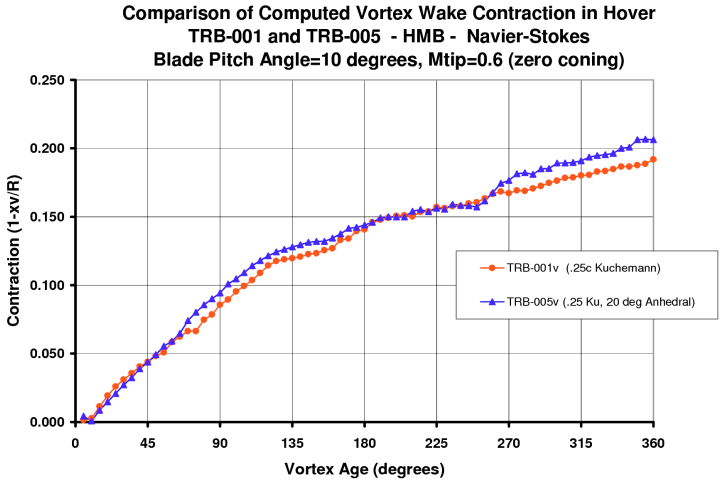

Figure 236: Vortex Trajectories from Navier-Stokes Predictions for the Flat Küchemann Tip, TRB-001v, and 20deg Anhedral Küchemann Tip, TRB-005 (Mtip=0.60). Compared to the Flat Küchemann Tip, TRB-005v shows Similar Contraction, Starts Lower, Passes Slightly Closer, and exhibits Less Final Vertical Displacement.

6.3 Flowfield Variations at High Pitch Angles

Since the tail rotor spends much of its time operating at relatively high pitch angles in hover (and during manoeuvres) it was always the purpose of this research project to compare, if at all possible, the selected tip shapes at high thrust conditions approaching the stall. Of particular interest to the rotorcraft design engineer is the point at which the profile power starts to diverge and it was hoped that at least this condition could be reached using a steady state Navier-Stokes solution (to avoid the prohibitively high computational expense of attempting comparisons using an unsteady approach).

An initial concern was that as the flow starts to separate at higher angles (initially near the tip for untwisted tail rotor blades) the solution may not converge as well as it did at low pitch, and fluctuations may start to occur in the integrated loads. It was expected that the HMB solver would respond to these flow oscillations, and the need for an unsteady solution to cope with the stall was anticipated. While these concerns appear to be well founded at very high pitch angles, an unexpected flowfield change occurred at more moderate pitch angles due an upwash in the central region of the rotor causing a re-positioning of the root vortices, and thereby influencing the induced flow (downwash) over the inboard part of the rotor. This change in flow state was unexpected, and greatly prolonged the analysis time and raised many concerns over the results which took time to fully understand. Many grid refinements and repeat-runs were undertaken before it became apparent that the problem was perhaps related to the configuration of the tail rotor and simplifications made in the hub region. The use of a long slender cylindrical hub, rather than a representative hub, together with a large root cut-out and zero-twist blade were probably the underlying cause of the flow initially moving upwards in the central region of the rotor, and then suddenly changing as the root-vortex re-formed below the rotor. This problem is probably independent of the solver used, although HMB has third-order spatial accuracy and so fully captures all features of the flow. Also the nature of the multi-block grid provides many small cells in the central region which also help to resolve, rather than smear the flow, and interactions between the root vortical flow and the cylindrical hub itself cannot be ruled out.

Two factors, which were not fully appreciated at the outset of this research also made the task of computing rotor performance at high pitch more difficult than it might otherwise have been. Firstly, while it was logical to continue to use the datum blade from the WHL model tail rotor as a basis for comparisons, Navier-Stokes computations were started at a model scale Reynolds Number and, even taking into account a tip Mach number of 0.6, typical of a modern tail rotor, the tip Reynolds Number is only 1,166,800. This value was retained for all subsequent cases to allow direct comparisons. This value of Reynolds number is about half that of a full-scale old-style narrow-chord tail rotor, but a modern tail rotor with a low R/c blade and perhaps a slightly higher tipspeed may operate with a Reynolds number up to about 4 times greater. Thus there was an expectation that separation may occur earlier on the model rotor. Secondly, the example blades considered here were chosen to have zero twist in order to simply focus on the tip shape question. In retrospect, some twist would have been useful to help to suppress the onset of stall near the tip, and would perhaps have also delayed the problems encountered beyond the the most critical angles near 16 degrees, since the inboard loading would have been better maintained. [16]

In attempting to evaluate the tail rotor tip designs at high pitch conditions using a steady Navier-Stokes approach, various difficulties may be encountered. At low to moderate pitch angles, the solution initially appears to converge well and the thrust, torque and moments settle towards constant values (to better than 0.5% at low pitch, with perhaps up to 2% variation at 10 degrees pitch for the cases considered here). However, as the pitch is increased further there is a progressively greater tendency for flow separation to occur, or as eventually discovered for the present configuration, the state of the flow field in the central region of the rotor may change and this results in the solution slowly responding and drifting towards a higher thrust and torque level. Of course the performance of the rotor is very sensitive to any changes in the flowfield that induce changes in thrust and torque. In several cases it was found that the torque may become relatively low in relation to the thrust, at least at moderate pitch angles, suggesting a change in the induced power. At very high pitch angles, of 18-20 degrees, the solution may alternate more vigorously (with thrust changes up to about 10%) and it

[16] Recent use of HMB by the author at AgustaWestland (Yeovil) to evaluate the aerodynamic performance of a new tail rotor design (ie with a refined tip shape, moderate twist, a relatively small root cut-out and modern aerofoils), showed few problems with convergence until very high pitch angles were reached, since the onset of stall near the tip had been delayed until near the point of maximum manoeuvre thrust. Pitch angles in the region of 22 degrees (at 75%R) were achieved without difficulty, although some uncertainty was eventually found at 24 degrees and beyond [AW Internal Report, 2011]. This wide-chord tail rotor also operated at a relatively high Reynolds number which also helped to suppress separation.

becomes more difficult, if not impossible, to decide which level is valid. In fact, in a normal flow situation (like that for a 2D aerofoil, as considered in Chapter 3 for the stalling of NACA0012), if the residuals are not smooth and do not remain low and stable, then this is an indication that the flow contains an element of unsteadiness, suggesting that the results should be ignored and an unsteady solution should be used. However, for the rotor case the situation is not so simple and reasons for the changes first need to be identified.

Initially, many runs were stopped after the residuals reduced to acceptable low levels (preferably better than 10^{-5} for rotor cases) and the solution first appeared to settle to a reasonably constant value. However, as the pitch angle was increased, it became more difficult to know where to take the solution, and the run was then extended, or repeated. In many instances, since the data files were large, the intermediate results were not stored. Also, many runs had to be carried out remotely, with an unavoidable delay in obtaining the full datasets and, in the majority of cases, the final solution could not be compared to an earlier solution state if the latter had not been saved. Visualisation of individual cases did not necessarily reveal the problem which becomes more apparent when comparing the early and later flowfields.

Another concern was that the wake below the rotor did not always connect to the far field outlet, but this in itself probably made little difference to the results.

In order to illustrate some of the problems encountered, some examples of convergence histories are shown in Figure 237 for steady Navier-Stokes cases at 15 degrees of pitch for each of the 3 tail rotor blades, TRB-000v, 001v, and 005v (the 'v' simply denotes that these were indeed viscous runs). Irrespective of the tip shape, the residuals do not settle to a particularly low level and show a tendency to fluctuate (although the flow residuals reduce to about 10^{-5} and the turbulence residuals fall below 10^{-6}). However, the varying nature of the integrated forces and moments histories suggests that the flowfield is still changing (while the viscous skin friction terms vary less). In addition to the standard runs carried out with HMB-1.4 (CFL=1), a recently repeated and extended case has been included here for TRB-000v using HMB-2.0, now able to run with CFL=3 (which explains why the integrated load monitors appear slightly out of phase with the earlier runs, and the stable states appear to be more transient), but this is of no consequence to the main argument being pursued here. Experience has shown that converged results from the new solver usually confirm earlier results. This recent data is utilised here because the full flow field data is available at a series of intermediate steps for TRB-000v. There is also one set of intermediate and final results available for TRB-005v, but the first data was stored just after the first solution stage is reached (these results will be included later).

It must be emphasised that all the convergence histories for the integrated loads presented in Figure 237 are plotted on deliberately expanded vertical scales (and contracted horizontal scales to include an unduly large number of iterations), such that even quite small variations in the loads may appear very large. Conversely, when a smooth level trace is seen with these expanded scales it is reassuring that the solution is particularly well settled and the loads are absolutely constant. It should also be noted that some of the outputs are from pressure integrations (and therefore not yet corrected for viscous effects, or properly scaled), although the rotor specific coefficients, CT, CQ and FoM are correctly scaled to rotor values. The pitching moment, CMx, from pressure integration needs to be divided by R/c (=6.402), and the viscous terms, CMz_τ, Cz_τ and CMx_τ, also need dividing by $(\pi.(R/c)^3)/N$ (=206.1), $(\pi.(R/c)^2)/N$ (=32.19) and $\pi.(R/c)^3$ (=824.3), respectively, alhtough the last two terms are in any case relatively small.

The CT and CQ histories in Figure 237 show a first stage solution in the range 30-40,000 iterations where the traces initially flatten. This first-stage steady state solution appears to follow the trends of the results found at lower pitch angles, at least for moderate pitch angles (the flow field itself will be illustrated in subsequent figures). However, the flow does not remain stable, and gradually takes up a new state at which higher CT and CQ values are found. Noting the relatively small changes in the viscous terms, the CT and CQ changes therefore suggest a reduction in the induced power factor arising through a re-distribution of the downwash. In some moderate pitch cases, the solution remains very stable at the 'high-CT' level, although at higher pitch the flow states may continue to alternate. However, while some of the histories appear settled after a large number of iterations, it is noted that the pitching moment history sometimes shows some notable activity, particularly for TRB-005v, where the results may become oscillatory (the mean of the actual pitching moment is small, CM=-0.0036, but varies from +0.0031 to -0.018). The recent results for TRB-000v show even greater variation. For this 15 degree case, the viscous torque, CMz_τ, remains fairly constant for all the blades, despite the fact that the flow field may be changing (and, as expected, the two Küchemann tip blades have slightly lower skin

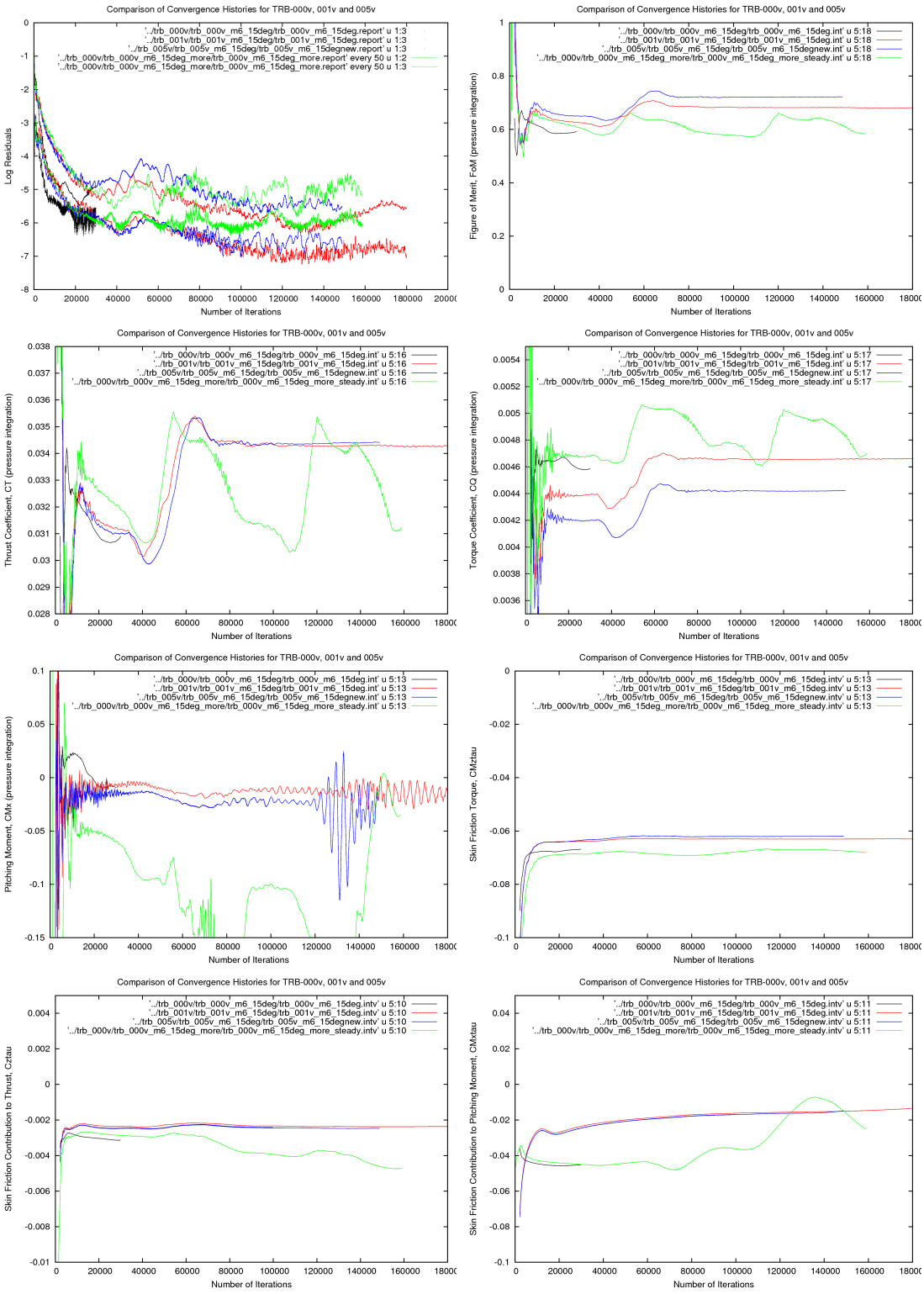

Figure 237: Example of Solution Convergence for TRB-000v, 001v and 005v at a Pitch Angle of 15 degrees where the Flowfield Exhibits to Two Different States. Raw Data from Steady Navier-Stokes with Modified k-ω Turbulence Model. Top Left: Log Residuals, Top Right: FoM, Upper Middle Left: CT, Upper Middle Right CQ, Lower Middle Left: CMx, Lower Middle Right: CMz_τ, Lower Left: CZ_τ, Lower Right: CMx_τ. (Final run for TRB-000v used HMB2 at a higher CFL number included for comparison)

friction drag than the datum blade). However, the newer version of the solver shows some variation for the datum blade. This is also the case for the remaining viscous terms, although these have an almost negligible effect on the overall results, and were only included here for completeness.

In an effort to maximise the usefulness of the steady Navier-Stokes solutions, a considerable amount of time was spent examining the solutions, and plotting the resulting integrated loads. One concern was that the different levels in the integrated results might be due to the wake of the rotor not joining to the wake outlet on the downstream Froude boundary. Certainly this has been observed in some cases, and at low thrust certain cases sometimes took many iterations to achieve this flow connection. However, this is perhaps a lesser concern at higher thrust levels, as illustrated by the w-velocity (downwash) contours shown in Figure 238. The visualisation in the upper part of this figure is presented at a first stage in the solution (30000 iterations), where the thrust and torque have settled to low values, and in the lower part of the figure at a later stage (130,000 iterations) where the thrust and torque have settled to higher values. For the the datum blade, TRB-000v, at 15 degrees, the flowfield solutions are available at various stages of the run, and the number of iterations was also massively increased to pursue the idea that the best solution would be reached when there were no longer any variations in the integrated loads.

However, even when the major integrated loads had stabilised, the residuals were not always low and smooth, but were often rather noisy, and some variation was likely to remain in the pitching moment parameter, CMx. This parameter is quite sensitive to any change in flowfield along the blade, especially when changes might occur near the root or tip of the blade. At the very highest pitch angles, the residuals continued to fluctuate, and there was a tendency for the solution to drift more rapidly, and eventually oscillate between flow states.

The main reason for the variation in the flow states appears to be that the root vortex re-positions itself, thus bringing about a change in the induced flow field with consequent influence on the blade loading. This effect is quite clearly illustrated in Figure 239, where contours of vorticity show the structure of the wake. The tip vortices, trailing vortex sheets, and the root-vortex features can all be seen in this cross-section of the flowfield. The top picture in Figure 239 represents a first stable solution (30,0000 iterations), prior to the solution reaching a second, higher level of thrust and torque (at 130,000 iterations), as shown in the lower part of this figure. For the first 'low-CT' solution, there is some upwash in the central region adjacent to the wall of the cylindrical hub, and the root vortices (from the preceding blade, and from the subject blade) induce a strong downwash over the inboard part of the blade. This downwash not only displaces the trailed vortex sheet of the preceding blade, but also reduces the local angles of attack and so diminishes the blade loading over the inboard half of the blade (as confirmed by loading distributions shown earlier). The visualisation in the lower picture, shows how the flow has settled in the 'high-CT' state, after a further 100,000 iterations. The root vortices are now below the blade and generally less intense. Since the downwash is reduced the blade now carries more loading over the inboard and middle region, and the thrust and torque accordingly increase. The strong upwash that was previously in the central region of the rotor (due to the raised pressure field below the blades), has now diminished (see again Figure 238) and the weaker root vortices now sit below the rotor disc. Some unevenness in downwash and vorticity also persists near the walls of the cylindrical hub below the rotor, and these fluctuations in the flow may take a long time to settle.

As suggested earlier, this phenomenon appears to be aggravated by the blades having no twist, together with a large root cut-out. Indeed, had the blades been twisted and extended further towards the root, this flow switching problem probably would not have occurred. Also, had a realistic hub (and feathering bearings) been present, this blockage (and source of small scale turbulence) may also have alleviated this problem by preventing the upwash and diffusing the vortical flows in the root region.

The changes to the downwash field in the root region of the blade are clearly quite significant, but even so it is rather surprising that such a large effect on thrust and torque was found. The influence on the blade loading must therefore extend over a significant portion of the blade. In order to investigate this further, the blade loading distributions were extracted for the 15 degree case, at the 'low-CT' and 'high-CT' solution states. The blade loading distributions are shown in Figure 240 and Figure 241, for the thrust and pitching moments, respectively (both in terms of the local aerofoil sectional values and after weighting to give the total loading). It can be seen that the loading, and therefore the downwash induced by the changes in the flowfield from one solution stage to another, affects a large part of the blade, from the root to as far outboard as 70%R, thus

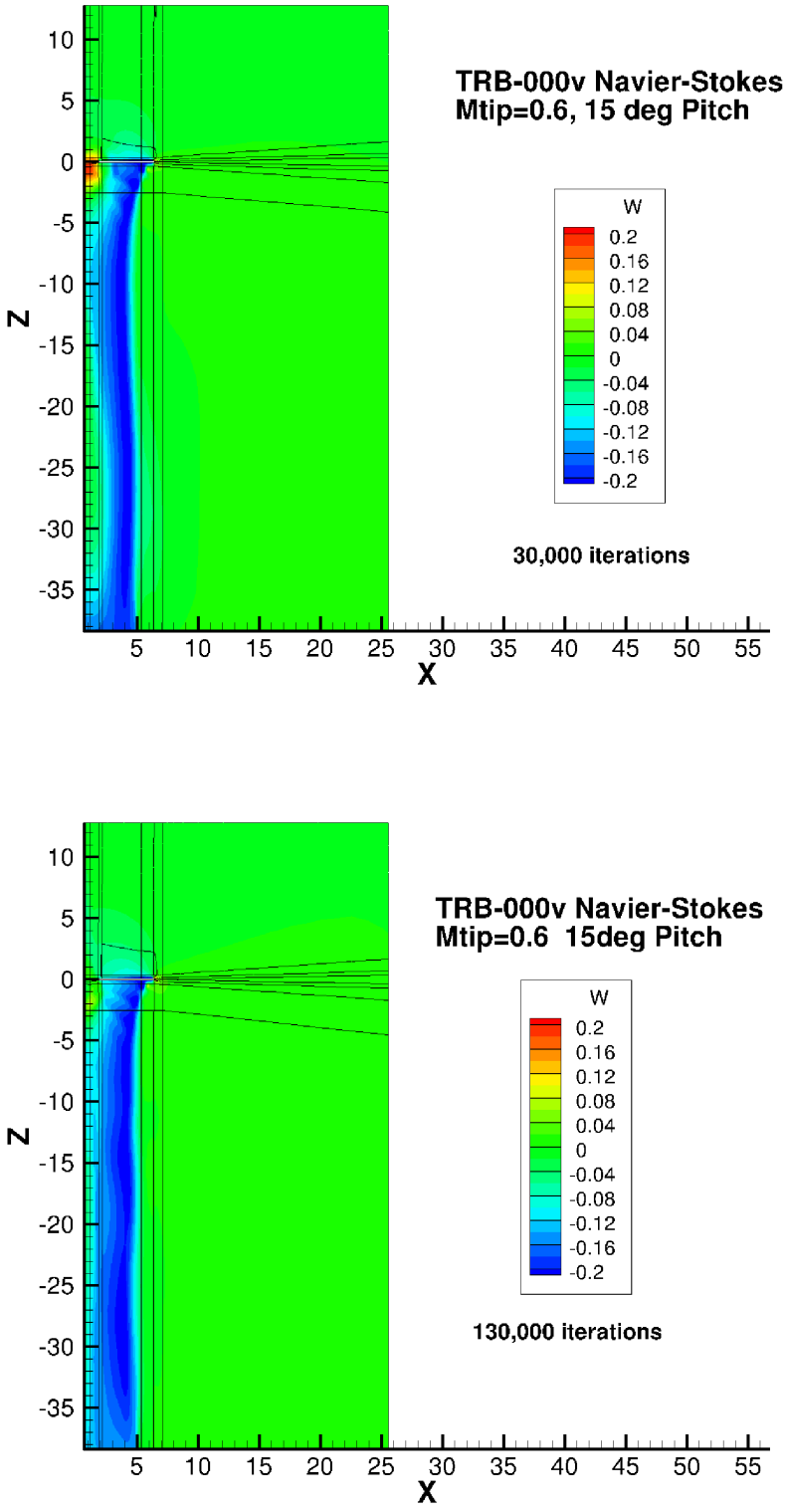

Figure 238: Visualisation of the Wake using w-Velocity Contours for TRB-000v at 15 degrees Pitch, Mtip=0.6. Steady Navier-Stokes with Modified k-ω Turbulence Model. The Top Illustration Shows the Flowfield for the First-Level Solution, and the Lower Graphic Shows the Second-Level Solution

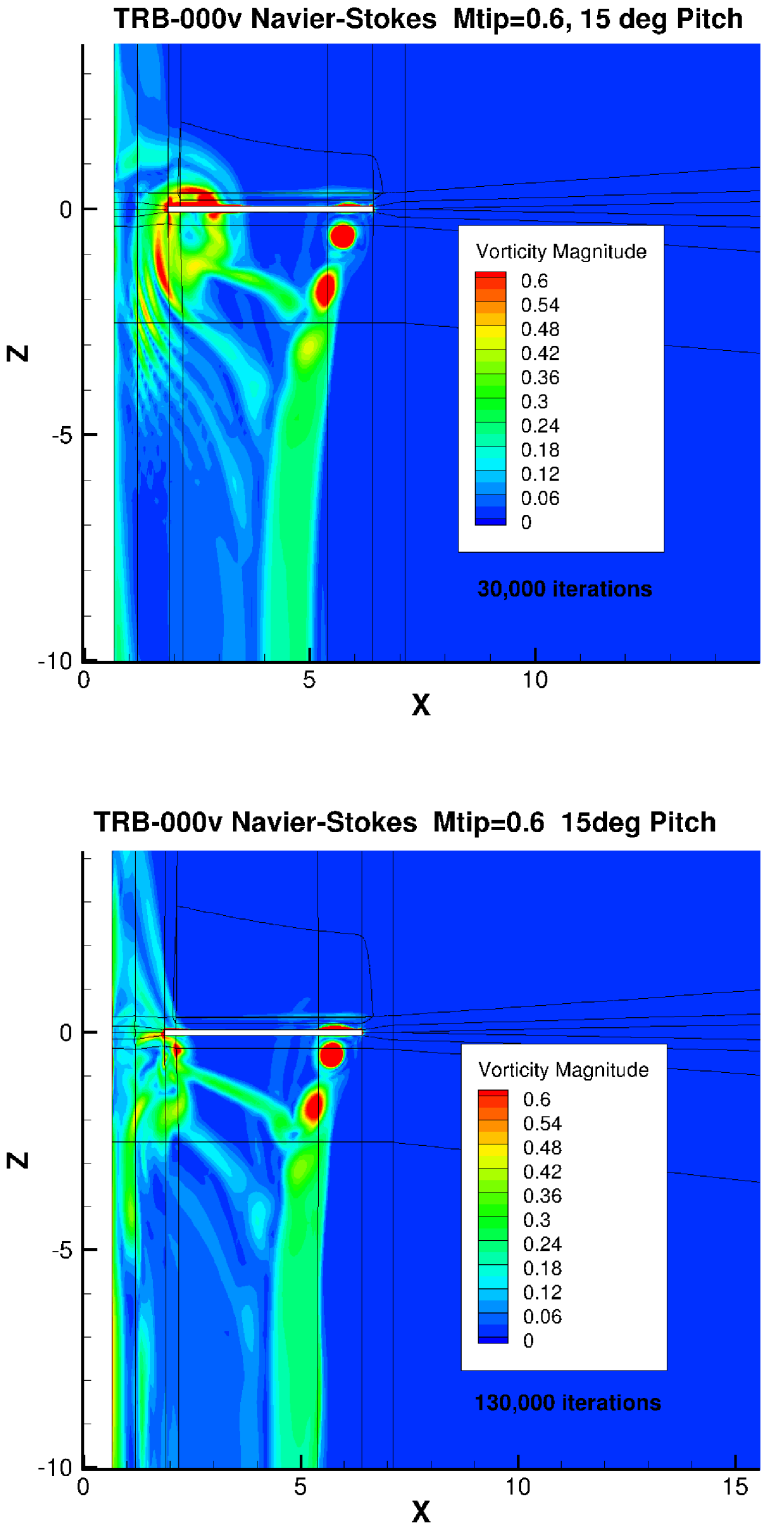

Figure 239: Visualisation of the Wake for TRB-000v at 15 degrees Pitch, Mtip=0.6. The Vorticity Contours Highlight the Tip and Root Vortices and the Trailing Vortex Sheets (Detached from the Tip Vortices) for this 4-blade Rotor. Steady Navier-Stokes with Modified k-ω Turbulence Model. The Top Illustration Shows the Flowfield for the First-Level Solution, and the Lower Part Shows the Second-Level Solution

accounting for the significant changes experienced in the solver-integrated pressures which yield the thrust, torque and moments (while in many cases the viscous skin friction is little affected since the flow is attached).

The loading distributions show the effect on the loads which arise from the pressure integrations, and these vary greatly in the region of 40-55%R due to the changes in the induced flow, and hence affect the thrust, torque and moment. In this example case for the datum blade at 15 degrees, there also appears to be some small changes to the loading further outboard (but inboard of the tip itself), perhaps as a consequence of disturbing the trajectory of the tip vortices. This disturbances may be less evident with a more diffusive solver than that used in the present work. In fact the moment appears to be very sensitive to these changes, and if the moment is well settled it is a good indication that the solution has stabilised. At higher pitch angles, the pitching moment often continuously varies and sometimes becomes erratic over large numbers of iterations suggesting that fluctuations are then due to flow separations and perhaps an unsteady solution is required when the rotor is near stall.

It is observed in Figure 240 that the value of Cz falls dramatically in the region of 40-60%R due to the changes in the induced flow. Here Cz changes from about 0.15 (at 30,000 iterations) to about 0.45 (at 130,000 iterations). These relatively low values of Cz suggest that the flow must be attached in this area, as confirmed by the Cp plots in Figure 242.

Outboard of 75%R, the loading is fairly similar for the two solution states, and the loading peak at the very end of the blade varies little. On this rectangular planform tip, the isobars bunch up in the forward leading edge corner, and there is an additional aft suction due to the tip vortex rolling-up over the trailing edge at the extreme end of tip. Just inboard of this peak the flow is well attached, and little difference can be seen in the loading. These features are clearly shown in the Cp plots of Figure 242, for 50, 82.5, 94 and 98%R. Most variation is seen at 50%R, where the angle of attack changes are greatest. Further outboard the changes are very small. In the top right graph a comparison is also shown at 82.5%R with an MSES 2D prediction. This comparison was achieved by varying the incidence in MSES (at the appropriate Mach number and Reynolds number) until a reasonable match with the Cp distribution was found, inferring an angle of attack of about 5.2 degrees at this radial station. This confirms that the flow in this region is attached as expected.

For the majority of work reported here the modified k-ω turbulence model was used, but a few check cases were run with the standard k-ω model and the shear-stress transport SST-k-ω variant. Changing the turbulence model seemed to make little difference to the flow changing states. Some results at high pitch, using the SST model are shown later in Section 6.4.

The lack of loading over the inboard half of the blade when there is a large downwash velocity over the blade is reminiscent of the loading distribution that may be obtained from a uniform downwash momentum-theory, where the lift coefficient falls off rapidly inboard and may become negative at the root, as shown in Figure 243. In contrast, blade-element (annulus) momentum theory shows a more uniform lift coefficient (hence angle of attack) due to the lower calculated downwash as one moves inboard towards the root. Most vortex models assume a location for the root vortex and this rounds off the loading at the root. However, the wake near the root of the blade is rarely distinct in flow visualisation photographs, eg Fradenburgh.[115] The early WHL vortex model employed a prescribed wake model with the vortices positioned according to Landgrebe,[174] and it was later found that the vortex locations given by Kocurek and Tangler[166] were preferable, particularly for tail rotors. (Note that the loading peak at the tip is due to the trailed vortex in the lift-line theory, and the tip-edge loading spike of the current work is not present). This diagram was included here for interest, but perhaps gives a feel for the magnitude of the changes in the induced flow field that were generated in the CFD simulations.

To confirm that the flow field changes are driven by the vortical flow features near the root, and are independent of the tip shape, a further comparison is included for the Küchemann tip blade with anhedral, TRB-005v. These cases employed an improved grid for the 15 degree case. Grid refinements were focused in the area of the root in particular, but also near the tip, and below the blade to ensure the wake vortices were well captured. As it happened, the first stage solution was saved rather late and the thrust is starting to rise (after the dip) at 51,000 iterations. In Figure 244 the final, higher thrust state looks well converged after 100,000 iterations, but CMx shows oscillations, possibly due to minor changes just inboard of the tip where the loading, and hence tendency for separation is greatest. Note that, as for the datum blade, the first stable

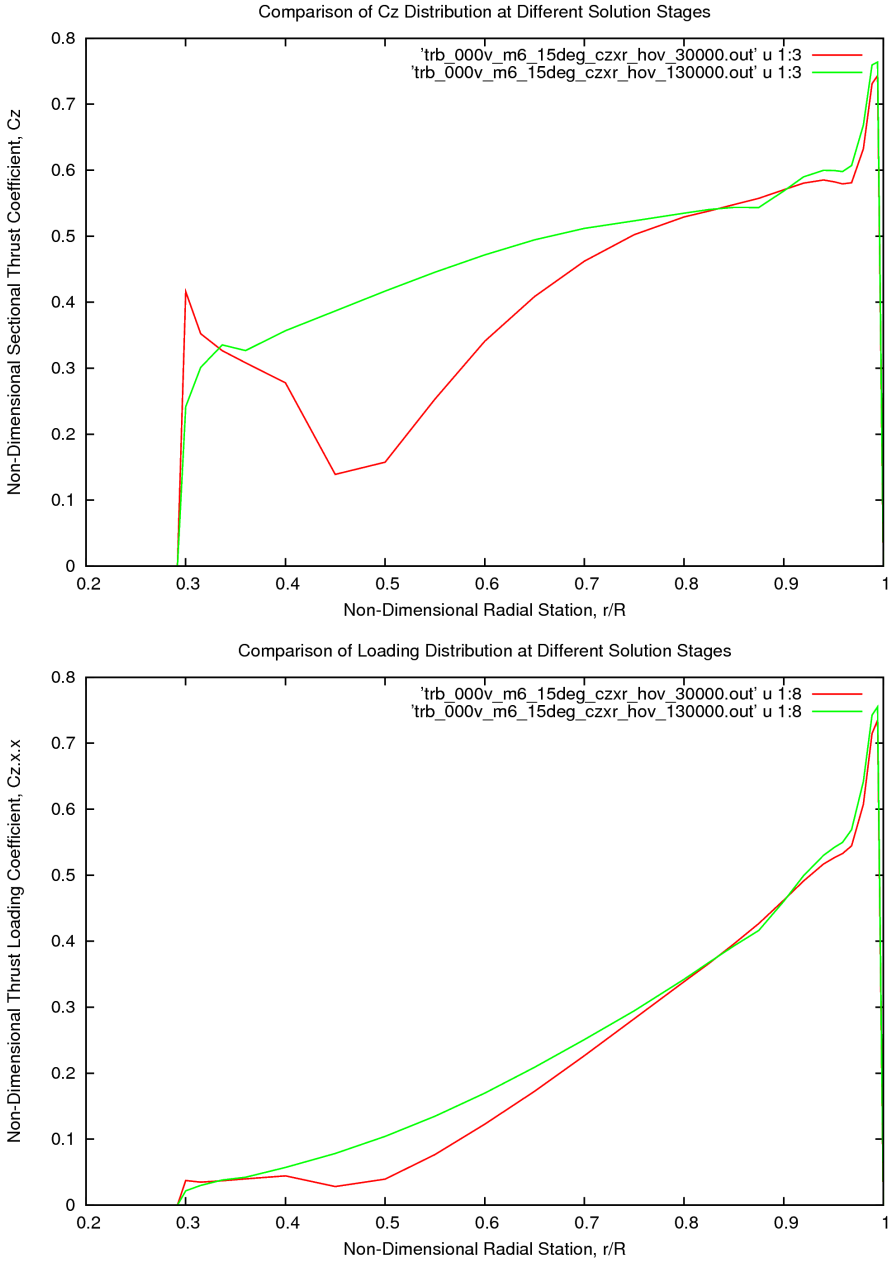

Figure 240: Sectional and Loading Distributions in the thrust direction for TRB-000v at 15 degrees Pitch, Mtip=0.6. Steady Navier-Stokes with Modified k-ω Turbulence Model. The Red and Green Lines Show the Loading at the First-Level Solution, and at the Second-Level Solution

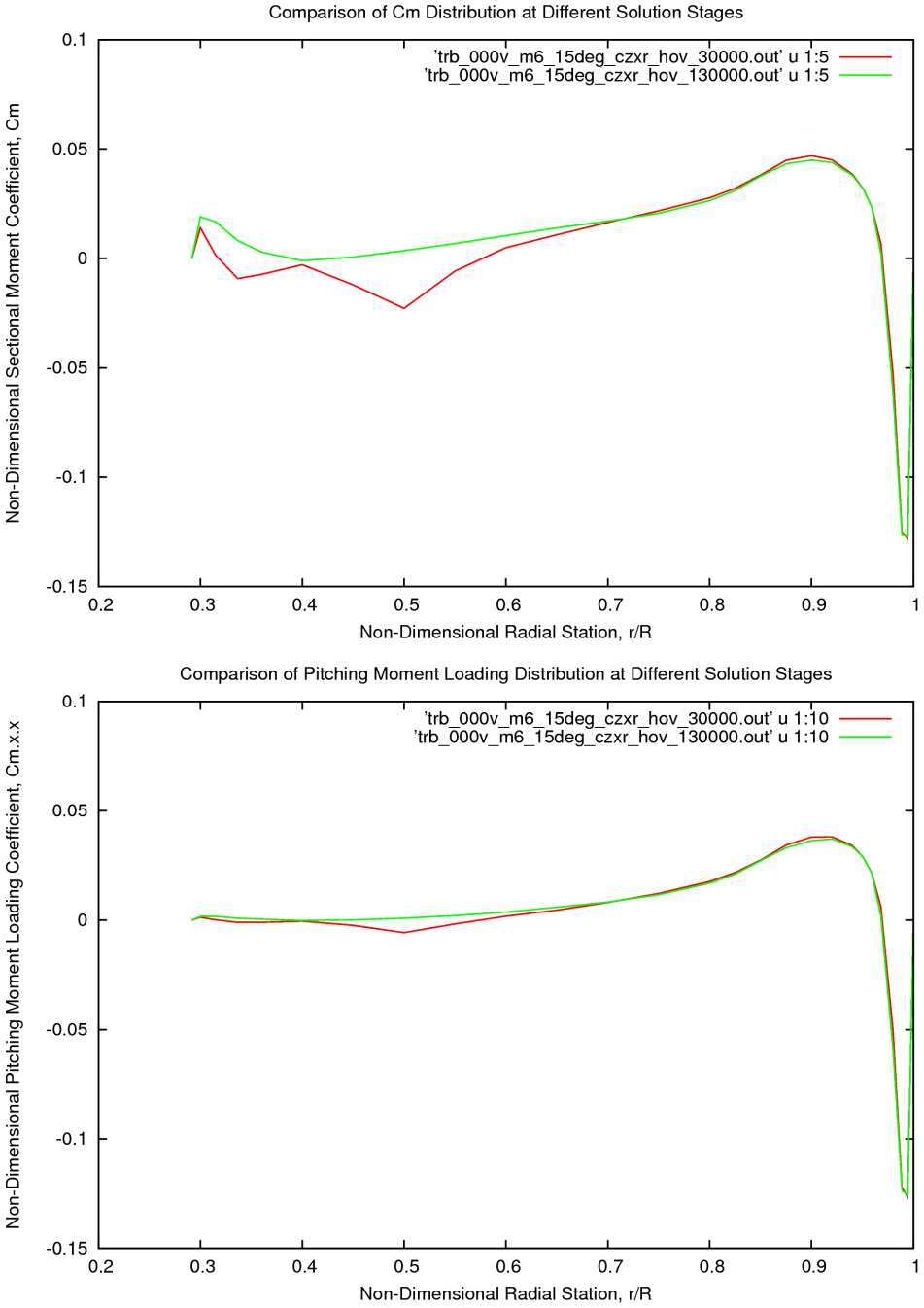

Figure 241: Sectional and Total Pitching Moment Distributions for TRB-000v at 15 degrees Pitch, Mtip=0.6. Steady Navier-Stokes with Modified k-ω Turbulence Model. The Red and Green Lines Show the Pitching Moments at the First-Level Solution, and at the Second-Level Solution

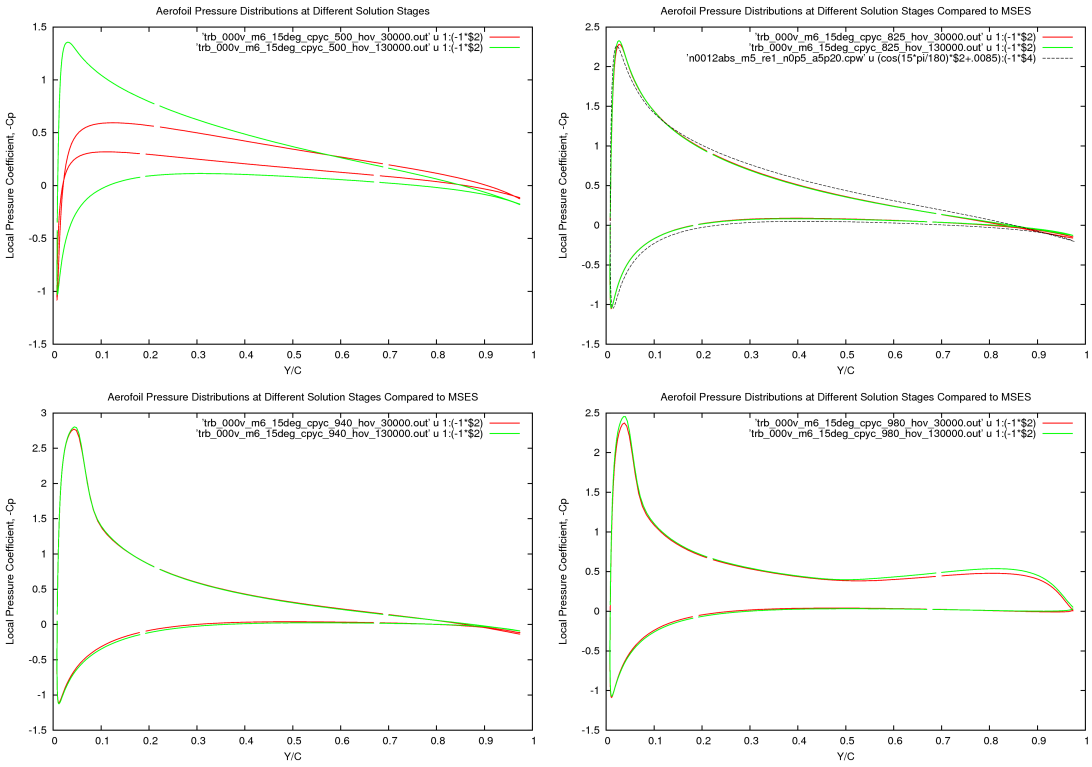

Figure 242: Pressure Distribution at 50, 82.5, 94 and 98% Radius for TRB-000v at 15 degrees Pitch, Mtip=0.6. Steady Navier-Stokes with Modified k-ω Turbulence Model. The Red and Green Lines Show the Surface Cp at the First-Level Solution, and at the Second-Level Solution, and Cp at 82.5% is Compared to MSES Predictions

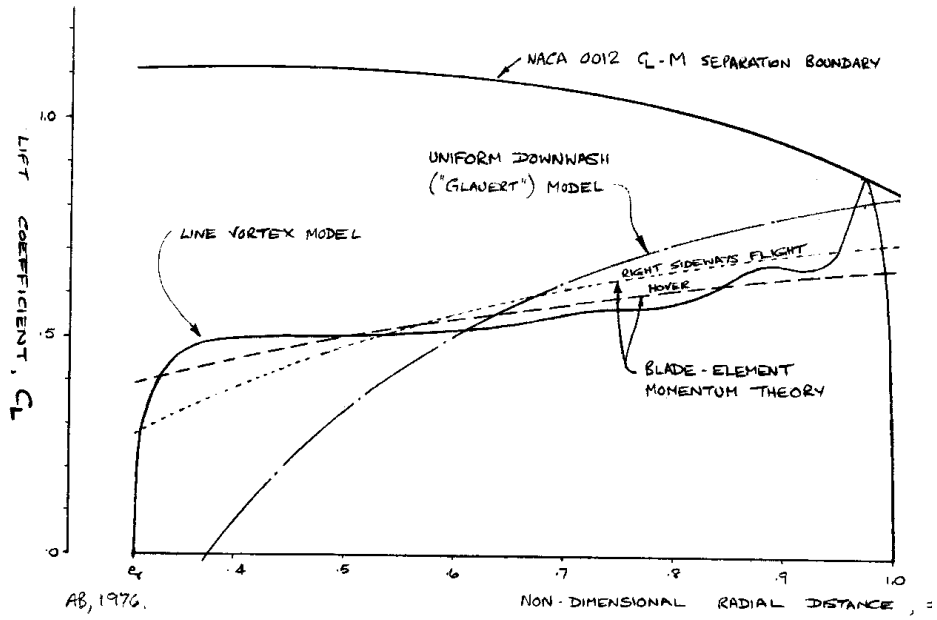

Figure 243: Comparison of Lift Coefficient Distributions calculated from Uniform Downwash, Blade-Element Momentum and Vortex Theory (taken from work done in 1976). The differences in Inboard Loading are similar to those experienced in the Navier-Stokes Simulations.

state for this case falls in line with the trend extrapolated from the lower pitch results, but the final CT is close to, but just below, the original Euler solution for this blade, and the power seems remarkably low (see later discussion and Figures in Section 6.4).

For TRB-005v at 15 degrees, the first solution state again shows a strong circulation around the root region of the blade as shown in the top left w-velocity contour plot in Figure 244. Therefore the blade will see a strong downwash over the inboard region, and this will tend to suppress the loading. It is also clear that the wake does not fully connect with the Froude outlet condition. It may be that the wake has not yet established a connection, or that it has since shifted. However, this probably has only a small effect on the flow close to the rotor.

The upper surface pressure contours in the lower part of Figure 244 confirm the above deductions and show significant changes inboard, with the solution at 51,000 having a weaker suction peak in this region, while the loading appears more continuous in the middle and inboard regions after 100,000 iterations. The isobar pattern in the tip region shows no significant changes, consistent with the result found previously for the datum blade.

The fact that the tip region is little affected by the changes of induced flow inboard is an important observation and justifies further analysis of the computational results to explore tip characteristics, as discussed in the following section of this report.

Both the flow states generated by the solver during these high pitch tail rotor cases may be not unrealistic considering the given geometry and boundary conditions imposed, particularly in view of the large root cut-out and lack of any hub blockage effect. Thus the inboard region of the blade is first influenced by an artificially strong central upwash and vortical flow near to and above the root of the blade, the downwash from which off-loads the inboard region of the blade. This mechanism later collapses when the inboard loading becomes sufficiently great to displace the root vortices down below the rotor. The change in the downwash brings about a change in the thrust and torque experienced by the rotor. For a low twist rotor with a large root cut-out this change in flow states occurs at moderate to high pitch.

Another aspect of the final solutions is that they point to a substantial benefit in performance, compared to the generally higher power trends of the initial results. It would appear that in the final flow state, as may be reached after many iterations of the solver, the adverse upwash (fountain effect) in the centre of the rotor (which also convects the root vortices upwards) is virtually eliminated, so that the rotor becomes more efficient since the downwash becomes more uniform.

In practice it is likely that, due to hub blockage and turbulence, the upwash generated in the central region would not be as large as predicted here, and that transition to the final flow state may also be a more gradual process.

For many years the design advice has been to reduce the root cut-out of the tail rotor as far as possible to minimise the induced power. Recent tail rotor designs employ sleeved flex-beams and shrouded feathering bearings in an attempt to bring the root-end of the blade further inboard. These design features may also help to stabilise the flow in steady hovering rotor computations.

In summary, the computational geometry used in this research employed a simplification of the actual geometry of the model tail rotor. A long cylindrical hub was used (as a convenience to simplify the blocking) and this, together with the desire to avoid geometries which could give rise to flow separations in the hub and root region, has led to the flow being free to switch from one state to another in the CFD simulations at moderately high pitch. At small pitch angles, there was no sign of this problem, and it only became noticeable at pitch angles greater than about 12 degrees in some cases, but became more significant by 15 or 16 degrees. At these angles and beyond, quite significant changes in thrust and torque were experienced, although the final solution, only reached after many iterations, was the most stable. At pitch angles of 18 or 20 degrees, where stall was present in the tip region the solution became difficult to settle, but with perhaps less variation of inboard loading (see loading distribution plots in the next section). The problem of these inboard induced flow changes was apparently made worse by the choice of a tail rotor blade which had zero twist, and a large root cut-out. With hindsight, a better choice would have been to use a twisted blade with a smaller root cut-out as a carrier for the various tip designs.

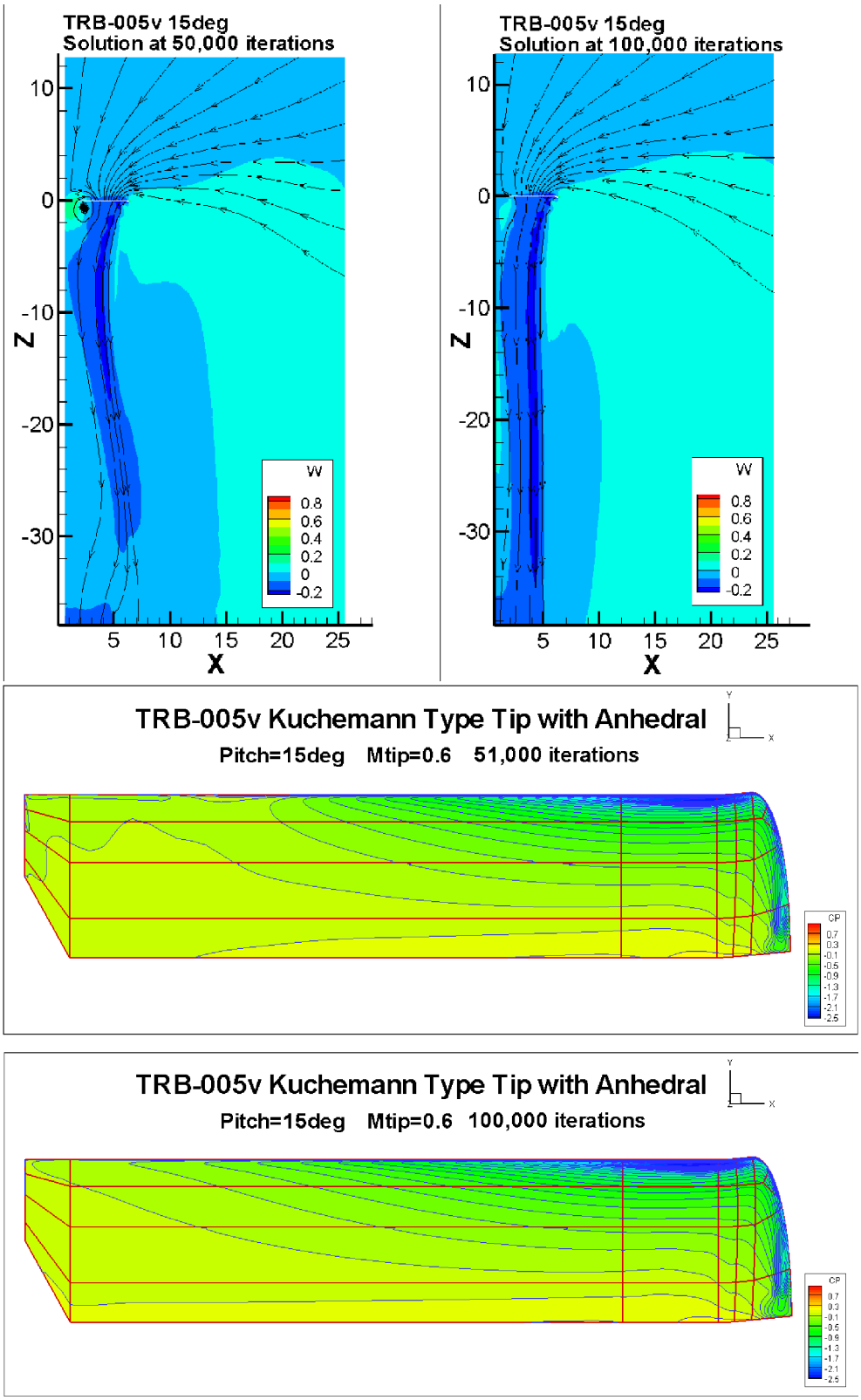

Figure 244: Top: Visualisation of the Wake for the Küchemann, Anhedral blade, TRB-005v, at 15 degrees Pitch, Mtip=0.6. Bottom: Surface Pressure Contours for TRB-005v Showing Variation of Loading Inboard and No Significant Changes at near Tip. Steady Navier-Stokes with Modified k-ω Turbulence Model. First-Level Solution at 51,000 and the Second-Level Solution is at 100,000 iterations

In following sub-section of this thesis, the steady CFD predictions for all pitch angles are gathered together and in some cases tend to show double trends for the thrust and power. However, since the changes in flow field mainly affect the inboard and middle region of the blade, with little influence near the tip as shown by the loading distributions, it is possible to extract some useful information to further compare the performance of the three selected tip shapes, despite the difficulties encountered.

Since the mechanism behind the tendency for the flow to shift was only understood towards the end of this research project, further work is therefore required to find a practical solution which would suppress the tendency for the flow to suddenly shift, and would therefore furnish a more realistic steady solution over a range of pitch angles. Since it was considered unlikely that simply enlarging the radius of the cylindrical hub would provide an adequate fix, this option was not pursued in the present work. A more likely solution would be to locally expand shape the cylindrical hub and attach it to the blade with a small chord thick aerofoil shape to represent the feathering bearings (perhaps leaving a small gap to facilitate pitch changes). The problem is to represent the blockage presented by the central hub, the hub-shanks, and feathering bearings whilst avoiding any significant separated flows such that a steady solution remains viable. Alternately, employing an unsteady solution would allow all the hub components to be modelled in detail, although the grid would then become more challenging. Both the hub-blockage effect and the diffusive effect of the turbulence generated by the other components could then be properly included in the simulation. However, this level of complexity would lead to a large grid (containing the hub components and all 4 blades), and the solution time would be very long in comparison to a steady solution. The use of an unsteady solution is considered in Chapter 8, where a simplified hub and feathering bearing arrangement is modelled as a first step.

6.4 Performance Comparisons at High Pitch

It has already been shown that the Küchemann-type tip shapes put forward in this thesis have yielded substantial benefits in both induced power factor and profile power for the example tail rotor blades at low-to-moderate pitch angles. However, the fact that the tail rotor has to both compensate the main rotor torque and generate additional thrust in manoeuvres in the hover and low speed flight means that it often has to operate close to the onset of stall, where the profile power may start to diverge. Modern tail rotors use advanced aerofoils and twist to delay the onset of stall and so maximise the manoeuvre thrust before power diverge occurs. While the question of maximum useful thrust is beyond the scope of this research, the performance near the onset of stall and the associated power divergence may be affected by the tip shape and therefore requires investigation. Hence it was desired to investigate, as far as possible, the performance of the rotor at high pitch angles where some separated flow will be present. Since an unsteady Navier-Stokes solution would be very expensive in computation, and well beyond the current capabilities of industry for repeated use in design, it is highly desirable to continue to use an steady Navier-Stokes to simulate the rotor approaching stall.

However, as discussed in the previous section, as the pitch was increased a change in the flowfield was encountered due to a change in the induced velocity near the root of the blade bought about by a sudden shifting of the root vortices. This resulted in the solver almost converging to what may be considered as a 'low-CT' solution, before switching towards a 'higher-CT' level. At very high pitch the solution was generally reluctant to settle and probably the separated flow near the tip was a limiting factor. This variability in the results caused much confusion and concern, and indeed many grid improvements and repeat runs were carried out. At low pitch, the solver gave the expected results, but above about 16 degrees, in the area of interest for power divergence, it became difficult to rationalise the results for the integrated thrust and torque. Eventually, it became apparent that the changes in induced flow mainly affected the loading in the root and inboard region of the blade, and had only a relatively small effect on the tip.

In the following Figures, both the 'low-CT' and 'high-CT' results have been included. Their applicability depends on how the flowfield near the root of the blade develops, and while either flowfield could be realistic for a given pitch angle, it seems likely that the real answer would lie somewhere between the two results. It interesting that the results tend to divide into two separate trends according to how the induced flow, or downwash builds up. However, near the tip the influence of the inboard flow field is relatively small, and some further information about the aerodynamics of the tips may be extracted from the steady Navier-Stokes solutions.

6.4.1 Performance Near Stall

Figure 245 presents the thrust pitch results for all pitch angles up to 20 degrees. It will be shown later that stall occurs near the tip of all three blades at 18 and 20 degrees, but even at moderate pitch, dual solutions were found. The 'high-CT' solutions between about 12 and 18 degrees for the flat blades, TRB-000v (datum, rectangular) and TRB-001v (0.25c Küchemann), all lie close to the Euler line and therefore seem unrealistically high. In contrast, for the Küchemann-type tip with 20 degrees of anhedral, TRB-005v, the 'high-CT results tend to follow the trend of the Navier-Stokes predictions from lower pitch angles, while the 'low-CT' results fall on the low side of the expected trend. It may be that the anhedral tip may have a greater tendency for separation due to the local effect of the anhedral crank which appears to disturb the loading. Some of the variability in the results is probably due to the variation in the proximity of the tip vortex from the preceding blade coupling with the effects of the inboard flowfield changes. The additional points obtained with the SST turbulence model, at 18 and 20 degrees for TRB-001v, seem to lie on an extended line of the 'low-CT' solutions.

It is also instructive to look at the CQ-Pitch curve as given in Figure 246, here it is apparent that the torque associated with the 'high-CT' for the datum blade, TRB-000v, are all higher than might be expected, while the results for the other two blades fall within more reasonable bounds. Again the points for TRB-005v tend to vary from the low side to high side of the general trend. The additional points for TRB-001v with the SST model are now closer to the 'high-CT' solutions of the torque-pitch curve.

The CQ-CT curve in Figure 247 suggests that the 'low-CT' and 'high-CT' results might fall into groups that have different induced or profile powers, while at very high pitch the results come closer together again. The results for TRB-005v suddenly switch from a low power to a high power trend. The low power trend of TRB-001v diverges later. A change in the induced power would be consistent with a change in the induced

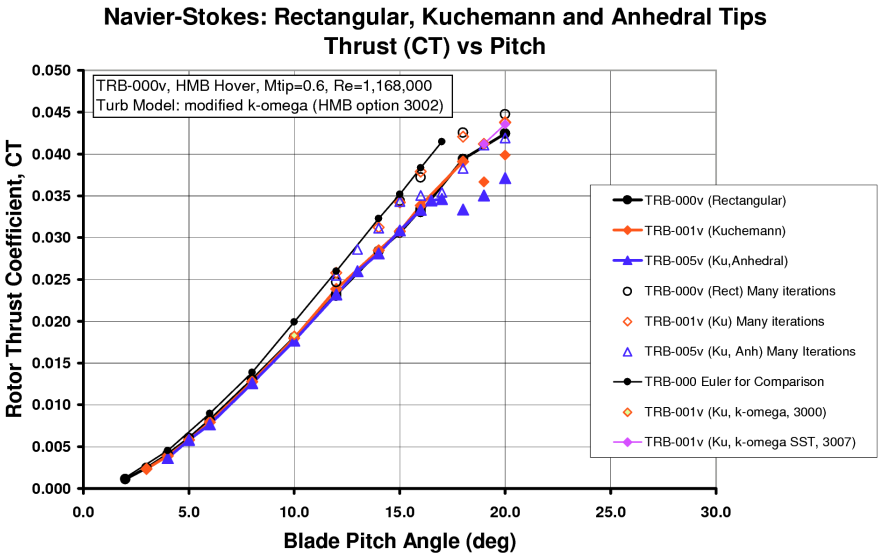

Figure 245: Steady Navier-Stokes Thrust-Pitch Predictions for All Pitch Angles for the Datum, Rectangular tip, TRB-000v, the Küchemann tip, TRB-001v, and the Küchemann tip with Anhedral, TRB-005v, using a Modified k-ω Turbulence Model, Mtip=0.6

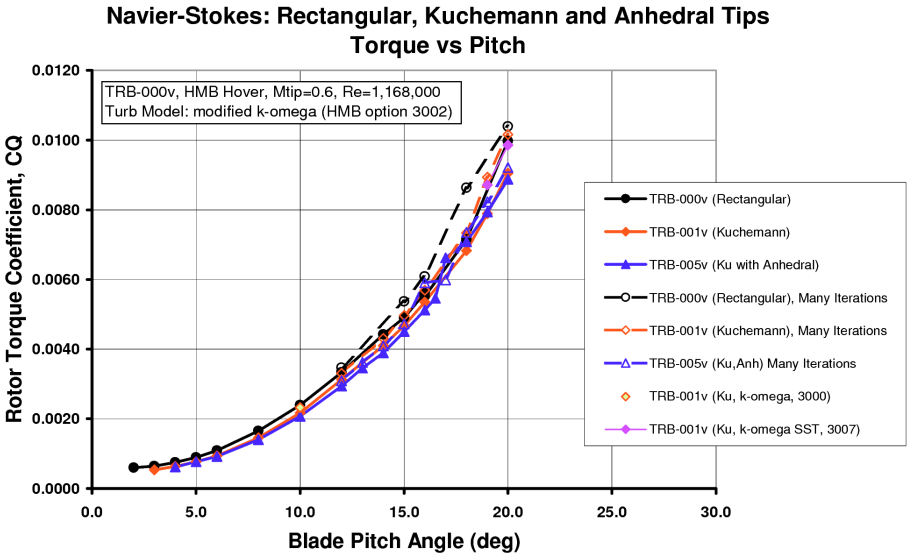

Figure 246: Steady Navier-Stokes Torque-Pitch Predictions for All Pitch Angles for the Datum, Rectangular tip, TRB-000v, the Küchemann tip, TRB-001v, and the Küchemann tip with Anhedral, TRB-005v, using a Modified k-ω Turbulence Model, Mtip=0.6

flowfield which has been seen to occur. A change in profile power seems unlikely at moderate pitch as it was shown earlier that the flow was attached on the inboard part of the blade and the tip loadings appear similar. At very high pitch some variation in the profile power could occur due to tip-vortex induced increments in the angle of attack, but even here the dominant effect of the shift in the flow field, if it affects the tip vortex trajectories at all, is likely to be seen in the induced power. This hypothesis is investigated further by re-plotting the results in the form CQ-$CT^{1.5}$, as shown in Figure 248. At pitch angles up to about 15 or 16 degrees the original (solid symbol) 'low-CT' trends continue. For the 'high-CT' (open symbol) points it is apparent that, between about 12 and 16 degrees, each blade could have a lower induced power factor than that determined earlier from the results at low pitch. The datum blade appears to follow the 'low-CT' trend, until it diverges, and the 'high-CT' results perhaps continue the original trend. Again 'high-CT' results for TRB-005v switch from a low power line and scatter high. The 'high-CT' points for TRB-001v similarly follow a lower power trend, but then suddenly diverge towards an extrapolation of the 'low-CT' trend at very high pitch.

Using the same induced power factors as previously derived from the CFD results at low-to-moderate pitch, in Section 6.2, the profile power in terms of the equivalent blade CD is shown in Figure 249 together with the results at higher pitch. The datum blade, TRB-000v, has a couple of 'high-CT' results that fall low on this plot, but if these are ignored, the profile power (drag) appears to follow the original trend until it rapidly diverges. For TRB-001v and TRB-005v between about 12 and 16 degrees, where the solution has a 'high-CT', the profile power would appear to be unrealistically low, suggesting that the changes are due to induced flow effects, as first supposed. However, it is doubtful if such low induced power could be realised in practice from this untwisted blade with such a large root cut-out. For TRB-005v there is considerable variation in the results in the range 15 to 16 degrees, possibly due to the close proximity of the tip vortices influencing the loading on this tip (which has a relatively sharp 20 degree anhedral crank). The 'low-CT' results for this blade appear to diverge early, crossing over the 'low-CT' trend for the flat Küchemann tip, TRB-001v. The 'low-CT' trend for TRB-001v continues to about the same CT/s as the datum blade.

Similarly, the 'high-CT' points appear to be over-optimistic on the Figure of Merit plot of Figure 250 for the model tail rotor in question, and are unlikely to be achieved in practice (compare with the Model Rotor results presented in the validation Chapter 3.4, remembering that there may also be a small effect due to Mach number). However, as suggested earlier in Section 6.3, it might be considered that the rotor is now behaving as though it had more area, or has lost the penalty of any upward flow in the centre. The 'low-CT' points for TRB-005v show a dramatic fall in the Figure of Merit for pitch angles above about 15 degrees, while the 'high-CT' results for this blade, post 15 degrees, appear to suggest the blade is gradually stalling. The Figure of Merit for TRB-001v peaks and then falls more gradually, while the trend for the datum, rectangular blade is surprisingly flat as CT increases, but this is probably the influence of the last point before stall. The additional SST results (at many iterations) for TRB-001v again suggest how the Figure of Merit might reduce due to stall. The performance of all the blades falls due to tip stall at 18 and 20 degrees.

The variability in the integrated results makes it difficult to obtain an accurate comparison of the performance of the three selected tip shapes. However, in Section 6.3 it was found that while the induced flow changes at the root of the blade influenced the integrated forces and moments, the loading at the tip of the blade appeared to be unaffected. The next logical step, therefore, is to examine the surface pressures and loading distributions in the tip region to see if a better comparison of the relative performance of the tip shapes can be obtained in these important high-pitch conditions.

6.4.2 Loading and Pressure Distributions

The surface pressure distributions near the tip for the three blades in question are shown in Figure 251. The contour plots for each tip shape were taken from available results, and hence have different convergence states (TRB-000v is taken early at 'low-CT', while TRB-001v and 005v have a 'high-CT'). Nevertheless, since the 'low-CT' and 'high-CT' results are mainly a consequence of the change in loading inboard, much can be learnt from examining and comparing the pressure patterns in the tip region. In these illustrations, the block boundaries are depicted in red while the pressure contours are outlined in black. Note that the pressure contours are smooth and also cross the block boundaries smoothly in each case, confirming that the solutions are all adequately converged in this region.

At the top of Figure 251, the datum blade, TRB-000v, clearly shows the isobars bunching up in the leading edge corner to form a strong leading edge suction peak, with a strong adverse pressure gradient just downstream

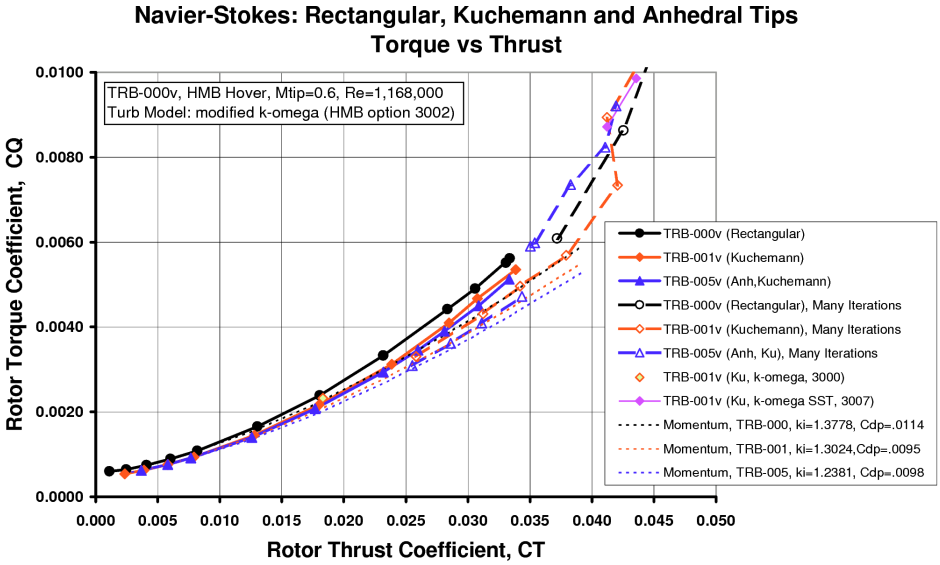

Figure 247: Steady Navier-Stokes Torque-Thrust Predictions for All Pitch Angles for the Datum, Rectangular tip, TRB-000v, the Küchemann tip, TRB-001v, and the Küchemann tip with Anhedral, TRB-005v, using a Modified k-ω Turbulence Model, Mtip=0.6

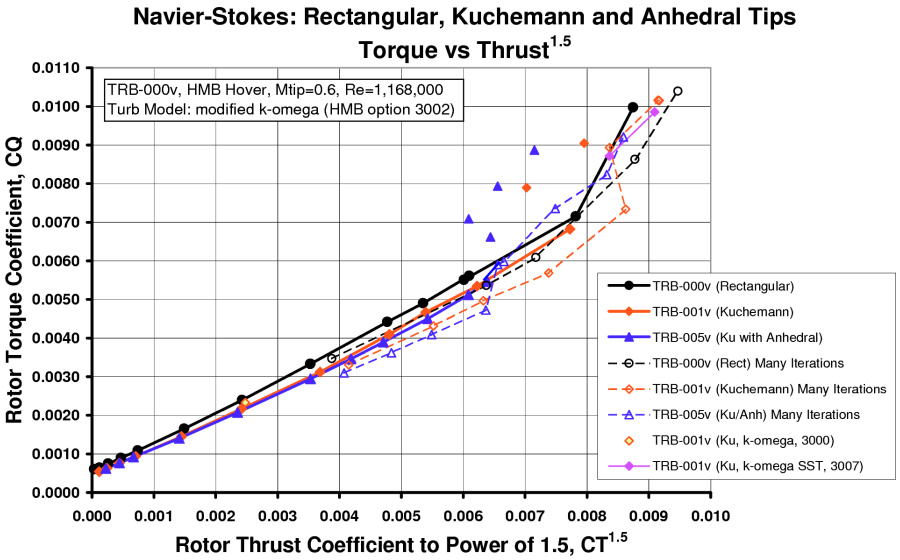

Figure 248: Steady Navier-Stokes Torque-Thrust$^{1.5}$ Predictions for All Pitch Angles for the Datum, Rectangular tip, TRB-000v, the Küchemann tip, TRB-001v, and the Küchemann tip with Anhedral, TRB-005v, using a Modified k-ω Turbulence Model, Mtip=0.6

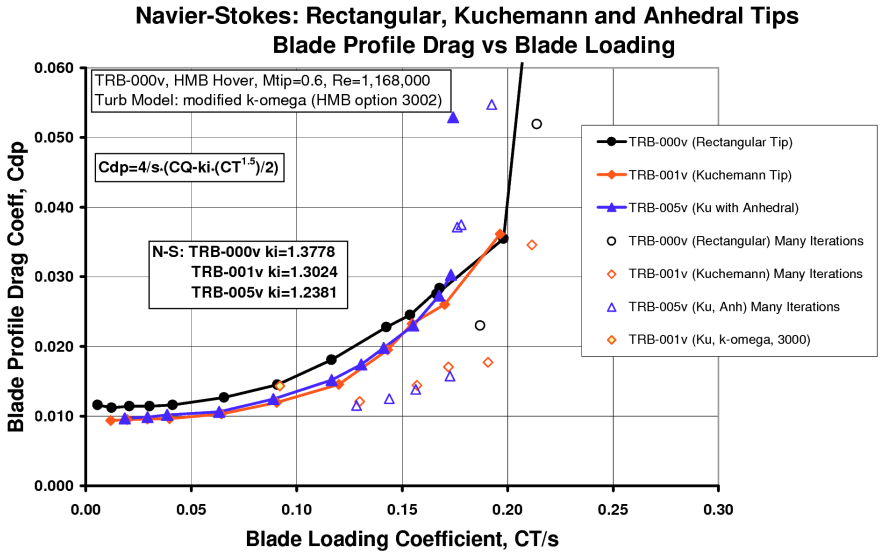

Figure 249: Steady Navier-Stokes Profile Power Results for All Pitch Angles for the Datum, Rectangular tip, TRB-000v, the Küchemann tip, TRB-001v, and the Küchemann tip with Anhedral, TRB-005v, using a Modified k-ω Turbulence Model, Mtip=0.6

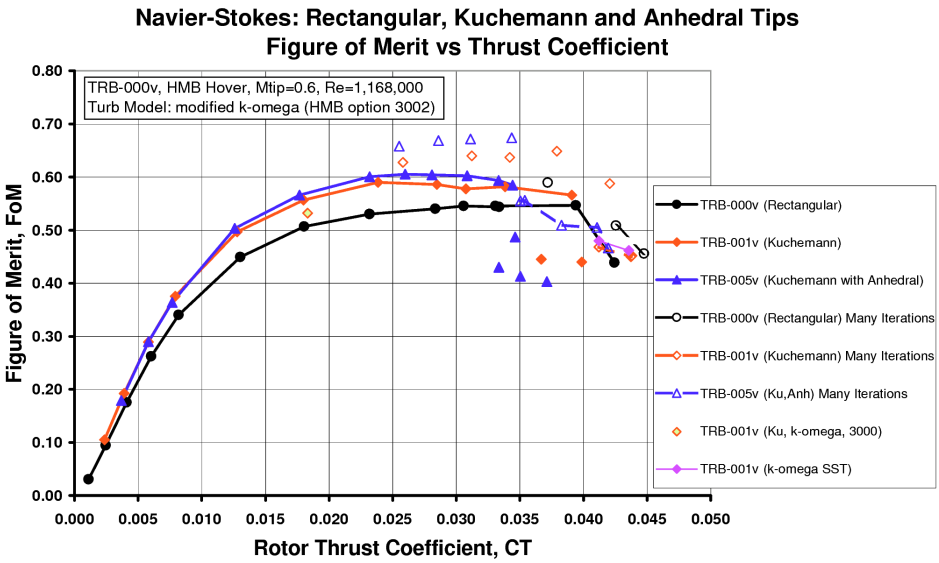

Figure 250: Steady Navier-Stokes Figure of Merit Predictions for All Pitch Angles for the Datum, Rectangular tip, TRB-000v, the Küchemann tip, TRB-001v, and the Küchemann tip with Anhedral, TRB-005v, using a Modified k-ω Turbulence Model, Mtip=0.6

(at about 12% chord in the region of 85-95%R). However, the pressure appears to recover towards the trailing edge, suggesting that only a small amount of separation may be present, probably greatest near 90%R, judging by the contour that wanders closer towards the trailing edge . The local suction field of the tip vortex can also be seen, but it perhaps appears here as a weaker feature than expected, although it still generates significant suction. Possibly, the vortex is tending to form some distance above the blade surface as it separates from the outer square-cut tip edge. The middle part of Figure 251 shows how the leading edge suction peak is relieved in the forward-outer tip region of TRB-001v, thus alleviating the associated adverse pressure gradient, although this is still a feature further inboard. For this tip the pressure recovery is slightly better. The formation of the tip vortex generates a suction along the curved part of the tip and this only tends to reduce (perhaps lifting away from the surface) aft of about 80% chord. On this Küchemann tip blade, the pressure contours are all nice and smooth. At the bottom of Figure 251, the effect of the anhedral of TRB-005v on the pressure contours can be observed. Just inboard of the blended anhedral crank the leading edge suction peak narrows and just inboard again (near 90%R) the pressure recovery is less complete, possibly as a consequence of a closer interaction with the vortex from the preceding blade, or as a conseqence of the anhedral crank itself. However, the pressure recovers quite well in the region of 96%R, and the tip is not yet in a stalled condition. The 20 degrees of anhedral appears to have reduced the amount of suction generated by the formation of the tip vortex, compared to the flat Küchemann tip. While it is perhaps too early to draw a firm conclusion, it would appear that a more gradual anhedral geometry may be preferable in order to alleviate some of these effects.

Having gained some ideas of how the surface pressures on the tips develop near to, but just below the onset of stall, the blade surface pressures can also be studied to see what happens at higher pitch when stall starts to occur. Since it became difficult to converge the steady solutions with this degree of separation occurring, and possibly still with the influence of flow changes near the root of the blade, the maximum pitch angle considered here was limited to 20 degrees. This pitch angle is near the maximum used in practice for such highly loaded rotors. [17] For the example untwisted model tail rotor, it is anticipated that the stall will first occur near the tip. For more modern tail rotors, with 8-10 degrees of twist, it should be possible to reach larger pitch angles (as measured at 75%R). The use of twist delays the power divergence due to the onset of stall, but the twist is limited to avoid the possibility of the whole blade stalling at once.

Considering now the HMB predictions for the highest pitch angle of 20 degrees, Figure 252 presents 3D plots of the pressure distributions for each of the subject blades. Here, the negative pressure coefficient, -Cp, has been plotted upwards on the vertical axis, so that the suctions and pressures follow the planform of the blade (looking from the root (left) towards the tip (right) in the figure), and give a 3D picture representative of the actual airload distribution. In these cases, which were all taken at a fairly early stage in the convergence history, there are no notable peaks or troughs in the loading at the root end of the blade, and the lower surface pressure and upper surface suction loads increase gradually along the radius. As expected, for these untwisted blades, the stall starts to develop in the tip region. The separated flow in the tip region is evidenced by the lack of recovery in the pressure distributions which are elevated at the trailing edge. The different tip shapes exhibit different peak suctions. For the datum, rectangular blade, TRB-000v, there is a strong suction region and associated adverse pressure gradients along the outer part of the blade. The lift falls off rapidly in the tip region, before the tip-edge suction is encountered (note any suctions on the vertical face of the outer edge of the tip will be plotted by a very thin pressure spike, and this contributes little to the thrust). For this blade, the lack of pressure recovery is greatest, and strongest in the outer tip region at about 95%R. The loading on the flat Küchemann tip blade, TRB-001v, is a little more complex, and the effect of the vortex from the preceding blade, since it may pass close beneath the blade, is more in evidence. Aft of this loading peak, the pressure again fails to recover due to separation, while the strong suctions along the tip edge are retained. Compared to the datum blade there is better overall pressure recovery in the tip region. The main loading peak on the anhedral Küchemann tip, TRB-005v, occurs further inboard, and it appears that the interaction with the tip vortex from the preceding blade has possibly brought about a deeper stall in the tip region with a collapse of the suction peak, just inboard of the tip. Even so, a fair amount of loading is still maintained over the outer tip trailing edge region. Just inboard of the tip, the pressure fails to recover as well as for the flat Küchemann tip.

[17] On the untwisted NACA0012 Sea King tail rotor, the pitch is limited to 22 degrees to avoid excessive torque in the tail rotor gearbox, and also to stay clear of buzz-bang blade stability concerns. For the untwisted Lynx and early EH101 tail rotors, which had cambered aerofoils, a limit of about 26 degrees is imposed for the same reasons. This pitch range provides good agility in hover and also enables these helicopters to meet a 35-50kts sideways flight requirement.

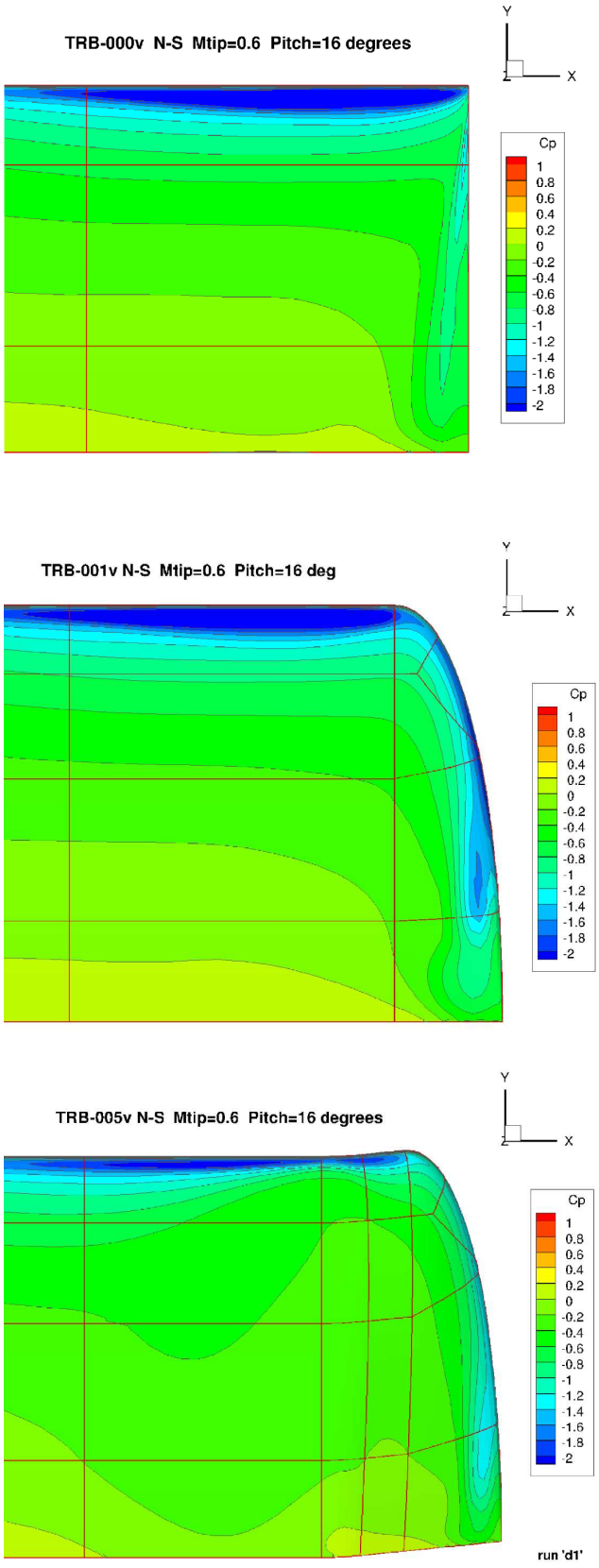

Figure 251: Surface Pressure Distributions for the 3 Tip Shapes at 16 Degrees Pitch. Top: TRB-000v (Datum, Rectangular). Middle: TRB-001v (Küchemann). Bottom: TRB-005v (Küchemann with Anhedral)

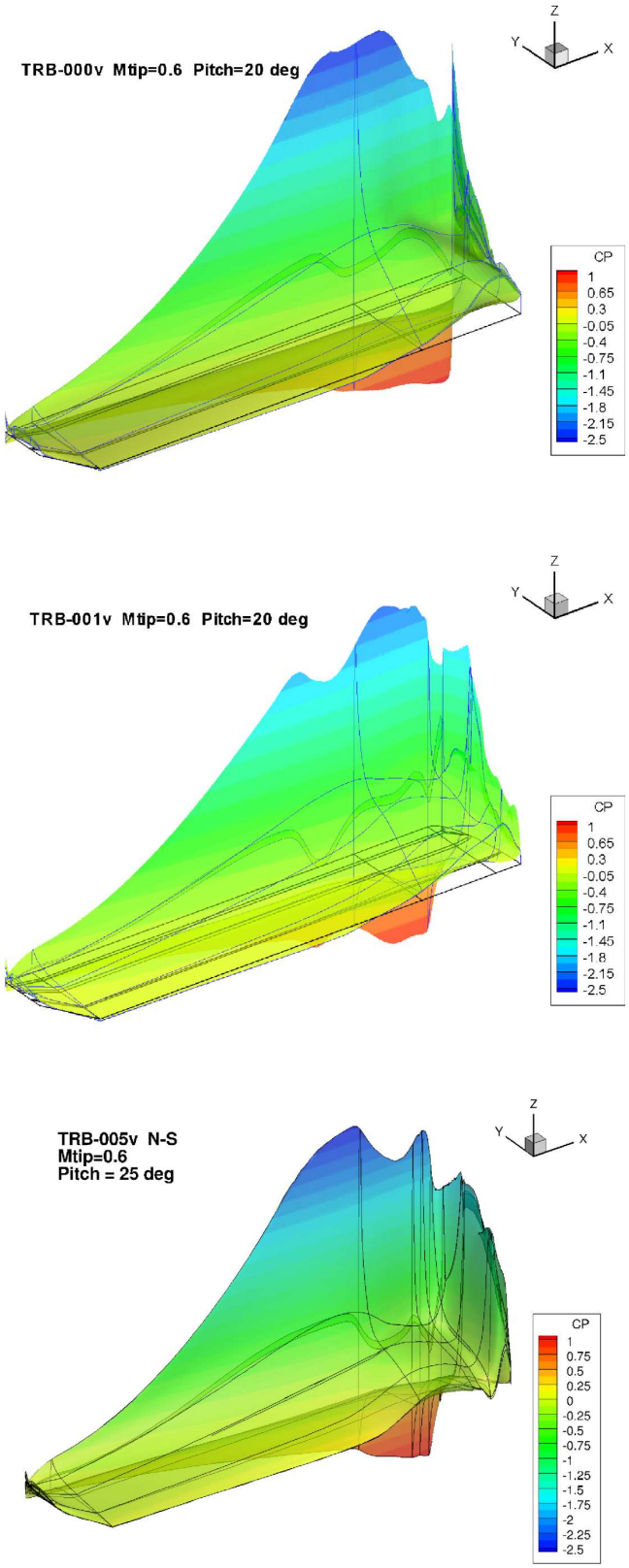

Figure 252: 3D Pressure Distributions for the 3 Tip Shapes at 20 Degrees Pitch Showing Lack of Pressure Recovery Near the Tip due to Stall. Top: TRB-000v (Datum, Rectangular). Middle: TRB-001v (Küchemann). Bottom: TRB-005v (Küchemann with Anhedral)

It is also useful to consider the blade loading distributions at the higher pitch angles up to 20 degrees, as presented in Figures 253 to 256. Here the data for TRB-000v was only available at an early stage in the convergence, while in the main, the results for TRB-001v and TRB-005v were taken later (except for TRB-001v at 10 degrees). The available lower pitch cases at 10 or 12 degrees are included to provide a commonality with the results shown earlier in Section 6.2. Again, the increased peaks in the loading coefficient are influenced by the taper of the blade at the tip, and at the inner-most root stations of the blade. In the top graph, the results for TRB-000v show a notable dip in the loading in the 40-60%R region, due to the high induced flow experienced inboard for 16 degrees and below for these 'low-CT' cases. The results for TRB-001v, show a similar characteristic loss in loading in this region for the 10 degree case. This feature is not present in the remaining results for TRB-001v and TRB-005v, below 16 degrees since these are 'high-CT' results, and is absent from all the results at 18 and 20 degrees. However, while it cannot be stated with any certainty that the tip loading will not be affected by these inboard changes when a degree of stall is present at the tip, it still seems likely that this will be the case, and what is of interest here is how each tip behaves at the higher pitch conditions. The non-dimensional loading coefficients, based on the local chord in the tip region are higher than on the datum blade because the chord reduces towards the tip, but this reduction is similar for the two Kücheman-like tips of TRB-001v and TRB-005v.

In Figures 254 and 256, the loading near the tip for the datum blade, TRB-000v, clearly shows that the aerofoil has reached its stall boundary. The loading is consequently reduced in the tip region, reaching a peak at about 88%R, and falling gradually over the middle region of the blade where the flow is attached (and the angle of attack is generally fairly high). The Küchemann tip blades, TRB-001 and TRB-005v, also show this sort of behaviour, but the situation is complicated by a stronger blade-vortex interaction in addition to the favourable influence of the tip. For the anhedral tip, TRB-005v, there is a notable dip in the tip loading at 90-98%R, at 16, 18 and 20 degrees, suggesting that the flow over this tip is breaking down earlier than on the flat Küchemann tip blade, possibly due to the effect of the anhedral crank at 96%R, despite the blending. The loading distribution for TRB-005v suggests that this blade is generating less thrust than the other blades, consistent with the variation seen earlier in the integrated results.

The pitching moment distributions in Figures 255 and 256 show how the pitching moment becomes strongly nose-down in the stalled region. This is a direct consequence of the separated flow preventing a more complete pressure recovery over the rear of the aerofoil, with perhaps also a reduction in nose-up suction near the leading edge. Prior to stall, the nose-up moment just inboard of the tip builds gradually, while the tip-edge nose-down spike also increases to provide some balance to the total moments. For the datum blade, TRB-000v, at 18 and 20 degrees, it is found that the tip-edge suction has disappeared completely and the whole of the tip region, outboard of about 85%R, suffers a nose-down moment due to stall. In contrast the Küchemann tip blades, TRB-001v and TRB-005v, both maintain the vortex-induced suction spike at the extreme tip-edge, for as far as results are available, except that there is some reduction in the tip-edge suction spike for TRB-001v at 20 degrees. Probably the vortex will eventually breakdown, or lift clear of the surface when the tip becomes more deeply stalled, but it is interesting to see that changing the tip shape has considerably delayed this process. It can also be more clearly seen in the pitching moment loads that the anhedral tip, TRB-005v, suffers a nose-down moment due to separation at only 16 degrees. At 16, 18 and 20 degrees, the spanwise extent of the dip in the moments is constrained to between 80 and 95%R.

The pitching moment is a useful stall monitor, either in the form of the total moment (as though measured at the root-end of the blade or reacted by a pitch link), or perhaps even better the local moment coefficient at 94%R may help to remove some of the variation in the results. In addition, the local force coefficient, Cz at 94%R, can also be used as a stall indicator. For this parameter, the gradient with pitch may start to reduce at the onset of stall and level off as the blade becomes more grossly stalled. The total pitching moment is normally available directly from the solver (from integration of the surface pressures with a tiny viscous correction). Unfortunately, some of the early rotor Navier-Stokes computations for TRB-000v contained errors (which were later corrected, but not all the cases were able to be repeated). It was also found from the convergence histories that CMx was particularly slow to settle for moderate-to-high pitch cases, and often wandered or oscillated due to continuing small fluctuations which affect this extremely sensitive parameter (in fact, this is the best parameter to use for monitoring the convergence of rotor cases, but one that is often thought of a secondary). Therefore all the following results for the higher pitch cases have been taken from the post-processed output of the Rotor-Analyser program (see Appendix G). Therefore these cases either fall into an early, notionally 'low-CT' state, or if the case was run to a greater number of iterations, may be at

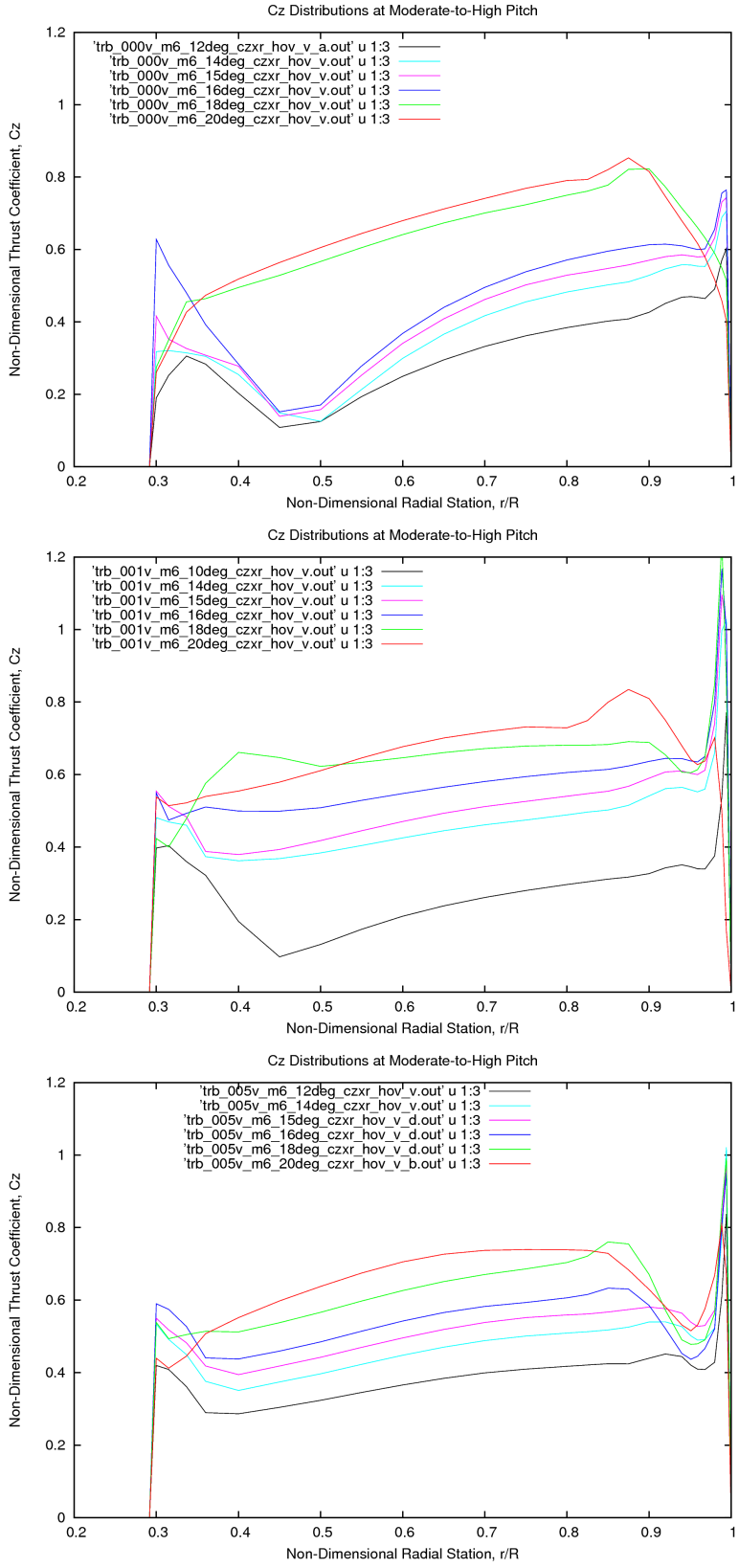

Figure 253: Predicted Thrust Coefficient Distributions for the 3 Tip Shapes at Moderate-to-High Pitch. Top: TRB-000v (Datum, Rectangular). Middle: TRB-001v (Küchemann). Bottom: TRB-005v (Küchemann with Anhedral)

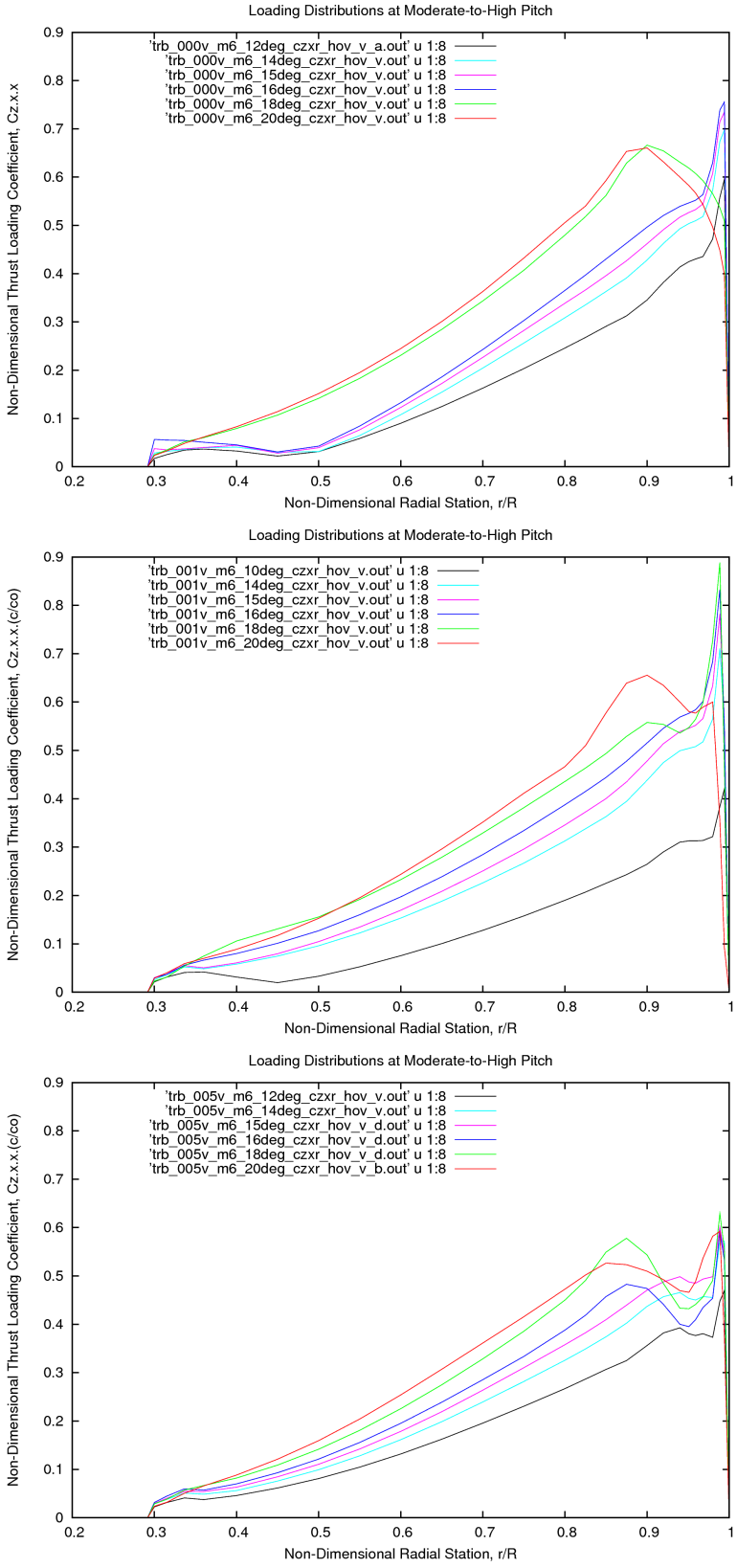

Figure 254: Predicted Thrust-Loading Distributions for the 3 Tip Shapes at Moderate-to-High Pitch. Top: TRB-000v (Datum, Rectangular). Middle: TRB-001v (Küchemann). Bottom: TRB-005v (Küchemann with Anhedral)

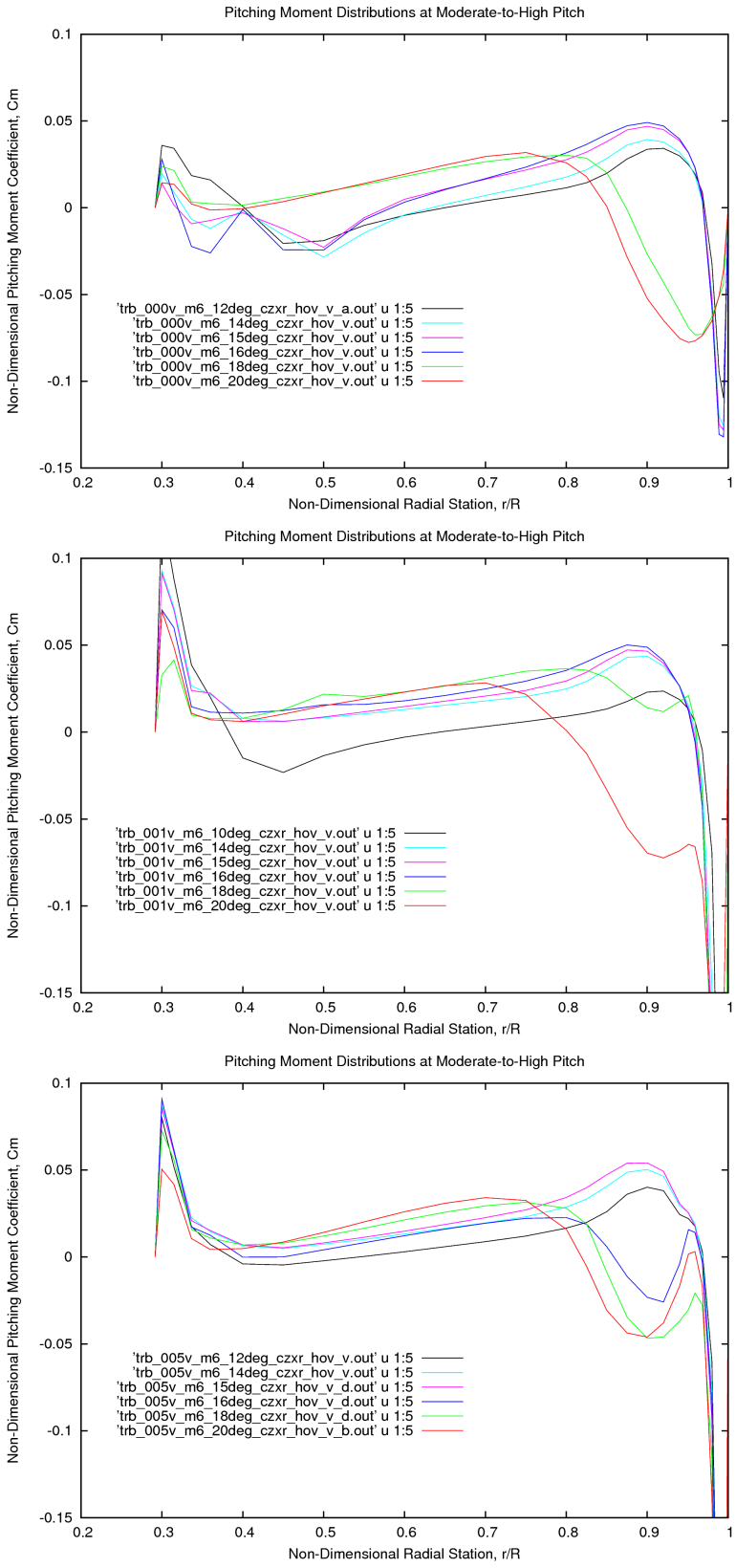

Figure 255: Predicted Pitching Moment Coefficient Distributions for the 3 Tip Shapes at Moderate-to-High Pitch. Top: TRB-000v (Datum, Rectangular). Middle: TRB-001v (Küchemann). Bottom: TRB-005v (Küchemann with Anhedral)

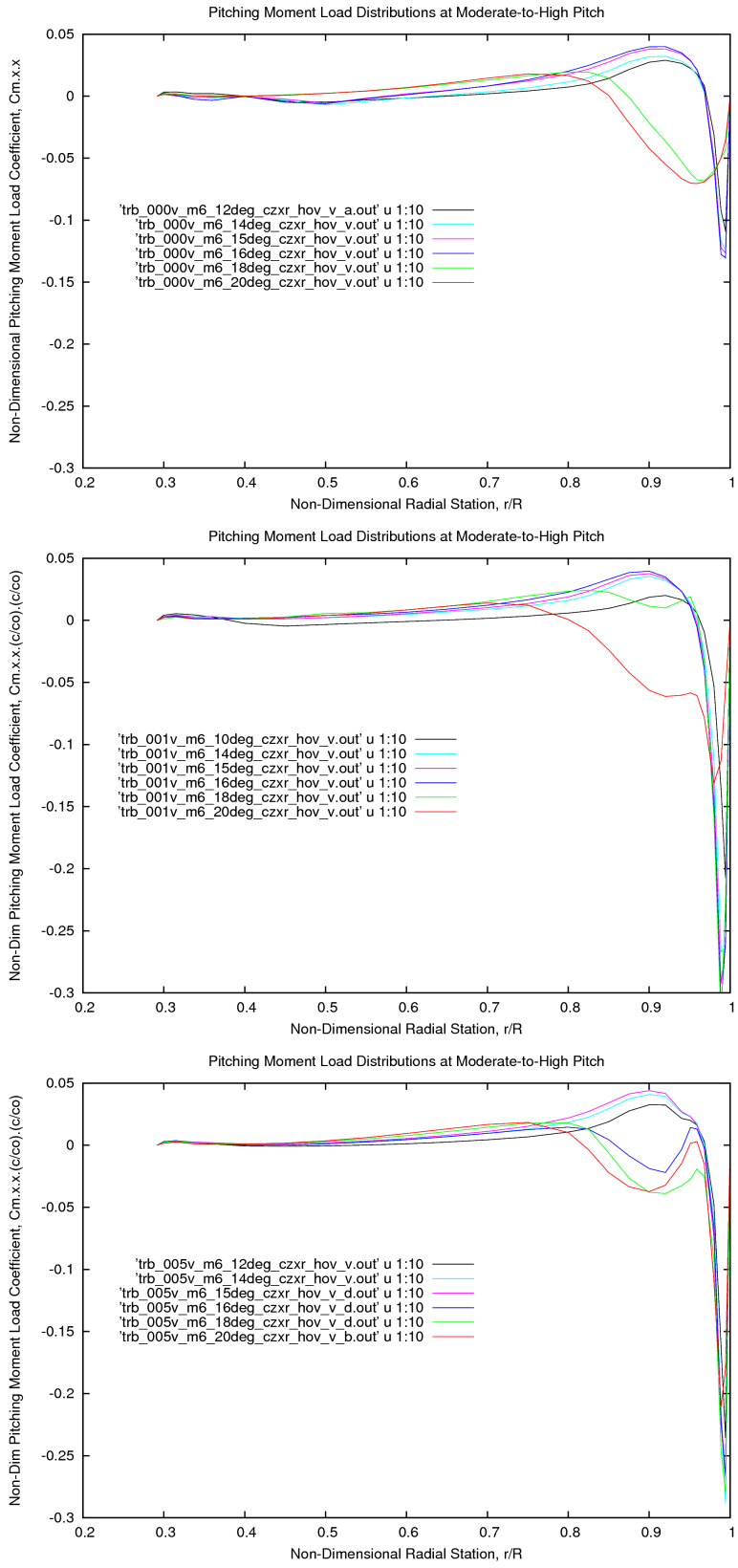

Figure 256: Predicted Pitching Moment Load Distributions for the 3 Tip Shapes at Moderate-to-High Pitch. Top: TRB-000v (Datum, Rectangular). Middle: TRB-001v (Küchemann). Bottom: TRB-005v (Küchemann with Anhedral)

a 'high-CT' state, depending on the induced-flow state near the root of the blade. Thus two sets of points are available, and both have been included in the following plots, the 'low-CT' points, which seem to be more realistic at low-to-moderate pitch, are shown by solid points, and the 'high-CT' solutions by open symbols. For ease of identification, these symbols have been joined by straight lines, either a full-line or a dashed line, respectively. In some cases these lines also help to show the trend while in other cases they can distract the eye, especially when only a few results are available.

The total thrust and pitching moments are presented in Figure 257. The total thrust is included for completeness, and is presented in terms of the blade loading coefficient, CT/s. These results again reflect the variation in the results due to changes in flow state. The total pitching moments show the expected gradual nose-up trend prior to the onset of stall, partly due to the NACA0012 aerofoil at mid-Mach number, but also due to the balance between the nose-up and nose-down moments at the outer end of the blade. The total pitching moment becomes negative when the tip begins to stall, as already noted from the trends in the loading distributions. It appears from these total pitching moment plots that the flat Kuchemann tip blade, TRB-001v, may encounter stall later than the other blades, and that the anhedral blade may perhaps break earlier. However, it is difficult to accurately determine the break point from the total moments due to the limited number of results available and the variability that is present.

Figure 258 presents the local Cz and Cm coefficients at 94%R. For the datum blade, TRB-000v, the results fall closer together, confirming that the effect of the flow changes near the root of the blade does not greatly affect the flow over the tip. The 18 degree point appears to fall on a continuation of the 'low-CT' thrust-pitch curve, while the 20 degree result falls off due to stall. This blade would appear to be free of stall at 16 degrees, but eventually the moments may diverge rapidly. The results for TRB-001v and TRB-005v are less clear. For TRB-001v, the trends may be better appreciated if the line joining the 'low-CT' points is ignored, and the overall impression gained is that this tip progresses into stall more gradually than the others. For TRB-001v, the pitching moment appears not to break until after 17 degrees. TRB-005v is perhaps more sensitive to flow variations and could either break early at 15 degrees or hold on to 16.5 degrees, perhaps as a consequence of the tip vortex from the preceding blade passing closer below the tip, or the sharpness of the anhedral crank itself eroding the performance near stall, despite the careful blending used.

In order to obtain a better understanding of the flow in the region of 94% radius some cross-sections of the flowfield are presented at a pitch angle of 16 degrees in Figure 259 and at 20 degrees in Figure 260. These figures show contours of the velocity-magnitude and streamtraces have been added to help visualise the flow in a plane normal to the blade surface. Here the local velocity of the blade in the rotating mesh has been added to the V-velocity component before computing the velocity-magnitude of the flow over the blade:

$$\mathrm{V}_{rel} = \mathrm{V} - \mathrm{X}/(\mathrm{R}/\mathrm{c}) \tag{31}$$

where V is the V-velocity component, X is the distance along the reference axis of the blade (in chords) and for the model tail rotor R/c=6.402439. For the anhedral blade, the cross-section should be taken normal to the surface of the blade, so that the upward component of velocity, W_δ, in this tilted plane becomes:

$$\mathrm{W}_\delta = \mathrm{W}\cos(\delta.\pi/180) + \mathrm{U}\sin(\delta.\pi/180) \tag{32}$$

where W is the vertical (or axial) velocity and δ is the anhedral angle. The velocity-magnitude in this plane is then given by:

$$\mathrm{V}_{mag} = \sqrt{(\mathrm{U}^2 + \mathrm{V}_{rel}^2 + \mathrm{W}_\delta^2)} \tag{33}$$

and finally the Cp based on the local Mach number is given by:

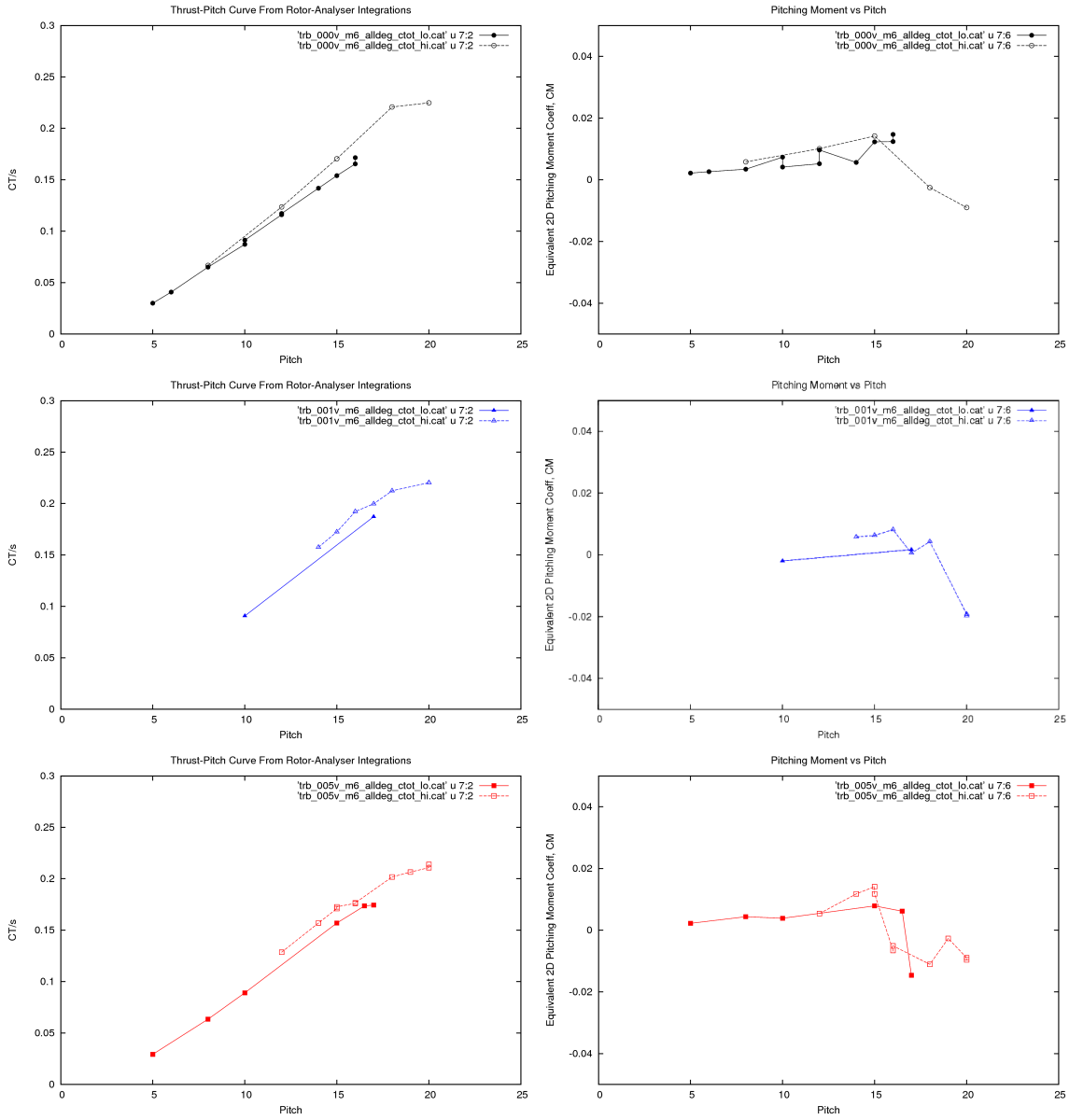

Figure 257: Total Thrust and Pitching Moment from Steady Navier-Stokes Predictions using a Modified k-ω Turbulence Model, Mtip=0.6. Top: the Datum, Rectangular tip, TRB-000v, Middle: Küchemann tip, TRB-001v, Lower: Küchemann tip with Anhedral, TRB-005v. Solid Symbols 'Low-CT' Solution, Open Symbols: 'High-CT' Solution

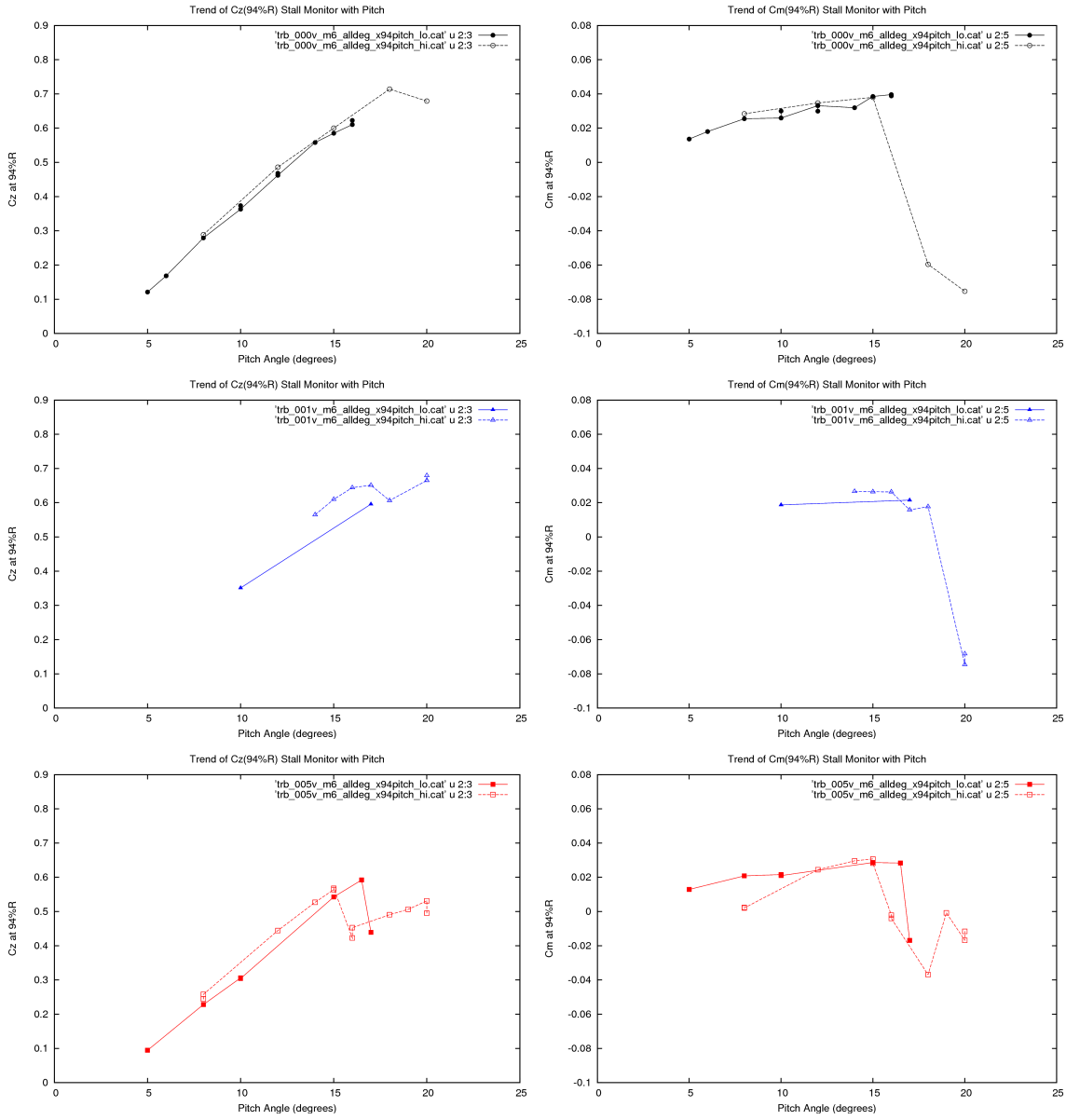

Figure 258: Sectional Thrust-Force and Pitching Moment Coefficients at 94%R from Steady Navier-Stokes Predictions. Top: the Datum, Rectangular tip, TRB-000v, Middle: Küchemann tip, TRB-001v, Lower: Küchemann tip with Anhedral, TRB-005v. Solid Symbols 'Low-CT' Solution, Open Symbols: 'High-CT' Solution

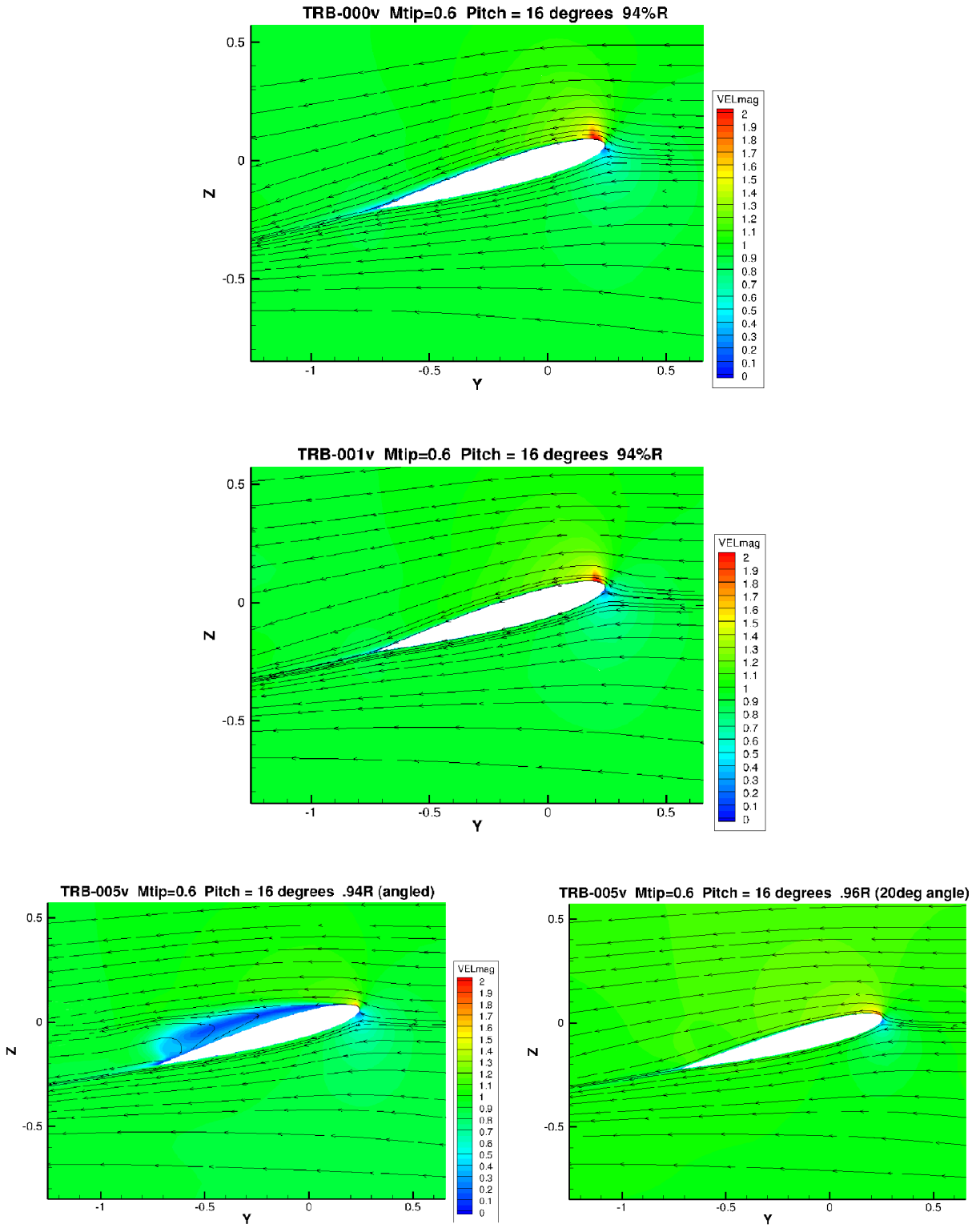

Figure 259: Contours of Velocity Magnitude and Stream Traces in Cross-Section Planes at 94% (TRB-005v also at 96%R) Radius for the 3 Tip Shapes at 16 degrees Pitch. Top: TRB-000v (Datum, Rectangular). Middle: TRB-001v (Küchemann). Bottom: TRB-005v (Küchemann with 20degrees Anhedral) Sectioned Angled Normal to Surface at 94 and 96%R.

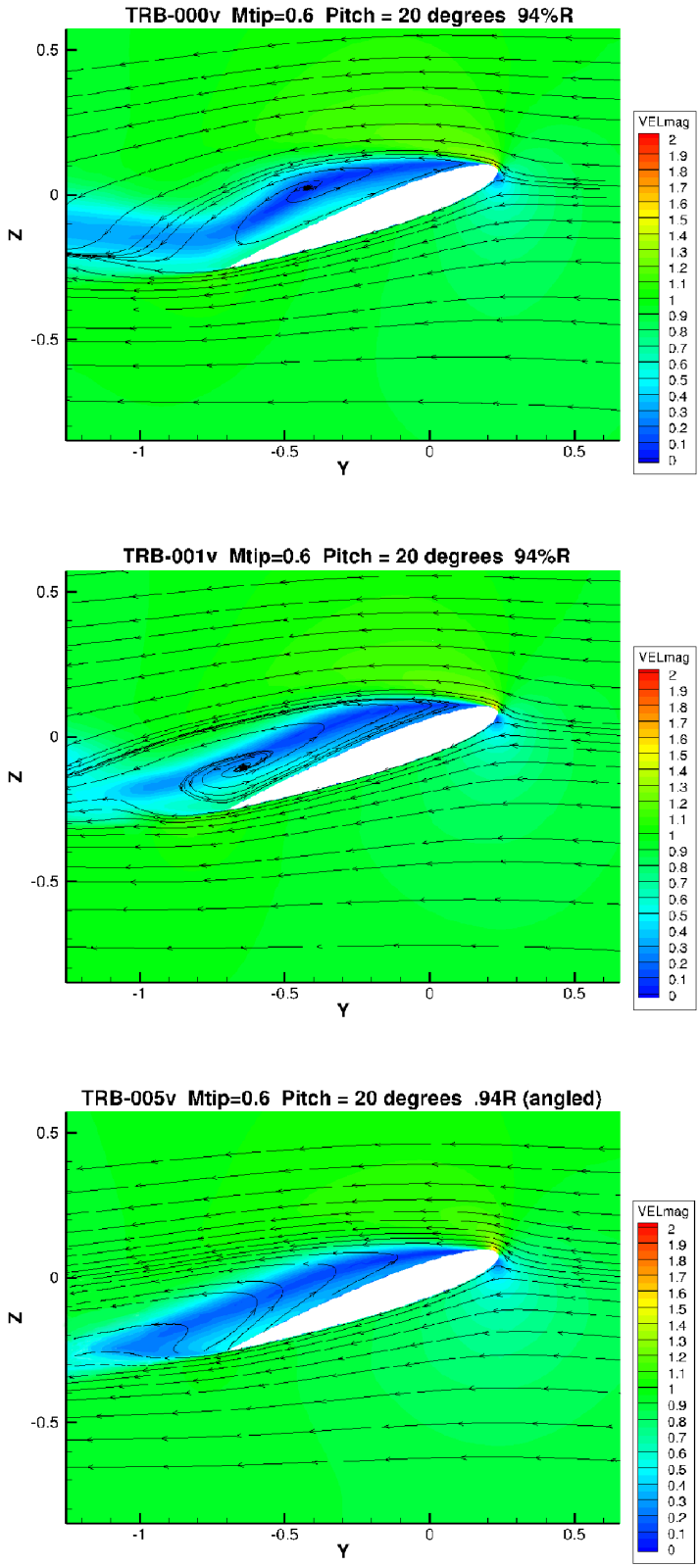

Figure 260: Contours of Velocity Magnitude and Stream Traces in Cross-Section Planes at 94% Radius for the 3 Tip Shapes at 20 degrees Pitch. Top: TRB-000v (Datum, Rectangular). Middle: TRB-001v (Küchemann). Bottom: TRB-005v (Küchemann with 20degrees Anhedral) Sectioned Angled Normal to Surface.

$$C_p=2(P - 1/(\gamma.M^2.x^2)) \tag{34}$$

where P is the pressure, γ is the ratio of specific heat (1.4 for air), M is the tip Mach number and x is the radial station as a fraction of the radius.

In the 16 degree case, Figure 259, the flow appears to be fairly well attached for the flat Küchemann tip, TRB-001v, and for the datum rectangular blade, TRB-001v, some additional thickening of the boundary layer can be seen on the upper surface trailing edge of the blade. For the datum blade a weak shock is present near the leading edge, and the strength of this feature is diminished for the Küchemann tip blade, TRB-001v, due to the rounding of the leading edge corner of the tip. For the anhedral tip, TRB-005v, the shock is similarly weak, but at 94%R the flow is separated (aft of the shock). The 94% radial station is centred on the (blended) crank of the anhedral (and the section here is therefore inclined at an angle of 10 degrees). The chord is constant in this region. However, just 2%R (12.8% chord) further outboard it was noticed that the flow is still fairly well attached with just a little thickening of the boundary layer near the trailing edge for TRB-005v at 16 degrees. This is consistent with the previous illustrations which depicted the surface pressures, but here the velocity contours make the change with radial position more striking. The 96% radial station is at the start of the Küchemann tip (and the section is inclined at 20 degrees on the anhedral tip). It may be that the angular style of anhedral adds to the adverse pressure gradients near the leading edge at the anhedral station, and perhaps it would have been better to more smoothly blend the anhedral and fair it with the shape of the tip in a single panel, although this may also mean having to scarifice some tip displacement or widen the tip.

Figure 260 shows the amount of separated flow at 94%R and 20 degrees for each of the tips. The datum rectangular tip would appear to be more strongly separated, and there is a hint that in reality the separation would be unsteady and 'blobs' of vorticity would be shed from the blade and the wake behind the blade would oscillate. This process is here being effectively 'time-averaged', or smeared, by the use of a steady solution.

6.4.3 Stall Monitors

In order to more precisely determine the point of stall onset, alternative stall monitors are now considered. These techniques have been used previously in industry, eg Isaacs and Harrison,[153] and by research establishments, Wilby,[319] both for 2D aerofoils and rotor blades in flight, but are less commonly used to extract results from CFD simulations. Following the ideas put forward by Brotherhood and Riley[63] in their flight tests on the Puma, two different stall monitors may be applied to the present problem. The development of the leading edge pressure, say at 2% chord on the upper surface, will not only give an indication of the angle of attack (as discussed in Chapter 7), but will also show when the leading edge pressure starts to collapse, either due to a leading edge separation, or more progressive trailing edge separations, depending upon the freestream conditions and the local geometry. Another useful parameter to monitor is the divergence of the upper surface trailing pressure which also occurs when the flow separates. To get some idea of the likely effectiveness of the stall monitors, these parameters were first extracted from earlier 2D aerofoil HMB Navier-Stokes computations (Chapter 3), for NACA0012 at a Mach number of 0.5 and Re=1 million, and are plotted in Figure 261. At this Mach number a weak shock develops behind the suction peak, and separation occurs due to the resulting strong adverse pressure gradient as the angle of attack is increased prior to the stall developing. The Cp at the leading edge increases gradually at first and then the gradient becomes steeper before it reduces markedly and even reduces a little as the aerofoil stalls. The trailing edge pressure shows a very gradual increase with angle of attack while the flow is essentially attached, but the gradient steepens as the boundary layer starts to thicken and eventually separates at stall. As the stall starts to occur the trailing edge pressure diverges quite rapidly.

Fortunately, all the required information for these stall parameters is available in the rotor CFD solutions, and can most easily be obtained from the output files of the Rotor-Analyser Fortran program (see Appendix G) after first taking slices across the blade in Tecplot at a series of chosen radial station. By referring to the pressure plots and loading distributions already presented, 94% radius was again chosen as the station at which the leading edge pressure (suction) and trailing edge pressure would be monitored.

Applying these stall monitors to the tail rotor results, the two sets of points on the plots of the datum blade, TRB-000v, again come close together in the top graphs in Figure 262. It would appear from the trailing edge pressure that there is very little separation at 15 degrees and some light stall may be present at about

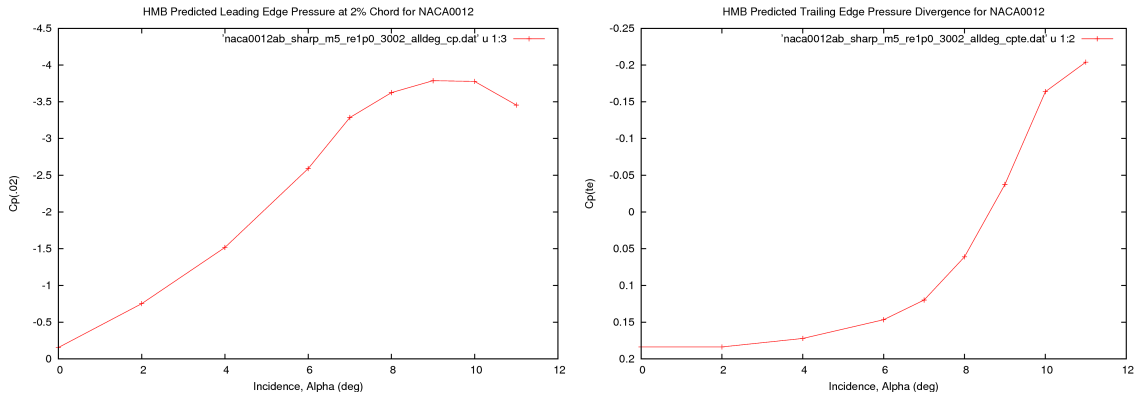

Figure 261: Steady HMB Predictions of Leading Edge and Trailing Edge Pressures Trends Into Stall for 2D NACA 0012 Aerofoil at M=0.5 and Re=1 million using a k-ω Turbulence model. Left: Leading Edge Suction Peak Development, Right: Trailing Edge Pressure Divergence. Solid Symbols 'Low-CT' Solution, Open Symbols: 'High-CT' Solution

16 degrees. The stall then develops as the pitch is increased to 18 degrees, with the 20 degree point having diverged to Cpte=-0.4, inferring almost complete separation at this radial station. The leading edge pressure also rolls over and starts to fall, with the maximum probably close to 16degrees, or just over. The middle pair of graphs in Figure 262 are for the flat Küchemann tip, TRB-001v. Ignoring the solid line (which simply joins two points at vastly different pitch angles), the 'high-CT' points show a similar rounding of the leading edge pressure with a peak at about 16 degrees and this holds until about 18 degrees, similar to the datum blade. The trailing edge pressure starts to show a lack of recovery between 16 and 17 degrees (inferring light stall at 17 degrees), and has started to diverge by 18 degrees of pitch, and again at 20 degrees has diverged to Cpte=-0.4. The lower graphs in Figure 262 for the anhedral, Küchemann tip, TRB-005v, show more variation between the 'low-CT' and 'high-CT' results. Here, it would appear that the leading pressure may fall more suddenly after about 15 or 16 degrees of pitch has been reached. The trailing edge pressure may hold on to 16.5 degrees, but may then diverge more sharply for TRB-005v. Interestingly, the trailing edge pressure does not diverge to the high negative values noted above, and seems to hold at around Cpte=-0.2 for the Küchemann tip with anhedral.

The local pitching moment, leading edge pressure and trailing edge pressure, at 94%R, have been successfully used as stall monitors, and the aerodynamic performance of the three tip shapes has been able to be characterised. The flat Küchemann tip has been found to give a significant reduction in induced power, to also have a lower profile drag. In addition, this part of the analysis has found that, for this tip, the onset of stall is delayed by up to about 2 degrees, relative to a rectangular tip blade. The anhedral Küchemann tip brought about a further reduction in induced power at low-to-moderate pitch angles, together with low profile drag, but appears to be more prone to stall onset than the flat Küchemann tip. It may be that a slight reduction in anhedral, and a more blended anhedral shape tip would be preferable to the simple cranked/blended anhedral of TRB-005v.

Much more reliable predictions and comparisons could have been made if the vortical flow instability near the root-end of the blade had been identified earlier and could have been suppressed by some means, such as using a more representative geometry as suggested in Section 6.3. If this was successful, or if twisted blades with a smaller root cut-out had been chosen as a carrier, it is reasonable to expect that the steady solver may be used safely up to the onset of stall, although as flow separation increases it becomes progressively more difficult to obtain a converged solution. However, when the residuals do not adequately reduce and the integrated pitching moment does not settle, an unsteady Navier-Stokes method is then called for. Application of an unsteady method also opens the door to a more comprehensive simulation, which may include the hub components, and removes the concerns of convergence when strongly separating flows may occur, and indeed other parts of the airframe may also be included.

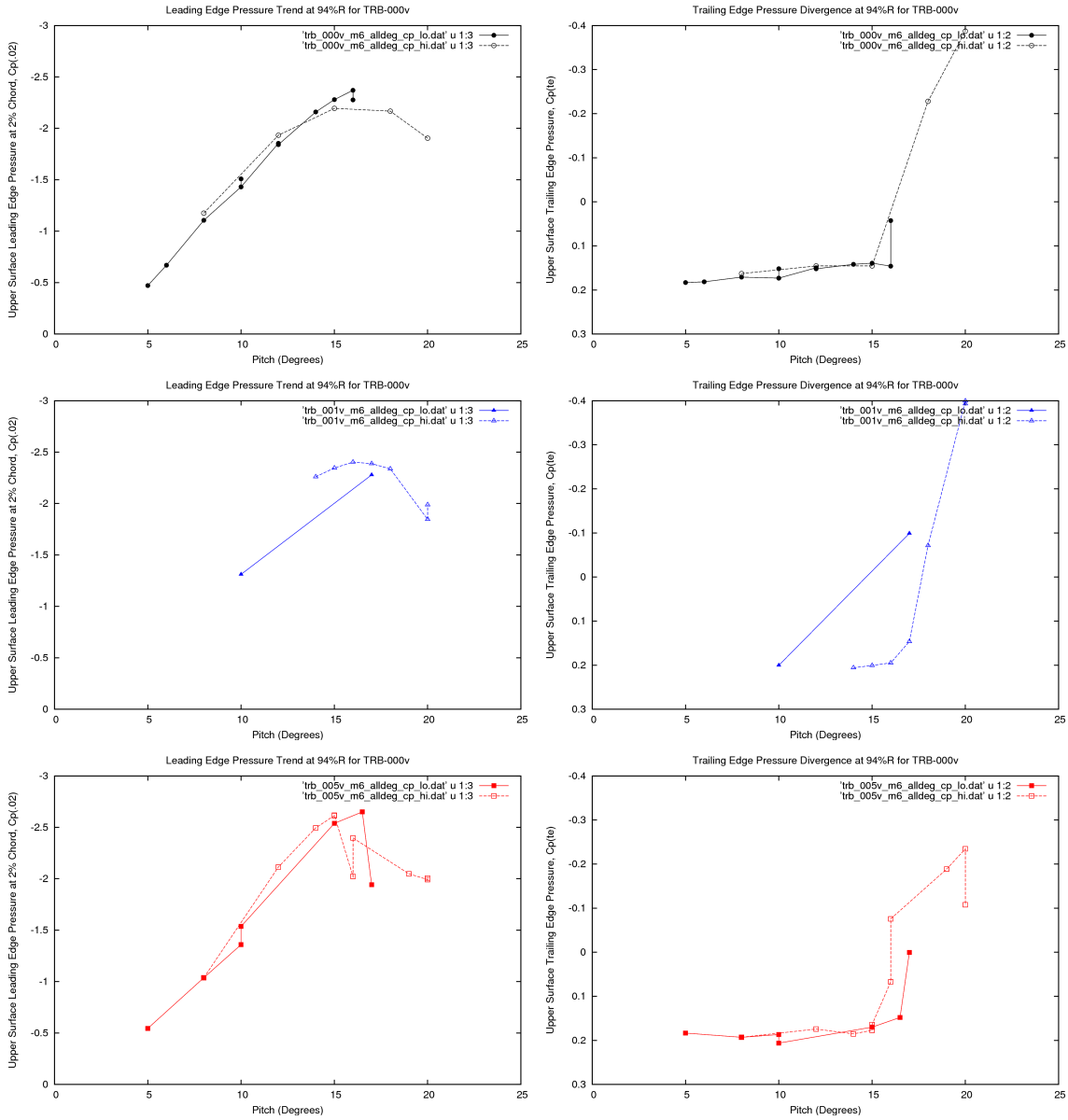

Figure 262: Stall Monitors: Leading Edge Suction Peak Development and Trailing Edge Pressure Divergence from Steady Navier-Stokes Predictions using a Modified k-ω Turbulence Model, Mtip=0.6. Top: the Datum, Rectangular tip, TRB-000v, Middle: Küchemann tip, TRB-001v, Lower: Küchemann tip with Anhedral, TRB-005v. Solid Symbols 'Low-CT' Solution, Open Symbols: 'High-CT' Solution

7 Further Analysis of CFD solutions

The numerical analysis methods used to solve the flowfield around the blade of a helicopter rotor furnish a great wealth of information. At all points in the flow field, the density, the pressure (and temperature) and the three orthogonal velocity components are computed, and for a Navier-Stokes solution the effects of viscosity are taken into account and the three components of the skin friction on the blade surface may also be available. The integrated forces and moments provide useful performance data, and the blade surface pressures are available as more detailed information. Visualisation of the solution may also be used to reveal details of the wake. However, some post-processing is often required to extract the blade loading distributions which are most conveniently extracted from the CFD in rotor (or body) axes, rather than as a distribution of CL and CD which act in the direction of the angle of attack (ie in wind axes) as employed in more traditional lifting-line type rotor models. The familiar parameters of downwash and angle of attack are therefore not available to the rotorcraft engineer, and he is unable to make direct comparison to assess the results in familiar terms. This section of the thesis considers several possible ways of extracting the downwash and angle of attack from a computational solution.

Traditional rotor lifting-line based analysis methods, whether using a prescribed or a free wake, often make use of aerofoil tables, or curve-fitted trends, based on wind tunnel data, sometimes with empirical corrections. Hence the lift, drag and moment coefficients acting on the blades are determined from the calculated angle of attack and local Mach number. The lift and drag coefficients are based on wind axes, and act normal and tangential to the local freestream direction. Since the inflow angles are calculated in the model, either from momentum, blade-element-momentum, or vortex theory, these local coefficients may therefore be resolved and integrated along the blade to obtain the thrust and torque. The angle of attack is obtained from the difference between the local geometric pitch angle and the local inflow. In hover, the inflow is simply the induced flowfield, or downwash (and any swirl velocity), which is thought of as a mean value acting on a local blade element. In contrast, the angle of attack and inflow are not explicitly used in the CFD approach, and the resulting surface pressures are simply resolved and integrated to give the overall forces and moments on the blade. Hence in the CFD solution there is no explicitly defined angle of attack, and the induced velocity is implicit in the flowfield and not singularly defined as a representative value acting on a blade element.

For a regular structured grid, such as may be used on the datum, rectagular blade, the predicted surface pressures may be readily integrated around the chord to provide force and moment coefficients in either body axes (Cn and Cc), or rotor axes (Cz and Cy). However, for a more complex tip shape, the orientation of the grid may change, such that a chordwise integration becomes more difficult, and the surfaces pressures first need to be interpolated. This could be done in the solver, but would prolong the runtime and the information is not always required until the final step of a steady solution (for an unsteady forward flight solution, knowledge of the time-varying local Cn and Cm would be extremely useful, but the problem then becomes one of storing this extra information). In the current work, the necessary interpolation and integrations are carried out in a post-processing operation by the combined use of Tecplot, to extract slices across the blade, and Rotor-Analyser to perform the chordwise (and confirmatory spanwise) integrations. However, having obtained the local Cz and Cy, or Cn and Cc, these quantities are not in wind axes and so there is still no ready means for the rotor engineer to relate these quantities to the (steady) angle of attack or the (time-averaged) downwash distribution.

One solution, and that used in many of the graphs presented in this thesis, is to present the CFD results in terms of force coefficients in the thrust and torque directions (as obtained from post-processing). Indeed, it should be a relatively straightforward matter to resolve the CL and CD of the classical rotor hover model from wind axes to rotor axes in order to accurately compare results. After all, this resolution is already done, or should be done unless small angle approximations are being used, to obtain the overall forces and moments on the rotor blades from the classical approach. While a rough comparison may be acceptable in some instances, at high pitch angles, such as those considered here for highly loaded tail rotors (but also for propellers and prop-rotors), careful resolution is necessary. However, this does not answer the rotorcraft designer's need to gain some idea of the local angle of attack, or to be able to compare downwash distributions.

7.1 Angle of Attack from Time Averaged Downwash

In hover, the angle of attack, α, is simply given by the difference between the local pitch angle, θ, and the induced flow:

$$\alpha = \tan^{-1}(\theta \text{ - } \lambda_i/(\text{x-}\lambda_\psi) \tag{35}$$

where λ_i is the local axial downwash and λ_ψ is the tangential or swirl velocity. In many instances, this latter term is small compared to the rotational speed, represented here by the non-dimensional radius, x (after dividing through by ΩR). For main rotor applications, the swirl velocity may indeed be small, and since the angle of attack is small the above equation can be simplified to:

$$\alpha = \theta \text{ - } \lambda_i/\text{x} \tag{36}$$

This form is often used in simple momentum analyses for main rotors, but for the highly loaded tail rotor, and for prop-rotors and fenestron applications, where the pitch angles are high and the swirl term is likely to be significant, equation 35 should be used (with any other appropriate inflow terms also included if in axial or edgewise flight).

Therefore, if the local downwash velocity can be determined from the CFD solution the angle of attack can be simply calculated. However, extracting a downwash velocity which is equivalent to that used in a lower-order method is not straight forward, even for an apparently simple hovering rotor case.

Figure 263 provides a 3D visualisation of the w-velocity component 0.25c below the rotor. In this lower part of this figure, the w-velocity (downwash) has been plotted on the vertical axis to give a 3D graphical representation of one blade-segement of the wake (in this case for $\psi = +/-45$ degrees, ahead of and behind the blade). The flow distortions local to the blade, and the edge of the wake are clearly visible, as is the upwash inboard of the root. At the edge of the wake the downwash peaks, and outside the wake, and ahead of the blade there is a strong upwash induced by the trailng vortices. It is therefore clear that there is not single value of the downwash that can be simply extracted as acting on the blade.

The problem is further illustrated in Figure 264 where Tecplot has been used to slice the wake, firstly in the plane of the rotor, and secondly in the contracted wake, well below the rotor plane. As expected, the flow gradually accelerates as it approaches the rotor disc, and following momentum theory, eventually reaches a mean velocity which is approximate double the speed at the rotor disc when the wake has fully contracted. So, not only is there an azimuthal and radial variation, as illustrated in the upper part of Figure 264, but both the distribution and the magnitude of the induced velocity changes as the flow passes through the plane of the rotor.

Some early work undertaken to explore the balance between the mass-flux and thrust produced from the change in mometum of the averaged flow field gave the result that the downwash should be taken in a plane very close to the rotor disc. However, as Figure 264 shows, this is not possible without intersecting the blade. For this analysis, the blade locations were simple skipped, and the remaining velocities were effectively time-averaged in the plane of the rotor by summation around the azimuth for a range of radial stations. However, when a section is taken in the rotor plane through the computational grid, the points obtained are not in a structured pattern and need interpolating onto radial and circumferential lines.

For convenience this was done by over-laying a cylindrical grid and interpolating the data in Tecplot, as shown in Figure 265. A coarse grid was used in initial explorations which covered a larger part of the wake, and finally a finer grid was chosen for extracting the w-velocity in z-planes closer to the rotor disc. Once the data had been interpolated onto the cylindrical grid it was written to a data file and subsequently integrated around the azimuth with a Fortran program to give the time-averaged, or mean, downwash at each radial location.

The results of taking a cross-section at the rotor disc, integrating for the downwash and the computing the angle of attack are shown in Figure 266 for the case of the datum blade at a pitch angle of 10degrees and

a tip Mach number of 0.6 (Navier-Stokes computations for the three selected tail rotor tip confirugations are described in Chapter 7). In the top part of Figure 266, the azimuthally-averaged, or time-averaged, hover downwash distribution shows significant variation over the radius, and there is a region of strong upwash adjacent to the cylindrical hub (used as a simplification for the computational domain). The mean downwash increases gradually along the blade, but then near the tip the edge of the wake and the effects of the wake contraction that takes place ahead of the blade comes into playand causes a sharp reduction in the downwash which becomes slightly positive at the extreme tip. The downwash distribution extracted from the CFD solution is also compared to the variation of downwash from the WHL (Lifting-Line) Hover Program. The agreement is fairly good between 50% and 94%, although there appears to be a vertical shift with the downwash extract from the CFD being greatest and near the root and tip of the blade there are significant discrepancies (in the CFD the blade tapers at the root from unit chord at 33.33%R, to 0.5 chords at 29.17%R where it is cut-off, while in the hover program a root cut-out of 33%R was used). The lower part of Figure 266 compares the angle of attack as calculated from the downwash, and from the Hover Program. Again, the agreement is remarkably good over most of the blade, while there is large disparity at the root and tip of the blade. Of course, the flow is highly three-dimensional in these regions, so some differences are to be expected. However, even small changes in the angle of attack have a large impact on the blade loading and it in these regions were the rotorcraft engineer would most like to know what the true angle of attack really is.

The comparisons also show an inconsistency in that the angle of attack itself is in close agreement whilst the agreement for the downwash is not so close. This could be due to a momentum top-up used in the Hover Program, or it could be that the swirl velocity was not properly taken into account in either approach, and the particularly close agreement for the angle of attack is due to comparing at the same CT (the Hover Program tends to over-predict the thrust for model rotor blades having very low Reynolds numbers, despite utilising low-Re data). Of course, the value of z/R at which the cross-section of the wake was taken in extracting the downwash from the CFD will have a bearing on the results. Taking a cross-section lower in the wake would tend to further increase the magnitude of the downwash and add to the wake contraction, while taking it just above the rotor seems a rather arbitrary choice, although it would reduce the magnitude and perhaps avoid some dofferences at the root and tip.

These issues were not pursued further in the current work, as the main focus was on ways of evaluating the performance of the selected tip shapes, and it seems that the accuracy needed for a deeper understanding could not be achieved from this avenue of the research. There are however, other perhaps more direct ways of determining angle of attack that would satisfy the need to compare with traditional rotor codes and at the same time offer further insight into the tip design.

However, before closing this brief study of the downwash it is perhaps worth remarking that, in principle, any change in blade design should be able to be seen in the induced velocities in the wake. It has already been shown that different rotor designs affect the details of the vortex trajectories, and it is also expected that these changes will also be seen in the downwash distribution (even if questions remain in the tip region).

Clearly, a blade design parameter such as twist should be reflected in the downwash distributions both at and below the rotor, and this was found to be the case when the Euler solutions for the twist model rotor blades were analysed using the methods outlined above. The effect of twist on the downwash distributions was shown earlier in Chapter 3.4, Figure 167. It was observed that the greater the twist, the more uniform is the distribution of downwash, and carrying more load inboard helps to make the rotor more efficient by making the downwash everywhere more uniform.

Euler solutions were also analysed to explore the effect of anhedral. In this analysis the datum rectangular blade, TRB-000, is compared to the rectangular blade with 20 degrees of anhedral, TRB-004. The time-average downwash distributions, both in the plane of the rotor and in the fully contracted wake are shown in the top part of Figure 267. Differences in the downwash are apparent near the tip (at the edge of the wake), particularly in the plane of the rotor, and it would appear that the anhedral tip has been effective in reducing the strength of the tip vortex, consequently bringing about a reduced downwash between about 75% and 95% radius. The changes further down in the wake are very subtle, although they suggest a tendency for the wake contraction to increase, consistent with the earlier results of extracting and plotting the wake trajectories (see Figure236 in Section 6.1). The reduced downwash inboard of the tip tends to load up the blade in this region, as shown by the increased angle of attack in the bottom part of Figure 267. Note that whilst the magnitude of the angle

of attack near the tip is clearly incorrect, the results for these blades cross over at about 95%R, suggesting that the effect of anhedral is also to off-load the tip. This is consistent with the changes seen in the loading distributions in Section 5.1.2.

The results from obtaining the angle of attack from the time-averaged downwash are compared to alternative methods of determining the angle of attack, as discussed below, in Figure 273 of Section 7.3. The results for the angle of attack from the downwash are seen to be in generally good agreement with the other methods, and are particularly close to those obtained from Cp-matching. Near the tip, the results obtained from the downwash climb steeply, while those from the stagnation and Cp-matching remain at about 4 degrees.

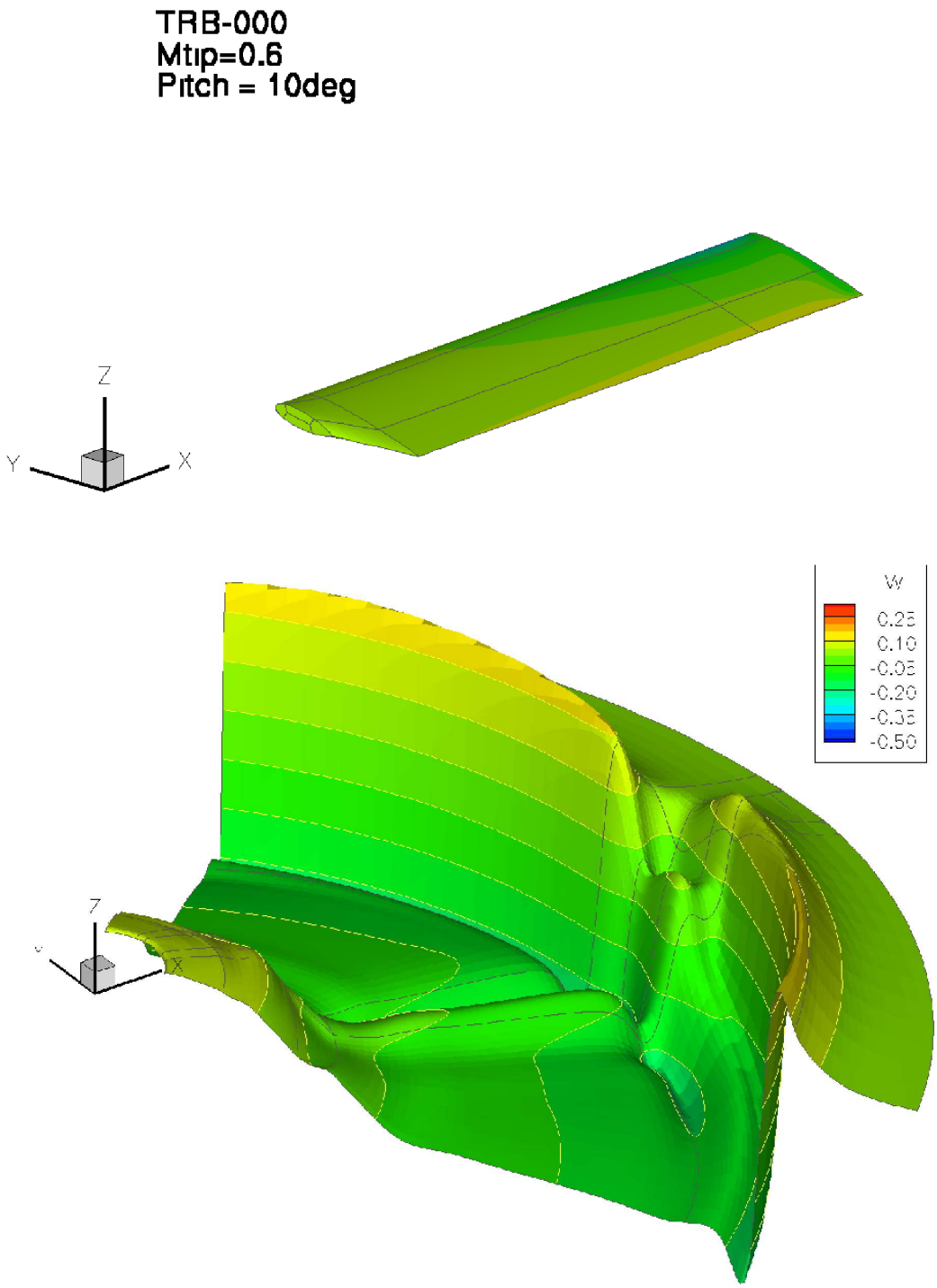

Figure 263: 3D Visualisation of the Downwash Distribution at 0.25 chords Beneath the Rotor Show Radial and Azimuthal Variations in w-Velocity

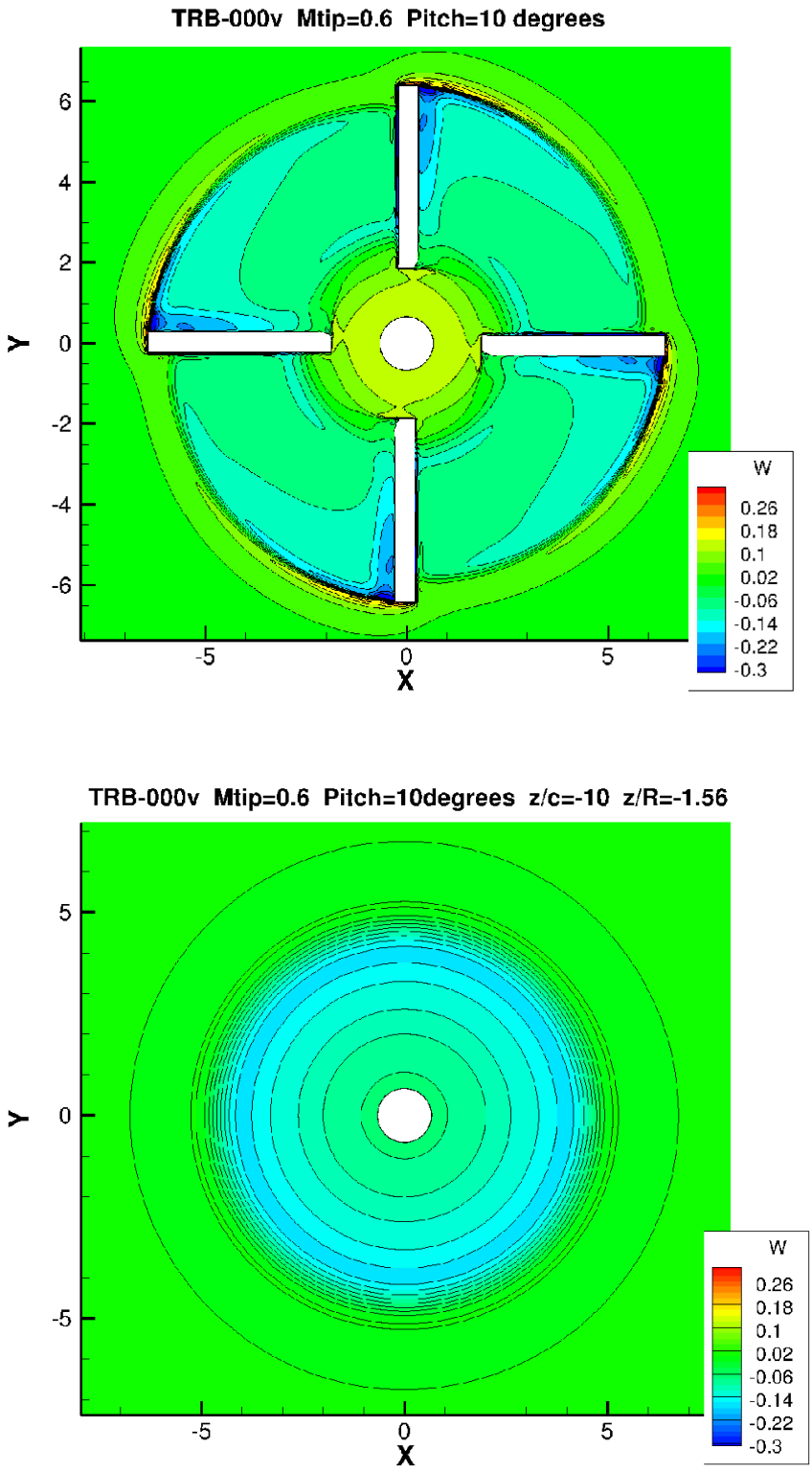

Figure 264: Contours of the Vertical w-Velocity Component (Axial Downwash) for the Datum Rectangular Blades at 10 degrees Pitch Angle. Top: In the Plane of the Rotor the Downwash is Strongest Behind the Blade and also Around the Periphery of the Disc Inside the Contracting Wake. Note the Upwash in the Centre of the Rotor. Bottom: In a Plane -10 Chords below the Rotor, z/R=-1.56.

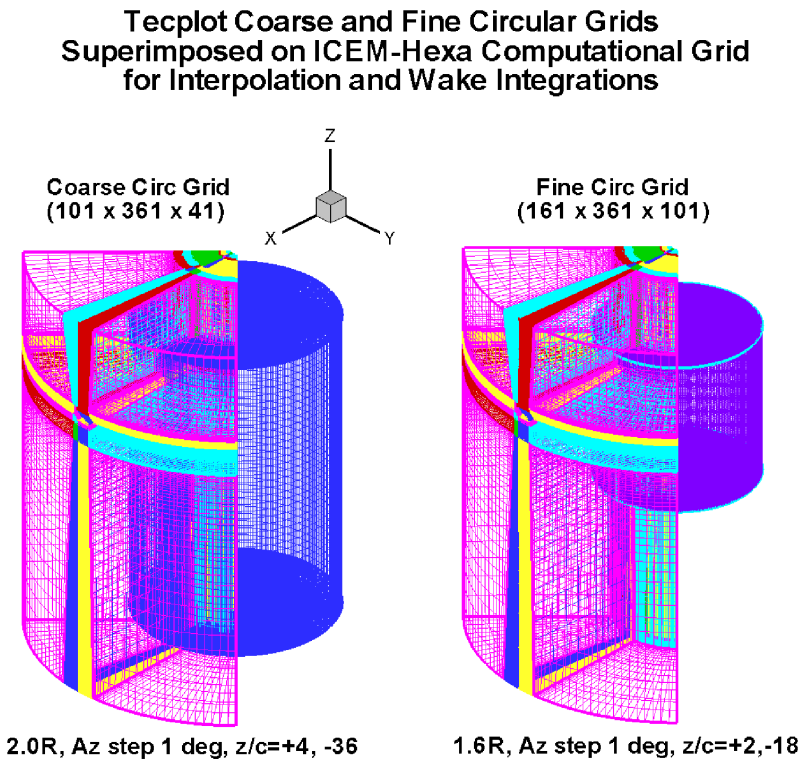

Figure 265: Coarse and Fine Circular Grids in Tecplot for Interpolation of Variables onto a Series of Planes Through the Wake

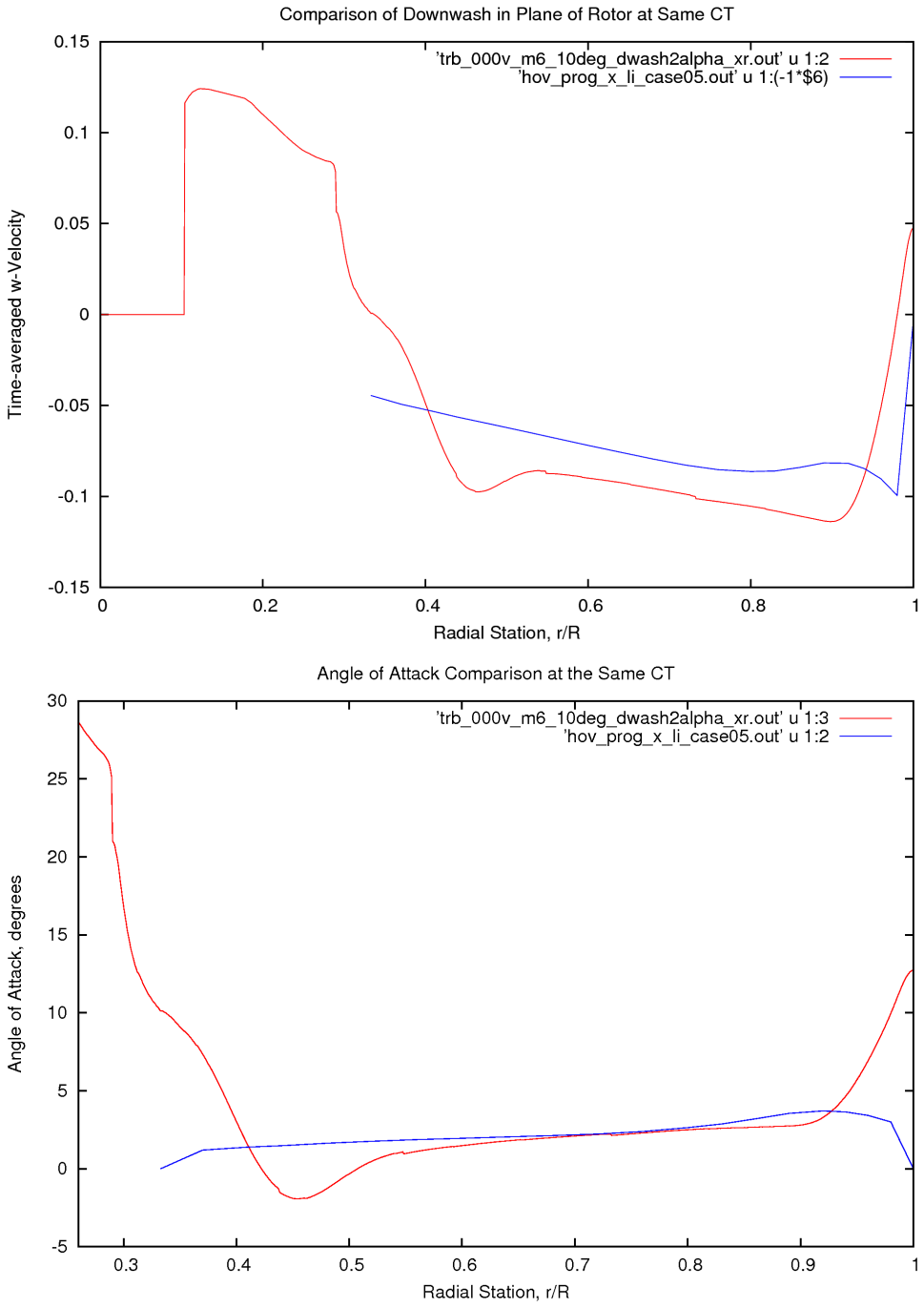

Figure 266: Time-Averaged Downwash and Angle of Attack from a Navier-Stokes Solution for the Datum Rectangular Blade, TRB-000v, at 10 degrees Pitch in Hover. Top: Average Downwash Distribution in the Plane of the Rotor Disc. Bottom: Resulting Angle of Attack Distribution.

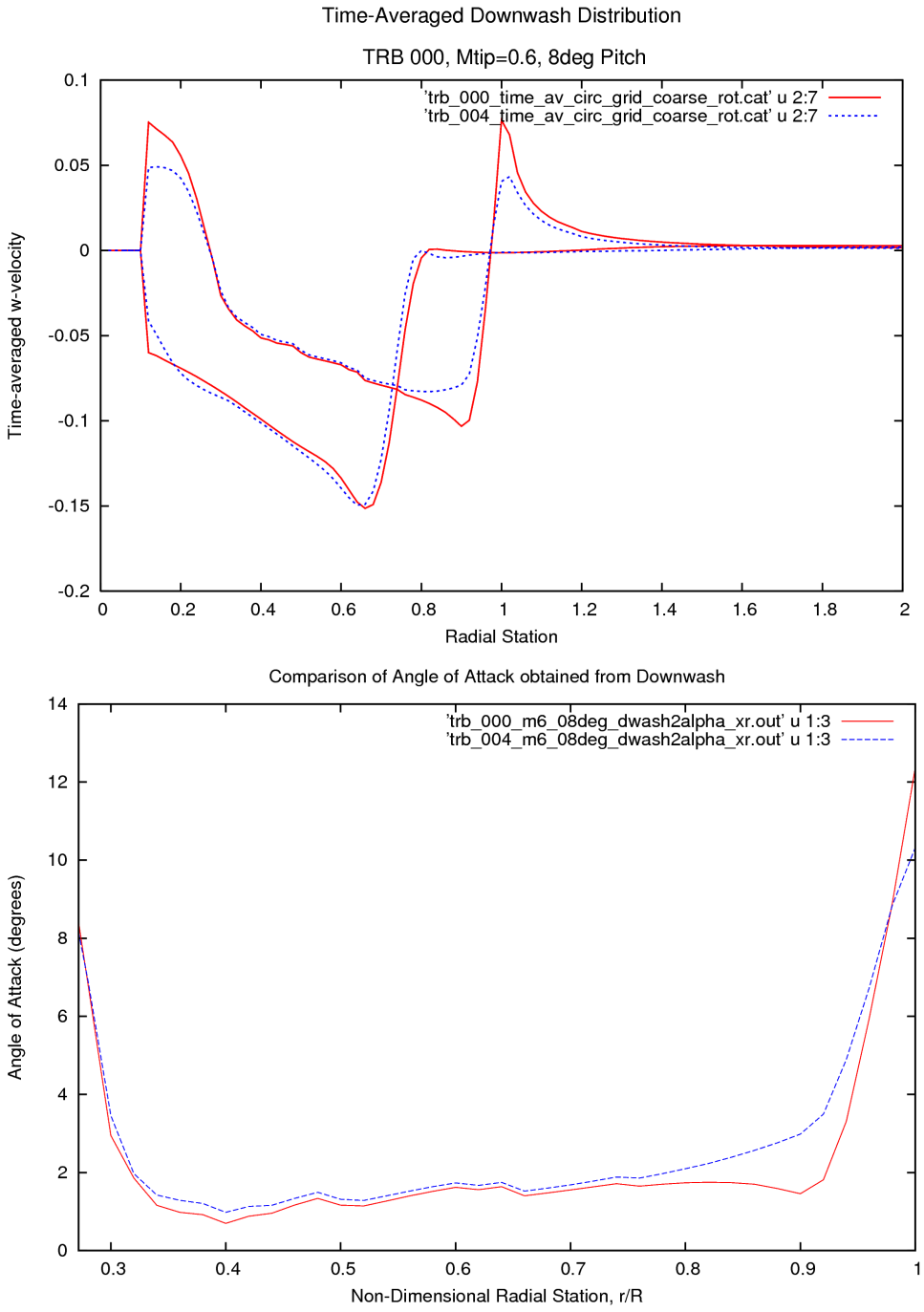

Figure 267: Comparison of the Time-Averged Downwash from Euler Solutions for the Datum Rectangular Blade, TRB-000, and the Rectangular Anhedral blade, TRB-004, in Hover at 8 degrees Pitch and Mtip=0.6. Top: Average Downwash Distribution in the Plane of the Rotor Disc and 12 chords, or 1.875R below the rotor. Bottom: Resulting Angle of Attack Distributions in the plance of the rotor.

7.2 Angle of Attack from Stagnation Point

One way to determine the angle of attack on the rotor blade is to identify the chordwise location of stagnation point. This approach should work well when the flow is reasonably normal to the leading edge, as in the middle section of the rotor blade, and elsewhere where there is a well defined stagnation point, or stagnation line on the surface of the blade. From the flow solutions generatred in Chapter 5 and 7, a stagnation point may be found on the lower surface of the rotor blade and the xyz position of any point on that line can be found via the probe in Tecplot, or by interpolating the solution via some other post-processing program. Towards the tips, the stagnation line may start to bend aft, and then becomes a flow-divergence line where the flow divides but does not stagnate as the outer edge of the tip is approached. Some of the flow is swept along the lower surface and some goes around the edge of the tip. Clearly the method will break down in this region, since the flow no-longer approximates the 2D ideal. As the stall is approached the rearward movement of the stagnation point will slow down, and could even reverse if the lift reduces.

The problem was therefore to relate the stagnation point location to the angle of attack. It was expected that a formula would be available from aerofoil theory, but nothing was found in the literature until after the following curve-fit to computational results was established. In 2007, Kang and Altman[160] published a paper in which they first quote a simple formula for the location of the stagnation point on a flat plate (actually it is mis-quoted, and that given in Katz and Plotkin,[163] their Ref 4, reads:

$$\text{xs=-(c/2).sin(2.}\alpha\text{))} \tag{37}$$

They then develop an equation for symmetrical 4-digit series NACA aerofoils using conformal mapping, introducing an additional term to account for thickness, but argue that camber has only a minor influence.

The formula for the stagnation point given by Kang and Altman is:

$$\text{Ds=((-0.9}\alpha^2 + 20\alpha - 2)t + 30\alpha^2 - 30\alpha + 6).10^{-5} \tag{38}$$

where Ds is the distance around the aerofoil from the leading edge to the stagnation point, t is the thickness in perent chord, and α represents the angle of attack. For NACA0012 this reduces to:

$$\text{Ds=(22.8}\alpha^2 + 210\alpha - 18).10^{-5} \tag{39}$$

However, this formula does not take into account compressible or viscous effects (although it could perhaps be modified to do so) and, since the NACA0012 of the model rotor blades operates between about M=0.3, Re=0.5 million at 50%R, and M=0.5 and Re=1.0 million at 83%R, to M=0.6 and Re=1.1668 million at the tip, it is essential to employ a technique that takes this into account.

For expediency, the MSES 2D aerofoil code was used to compute the characteristics of NACA0012 at the M=0.3 and M=0.5 conditions, and the stagnation point was obtained from the resulting Cp. These calculations were later checked against predictions from HMB and very close agreement was found. Some points from HMB have been added to the following plots. In retrospect it would have been better to use HMB to be consistent with the model rotor simulations.

The top graph in Figure 268 shows how the lift-curve of NACA0012 varies with Mach number. The NACA0012 used here has a sharp trailing edge so as to be compatible with the model rotor blade use in the computations. The slope of the lift-curves were checked against a simple Prandtl-Glauert relationship and the overall lift characteristics were also re-constructed using the method of Beddoes,[29] as part of the initial

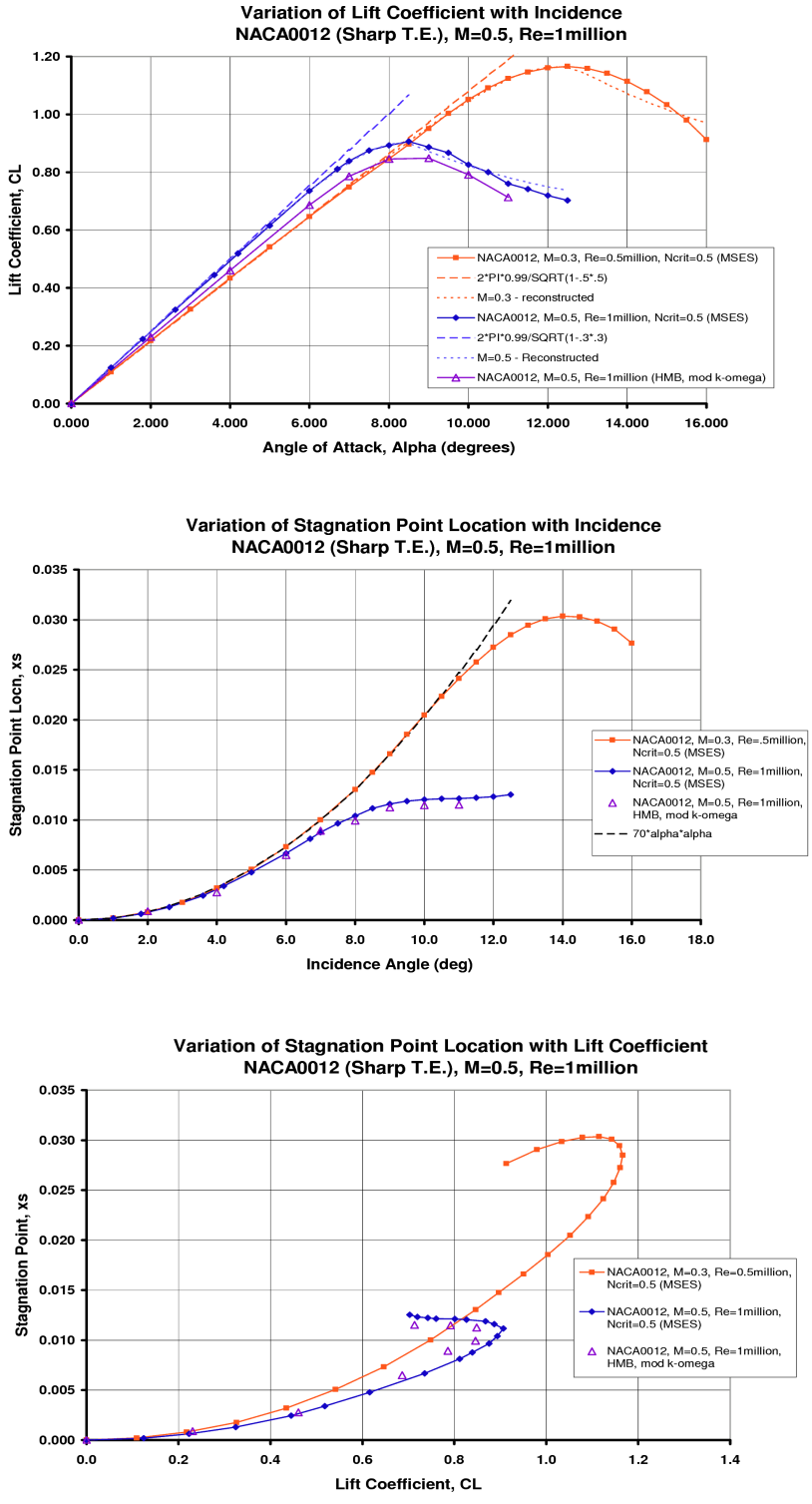

Figure 268: Predicted 2D Characteristics for NACA0012 at M=0.30 and M=0.50. Top: Lift-Curve. Middle: Variation of Stagnation Point Location with Angle of Attack (2D Incidence). Bottom: Variation of Stagnation Point Location with Lift-Coefficient

investigation. Subsequently 2D HMB results were also added for M=0.5, and show a small reduction in lift-curve slope which probably arises from the fact that MSES has an initially laminar boundary layer which allows a slightly higher suction peak to be generated over the leading edge of the aerofoil ahead of transition. This minor discrepancy is not important for the present purpose, as the intention is to demonstrate this process to determine the angle of attack. As shown on the middle and lower graphs of Figure 268 the results from the two methods are quite close in terms of stagnation point location and angle of attack. In this work it was found most convenient to measure the stagnation point in the chordwise direction, rather than around the leading edge as done by Kang and Altman, but the choice is a matter of convenience. Notice how the stagnation point moves gradually aft at first, and then more rapidly aft with angle of attack (or 2D incidence) until the stall is reached, when it may move forward again as the lift decreases post-stall, depending upon the Mach number and how the stall develops. Below the stall, this variation was found to be parabolic (as shown by the dashed line in the middle graph) in broad agreement with the work of Kang and Altman cited above. The reversal of the stagnation point at stall is most apparent at the lower Mach number, and at a Mach number of 0.5, or higher, the stagnation point tends to become invariant with increasing angle of attack once the separation boundary has been reached. The bottom graph in Figure 268 plots the stagnation point against CL and therefore places emphasis on this behaviour. It is observed that the stagnation point only starts to move forward after the maximum lift has been reached. Clearly, care is required if it is desired to obtain CL directly from the location of the stagnation point.

However, what is required here is to make the stagntion point the independent variable in order to obtain the angle of attack. The 2D CFD predictions were therefore replotted in this form as shown in the top graph of Figure 269. A square root function was used to fit the lower Mach number (M=0.3) curve in the middle graph of Figure 269, and an exponential growth was added to maintain the fit near stall. In the bottom graph of Figure 269, for M=0.5, a quardratic correction term was added to the square root function to allow for the effect of Mach number. Again an exponential growth was used as the stall was approached, and a further linear growth was also added. As illustrated in the graphs, the fitted curves closely follow the computational predictions, despite their simple nature.

The fit to the 2D predicted position of the stagnation point to allow the angle of attack to be found for NACA0012 at M=0.3, is given by:

$$\alpha = 70\sqrt{x_s} \qquad :\alpha < 10 \text{ degrees} \tag{40}$$

$$\alpha = 70\sqrt{x_s} + (e^{14000(xs-.0222)^2} - 1) \qquad :10 \leq \alpha < 14 \text{ degrees} \tag{41}$$

$$\alpha = 70\sqrt{x_s} + (e^{14000(xs-.0222)^2} - 1) + \sqrt{(x_{s14}-x_s)} \qquad :\alpha > 14 \text{ degrees} \tag{42}$$

where x_s is the chordwise location of the stagnation point as a fraction of the chord, and α is the angle of attack in degrees.

and for M=0.5, the fit is given by:

$$\alpha = 70\sqrt{x_s} + 6000.x_s^2 \qquad :\alpha < 7.5 \text{ degrees} \tag{43}$$

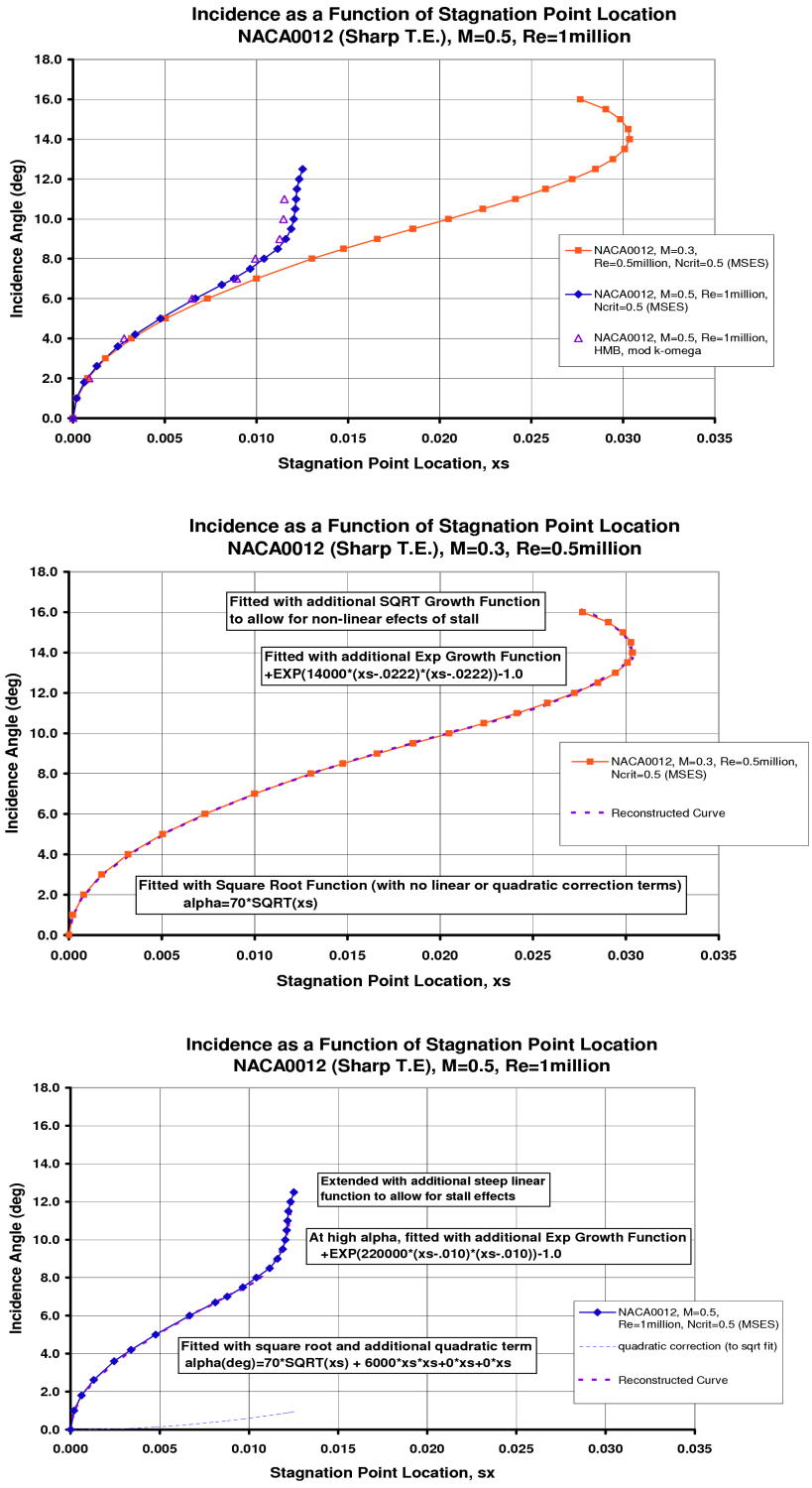

Figure 269: Curve-fits to Predicted Stagnation Point Locations for NACA0012 at M=0.30 and M=0.50. Top: Angle of Attack (2D Incidence) as a function of Stagnation point location. Middle: Curve-Fit for M=0.3. Bottom: Curve-Fit for M=0.5

$$\alpha = 70\sqrt{x_s} + 6000.x_s^2 + (e^{22000(xs-.0100)^2} - 1) \qquad 7.5 \leq \alpha < 10 \text{ degrees} \tag{44}$$

$$\alpha = 70\sqrt{x_s} + 6000.x_s^2 + (e^{22000(xs-.0100)^2} - 1) + 2000(x_s - x_{s10.5}) \qquad 10 \leq \alpha < 12.5 \text{ degrees} \tag{45}$$

The chordwise stagnation points along the blade are obtained from probing for the maximum pressure on the lower surface (in Tecplot), or by reading from the surface.plt file and interpolating for the maximum Cp. Provided the grid is sufficiently fine, the latter method may be the most accurate, while the former is convenient to establish the method but may be prone to small errors. If the stagnation region is found using Tecplot it is useful to adjust the contour levels to help identify and record the xyz location of the stagnation point. It is also useful to run the slicing macro, previously used with the Rotor-Analyser Fortran program (Appendix G), as an aid to obtaining data at convenient radial stations. This data is then rotated through the local pitch angle of the blade using a Fortran program such that the chordwise location of the stagnation point is found and the angle of attack computed according to the above formulae.

Figure 270 shows an example of the pressure contours on the lower surface near the tip of the datum blade, and also at the root-end of the blade. On the rectangular blade the stagnation line extends almost to the tip edge, whereas on the Küchemann tips the flow divides and flows around the tip before reaching the full stagnation pressure. Note however, how the stagnation region under the anhedral crank region is extended outboard compared to the Küchemann tip without anhedral.

Some results of using this procedure to locate the stagnation point and hence find the angle of attack on the three selected blades at 10 degrees pitch are shown in Figure 271. Near the tip the angle of attack for the datum rectangular blade, TRB-000v, continued to increase almost all the way to the tip, before falling off. For the Küchemann tip, TRB-001v, the angle of attack reaches a peak and starts to reduce further inboard. The angle of attack for the anhedral blade reaches a slightly higher peak near 94%R, before it similarly reduces in the outer tip region. The peak angle of attack is near the anhedral crank, and the angle of attack is generally higher over the outer part of the blade for this blade. The angle of attack, and hence the local lift-coefficient, is large at the root due to the effect of the chord taper at the root.

The results from determining the angle of attack from the stagnation point are compared to those obtained from the averaged downwash and Cp matching (discussed below) at the end of the next section of this chapter in Figure 273. Reasonably good agreement is found between all the methods compared, but the stagnation point method gave angles of attack that were generally greater than the other methods, although fairly close agreement was found near the tip. At the tip the angle of attack from the downwash increases, while that from the stagnation point and Cp-matching remains fairly constant.

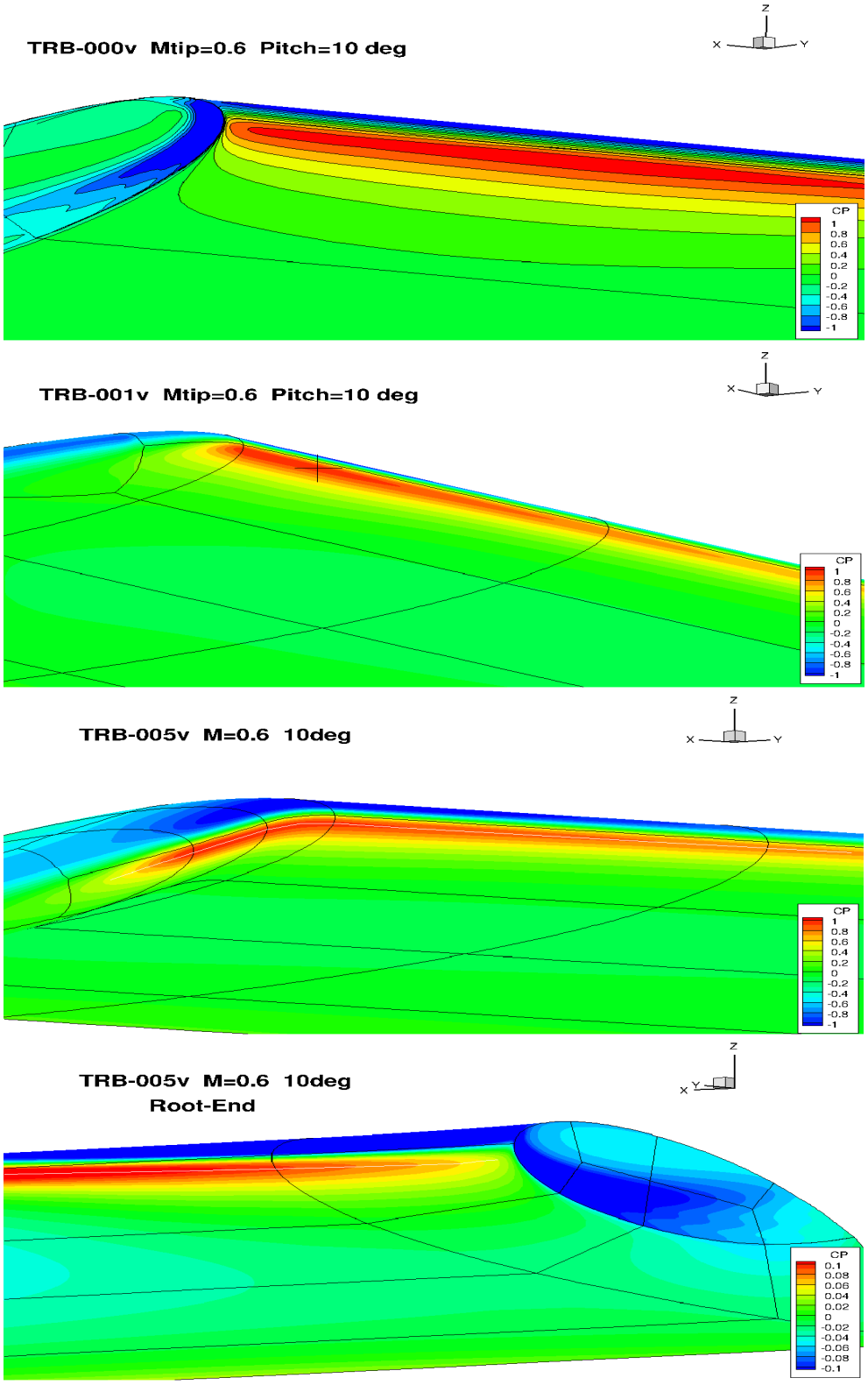

Figure 270: Contours of Pressure Coefficient (Based on Mtip) Near the Stagnation Region on the Lower Surface of the Selected Blades. Top: TRB-000v (Cp outlined). Upper Middle: TRB-001v (with probe cursor). Lower Middle: TRB-005v (with stagnation line highlighted). Bottom: Root-End (Cp re-scaled)

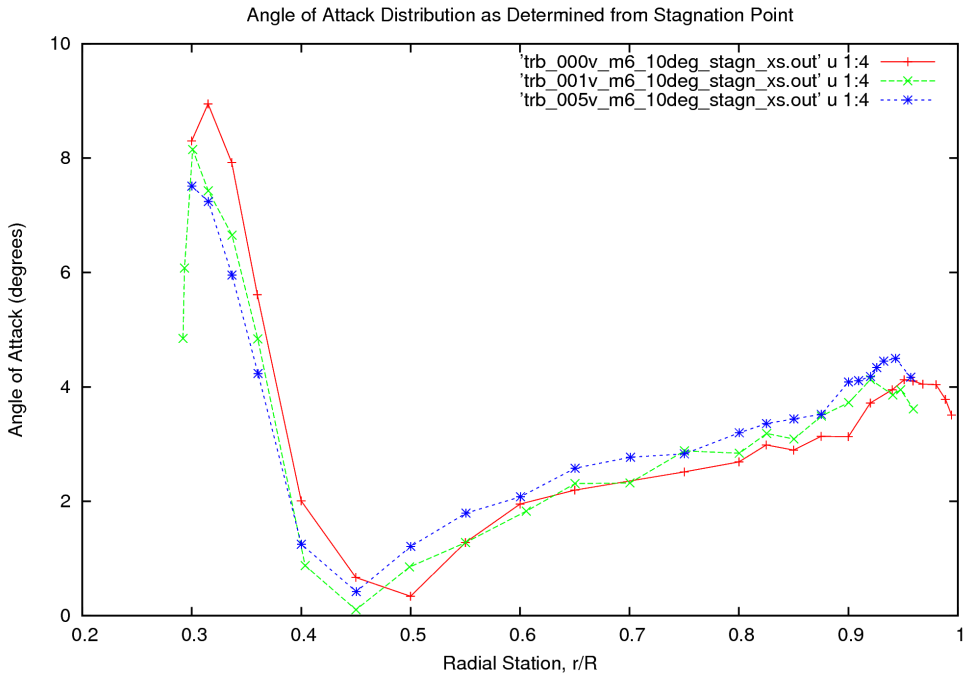

Figure 271: Angle of Attack Distribution as Determined from the Location of the Stagnation Point for the Datum Rectangular Blade, TRB-000v, the Küchemann tip, TRB-001v,and the anhedral Küchemann tip blade, TRB-005v.

7.3 Angle of Attack from Cp Matching

An alternative to using the stagnation point to find the angle of attack is to consider the upper surface pressure at a point near the leading edge. This method was used in flight tests by Brotherhood and Riley,[63] and has been used as a stall detector by Wilby,[319] and has already been applied for the latter purpose in Chapter 6.4. However, provided the flow is attached, the leading edge pressure coefficient obtained at, say 2% chord, may be used to determine the angle of attack as long as the flow can be considered to be close to two-dimensional. A similar curve-fit procedure is required to that used above to relate the extracted Cp to the angle of attack, and hence CL.

As shown in Chapter 6.4, Figure 261, Cp(.02) does not vary linearly with angle of attack, but the curve steepens with increasing incidence before rounding over as the stall is approached. Therefore, while the stagnation point may continue to move aft as the stall is approached (unless it relaxes again as the shock moves forward again as the lift reduces post-stall), Cp(.02) may tend to level off and becomes a poor indicator of the angle of attack near stall.

In fact, all the methods described above have some advantages and some limitations. The time-averaged downwash technique may be one of the most useful for the rotor engineer, but may not be at all accurate the tip region as it is not obvious over what distance upstream or downstream of the blade to carry out the averaging process in the highly 3D flowfield. The results here seem to suggest that averaging over each blade segment over-estimates the angle of attack near the tip compared to the other methods. The stagnation point approach is effective provided that a stagnation point, or line, exists along a leading edge which should be reasonably straight (ie parallel to the blade reference axis) to ensure 2D flow. Over the middle part of the blade identifying the stagnation point will continue to provide the angle of attack up to and into stall, whereas the use of the leading edge pressure only relates directly to angle of attack well below the stall. Another alternative, considered next, is to seek a best-fit to the chordwise Cp-distribution.

Strip theory is often used in traditional analyses of helicopter rotors with the implicit assumption that the flow will be reasonably two dimesnional over much of the blade. If this is the case, a 2-D aerofoil code, or 2D-CFD model, should be able to match the Cp-distribution exactly, given the Mach number and Reynolds number at the radial station in question. In reality, this is unlikely to be the case near the ends of the blade, and towards the tip the loading is highest and a strong tip vortex develops. In hover the vortex from the preceding blade also adds to the three-dimensionality of the flowfield near the tip. The matching process will become more difficult as the local conditions become less 2-D, and may prove impossible in highly 3D situations very close to the tip. However, despite these limitations, this method may be useful to the rotorcraft engineer, since it will also provide an indication of the difference between a truely 2D-distribution and the pressure distribution taken from the fully 3D predictions.

As an example of the matching process, a series of surface pressure distributions were again extracted from the HMB solution for TRB-000v at 10 degrees, and have been compared to 2D-Cp distributions results from the 2D aerofoil code MSES. As described in Chapter 2, the MSES code solves the Euler equations along streamlines, and also uses a coupled integral boundary layer with an e^N transition model. Using a small value of Ncrit gives transition close the leading edge and provides a solution comparable to HMB using a modified k-ω model. This was done to reduce the computing time in matching the distributions, but potential exists to automate the fitting process and consistent use of the HMB method would have been preferable. However, as established in Chapter 3, the agreement between MSES and HMB is very good in this mid-Mach number and low Reynolds number range. Further cross-checks were carried out during this matching investigation and very close agreement was found, with just minor descrepencies near the leading edge suction peak due to the initial laminar boundary layer of MSES. This is only a problem if Ncrit is greater than unity, and the value of Ncrit=0.1 used here sets transition near the suction peak.

Figure 272 shows Cp-distributions for a range of radial stations along the datum blade at which comparisons were made. At each location the incidence was varied until a reasonable match was achieved (by eye), with a focus on matching the peak suction near the leading edge, and the pressure in the stagnation region on the lower surface, but also with regard to the shape of the distribution and checking for any trailing edge pressure divergence. As expected, near the root and the tip of the blade it becomes more difficult to find a match and differences in the chordwise pressure distribution may become significant. However, whilst this then spoils the

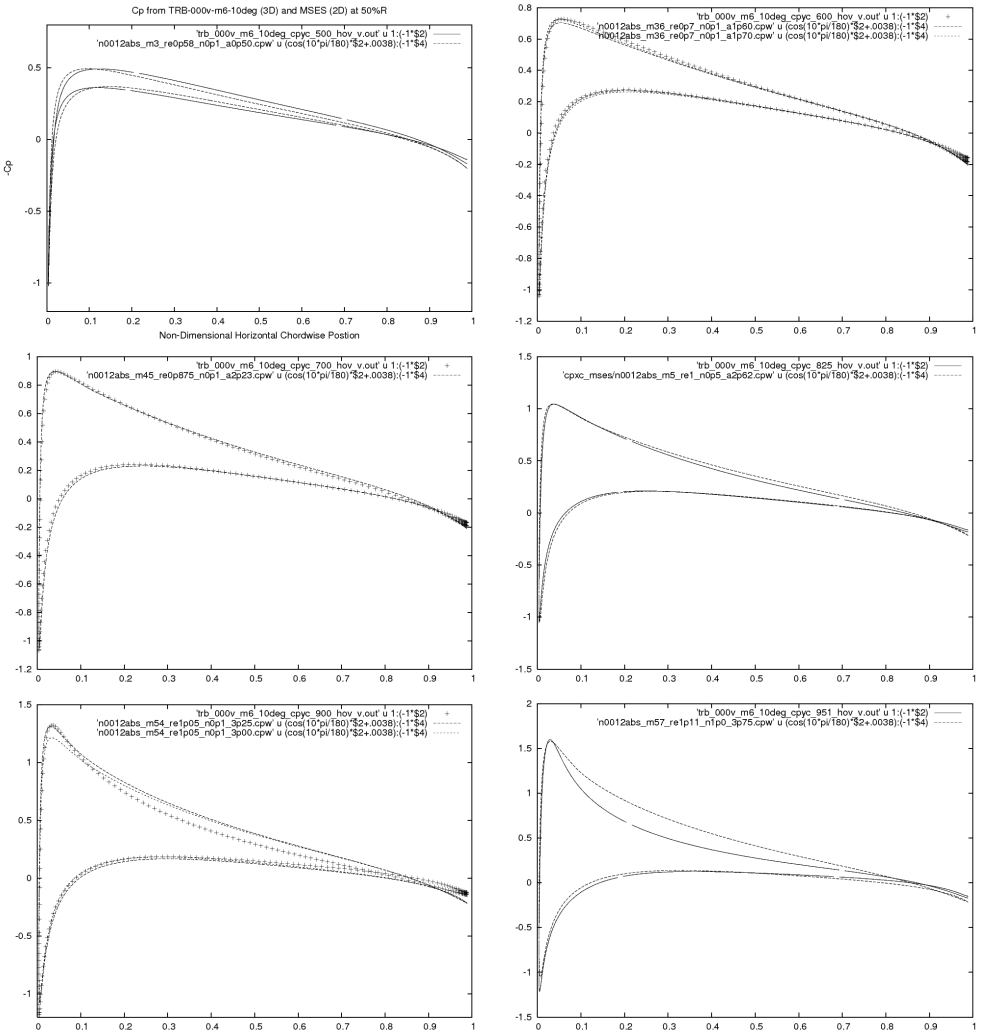

Figure 272: Matching Cp Distributions from the HMB flow solver for TRB-000v at 10degrees Pitch and the 2D aerofoil code MSES at 50, 60, 70, 82.5, 90 and 95.1%R.

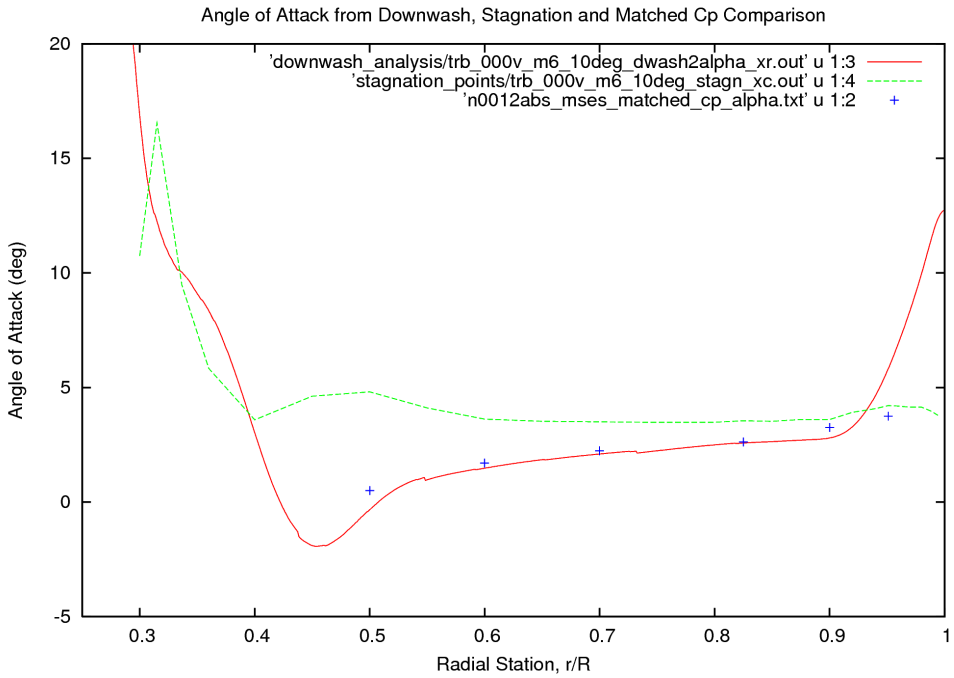

Figure 273: Comparison of Different Methods of Determining the Angle of Attack from Analysing the Navier-Stokes Solution for the Datum Rectangular Blade, TRB-000v at 10 degrees Pitch in Hover: Angle of Attack from Time-Averaged Downwash, from Stagnation Point Location, and from Matching the Cp Distribution at Selected Radial Stations.

idea of extracting the angle of attack (remembering that there may not be a stagnation region near the tip, and the flow here is highly 3-dimensional), it provides a useful indication of how the pressure distributions vary in the tip region. This information may be quite useful to the blade designer, and clearly potential exists to feed-back this information to help refine lower order methods to allow a better representation of rotor blades with specific tip shapes.

The results from finding the angle of attack from the Cp-matching process are compared to those obtained from the averaged downwash and stagnation point (discussed above) in Figure 273. As stated previously, reasonably good agreement is found between all the methods away from the root region, and the results of the Cp-matching are closely aligned with those extracted from the averaged downwash over much of the blade, and in close agreement with those from the stagnation point method closer to the tip.

The above methods of extracting the angle of attack and downwash provide additional insight into rotor aerodynamics from information that is not directly available from the CFD solution files. They usefully allow the rotor engineer to make comparisons to verify methods using familiar variables. However, it has been found that all the above methods have limitations, mainly related to the underlying assumption that the flow is primarily 2D (as in strip theory), and are therefore likely to be least accurate in the important tip region. This result in perhaps not surprising in view of the fact that the computational approach closely models the physics of the flow around a blade which is fully defined by its surface geometry and the given boundary conditions, and therefore well suited to capturing the 3D flow about the blade tip. It is therefore questionable as to whether there is any advantage in attempting to impose 2D ideas in the 3D environment of the tip. The only reason for doing so is to enhance the development of simpler rotor models which have the advantage of very much faster run-time for routine performance calculations. If it is required to make comparisons, it may be preferable to cast the traditional rotor code results into coefficients, such as Cz and Cy, in order to ensure accuracy. These coefficients are easy to extract from the CFD results and are also available from lower order methods. While extracting information from the flowfield has confirmed the influence of parameters such as twist and anhedral, in order to gain a deeper understanding of the aerodynamics in the tip region it is preferable to visualise the CFD solution and extract local pressure distributions in the tip region.

7.4 Surface Pressures at Tip

As discussed above, the central portion of the blade experiences conditions that are close to 2D, but at the tip the flow is highly 3D, and to gain further insight into the tip aerodynamic design it is necessary to consider alternative ways of displaying the predicted loading information in the tip region.

Previous experience of wind tunnel tests on the Lynx-BERP blade (tested as a wing in the Westland wind tunnel by the author during a collaborative program with NASA), Brocklehurst and Duque,[58] led to the idea of plotting the surface pressures on sections normal to the leading edge. Further details of the tip-edge pressures were also extracted from this data for comparison with HMB and were presented by the author in 2003.[60] It would therefore seem appropriate to consider a similar approach here, where the predicted pressure distributions are displayed along sections normal to the leading edge of the tip. Whilst still looking at a planar (2D) sections this approach allows the tip to be considered as a 3D entity. Relating the loading on the tip, outboard of the tip station, to the stagnation pressure near 96%R, and hence the angle of attack, as determined above, may also be useful in support of the development of lower-order models. Indeed, the forces and moments acting on the tip may be obtained by integrating the surface pressures over the area of the tip directly from the numerical solution.

The surface pressures over the three selected tip shapes are compared in detail in Figures 274, 275 and 276. In the main part of these Figures, the surface pressure distributions have been obtained by taking sections (A-H) normal to the leading edge at outer edge of the tip. However, for the rectangular blade, sections were taken normal to the leading edge and normal to the outer edge of the tip. For the Küchemann tips, some sections inboard of the start of the tip (ie up to 96%R) were taken chordwise and others around the tip were taken normal to the leading edge. The inset at top left shows the surface pressure contours and illustrates where the sections were taken for each individual tip shape. The inset at top right shows the surface pressure distribution on conventional chordwise sections after the blade has been rotated into the horizontal plane (so that in this case the Cp's are plotted normal to the chord-line which would enable Cn, rather than Cz, to be obtained for the tip, if desired, depending upon how the results would be used). The pressure distributions near the extreme tip edge of the datum rectangular blade, TRB-000v, are shown in Figure 274. The peak loading is at about 94%R near the leading edge and reduces as the tip edge is approached. At 98 and 99%R the Cp distribution is dominated by the aft-loading due to the tip vortex, but even very close to the tip edge the lower surface experiences the full stagnation pressure near the leading edge of the blade. The sections normal to the tip edge show the shape of the vortex induced suction region in much greater detail, and as expected the suction spike at the tip edge suggests that some edge separation occurs. The vortex induced loading starts as a high local peak near 20% chord, and reduces and moves inboard towards the trailing edge. Figure 275 show the Cp-distributions for the Küchemann tip. As noted previously, the rounding of the leading edge corner reduces the suction peak, and hence also reduces the adverse gradients in this region. Around the curved leading edge of the tip at the first few slanted sections, A-D, the suction peak is smooth, although a spike appears towards the trailing edge for sections, E-H. For the Küchemann tip with 20 degrees of anhedral the sections were taken normal to the anhedral plane. Strong adverse gradients are seen near the leading edge as the flow starts to separate near the 92% and 94% stations. The pressure recovery is more gradual at 96%R, due to the favourable leading edge shaping of the tip. Again the first 4 or 5 sections normal to the tip edge show smooth pressure peaks for attached flow, and the flow separates as it travels around the edge of the tip at the last 3 stations, F-H. As expected, as the leading edge curves away from the tip station at 96%R, the full stagnation pressure is not reached on the lower surface, helping to reduce the drag experienced by these Küchmann-type tip shapes.

Clearly, the tip loading and flowfield around the tip are highly three-dimensional, and the use of a steady Navier-Stokes CFD method has furnished a very detailed solution from which the engineer can gain a deeper insight into the tip design problem.

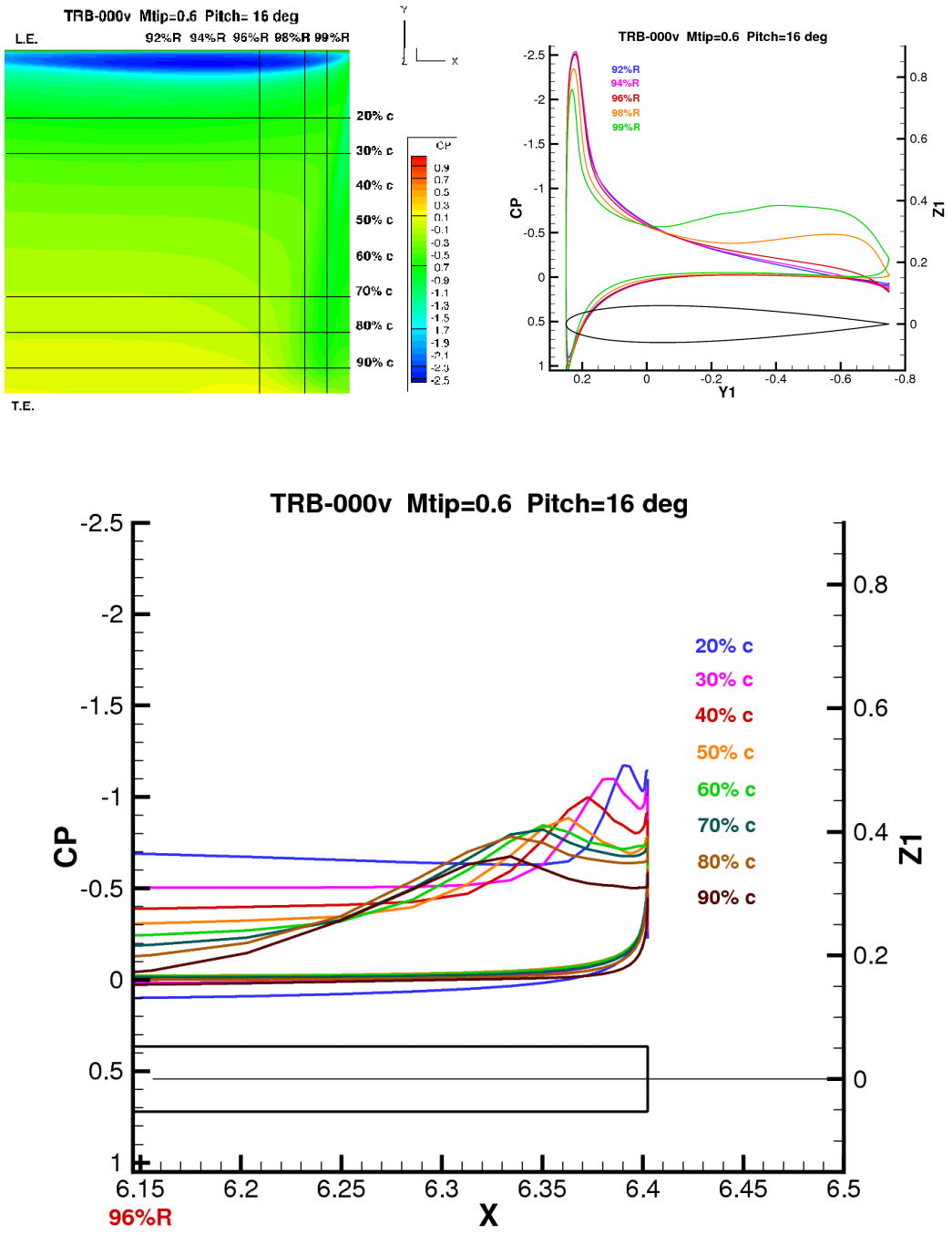

Figure 274: Pressure Distributions in the Tip Region of the Datum Rectangular Tip Blade, TRB-000v, at 16 degrees Pitch. Top Left: Cp Contours and Sections. Top Right: Cp vs Chord at 92, 94, 96, 98 and 99%R. Bottom: Cp Normal to Tip Edge

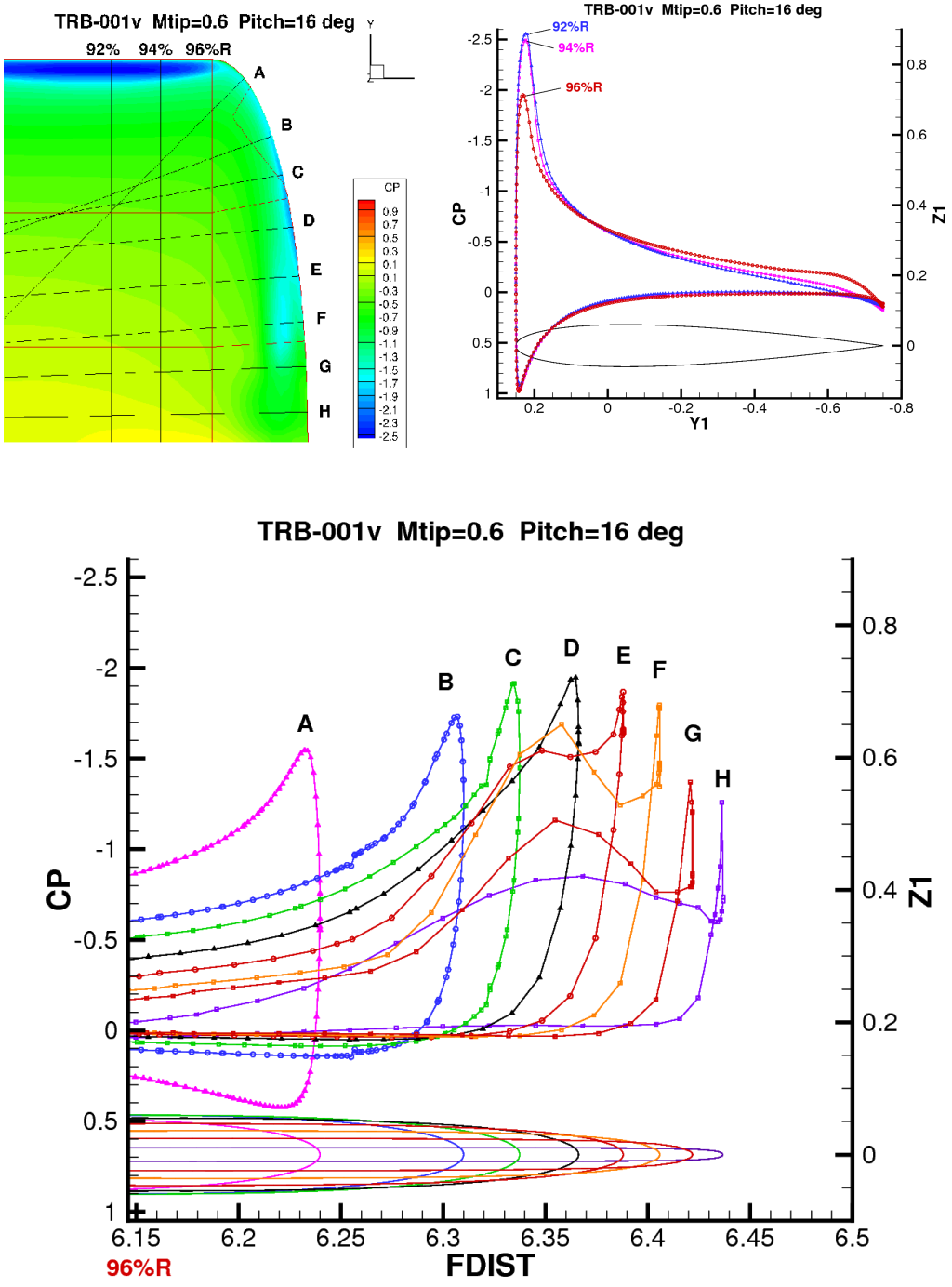

Figure 275: Pressure Distributions in the Tip Region of the Küchemann Tip Blade, TRB-001v, at 16 degrees Pitch. Top Left: Cp Contours and Sections. Top Right: Cp vs Chord at 92, 94 and 96%R. Bottom: Cp vs Distance (in chords) Normal to Leading Edge

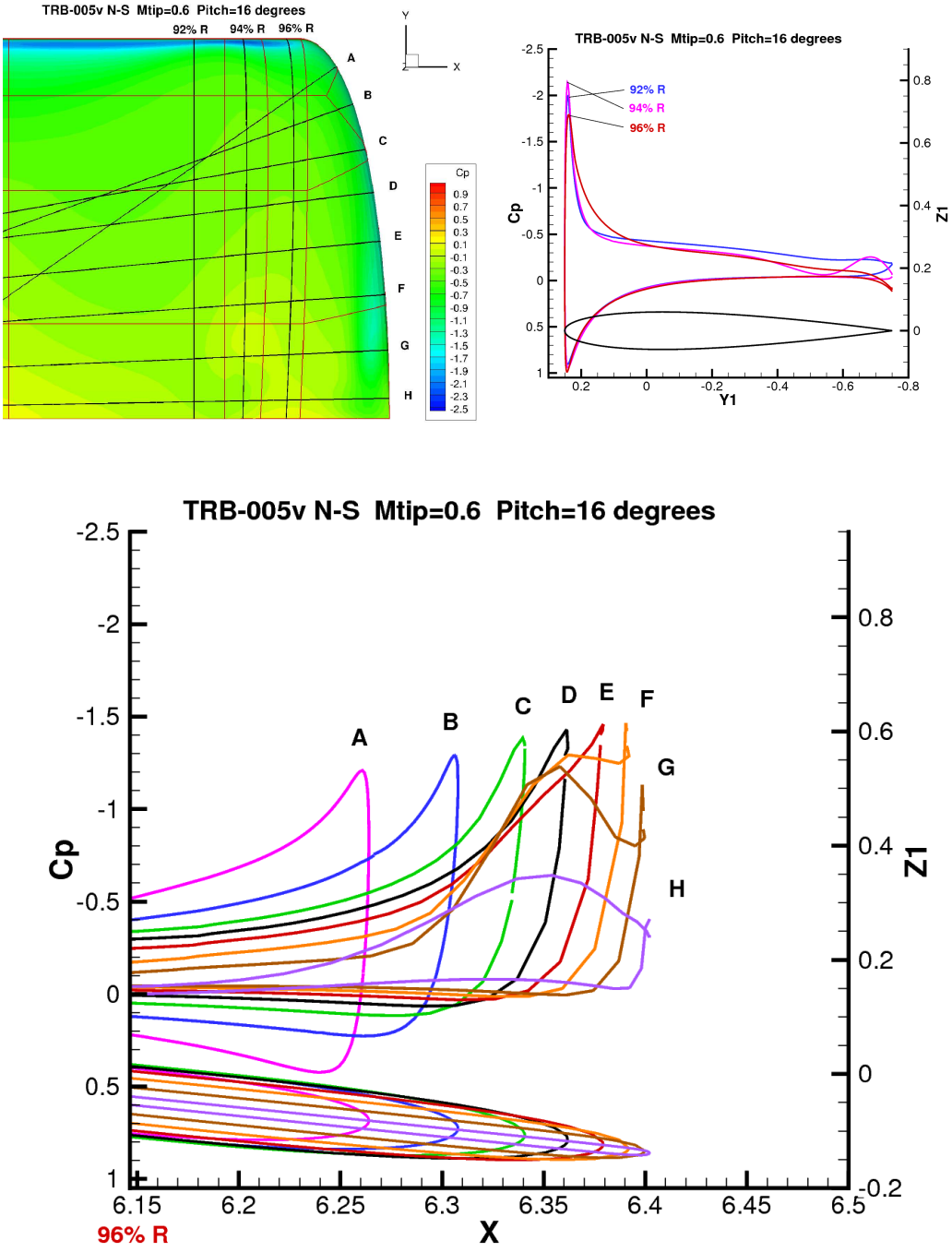

Figure 276: Pressure Distributions in the Tip Region of the 20 deg Anhedral Küchemann Tip Blade, TRB-005v, at 16 degrees Pitch. Top Left: Cp Contours and Sections. Top Right: Cp vs Chord at 92, 94 and 96%R. Bottom: Cp vs Distance (in chords) Normal to Leading Edge

8 Application of Unsteady Navier-Stokes

This section of the thesis sets out ideas for the application of unsteady Navier-Stokes computations to the helicopter tail rotor aerodynamic performance problem. An unsteady solution requires significantly more computational resource than a steady single blade segment solution, but offers to capture separation and transient flow features. An unsteady approach should therefore be useful in studying the rotor at the onset of stall, and also allows the rotor to be operated in proximity to other parts of the airframe.

In previous sections, a steady solution was used in an attempt to evaluate tail rotor performance with sufficient resolution and fidelity to evaluate design features such as new tip shapes. However, a steady solution is limited to attached flow conditions where boundary layer separations are minimal, and strong vortex shedding does not occur. Changing from a steady solution, where some simplification at the root-end of the blade and hub may be necessary, to an unsteady method, allows the separated flows over the hub components to be modelled. For a highly loaded rotor with a large root cut-out, the blockage effect of the hub and turbulence generated by the bearings and blade attachments may have an impact on the overall flowfield. Inclusion of such details, whilst not part of the tip design question, may help to stabilize the flowfield and ensure a realistic result for highly loaded rotors in hover.

In many unsteady cases it may be no longer possible to assume periodicity on planes between the blades, and a grid containing the whole rotor has to be employed. Including additional mechanical and airframe components may also increase the gridsize. The solution must also be iterated at each small time step, and the runtime is likely to be at least an order of magnitude longer than for a steady solution, depending upon how many rotor revolutions are necessary. In today's environment, application of an unsteady approach is therefore limited to a few special cases, but this situation will change in the future as computing resources continue to expand.

Unsteady solutions have been applied to the helicopter forward flight problem, and indeed, the fuselage and tail rotor have also been included, eg Steijl and Barakos.[282] In this flight mode, where there is a strong free-stream component, rotor solutions have been found to settle to a repeatable cyclical pattern after 3, or maybe 5, revolutions of the rotor, although up to 12 have been used in difficult cases. However, except for tilt-rotor problems, where rotor-airframe interactions are important, Potsdam,[74] the unsteady Navier-Stokes method does not yet appear to have been applied to a main rotor in hover. To date, the faster runtime of the steady periodic solution provides information about the rotor design and performance, and has taken priority over any desire to determine the Figure of Merit of the rotor-fuselage combination. As yet, helicopter interactional aerodynamics in low speed manoeuvring flight have not been addressed by CFD methods, although the challenge of the helicopter-ship problem has been taken up, but even here there is dominant freestream direction.

A sliding plane approach was developed by Steijl, et al[284] under the UK-DARP and EU-GOAHEAD projects to provide a framework for the application of unsteady CFD to the helicopter problem. This approach is used here to interface between the stationary fin and rotating blades. Against this background, the tail rotor problem in hover seemed tractable, but the problem needed to be re-formulated based on the the tipseed, rather than the forward flight Mach number. The following sections of this thesis illustrate the application of an unsteady Navier-Stokes CFD method to the tail rotor problem and include fin-blockage as a first demonstration case.

Model tail rotor test data was again available for comparison and it was planned to run the rotor alone and with the fin in place, at a impressed pitch angle of 8 degrees, before attempting a higher pitch condition. In the event, problems were encountered with the wake not developing sufficiently well, probably due to the inadequacy of the low Mach number preconditioning that was in use at the time. Since computational resources were limited, effort was re-focused on the steady solutions for the main part of this thesis.

As discussed in the following sections, the results of the fin-blockage simulation highlight the benefits of the unsteady approach, and have the potential to provide the design engineer with useful insight into unsteady loading effects which were previously not apparent. However, a more contemporary approach to this problem may be to apply the harmonic balance method developed recently by Woodgate and Badcock.[325] This would appear to be an ideal method for obtaining a solution for cyclically varying loading on the fin and the rotor, although this approach may not be suitable for an isolated rotor at high pitch where stall is present.

8.1 Tail Rotor Fin Blockage Test Case

This test case was undertaken as a first demonstration of the unsteady Navier-Stokes method applied to the tail rotor problem. While the main focus of this thesis has been to evaluate the performance of different tip shapes on an example tail rotor, an unsteady approach may ultimately be required to predict the performance of the tail rotor in situ, or at high pitch where stall may be present. An unsteady method may also be required to provide a more realistic model of the flowfield when the influence of the rotor hub and blade attachments may affect the flow near the centre of the rotor and impact the overall performance of the rotor. The unsteady approach may therefore overcome the problems experienced in Chapter 6. Once an unsteady approach has been adopted, this also opens the door to the solution of many practical problems where the tail rotor cannot be considered in isolation. Interaction between the tail rotor and the fin is one such interaction where CFD may be used to obtain a better understanding and hence a better prediction of this aspect of helicopter performance.

In considering the unsteady problem, it was thought preferable to run a relatively low pitch case to begin with, where the flow would be mainly attached, and the rotor wake should be able to be established without disturbances due to stall near the tip. A suitable test case, against which results could be compared, was the model tail rotor fin blockage tests, where not only could the benefits of an unsteady approach be demonstrated, but an isolated rotor with the same hub configuration could also be studied. If successful, further cases could then be run to further evaluate tip design issues at high pitch angle.

The experimental arrangement used for the fin-blockage tests is shown in Figure 277. The rotor was arranged to thrust downwards with the fin mounted below the rotor. The fin was therefore on the inflow side of the rotor as in a 'pusher' configuration. This configuration helps to minimse the fin-force which subtracts from the shaft thrust of the tail rotor to give a lower useful net thrust, as reported by Lynn, et al.[193] The fin, which had an elliptical cross-section, was mounted on load-cells to measure the total (average) fin-force (see top-left photo). The fin was also fitted with static pressure tappings along a projected arc of 90% rotor radius, to measure the (time-averaged) pressure distribution over the fin (the tubes exiting the fin are visible in the upper-right photo). Smoke was introduced to visualise the flow into the tail rotor, and as the flow accelerated around the edges of the fin and was pulled inwards, a vortex formed above and along the leading and trailing edges of the fin upper surface (see middle-left photo). Wool tufts were also used to visualise the flow on the surface of the fin and confirmed the presence of these vortical flows in the inflow to the tail rotor. Various strakes, and plates normal to the fin surface were tested, but had little impact on the vortical flow being generated on the suction side of the fin adjacent to the rotor. The lower photo shows the rotor stationary and provides a view of the rotor hub, spider, pitch links and feathering bearings. The blade root-attachments are at 29%R while the aerofoil at the root of the blade is at 33%R, typical of a tail rotor.

The results from measuring the mean load on two different fins are shown in Figure 278. Only the larger fin (with s/A=0.412, y/R=0.35) was pressure tapped and was also in place for the vortex wake measurements, and was therefore chosen for the simulations. The fin blockage ratio, k_B, is defined as the ratio of the fin-force to the tail rotor shaft thrust and was found to remain fairly constant as the tail rotor pitch, and hence thrust, was increased. As the stall is approached, the measurements suggest that the fin-blockage ratio may increase slightly. In the tests the main focus was on determining the mean fin-blockage ratio and the mean-flow mechanism by which it was generated. No unsteady measurements were taken. However, in addition to the rotor thrust and torque, the flapping was measured, as it was recognised that the disturbance of the fin in the rotor inflow causes blade flapping to occur, as first discovered from flight tests and confirmed in the model rotor tests. However, the low Lock number of this model tail rotor meant that the coning and cyclic flapping is relatively small in these tests. The model rotor has 45 degrees of conventional pitch-flap coupling ($d\theta/d\beta$=-1). While this 'fin-induced' flapping is small, it creates a cyclical variation in the aerodynamic loading experienced by the rotor blades. The coning, flapping and pitch harmonics were included in the unsteady Navier-Stokes simulation. Figure 279, shows the relationship of the flapping to the blade passing the leading and trailing edges of the fin.

Simplistically, the blockage caused by the fin can be considered to result in an azimuthal variation of the downwash at the rotor disc and, at the time of the tests, this idea was used to determine Glauert downwash factors, see Gessow and Myers,[118] to calculate the flapping for any given tail rotor and fin configuration. It was also anticipated that the trajectory of the tip vortices would be affected by the presence of the fin, and the experiments provided an opportunity to measure the location of the vortices in the wake, using the techniques

developed in earlier isolated rotor tests. This information was intended to support the development of a more detailed vortex wake model, but is now available to compare CFD simulations, with and without the fin.

The measured vortex trajectories, and their vertical displacement and contraction with azimuth (vortex age), are shown in Figure 280, both at the azimuth of the fin centre and at the opposite side of the disc away from the fin. The measurements opposite the fin, not surprisingly, show little change due to fin interference, with only a small increase in vertical displacement and little change in contraction compared to measurements with no fin present. At an azimuth aligned with the middle of the fin, the vortices have a much lower rate of descent prior to the next blade passage, and the contraction is increased so that the whole trajectory lies well inside that measured without the fin. This variation in the proximity of the tip vortex to the following blade will cause a variation in the loading and, at high pitch angles, may cause the blade to enter stall prematurely as it passes over the fin.

The geometry and surfaces for this model rotor and fin configuration were drawn in Rhino, along with all necessary support curves. An upper domain, 4R in radius and 2.875R high (above the sliding plane), was used to contain the stationary fin as shown in Figure 281. Below the stationary domain of the fin, a sliding plane was used to interface with the blades in a rotating frame of reference. A cylindrical hub with a radius of 0.25 chords projected from the fin, and terminated in a domed cap. The spider and control rods were not modelled. The rotor was located .125R below the sliding plane. One blade quadrant was drawn and meshed, and then copied and rotated to make up the complete rotor. The underlying geometry is shown in Figure 282. At the far field, set at 6R below the rotor plane, the usual Froude boundary condition was applied.

Figure 283 shows the master blade at the downstream, $\psi = 0$, reference position. In this example the rotor has top-blade-aft rotation (this is the preferred tail rotor rotation to alleviate main rotor - tail rotor interactional effect in quartering flight, Sheridan and Smith[258]). A gap was left between the inboard face of the feathering bearing and the hub to facilitate future pitch changes. An alternative option would have been to use a solid tie-bar in this region and adjust the blocking to re-establish the mesh quality. As shown in Figure 284, the feathering bearings were drawn with a sharp rear edge to be compatible with the blocking of the sharp trailing edge blade (more complex blocking could be used for greater realism). The feathering bearings and blade attachment forks were represented by simplified shapes to avoid any excessive vortex shedding in this first attempt at an unsteady analysis.

The upper domain for the fin and lower domain containing the rotor blade, were meshed separately in ICEM and then the grids were assembled. Figure 285 shows a view on the port side, looking towards the leading edge of the fin. For clarity, only the surface meshes of the fin, rotor blades and central hub are shown. The grid comprised just over 24 million points in 1234 blocks, 952 of which were in the lower grid around the rotor. This unsteady Navier-Stokes case was run using 87 processors and completed just over 2 rotor revs in 0.25 degree increments before being stopped for inspection. It was found that the wake had not developed as well as expected and the case was not run further as computational resources were limited.

However, visualisation of the pressure contours on the fin clearly showed that a reduced pressure field associated with the blade moved across the fin surface. This induced unsteady loads on the fin, giving rise to some structural vibration at a frequency of 4 per tail rotor revolution. Whilst some blade passing effect was anticipated, seeing this suction field pass over the surface of the fin greatly improved understanding of the mechanism by which the fin force is created, and was certainly not appreciated at the time of the experiment when only the mean fin force was measured. Since the simulation was incomplete, the mean fin loads were not compared. The shape of the pressure pulse shown in Figure 285 should also be considered as a preliminary result and could be subject to change as the solution has yet to reach cyclic repeatability with a fully developed wake. Since the pressures over the fin fluctuate significantly, the pressure distribution in Figure 285 is presented at one instant in time and could form one frame of an animation. The pressures everywhere on the fin surface need to be time-averaged before the mean fin-force can be integrated to compare with the test. Note that the pressures on the starboard side of the fin, away from the rotor, are much smaller in magnitude, but will also fluctuate as each blade passes.

While this similation was only partially successfully a great deal has been learnt from the preliminary results, and running this demonstration case has established the feasibility of applying an unsteady Navier-Stokes code to the tail rotor and fin blockage problem, with the prospect of using this method to evaluate future helicopter designs.

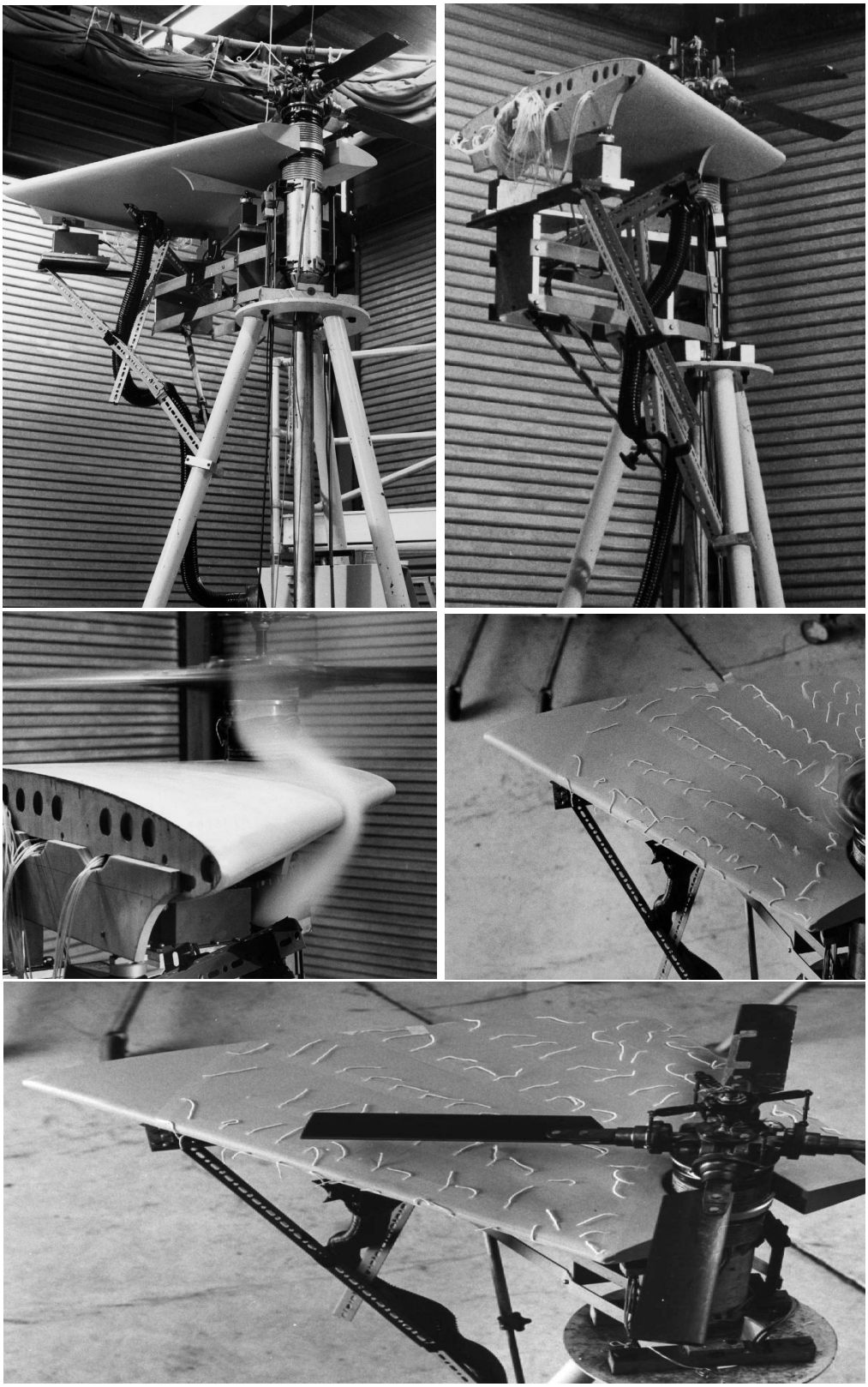

Figure 277: The WHL Tremor Rig used for the Model Tail Rotor Fin-Blockage Tests in 1984. In addition to the Load Cells and Pressure Taps used to Measure the Mean Fin Loads, Smoke and Wool-Tufts were used to Visualise the Vortical Inflow to the Rotor.

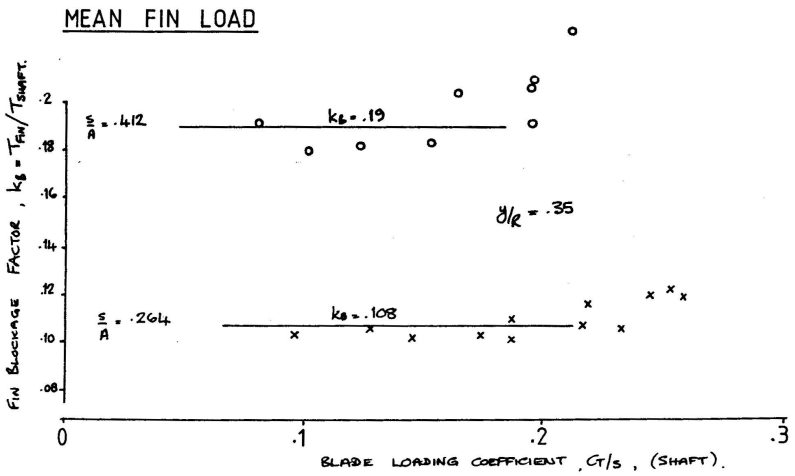

Figure 278: Fin Force as a Fraction of Tail Rotor Shaft Thrust as Measured in the 1984 Experiment

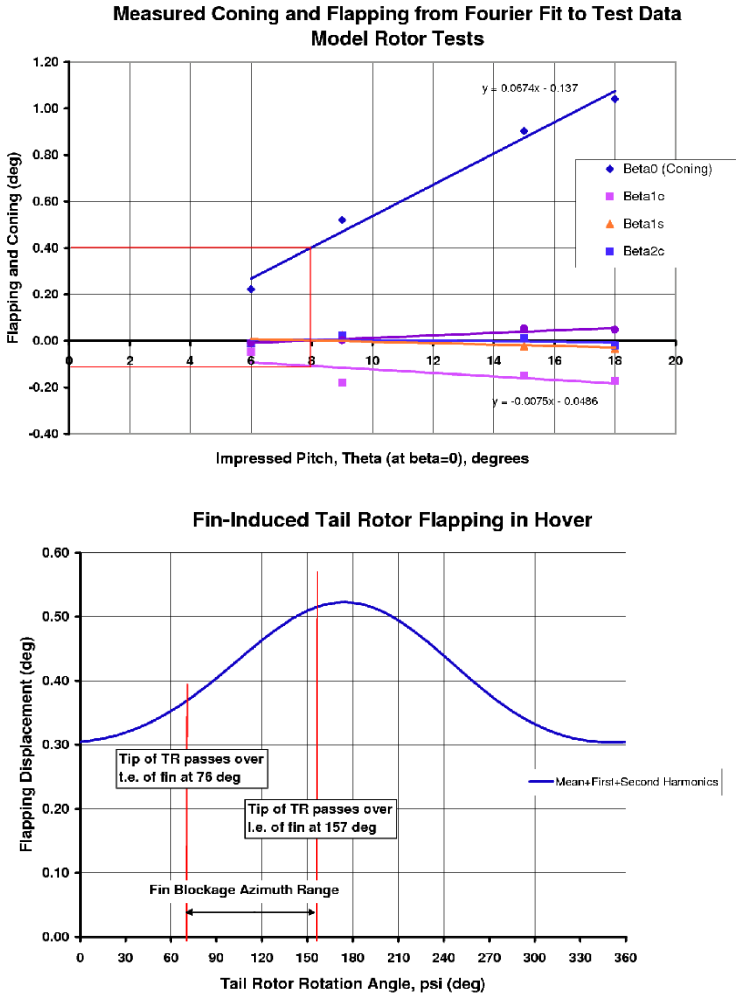

Figure 279: Tail Rotor Coning and Blade Flapping Response due to Presence of Fin in Hover

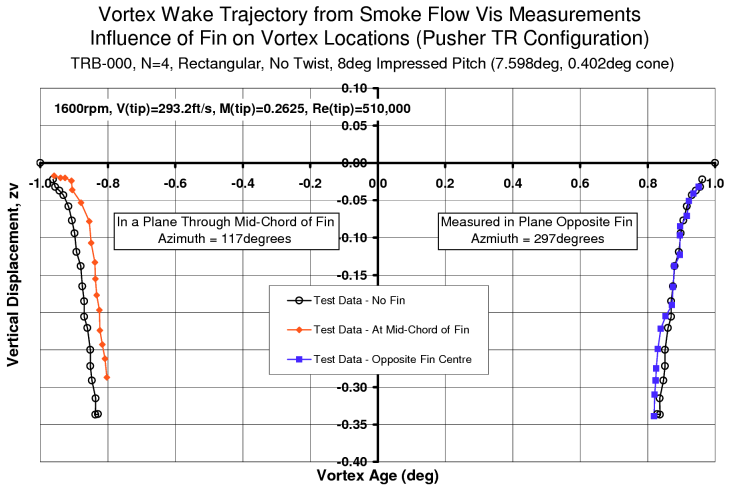

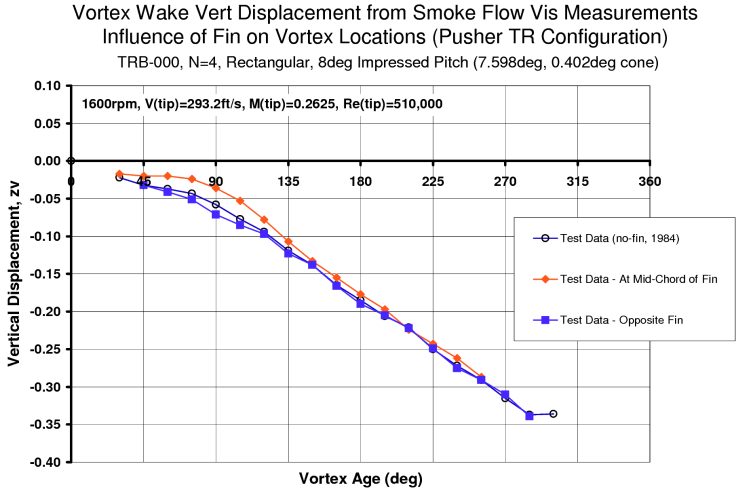

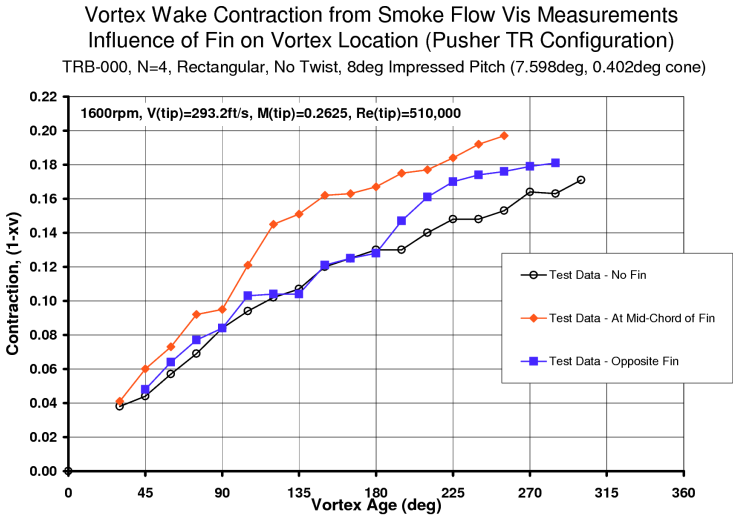

Figure 280: Vortex Wake Measurements from the Fin Blockage Tests Showing the Influence of the Fin on the Tail Rotor Wake. Top: Vortex Trajectories, Over Fin and Away from Fin. Middle: Vortex Vertical Displacement vs Azimuth. Bottom: Wake Contraction vs Azimuth

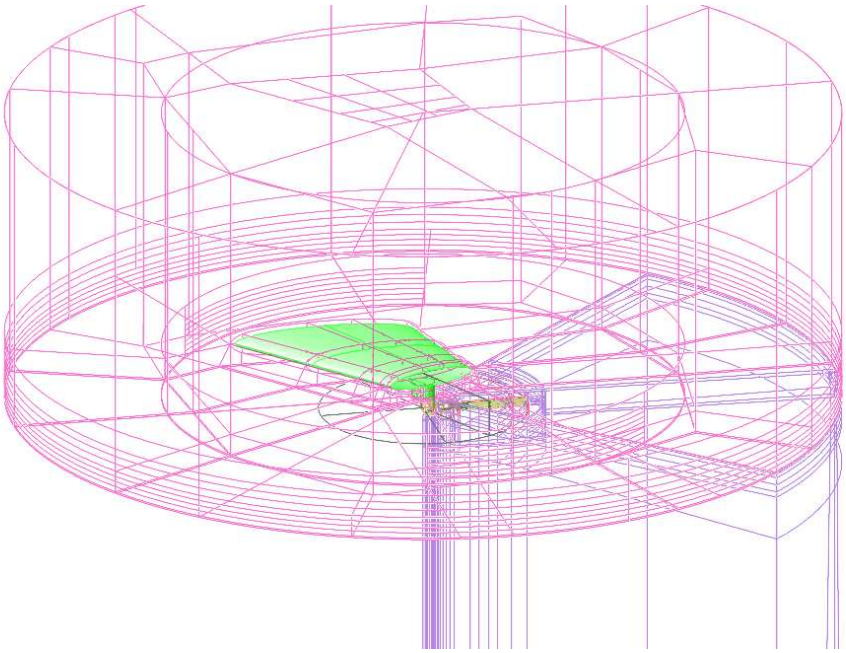

Figure 281: Stationary Upper Domain Containing the Fin Extends 4R Radially, and 2.875R Above the Sliding Plane Interface (3R Above the Rotor Plane). Fin-Rotor Spacing is 0.35R

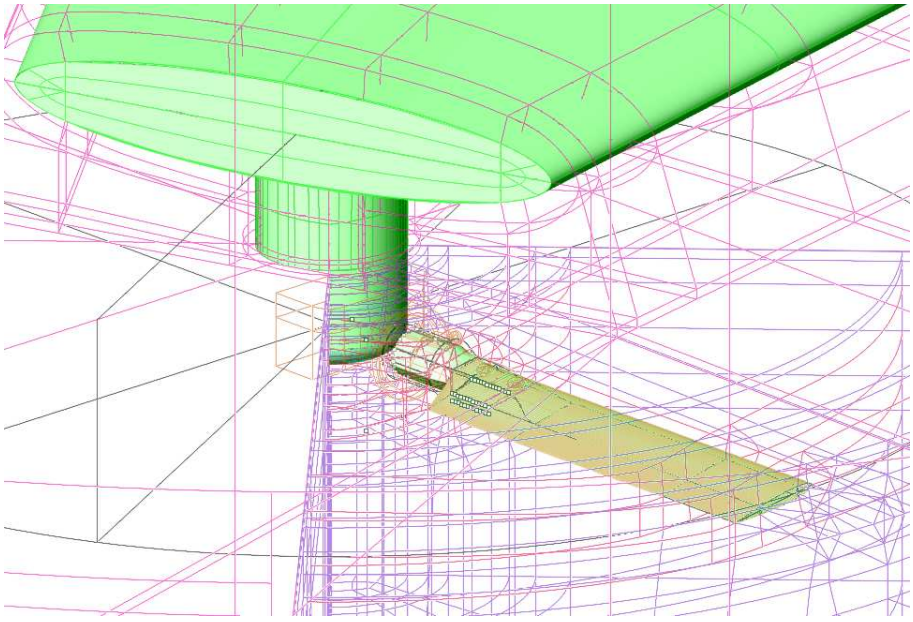

Figure 282: Rotating Lower Domain for the Tail Rotor Extends 4R Radially, and 6.125R Below the Sliding Plane Interface. The Simplified Tail Rotor Hub is Represented by a Cylinder with a Domed Cap.

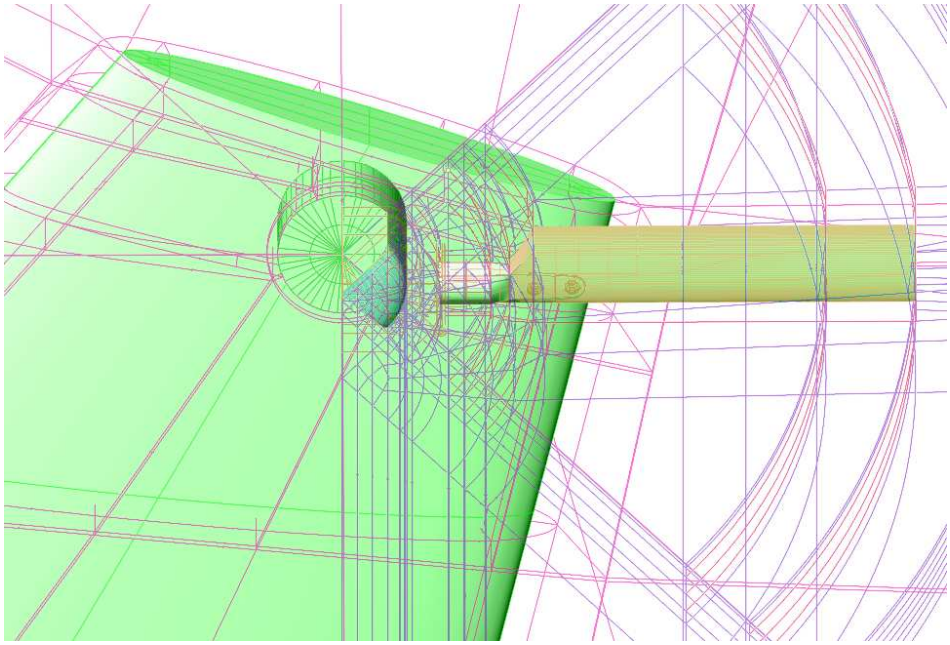

Figure 283: Side View of Geometry for the Model Tail Rotor Fin-Blockage Simulation. The Tail Rotor has Top-Blade-Aft Rotation and Thrusts Towards the Fin.

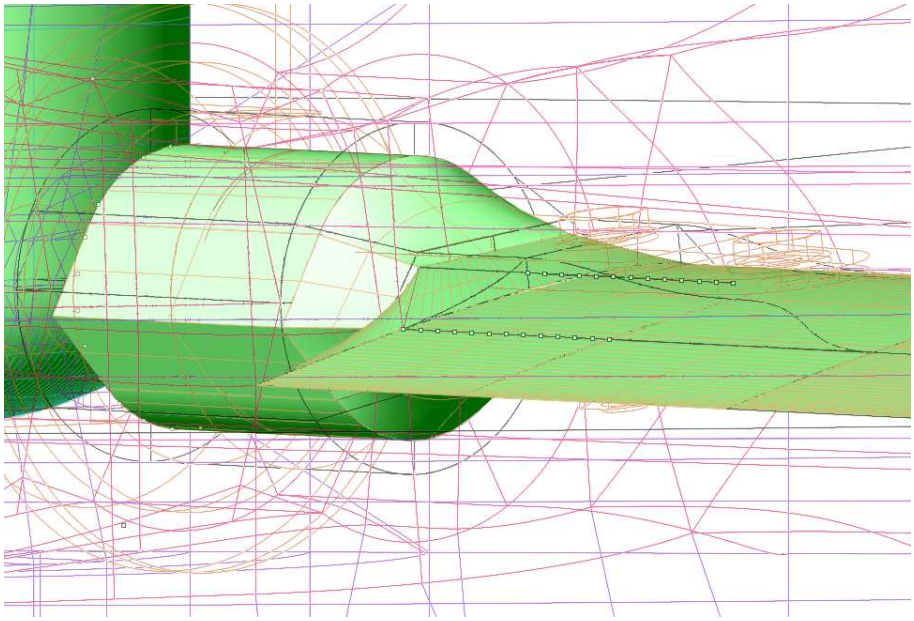

Figure 284: Close-Up View of Simplified Representation of Feathering Bearings and Blade Attachement Forks at Root of the Blade. In this Example, the Gap Between the Feathering Bearing and Hub Facilitates Pitch Change.

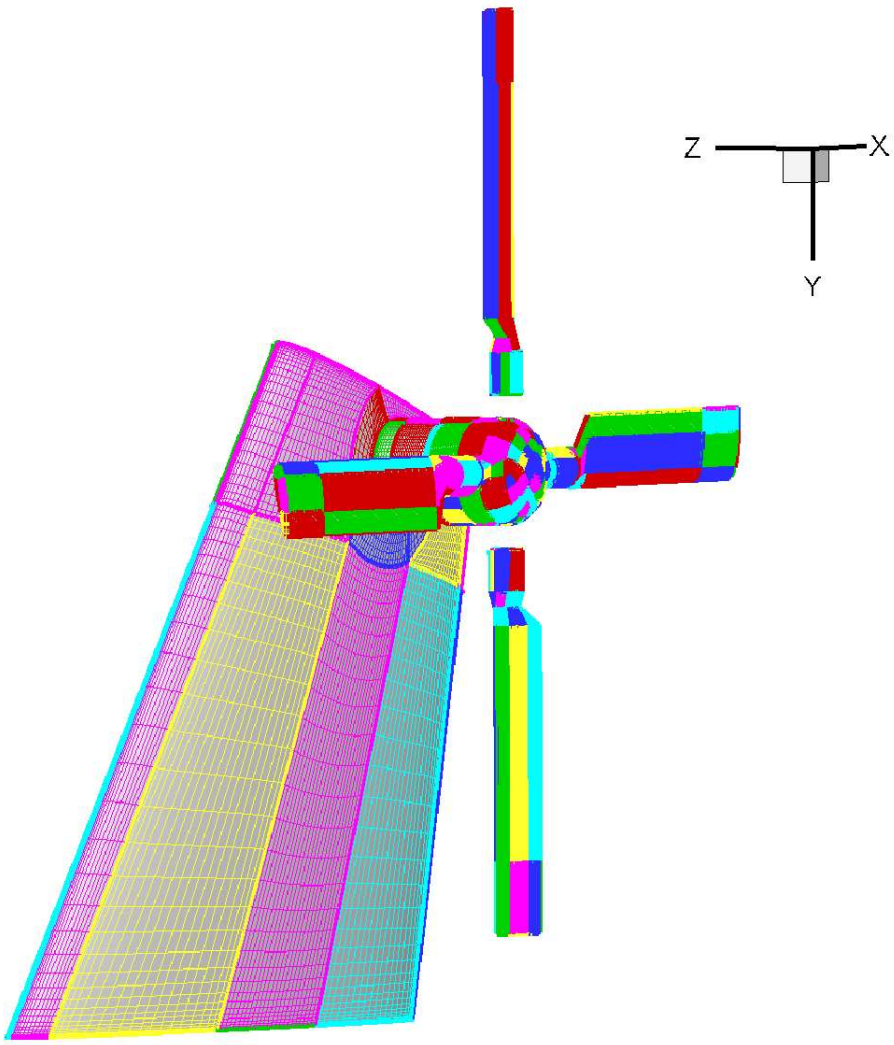

Figure 285: Multi-Block Structured Grids were used for the Tail Rotor Fin-Blockage Simulation

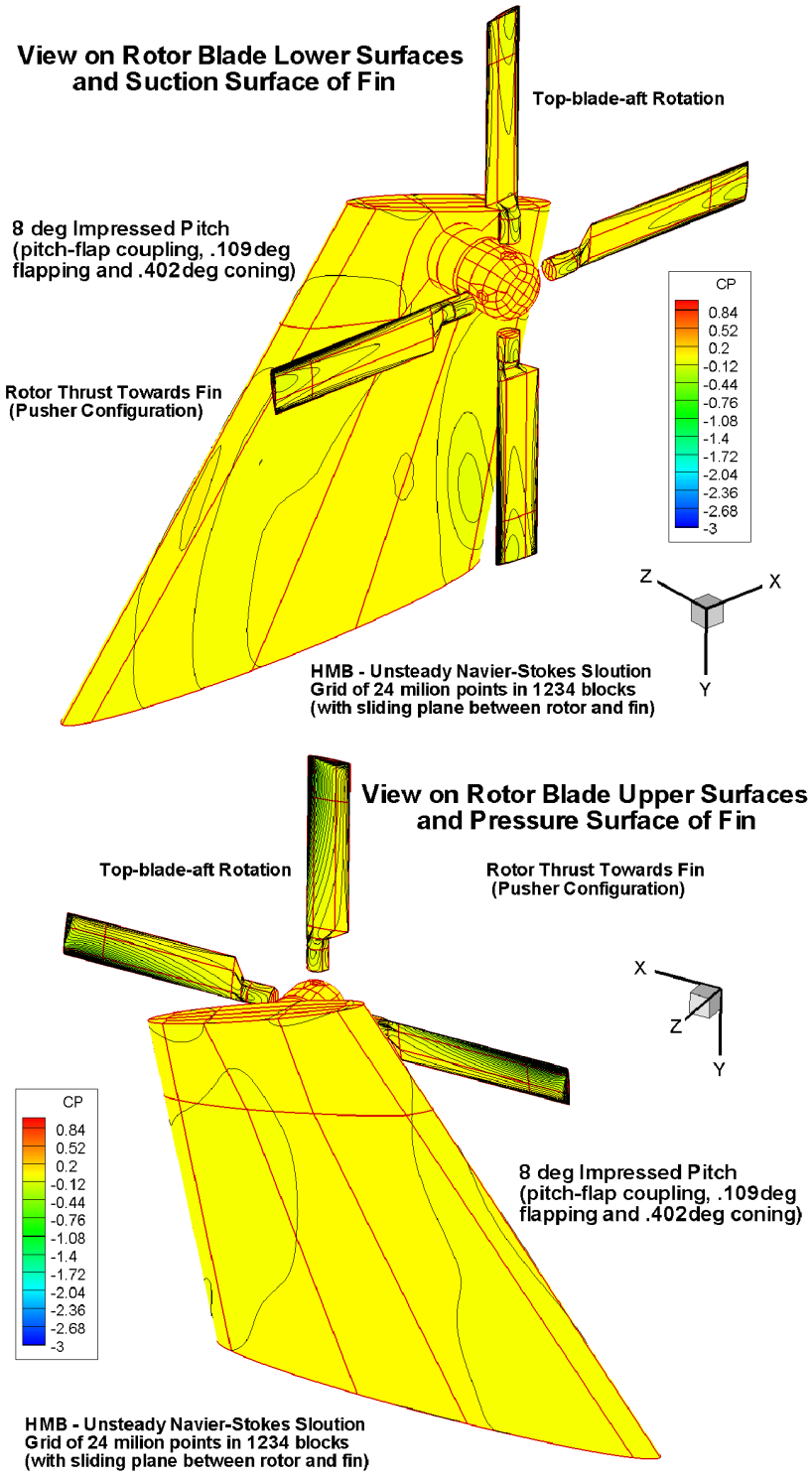

Figure 286: Results of Tail Rotor Fin Blockage Simulation Showing Pressure Contours on Fin and Tail Rotor at a Given Instant in Time

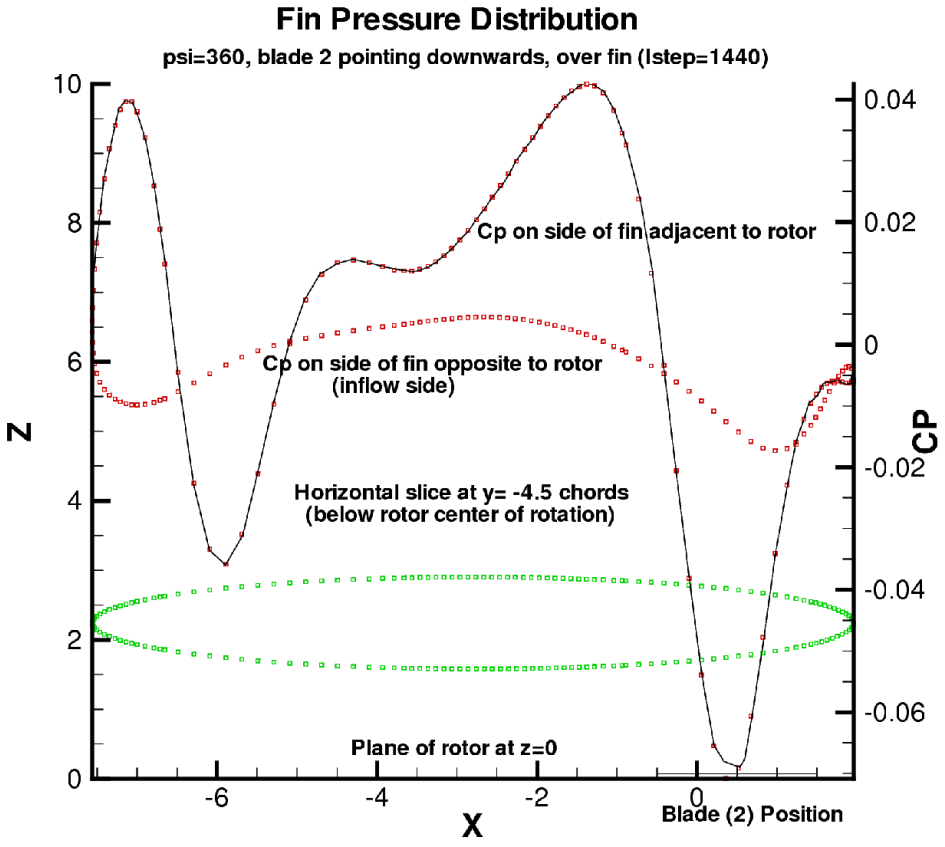

Figure 287: Predicted Unsteady Fin Airloads on Fin Surfaces at a Given Instant in Time

8.2 Unsteady Isolated Rotor

For the isolated rotor case, the rotor geometry from the fin-blockage study was re-used. The simplified feathering bearings and blade attachment, together with the cylindrical domed hub, was retained and the pitch was unchanged at just under 8 degrees. The rotor blocking was also re-used by simply enlarging the blocks above the rotor to cover the upper part of the domain and re-distributing the mesh appropriately. The blade segment was then copied to give a total grid size of about 23 million points for all 4 blades. The upper part of the domain therefore simply contained an extrusion of the cylindrical hub on the inflow side of the rotor, as shown in Figure 288.

The aim was to see if the wake could be established without the upstream disturbance of the fin. The complexity of this case was further reduced by removing the need to interpolate the flowfield on the sliding plane that had been esential when the fin was in place, although the interpolations themselves were not in question.

Prior to attempting this unsteady case, a steady Navier-Stokes solution was also obtained for TRB-000v at the same blade angle of 7.598 degrees and a coning of 0.402 degrees as measured in the test, but with the standard TRB geometry and grid. As in all previous steady Navier-Stokes cases, a long-cylindrical hub was used which extended from the top to the bottom of the domain, and the blade had the usual taper at the root with no feathering bearings. The standard Froude boundary conditions were applied, with the outlet at 6R below the rotor.

The tip vortex locations from the steady case were extracted and compared with the model tail rotor measurements and the earlier Euler case, as already presented in Chapter 6. It was noted that the Navier-Stokes results had very slightly less contraction than obtained from Euler, and had a slightly lower rate of descent after the first blade passage in close agreement with the data.

However, it was found that this steady case was particularly slow to establish the wake connection from about 1.5R beneath the rotor to the Froude outlet, even after several attempts with different turbulence models, and a final run with the modified k-ω model to 90,000 iterations. While the residuals reduced quickly and remained fairly low and the forces and moments appeared well settled, when viewed on a much expanded scale these parameters actually took many iterations to level off. It was suggested that this may be a consequence of the particularly low tip Mach number of only 0.263, and the associated low Reynolds number of only 510,000. It was concluded that planned improvements in the low Mach number preconditioning might be helpful in future cases.

As in the fin blockage case, the isolated rotor unsteady case was again found to have some problems in establishing the wake and was stopped after 2.8 revolutions. Figure 288 shows how the solution was developing at this stage, with the blade surface pressure distributions starting to develop in a reasonably realistic manner, confirming that the basic formulation and non-dimensionalisation within the solver for this flow condition was correct. One problem was thought to be that the wake may be slow to evolve for this relatively lightly loaded hovering rotor case. (At least 10 rotor revolutions would be required for an established helical wake to wind its way to the farfield, and perhaps a similar number of turns for it to initially form, leading to very long runtimes.) This scenario contrasts sharply with previous experience of unsteady forward flight rotor cases, or axial flow propellers, where there is a strong freestream flow to help establish the flow field, and cyclic repetition may be achieved after 3 or 4 revolutions.

However, the main concern was the need for an improved low Mach number pre-conditioner to help converge the parts of the solution where the Mach number is particularly low and the flow may be slow to develop. Such improvements have since been made, see Woodgate and Barakos[324,325]. This unsteady case was not pursued at the time in view of the limitations on computer resources and the difficulties which might be encountered running further unsteady cases at high pitch angle where tip-stall may be encountered. This decision allowed the focus of the research to return to the steady-state Navier-Stokes cases, where several cases were being repeated and extended in an effort to understand the apparent shifts in the flowfield at moderate-to-high pitch angles, as already discussed in Chapter 6.

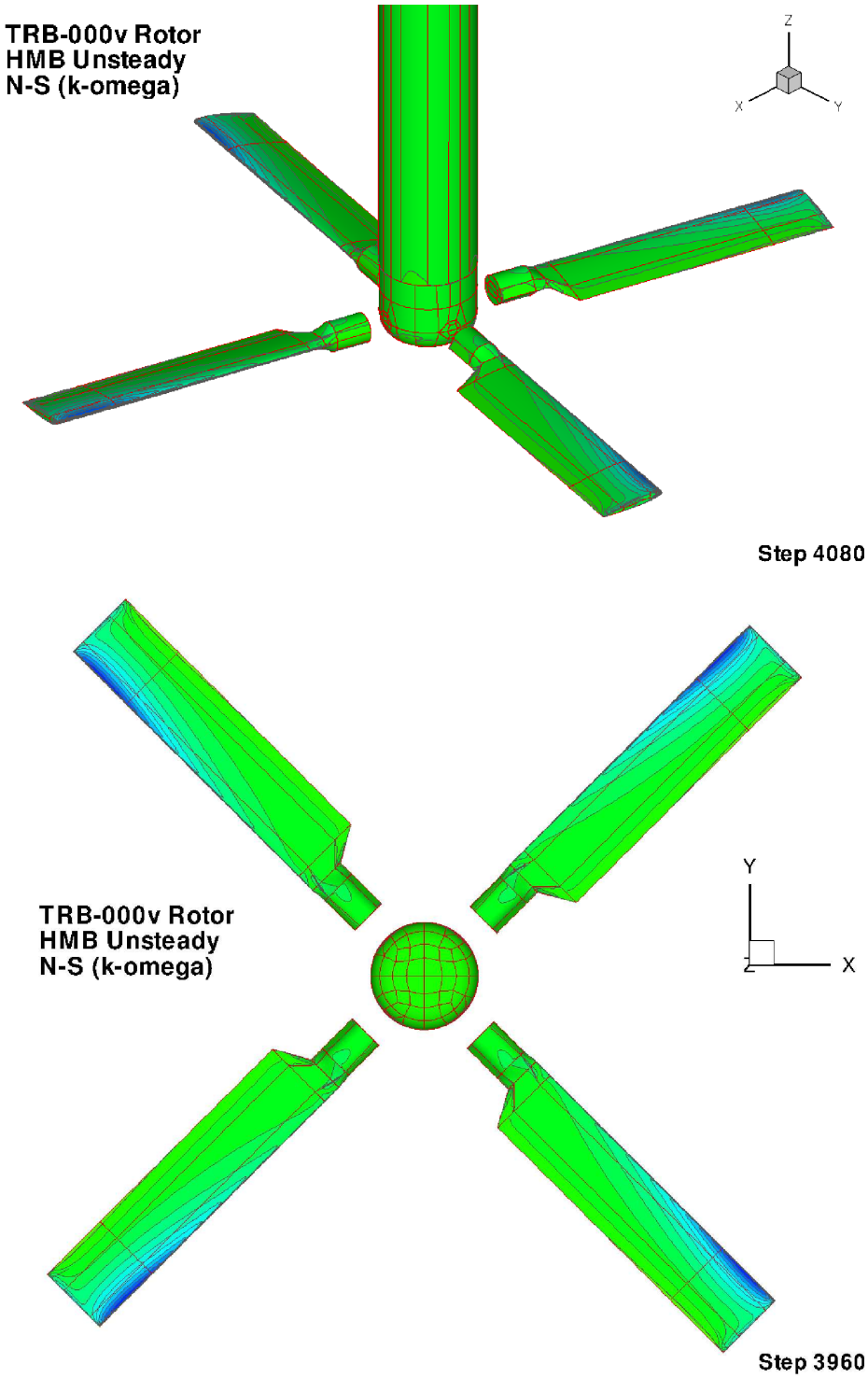

Figure 288: Preliminary Results from Unsteady Navier-Stokes for the Datum Model Tail Rotor Blade with Simplified Feathering Bearings and Cylindrical Domed Hub. Impressed Pitch of 8 Degrees, and 0.402 Degrees Coning. Modified k-ω Turbulence Model, Mtip=0.263, Retip=510,000

8.3 Unsteady Navier-Stokes - Discussion

The application of unsteady Navier-Stokes to the tail rotor fin-blockage problem has been demonstrated in this chapter of the thesis. Despite the problems encountered and the general difficulty of obtaining an unsteady Navier-Stokes solution for a helicopter rotor in hover, the results have been quite illuminating, and the benefits of using an unsteady method are now clear. In the fin blockage case, the preliminary solution that was obtained showed a pressure pulse travelling with the blade and passing over the fin, providing fresh insight into the aerodynamic mechanism by which the fin force is generated. As experienced in flight tests, the tail rotor therefore imparts a 4-per-rev vibratory loading on the fin. In the experimental work available for comparison, only the mean time-averaged fin load had been considered previously, while time-averaged smoke flow visualisation revealed vortical structure in the flow over the fin as accelerated towards the rotor. In this first simulation, the measured flapping and pitch changes induced by the fin were used as input, but the blade response may ultimately be able to be predicted.

The problems encountered with wake development prevented futher work towards a full unsteady simulation of the tail rotor at very high pitch. However, this computationally challenging problem remains a possibility for the future and it is anticipated that, as the solver is developed further and computer resources expand, it will become more tractible. One such development, already available in HMB-2, is the harmonic balance method of Woodgate and Badcock,[325] and this offers a faster solution for cases where the flow and rotor loads vary cyclically, such as in the fin-blockage case. In this frequency domain approach, several modes of the solution are computed in a series of steady runs. However, whilst this approach may be suitable for the fin-blockage case, the technique may not be appropriate for the stalled rotor case due to the likely randomness of the vortex shedding and associated wake couplings.

The concept of using an unsteady approach for rotor performance, opens the door to dealing with both transient problems and interactional aerodynamic effects which often occur in low-speed manoeurving flight. The fin-blockage example is just one such interactional problem faced by helicopter designers, and the hovering flight condition just one of several flight regimes of interest. The addition of a freestream flow, as in forward flight, or low-speed quartering or sideways flight, would alter the flowfield significantly, and in right sideways flight the fin blockage may increase dramatically.

In changing to an unsteady solution, any flow constraints due the usual periodic planes bounding a single blade segment were removed (clearly necessary in the fin-blockage case, but a less obvious requirement for the general isolated rotor case). Another advantage of the unsteady approach, identified in the current work, is that it enables the various components of the hub, such as feathering bearings and blade root attachments, to be included into the simulation without fear that the vortex shedding and turbulence generated in this region would prevent convergence of a steady-state solution. If these effects cannot be otherwise overcome, an unsteady solution may provide the necessary realism and could overcome the unstable root-end vortical flow problems encountered in some of the steady simulations undertaken in this research. The recent development of interpolating planes that allow non-matching structured grids to be employed, or the use of an unstructured grid locally in the root region, may make meshing the hub details much easier. Here great accuracy is perhaps not so vital to the overall simulation, since the major thrust and torque contributions are generated outboard near the tip, but the blockage and disturbance of the hub and proximity of other components, could strongly influence the overall flowfield.

While the problem of establishing and settling the wake for an isolated rotor unsteady simulation remain, there is still a need to evaluate tail rotor performance at very high pitch angles, up to and including the stall. From an industry perspective, the helicopter designer needs to know the maximum thrust capability of the rotor and how much gearbox power is required to generate this thrust, especially during transient low speed manoeuvres. Indeed, any new tip shape or other blade design feature must be well suited to operating near stall, in addition to offering overall performance enhancement at less extreme design conditions.

9 Conclusions and Outlook

The research carried out in this thesis was aimed at discovering if Computational Fluid Dynamics (CFD) methods could be used to accurately determine the aerodynamic performance characteristics of new helicopter blade tip designs. It is concluded that CFD is excellent for this purpose and is the only method which includes both the complexity of the geometry and the detailed flow physics to correctly predict rotor performance. For a helicopter rotor it is essential that both compressibility and viscous effects are taken into account by using a Navier-Stokes method.

The application of CFD avoids the need for approximations and empiricisms necessary in traditional rotor codes, and is truly predictive. The HMB code employs a multi-block structured grid that helps maintain accuracy, both close to the surface of the blade and in the wake. The code has third order spacial accuracy, allowing it to capture tip vortices in the wake as well as many other flow features, and it is therefore well suited to resolving helicopter rotor flows. The solver is versatile, efficient and designed for parallel execution. Alongside the research reported here, HMB has been greatly developed over the last 10 years and now finds application in the helicopter industry.

At the start of this research, the literature review highlighted three different tip shapes for main rotors, originating from the UK, Europe and the US, but found little work had been published on tail rotor blade development. The availability of a CFD method now opens the door to a more detailed appraisal of existing designs and some new concepts are starting to emerge. The Küchemann-type tip shape has a long history, but has not been previously applied to helicopter rotors. This tip has a number of key features which offer a general improvement in performance over previous practice. CFD allows greater insight and opportunity to better optimise rotor designs to obtain greater efficiency or suit a particular purpose.

Euler solutions were used initially to obtain an economic first assessment of eight different tip designs, and gave a good indication of improvements in induced power that might be obtained from changes in tip shape and the use of anhedral (the effect of twist was separately confirmed as part of the validation studies). However, a new tip shape must offer an overall benefit, and it was recognised from the outset that viscous effects which contribute to the profile power were particularly important at the mid-subsonic Mach numbers and low Reynolds numbers at which helicopter rotors operate. Three tip shapes were selected for further analysis with a full Navier-Stokes method.

Application of a steady Navier-Stokes method is an extremely useful and accurate way of determining rotor performance for pitch angles up to and including the onset of stall (provided that the flow is predominantly attached, and residuals remain acceptably low). However, care must be taken to ensure that the computational geometry is not over-simplified so that simulations remain realistic and any tendency for flow-changes are avoided when seeking steady solutions. This level of CFD simulation furnishes a rich database of information, from which much insight may be gained. The understanding obtained from CFD could help to develop more traditional (faster) methods for application to radically new rotor designs. If desired, the time-averaged downwash and angle of attack can be extracted from the CFD solution so that the rotor engineer can make comparisons in familiar terms, although a more accurate approach may be to make direct comparison with the predicted thrust and torque-loading distributions. However, CFD now offers a more holistic approach, and perhaps the philosophy should be to move away from 2D strip theory concepts and seek more efficient ways of working with the 3D solution. For example, in the tip region it was found useful to display surface pressures normal to the leading edge to highlight both the radial and chordwise loading distributions.

The example used here was for a model tail rotor (compatible with that tested at WHL in the 1980's) which acted as a carrier for the various tip shapes considered. The basic features of this rotor blade, whilst simple, led to some unforeseen root-end flow variation problems aggravated by zero-twist and a large root cut-out together with unforeseen consequences of omitting hub-blockage effects in the simulations. However, these problems did not prevent valuable information being discovered about the impact of the tip design. Further high-quality test data would be useful to verify some of the modelling choices involved, especially for advanced rotor configurations operating at high pitch angles when stall may be encountered.

Three selected tip shapes have been evaluated by use of a steady Navier-Stokes method. The idea of using a Küchemann-type tip shape has resulted in a significant improvement in tail rotor performance, compared to the

datum rectangular tip. The 0.25 chord wide Küchemann tip (without anhedral) was predicted to give a 5.5% improvement in induced power factor and a 16% reduction in profile power, relative to the datum rectangular blade. In terms of Figure of Merit, a 5-point improvement was realised, and the Küchemann tip was found to delay the onset of tip stall and power divergence by up to 2 degrees in pitch. The addition of 20 degrees of anhedral gave a further reduction in the induced power factor at low pitch, and a further 1-point improvement in the peak Figure of Merit was obtained. The detailed results suggest that the form of the anhedral could be refined to better optimise this tip design. The HMB code offers an ideal tool to pursue improvements in rotor blade design.

However, what is important here is not so much the benefits which were obtained, but the new capability to quantify the flow physics with good accuracy, such that subtle changes in tip geometry arising from intuitive design thinking can be confirmed, permiting further design refinement and optimisation using CFD as a tool in the future.

Adopting an unsteady approach allows the effects of fluctuating flow separations to be captured at high pitch, and may also remove the need to simplify the geometry allowing many practical details of the rotor blades and hub to be included. Airframes components such as the fin and gearbox fairing, or fuselage and engine fairings may also to be taken into account. Unsteady methods have previously been used for forward flight applications where there is a strong freestream flow component, but are not commonly used in the hover where the flowfield starts from rest. The attempted isolated rotor case was only partially successful, and was limited by the need for further code development at that time together with constraints on computing resource. Application of the unsteady method to a tail rotor fin-blockage case was also demonstrated, and highlighted the cyclic nature of the loads on the fin and rotor. The unsteady method offers potential to model the rotor in stall during manoeuvres. The capability to move from a detail design evaluation to an installed rotor simulation using the same computational method represents a significant step forward.

While today the computational cost seems high, the unsteady approach offers a powerful tool for future application to model the tail rotor at off-design conditions, such as found in manoeuvres, and it is now feasible to model the complete helicopter to gain insight into interactional aerodynamics. Problems yet to be addressed are the sudden application of pitch and use of very high pitch in manoeuvring flight where the maximum thrust and power are often in question for new designs. For some applications, such as for a tail rotor next to the fin, or a main rotor close to the fuselage, the recently developed harmonic balance method may prove extremely useful in providing an answer in shorter time, but for some rotor problems, where periodic or cyclic loading cannot be pre-supposed due to random flow fluctuations near stall, a time-accurate method may be required.

The example cases used in this thesis took advantage of the rigidity of the short-stiff blades of the tail rotor, but it is important to include aeroelastic deformations when dealing with more flexible rotor blades, using either strongly or loosely coupled techniques. Also the low Reynolds number of the model rotor raised questions about transition in the boundary layer and how the stall mechanism could be adequately captured. These details are important for all aspects of helicopter rotor aerodynamics if accurate results for performance, vibration and noise are to be obtained.

Navier-Stokes methods are now finding application in industry because of their capability to provide highly detailed predictive results, and with further development and investment, will become indispensable in the design process. In the future, it is anticipated that much larger, more comprehensive CFD simulations will be possible, but enhanced computational resources also bring the opportunity to run many smaller, more specific cases to quickly shed light on a new design features or investigate a particular problem. CFD has the versatility and represents the physics sufficiently well to do this, as demonstrated here for the evaluation of enhanced tail rotor tip shapes.

References

[1] Abbott, I.H. and von Doenhoff, A.E. *Theory of Wing Sections*. Dover, 1959.

[2] Ahmad, J.U. and Duque, E.P.N. Helicopter Rotor Blade Computation in Unsteady Flows Using Moving Overset Grids. *Journal of Aircraft*, 33(1):54–60, January-February 1996. Presented as Paper AIAA 94-1922 at the 12th AIAA Applied Aerodynamics Conference, Colorado Springs, CO, June, 1994.

[3] Ahmad, J.U. and Strawn, R.C. Hovering Rotor and Wake Calculations with an Overset Grid Navier-Stokes Solver. In *55th Annual Forum of the American Helicopter Society, Montreal, Canada*, May 1999.

[4] Ahmed, S.R. and Vidjaja, V.T. Unsteady Panel Method Calculation of Pressure Distribution on a Bo105 Model Rotor Blade. *Journal of the American Helicopter Society*, 43(1):47–56, January 1998. Presented at the 50th Annual Forum of the American Helicopter Society, Washington, DC, May, 1994.

[5] Aiken, E.W., Ormiston, R.A. and Young, L.A. Future Directions in Rotorcraft Technology at NASA Ames Research Center. In *56th Annual Forum of the American Helicopter Society, Virginia Beach, VA*, May 2000.

[6] Alansky, I, Faull, R., and Skonieczny, J. Handling Qualities of the SH-60B SEAHAWK. In *37th Annual Forum of the American Helicopter Society, New Orleans, LA.*, pages 288–306, May 1981.

[7] Allen, C.B. and Rogers, J.R.W. Extension and Application of the GEROS Grid Generation System. In *CEAS Conference, Cambridge*, June 2002.

[8] Allongue, M., Marze, H.J. and Potdevin, F. The Quiet Helicopter - From Research to Reality. In *55th Annual Forum of the American Helicopter Society, Montreal, Canada*, May 1999.

[9] Althaus, D. Stuttgarter Profilekatalog I, 1962-1972. Technical report, Institut fur Aerodynamik und Gasdynamic der Universitat Stuttgart, Germany, 1972.

[10] Amer, K.B. and Prouty, R.W. Technology Advances in the AH-64 Apache Advanced Attack Helicopter. In *39th Annual Forum of the American Helicopter Society, St Louis, Missouri*, May 1983.

[11] Anderson, E.A. and Lawton, T.A. Correlation between Vortex Strength and Axial Velocity in a Trailing Vortex. *Journal of Aircraft*, 40(4):699–704, July-August 2003.

[12] Anderson, J.D. *Computational Fluid Dynamics - The Basics with Applications*. McGraw Hill International Edition, Mechanical Engineering Series, 1995. ISBN 0-07-001685-2.

[13] ANSYS Inc. ICEM-CFD Hexa Mesh Generation Software. http://www.ansys.com/products/icemcfd.asp.

[14] Antoniadis, A.F., Drikakis, D., Zhong, B., Barakos, G., Steijl, R. Biava, M., Vigevano, L., Brocklehurst, A., Boelens, O., Dietz, M., Embacher, M. and Khier, W. Assessment of CFD Methods against Experimental Flow Measurements for Helicopter Flows. *Aerospace Science and Technology, Elsevier, doi:10.1016/j.ast.2011.09.003*, September 2011.

[15] Aoyama, T., Kawachi, K. and Saito, S. Effect of Blade Tip Planform on Shock Wave of Advancing Helicopter Blade. *Journal of Aircraft*, 32(5):955–961, September-October 1995.

[16] Ardonceau, P.L. Aerodynamic Properties of Crescent Wing Planforms. *Journal of Aircraft*, 31(2):462–465, March 1994. Engineering Note.

[17] O. Axelsson. *Iterative Solution Methods*. Cambridge University Press, Cambridge, MA, 1994.

[18] Baeder, J.D. Passive Design for Reduction of High-Speed Impulsive Rotor Noise. *Journal of the American Helicopter Society*, 43(3):222–234, July 1998. Presented at the 52nd Annual Forum of the American Helicopter Society, Washington, DC, May, 1996.

[19] Bagley, J.A. and Beasley, J.A. The Shapes and Lift-Dependent Drags of Some Sweptback Wings Designed for M=1.2. Technical report, Royal Aircraft Establishment, Farnborough, Report No. Aero. 2620 (unclassified), June 1959.

[20] Balch, D.T. Impact of Main Rotor Tip Geometry on Main Rotor/Tail Rotor Interaction in Hover. In *40th Annual Forum of the American Helicopter Society, Washington, DC.*, pages 349–358, May 1984.

[21] Barakos, G., Badcock, K., et al. HMB User Manual, TN04. Technical report, CFD Laboratory, University of Glasgow, July 2005.

[22] Barakos, G., Steijl, R., Badcock, K. and Brocklehurst, A. Development of a CFD Capability for Full Helicopter Engineering Analysis. In *31st European Rotorcraft Forum, Florence, Italy*, September 2005.

[23] Barakos, G.N., Steijl, R. and Woodgate, M. Towards CFD Analysis of Complete Helicopter Configurations. In *3rd International Basic Research Conference on Rotorcraft Technology, Nanjing, China*, October 2009.

[24] Beaumier, P. and Delrieux, Y. Description and Validation of the ONERA Computational Method for the Prediction of Blade-Vortex Interaction Noise. In *29th European Rotorcraft Forum, Friedrichshafen, Germany*, September 2003.

[25] Beaumier, P., Chelli, E. and Pahlke, K. Navier-Stokes Prediction of Helicopter Rotor Performance in Hover Including Aero-Elastic Effects. In *56th Annual Forum of the American Helicopter Society, Virginia Beach, VA*, May 2000.

[26] Beaumier, P, Chelli, E. and Pahlke, K. Navier-Stokes Prediction of Helicopter Rotor Performance in Hover Including Aeroelastic Effects. *Journal of the American Helicopter Society*, 46(4):301–309, October 2001.

[27] Beaumier, P., Zibi, J., and Costes, M. CFD Drag and Power Prediction for a Rotor in Hover or Forward Flight - Formulation and First Applications. *Journal of the American Helicopter Society*, 42(4):327–336, October 1997. Presented at the 52nd Annual Forum of the American Helicopter Society, Washington, DC, June, 1996.

[28] Bebesel, M., Polz, G. and Scholl, E. Aerodynamic and Aeroacoustic Layout of the ATR (Advanced Technology Rotor). In *55th Annual Forum AHS, Montreal, Canada*, May 1999.

[29] Beddoes, T.S. Representation of Airfoil Behaviour. *Vertica*, 7(2):183–197, 1983.

[30] Beddoes, T.S. Two and Three Dimensional Indicial Methods For Rotor Dynamic Airloads. In *AHS National Specialists' Meeting on Rotorcraft Dynamics, Arlington, Texas.*, November 1989.

[31] Beddoes, T.S. A 3-D Separation Model for Arbitary Planforms. In *47th Annual Forum of the American Helicopter Society, Phoenix, Arizona.*, May 1991.

[32] Beddoes, T.S. A Near Wake Dynamic Model. In *Annual Forum of the American Helicopter Society*, c.1992.

[33] Beedy, J. Numerical Study of the Flow Field Around the Tip of Oscillating Wings. In *Proceedings of the University of Glasgow Helicopter Study Weekend, The Burn, Scotland*, April 2003.

[34] Beedy, J. *Using Computational Fluid Dynamics to Improve Rotorcraft Aerodynamic Codes*. PhD Thesis, University of Liverpool, 2006.

[35] Beedy, J., Barakos, G., Badcock, K. and Richards, B. Improving Rotorcraft Aerodynamics Using Computational Fluid Dynamics. In *29th European Rotorcraft Forum, Friedrichshafen, Germany*, pages 72.1–72.13, September 2003.

[36] Berkman, M.E., Sankar, L., Berezin and Torok, M.S. A Navier-Stokes / Full Potential / Free Wake Method for Advancing Multi-Bladed Rotors. In *53rd Annual Forum of the American Helicopter Society, Virginia Beach, VA*, pages 305–314, May 1997.

[37] Berry, J.D. Quarter-Scale Testing of an Advanced Rotor System for the UH-1 Helicopter. In *37th Annual Forum of the American Helicopter Society, New Orleans, LA.*, pages 456–462, May 1981.

[38] Berton, E., Favier, D., Maresca, C., Mba, M.N., Vozhdaev, E., Golovkin, V., Tarasov, N. and Maslennikov, A. Experimental and Numerical Results Obtained at LABM and TSAGI on Aerodynamics of Helicopter Rotor Blades in Hover. In *29th European Rotorcraft Forum, Friedrichshafen, Germany*, pages 81.1–81.14, September 2003.

[39] Bhagwat, M., Moulton, M.A. and Caradonna, F.X. Recent Advances in the Embedded-Wake Approach to Hover Performance Prediction. In *4th AHS Specialists' Conference on Aeromechanics, San Francisco, CA*, pages 5.1:1–17, January 2004.

[40] Bhagwat, M.J. and Leishman, J.G. On the Relationship Between Blade Circulation and Tip Vortex Characteristics. In *54th Annual Forum of the American Helicopter Society, Washington, D.C.*, pages 557–575, May 1998.

[41] Bhagwat, M.J. and Leishman, J.G. Correlation of Helicopter Rotor Tip Vortex Measurements. *AIAA Journal*, 38(2):301–308, February 2000.

[42] Bhagwat, M.J. and Leishman, J.G. Measurements of Bound and Wake Circulation on a Helicopter Rotor. *Journal of Aircraft*, 37(2):227–234, March-April 2000.

[43] Bhagwat, M.J., and Leishman, J.G. On the Aerodynamic Stability of Helicopter Rotor Wakes. In *56th Annual Forum of the American Helicopter Society, Virginia Beach, VA*, May 2000.

[44] Bhagwat, M.J., Franke, M., Martin, P.B. and Leishman, J.G. Flow Visualisation and Measurement in the Wake of a Rotor with a Subwing Tip. In *55th Annual Forum of the American Helicopter Society, Montreal, Canada*, May 1999.

[45] Biava, M. and Vigevano, L. The Effect of Far-Field Boundary Conditions on Tip Vortex Path Predictions in Hover. In *CEAS Conference, Cambridge*, June 2002.

[46] Biava, M. and Vigevano, L. Assessment of the Vorticity Confinement Technique Applied to Rotorcraft Flows. In *21st Applied Aerodynamics Conference, Orlando, Florida*, June 2003.

[47] Bingham, G.J. The Aerodynamic Influences of Rotor Blade Airfoils, Twist, Taper and Solidity on Hover and Forward Flight Performance. In *37th Annual Forum of the American Helicopter Society, New Orleans, LA.*, pages 37–50, May 1981.

[48] Boelens, O.J., Barakos, G., Biava, M., Brocklehurst, A., Costes, M., D'Alascio, A., Dietz, M., Drikakis, D., Ekaterinaris, J., Humby, I., Khier, W., Knutzen, B., Kok, J., LeChuiton, F., Pahlke, K., Renaud, T., Schwartz, T., Steijl, R., Sudre, L., van der Ven, H., Vigevano, L. and Zhong, B. The Blind-Test Activity of the GOAHEAD Project. In *33rd European Rotorcraft Forum, Kazan, Russia*, September 2007.

[49] Boelens, O.J., van der Ven, H., Kok, J.C., and Prananta, B.B. Rotorcraft Simulations Using a Sliding-Grid Approach. In *34th European Rotorcraft Forum, Liverpool, UK.*, September 2008.

[50] Bourdin, P. Planform Effects on Lift-Induced Drag. In *20th AIAA Applied Aerodynamics Conference, St Louis, Missouri, AIAA Paper 2002-3151*, June 2002.

[51] Bousmann, W.G. Putting the Aero Back Into Aeroelasticity. In *Eighth Annual ARO Workshop on Aeroelasticity of Rotorcraft Systems*, October 1999.

[52] Brady, C. Advanced Blended Winglets. *The B737 Technical Site (www.b737.org.uk winglets.htm)*, 2003.

[53] Brocklehurst, A. Unsteady 2D Pitching Aerofoil in Compressible Viscous Flow. In *Fluent CFD User Group Meeting*, March 2002.

[54] Brocklehurst, A. Application of CFD to Aerofoils, Blades and Helicopters. In *The University of Glasgow Helicopter Study Weekend, The Burn, Edzell, Scotland*, April 2003.

[55] Brocklehurst, A. Recent Application of CFD to Helicopter Rotors at WHL. In *The University of Glasgow Helicopter Study Weekend, The Burn, Edzell, Scotland*, April 2005.

[56] Brocklehurst, A. and Barakos, G. Performance Analysis of Rotor Tip Shapes in Hover Using Computational Fluid Dynamics. In *The University of Glasgow Helicopter Study Weekend, The Burn, Edzell, Scotland*, March 2006.

[57] Brocklehurst, A. and Barakos, G. Effect of Tip Shape and Twist on Rotor Performance. In *The University of Glasgow Helicopter Study Weekend, The Burn, Edzell, Scotland*, March 2007.

[58] Brocklehurst, A. and Duque, E.P.N. Experimental and Numerical Study of the British Experimental Rotor Programme Blade. In *8th Applied Aerodynamics Conference, Portland, Oregon, AIAA-90-3008*, August 1990.

[59] Brocklehurst, A. and Pike, A.C. Reduction of BVI Noise Using a Vane Tip. In *AHS Specialists' Conference on Aerodynamics, Dynamics and Acoustics, San Francisco*, January 1994.

[60] Brocklehurst, A., Beedy, J., Barakos, G., Badcock, K. and Richards, B. Experimental and CFD Investigation of Helicopter BERP Tip Aerodynamics. In *Conference on Computational and Experimental Methods, University of Glasgow*, September 2003.

[61] Brocklehurst, A., Steijl, R. and Barakos, G. CFD for Tail Rotor Design and Evaluation. In *34th European Rotorcraft Forum, Liverpool*, September 2008.

[62] Brocklehurst, A., Steijl, R. and Barakos, G. Using CFD to Understand and Evaluate Tail Rotor Blade Design. In *AHS Aeromechanics Specialists' Conference, San Francisco, CA.*, January 2008.

[63] Brotherhood, P. and Riley, M.J. Flight Experiments on Aerodynamic Features Affecting Helicopter Blade Design. In *Third European Rotorcraft Forum, Aix-en-Provence, France*, September 1977.

[64] Brown, R.E. Rotor Wake Modeling for Flight Dynamics Simulation of Helicopters. *AIAA Journal*, 38(1):57–63, January 2000.

[65] Brown, R.E., Leishman, J.G., Newman, S.J. and Perry, F.J. Blade Twist Effects on Rotor Behaviour in the Vortex Ring State. In *28th European Rotorcraft Forum, Bristol*, September 2002.

[66] Brown, R.E., Line, A.J. and Ahlin, G.A. Numerical Investigations into the Vortex Ring State Phenomenon. In *Proceedings of the University of Glasgow Helicopter Study Weekend, The Burn, Scotland*, March 2004.

[67] Burkett, C.W. Reduction in Induced Drag by the use of Aft Swept Wing Tips. *Aeronautical Journal*, pages 400–405, December 1989.

[68] Bushnell, D.M. Aircraft Drag Reduction - A Review. In *Proceedings of the Institution of Mechanical Engineers, Vol.217 Part G-00602, Journal of Aerospace Engineering*, pages 1–18, 2003.

[69] Byham, G.M. An Overview of Conventional Tail Rotors. In *RAeS Conference, London*, 1987.

[70] Callahan, C.B. and Straub, F.K. Design Optimisation of Rotor Blades for Improved Performance and Vibration. *Journal of the American Helicopter Society*, 38(4):62–70, October 1993.

[71] Canonne, E., Benoit, C. and Jeanfaivre, G. Cylindrical Mesh Adaption for Isolated Rotors in Hover. In *58th Annual Forum of the American Helicopter Society, Montreal, Quebec, Canada*, June 2002.

[72] Caradonna, F.X. and Tung, C. Experimental and Analytical Studies of a Model Helicopter Rotor in Hover. *Vertica*, 5:149–161, 1981.

[73] Caradonna, F.X. and Tung, C. Experimental and Analytical Studies of a Model Helicopter Rotor in Hover. Technical report, NASA TM-81232, September 1981.

[74] CFD Simulations of Tilt Rotor Configurations in Hover. Potsdam, M.A. and Strawn, R.C. In *58th Annual National Forum of the American Helicopter Society, Montreal, Canada*, June 2002. Also published in AHS Journal, Vol.50, No.1, January, 2005.

[75] Chae, S., Yee, K., Yang, C., Aoyama, T., Jeong, S. and Obayashi, S. Helicopter Rotor Shape Optimisation for the Improvement of Aeroacoustic Performance in Hover. *Journal of Aircraft*, 47(5):1770–1783, September-October 2010.

[76] Chang, J.W., Park, S.O. An Experimental Study of a Tip Vortex Roll-up of an Oscillating Wing. In *AIAA 37th Aerospace Sciences Meeting, Reno, NV., AIAA Paper 99-0142*, January 1999.

[77] Chao, D.D. and van Dam, C.P. Airfoil Drag Prediction and Decomposition. *Journal of Aircraft*, 36(4):675–681, July-August 1999.

[78] Cook, C.V. The Structure of the Rotor Blade Tip Vortex. In *AGARD-CP-111*, pages 3.1–3.14, September 1972.

[79] Cook, C.V. A Review of Tail Rotor Design and Performance. *Vertica*, 2:163–181, November 1978.

[80] Corsiglia, V.R., Schwind, R.G., Chigier, N.A. Rapid Scanning Three-Dimensional Hot-Wire Anemometer Surveys of Wing-Tip Vortices. *Journal of Aircraft*, 10(12), December 1973.

[81] Costes, M., LeBalleur, J.C., Gasparini, L., Vigevano, L., Hounjet, M.H.L., Kokkalis, A., Miller, J.V., Spruce, M., Pagano, A., Renzoni, P., Rocchetto, A., Toulmay, F. Development of a Common European Unsteady Full Potential CFD Code for Helicopter Rotors in Hover and Forward Flight. In *53rd Annual Forum of the American Helicopter Society, Virginia Beach, VA*, pages 330–342, May 1997.

[82] Coton, F.N. and Galbraith, R.A.McD. An Examination of Dynamic Stall on an Oscillating Rectangular Wing. In *21st Applied Aerodynamics Conference, Orlando, Florida. Paper AIAA-2003-3675*, June 2003.

[83] Coton, F.N., Galbraith, R.A.McD. and Green, R.B. The Effect of Wing Planform Shape on Dynamic Stall. *The Aeronautical Journal*, 105(1045):151–159, March 2000.

[84] Cowan, J., Dadone, L., Gangwani, S. Wind Tunnel Test of a Pressure Instrumented Model Scale Advanced Rotor. In *42nd Annual Forum of the American Helicopter Society, Washington-DC.*, pages 217–229, June 1986.

[85] Crouch, J.D., Crouch, I.W.M. and Ng, L.L. Transition Prediction for Three-Dimensional Boundary Layers in Computational Fluid Dynamics Applications. *AIAA Journal*, 40(8):1536–1541, August 2002.

[86] Curtiss, H.C., Carson, F., Hill, J. and Quankenbush, T. Performance of a Sikorsky S-61 with a New Main Rotor. *Journal of the American Helicopter Society*, 48(3):211–215, July 2003.

[87] D'Alascio, A., Pahlke, K., Castellin, C. and Costes, M. Application of the Navier-Stokes Codes Developed in the Framework of the Joined German/French CFD Research Program CHANCE. In *27th European Rotorcraft Forum, Moscow*, pages 38.1–38.10, September 2001.

[88] D'Andrea, A. Development of a Multi-Processor Unstructured Panel Code Coupled with a CVC Free Wake Model for Advanced Analysis of Rotorcraft and Tilt-Rotors. In *64th Annual Forum of the American Helicopter Society, Montreal, Canada.*, April-May 2008.

[89] Datta, A. and Chopra, I. Validation of Structural and Aerodynamic Modelling Using UH-60A Flight Test Data. In *59th Annual Forum of the American Helicopter Society, Phoenix, Arizona*, May 2003.

[90] deMattos, B.S., Macedo, A.P., Filho, D.H.S. Considerations About Winglet Design. In *21st Applied Aerodynamics Conference, Orlando, Florida*, June 2003.

[91] Desabrais, K.J., Johari, H. Direct Circulation Measurement of a Tip Vortex. *AIAA Journal Technical Note*, 38(11):2189–2191, November 2000.

[92] Devenport, W.J., Rife, M.C., Liapis, S.I. and Follin, G.J. The Structure and Development of a Wing-Tip Vortex. *Journal Fluid Mechanics*, 312:67–106, 1996.

[93] Dietz, M., Kessler, M. and Kramer, E. Trimmed Simulation of a Complete Helicopter Configuration Using Fluid-Structure Coupling. *Journal of High Performance Computing in Science and Engineering*, 2007. Presented at the CICA Conference, Italy, July, 2007.

[94] Dindar, M., Lemnios, A., Shephard, M., Jansen, K. and Kenwright, D. Effect of Tip Vortex Resolution on UH-60A Rotor Blade Hover Performance Calculations. In *54th Annual Forum of the American Helicopter Society, Washington, D.C.*, pages 45–57, May 1998.

[95] Drees, J.M. Prepare for the 21st Century - The 1987 Alexander Nikolsky Lecture. *AIAA Journal*, pages 3–14, July 1987. Presented at the 43rd Annual Forum of the American Helicopter Society, St Louis, May 1987.

[96] Drela, M. An Analysis and Design System for Low Reynolds Number Airfoils. In *Low Reynolds Number Aerodynamics, T.J. Muller (editor), Proceedings of the Conference, Notre Dame, Indiana, USA, 5-7 June 1989, Springer-Verlag*, pages 1–12, June 1989.

[97] Drela, M. Transonic Low Reynolds Number Aerofoils. *Journal of Aircraft*, 29(6):1106–1113, Nov-Dec 1992.

[98] Drela, M. Variation of Ncrit with Turbulence Level. Technical report, MSES Documentation, M.I.T., 1997.

[99] Drela, M. and Giles, M.B. Viscous-Invicid Analysis of Transonic and Low Reynolds Number Airfoils. *AIAA Journal*, 25(10):1347–1355, October 1987.

[100] Duque, E.P.N. A Numerical Analysis of the British Experimental Rotor Program Blade. In *45th Annual Forum of the American Helicopter Society, Boston, MA*, pages 523–532, May 1989. National 1989 Lichten Prize Winner.

[101] Duque, E.P.N. A Numerical Analysis of the British Experimental Rotor Program Blade. In *15th European Rotorcraft Forum, Amsterdam*, September 1989.

[102] Duque, E.P.N. A Numerical Analysis of the British Experimental Rotor Programme Blade. *Journal of the American Helicopter Society*, 37(1):46–54, January 1992.

[103] Duque, E.P.N. and Dimanlig, A.C.B. Navier-Stokes Simulation of the AH-66 (Comanche) Helicopter. In *AHS Specialists' Conference, San Francisco, CA.*, January 1994.

[104] Duque, E.P.N. and Srinivasan, G.R. Numerical Simulation of a Hovering Rotor Using Embedded Grids. In *48th Annual National Forum of the American Helicopter Society, Washington, D.C.*, June 1992.

[105] Egolf, T.A., and Sparks S.P. A Full Potential Rotor Analysis With Wake Influence Using an Inner-Outer Domain Technique. *Journal of AHS*, 32(8):15–24, July 1987. Presented at the 42nd Annual Forum of the American Helicopter Society, Washington, June, 1986.

[106] Eppler, R. Induced Drag and Winglets. *Aerospace Science and Technology*, 1(1):3–15, January 1997. Presented at the OSTIV Congress, New Zealand, January, 1995.

[107] Eppler, R. and Somers, D.M. A Computer Program for the Design and Analysis of Low Speed Airfoils. Technical report, NASA-TM-80210, March 1980.

[108] Esquieu, S. Aircraft Drag Extraction From Patched Grid Computations. In *AIAA 2003-3659, 21st Applied Aerodynamics Conference, Orlando, Florida*, June 2003.

[109] Faury, G. Eurocopter EC225 / 725 - An Example of Risk Management. In *27th European Rotorcraft Forum, Moscow*, pages 21.1–21.8, September 2001.

[110] Favier, D., Nsi-Mba, M., Barbi, C. and Maresca, C. A Free Wake Analysis for Hovering Rotors and Advancing Propellers. In *11th European Rotorcraft Forum, City University, London*, pages 29.1–29.22, September 1985.

[111] Felker, F.F, Maisel, M.D., and Betzina, M.D. Full-Scale Tilt-Rotor Hover Performance. In *41st Annual Forum of the American Helicopter Society, Fort Worth, Texas, 1985*, pages 501–513, May 1985.

[112] Ferguson, H.J. Booster Tips. *Flight*, c1980.

[113] Flechner, S.G., Jacobs, P.F., and Whitcomb, R.T. A High Subsonic Speed Wind Tunnel Investigation on a Representative Second-Generation Jet Transport Wing. Technical Report NASA TN D-8264, NASA Langley, July 1976.

[114] Flowers, J.W. and Collar, A.R. A Circulation Meter. *Unpublished note. Personal communication from F.G. Maccabee, Loughborough University of Technology*, October 1966.

[115] Fradenburgh, E.A. Flow Field Measurements for a Hovering Rotor Near the Ground. In *Fifth Annual Western Forum, Los Angeles, CA*, September 1958.

[116] Francis, M.S. and Kennedy, D.A. Formation of a Trailing Vortex. *Journal of Aircraft*, 16(3):148–154, March 1979.

[117] Freestone, M.M. Pressure Probes for Determining Vorticity. *Unpublished Note*, April 1983.

[118] Gessow, A. and Myers, G. *Aerodynamics of the Helicopter*. Frederick Ungar, New York, 1952.

[119] Glauert, H. *The Elements of Aerofoil and Airscrew Theory*. Cambridge University Press, second edition, 1959.

[120] Grant, J. Calculation of the Supercritical Flow Over the Tip Region of a Non-Lifting Rotor Blade at Arbitary Azimuth. Technical report, Royal Aircraft Establishment, Farnborough, December 1977.

[121] Grant, J. The Prediction of Supercritical Pressure Distributions on Blade Tips of Arbitary Shapes. *Vertica*, 3:275–292, 1979. Presented at the 4th European Rotorcraft and Powered Lift Aircraft Forum, Stressa, September 1978.

[122] Gray, R.B., McMahon, H.M., Shenoy, K.R. and Hammer, M.L. Surface Pressure Measurements at Two Tips of a Model Helicopter Rotor in Hover. Technical report, NASA CR-3281, May 1980.

[123] Grenon, R. and Bourdin, P. Numerical Study of Unconventional Wing Tip Devices for Lift-Induced Drag Reduction. In *CEAS Conference, Cambridge*, June 2002.

[124] Hall, C.M. and Long, L.N. High Order Accurate Simulations of Wake and Tip Vortex Flowfields. In *55th Annual Forum American Helicopter Society, Montreal, Canada*, May 1999.

[125] Hall, S. The Hoerner Wing Tip. *Soarer, SSA*, page 16, c1990.

[126] Hall, S.R. and Anand, V.R. Active Flap Control of the Smart Rotor for Vibration Reduction. In *65th Annual Forum of the American Helicopter Society, Grapevine, Texas*, May 2009.

[127] G Haller. An objective definition for a vortex. *Journal of Fluid Mechanics*, 525:1–26, 2005.

[128] Han, Y.O. and Leishman, J.G. Investigation of Helicopter Rotor-Blade-Tip-Vortex Alleviation Using a Slotted Tip. *AIAA Journal*, 42(3):524–535, March 2004.

[129] Hansford, R.E. Rotor Load Correlation with the British Experimental Rotor Program Blade. *Journal of the American Helicopter Society*, 32(3):43–53, July 1987.

[130] Hardin, J.C. and Lamkin, S.L. Concepts for Reduction of Blade/Vortex Interaction Noise. *Journal of Aircraft*, 24(2):120–124, February 1987. Presented at the 10th AIAA Aeroacoustics Conference, Seattle, WA.

[131] Hariharan, N. Rotary-Wing Wake Capturing: High Order Schemes Toward Minimizing Numerical Vortex Dissipation. *Journal of Aircraft*, 39(5):822–829, September-October 2002.

[132] Hariharan, N.S. and Sankar, L.N. First-Principles Based High Order Methodologies for Rotorcraft Flowfield Studies. In *55th Annual Forum AHS, Montreal, Canada*, May 1999.

[133] Hepperle, M. Winglets - A Close Look. In *International Nurflugelmeeting des MFC Osnabruck (see www.mh-aerotools.de airfoils winglets.htm)*, May 1993.

[134] Hill, J., Shaw, S., and Qin, N. Engineering Prediction of Laminar/Turbulent Transition for Isolated Helicopter Rotors in Hover. In *RAeS Aerodynamics Conference, London*, September 2004.

[135] Hill, J.L. PhD Thesis: Development of a Boundary Layer Transition Model for Helicopter Rotor CFD. Technical report, Cranfield University, March 2005.

[136] Hill, J.L., Shaw, S.T. and Qin, N. Development and Application of Engineering Transition Model for Rotorcraft Aerodynamics. In *30th European Rotorcraft Forum, Marseille, France*, September 2004.

[137] Hill, J.L., Shaw, S.T. and Qin, N. Investigation of Transition Modelling for Aerofoil Dynamic Stall. In *22nd Congress of the International Council of the Aeronautical Sciences*, June 2004.

[138] Hoad, D.R. Helicopter Model Scale Results of Blade-Vortex Interaction Impulsive Noise as Affected by Tip Modification. In *36th Annual Forum of the American Helicopter Society, Washington*, May 1980.

[139] Hoerner, S. Aerodynamic Shape of The Wing Tips. Technical report, USAF, Air Materiel Command, Wright-Patterson Air Force Base, Dayton, Ohio, Technical Report No 5752, July 1949.

[140] Hoerner, S.F. *Fluid Dynamics of Drag*. Mrs L.A. Hoerner, 1965.

[141] Hu, G., Grossman, B. and Steinhoff, J. Numerical Method for Vorticity Confinement in Compressible Flow. *AIAA Journal*, 40(10):1945–1953, October 2002.

[142] Hu, H. Application of Multigrid CFD Methods to Rotor Analysis. In *Proc 2nd International AHS Aeromechanics Specialists' Conference, Bridgeport, Connecticut*, pages 6.59–6.67, October 1995.

[143] Hu, H. A Tilt Rotor Tip-Shape Analysis using CFD. In *Proc AHS Technical Specialists' Meeting for Rotorcraft Acoustics and Aerodynamics, Williamsburg, VA.*, October 1997.

[144] Hu, H. A Multigrid Navier-Stokes CFD Code for Rotor Computations. *Computer Methods in Applied Mechanics and Engineering*, 167(1-2):127–137, 1998.

[145] Hu, H. Computational Analysis of Effects of Blade Shapes on Tip-Vortices. *Advances in Engineering Software*, 34:279–286, January 2003. Published by Elsevier Science.

[146] Huber, H. Helicopter Flight Characteristics Improvement Through Swept-Tip Rotor Blades. In *Fifth European Rotorcraft and Power Lift Aircraft Forum, Amsterdam*, pages 29.1–29.20, September 1979.

[147] Humpert, A. and Schley, C. Design Development and Flight Testing of the New Eurocopter EC145 Medium Twin. In *27th European Rotorcraft Forum, Moscow*, pages 37.1–37.10, September 2001.

[148] Humphreys, C. The Dynamic Approach to Rotor Blade Research - ARA's Oscillatory Test Facility. In *Presented at ICAS Conference*, c1985.

[149] Hunt, D.L. Development and Application of Farfield Drag Extraction Techniques for Complex Viscous Flows. *The Aeronautical Journal*, 105(1045):161–169, March 2001.

[150] Hwang, C., Joo, G., Pike, A.C. and Perry, F.J. Parametric Study for the Low BVI noise BERP Blade - KBERP Design Using DEAF. In *27th European Rotorcraft Forum, Moscow*, pages 13.1–13.9, September 2001.

[151] Imiela, M. High Fidelity Optimisation Framework for Helicopter Rotors. In *35th European Rotorcraft Forum, Hamburg*, September 2009.

[152] Imiela, M. Investigation of Aeroelastic Effects for a Helicopter Main Rotor in Hover. In *36th European Rotorcraft Forum, Paris*, September 2010.

[153] Isaacs, N.C.G. and Harrison, R.J. Identification of Retreating Blade Stall Mechanisms Using Flight Test Pressure Measurements. In *45th Annual Forum of the American Helicopter Society, Boston, MA*, pages 265–279, May 1989.

[154] Jeong, J. and Hussain, F. On the Indentification of a Vortex. *J. Fluid Mech.*, 285:69–94, 1995.

[155] Johari, H., Moreira, J. Direct Measurement of Delta-Wing Vortex Circulation. *AIAA Journal*, 36(12), December 1998.

[156] Johnson, C.J. and Barakos, G.N. Development and Demonstration of a Framework for Optimising Aspects of Rotor Blades in Forward Flight. In *AIAA Applied Aerodynamics Conference, Orlando, Florida*, January 2011.

[157] Johnson, W. Rotocraft Aerodynamics Models for a Comprehensive Analysis. In *54th Annual Forum of the American Helicopter Society, Washington, D.C.*, pages 71–93, May 1998.

[158] Joncheray, P. Aerodynamics of Helicopter Rotor in Hover - The Lifting-Vortex Line Method Applied to Dihedral Tip Blades. *Aerospace Science and Technology*, 1(1):17–25, January 1997. ISSN 0034-1223, Ecole Super Ingenieurs, Marseille.

[159] Kampa, K., Enenkl, B., Polz, G. and Roth, G. Aeromechanic Aspects in the Design of the EC135. *Journal of the American Helicopter Society*, 44(2):83–93, April 1999. Presented at the 23rd European Rotorcraft Forum, Dresden, Germany, September, 1997.

[160] Kang, H. and Altman, A. Generalised Empirical Airfoil Stagnation Point Location Prediction. *Journal of Aircraft, Engineering Note*, 44(2):698–701, March-April 2007.

[161] Kang, H.J. and Kwon, O.J. Effect of Wake Adaption on Rotor Hover Simulations Using Unstructured Meshes. *Journal of Aircraft*, 38(5):868–877, September-October 2001. Presented as Paper 2000-0258 at the AIAA 38th Aerospace Sciences Meeting and Exhibit, Reno, NV, January, 2000.

[162] Kang, H.J., Kwon, O.J. Viscous Flow Simulation of a Lifting Rotor in Hover Using Unstructured Adaptive Meshes. In *57th Annual Forum of the American Helicopter Society, Washington, DC.*, May 2001.

[163] Katz, J. and Plotkin, A. *Low-Speed Aerodynamics - From Wing Theory to Panel Methods*. McGraw-Hill, 1991, ISBN 0-07-050446-6, 1991.

[164] Kelley, H.L., and Wilson, J.C. Aerodynamic Performance of a 27-percent-scale AH-64 Wind Tunnel Model with BaseLine/Advanced Rotor Blades. In *41st Annual Forum of the American Helicopter Society, Fort Worth, Texas, 1985*, pages 491–498, May 1985.

[165] Kim, K-C. and Chopra, I. Aeroelastic Analysis of Swept, Anhedral, and Tapered Tip Rotor Blades. *Journal of the American Helicopter Society*, 37(1):15–30, January 1992.

[166] Kocurek, J.D. and Tangler, J.L. A Prescribed Wake Lifting Surface Hover Performance Analysis. In *32nd Annual National Forum of the American Helicopter Society, Washington DC*, May 1976.

[167] Kondo, N, Nishimura, H., Nakamura, H., Aoki, M., Tsujiuchi, T., and Yamakawa, E. Preliminary Study of a Low Noise Rotor. In *54th Annual Forum of the American Helicopter Society*, pages 22.1–22.14, 1998.

[168] Kondo, N., Ochi, A., Nakamura, H., Aoyama, T., Saito, S. and YamakawaE. Validation of Rotor Aerodynamic and Acoustic Prediction Methods. In *26th European Rotorcraft Forum, The Hague, NL*, pages 102.1–102.10, September 2000.

[169] Küchemann, D. *The Aerodynamic Design of Aircraft*. Pergamon Press, ISBN 0-08-020514-3, 1978.

[170] Kufeld, R.M. and Bousman, W.G. High Load Conditions Measured on a UH-60A in Maneuvering Flight. *Journal of the American Helicopter Society*, 43(3):202–211, July 1998.

[171] Kufeld, R.M. and Bousman, W.G. Technical Note: UH-60A Airloads Program Azimuth Reference Correction. *Journal of the American Helicopter Society*, 50(2):211–213, April 2005.

[172] Kulfan, R.M. Wing Geometry Effects on Leading Edge Vortices. In *AIAA Aircraft Systems and Technology Meeting, NY. AIAA-79-1872*, August 1979.

[173] La Roche, U., La Roche, H.L., and To, F. A Fanned Winglet Wing Tip with Parallel Blades, Fluid Dynamics and Design. In *La Roche Consulting 02, Working Paper, Source www*, January 2004.

[174] Landgrebe, A.J. The Wake Geometry of a Hovering Helicopter Rotor and Its Influence on Rotor Performance. In *28th Annual National Forum of the American Helicopter Society*, May 1972.

[175] Landgrebe, A.J. and Bellinger, E.D. Experimental Investigation of Model Variable-Geometry and Ogee Tip Rotors. Technical report, NASA CR-2275, February 1974.

[176] Landgrebe, A.J. and Egolf, T.A. Prediction of Helicopter Induced Flow Velocities using the Rotorcraft Wake Analysis. In *32nd Annual National Forum of the American Helicopter Society, Washington DC*, May 1976.

[177] LaRoche, U. and Palffy, S. WING-GRID, A Novel Device for Reduction of Induced Drag on Wings. In *20th ICAS Congress, 1996, Vol2, ICAS-96.2.10*, pages 2303–2309, 1996.

[178] Le Chuiton, F., D'Alascio, A., Barakos, G., Steijl, R. and Schwamborn, D. EC145 Helicopter Fuselage - An Industrial Case. In *Progress in Aerospace Sciences, EU-Framework-VI, DECIDER Project, Chapter IV - Applications, Springer-Verlag*, pages 250–260, 2009.

[179] Le Pape, A., Beaumier, P. Numerical Optimization of Helicopter Rotor Aerodynamic Performance in Hover. In *29th European Rotorcraft Forum, Friedrichshafen, Germany*, pages 71.1–71.11, September 2003.

[180] Lednicer, D. Airfoil Tools. *Internet site: http://airfoiltools.com*, 2003.

[181] Leishman, J.G. *Principles of Helicopter Aerodynamics*. Cambridge University Press, 2000, ISBN 0-521-66060-2, 2000.

[182] Leishman, J.G. Achieving the Ultimate Potential of the Helicopter. In *45th Cierva Memorial Lecture, Royal Aeronautical Society*, October 2006.

[183] Leishman, J.G. *The Helicopter: Thinking Forward, Looking Back*. The College Park Press, Maryland, USA. ISBN 978-0-9669553-1-6, 2007.

[184] Li, J., Li, F.L, and Qin, E. Far-Field Drag Prediction Technique Applied to Wing Design for Civil Aircraft. *Journal of Aircraft*, 40(3):425–431, 2003.

[185] Lin, C.S. Ng, T.T., Skaff, A. An Experimental Study of Wing Tips for Wing Performance Improvement. In *14th AIAA Applied Aerodynamics Conference, New Orleans, AIAA Paper 96-2412*, June 1996.

[186] Line, A.J. and Brown, R.E. High Resolution Wake Modelling Using A Semi-Lagrangian Adaptive Grid Formulation. In *European Rotorcraft Forum, Friedrichshafen, Germany*, pages 27.1–27.10, September 2003.

[187] Liu, Z., Sankar, L.N. and Hassan, A.A. Alteration of the Tip Vortex Structure of a Hovering Rotor by Blowing. In *37th AIAA Aerospace Sciences Meeting and Exhibit AIAA-99-0906*, January 1999.

[188] Lock, R.C. and Williams, B.R. Viscous-Inviscid Interactions in External Aerodynamics. *Progress in Aerospace Sciences*, 24:51–171, 1987.

[189] Loftus, R. Swept Tip Design Trade Study - New Affordable Main Rotor Blade for the AH-64D Apache Attack Helicopter. In *60th Annual Forum of the American Helicopter Society, Baltimore*, June 2004.

[190] Lorber, P.F. Aerodynamic Results of a Pressure-Instrumented Model Rotor at the DNW. *Journal of the American Helicopter Society*, 36(4):66–75, October 1991. Presented at the 46th Annual Forum of the American Helicopter Society, Washington, DC, May 1990.

[191] Lorber, P.F., Stauter, R.C., and Landgrebe, A.J. A Comprehensive Hover Test of the Airloads and Airflow of an Extensively Instrumented Model Helicopter Rotor. In *45th Annual Forum of the American Helicopter Society, Boston, MA*, May 1989.

[192] Lorber, P.F., Stauter, R.C., Pollack, M.J. and Landgrebe, A.J. A Comprehensive Hover Test of the Airloads and Airflow of an Extensively Instrumented Model Helicopter Rotor - Vol 1 Rotor Airloads and Performance. Technical report, USAAVSCOM TR 91-D-16A, October 1991.

[193] Lynn, R.R., Robinson, F.D., Batra, N.N. and Duhon, J.M. Tail Rotor Design, Part 1: Aerodynamics. *Journal of the American Helicopter Society*, 15(4), October 1970. Presented at the 25th Annual National Forum of the American Helicopter Society, May 1969.

[194] Maier, T.H. and Abrego, A.L. Analytical Model Sensitivity Study for Aeroelastic Stability of Straight and Swept-Tip Rotor Blades. In *26th European Rotorcraft Forum, The Hague, NL*, pages 70.1–70.15, September 2000.

[195] Manke, J.W., Hirsh, J.E., Oh, B.K., Wicks, T.M. and Dadone, L. Improved Rotor Tip Relief Modeling by Coupling Comprehensive Rotor Analysis and Rotor Aerodynamics Codes. In *Advances in Engineering Software, Elsevier Science Ltd*, volume 29:3-6, pages 475–480, 1998.

[196] Mantay, W.R., Yeager, W.T.Jr. Parametric Tip Effects for Conformable Rotor Applications. In *9th European Rotorcraft Forum, Stresa, Italy*, pages 53.1–53.29, September 1983.

[197] Margaris, P. and Gursul, I. Effect of Steady Blowing on Wing Tip Flowfield. In *2nd AIAA Flow Control Conference, Portland, Oregon*, AIAA-2004-2619, June 2004.

[198] Martin, B.P., Leishman, J.G., Pugliese, G.J. and Anderson, S.L. Stereoscopic PIV Measurements in the Wake of a Hovering Rotor. In *56th Annual Forum of the American Helicopter Society, Virginia Beach, VA*, May 2000.

[199] Martin, P.B. and Leishman, J.G. Trailing Vortex Measurements in the Wake of a Hovering Rotor Blade with Various Tip Shapes. In *58th Annual Forum of the American Helicopter Society, Montreal, Quebec, Canada*, June 2002.

[200] Martin, P.B., Pugliese, G.J. and Leishman, J.G. High Resolution Trailing Vortex Measurements in the Wake of a Hovering Rotor. In *57th Annual Forum of the American Helicopter Society, Washington DC*, May 2001.

[201] Maskew, B. Influence of Rotor Blade Tip Shape on Tip Vortex Shedding - An Unsteady, Inviscid Analysis. In *36th Annual Forum of the American Helicopter Society, Washington, DC.*, May 1980.

[202] Matthewson, C.S., Vakili, A.D., Gowanlock, D.K. Adaptive Control of Wing Tip Vortex. In *36th AIAA Aerospace Sciences Meeting and Exhibit, Reno, NV.*, January 1998.

[203] Maughmer, M.D. The Design of Winglets for High-Performance Sailplanes. In *19th AIAA Applied Aero Conf, Anaheim, CA., AIAA Paper 2001-2406*, June 2001.

[204] Maughmer, M.D., Swan, T.S. and Willits, S.M. Design and Testing of a Winglet Airfoil for Low Speed Aircraft. *Journal of Aircraft*, 39(4):654–661, July-August 2002.

[205] McAlister, K.W., Schuler, C.A., Branum, L. and Wu, J.C. 3-D Wake Measurements near a Hovering Rotor for Determining Profile and Induced Drag. Technical Report NASA Technical Paper 3577, NASA, August 1995.

[206] McAlister, K.W., Tung, C., and Heinech, J.T. Forced Diffusion of Trailing Vorticity From a Hovering Rotor. In *57th Annual Forum of the American Helicopter Society, Washington, DC.*, May 2001.

[207] McCormick, B.W. *Aerodynamics, Aeronautics and Flight Mechanics.* John Wiley and Sons, 1979.

[208] McVeigh, M.A., and McHugh, F.J. Influence of Tip Shape, Chord, Blade Number, and Airfoil on Advanced Rotor Performance. *Journal of the American Helicopter Society*, pages 55–62, October 1984. Presented at 38th Annual Forum of the American Helicopter Society, Anaheim, CA.

[209] Menter, F.R. Zonal Two Equation k-omega Turbulence Models for Aerodynamic Flows. *AIAA 24th Fluid Dynamics Conference, Orlando, FL, AIAA Paper 93-2906*, 1993.

[210] Menter, F.R. Two Equation Eddy-Viscosity Turbulence Models for Engineering Applications. *AIAA Journal*, 32(8):269–289, 1994.

[211] Morvant, R., Badcock, K.J. and Barakos, G.N. Airfoil-Vortex Interaction Simulation Using the Compressible Vorticity Confinement Method. In *29th European Rotorcraft Forum, Friedrichschafen, Germany*, September 2003.

[212] Mosher, M. Acoustic Measurements of a Full-Scale Rotor with Four Tip Shapes: Vol.1, Text, Appendix A and B. Technical report, NASA Technical Memorandum 85878, 1983.

[213] Muller, R. The Influence of Winglets on Rotor Aerodynamics. In *Twelfth European Rotorcraft Forum*, pages 34.1–34.15, September 1986.

[214] Muller, R.H.G. Winglets on Rotorblades in Forward Flight - A Theoretical and Experimental Investigation. In *14th European Rotorcraft Forum, Milano, Italy*, September 1988.

[215] Muller, R.H.G. Special Vortices at a Helicopter Rotor Blade. *Journal of the American Helicopter Society*, 35(4):16–22, October 1990.

[216] Muller, R.H.G., Pengel, K. and van der Wall, B.G. Blade Deflection Measurement of the Low Noise ERATO Rotor. In *26th European Rotorcraft Forum, The Hague, NL*, pages 104.1–104.9, September 2000.

[217] Murashige, A., Kobiki, N., Tsuchihashi, A., Inagaki, K., Tsujiuchi, T., Hasegawa, Y., Nakamura, H, Yamamoto, Y. and Yamakawa, E. Second ATIC Aeroacoustic Model Rotor Test at DNW. In *26th European Rotorcraft Forum, The Hague, NL*, pages 99.1–99.12, September 2000.

[218] Murashige, A., Kobiki, N., Tsuchihashi, A., Tsujiuchi, T., Inagaki, K. and Yamakawa, E. Final Report of ATIC Model Rotor Test at DNW. In *57th Annual Forum of the American Helicopter Society, Washington DC*, May 2001.

[219] Nangia, R.K., Palmer, M.E. and Tilmann, C.P. Unconventional High Aspect Ratio Joined-Wing Aircraft Incorporating Laminar Flow. In *21st Applied Aerodynamics Conference, Orlando, Florida. Paper AIAA-2003-3927*, June 2003.

[220] Nathman, J. *VSAERO 7.0 Manual*. Analytical Methods Inc, May 2003.

[221] ONERA. Eurocopter Introduces New Low Noise Rotor Blade, Blue Edge, Reflecting 30 Years of Forward-Looking Research at ONERA. *ONERA Press-Release*, 2011.

[222] S. Osher and S. Chakravarthy. Upwind schemes and boundary conditions with applications to euler equations in general geometries. *Journal of Computational Physics*, 50:447 – 481, January - February 1983.

[223] Ota, T., Hashiguchi, Y. and Tsukahara, T. BVI Noise Reduction Research with Canard Blade Tip. In *27th European Rotorcraft Forum, Moscow*, pages 23.1–23.11, September 2001.

[224] Pahlke, K. and van der Wall, B. Calculation of Multibladed Rotors in High Speed Forward Flight with Weak Fluid-Structure Coupling. In *27th European Rotorcraft Forum, Moscow*, pages 27.1–27.11, September 2001.

[225] Pahlke, K. and van der Wall, B. Progress in Weak Fluid-Structure Coupling for Multibladed Rotors in High-Speed Forward Flight. In *27th European Rotorcraft Forum, Bristol*, pages 67.1–67.12, September 2002.

[226] Pahlke, K., Chelli, E. Calculation of Multibladed Rotors in Forward Flight. In *26th European Rotorcraft Forum, The Hague, NL*, pages 48.1–48.18, September 2000.

[227] Pahlke, K.G. The GOAHEAD Project. In *33rd European Rotorcraft Forum, Kazan, Russia*, September 2007.

[228] Paparone, L. and Tognaccini, R. Computational Fluid Dynamics-Based Drag Prediction and Decomposition. *AIAA Journal*, 41(9):1647–1657, September 2003.

[229] Park, P.S. Effects of a Winglet Rudder on Lift-to-Drag Ratio and Wake Vortex Frequency. In *21st Applied Aerodynamics Conference, Orlando, Florida. Paper AIAA-2003-4069*, June 2003.

[230] Parthasarthy, S.P., Cho, Y.I. and Back, L.H. Wide-Field Shadowgraph Flow Visualization of Tip Vortices. In *AIAA 85-1557*, 1985.

[231] Patt, D. and Karem, A. Anhedral Tip Blades for Tilt-Rotor Aircraft. Technical report, United States Patent, US 2011/0024552 A1 (Karem Aircraft Inc.), February 2011.

[232] Peace, A.J. Maximising the Impact of CFD in the Design Office: ARA's Role. Technical report, ARA Tech Memo TM466, September 2002. Presented at ARA 50th Aniversary Technical Forum, Cranfield, May 2002, and at the 23rd ICAS Congress, 8-13th September 2002, Toronto, Canada.

[233] Perry, F.J. Aerodynamics of the World Speed Record. In *43rd Annual Forum of the American Helicopter Society*, May 1987.

[234] Perry, F.J. The Contribution of Planform Area to the Performance of the BERP Rotor: A Reply to K.B. Amer. *Journal of the American Helicopter Society*, pages 64–65, January 1989.

[235] Perry, F.J., Brocklehurst, A. and Harrison, R.J. Splitting Tip Vortex on Swept Tip. *US Patent No 5992793 (30.11.99), and GB Pat Appl No 9600123.5*, 4 January 1996.

[236] Perry, F.J., Wilby, P. and Jones, A.F. The BERP Rotor - How Does It Work, and What Has It Been Doing Lately? *Vertiflite: Published by the American Helicopter Society*, 44(2):44–48, Spring 1998.

[237] Philippe, J-J. ONERA Makes Progress in Rotor Aerodynamics, Aeroelasticity, and Acoustics. *Vertiflite: Published by the American Helicopter Society*, 38(5):48, September/October 1992.

[238] Pike, A.C. and Harrison, R.J. Helicopter Noise Measurements at High Advancing Blade Mach Number - A Novel Approach to Full-Scale Flight Testing. In *Northeast Region Aeromechanics Specialists' Meeting*, October 1995.

[239] Piziali, R.A. 2-D and 3-D Oscillating Wing Aerodynamics for a Range of Angles of Attack Including Stall. Technical report, NASA Ames Research Center, Moffett Field, CA., NASA Tech Memo 4632, USAATCOM Tech Rpt 94-A-011, September 1994.

[240] Pomin, H. and Wagner, S. Navier-Stokes Analysis of Helicopter Rotor Aerodynamics in Hover and Forward Flight. *Journal of Aircraft*, 39(5):739–749, September-October 2002.

[241] Pope, A. *Basic Wing and Airfoil Theory*. McGraw-Hill Book Company Inc, 1951.

[242] Prandtl, L. Application of Modern Hydrodynamics to Aeronautics. Technical report, NACA Report 116 (NACA Translation, not dated), c1921.

[243] Prouty, R.W. and Amer, K.B. The YAH-64 Empennage and Tail Rotor - A Technical History. In *38th Annual Forum of the American Helicopter Society*, pages 247–261, May 1982.

[244] Quackenbush, T.R. Computational Studies in Low Speed Rotor Aerodynamics. In *AHS Specialists' Meeting on Aerodynamics and Aeroacoustics, Arlington, Texas*, February 1987.

[245] Rajagopalan, R.G. and Lim, C.K. Laminar Flow Analysis of a Rotor in Hover. *Journal of the American Helicopter Society*, 36(1):12–23, Jan 1991.

[246] Ramaprian, B.R. and Youxin Zheng. Near Field of the Tip Vortex Behind an Oscillating Rectangular Wing. *AIAA Journal*, 36(7):1263–1269, July 1998.

[247] Rezoni, P., d'Alascio, A., Kroll, N., Peshkin, D., Hounjet, M.H.L., Boniface, J.C., Vigevano, L., Allen, C.B., Badcock, K., Mottura, L., Scholl, E. and Kokkalis, A. EROS - A Common Eurpoean Euler Code for the Analysis of Helicopter Rotor Flow Fields. *Progress in Aerospace Sciences*, 36:437–485, 2000.

[248] Rezoni, P., d'Alascio, A., Kroll, N., Peshkin, D., Hounjet, M.H.L., Boniface, J.C., Vigevano, L., Allen, C.B., Badcock, K., Mottura, L., Scholl, E. and Kokkalis, A. EROS - A Common Eurpoean Euler Code for the Analysis of Helicopter Rotor Flow Fields. *Progress in Aerospace Sciences*, 36:437–485, 2000.

[249] Riley, M.J., and Miller, J.V. Pressure Distributions on a Helicopter Swept Tip from Flight Tests and from Calculations. In *9th European Rotorcraft Forum, Stresa, Italy*, pages 9.1–9.12, 1983.

[250] Robinson, K. and Brocklehurst, A. BERP-IV Aerodynamics, Performance and Flight Envelope. In *34th European Rotorcraft Forum, Liverpool*, September 2008.

[251] Roesch, P. Aerodynamic Design of the Aerospatiale SA365N Dauphin2 Helicopter. In *6th European Rotorcraft and Powered Lift Aircraft Forum, Bristol*, pages 28.1–28.10, September 1980.

[252] Russell, J.W., Sankar, L.N., and Tung, C. High Accuracy Studies of the Tip Vortex Structure from a Hovering Rotor. In *28th AIAA Fluid Dynamics Conference, Snowmass Village, CO.*, 29 June-2 July 1997.

[253] Sakrison, D. A German Aerodynamicist, A Californian Character, and a Corkscrew. *www.metcoaire.com/technical*, 2012.

[254] Sakrison, D. Why They Work - The Hoerner Design. *www.metcoaire.com/technical*, 2012.

[255] Sampson, R.G. An Experimental and Theoretical Investigation of the Structure of a Trailing Vortex Wake. *Journal of the Royal Aeronautical Society*, February 1976.

[256] Sato, A. Research and Development in Japan, Year 2000. In *57th Annual Forum of the American Helicopter Society, Washington, DC*, May 2001.

[257] Schreck, S.J., Faller, W.E. and Robinson, M.C. Unsteady Separation Processes and Leading Edge Vortex Precursors: Pitch Rate and Reynolds Number Influences. *Journal of Aircraft*, 39(5):868–875, September-October 2002. Presented as Paper 2000-2605 at the AIAA Fluids 2000 Conference, Denver, CO, June 2000.

[258] Sheridan, P.F. and Smith, R.P. Interactional Aerodynamics - A New Challenge to Helicopter Technology. In *35th Annual National Forum of the American Helicopter Society, Washington, D.C., Paper No 59*, May 1979.

[259] Shijianzhuang Aircraft. Chinese Version of AN2. *http://www.home.hiway.net/jlwebs/chinese.htm*, 2004.

[260] Shinoda, P.M., Yeo, H., Norman, T.R. Rotor Performance of a UH-60 Rotor System in the NASA Ames 80- by 120-Foot Wind Tunnel. *Journal of the American Helicopter Society*, 49(4):401–413, October 2004.

[261] Shivananda, T.P., McMahon, H.M. and Gray, R.B. Surface Pressure Measurements at the Tip of a Model Helicopter Rotor in Hover. *Journal of Aircraft*, 15:460–467, August 1978.

[262] Sides, J., Pahlke, K. and Costes, M. Numerical Simulation of Flows around Helicopters at DLR and ONERA. *Aerospace Science and Technology*, 5(1):35–53, Jan 2001. Article based on the presentation at the ODAS Conference, Paris, 1999.

[263] Snyder, D.O. and Spall, R.E. Numerical Investigation into Multiple Vortex Structures of Flat End-Cap Wings. *AIAA Journal*, 38(8):1486–1489, August 2000.

[264] Spall, R.E. Numerical Study of a Wing Tip Vortex Using the Euler Equations. *Journal of Aircraft*, 38(1):22–27, January-February 2001.

[265] Spentzos, A., Barakos, G., Badcock, K., and Richards, B. Investigation of Three-Dimensional Dynamic Stall Using Computational Fluid Dynamics. *AIAA Journal*, 43(5):1023–1033, May 2005.

[266] Spentzos, A., Barakos, G.N., Badcock, K.J., Richards, B.E., Coton, F.N., Galbraith, R.A.McD., Berton, E. and Favier, D. Computational Fluid Dynamics Study of Three-Dimensional Stall of Various Planform Shapes. *Journal of Aircraft*, 44(4):1118–1128, July-August 2007.

[267] Spentzos, A., Barakos, G.N., Badcock, K.J., Richards, B.E. Wernert, P., Schreck, S. and Raffel, M. CFD Investigation of 2D and 3D Dynamic Stall. In *AHS 4th Decennial Specialists' Conference on Aeromechanics, San Francisco*, pages 2.4:1–20, January 2004.

[268] Spillman, J.J. The Use of Wing Tip Sails to Reduce Vortex Drag. *Aeronautical Journal*, pages 387–395, September 1978.

[269] Spillman, J.J. and Allen, J.E. The Use of Wing Tip Sails to Reduce Vortex Drag. Technical report, Aeronautical Research Council ARC 37 190, Perf 3550, February 1987.

[270] Spivey, R.F. Blade Tip Aerodynamics - Profile and Planform Effects. In *24th Annual National Forum of the American Helicopter Society, Washington, DC. Paper 205*, May 1968.

[271] Spivey, W.A. and Morehouse, G.G. New Insights into the Design of Swept-Tip Rotor Blades. In *26th Annual National Forum of the American Helicopter Society*, June 1970.

[272] Srinivasan, G.R. and Baeder, J.D. TURNS: A Free Wake Euler/Navier-Stokes Numerical Method for Helicopter Rotors. *AIAA Journal*, 31(5):959–962, May 1993.

[273] Srinivasan, G.R. and McCroskey, W.J. Navier-Stokes Calculations of Hovering Rotor Flowfields. *Journal of Aircraft*, 25(10):865–874, October 1988.

[274] Srinivasan, G.R., Baeder, J.D., Obayashi, S. and McCroskey, W.J. Flowfield of a Lifting Hovering Rotor - A Navier-Stokes Simulation. In *16th European Rotorcraft Forum, Glasgow, Paper No I.3.5*, pages 1–15, September 1990.

[275] Srinivasan, G.R., McCroskey, W.J., Baeder, J.D. and Edwards, T.A. Numerical Simulation of Tip Vortices of Wings in Subsonic and Transonic Flows. *Journal of Aircraft*, 26(10):1153–1162, October 1988.

[276] Srinivasan, G.R., Ragavan, V., Duque, E.P.N. and McCroskey, W.J. Flowfield Analysis of Modern Helicopter Rotors in Hover by Navier-Stokes Method. *Journal of the American Helicopter Society*, pages 3–13, July 1993. Presented at the AHS International Specialists' Meeting on Rotorcraft Acoustics and Rotor Fluid Dynamics, Philadelphia, PA.

[277] Steijl, R. and Barakos, G. Sliding Mesh Algorithm for CFD Analysis of Helicopter Rotor-Fuselage Aerodynamics. In *33rd European Rotorcraft Forum, Kazan, Russia*, September 2007.

[278] Steijl, R. and Barakos, G. Computational Analysis of Rotor-Fuselage Interactional Aerodynamics Using Sliding Plane CFD Method. In *34th European Rotorcraft Forum, Liverpool*, September 2008.

[279] Steijl, R. and Barakos, G. Sliding Mesh Algorithm for CFD Analysis of Helicopter Rotor-Fuselage Aerodynamics. *Int. J. Numer. Meth. Fluids*, 58:527–549, 2008.

[280] Steijl, R. and Barakos, G. A Computational Study of Helicopter Rotor-Fuselage Aerodynamic Interactions. In *35th European Rotorcraft Forum, Hamburg, Germany*, September 2009.

[281] Steijl, R. and Barakos, G. CFD Analysis of Complete Helicopter Configurations: Lessons Learnt from the GOAHEAD Project. In *36th European Rotorcraft Forum, Paris, France*, September 2010.

[282] Steijl, R. and Barakos, G.N. Computational Study of Helicopter Rotor-Fuselage Aerodynamic Interactions. *AIAA Journal*, 47(9):2143–2157, September 2009.

[283] Steijl, R., Barakos, G. and Badcock, K. A Computational Study of the Advancing-Side Lift Problem. In *31st European Rotorcraft Forum, Florence, Italy*, September 2005.

[284] Steijl, R., Barakos, G. and Badcock, K. A Framework for CFD Analysis of Helicopter Rotors in Hover and Forward Flight. *International Journal for Numerical Methods in Fluids*, 51:819–847, January 2006.

[285] Steijl, R., Barakos, G.N. and Badcock, K.J. A CFD Framework for Analysis of Helicopter Rotors. In *17th AIAA Computational Fluid Dynamics Conference, Toronto, Canada, AIAA Paper 2005-5124*, June 2005.

[286] Stepniewski, W.Z. and Keys, C.N. *Rotary Wing Aerodynamics*. Dover, 1984.

[287] Strawn, R.C. and Djomehri, M.J. Computational Modeling of Hovering Rotor and Wake Aerodynamics. In *57th Annual Forum AHS, Washington, DC*, May 2001.

[288] Strawn, R.C. and Djomehri, M.J. Computational Modelling of Hovering Rotor and Wake Aerodynamics. *Journal of Aircraft*, 39(5):786–793, September-October 2002.

[289] Summa, J.M. Advanced Rotor Analysis Methods for the Aerodynamics of Vortex-Blade Interactions in Hover. *Vertica*, 9(4):331–343, 1985. Presented at the 8th European Rotorcraft and Powered Lift Aircraft Forum, Aix-en-Provence, France, August 1982.

[290] Tang, L. and Baeder, J.D. Improved Euler Simulation of Hovering Rotor Tip Vortices With Validation. In *55th Annual Forum AHS, Montreal, Canada*, May 1999.

[291] Tangler, J.L. The Design and Testing of a Tip to Reduce Blade Slap. In *31st Annual Forum of the American Helicopter Society, Washington, DC*, May 1975.

[292] Tauber, M.E. Computerized Aerodynamic Design of a Transonically "Quiet" Blade. In *40th Annual Forum of the American Helicopter Society, Crystal City, VA*, pages 401–418, May 1984.

[293] Tauber, M.E. and Hicks, R.M. Computerised Three-Dimensional Aerodynamic Design of a Lifting Rotor Blade. In *36th Annual National Forum of the American Helicopter Society*, May 1980.

[294] Tavella, D., Wood, N. and Harrits, P. Measurements on Wing Tip Blowing. Technical Report JIAA TR-64, Joint Institute of Aeronautics and Acoustics, Standford, June 1985.

[295] Tecplot. *CFD Analyser 3.0 User's Manual*. Tecplot Inc, Bellevue, WA, 2002.

[296] Thompson, D.H. A Flow Visualisation Study of Tip Vortex Formation. Technical report, Australian ARL Aerodynamics Note 421 AR-002-988, 1998.

[297] Tsukahara, T., Ota, T., Obukata, M., Araki, R., Obayashi, S. and Nakahashi, K. Numerical Analysis Around Rotor Blade by Vortex Confinement. In *58th Annual Forum of the American Helicopter Society, Montreal, Quebec, Canada*, June 2002. Aeroacoustics.

[298] Tung, C., Pucci, S.L., Caradonna, F.X., and Morse, H.A. The Structure of Trailing Vortices Generated by Model Rotor Blades. Technical report, NASA Technical Memorandum, TM-81316, USAAVRADCOM TR-81-A-25, NASA Ames, Moffett Field, CA., August 1981.

[299] Uygun, M. and Tuncer, I.H. A Computational Study of Subsonic Flows Over A Medium Range Cargo Aircraft. In *21st Applied Aerodynamics Conference, Orlando, Florida. Paper AIAA-2003-3661*, June 2003.

[300] Vakili, A.D., Matthewson, C.S., Gowanlock, D.K. Control of Helicopter Blade Tip Vortex. In *AIAA/CEAS 4th AeroAcoustics Conference, Toulouse, France, AIAA Paper 98-2240*, June 1998.

[301] van Aken, J.M. An Investigation of Tip planform Influence of the Aerodynamic Load Characteristics of a Semi-Span Unswept Wing and Wing-Tip. Technical report, University of Kansas, NASA CR-177110, CRINC Report 5171-1, December 1985.

[302] van Dam, C.P. Drag-Reduction Characteristics of Aft-Swept Wing Tips. *Journal of Aircraft*, 24(2):115–119, 1986. Also presented at AIAA Applied Aerodynamics Conference as paper AIAA-86-1824.

[303] van Dam, C.P. High Angle of Attack Aerodynamic Characteristics of Crescent and Elliptic Wings. Technical report, NASA-CR-184992, University of California, Davis, CA., May 1989.

[304] van Dam C.P. Recent Experience with Different Methods of Drag Prediction. *Progress in Aerospace Sciences*, 35((8)):751–798, Nov 1999.

[305] van Dam, C.P., Nikfetrat, K., Wong, K.W. and Vijgen, P.M.H.W. Drag Prediction at Subsonic and Transonic Speeds Using Euler Methods. *Journal of Aircraft*, 32(4):839–845, July-August 1995.

[306] van Dam, C.P., Vijgen, P.M.H.W., and Holmes, B.J. Experimental Investigation on the Effect of Crescent Planform on Lift and Drag. *Journal of Aircraft*, 28(11):713–720, 1991.

[307] van Dam, C.P., Vijgen, P.M.H.W., Holmes, B.J. Aerodynamic Characteristics of Crescent and Elliptic Wings at High Angles of Attack. *Journal of Aircraft*, 28(4):253–260, April 1991.

[308] B. van Leer. Flux-vector splitting for the euler equations. In *Eighth International Conference on Numerical Methods in Fluid Dynamics*, volume 170 of Lecture Notes in Physics, pages 507 – 512, Berlin / Heidelberg, 1982.

[309] Vijgen, P.M.H.W., van Dam C.P. and Holmes, B.J. Sheared Wing Tip Aerodynamics: Wind Tunnel and Computational Investigation. *Journal of Aircraft*, 26(3):207–213, March 1989. Presented as Paper 87-2481 at the AIAA 5th Applied Aerodynamics Conference, Monterey, CA, August, 1987.

[310] Wachspress, D.A., Quackenbush, T.R. and Boschitsch, A.H. Rotorcraft Interactional Aerodynamics Calculations with Fast Vortex/Fast Panel Methods. In *56th Annual Forum of the American Helicopter Society, Virginia Beach, VA*, May 2000.

[311] Wachspress, D.A., Quackenbush, T.R. and Boschitsch, A.H. First Principles Free Vortex Wake Analysis For Helicopters and Tiltrotors. In *59th Annual Forum of the American Helicopter Society, Pheonix, AZ.*, May 2003.

[312] Wagner, W.J. Comparative Measurements of the Unsteady Pressures and the Tip-Vortex Parameters on Four Oscillating Wing Tip Models. In *European Rotorcraft Forum*, pages 9.1–9.17, September 1984.

[313] Wake, B.E. and Baeder, J.D. Evaluation of a Navier-Stokes Analysis Method for Hover Performance Prediction. *Journal of the American Helicopter Society*, 41(1):7–17, January 1996.

[314] Wenren, Y., Fan, M., Wang, L., Xiao, M. and Steinhoff, J. Application of Vorticity Confinement to Prediction of the Flow over Complex Bodies. *AIAA Journal*, 41(5):809–816, May 2003.

[315] Whitcomb, R.T. A Design Approach and Selected Wind Tunnel Results at High Subsonic Speeds for Wing Tip Mounted Winglets. Technical Report NASA TN D-8260, NASA Langley, July 1976.

[316] Wigeland, A., Ahmed, M. and Nagib, H.M. Vorticity Measurements Using Calibrated Vane-Vorticity Indicators and Crosswires. *AIAA Journal*, 16(12), December 1978.

[317] Wilby, P. Shock-Waves in the Rotorcraft World - A Personal Perspective of 30 years of Rotor Aerodynamic Developments in the UK. In *Royal Aeronautical Society - The 1997 Cierva Memorial Lecture*, 1997.

[318] Wilby, P. Shockwaves in the Rotorcraft World - A personal Perspective of 30 years of Rotor Aerodynamic Development in the UK. *Aeronautical Journal*, pages 113–127, March 1998. The 1997 Cierva Lecture to the Royal Aeronautical Society.

[319] Wilby, P. The Development of Airfoil Testing in the UK. *Journal of the American Helicopter Society*, 46(3):210–220, July 2001. Presented at the 22nd European Rotorcraft Forum, Brighton, September, 1996.

[320] Wilby, P.G. and Phillipe, J-J. An Investigation of the Aerodynamics of an RAE Swept Tip Using a Model Rotor. In *8th European Rotorcraft Forum, Aix-en-Provence, 1982*, September 1982. Also presented at the 39th Annual Forum of the American Helicopter Society, St Louis, Missouri, May 1983.

[321] Wilcox, D.C. Multiscale Model for Turbulent Flows. *AIAA Journal*, 26(11):1311–1320, November 1988.

[322] Wilcox, D.C. *Turbulence Modeling for CFD, 2nd Edition*. DCW Industries, Inc, 2004. ISBN 1-928729-10-X.

[323] Wong, K.J. and van Dam, C.P. Numerical Study on the Effect of Tip-Cap Shape on Wing Aerodynamic Characteristics. In *33rd Aerospace Sciences Meeting and Exhibit, Reno, NV. Paper AIAA-95-0042*, January 1995.

[324] Woodgate, M and Barakos, G.N. Implicit CFD Methods For Fast Analysis of Rotor Flows. In *36th European Rotorcraft Forum, Paris*, September 2010.

[325] Woodgate, M. and Barakos, G.N. Implicit Computational Fluid Dynamics Methods for Fast Analysis of Rotor Flows. *AIAA Journal*, 50(6):1217–1244, June 2012.

[326] Yang, C., Baek, J., Saito, S., Masataka, S., Suenaga, H. Yamada, R., Nishizawa, U., Tan, A., Kanehira, N and Shindo, S. Numerical and Experimental Investigations of Tip Vortex With Lateral Wing Tip Blowing. In *26th European Rotorcraft Forum, The Hague, NL*, pages 44.1–44.18, May 2000.

[327] Yang, G.W. and Zhuang, L.X. Numerical Simulation of Rotor Flow in Hover. *Journal of Aircraft*, 37(2):221–226, March-April 2000.

[328] Yates, J.E. and Donaldson, C. A Fundamental Study of Drag and an Assessment of Conventional Drag-Due-To-Lift Reduction Devices. Technical Report NASA CR 4004, AeroResearch Associates of Princeton, for NASA Langley, September 1986.

[329] Yen, J.G. Effects of Blade Tip Shape on Dynamics, Cost, Weight, Aerodynamic Performance, and Aeroelastic Response. *Journal of the American Helicopter Society*, 39(4):37–45, October 1994.

[330] Zimmer, H. The Aerodynamic Optimisation of Wings at Subsonic Speeds and the Influence of Wingtip Design. Technical report, NASA TM-88534, May 1987.

[331] Zografakis, G., Barakos, G., Johnson, M. Transition Modelling for Rotorcraft CFD. In *34th European Rotorcraft Forum, Liverpool*, September 2008.

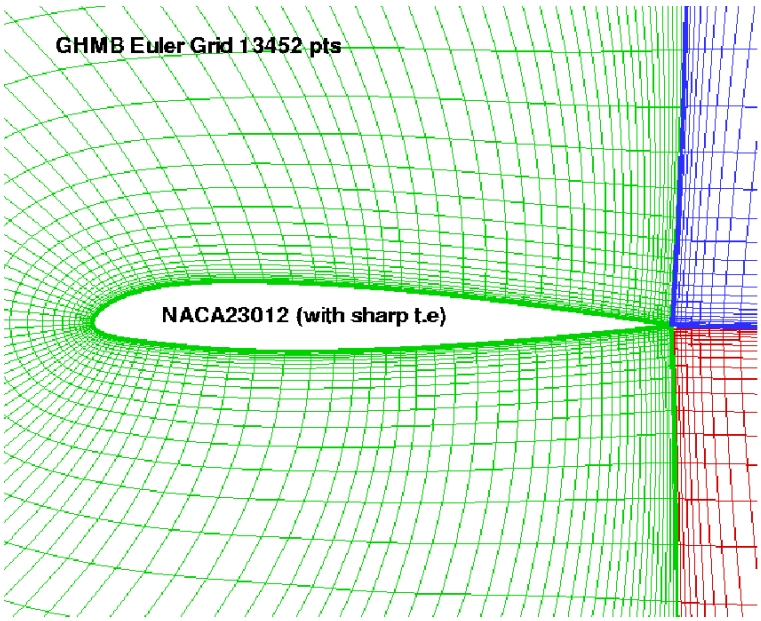

Figure 289: Example Coarse Grid for Euler Solution

A 2D Euler Grid Sensitivity

Exploratory Study - HMB 2D Euler Grid - NACA 23012 Aerofoil

This study was carried out at the begining of this research project and was instructive in guiding the construction of all further Euler grids, whether for 2D aerofoils, 3D wings, or later, for rotors in hover and forward flight. The underlying assumption for application of an Euler solution is that the flow should be well attached, yet for 2D aerofoils at increasing incidence, and also near wing tips in 3D, the flow often reaches a point of pending separation due to the generation of large adverse pressure gradients. Consequently, numerical losses may build up in the Euler computations and artificial flow separation, or breakdown, can occur. At first glance this can appear as though it is a real flow phenomena (prior to total breakdown when the solution will not converge). Of course, in many practical cases the tendency for separation is of great interest, and it is highly desirable to avoid any premature initiation of so-called Euler-breakdown of the flow wherever possible. At the start of this research, computational resources were such that 3D Navier-Stokes solutions were not always feasible, and it was therefore natural to carry out initial explorations with an Euler approach. The thinking here is that knowledge gained in simple 2D cases may be applied to grid generation in more complex 3D situations, by striving to maintain the optimum first cell spacing and a gradual growth away from the surface. The final numerical solution should therefore offer the best possibility of avoiding premature onset of numerical breakdown, and its engineering value will therefore be enhanced.

The NACA23012 aerofoil was chosen for these studies since it has been previously used in rotor applications, due to it's moderate camber yet relatively low pitching moment, and is a well known algebraically defined aerofoil.

The GHMB grid generator was used to vary the grid parameters for an Euler solution of the flow over a NACA23012 with sharp trailing edge (na23012s). The co-ordaintes for this aerofoil are given in Appendix E An example coarse grid of 13,452 points is shown in Figure 289.

In general, it was found that the pressure drag from the 2D Euler solution decreased as the height of the first cell (y_1) normal to the aerofoil was decreased towards .001. The drag remained very small within a limited incidence range, but was found to increase significantly with incidence in a similar manner to aerofoil profile drag.

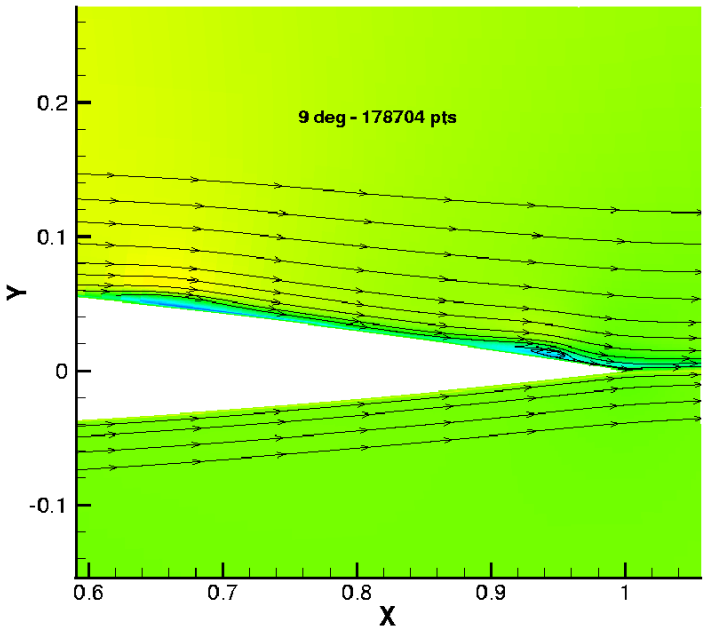

Figure 290: Example of Flow Breakdown in an Euler Solution at 9 degrees Incidence

Attempting to reduce the drag by using a finer grid, appeared to increase numerical dissipation and cause the drag to rise. As the incidence was increased, numerical viscosity effects formed instability waves in the flow on the upper surface trailing edge, Figure 290, leading to erratic behaviour of the lift, drag and moment. In cases with a coarser grid a more gradual and smooth flow separation was noted. The tendency for the drag to increase with incidence and the flow to start to separate at high incidence may be thought of as an Euler-stall.

The lift drag and moment results of this grid sensitivity exercise are summarised in Figures 291 to 294.

For a typical 2D aerofoil such as the NACA23012 (in this case at low mach number) the optimal first cell spacing was found to be about .0005c, and for a 20c radius far-field the associated grid size was approximately 52,000 points. Even with this grid, the flow was observed to separate from the upper surface trailing edge at high incidence, causing the drag to grow, although the lift did not fall. Coarsening the grid by reducing to 13,000 points and a first cell spacing of .002c, caused significant increase in pressure drag from Cdp=.002 to Cdp=.005 at Cl=1.0, while a first spacing of .001c gave Cdp=.003 at CL=1.0. The 3 coarser grids all exhibited a parabolic growth of pressure drag with incidence, while the lift continued to rise linearly to the maximum incidence of 20 degrees used here (purposely well in excess of the normal range for Euler solution). Rather surprisingly, refining the grid to 80,000 points, with the first spacing reduced to .0001 caused the drag values to become erratic beyond about 3 degrees of incidence, although the lift did not break until 9 degrees. The finer grids caused an initial fall-off in lift and then either a sudden drop, or an overshoot before finally collapsing. The behaviour of the lift is also reflected in the pitching moment.

In this study, the number of points around the aerofoil, and the leading edge and trailing edge clustering also varied with the grid size. The leading and trailing edge spacing for the 52,000 point grid was .001c, with .016c mid-chord spacing, with 217 points around the aerofoil, 73 points normal, and 67 points in the wake.

First-hand knowledge of the sensitivity of an Euler solution to grid parameters has proved extremely useful in subsequent work on 3D rotor problems where the number of cells is often at a premium. Ideally, these grid dependency checks should be repeated at different Mach numbers.

Another aspect of preparing a grid for a helicopter rotor simulation is that further geometric constraints are encountered due to the need for symmetry on the periodic boundary, and the simple C-H topology considered above may not be able to be maintained. In this case the need is to not only achieve the best first spacing, and a gradual growth, but also avoid sudden changes in grid spacing which may occur if the location of the

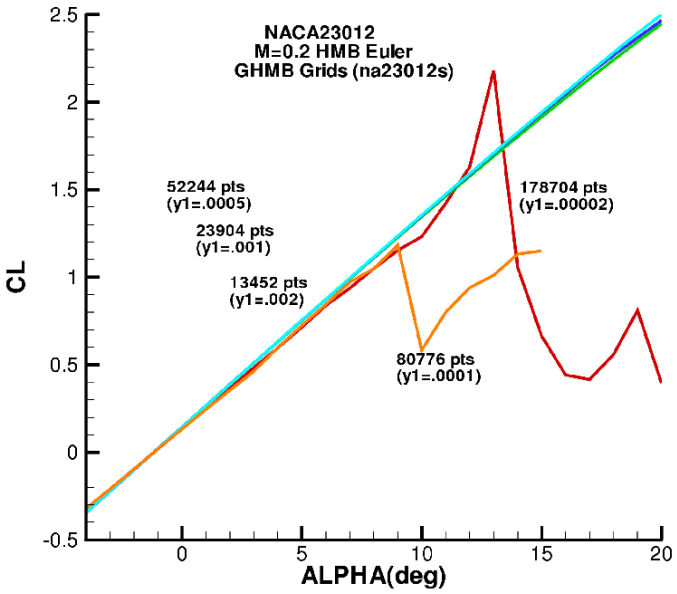

Figure 291: HMB Euler Results: CL vs Incidence

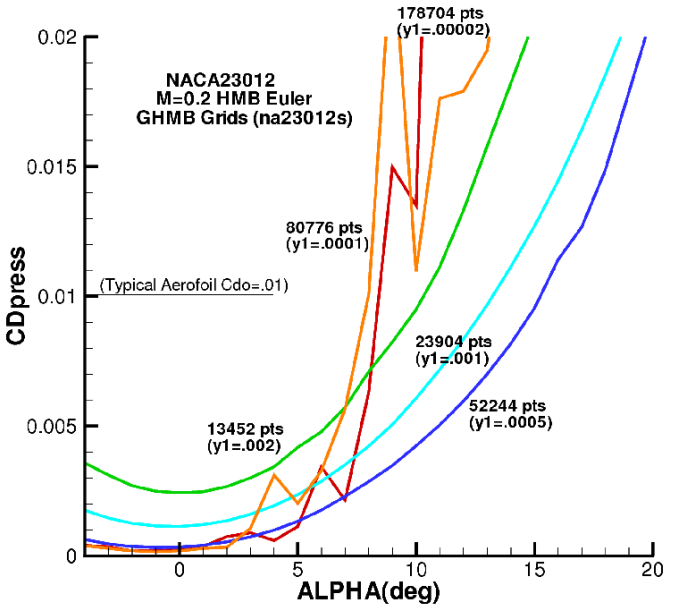

Figure 292: HMB Euler Results: CD vs Incidence

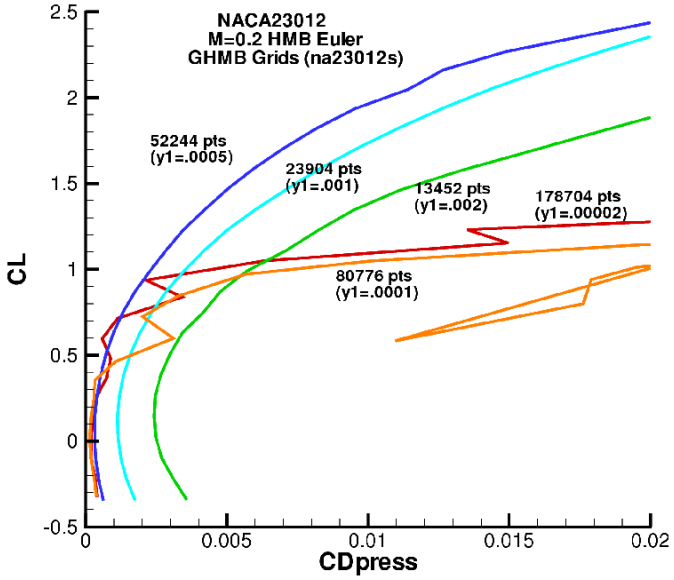

Figure 293: HMB Euler Results: CL vs CD

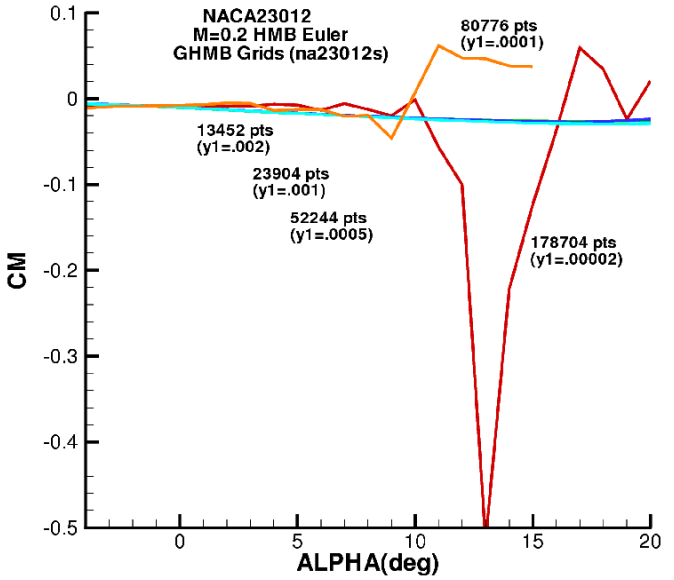

Figure 294: HMB Euler Results: CM vs Incidence

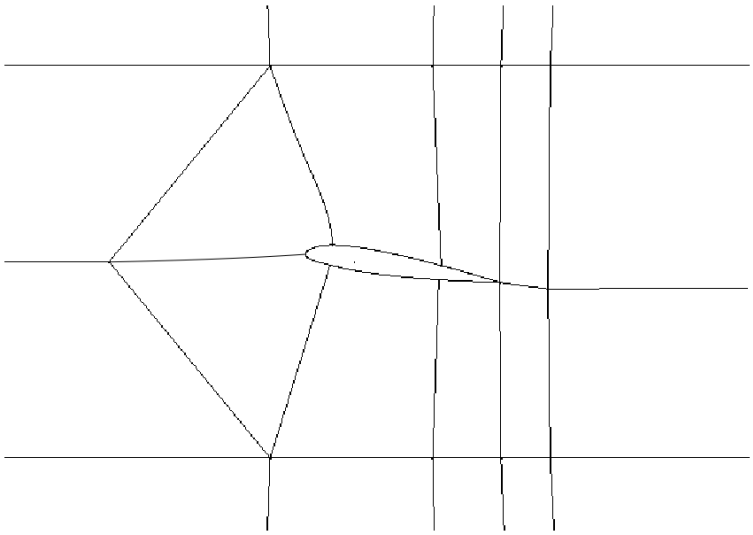

Figure 295: 2D Rotor-Type Grid Requires the Same Number of Points on Both the Upstream and Downstream Boundaries, which also Dictates the Number of Points used on the Leading Edge of the Aerofoil

block-boundaries are not well designed. Again, some aspects of this problem may be explored in 2D, before attempting a 3D solution. The aim here is to ensure a well designed (ICEM) multi-block grid prior to running a large rotor simulation.

The 2D aerofoil case described above used a C-H type grid with gradually increasing (exponential or hyperbolic) spacing between the aerofoil and the 20c far-field, and with freedom to vary the spacing and number of points, both around the aerofoil and in the wake, thus maintaining a reasonable cell aspect ratio and ensuring gradual volume changes. Lines radiating from the aerofoil may be curved as desired to preserve orthogonality. For the rotor case, where periodic boundaries are used, the blocks on the downstream boundary must exactly match the blocks on the up-stream boundary, as shown in Figure 295. To achieve this, the C-type grid around the leading edge must be converted back to an H-type grid before the periodic boundaries are reached. This type of grid leads to the need to use the same number of nodes along the edges of the blocks surrounding the aerofoil, in both the i and j directions, at least near the leading edge (and often in other regions of the aerofoil if constaints arise from the tip, root end of the blade, or hub connections). Care must therefore be taken to choose the optimum distance above and below the aerofoil when laying out the grid, such that a good quality grid is obtained. If desired, the block boundaries could be smoothed by using B-spline curves. This is much easier to plan in 2D.

In the 2D rotor-type grid, the aerofoil is bounded between lines representing a plane above and below the rotor, and is constructed with an initial pitch which helps to minimise distortions in the outer blocks when the blade-fixed blocks are rotated to achieve the desired trim angle. Two extra blocks have been introduced to maintain the start of the wake line tangent to the mean trailing edge angle. The distance from the aerofoil surface to the first supporting block-boundary curve was found to be a key parameter to ensure a well spaced grid. A distance of about 0.5 to 0.67 chord is appropriate for an Euler solution, and decreasing this distance to 0.25 chord for a Navier-Stokes grid is recommended. Experience gathered in 2D can now be applied to the 3D rotor problem.

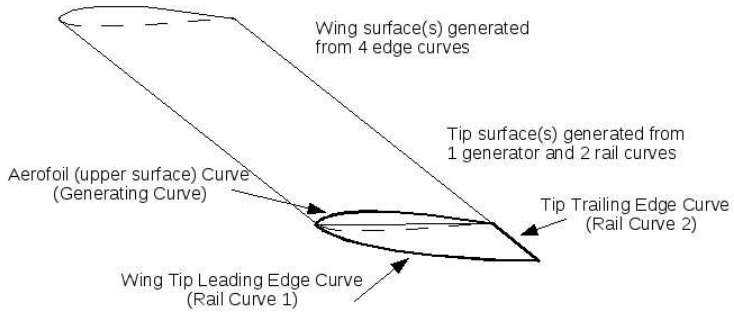

Figure 296: Illustration Showing Construction of Surfaces for the Küchemann-Type Tip

B 3D Wing Exploratory Study

At an early stage in this research, prior to undertaking rotor computations, HMB performance predictions for a finite wing were explored. In many ways this was a natural starting point, partly because it provided an opportunity to compare with classical wing aerodynamics, and also because it allowed an exploration in geometry preparation and grid generation for an arbitary wing with a tip shape of interest. This work also highlighted the need for a sufficiently fine grid to resolve and conserve flow features such as tip vortices in order to obtain an accurate simulation.

The geometry for the wing, referred to here as 'Wing-1', or 'Wing-1-symm', was prepared using the Rhino 3D solid modelling package. The aspect ratio was arbitarily set at 5, and the aerofoil chosen was the SC1095, since this aerofoil had recently been smoothed in anticipation of running the UH-60A model rotor validation case, as reported in Chapter 3. The co-ordinates for the smoothed SC1095 aerofoil are given in Appendix D This aerofoil was defined with a sharp trailing edge to simplify grid generation and for compatibility with an Euler solution, and was extruded over the main part of the wing between the spanwise stations from which the tips were formed. It was found that one of the Rhino surfacing tools, employing 2 rail-curves and one generating curve, was capable of forming a smooth Küchemann-type tip on this otherwise rectangular planform constant chord wing, as shown in Figure 296. The rail curves used were the curved tip leading edge and the straight tip trailing edge, and the generating curve was either the upper or lower surface curve of the aerofoil (subsequently this method of tip surface generation has been used throughout this research).

The geometry was then imported into ICEM for generation of the multi-block grids. The blocking evolved as an H-H scheme in order to readily accommodate the tip shape, Figure 297. This blocking strategy raised questions regarding the quality of the grid at the leading edge and the difficulty of transferring similar blocking to a grid for a rotor blade (compare and contrast this type of grid with the 2D rotor grid example, illustrated in Appendix A).

Figure 298 shows pressure contours on the surface of the wing and a section through the grid near the mid span symmetry plane of the wing. This illustration is taken from an early coarse grid case and shows a region of sparse cells ahead of the leading edge.

The grid was gradually refined by increasing the number of points. The predicted wing characteristics for a range of grid sizes are shown in Figures 299 to 302. Clearly, it is important to use a sufficient number of correctly spaced cells. For the finest grid of 3.5 million points, the pressure drag of the wing was very small at low lift (due to some small Euler numerical pressure losses), and was found to be very close to the induced drag predicted by lifting line theory for a rectangular wing of the same aspect ratio. While an Euler solution may be expected to be valid up to about 8 degrees, larger angles have been deliberately explored here to see the trends (a Navier-Stokes analysis would normally be required at high incidence).

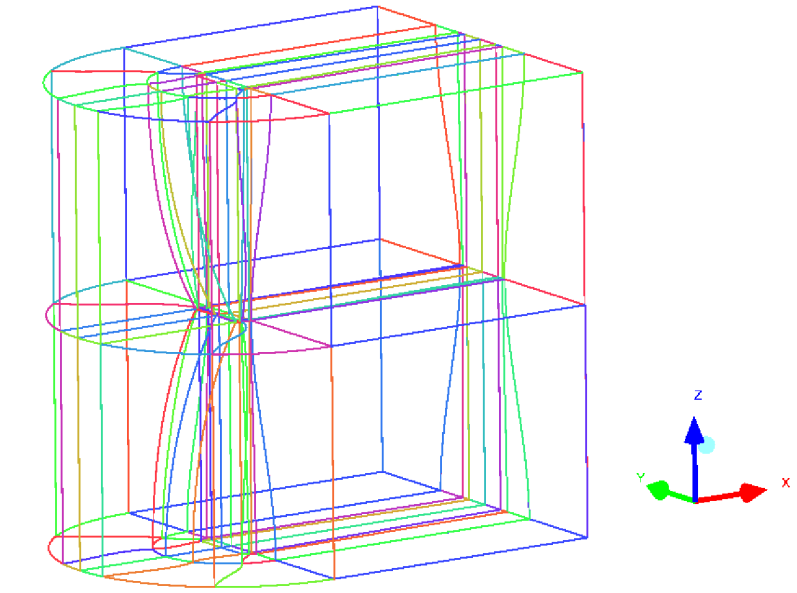

Figure 297: Support Curves Used to Generate H-H Multi-block Topology for Wing-1 with Küchemann-Type Tip

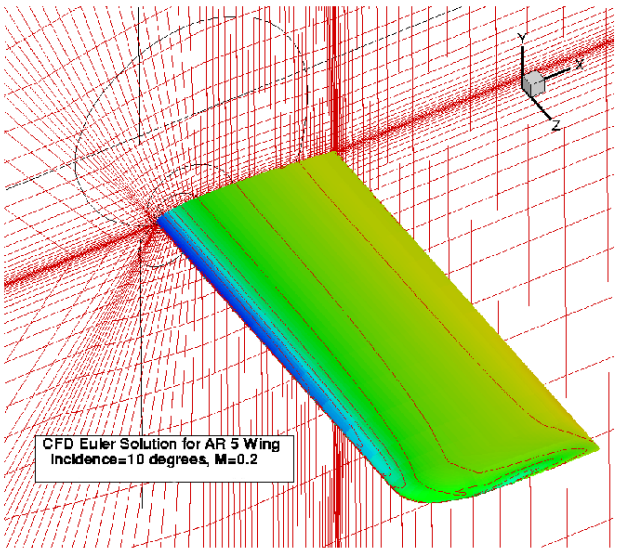

Figure 298: Pressure Contours on Wing Upper Surface and Central Grid-Plane for Wing-1 at M=0.2 and 10 degrees

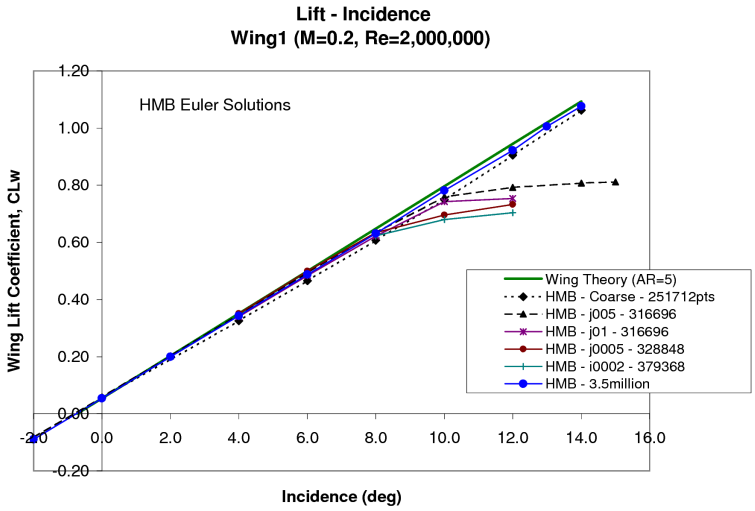

Figure 299: Predicted Lift Characteristics of Wing1 Compared to Theory

For the coarse grid, stream-traces on a cross-section at 50%span revealed an amount of flow separation and recirculation, despite this being an Euler solution. For the finer grid, this problem was greatly alleviated. Near the tip, the leading edge pressure gradually reduced in the expected manner and a suction peak was observed along the outer tip edge due to the tip vortex. At high incidence, this tended to give the wing a more nose down pitching moment. It is considered that this type of tip shape, with a streamwise outer edge, allows the vortex to form cleanly, leaving the tip vortex displaced as far outboard as possible, minimising the induced drag. As can be seen in the pressure contours, the rounded leading edge corner avoids the isobars clustering near the leading edge of the tip. To evaluate these features in greater detail calls for a Navier-Stokes analysis to reveal benefits arising from this and other tip shapes so that viscous effects are taken into account, especially in the rotor case where the tip is often highly loaded.

This preliminary analysis of a 3D wing has shown that, with a carefully designed grid, a good estimate of the induced drag can be obtained from the integrated surface pressures predicted by an Euler solution.

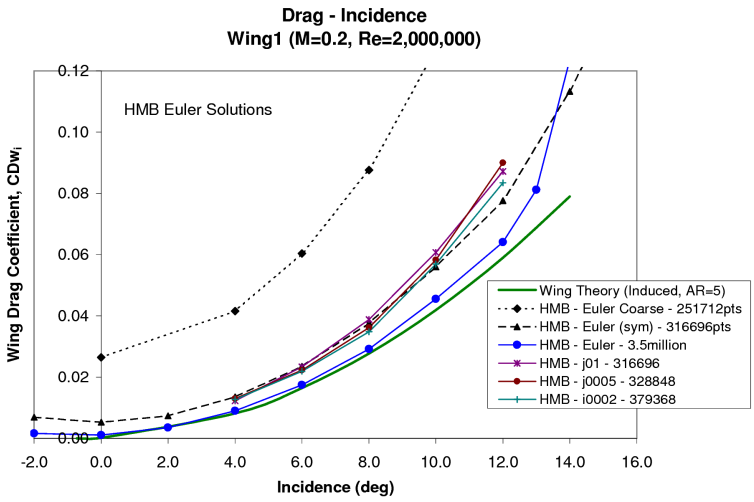

Figure 300: Predicted Drag Characteristics of Wing1 Compared to Theory

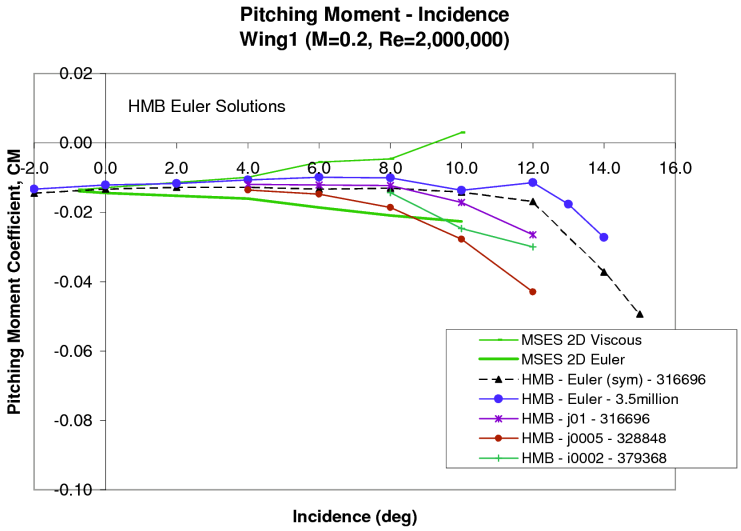

Figure 301: Predicted Moment Characteristics of Wing1 Compared to Theory

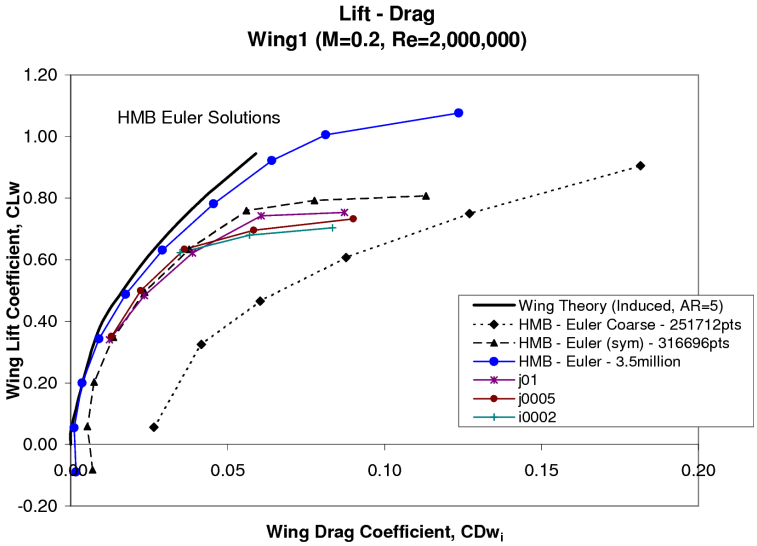

Figure 302: Predicted Lift-Drag Characteristics of Wing1 Compared to Theory

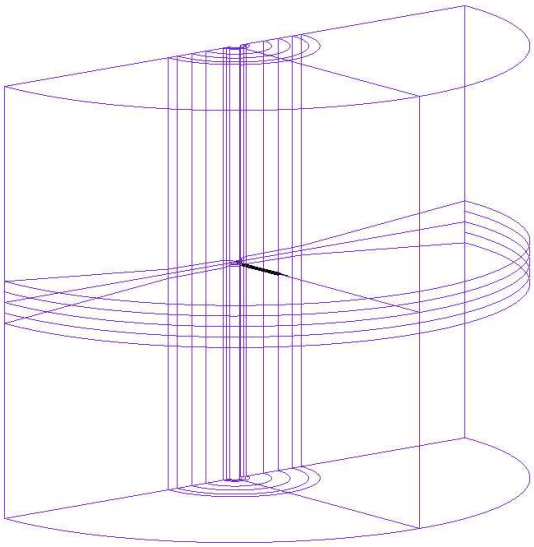

Figure 303: Diagram Showing the Computational Domain Used for the Computations of the R/c=13.7 Model Rotor of Tung, Pucci, Caradonna and Morse. For this 2-blade rotor the periodic planes are 180 degrees apart.

C Further Model Rotor Validation (R/c=13.7)

Comparison of HMB and Model Rotor with R/c=13.7

This Appendix contains an additional 'validation' case to compare results of HMB against the thrust and torque at a given pitch for the higher apsect ratio (R/c=13.7) model rotor of Tung, Pucci and Caradonna and Morse.[298] Since the main aim of the experiment was to investigate the structure of the tip vortices, the torque measurements appear to have been a by-product of the testing, and as such there may be some inaccuracies in the 3 data points that are available. No blade surface pressure measurements were taken in this experiment, unlike in the classical Caradonna and Tung lower aspect ratio (R/c=6) model rotor experiments against which HMB has already been validated (see previous references in Chapter 3). Both these 'Caradonna and Tung' model rotors had 2-blades, and the one considered here is representative of a main rotor, with zero twist. Unfortunately, time and resources did not permit similar comparisons to be made for the 8 degree twist case, as also described in the above referenced report. Further validation could be carried out against the hot-wire data, but this has not been pursued here, since this aspect has already been covered by the writer's own tests on the WHL model tail rotor in Chapter 3.

The rotor radius quoted in the Table 1 of TM-81316 is quite difficult to read in the copied report, but appears to be 105.2 cm which would give R/c=13.805, rather than the quoted value of 13.7. However, the 13.7 figure tallys with the stated radius of 104.5 cm in the text of the report. There is no doubt about the chord which was quoted in the same table as 7.62 cm, or 3". The uncertainty in radius could be due to a tip cap, or it could simply be a mistake in the report, unless an end-plate was used at the root of the blade which extended the radius by 7 mm (but perhaps this is unlikely). Personnal communication with Frank Caradonna still left some doubt as to the use of an end plate at the root, and therefore the exact radius of the rotor, here taken to be 1045 mm, might contain a tiny (less than 1%) error. The root cut-out radius was taken to be at 20%R and the blade aerofoil was NACA 0012. However, the tip shape is not described in detail, but (after enquirey) it is assumed to be a square-cut rectangular tip. The rotational speed was 1250 rpm, giving a tip Mach number of 0.40.

The blade geometry was prepared in the Rhino solid modelling CAD package. The blade was drawn at a pitch angle of 8 degrees and was set at a pre-cone of 0.5 degrees which was left unchanged throughout for this metal 2-blade model rotor. The structured multi-block grid was constructed using ICEM-Hexa, and employed periodic boundaries on the symmetry walls which were 180 degrees apart for this 2-bladed rotor. The gridsize

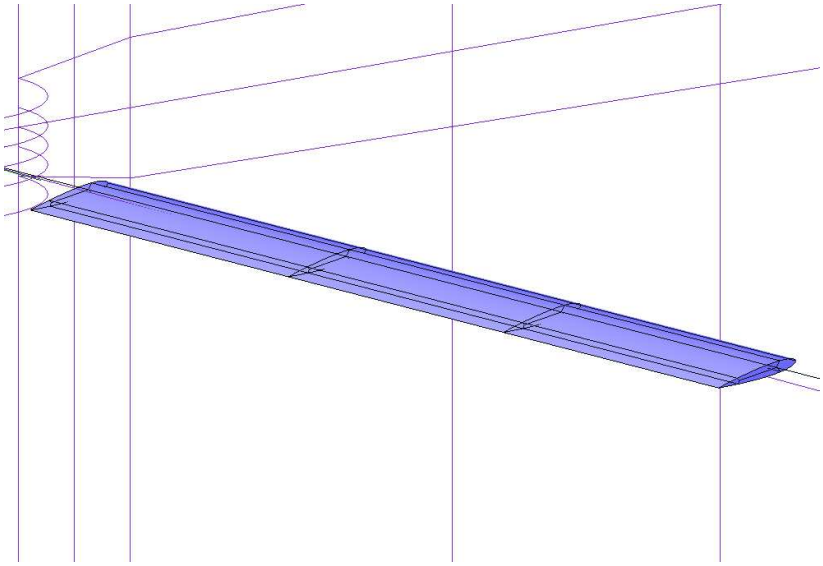

Figure 304: 3D View of the Blade of the R/c=13.7 Model Rotor of Tung, Pucci, Caradonna and Morse

was 16.7 million points in 170 blocks. The computational domain extended 4R above the rotor, 4R below and was 4R in radius as shown in Figure 303. A closer 3D view of the blade is given in Figure 304.

As usual for an hover case, the computations were carried out using a so-called 'Froude' boundary condition to allow the rotor wake to exhaust from the bottom of the domain, balanced by the inflow towards the rotor elsewhere. The HMB code was run as a Navier-Stokes solver with a k-ω turbulence model, until it was well converged.

The results from the HMB Navier-Stokes computations are compared with the untwisted, R/c=13.7, model rotor test data in Figures 305 to 308.

The thrust-pitch comparison is presented in Figure 305, where the test data lies above the predictions. The 5 degree point is very close to the predictions, while the 8 degree point is scatters high. There could also be a slight shift present in the test data, and a small amount of aeroelastic distortion cannot be ruled out. Some rounding-off of the thrust-pitch curve between 8 and 12 degrees is discrenable in the predictions and the test data is not at odds with this. Some early rounding-off of the thrust-pitch curve would be expected due to the relatively low Reynolds number of the model rotor. In all previous work, HMB has generally shown good agreement for the thrust-pitch curve, especially when the grids are sufficiently fine, as is the case here. The scatter in the test data could also be a consequence of recirculation or wake-venting effects in the test facility, or just some inaccuracy in the measurements.

Figure 306 shows the predicted results compare to test data in terms of thrust and torque. The HMB results sit fairly close to the test data, with the thrust differences noted above showing through. Whilst the torque at the two lower pitch angles appears to be slightly over-predicted, the torque data point at 12 degrees falls beyond, but in line with the trend of the predictions.

Figure 307 replots only the HMB predictions in the linearised form of CQ vs $CT^{1.5}$, in an attempt to discover the induced power factor, ki, for this 2-blade model rotor (the test data is put to one side here because the data is sparse and an amount of scatter is present). The 3 computed points appear to follow the expected, almost linear trend, with a small amount of power growth being predicted, either through a slight non-linear increase in induced power, or most likely, due to an increase of profile power at the low Reynolds number of the model rotor. An initial linear curve fit through the predicted points gave a rather high value of ki of 1.446, whilst just fitting a line to the first two points suggested a lower ki value of 1.311 (over the range from 5 to 8 degrees of pitch). Both these values seem high for a blade with moderately high R/c, even allowing for the low Reynolds number of only 715,000 and Mtip=0.4. Changing to a 2nd order polynomial curve fit, as put forward

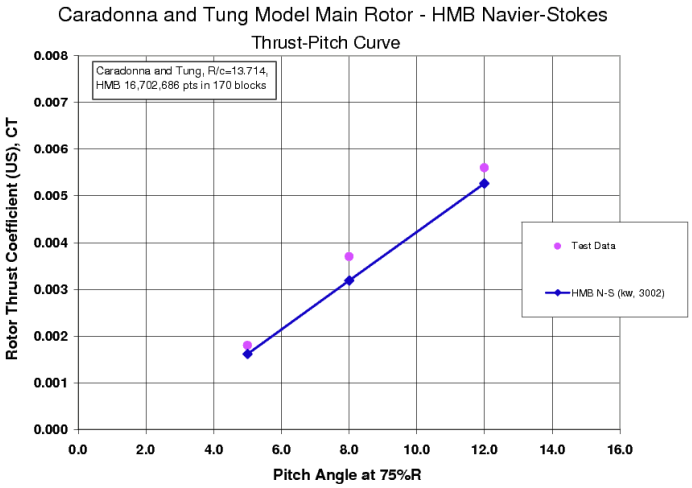

Figure 305: Comparison of HMB Navier-Stokes Results with Test Data for the 2-Blade Model Rotor of Tung, Pucci, Caradonna and Morse:[298] Thrust Coefficient versus Pitch

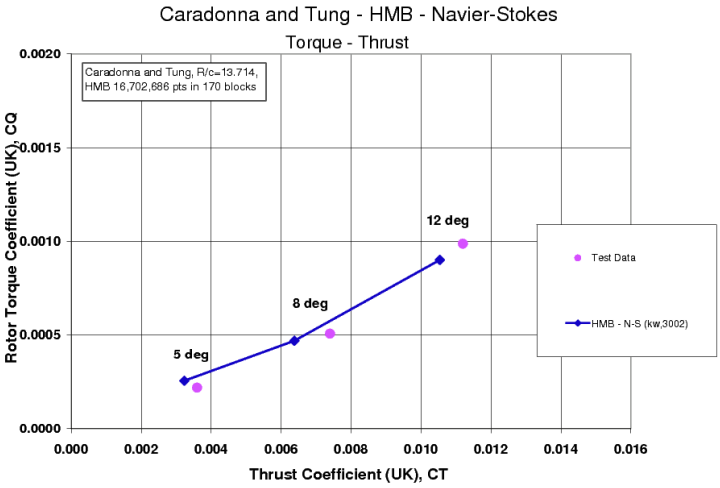

Figure 306: Comparison of HMB Navier-Stokes Results with Test Data for the 2-Blade Model Rotor of Tung, Pucci, Caradonna and Morse:[298] Torque Coefficient versus Thrust Coefficient

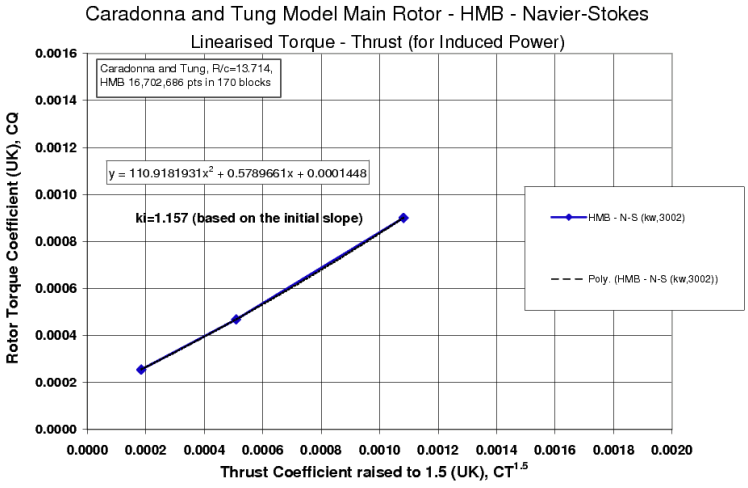

Figure 307: Comparison of HMB Navier-Stokes Results with Test Data for the 2-Blade Model Rotor of Tung, Pucci, Caradonna and Morse:[298] Torque Coefficient versus $CT^{1.5}$ to find the induced power factor, ki

in this thesis, yields a lower initial slope (as though projected back to at zero thrust), and hence a value of ki of 1.157 which is, perhaps, closer to what might be expected. The coefficient of the squared term in the polynominal fit is indicative of some profile power growth, but is not too dissimilar to values seen previously for other model rotors. The value of the constant term reveals an equivalent aerofoil drag coefficient for the blades of 0.0128 (at zero thrust). This is a very acceptable result, considering the low Reynolds number and the fact that only 3 points were computed, suggesting good accuracy for the HMB results.

Finally, the trend of Figure of Merit against CT from the HMB predictions is compared to test data in Figure 308. The discrepency in Figure of Merit is due to the measured thrust being higher and the measured torque being lower than the HMB predictions (contrary to expectations), probably due to the difficulty of making accurate measurements on the rotor test rig. While the trend of the results is similar, it is unlikely that a FoM as high as 0.5 would be reached at only 5 degrees of pitch. At 12 degrees, the test data shows a fall-off in Figure of Merit, while at first sight the HMB results appear to show an increasing trend since the computed points were joined with straight lines, and there are no results in the region of 10 degrees which may be near where the peak Figure of Merit actually occurs. It is well know that Figure of Merit is a sensitve parameter on which to compare rotor performance, however the measured and predicted values of Figure of Merit are in close agreement values at 12 degrees.

Despite the minor queries regarding the precise geometry of this rotor, and the fact that the experiment was not designed to provide data for CFD validation and includes only 3 data points, the overall agreement is good and any differences are mainly due to scatter in the data. A reasonable induced power factor was able to be extracted from the computational results using the method put forward in this thesis. This exercise has been useful to once again verify the HMB CFD code, and provides further confidence in the accuracy of the predictions, confirming that Computation Fluid Dynamics provides a truely predictive tool for the rotor designer. Further validation is presented in Chapter 3 of this thesis.

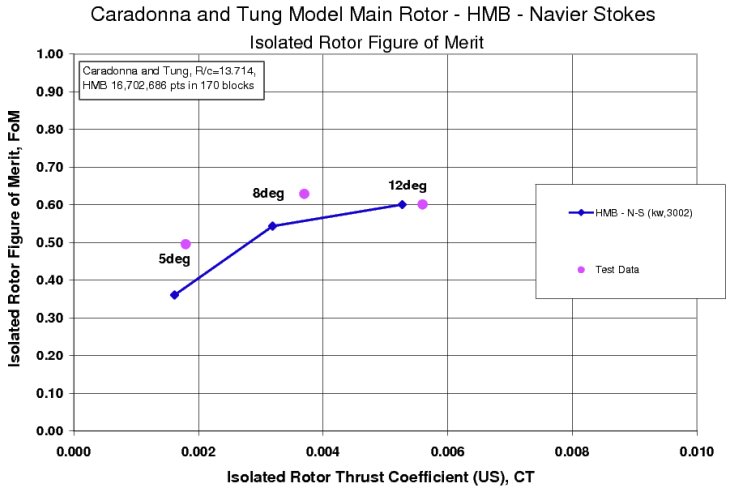

Figure 308: Comparison of HMB Navier-Stokes Results with Test Data for the 2-Blade Model Rotor of Tung, Pucci, Caradonna and Morse:[298] Figure of Merit versus Thrust Coefficient

D Smoothed Co-ordinates for SC1095 and SC1095R8

This appendix records the final, smoothed co-ordinates used for the Sikorsky SC1095 and SC1095R8 aerofoils which were used during the validation study of the UH-60A model rotor case of Chapter 3. The smoothed, sharp trailing edge aerofoils used in the Euler simulation are listed in the following table.

SC1095SS (Smooth, Sharp T.E.)

x/c(upper)	y/c(upper)	y/c(lower)
0.000000	0.0000000	0.0000000
0.000602	0.003449081	-0.00321978
0.002408	0.007305288	-0.006422138
0.005412	0.01153227	-0.009655564
0.009607	0.01589606	-0.01299584
0.014984	0.02032041	-0.01636648
0.021530	0.02471978	-0.0196396
0.029228	0.02896537	-0.02273393
0.038060	0.03287742	-0.02558716
0.048005	0.03636286	-0.02811637
0.059039	0.03943912	-0.03024623
0.071136	0.04216359	-0.03195386
0.084265	0.04457669	-0.03336983
0.098396	0.04669247	-0.03458216
0.113495	0.04854341	-0.03564249
0.129524	0.0501595	-0.03656963
0.146447	0.05157573	-0.0373679
0.164221	0.05280573	-0.03803196
0.182803	0.05383448	-0.03855805
0.202150	0.05463564	-0.03895391
0.222215	0.05518367	-0.03923123
0.242949	0.05548596	-0.03939179
0.264302	0.05557307	-0.03943833
0.286222	0.05548846	-0.03937881
0.308658	0.05525818	-0.03922084
0.331555	0.054889	-0.03896361
0.354858	0.0543812	-0.03860767
0.378510	0.05373745	-0.03815574
0.402455	0.05296217	-0.03761109
0.426635	0.05205903	-0.03697398
0.450991	0.05102942	-0.03624638
0.475466	0.04987485	-0.03542833
0.500000	0.04859724	-0.03452237
0.524534	0.04720155	-0.03353149
0.549009	0.04569062	-0.03245625
0.573365	0.04407169	-0.03129864
0.597545	0.04234781	-0.03006272
0.621490	0.04052793	-0.02875145
0.645142	0.0386205	-0.02737337
0.668445	0.0366360	-0.02593979
0.691342	0.0345852	-0.02445842
0.713778	0.0324811	-0.02293941
0.735698	0.0303390	-0.02139822
0.757051	0.0281790	-0.01984747

SC1095SS (Smooth, Sharp T.E.) (continued)

x/c(upper)	y/c(upper)	y/c(lower)
0.777785	0.0260183	-0.01830098
0.797850	0.0238750	-0.01677199
0.817197	0.0217662	-0.015272
0.835780	0.0197047	-0.01381161
0.853553	0.0177053	-0.0123996
0.870476	0.0157787	-0.01104348
0.886505	0.0139303	-0.009749902
0.901604	0.0121706	-0.008517988
0.915735	0.0104934	-0.007344271
0.928864	0.0089019	-0.006231391
0.940961	0.0074120	-0.005188741
0.951995	0.0060379	-0.00422723
0.961940	0.0047913	-0.0033546
0.970772	0.0036797	-0.002576685
0.978470	0.0027095	-0.001897491
0.985016	0.0018845	-0.001319692
0.990393	0.0012071	-0.0008454656
0.994588	0.0006795	-0.0004759892
0.997592	0.0003022	-0.0002117069
0.999398	0.0000755	-0.00005291755
1.000000	0.0000000	0.0000000

SC1095R8SS (Smooth, Sharp T.E.)

x/c(upper)	y/c(upper)	y/c(lower)
-0.0094542	-0.0175869	-.0175869
-0.0093525	-0.0157140	-0.0194027
-0.0086411	-0.0119236	-0.0226306
-0.0074215	-0.0079999	-0.0253610
-0.0053887	-0.0033886	-0.0281575
-0.0028478	0.0009664	-0.0303701
-0.0003069	0.0045391	-0.0317638
0.0027421	0.0082095	-0.0329144
0.0088403	0.0143613	-0.0344560
0.0126059	0.0176027	-0.0351369
0.0187041	0.0222115	-0.0360274
0.0248022	0.0260965	-0.0367231
0.0309004	0.0293528	-0.0372651
0.0369986	0.0321005	-0.0376946
0.0430967	0.0344443	-0.0380445
0.0512276	0.0370883	-0.0384168
0.0613912	0.0398159	-0.0387607
0.0715548	0.0420805	-0.0390079
0.0817184	0.0440012	-0.0391829
0.0918820	0.0456472	-0.0393009
0.1020456	0.0470674	-0.0393741
0.1172910	0.0488692	-0.0394179
0.1325364	0.0503607	-0.0394229
0.1477818	0.0516182	-0.0394250
0.1630272	0.0526823	-0.0394270
0.1782727	0.0535684	-0.0394290
0.1935181	0.0542817	-0.0394301
0.2087635	0.0548257	-0.0394311
0.2240089	0.0552057	-0.0394321
0.2392543	0.0554418	-0.0394331
0.2538202	0.0555548	-0.0394298
0.264302	0.05557307	-0.03943833

The trailing edge region aft of 0.264302 has the same co-ordinates as the SC1095, given above.

E Co-ordinates for NACA 23012 with Sharp T.E.

This appendix records the co-ordinates used for the sharp trailing edge version of the NACA 23012 aerofoil as in the validation studies in Chapter 3. The co-ordinates were computed from the modified NACA 4-digit series equations given by Abbot and von Doenhoff[1] and written out to 7 figure accuracy to maintain smoothness.

Aerofoil Co-ordinates for NACA 23012 with Sharp T.E. (na23012s)

x/c(upper)	y/c(upper)	x/c(lower)	y/c(lower)
0.0000000	0.0000000	0.0000000	0.0000000
-0.0006312	0.0043287	0.0018352	-0.0039626
-0.0000321	0.0089284	0.0048481	-0.0074778
0.0018097	0.0137720	0.0090143	-0.0105635
0.0050717	0.0188719	0.0141423	-0.0133035
0.0097122	0.0241586	0.0202558	-0.0157234
0.0157453	0.0295652	0.0273147	-0.0178730
0.0231723	0.0350106	0.0352837	-0.0198042
0.0319828	0.0404053	0.0441372	-0.0215697
0.0421520	0.0456536	0.0538580	-0.0232204
0.0536401	0.0506590	0.0644379	-0.0248037
0.0663932	0.0553301	0.0758788	-0.0263618
0.0803404	0.0595844	0.0881896	-0.0279301
0.0954015	0.0633565	0.1013905	-0.0295358
0.1114831	0.0665999	0.1155069	-0.0311954
0.1284811	0.0692921	0.1305669	-0.0329123
0.1462887	0.0714374	0.1466053	-0.0346746
0.1647902	0.0730677	0.1636519	-0.0364516
0.1838706	0.0742434	0.1817354	-0.0381903
0.2034185	0.0750519	0.2008815	-0.0398127
0.2235050	0.0755814	0.2209250	-0.0412284
0.2442551	0.0758500	0.2416429	-0.0424128
0.2656187	0.0758611	0.2629853	-0.0433670
0.2875441	0.0756198	0.2848999	-0.0440938
0.3099803	0.0751327	0.3073357	-0.0445977
0.3328725	0.0744084	0.3302376	-0.0448847
0.3561658	0.0734565	0.3535502	-0.0449621
0.3798035	0.0722882	0.3772165	-0.0448384
0.4037299	0.0709157	0.4011801	-0.0445235
0.4278871	0.0693519	0.4253829	-0.0440277
0.4522166	0.0676109	0.4497654	-0.0433624
0.4766614	0.0657067	0.4742706	-0.0425393
0.5011621	0.0636543	0.4988379	-0.0415705

Aerofoil Co-ordinates for NACA 23012 with Sharp T.E. (na23012s) (continued)

x/c(upper)	y/c(upper)	x/c(lower)	y/c(lower)
0.5256597	0.0614686	0.5234082	-0.0404684
0.5500959	0.0591646	0.5479222	-0.0392454
0.5744105	0.0567574	0.5723194	-0.0379139
0.5985472	0.0542617	0.5965428	-0.0364861
0.6224471	0.0516920	0.6205329	-0.0349741
0.6460526	0.0490628	0.6442314	-0.0333896
0.6693079	0.0463880	0.6675821	-0.0317440
0.6921563	0.0436813	0.6905277	-0.0300485
0.7145430	0.0409559	0.7130130	-0.0283142
0.7364134	0.0382252	0.7349826	-0.0265516
0.7577166	0.0355015	0.7563854	-0.0247710
0.7784010	0.0327973	0.7771690	-0.0229826
0.7984168	0.0301249	0.7972832	-0.0211964
0.8177152	0.0274965	0.8166789	-0.0194225
0.8362494	0.0249240	0.8353086	-0.0176707
0.8539767	0.0224188	0.8531293	-0.0159505
0.8708544	0.0199925	0.8700976	-0.0142717
0.8868396	0.0176569	0.8861704	-0.0126441
0.9018967	0.0154228	0.9013113	-0.0110768
0.9159877	0.0133014	0.9154823	-0.0095796
0.9290790	0.0113034	0.9286490	-0.0081615
0.9411407	0.0094390	0.9407813	-0.0068314
0.9521421	0.0077184	0.9518480	-0.0055981
0.9620573	0.0061509	0.9618227	-0.0044699
0.9708626	0.0047453	0.9706815	-0.0034544
0.9785370	0.0035096	0.9784030	-0.0025587
0.9850628	0.0024510	0.9849691	-0.0017892
0.9904231	0.0015759	0.9903629	-0.0011516
0.9946050	0.0008897	0.9945710	-0.0006507
0.9975995	0.0003965	0.9975844	-0.0002902
0.9993999	0.0000992	0.9993961	-0.0000726
1.0000000	0.0000000	1.0000000	0.0000000

F Co-ordinates for NACA 0012 with Sharp T.E.

This appendix records the co-ordinates used for the sharp trailing edge version of the NACA 0012 aerofoil as used throughout this research. The co-ordinates were computed from the equation for the sharp aerofoil and written out to 7 figure accuracy to maintain smoothness. The sharp trailing edge was initially chosen to suit the Euler computations, and was also used for consistency in the Navier-Stokes computations where it also simplifies grid generation. (Details of the model rotor aerofoil are noted below).

Aerofoil Co-ordinates for NACA 0012 (naca0012ab_sharp)

x/c(upper)	y/c(upper)	y/c(lower)
0.0000000	0.0000000	0.0000000
0.0006023	0.0043262	0.0043262
0.0024076	0.0085577	0.0085577
0.0054117	0.0126895	0.0126895
0.0096074	0.0167150	0.0167150
0.0149844	0.0206263	0.0206263
0.0215298	0.0244142	0.0244142
0.0292280	0.0280684	0.0280684
0.0380602	0.0315779	0.0315779
0.0480054	0.0349310	0.0349310
0.0590394	0.0381158	0.0381158
0.0711357	0.0411203	0.0411203
0.0842652	0.0439330	0.0439330
0.0983962	0.0465426	0.0465426
0.1134948	0.0489390	0.0489390
0.1295244	0.0511129	0.0511129
0.1464466	0.0530562	0.0530562
0.1642205	0.0547626	0.0547626
0.1828034	0.0562270	0.0562270
0.2021504	0.0574463	0.0574463
0.2222149	0.0584191	0.0584191
0.2429487	0.0591458	0.0591458
0.2643017	0.0596286	0.0596286
0.2862225	0.0598714	0.0598714
0.3086583	0.0598798	0.0598798
0.3315551	0.0596611	0.0596611
0.3548577	0.0592237	0.0592237
0.3785099	0.0585776	0.0585776
0.4024549	0.0577337	0.0577337
0.4266348	0.0567037	0.0567037
0.4509914	0.0555001	0.0555001
0.4754662	0.0541362	0.0541362
0.5000000	0.0526252	0.0526252

Aerofoil Co-ordinates for NACA 0012 (naca0012ab_sharp) (continued)

x/c(upper)	y/c(upper)	y/c(lower)
0.5245339	0.0509810	0.0509810
0.5490086	0.0492171	0.0492171
0.5733653	0.0473472	0.0473472
0.5975451	0.0453850	0.0453850
0.6214901	0.0433436	0.0433436
0.6451424	0.0412362	0.0412362
0.6684449	0.0390755	0.0390755
0.6913418	0.0368739	0.0368739
0.7137775	0.0346436	0.0346436
0.7356984	0.0323962	0.0323962
0.7570514	0.0301435	0.0301435
0.7777852	0.0278967	0.0278967
0.7978497	0.0256670	0.0256670
0.8171966	0.0234653	0.0234653
0.8357795	0.0213025	0.0213025
0.8535534	0.0191893	0.0191893
0.8704756	0.0171363	0.0171363
0.8865052	0.0151541	0.0151541
0.9016038	0.0132530	0.0132530
0.9157348	0.0114433	0.0114433
0.9288643	0.0097348	0.0097348
0.9409606	0.0081372	0.0081372
0.9519947	0.0066599	0.0066599
0.9619398	0.0053117	0.0053117
0.9707720	0.0041008	0.0041008
0.9784701	0.0030348	0.0030348
0.9850156	0.0021206	0.0021206
0.9903926	0.0013641	0.0013641
0.9945883	0.0007704	0.0007704
0.9975924	0.0003434	0.0003434
0.9993978	0.0000860	0.0000860
1.0000000	0.0000000	0.0000000

Note: The WHL model rotor employed a standard NACA0012 aerofoil, as given in Abbott and von Doenhoff,[1] based on a 3.25" chord, with a small, constant thickness horizontal tab, aft of 98.46%c, taking the chord to 3.28" (83.312 mm). The purpose of the tab was to join the carbon t.e. skins and it was smoothly blended with the aerofoil. The total tab thickness was .023"(0.584 mm).

G Rotor-Analyser Fortran Program Listing

```
      program rotor_analyser

c     Read from Tecplot radial x,y pos/neg slices output '.dat' files
c     Integrate local force (CZ) and moment (CM), find theta, hence CN
c     Write output to files for subsequent plotting

c     Compiled with gfortran -o rotor_analyser rotor_analyser.f

c     (perhaps a better idea would be to read/interpolate HMB .plt files)
c     (this would have avoided many extraction problems from tecplot!)

c     Alan Brocklehurst
c     PhD Utility Program

c     University of Liverpool
c     Longburton, Dorset

c     Version Dev(1.01) - fwd flt ideas modified to suit hover analysis
c     Date 05 August 2006 - modified 3 Feb 07 for trb_005_m6_ns ...
c     - modified 11 Feb 07 when used for trb-001 - hover euler 10deg
c     - also used for trb_000_00, 08, 16 twist analysis
c     17 June 2008 - modified for trb_000v 10,12,15,18(surf),20deg
c     moved to rotor_analyser_ab directory re-comp for trb_000v_ 2deg
c     12 Feb 2011 - modifed for trb_005v - executable in ../hmb_progs/.
c     23-25 Jan 2013 - trb_000v 15deg more, 16deg new, 8 more, 12 more
c     25 Jan 2013 - trb_005v 10, 12, 14, 15, etc, all available re-done
c     27 Jan 2013 - trb_001v 10deg: array size from 50 to 51, +low pitch

c     Notes:
c     i-points on surface set to 50 (usually 30 or 31) - adjust as required
c     Now increased for trb-001v or maybe new tecplot slices to 51 not 50 !
c     j-blocks around aerofoil set to 8 for trb_005
c     k-radial slices - typically 25 (+root and tip) - adjust as required
c     NB avoid block boundaries in tecplot slices (and allow for flapping)
c     In the trb_005_m6 case there is no coning (and no flapping in hover)!
c     NB for 001 and 005 in .dat file replace I=9 with I=09, etc, and split
c     the blocks that wrap around the leading edge before running program!

      implicit none

      real x(51,8,25),y(51,8,25),z(51,8,25),p(51,8,25),cp(51,8,25)
      real cpc(51,8,25),xr(25),cz(25),cm(25),theta(25),theta_deg(25)
      real cc0(25),cz_blk(8,25),cpc_av(51,8,25),y_av(51,8,25),t(51,8,25)
      real cm_blk(8,25),del_y(51,8,25),yle(25),zle(25),yte(25),zte(25)
c     real mu_n(25)
      real del_z(51,8,25),z_av(51,8,25)
      real up(8,25),ymid(8,25),zmid(8,25),zchord(8,25)
      real cpmax(25),cpmin(25),delxr(25),chord(25)
      real z_anh(25),y_off(25),z_off(25),dist(51,8),le_dist(25)
      real dist_le(25),dist_te(25),chord_sum(25)
      real z_load(25),y_load(25),m_load(25)
      real n_load(25),c_load(25),cy(25),cn(25),cc(25)
```

Appendix G Rotor-Analyser Program Listing (continued)

```
      real roc,gamma_air,mtip,xchk ! psi_deg,psi,mu,mfwd
      real xsign,ysign,trb
      real solidity,xr_tip,xr_cutoff,cts,cmb,ct,cq,cqs,cmbar
      real sgn,pitch,pitch_deg
      real pi,dtr,rtd

      integer imax(8,25),jmax(25),ij_le(2),ij_te(2)
      integer i,j,j1,k,k1,kmax,lines
      integer ile,ite,jle,jte,iend,ixr

      character*1 xyswap
      character*3 xr_chrs,trb_chrs
      character*4 out_extn
      character*5 hov_chrs
      character*2 pitch_chrs !edit as required
      character*60 filename ! now using trim(), including '.dat'
      character*23 output_file1,output_file2,output_file3 !edit to suit
      character*80 header

      pi=4.*ATAN(1.)
      dtr=pi/180.
      rtd=180./pi

      write(6,*)
      write(6,*)'** Alan"s Rotor-Analyser (from Tecplot Slices) ***'
      write(6,*)

c     Setup: (for trb-001)
c     trb=1.0 ! = 0.0 for trb_000, =1 or 5 for trb001,005
c     psi_deg=180.0 !edit as required for each azimuth case
c     for the moment...assume that this is for a hover case only ...
c     trb_chrs='000'
      trb_chrs='001'
      hov_chrs='hov_v'
      out_extn='.out'
c     output_file1='trb_000v_m6_12deg_cpyc_' !edit as required
c     output_file2='trb_000v_m6_12deg_czxr_' !edit as required
c     output_file3='trb_000v_m6_12deg_ctot_' !edit as required
      output_file1='trb_001v_m6_20deg_cpyc_' !edit as required
      output_file2='trb_001v_m6_20deg_czxr_' !edit as required
      output_file3='trb_001v_m6_20deg_ctot_' !edit as required
```

Appendix G Rotor-Analyser Program Listing (continued)

```
      solidity=.198868
      roc=6.402439
      xr_cutoff=0.2917
      xr_tip=1.0
c     mu=0.4032
      mtip=0.60 !for most cases, except mtip=0.448 for trb_000_00,08,16
c     mtip=0.448 !for trb_000_00,08,16
      gamma_air=1.4
c     pitch_deg ! edit as required for each case!!!
      pitch_deg=20.0
      pitch=pitch_deg*dtr

c     mfwd=mu*mtip
c     psi=psi_deg*dtr

      !i points, j blocks per station, for k radial stations

      !imax() variable is read in from tecplot data file, edit to 'I=i2'

      kmax=25 !trb 25 slices (new at tip) (27 inc 29.17% and 100%R)

      if(trb_chrs.eq.'000')then
      do k=1,kmax
      jmax(k)=6 !for trb_000, etc there are only 6 blocks on aerofoil
      cc0(k)=1.0
      end do
      else
      do k=1,kmax-3
      jmax(k)=8 !these stations have 8 blocks around aerofoil trb_001/5
      end do !imax may require splitting at le on '23' and '24' 001
      jmax(23)=8 ! stn 6.2744 (98.00%R)- 8 after edit - trb001/5
      jmax(24)=8 ! stn 6.3300 (98.87%R)- 8 after edit - trb001/5
      jmax(25)=4 ! stn 6.3650 (99.42%R)- 4 after edit - trb001/5
      cc0(1)=.5995 ! 30.0% linear taper at inbd end, c-cutoff=0.5
      cc0(2)=.7798 ! 31.5%
      do k=3,kmax-4
      cc0(k)=1.0
      end do !_005 !c/c0 to account for tip shape on 001,005
      if(trb_chrs.eq.'001')then
      cc0(22)=.986697 !96.81% (trb_001)
      cc0(23)=.890232 !98.00% (trb_001)
      cc0(24)=.729445 !98.87% (trb_001)
      cc0(25)=.551488 !99.42% (trb_001)
      end if
      if(trb_chrs.eq.'005')then
      cc0(22)=.9934 !96.81%
      cc0(23)=.9062 !98.00%
      cc0(24)=.7498 !98.87% - 005 c/c0 approx!
      cc0(25)=.5669 !99.42%
      end if
      end if
```

Appendix G Rotor-Analyser Program Listing (continued)

```
        ! NB tecplot slices 'cut' vertically for zero-cone (hover)
        ! TRB-005 has nominally the same tip planform as TRB-001,
        ! but was drawn on the 20deg anhedral slant, giving small
        ! difference in the true chord lengths

        if(trb_chrs.eq.'004'.or.trb_chrs.eq.'005')then
        do k=1,18
        z_anh(k)=0.0
        end do
        z_anh(19)=-.004266 !vertical displacement of anhedral (chords)
        z_anh(20)=-.023303
        z_anh(21)=-.044303
        z_anh(22)=-.065410
        z_anh(23)=-.093214
        z_anh(24)=-.113455
        z_anh(25)=-.126194
        ! z_anh_tip=.13982 chords, or .02183 z/R
        else
        do k=1,kmax
        z_anh(k)=0.0
        end do
        end if

        do k=1,kmax
        y_off(k)=-z_anh(k)*SIN(pitch) !y_off is positive (fwds)
        z_off(k)=z_anh(k)*COS(pitch) !z_off is negative (down)
c       write(6,*)'k=',k,'y_off(k)=',y_off(k),' z_off(k)=',z_off(k)
        end do

c       1. Read input data files (from Tecplot, one zone per blk at each stn)

        write(6,*)'Enter filename:'
        write(6,*)'(eg trb_00Nv_m6_XXdeg_xpslices.dat):'
        read(5,5000)filename
5000    format(60a)
        write(6,*)
5001    format(a)

        write(6,*)'Enter 2 chrs for pitch_chrs:'
        read(5,5002)pitch_chrs
5002    format(a2)

        xsign=1.0
        ysign=1.0
```

Appendix G Rotor-Analyser Program Listing (continued)

```
      open(unit=11,file=trim(filename),status='OLD')

      do lines=1,5 !read first 5 lines, title, variables
      read(11,1101)header
      end do

      do k=1,kmax

      do j=1,jmax(k)

      read(11,1101)header !read zone and slice location
      write(6,6001)header !check zone and slice location
      read(11,*) !skip Tecplot360's STRANDID line

      read(11,1102)imax(j,k),j1,k1
      if(j1.eq.1.and.k1.eq.1)then
      write(6,6002)imax(j,k),jmax(k),j,k
      else
      write(6,*)'dummy j1 and k1 not read-in correctly!'
      stop
      end if
      if(imax(j,k).gt.51)then
      write(6,*)'number of i-points to be read exceeds array size!'
      STOP
      end if

      read(11,*) !skip DATAPACKING=POINT
      read(11,*) !skip DT=(SINGLE...)

      do i=1,imax(j,k)
      read(11,*)x(i,j,k),y(i,j,k),z(i,j,k),p(i,j,k)
      x(i,j,k)=xsign*x(i,j,k)
      y(i,j,k)=ysign*y(i,j,k)
      if(xyswap.eq.'y')then
      t(i,j,k)=x(i,j,k)
      x(i,j,k)=y(i,j,k)
      y(i,j,k)=t(i,j,k)
      end if
      end do !i-datapoints
      write(6,6003)x(1,j,k),y(1,j,k),z(1,j,k),p(1,j,k)
      write(6,6004)x(imax(j,k),j,k),y(imax(j,k),j,k),
      $ z(imax(j,k),j,k),p(imax(j,k),j,k)

      end do !j-blocks

      write(6,*)
      end do !k-stations
1101  format(80a)
1102  format(3x,i2,4x,i1,4x,i1) !NB edit input file to ensure 'I=i2'
6001  format(80a)
6002  format('imax=',i2,' jmax=',i2,' j=',i2,' k=',i2)
6003  format('i=1 :',e17.9,2f12.6,f10.4)
6004  format('imax:',e17.9,2f12.6,f10.4)

      close(unit=11)
```

Appendix G Rotor-Analyser Program Listing (continued)

```
c       2. Check for common radial stations and store non-dim rad in xr()

        do k=1,kmax
        xchk=x(1,1,k)
        write(6,*)'j=',1,' x(1,1,k)=',xchk
        do j=2,jmax(k)
        if(abs(x(1,j,k)-xchk).lt.0.000001)then
        xchk=x(1,j,k)
        write(6,*)'j=',j,' xchk=',xchk
        else
        write(6,*)'xstns are inconsistent!'
        stop
        end if
        end do
        xr(k)=int(xchk/roc*10000.+.5)/10000.
        write(6,6006)k,xr(k)
        end do
        write(6,*)
6006    format('xr(',i2,')=',f8.6)

c       3. Find leading edge, trailing edge and pitch angle at each rad stn
c       and confirm the chord is correct, +/-.005, compared to Rhino c/c0.

        ile=1
        jle=1
        ite=1
        jte=1
        do k=1,kmax
c       yle(k)=-.1
        le_dist(k)=-.1
        yte(k)=0.1
        dist=0.0 !re-initialise the array for finding distance to le/te
        do j=1,jmax(k)
        do i=1,imax(j,k)
        sgn=(y(i,j,k)-y_off(k))/ABS(y(i,j,k)-y_off(k))
        dist(i,j)=sgn*
        $ SQRT((y(i,j,k)-y_off(k))**2+(z(i,j,k)-z_off(k))**2)
        end do
        end do
        dist_le(k)=MAXVAL(dist)
        dist_te(k)=MINVAL(dist)
        ij_le=maxloc(dist)
        ij_te=minloc(dist)
cx      write(6,*)'ij_le=',ij_le
cx      write(6,*)'ij_te=',ij_te
        ile=ij_le(1)
        jle=ij_le(2)
        yle(k)=y(ile,jle,k)
        ite=ij_te(1)
        jte=ij_te(2)
        yte(k)=y(ite,jte,k)
```

Appendix G Rotor-Analyser Program Listing (continued)

```
      if(k.eq.kmax.and.(trb_chrs.eq.'001'.or.trb_chrs.eq.'005'))then
      do j=1,jmax(k)
      do i=1,imax(j,k)
      if(dist(i,j).le.le_dist(k))then
      ile=i
      jle=j
      yle(k)=y(ile,jle,k)
      end if
      end do
      end do
      end if

      zle(k)=z(ile,jle,k)
      zte(k)=z(ite,jte,k)

cx    write(6,*)'zle(k)=',zle(k),' z_off(k)=',z_off(k)
      if(k.le.kmax-2)then
      chord_sum(k)=dist_le(k)-dist_te(k)
      else
      chord_sum(k)=-dist_le(k)-dist_te(k)
      end if
      write(6,*)'dist_le=',dist_le(k),' dist_te=',dist_te(k),
     $ ' chord_sum=',chord_sum(k)
      chord(k)=SQRT((zle(k)-zte(k))**2+(yle(k)-yte(k))**2)
      theta(k)=ATAN((zle(k)-zte(k))/(yle(k)-yte(k)))
      theta_deg(k)=theta(k)*rtd
      if(abs(cc0(k)-chord(k)).le.0.005)then
      write(6,6007)k,xr(k),yle(k),zle(k),
     $ yte(k),zte(k),theta_deg(k),chord(k),cc0(k)
      else
      write(6,6008)k,chord(k)
      if(abs(cc0(k)-chord(k)).le.0.05)then
      write(6,6009)k,chord(k)
      end if
      write(6,6007)k,xr(k),yle(k),zle(k),
     $ yte(k),zte(k),theta_deg(k),chord(k),cc0(k)
      end if
      write(6,*)
      end do
      write(6,*)

6007  format('k=',i2,' xr=',f6.3,' yle=',f7.4,' zle=',f7.4,
     $ ' yte=',f7.4,' zte=',f7.4,' theta_deg=',f6.3,' chord=',f8.4,
     $ ' cc0=',f8.4)
6008  format('Chord err¿.005... at k=',i2,' chord=',f8.4,' !!!')
6009  format('Chord err¿.05.... at k=',i2,' chord=',f8.4,' !!!')
```

Appendix G Rotor-Analyser Program Listing (continued)

```
c   4. Determine whether block-surface data is on upper or lower surface

      do k=1,kmax
      do j=1,jmax(k)
      iend=imax(j,k)
      ymid(j,k)=(y(1,j,k)+y(iend,j,k))/2.
      zmid(j,k)=(z(1,j,k)+z(iend,j,k))/2.
      if(jmax(k).eq.2)then
      ymid(j,k)=y(int(imax(j,k)/2),j,k)
      zmid(j,k)=z(int(imax(j,k)/2),j,k)
      end if
      zchord(j,k)=zle(k)-.25*TAN(theta(k))+ymid(j,k)*TAN(theta(k))
      up(j,k)=0.0
      if(zmid(j,k).gt.zchord(j,k))then
      up(j,k)=1.0 !is an upper surface
      end if
      if(zmid(j,k).lt.zchord(j,k))then
      up(j,k)=-1.0 !is a lower surface
      end if

      if((trb_chrs.eq.'001').and.(k.eq.23.or.k.eq.24))then
c     up(1,k)=-1.0
c     up(2,k)=1.0
c     up(3,k)=1.0 !these may be suitable for 001 Euler hover
c     up(4,k)=-1.0 !or could be appropriate to 001 in fwd flight
c     up(5,k)=1.0
c     up(6,k)=-1.0
c     up(7,k)=-1.0
c     up(8,k)=1.0
c     up(1,k)=-1.0
c     up(2,k)=1.0
c     up(3,k)=1.0 !these are suitable only for 'original' 001v hov
c     up(4,k)=1.0 ! ie low-pitch cases
c     up(5,k)=-1.0
c     up(6,k)=-1.0
c     up(7,k)=-1.0
c     up(8,k)=1.0
      up(1,k)=1.0 !these are for the most recent 001v cases
      up(2,k)=-1.0
      up(3,k)=-1.0
      up(4,k)=1.0
      up(5,k)=-1.0
      up(6,k)=1.0
      up(7,k)=-1.0
      up(8,k)=1.0
      end if
```

Appendix G Rotor-Analyser Program Listing (continued)

```
if((trb_chrs.eq.'005').and.(k.eq.23.or.k.eq.24))then
up(1,k)=1.0
up(2,k)=-1.0
up(3,k)=-1.0
up(4,k)=1.0
up(5,k)=-1.0
up(6,k)=1.0
up(7,k)=-1.0
up(8,k)=1.0
end if

if(k.eq.25.and.(trb_chrs.eq.'001'.or.trb_chrs.eq.'005'))then
up(1,k)=-1.0
up(2,k)=1.0
up(3,k)=-1.0
up(4,k)=1.0
end if


if(up(j,k).eq.0.0)then
write(6,*)'Problem: Cannot determine upper or lower surfaces!'
stop
end if
write(6,*)'k=',k,' xr=',xr(k),
$ ' ymid=',ymid(j,k),' zmid=',zmid(j,k),
$ ' zchord=',zchord(j,k),' up=',up(j,k)
end do
write(6,*)
end do
```

Appendix G Rotor-Analyser Program Listing (continued)

```
c     5. Calculate the local Cp (non-dimensionalised by mtip/xr
c     Check max Cp (stagnation) and min Cp (peak suction)

      do k=1,kmax
      cpmax(k)=0.2
      cpmin(k)=-.2
      do j=1,jmax(k)
      do i=1,imax(j,k)
      cpc(i,j,k)=2.0*(p(i,j,k)-1.0/(gamma_air*mtip*mtip))
c     if reading in Cp (from surface.plt) instead of expected P (from .plt)
c     then all the is required is to equate the cp to p, rather than calc it
c     needed for trb_000v_18deg case, next should be commented out normally!
c     18deg cpc(i,j,k)=P(i,j,k) !for trb_000v_18deg using surf.plt file
      cpc(i,j,k)=cpc(i,j,k)*(1.0/xr(k))**2
c     mu_n(k)=xr(k)+mu*sin(psi) ! pressure -1/(gam*local-mach no)
c     cpc(i,j,k)=2.0*(p(i,j,k)-1.0/(gamma_air*mfwd*mfwd))
c     cpc(i,j,k)=cpc(i,j,k)*(mfwd/(mtip*mu_n(k)))**2
cx    write(6,*)'xr=',xr(k),' mu_n=',mu_n(k),' cpc=',cpc(i,j,k)
      if(cpc(i,j,k).lt.cpmin(k))then
      cpmin(k)=cpc(i,j,k)
      end if
      if(cpc(i,j,k).gt.cpmax(k))then
      cpmax(k)=cpc(i,j,k)
      end if
      end do
cx    write(6,*)
      end do
      write(6,*)'k=',k,' xr=',xr(k),
      $ ' cpmax=',cpmax(k),' cpmin=',cpmin(k)
      end do
      write(6,*)
```

Appendix G Rotor-Analyser Program Listing (continued)

```
c       6. Integrate the pressures over each block surface at each radial stn
c       upper=-(+1)*(-upwards suction)=+lift, lower=-(-1)*(+press)=+lift

        write(6,6060)
6060    format('Integrated local forces and moments about 1/4c axis:')
        k=0
        write(6,6061)k,xr_cutoff,0.0,0.0
        do k=1,kmax
        cz(k)=0.0 ! initialise total force and moment accumulator
        cy(k)=0.0
        cm(k)=0.0
        cn(k)=0.0
        cc(k)=0.0
        do j=1,jmax(k)
        cz_blk(j,k)=0.0 !initialise del-force and mom for each block
        cm_blk(j,k)=0.0
        do i=2,imax(j,k)
        cpc_av(i,j,k)=(cpc(i-1,j,k)+cpc(i,j,k))/2.
        y_av(i,j,k)=(y(i-1,j,k)+y(i,j,k))/2.
        z_av(i,j,k)=(z(i-1,j,k)+z(i,j,k))/2.
        del_y(i,j,k)=abs(y(i,j,k)-y(i-1,j,k)) !suppress blk dir
        del_z(i,j,k)=abs(z(i,j,k)-z(i-1,j,k)) !suppress blk dir
        cz_blk(j,k)=cz_blk(j,k)-up(j,k)*cpc_av(i,j,k)*del_y(i,j,k)
        cm_blk(j,k)=cm_blk(j,k)
        $ -up(j,k)*y_av(i,j,k)*cpc_av(i,j,k)*del_y(i,j,k)
        $ -z_av(i,j,k)*cpc_av(i,j,k)*del_z(i,j,k) !nose dwn
        end do
        cz(k)=cz(k)+cz_blk(j,k)
        cm(k)=cm(k)+cm_blk(j,k)
        end do
        cz(k)=cz(k)/cc0(k)
        cm(k)=cm(k)/(cc0(k)*cc0(k))
        write(6,6062)k,xr(k),cz(k),cm(k),theta_deg(k)
        end do
        write(6,6063)kmax+1,xr_tip,0.0,0.0

6061    format('k=',i2,' xr_cutoff=',f7.4' cz=',f8.4,' cm=',f8.4)
6062    format('k=',i2,' xr=',f7.4,' cz=',f8.4,' cm=',f8.4,' theta=',f7.3
        $ ' deg')
6063    format('k=',i2,' xr_tip=',f7.4' cz=',f8.4,' cm=',f8.4)
```

Appendix G Rotor-Analyser Program Listing (continued)

```
c       7. Radial integration for blade aerodynamic forces and moments

        write(6,*)
        write(6,6070)
6070    format('Radially Integrated forces and moments')

        delxr(1)=(xr(2)-xr_cutoff)/2.
        do k=2,kmax-1
        delxr(k)=(xr(k+1)-xr(k-1))/2.
        end do
        delxr(kmax)=(xr_tip-xr(kmax-1))/2.

        cts=0.0
        cqs=0.0
        cmb=0.0
        do k=1,kmax
        cts=cts+cc0(k)*cz(k)*delxr(k)*xr(k)*xr(k)
        cmb=cmb+cc0(k)*cc0(k)*cm(k)*delxr(k)*xr(k)*xr(k)
        write(6,6071)k,delxr(k),xr(k),cc0(k),cz(k),cts,cm(k),cmb
        end do
        ct=cts*solidity !convert to 'local' ct value for easy reference
        cq=cqs*solidity !convert to 'local' cq value for easy reference
        cmbar=cmb*3. !to get integrate mean Cm comparable with 2D aero

        write(6,*)
        write(6,6073)
6073    format('Total rotor coefficients')
        write(6,6072)ct,cts,cq,cqs,cmb,cmbar
        write(6,*)

6071    format('k=',i2,' delxr=',f7.4,' xr=',f7.4,' cc0=',f7.4,
        $' cz=',f7.4,' cts=',f7.4,' cm=',f7.4,' cmb=',f8.5)
6072    format('ct=',f7.5,' cts=',f6.4,' cq=',f8.6,' cqs=',f7.5,
        $ ' cmb=',f8.5,' cmbar=',f8.5)
```

Appendix G Rotor-Analyser Program Listing (continued)

```
c       8. Write results to file for subsequent plotting

c       8a. Write local sectional Cp to file

        do k=1,kmax
        ixr=int(1000.*xr(k)+.5)
        write(xr_chrs,1000)ixr
        open(unit=12,file=output_file1//xr_chrs//'_'//hov_chrs//out_extn)
        write(12,1201)
        do j=1,jmax(k)
        write(12,1202)xr(k),k,j,up(j,k)
        do i=2,imax(j,k) !edit to ouput '_av' values 2-imax (as req'd)
        write(12,1203)(0.25-y_av(i,j,k)),cpc_av(i,j,k) !changed to actCp
        end do
        write(12,*) !blank line avoids gnuplot fly-back
        end do
        write(12,*)
        close(unit=12)
        end do

1000    format(i3)
1201    format('# 0.25-y cpc')
1202    format('# xr=',f7.4,' k=',i2,' j=',i2,' up=',f4.1)
1203    format(2f12.6)


c       8b. Write integrated blade force and moment coefficients to file

        open(unit=14,file=output_file2//hov_chrs//out_extn)

        write(14,1401) !write headings
        write(14,1402)xr_cutoff,theta_deg(1),0.0,0.0,0.0,0.0,0.0,
        $ 0.0,0.0,0.0,0.0,0.0
        do k=1,kmax
        z_load(k)=cz(k)*cc0(k)*xr(k)*xr(k) !thrust z-dir
        y_load(k)=cy(k)*cc0(k)*xr(k)*xr(k) !torque y-dir
        m_load(k)=cm(k)*cc0(k)*cc0(k)*xr(k)*xr(k) !moment
        n_load(k)=cn(k)*cc0(k)*xr(k)*xr(k) !normal force
        c_load(k)=cc(k)*cc0(k)*xr(k)*xr(k) !chordwise force
        write(14,1402)xr(k),theta_deg(k),cz(k),cy(k),cm(k),cn(k),cc(k),
        $ z_load(k),y_load(k),m_load(k),n_load(k),c_load(k)
        end do
        write(14,1402)xr_tip,theta_deg(kmax),0.0,0.0,0.0,0.0,0.0,
        $ 0.0,0.0,0.0,0.0,0.0
1401    format('# xr theta cz cy cm cn ca',
        $ ' z_load y_load m_load n_load c_load ')
1402    format(2f10.4,5f10.4,5f10.4)

        close(unit=14)
```

Appendix G Rotor-Analyser Program Listing (continued)

```
c       8c. Write integrated blade force and moment coefficients to file

        open(unit=16,file=output_file3//hov_chrs//out_extn)


        write(16,1601)
        write(16,1602)ct,cts,cq,cqs,cmb,cmbar

1601    format(' ct cts cq cqs cmb cmbar')
1602    format(f10.5,f10.4,f10.6,f10.5,f10.5,f10.5)

        close(unit=16)

        stop

        end program rotor_analyser
```